useful models

JOURNAL OF GEOPHYSICAL RESEARCH, VOL. 87, NO. B10, PAGES 8491–8500, OCTOBER 10, 1982

Constraints on the Structure of the East Pacific Rise From Gravity

BRIAN T. R. LEWIS

School of Oceanography and Geophysics Program, University of Washington, Seattle, Washington 98195

Gravity data across the East Pacific Rise at 9°N and 12°N (the ROSE area) are characterized by a high of 12–20 mGal with a width of about 20 km. It is shown that this axial gravity high is not adequately explained by uncompensated constant density topography or an isostatically compensated thermally expanded ridge crest. It can be adequately explained by Airy compensation with a depth of compensation of at least 20 km or by elastic plate compensation with a flexural rigidity between 10^{18} and 10^{20} N m. The significance of the depth and flexural rigidity parameters is that in both cases they result in a gravity field from the compensation whose amplitude is below the data resolution for wavelengths less than about 50 km. That is, the gravity data do not require compensation of the rise axis for wavelengths less than about 50 km. This suggests that these wavelengths are either supported mechanically or by other forces (dynamic). The mechanical interpretation is not consistent with partial melt under the axis, indicating that dynamic forces may be important in supporting the rise axis. The same conclusion is arrived at from the thermal model. The thermal model can be made to fit the gravity data if we allow departures from isostasy and the addition of a dike-like body about 2 km wide in the crust having a positive density contrast of about 0.25 Mg m^{-3}. This geometry is consistent with a seismically determined low velocity zone in the crust in the ROSE area. In this model the nonhydrostatic pressures must be supported dynamically. A general conclusion of this study (for the portions of the East Pacific Rise studied here) is that the axial topography is not buoyantly supported by low density material in the crust. Therefore, either the crust under the rise axis mechanically supports the axial topography or a mass excess at the thermally expanded rise axis is supported by other forces, such as plate driving forces. The latter option is favored on the basis of heat flux and seismic data.

INTRODUCTION

The principal motivation for this study was to investigate if low velocities found under the axis of the East Pacific Rise, which are thought to represent partially molten rock, are associated with a gravity anomaly. Evidence for these low velocities has been found by *Orcutt et al.* [1976] at 9°N and by *Lewis and Garmany* [this issue] at 12°N, the ROSE area. The thermodynamics under a rise axis have been considered theoretically by *Lachenbruch* [1973, 1976], *Sleep* [1975], *Lister* [1977], and others with results that are consistent with evidence from submersible studies for hot rock under the rise axis.

The principal difficulty in interpreting gravity data across the rise axis involves the mechanism of isostatic compensation and the question of whether the axis is in fact in isostatic equilibrium. Nonisostatic or deviatoric stresses should not be ruled out by the a priori assumption of isostasy since the rise axis is the focus of plate driving forces [*Lachenbruch*, 1973; *Lewis*, 1981]. Previous interpretations of East Pacific Rise gravity profiles have generally used the elastic plate model to interpret the gravity data [*Cochran*, 1979; *McNutt*, 1980]. It is rather surprising that the elastic plate model fits the data as well as it does on the East Pacific Rise, considering that partial melt in the crust should produce very low mechanical strength. One might expect the thermal model, which predicts the topography very well [*Davis and Lister*, 1974] to predict also the rise axis gravity accurately. However, gravity calculations based on thermal models [*Pearson and Lister*, 1979; *Lewis*, 1981] do not in fact predict as large a gravity anomaly as observed.

On the basis of these results there appears to be a dilemma. On the one hand, the thermal model, which invokes thermally caused density changes to predict accurately the seafloor topography, does not fit the gravity data very well. On the other hand, the elastic plate model, which treats the rise axis region as a region of high mechanical strength (where we in fact expect low strength), predicts the observed gravity reasonably well.

I shall attempt to show that if we allow deviations from isostasy at the rise axis (which may be supported dynamically), the thermal model can be reconciled with gravity and other geophysical data. To do this one would like to use objective inversion methods, such as the ideal body theory of *Parker* [1975], but I have not done this because I am doubtful that they would provide useful results in this particular case. This is because one would be lumping density variations caused by topography, thermal effects, elastic plate effects, and possible rise axis inhomogeneities into one pot and trying to invert for one unique density distribution.

My approach in this paper is to examine several propositions and judge the merit of each on how well it satisfies the gravity data and is compatible with other geophysical data. The following propositions are tested with respect to the rise axis: (1) that the gravity is caused by uncompensated constant density topography, (2) that the gravity is caused by topography compensated by the Airy model, (3) that the gravity is caused by topography resting on an elastic plate, and (4) that the gravity is explainable by an isostatic thermal model. These propositions are graphically displayed in Figure 1.

DATA

Three lines crossing the East Pacific Rise are presented, and they are believed to be representative of accreting boundaries with half spreading rates of about 5 cm/year. Two of the lines are from the Siqueiros area and were

Paper number 1B1839.
0148-0227/82/001B-1839$05.00

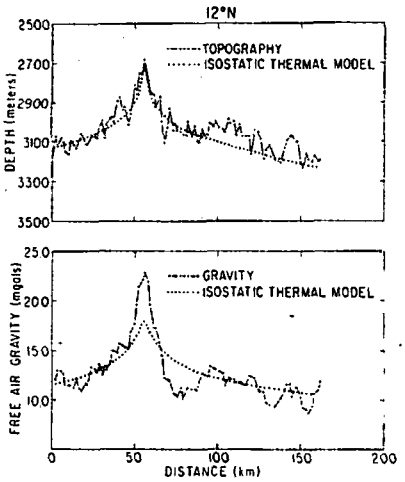

Fig. 11. Comparison of the 12°N data with topography and gravity computed from the isostatic thermal model (see text for parameters used).

Discussion

Four different methods for interpreting the rise axis gravity have been used, and some general inferences emerge.

1. The gravity data preclude the existence of low density material at crustal depths under the axis. If low density material were present to compensate the topography, the rise axis gravity anomaly would be significantly smaller. This result is clearly indicated by all four interpretation methods. In the thermal model the compensation is distributed over depth from very shallow depths (seafloor) to the base of the lithosphere, and yet this model also underestimates the axial anomaly.

2. There is a general pattern to the results obtained from the inversion method, the Airy model, and the elastic plate model. In all three cases the data indicate that the amplitude of the gravity field from the rise axis compensation is unresolvable for wavelengths less than about 50 km. This is most easily seen from the Airy model. Consider a gravity field due to topography at a depth of 3 km and compensation at 20 km. The ratio of these two fields will be $w = \exp(-2\pi 20/\lambda)/\exp(-2\pi 3/\lambda)$. Since the topographic field is about 10 mGal and the data resolution is about 1.5 mGal, we can find a value of λ for which $w = 0.15$. Below this wavelength the compensation gravity field will not be resolvable. This occurs for $\lambda = 50$ km. Therefore, the data are interpreted to imply that for wavelengths less than 50 km the rise axis is either uncompensated or the compensation is smoothed by a mechanical filter or it is too deep to be resolved. The merit of each of these alternatives is discussed next.

There are two principal arguments against the elastic model. First, the model predicts a thickening of the crust toward the rise axis because of the deflection of the crust mantle boundary. The reflection data of *Herron et al.* [1980] in the Siqueiros area clearly show that this is not occurring. Second, the refraction data of *Orcutt et al.* [1976] and *Lewis and Garmany* [this issue] indicate low velocities under the rise axis that can be interpreted as being caused by partial melt in the crust. If there is indeed partial melt under the axis, the mechanical strength must be very low, and therefore it is unlikely that the elastic plate model is applicable. In fact, it would be more appropriate to treat the axial region as a viscous fluid. For significant amounts of partial melt, the effective viscosity may be as low as several hundred poise [*Kushiro et al.*, 1976], in which case the rise axis should disappear rapidly in the absence of other sustaining forces.

Similar arguments can be made against the Airy model

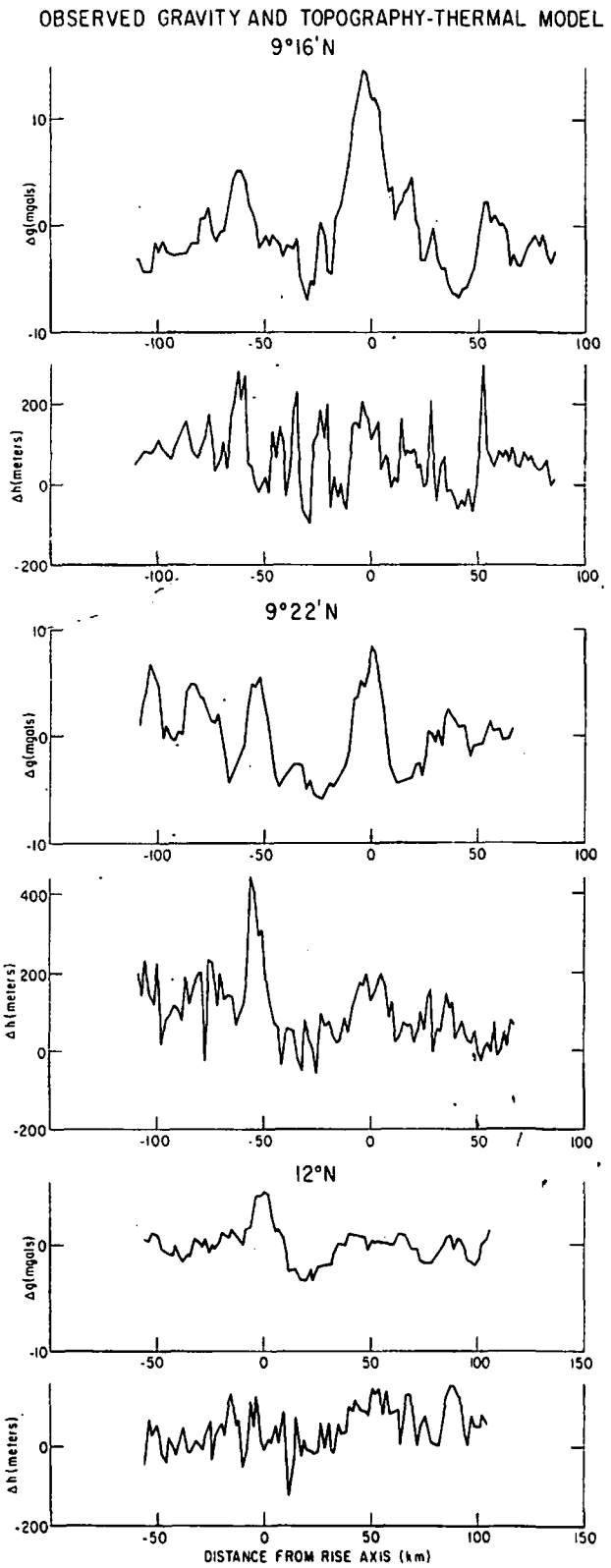

Fig. 12. Gravity and topographic residuals obtained by subtracting the thermal model in Figure 11 from the data.

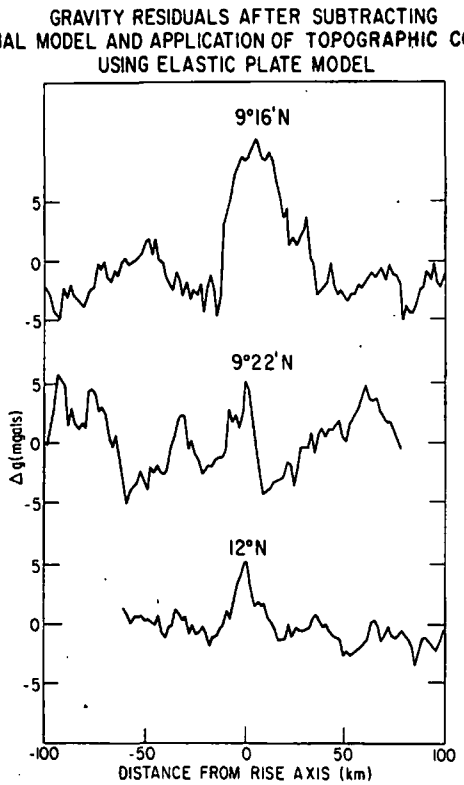

Fig. 13. Gravity anomalies obtained by applying a topographic correction to the residuals in Figure 12. The elastic plate model with $D = 10^{18}$ N m was used to compute the topographic corrections.

with a depth of compensation of at least 20 km. Although it is conceivable that the axial topography is supported buoyantly by low density at 20 km depth, the material between the seafloor and the compensation would be in a state of tensional stress as a result of the forces caused by the topography and the compensation. If the material had no strength, it would flow outward so as to remove the topographic anomaly. If it had finite mechanical strength, then the assumptions of the model would be violated and we should use the mechanical model. Therefore, if low mechanical strength does exist under the rise axis, the rise axis would disappear unless other dynamic forces kept it in existence. An additional argument against the Airy model is that it precludes the existence of thermally induced density changes above 20 km, which are thought to cause the axial topography and the observed heat flux. This is a major deficiency in both the elastic plate and the Airy models.

Since neither the elastic plate nor the Airy models provide a satisfactory physical explanation of the rise axis, we are led to infer that the rise axis may not be in isostatic equilibrium and therefore that it is supported by other forces, most likely dynamic.

A similar conclusion is reached from considering the thermal model. The thermal model, which accurately predicts the topography and heat flow versus age, does not accurately predict the gravity. To gain some insight into the modifications of the thermal model that are required to make it fit the gravity data some further numerical modeling has been performed.

In the 12°N area I have used the constraints of the refraction data on the size of the axial low velocity zone to see if a density anomaly corresponding to the low velocity zone can reasonably fit the gravity residuals shown in Figure 13. A dike model has been used to represent the intrusion zone by using equations from *Hammer* [1974]. The dimensions of the dike were selected to be consistent with the refraction model of *Lewis and Garmany* [this issue], that is, 2 km wide and 4 km high with a depth below sea level to the top of 4 km. A positive density contrast of 0.25 Mg m^{-3} was found to fit the gravity residuals (that is, the topographically corrected difference between the observed gravity and the thermal model). A comparison of the data and the model results is shown in Figure 14. This model would fit the 9°22'N data, but a larger mass anomaly is needed for the 9°16'W data.

The size of this uncompensated mass anomaly depends to some extent on the degree of partial melting in the mantle under the axis (i.e., on the density of the upper mantle). Lower upper mantle densities will require a larger mass anomaly in the crust. Figure 15 shows a model with up to 15% partial melt in the mantle and a crustal magma chamber having low density partially molten crustal material. The effect on the gravity is to reduce greatly the amplitude of the axial high. This model is in isostatic equilibrium.

Figure 16 shows a model with partial melt in the mantle and the intrusion of this upper mantle material into the crust. This model clearly fits the gravity data better and is consistent with the analysis using the other models. This model is not in isostatic equilibrium.

In both of these thermal models the diffusivity in the crust and mantle was adjusted until an optimum fit to the topography and gravity was obtained, the other parameters being the same as for the thermal model in Figure 11. For the model in Figure 15 this was the best fit to the gravity that could be obtained with the assumptions given above.

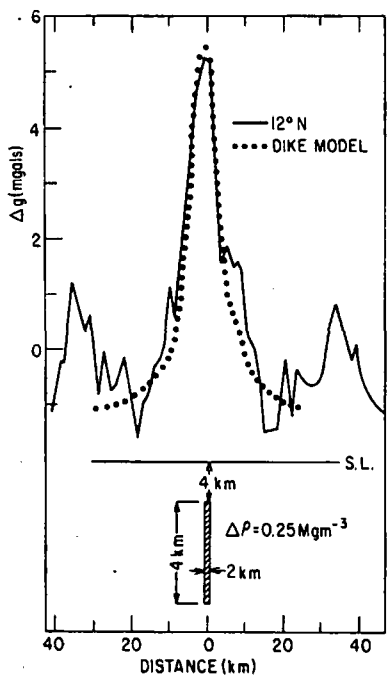

Fig. 14. Comparison of the gravity anomaly in Figure 13 for 12°N with the gravity field from a dike in the crust having the dimensions shown in the figure.

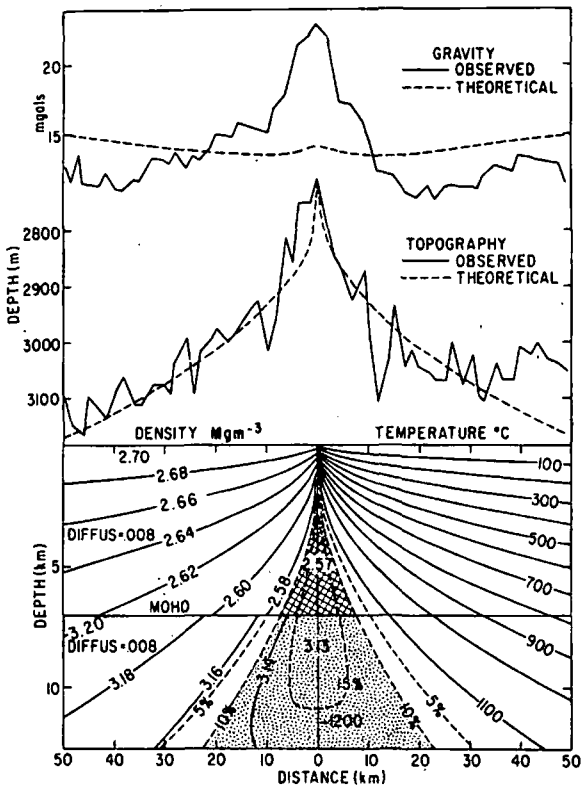

Fig. 15. Comparison of the 12°N data with an isostatic thermal model having partial melt in the crust and upper mantle. In the crust the partial melt is assumed to be of crustal compositoin (see *Lewis* [1981] for details on the method of calculating the amount of partial melt). The diffusivity is in units of 10^4 m^2 s^{-1}.

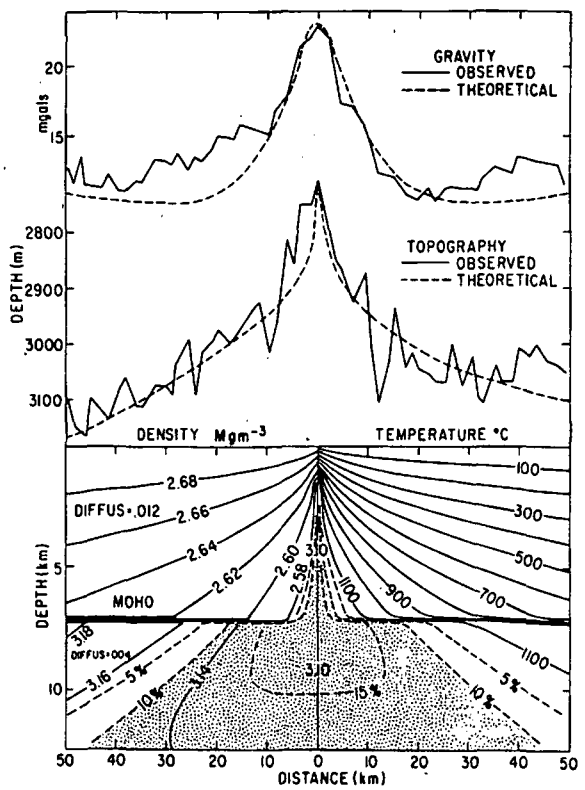

Fig. 16. Comparison of the 12°N data with a thermal model having partial melt in the mantle and the intrusion of this melt into the crust. Note that in this thermal model a high density body is required in the crust to fit the gravity data. The diffusivity is in units of 10^4 m^2 s^{-1}.

CONCLUSIONS

Three principal conclusions are arrived at from this study:

1. The gravity data on the segments of East Pacific Rise analyzed here do not allow the existence of low density material at crustal depths that would isostatically compensate the rise axis topography.

2. A consequence of the first conclusion is that the stresses due to the topographic load of the rise axis must be supported in the crust either by mechanical strength or by other forces (such as dynamic forces caused by plates moving apart) [*Lachenbruch*, 1973]. Although the elastic plate model can be made to fit the gravity data adequately, it is unlikely that this is the correct explanation because it is inconsistent with the inference of partial melt, and therefore low strength, under the axis, and with the seismic reflection data. This leads us to infer that other forces are supporting the axial load.

3. Analysis of the gravity and topography using the thermal model suggests that the excess mass at the rise axis may not be in the topography itself but in a subsurface mass associated with the axial intrusion zone. This conclusion is based on the fact that this model predicts the topography adequately but does not fit the gravity, requiring not a topographic anomaly but a subsurface axial mass excess. It was found that a dike-shaped body in the crust with a width of 2 km and a density contrast of 0.25 Mg m^{-3} is one possibility that is consistent with seismic constraints. This model is not in isostatic equilibrium, implying that other forces (probably dynamic) are supporting the nonhydrostatic pressures at the crust mantle boundary.

Acknowledgments. I am indebted to the Office of Naval Research for financial support of this work, under contract N-00014-80-C-0252. The IPOD data bank kindly provided the Conrad gravity data, and special thanks are due to A. Fudge for his diligence in the collection and reduction of the *Thompson* gravity data. I am also extremely grateful for constructive and helpful suggestions from anonymous JGR reviewers, suggestions that aided in focusing and clarifying the manuscript. Contribution 1231 of the School of Oceanography, University of Washington, Seattle, Washington.

REFERENCES

Banks, R. J., R. L. Parker, and S. P. Huestis, Isostatic compensation on a continental scale, local versus regional mechanisms, *Geophys. J. R. Astron. Soc., 51*, 431–452, 1977.

Cochran, J. R., Analysis of isostasy in the world ocean, 2, Mid-ocean ridge crests, *J. Geophys. Res., 84*, 4713–4729, 1979.

Davis, E. E., and C. R. B. Lister, Fundamentals of ridge crest topography, *Earth Planet. Sci. Lett., 21*, 405–413, 1974.

Hammer, S., Approximation in gravity interpretation calculations, *Geophysics, 39*, 205–222, 1974.

Herron, T. J., P. L. Stoffa, and P. Buhl, Magma chambers and mantle reflections—East Pacific Rise, *Geophys. Res. Lett., 7*, 989–992, 1980.

Kushiro, I., H. S. Yoder, and B. O. Mysen, Viscosities of basalt and andesite melts at high pressures, *J. Geophys. Res., 81*, 6351–6356, 1976.

Lachenbruch, A. H., A simple mechanical model for oceanic spreading centers, *J. Geophys. Res., 78*, 3395–3417, 1973.

Lachenbruch, A. H., Dynamics of a passive spreading center, *J. Geophys. Res., 81*, 1883–1902, 1976.

Lewis, B. T. R., Isostasy, magma chambers and plate driving forces on the East Pacific Rise, *J. Geophys. Res., 86*, 4868–4880, 1981.

Lewis, B. T. R., and J. D. Garmany, Constraints on the structure of the East Pacific Rise from refraction data, *J. Geophys. Res.*, this issue.

Lister, C. R. B., Estimates of heat flow and deep rock properties based on boundary layer theory, *Tectonophysics, 41*, 141–157, 1977.

Ludwig, W. J., and P. D. Rabinowitz, Geophysical measurements across the East Pacific Rise in the vicinity of the Siqueiros fracture zone (survey area pt-4), *Initial Rep. Deep Sea Drill. Proj., 54*, 37–42, 1980.

McKenzie, D. P., and C. Bowin, The relationships between bathymetry and gravity in the Atlantic Ocean, *J. Geophys. Res., 81*, 1903–1915, 1976.

McNutt, M., Compensation of oceanic topography, an application of the response function technique to the Surveyor area, *J. Geophys. Res., 84*, 7589–7598, 1979.

Oldenburg, D. W., The inversion and interpretation of gravity anomalies, *Geophysics, 39*, 526–536, 1974.

Orcutt, J. A., B. L. N. Kennett, and L. M. Dorman, Structure of the East Pacific Rise from an ocean bottom seismometer survey, *Geophys. J. R. Astron. Soc., 45*, 305–320, 1976.

Parker, R. L., The rapid calculation of potential anomalies, *Geophys. J. R. Astron. Soc., 31*, 447–455, 1972.

Parker, R. L., Theory of ideal bodies for gravity interpretation, *Geophys. J. R. Astron. Soc., 42*, 315–334, 1975.

Pearson, W. C., and C. R. B. Lister, The gravity signatures of isostatic thermally expanded ridge crests, *Phys. Earth Planet. Inter., 19*, 73–84, 1979.

Sleep, N. H., Formation of oceanic crust: Some thermal constraints, *J. Geophys. Res., 80*, 4037–4042, 1975.

(Received April 20, 1981;
revised October 22, 1981;
accepted December 4, 1981.)

JOURNAL OF GEOPHYSICAL RESEARCH, VOL. 87, NO. B10, PAGES 8417–8425, OCTOBER 10, 1982

Constraints on the Structure of the East Pacific Rise From Seismic Refraction Data

B. T. R. LEWIS AND J. D. GARMANY

University of Washington, Department of Oceanography and Geophysics Program Seattle, Washington 98195

University of Washington seismic data taken during ROSE phase 1 have been used to study the structure of the East Pacific Rise in the vicinity of 12°N. Off axis but within 50 km of the axis we find that the oceanic crust can be modeled with a rapid change in velocity in the top 2.5 km, a zone of low but uniform velocity gradient from 2.5 to about 5.5 km and a transitional zone about 1 km thick to mantle material. There is also evidence for substantial anisotropy in mantle velocity gradients, with a positive velocity gradient in the spreading direction and a negative velocity gradient parallel to the rise. Under the rise axis the data allow at most a very narrow zone of low velocity (less than about 2 km wide) in the crust.

INTRODUCTION

The ROSE experiment was a multi-institutional seismic experiment conducted in early 1979 to investigate the structure of the East Pacific Rise and its intersection with a fracture zone. An overview of the experiment has been given by *Ewing and Meyer* [this issue]. A unique aspect of this experiment was the data archiving system, and this is described by *LaTraille et al.* [this issue]. An analysis of the seismicity recorded on the Orozco fracture zone during phase 2 was reported by *Project ROSE Scientists* [1981].

This study deals with the active phase of the experiment, phase 1, and, in particular, the data subset pertaining to the rise axis structure. The specific goals in this analysis are (1) a determination of the presence or absence of crustal partial melt under the axis as revealed by low velocities, (2) an estimation of the size of the partial melt zone, if present, and (3) the velocity structure of the crust adjacent to the axial zone.

Fairly extensive and detailed studies with similar objectives have been undertaken previously by Scripps researchers in the Siqueiros area to the south and by the University of Washington [*Lewis and Snydsman*, 1979] in an area to the north of the ROSE phase 1 area. In the Siqueiros area, *Orcutt et al.* [1975] obtained evidence of a crustal low-velocity zone (LVZ) under the axis from refraction lines along the axis. Subsequently, *Herron et al.* [1980] used multichannel seismic reflection data to show that acoustic Moho could be traced to within a few kilometers of the axis.

Although the refraction experiments have been helpful in suggesting LVZ's in the crust under the axis, the data have been taken along the strike of the rise axis on the axis and have been interpreted in terms of flat lying homogeneous layers. At the rise axis this can be a serious oversimplification. In particular, if the width of the LVZ is less than the crustal thickness (say 2 or 3 km compared to 6 or 7 km), lateral refraction must be important since the horizontal velocity gradients may be at least as great as the vertical gradients. Neglecting this can lead to incorrect velocity models which have serious implications for petrologic models.

Paper number 2B0311.
0148-0227/82/002B-0311$05.00

To circumvent the lateral refraction problem and reduce the problem from a three-dimensional to a two-dimensional refraction analysis, we have restricted our interpretation of the rise axis structure to shot lines across the axis. This allows us to infer an axial LVZ from delayed first arrival travel times without reverting to the interpretation of data in terms of a detailed velocity depth function and its attendant assumptions. To obtain a reference for the axial delay times, we have used the off-axis structure obtained from shot lines within 50 km of the axis.

THE DATA

In this study we have restricted our analysis to shots in the vicinity of the rise axis and to data recorded by University of Washington ocean bottom seismometers (OBS's) [*Lister and Lewis*, 1976]. For this experiment the OBS's were used with metal tripod anchors rather than the concrete flower pots because they were to be emplaced, in general, on a hard rock bottom.

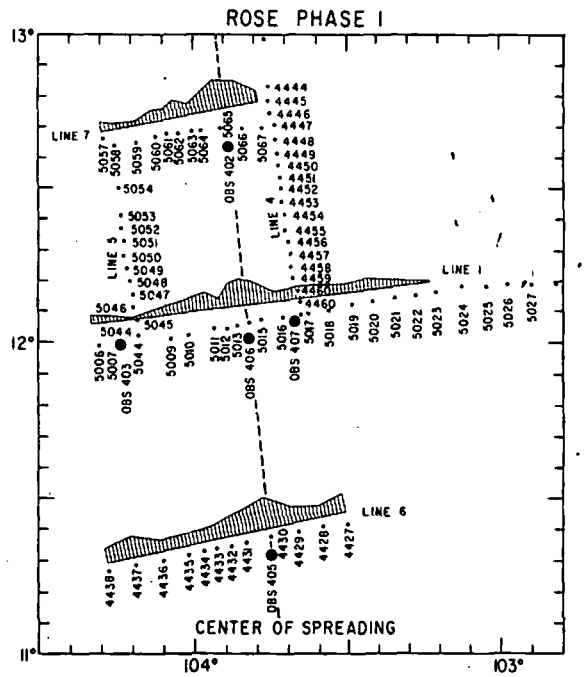

Fig. 1. Locations of shot lines and receivers used in this study. The numbered shots refer to large shots.

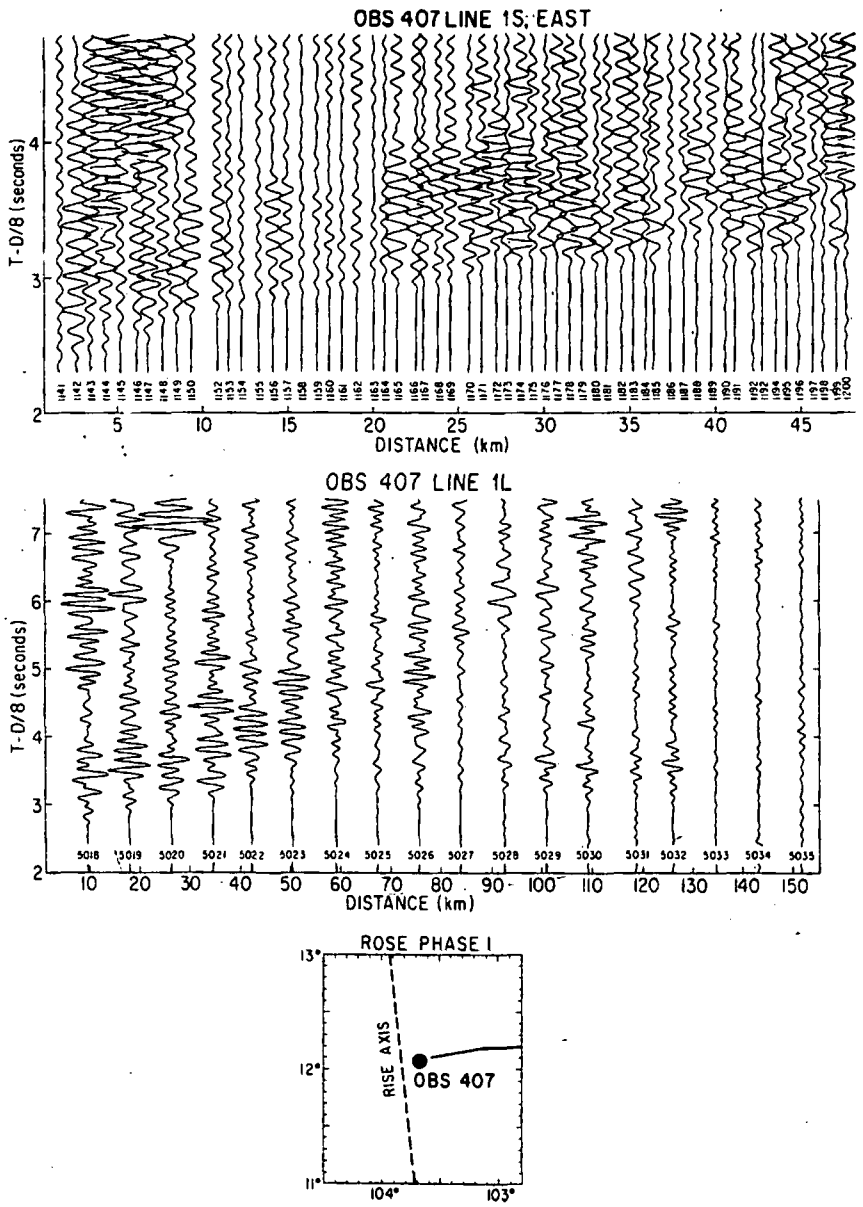

Fig. 2. Record section of large and small shot data along line 1 to OBS 407.

Because the interpretation of the axial structure is critically dependent on the quality and distribution of the seismic data, we emphasize in this paper the presentation of the data in record section form. The data have been uniformly treated in terms of display. All data (except where noted) have been corrected for shot size variations and distance according to $(W/W_0)^{2/3} \cdot (R/R_0)^{1.5}$, where W_0 and R_0 are a reference weight and distance, and W is the actual charge weight at distance R. The square root signal compression used during the analog recording has been corrected by bipolar squaring so that the amplitude relationships displayed are linear within the accuracy of the recording process, about 25%.

For the lines of large shots, distances from shot to receiver were computed from the published shot locations to OBS positions that were relocated using water wave travel times from the shots. For the lines of small shots the water wave travel times alone were used to compute distances because of the poor navigation on these shot lines.

The locations of the large shots and the receivers used in this study are shown in Figure 1. The small shots used were along lines 1, 4, and 5.

Except where noted, corrections have been applied to the travel times for topographic variations. These were made as small as possible by applying a correction which produced a constant thickness ocean of 3 km above the shots at a phase velocity of 7 km/s.

RESULTS

Off-Axis Structure

The seismic data from the series of small shots on lines 1, 4, and 5 were used to constrain the off-axis velocity structure. The linear programing method of *Garmany* [this issue] was used to derive bounds on structure and to supply candidate models for use in synthetic seismogram modeling. From the set of optimal feasible solutions which maximized or minimized the depth to several material slownesses, a few

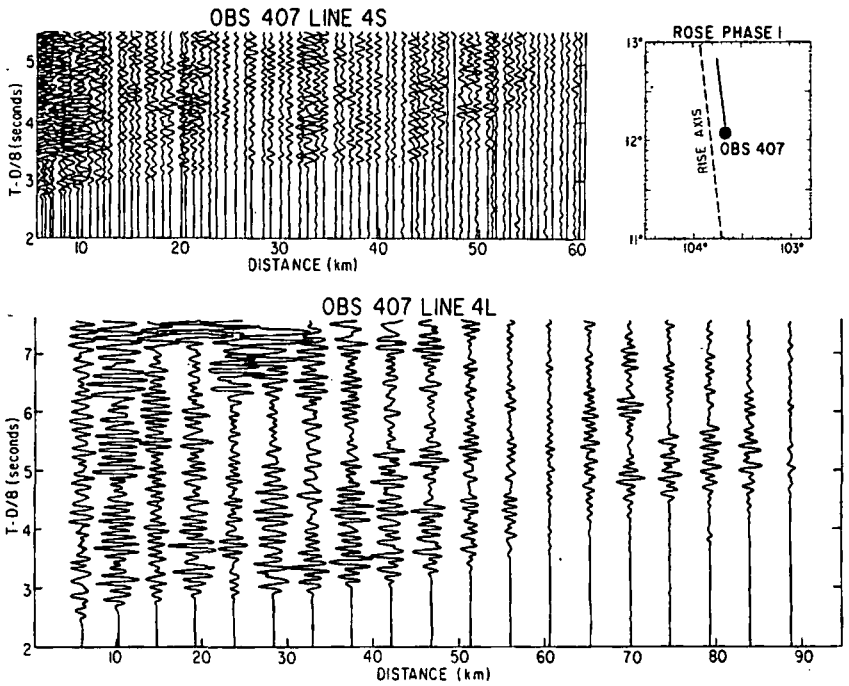

Fig. 3. Record section of large and small shot data along line 4 to OBS 407.

models were chosen which best fit the observed travel times as a function of distance. These models were used in a WKBJ synthetic seismogram program [*Chapman*, 1978], and the resulting synthetic record sections were compared with the observed data. The qualitative comparisons were used to suggest additional constraints on the kinematic variables delay time, distance, and the derivative of distance with respect to slowness (dX/dp). The linear programing routine would then be run with the added constraints and, the entire procedure was repeated until the qualitative fit could not be improved.

Only the data from the 10.9 kg (24 pounds) shots were used to minimize difficulties in measuring amplitudes and comparing waveforms. The peak-to-peak excursions from the first dilational to the second compressional peaks were used as the amplitudes. This convention was adopted because the first compressional peak is not well observed in these data beyond about 20 km. In regions of strong interference (caustics) a different method of estimating amplitudes was needed [*Garmany*, this issue]. These measurements were not so direct and were used sparingly.

Before discussing the final models, we will consider the major similarities and differences in the three record sections of the data (Figures 2–4). All three lines show a strong Moho

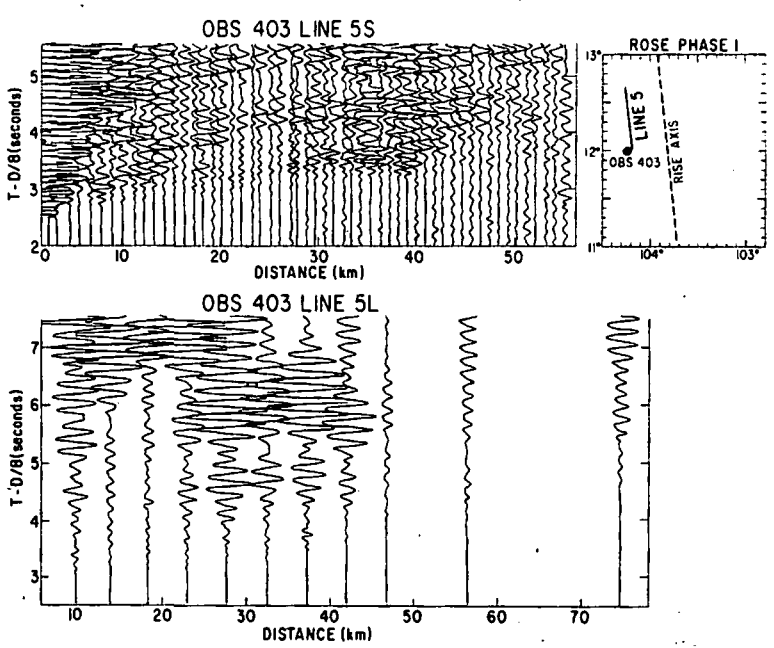

Fig. 4. Record section of large and small shot data along line 5 to OBS 403.

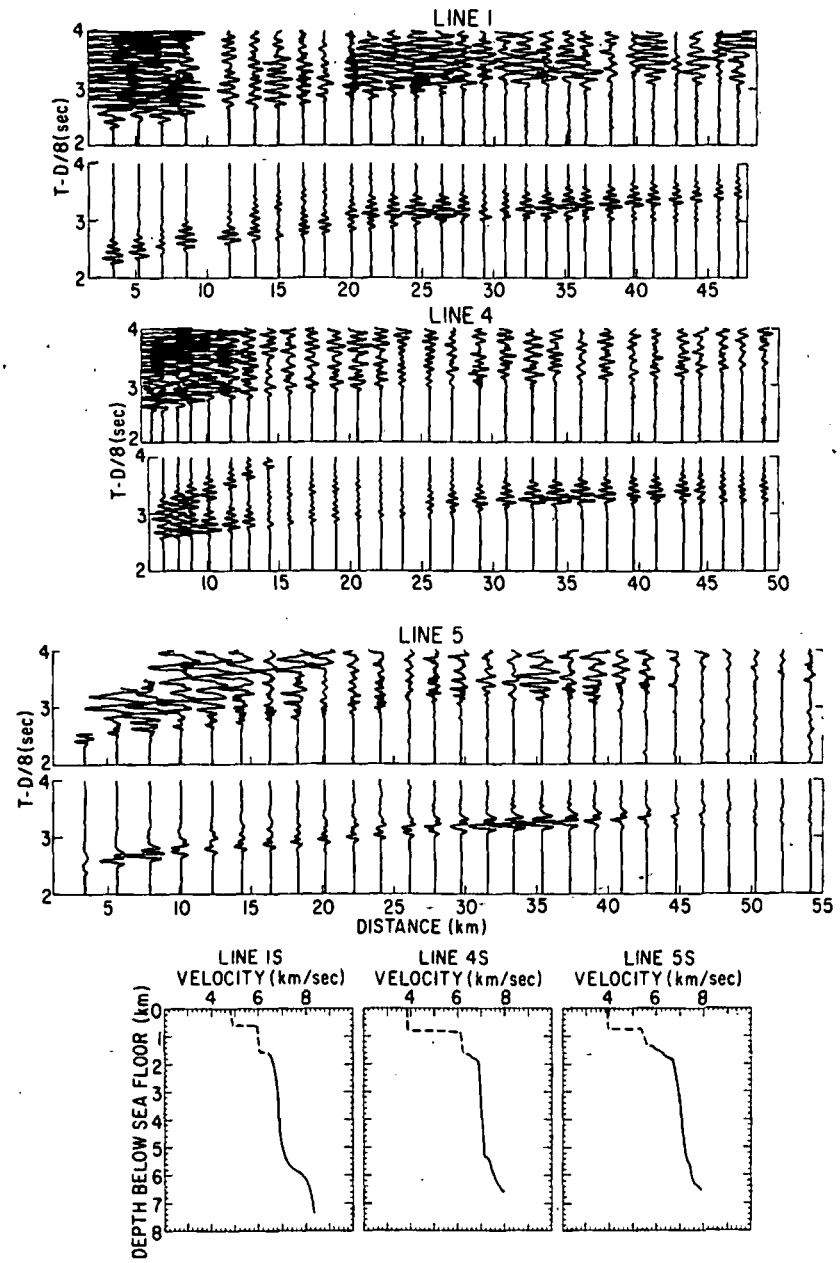

Fig. 5. Comparison of data on lines 1, 4, and 5 with synthetic seismograms computed with the WKBJ method and the corresponding models. The dashed lines in the models indicate where constraints are poor. The data have been corrected for distance by a factor (R/R_0). Topography is essentially flat, and travel times have been adjusted to a water depth of 3 km using a phase velocity of 7 km/s.

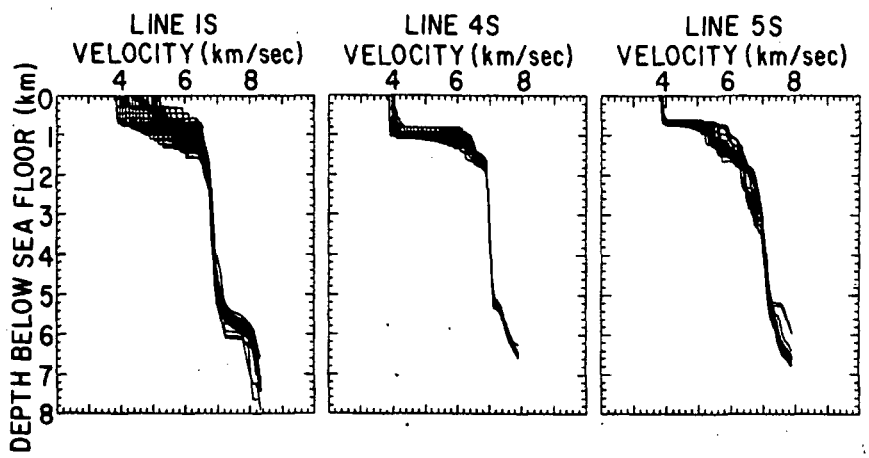

Fig. 6. All feasible solutions for each line based on amplitude data. Only a restricted subset of these adequately satisfy the travel time data, one of which is shown in Figure 5 for each line.

reflected (*PmP*) branch. The lines parallel to the strike (lines 4 and 5) have a near *PmP* caustic close to 27 km distance, while in the direction of spreading this caustic occurs at about 20 km distance. This difference is due to the greater mantle velocity in the direction of spreading. The total extent of these reflected branches is limited, the farthest observed *PmP* arrivals being at approximately 45 km distance. This is seen in the long-range large shot data, as well. Such behavior is consistent with a gradual transition at the Moho. A *Pn* branch on lines 4 and 5 is not observed, while this phase is quite visible on line 1. This implies that the velocity gradient below the Moho transition is probably negative for refracted waves along the strike of the rise and is definitely positive orthogonal to this direction. We feel that this is due to an increase in anisotropy with depth, as suggested by *Garmany* [1981] to account for similar observations in other young oceanic provinces. All the lines show layer 3 refractions of similar velocity. At about 10 km, all three lines show a region of higher amplitude which is associated with the layer 2–layer 3 transition.

The final results of this iterative process are shown in Figure 5. The dashed lines at the shallowest levels in the velocity models indicate the output of the linear programing routine that is poorly constrained and are not intended to represent earth structure. There is insufficient data at short distances to constrain this part of the structure. In addition, sharp corners in other parts of the structures must not be regarded as resolved details. These represent points where the linear programing routine has run up against a hard constraint and has wrapped around it. The source function used for the synthetics on lines 1 and 4 was an exponentially damped cosine curve of four cycles duration (0.4 s). Line 5 was received by another instrument and has rather different recording characteristics. An undamped wavelet of 1 cycle duration (0.12 s) was convolved with the broadband synthetics for this line.

Given the uncertainties in amplitudes caused by only approximate removal of the nonlinear signal compression, the variability of the explosive sources, and the distortion associated with coupling to the seafloor [*Sutton et al.*, 1981], we feel that the synthetic seismogram modeling has been quite successful. Special emphasis was placed on modeling the relatively weak *PmP* arrivals on line 4 between 30 and 50 km distance. This constraint and the limit on the distance to the observed far *PmP* caustic required an increase in veloc-

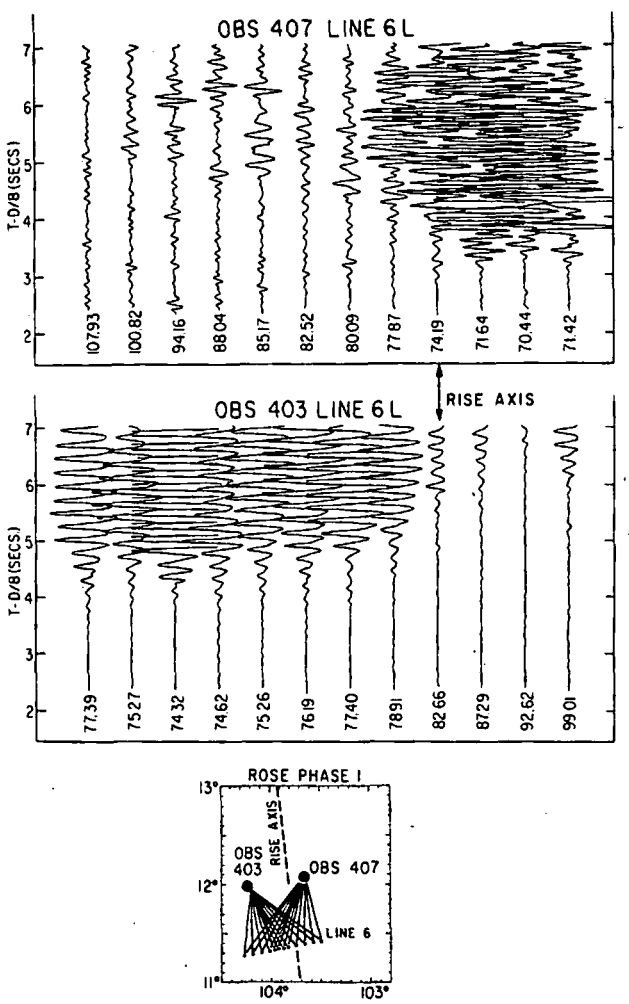

Fig. 7. Fan line 6 to OBS's 407 and 403. The data are plotted equally spaced, and distances from shot to receiver are shown below each seismogram.

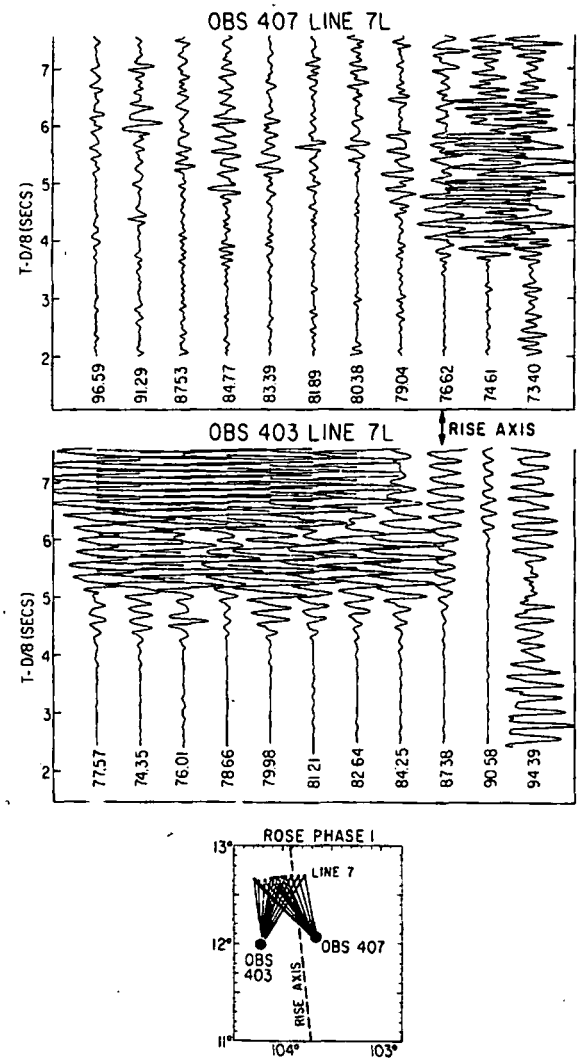

Fig. 8. Fan line 7 to OBS's 407 and 403. The data are plotted equally spaced, and distances from shot to receiver are shown below each seismogram.

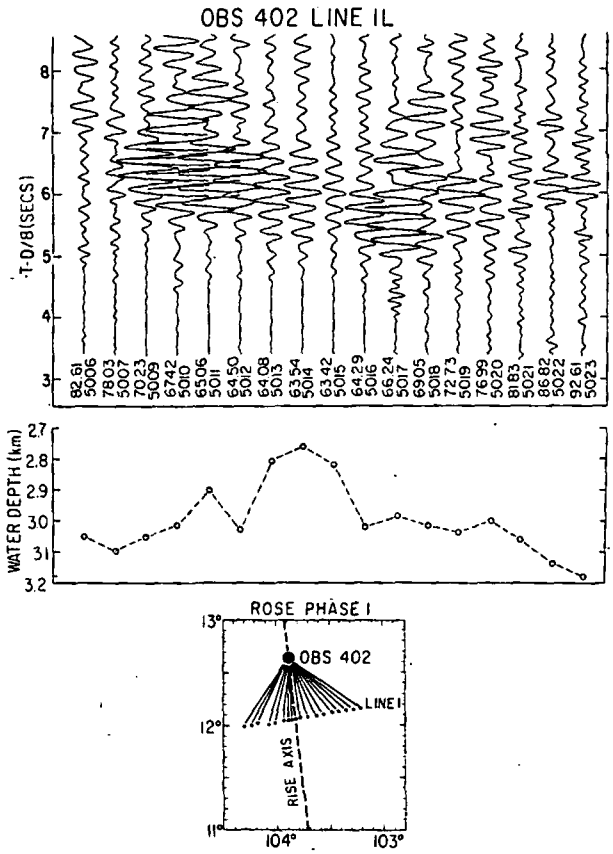

Fig. 9. Fan line 1 to OBS 402, which was on the rise axis.

ity gradient in the lower crust. On line 5 the extremely close limit on the distance of the far *PmP* caustic (about 40 km) required a similar gradient. The *Pn* arrivals in the synthetics on lines 4 and 5 correspond to zero velocity gradient in the mantle and are clearly too strong. This argues for a probable negative velocity gradient below the Moho transition. All three lines exhibited amplitude increases near 10 km distance which were modeled by a rapid layer 2–layer 3 transition followed by a gradual decrease in velocity gradient over a depth range of several hundred meters. Line 1 also shows a region of high amplitude at 15 km distance, suggesting a possible triplication with a caustic at that distance. The linear programing inversion was not constrained to yield such a triplication, but the models which best fit the $T(X)$ data included one. Layer 3 for all three lines was found to be nearly homogeneous, and there is no significant difference in layer 3 velocities between any of the models. The Moho transition for line 1 appears to be sharper than for the other two lines, and the stronger *Pn* requires a positive velocity gradient below the transition region. The differences in *Pn* velocities are also significant and are consistent with previously observed *Pn* anisotropy [*Bibee and Shor*, 1976; *Lewis and Snydsman*, 1979]. Velocities are 7.8–8.0 km/s along the strike of the rise and 8.2–8.3 km/s in the direction of spreading.

All the feasible solutions which maximized or minimized the depths to 25 evenly spaced slownesses (50 models in all for each line) are shown in Figure 6. The envelope of these solutions are the bounds on the velocity-depth structure inferred from the linear programing routine. The set of these solutions which best fit the travel times is considerably narrower, of course. The shapes of the structures at the greatest depths are extremely similar as a result of the very high order constraints due to the amplitude information.

Structure Under the Axis

Two types of data have been used to infer structure under the axis: the fan lines which involve ray paths crossing the axis obliquely and a reversed line across and perpendicular to the axis (line 1).

Data from lines 6L and 7L to OBS's 407 and 403 are shown in Figures 7 and 8 and represent travel times along paths that cross the rise axis obliquely. Data from line 1L to OBS 402 on the rise axis is shown in Figure 9 and represents travel times along paths oblique to the axis but not crossing the axis. The following features of these data are noted.

1. They are in the distance range 65–90 km, and the predominant energy corresponds to wave paths which are multiple reflections at the seafloor of the caustic caused by the velocity gradient at the crust-mantle transition. This has been verified by synthetic seismogram modeling, and it indicates that these waves are only affected by crustal properties and the crust-mantle transition.

2. They show clearly that some type of velocity inhomogeneity exists in the crust under the axis which causes a marked attenuation of energy crossing the axis (Figures 7 and 8). The change in amplitudes is directly related to the rise axis, and it indicates that the width of the inhomogeneity is certainly less than about 10 km. This is supported by the data in Figure 9 which show that for propagation along the axis the travel times are not retarded. This would be expected for a narrow low-velocity zone with lateral refraction in the faster material.

3. The abrupt change in amplitude for crustal paths crossing the axis could be caused by transmission loss through a low-velocity zone or the absence of the crust-mantle boundary at the axis or both. It is unlikely to be due to anelastic effects because the wavelengths are of the order of the width of the inhomogeneity and therefore the anelastic attenuation coefficient would have to be unrealistically high to cause the observed amplitude reduction.

Because the complicated ray paths make these data difficult to interpret, we have used the data on line 1 perpendicular to and crossing the axis to provide better constraints on the axial structure.

Figure 10 shows the large shot data on line 1L between OBS's 407 and 403. These data are uncorrected for topography, and they show that at distances corresponding to crustal arrivals (OBS 407) the propagation across the axis is not greatly affected by the axis except for a time offset of about 0.3 s. At distances where one might expect the first arrivals to be from mantle paths (OBS 403) the rise axis does appear to affect the propagation across the axis. This could be due to a negative velocity gradient in the mantle near the rise axis.

Because the topographic effects of the rise axis on the travel times are significant (about 0.2 s), these need to be included in any modeling procedure or corrected for in the data. Both procedures were implemented. In one case we used a two-dimensional ray trace method [*McMechan and Mooney*, 1980] and included the topography. In the other we first corrected for the topography and then applied the two-dimensional ray trace method. The topographic corrections were made using the method described in the section on data; that is, the travel times were corrected by adding or

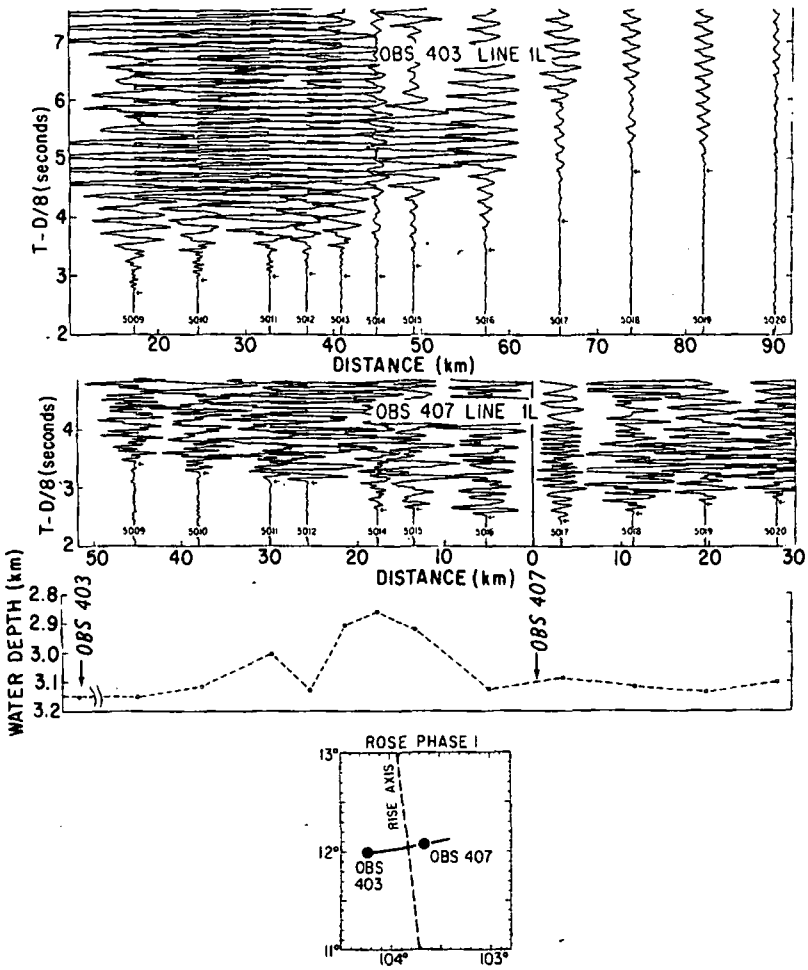

Fig. 10. Line 1L reversed between OBS's 407 and 403. This line crosses the rise axis and no topographic corrections have been made.

subtracting the travel time at a phase velocity of 7 km/s in a water layer whose thickness was the difference between the shot depth and 3 km. Because the mean ocean depth along this line is close to 3 km, this required the smallest corrections, less than 0.2 s, to simulate a constant thickness ocean above the shots. The application of the topographic corrections to line 1S data on OBS's 407 and 406 are shown in Figure 11.

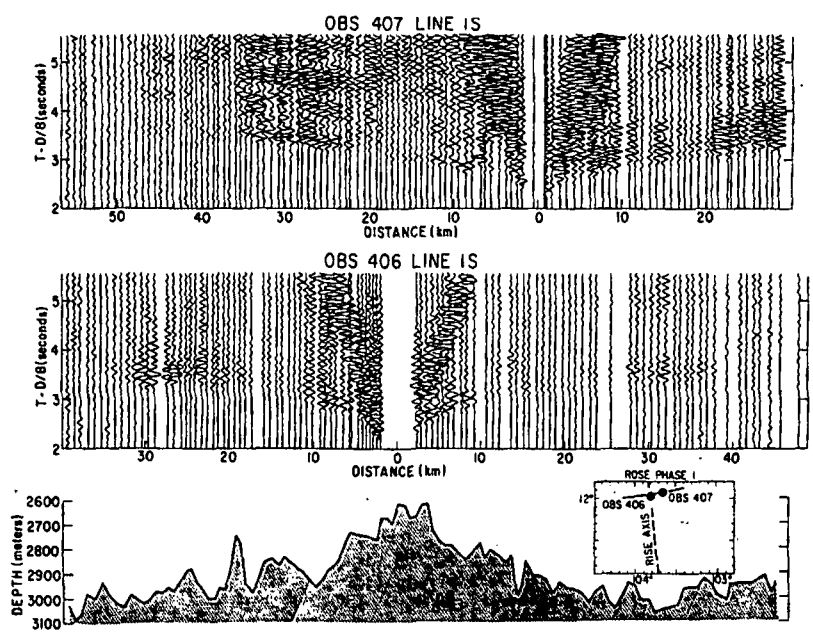

Fig. 11. Small shots across the rise axis to OBS's 407 and 406. Topographic corrections have been made.

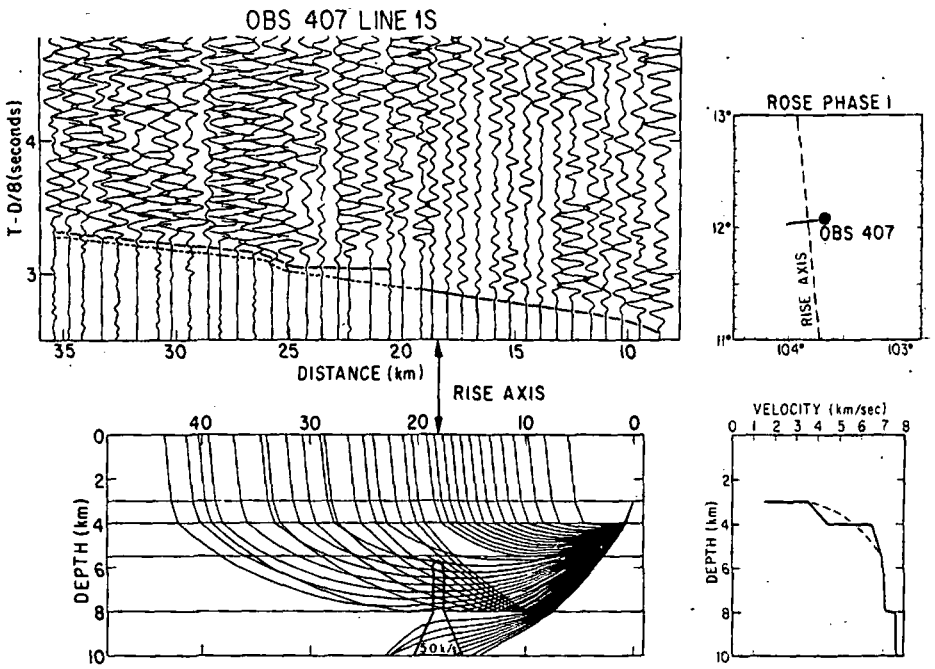

Fig. 12. An enlargement of the data in Figure 11 crossing the rise for OBS 407. Also shown is a model derived from two-dimensional ray tracing which satisfies the data.

Several interesting features of the data in Figure 11 are noted. First, we see that although OBS 406 was on the rise axis, the travel times are not significantly different from OBS 407, which was 17 km from the axis. This indicates again that any axial low-velocity zone in the crust must be narrow. Second, we see that amplitude increases in the distance range 20–45 km, which are caused by the crust-mantle transition, are found on all segments of the data, including data crossing the axis. This indicates that this transition is continuous under the region of the rise axis. Third, we note a slightly irregular behavior in the caustic on OBS 407 which is associated with travel paths under the rise axis.

These data show that if there is any unusual velocity behavior under the rise axis, it is very localized and has a subtle effect on the travel times.

To explore the range of axial velocity structures compatible with the data, we applied the two-dimensional ray trace method to the OBS 407 line 1S data. A model which is compatible with the data is shown in Figure 12, and a model which is definitely incompatible with the data (the Oman

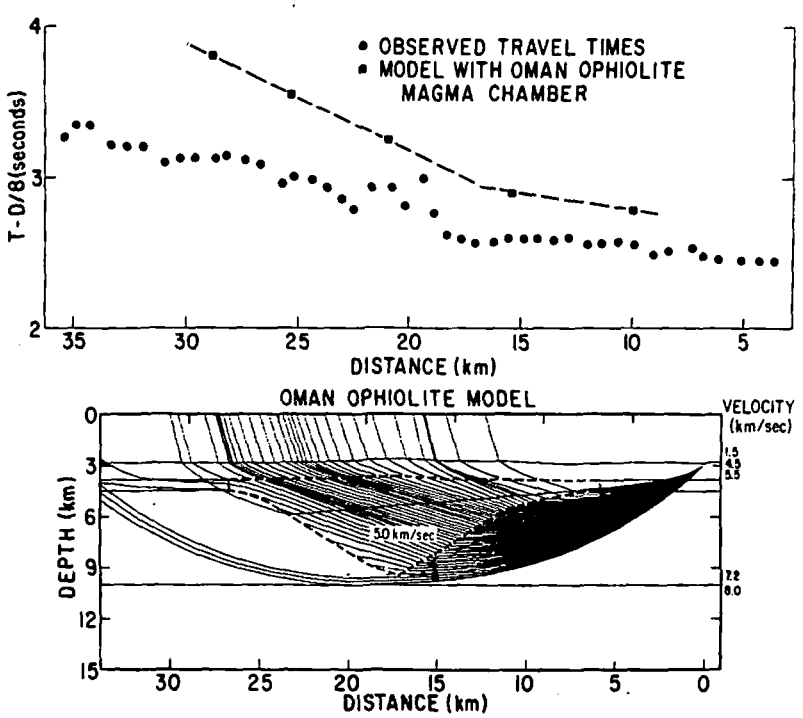

Fig. 13. Computed travel times for the Oman ophiolite model of *Pallister and Hobson* [1981] compared with the data in Figure 12 (uncorrected for topography).

ophiolite model, *Pallister and Hobson* [1981]) is shown in Figure 13. In Figure 12 it is seen that the only unusual feature of the data is an offset of about 0.1 s in the travel times beyond 25 km. The reduction in amplitude between 19 and 22 km can be adequately explained by the normally low gradient in velocity in the lower crust. The travel time offset can be due to a slowness difference dS applied over a distance x. For x = 1 km, dS = 0.1 s/km, which corresponds to a velocity decrease from 7 km/s (the velocity in the lower crust) to 4.12 km/s. For x = 3 km the corresponding low velocity is 5.68 km/s. Models having an axial low-velocity zone with different shapes were tried, but all nonparallel-sided shapes caused refraction effects which influenced the amplitudes in a detrimental manner.

Therefore we feel that the simplest model compatible with the data is that shown in Figure 12. Although we have not rigorously demonstrated that this model will also explain the oblique travel path data, one can argue that a narrow crustal low-velocity zone coupled with the absence of an underlying crust-mantle transition would channel energy, which crosses the rise axis obliquely, into the mantle, thereby causing the decrease in amplitudes.

DISCUSSION AND CONCLUSIONS

The off-axis velocity structure is characterized by a thin zone of low velocity at the seafloor (probably representing the zone of pillow basalts) underlain by a rapid transition to a nearly homogeneous and apparently isotropic layer 3. For rays refracted parallel to the strike of the East Pacific Rise near 12°N, the Moho seems to be a very gradual increase in velocity up to at least 7.8 km/s, but this is followed by a decrease in velocity below the transition. For rays refracted in the direction of spreading, the Moho transition may be somewhat sharper, and the strong *Pn* arrivals require a continuing increase in velocity with depth below the major transition. Observed *Pn* velocities are almost 8.3 km/s in this direction. These disparate velocity gradients are most probably due to a gradual increase in anisotropy just below the Moho.

An important result of this study is the strong constraint on the width of any magma chamber or partial melt zone in the crust under the rise axis. We have shown that the data crossing the axis do not exclude a narrow low-velocity zone under the axis. An upper limit to the width of this zone would be about 4 km at a velocity of 6 km/s (little partial melt). A lower limit on the width is about 0.5 km corresponding to the velocity of totally basaltic magma, about 3 km/s [*Murase and McBirney*, 1973].

We have shown that the magma chamber model postulated for the Oman ophiolite can be ruled out as a possibility for this part of the East Pacific Rise. Since the large magma chamber for the Oman ophiolite was postulated to explain the cumulate section, we infer that the Pacific crust in this area may not have a significant cumulate section. This is also in general agreement with the seismic velocities. *Christensen and Smewing* [1981] report velocities of about 7.5 km/s for the Oman layered gabbros. The refraction data do not require 7.5-km/s velocities in the lower crust except in the transition zone from crust to mantle.

Acknowledgments. We thank Jim McClain for his part in collecting the data, Sam Wade for his diligence in digitizing the data, the Office of Naval Research for supporting this research under contract N-00014-80-C-0252, and we note our appreciation for the opportunity to work with the other ROSE scientists. University of Washington contribution 1247.

REFERENCES

Bibee, L. D., and G. G. Shor, Jr., Compressional wave anisotropy in the crust and upper mantle, *Geophys. Res. Lett.*, *3*, 639–642, 1976.

Chapman, C. H., A new method for computing synthetic seismograms, *Geophys. J. R. Astron. Soc.*, *54*, 481–518, 1978.

Christensen, N. I., and J. D. Smewing, Geology and seismic structure of the northern section of the Oman ophiolite, *J. Geophys. Res.*, *86*, 2545–2555, 1981.

Ewing, J. I., and R. P. Meyer, Rivera ocean seismic experiment (ROSE) overview, *J. Geophys. Res.*, this issue.

Garmany, J. D., Anisotropic gradients in the upper mantle, *Geophys. Res. Lett.*, *8*, 955–957, 1981.

Garmany, J. D., Amplitude constraints in linear inversions of seismic data, *J. Geophys. Res.*, this issue.

Herron, T. J., P. L. Stoffa, and P. Buhl, Magma chambers and mantle reflections: East Pacific Rise, *Geophys. Res. Lett.*, *7*, 989–992, 1980.

LaTraille, S. L., J. F. Gettrust, and M. Simpson, The ROSE data storage and exchange facility, *J. Geophys. Res.*, this issue.

Lewis, B. T. R., and W. E. Snydsman, Fine structure of the lower oceanic crust on the Cocos plate, *Tectonophysics*, *55*, 87–105, 1979.

Lister, C. R. B., and B. T. R. Lewis, An ocean bottom seismometer suitable for arrays, *Deep Sea Res.*, *23*, 113–124, 1976.

McMechan, G. A., and W. D. Mooney, Asymtotic ray theory and synthetic seismograms for laterally varying structures: Theory and application to the Imperial Valley, California, *Bull. Seismol. Soc. Am.*, *70*, 2021–2036, 1980.

Murase, T., and A. R. McBirney, Properties of some common igneous rocks and their melts at high temperatures, *Geol. Soc. Am. Bull.*, *84*, 3563–3692, 1973.

Orcutt, J., B. Kennett, L. Dorman, and W. Prothero, A low velocity zone underlying a fast spreading rise crest, *Nature*, *256*, 475–476, 1975.

Pallister, J. S., and C. A. Hopson, Samail ophiolite suite: Field Relations, phase variations, cryptic variation and layering, and a model of a spreading ridge magma chamber, *J. Geophys. Res.*, *86*, 2593–2644, 1981.

Project ROSE Scientists, Microearthquake activity on the Orozco fracture zone: Preliminary results from project ROSE, *J. Geophys. Res.*, *86*, 3783–3790, 1981.

Sutton, G. H., B. T. R. Lewis, J. Ewing, F. K. Duennebier, B. Iwatake, and J. D. Tuthill, An overview and general results of the Lopez Island OBS experiment, *Mar. Geophys. Res.*, *5*, 3–34, 1981.

(Received June 8, 1981;
revised February 3, 1982;
accepted February 26, 1982.)

Geophys. J. R. astr. Soc. (1976) 47, 459–491

Crustal structure of the Mid-Atlantic ridge crest at 37° N

C. M. R. Fowler *Department of Geodesy and Geophysics, Madingley Road, Cambridge CB3 0EZ*

Received 1976 May 7

Summary. A structural model of the Mid-Atlantic Ridge at 37° N is proposed on the basis of travel-time data and synthetic seismograms. At the ridge axis the crust is only 3 km thick and overlies material with an anomalously low 'upper mantle' velocity of 7.2 km s^{-1}. Crustal thickening and the formation of layer 3 and a layer with velocity 7.2–7.3 km s^{-1} takes place within a few kilometres of the axis, producing a 6–7 km thick crust by less than 10 km from the axis. A normal upper mantle velocity of 8.1 km s^{-1} exists within 10 km of the axis. Shear waves propagate across the axis, thus precluding the existence of any sizeable magma chamber at shallow depth.

Introduction

The theory of plate tectonics is now generally accepted, but the details of plate creation and destruction are still poorly understood. There is little agreement about the processes by which layered oceanic crust is created at the axis of the mid-ocean ridge system. Many petrologists require that there should be a magma chamber beneath the ridge axis to produce the basaltic lavas erupted on the seabed at the axis, but the size and extent of such a magma chamber remains conjectural.

Cann (1970, 1974) proposed the existence of a large magma chamber situated in the crust at the top of a rising column of asthenosphere. Orcutt *et al.* (1975, 1976) and Rosendahl *et al.* (1976) reported a low-velocity zone, interpreted as such a magma chamber, at the crest of the East Pacific Rise at 9° N. Sleep (1975), modelling the temperature field at the ridge axis, has shown that for spreading rates less than 1 cm yr^{-1}, the half-width of any possible magma chamber in the crust is less than 0.5 km, which suggests that no large-scale permanent magma chamber can exist beneath a slow-spreading ridge. Seismologists working with teleseismic data from earthquakes (Molnar & Oliver 1969; Francis 1969; Solomon 1973) reported a sharply-defined zone of high attenuation in the upper mantle at the ridge axis through which S_n is not propagated. Solomon & Julian (1974) modelled the temperature field and hence the *P*-wave velocity field in the upper mantle in the axial zone. In order to account for the non-orthogonality of the nodal planes of ridge crest earthquakes, they concconcluded that there must be a *P*-wave low-velocity zone, with half-width several tens of

Detailed Near-Bottom Geophysical Study of the Gorda Rise[1]

TANYA ATWATER[2] AND JOHN D. MUDIE

University of California, San Diego
Marine Physical Laboratory of the Scripps Institution of Oceanography
La Jolla, California 92037

A deeply towed instrument package was used to survey the fine details of topography, sediment distribution, and magnetization of the Gorda rise, an active spreading center off northern California. The gross form of the central rift valley is the result of large-scale normal faulting. The surface is broken into long, narrow, tilted steps parallel to the spreading center. Topographic features just outside the rift valley also have a tilted blocky aspect and are lineated and symmetrical with respect to features of the same age on the opposite flank. Flat terrigenous turbidite sediments are found in the valley floor and in deeps on the west flank, as might be expected. They also are found on the tops of the steps high in the rift valley walls, implying that the steps are uplifted to form the walls as they move out from the center. The magnetic field measured near the ocean bottom can be approximately simulated by using straightforward model calculations. The extremely complex short-wavelength anomalies (width less than 1 km) generally are caused by topographic effects, and from them the bulk magnetization of the topographic features was estimated to be about 0.009 emu/cm^3 near anomaly 2 and 0.007 emu/cm^3 near anomaly 3. Assuming these values of magnetization for the entire magnetic layer, the magnitude of long-wavelength anomalies shows that it must be about 0.5 km thick. In crust formed at a spreading rate of 37 mm/yr, magnetic field polarity reversals are recorded in the magnetic layer as a gradual zone of transition about 2 km wide. Of this width, 0.1 to 0.7 km can be attributed to the time it takes for a reversal to be completed, and the remaining width, about 1.7 km, can be attributed to the process of emplacement of magnetic material. Comparisons with emplacement models show that most magnetic material was emplaced within 2 km of the center (within 0.7 km if a pure dike injection model is assumed). The 2-km width of the emplacement effect acts as a smoothing function for events in the magnetic field, so that the record in the magnetic layer of events of duration less than about 10,000 years should be greatly attenuated. Two medium-wavelength anomalies are interpreted as possible normal polarity events centered at 3.4 and 3.55 m.y.

The Gorda rise lies off northern California just north of the Mendocino fracture zone (Figure 1). Seismicity shows that it is an active plate boundary [*Tobin and Sykes*, 1968]; high heat flow, low mantle velocities, shallow symmetrical topography, and recognizable magnetic anomalies all indicate that it is an active spreading center [*Von Herzen*, 1964; *Shor et al.*, 1968; *McManus*, 1967; *Vine*, 1968]. Magnetic anomalies discussed by *Vine* [1966] show that the southern Gorda rise has spread slowly since about 2 m.y. and more quickly in earlier times.

In May 1967 a survey was conducted of the southern Gorda rise with a deep towed geophysical instrument package, hereafter called the Fish. Since it is towed very near the sea floor, the Fish reduces the resolution problems encountered by sea surface instruments, allowing one to study structures of the sea floor in great detail. The central portion of the southern Gorda rise was taken as an example of a slowly spreading rise (about 12 mm/yr), and most of the survey was concentrated in that region. Data were also collected along one long track crossing older crust that was formed by faster spreading (37 mm/yr). The purpose of this paper is to summarize the data collected with the Fish and to explore the implications of these data for the spreading phenomenon.

All spreading rates given in this paper are half rates, i.e., the rate at which one flank of the ridge was formed. The unit millimeter per year is adopted because it converts directly to

[1] Contribution of the Scripps Institution of Oceanography, new series.

[2] Now at Department of Earth and Planetary Sciences, Massachusetts Institute of Technology, Cambridge, Massachusetts 02139.

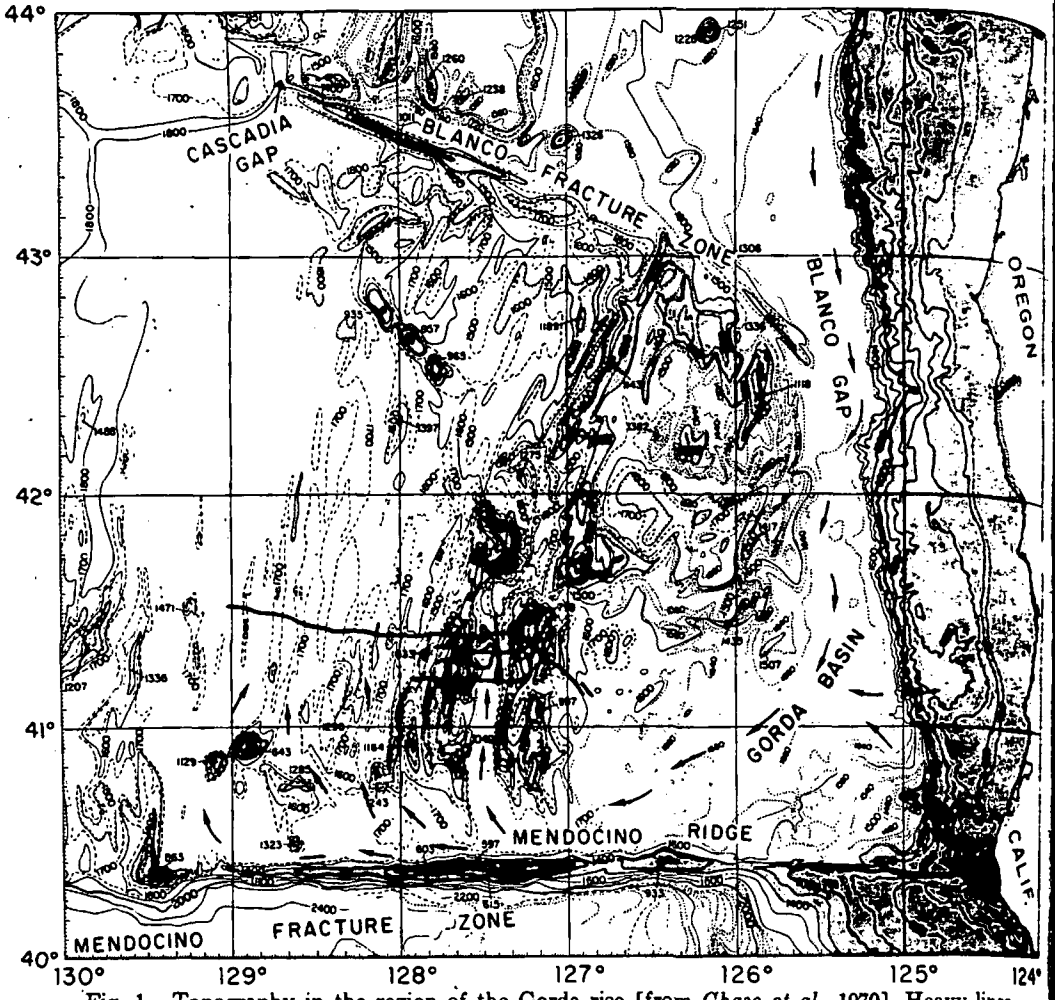

Fig. 1. Topography in the region of the Gorda rise [from *Chase et al.*, 1970]. Heavy lines show survey tracks of deep towed Fish. Contours are in uncorrected fathoms, and grey regions are shallower than 1400 fm (2.6 km). Arrows show probable paths followed by continentally derived turbidity flows.

kilometer per million years and conforms to the International System (SI) of Units [*Reilly*, 1972]. The second author wishes to note that 1 nT = 1 gamma and 1 amp/m = 0.001 emu/cm^3, where the nanotesla and amperes per meter are SI units.

Instrumentation and Data Processing

The data reported here were collected by the Marine Physical Laboratory deep towed Fish, described in detail by *Spiess and Mudie* [1971]. The Fish was generally towed 1–3 km behind the ship and 20 to 200 meters above the bottom. It was instrumented with sonars and a magnetometer. An up-looking sonar and a narrow-beam down-looking sonar give the depth of the Fish and the ocean bottom; a wide-beam 3.5-kHz down-looking sonar penetrates sediment bodies; and side-looking sonars display the character of the bottom and the shape of bottom features within 400 meters of either side. The sonars resolve objects as small as a few meters in size and delineate objects tens of meters or larger in size. The usual transponder navigation system was not used successfully in this survey. A proton precession magnetometer sensor was towed behind the Fish, and the ship towed a second proton precession magnetometer at the sea surface.

During postcruise data processing, all sound-

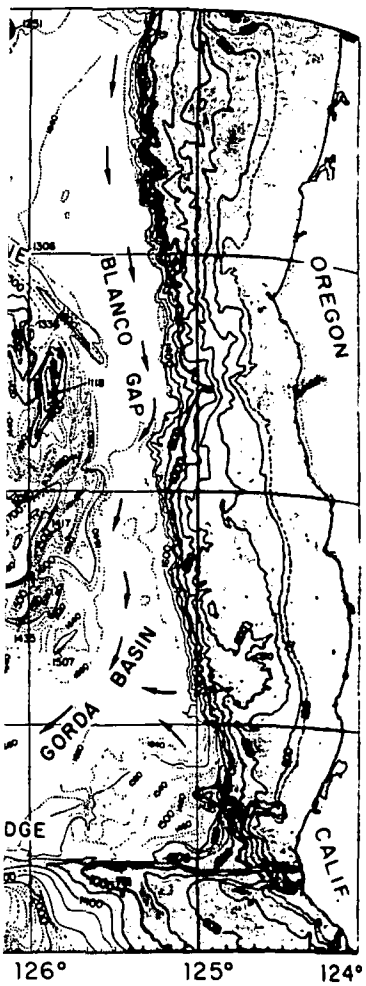

Chase et al., 1970]. Heavy lines
ected fathoms, and grey regions
aths followed by continentally

oking sonar give the depth of the
ocean bottom; a wide-beam 3.5-
oking sonar penetrates sediment
side-looking sonars display the
he bottom and the shape of bot-
within 400 meters of either side.
solve objects as small as a few me-
d delineate objects tens of meters
ze. The usual transponder naviga-
was not used successfully in this
ton precession magnetometer sen-
d behind the Fish, and the ship
d proton precession magnetometer
rface.
tcruise data processing, all sound-

ing data were corrected for varying water column velocities according to *Matthews* [1939] and were converted to meters (more recent estimates of water column sound velocity in this region, made in 1965 by R. Raitt and coworkers (personal communication), 1969, are essentially identical to those reported and used in Matthews' tables for the depths concerned). Where needed for comparisons to charts, depths are also given in uncorrected fathoms (assuming a sound velocity of 800 fm/sec).

NAVIGATION

Navigation of the ship was by Loran A, readings being taken every half hour. Inconsistencies among readings and between readings and approximately known ship speeds and headings indicate the Loran readings to be sometimes as much as 3 km in error in E-W positioning. N-S control was somewhat better because of the locations of the Loran stations. The Fish was not navigated directly. The usual practice of using a set of ocean bottom transponders to locate the Fish was not appropriate in this survey because of the extreme roughness of the topography and the long distances involved. Therefore the Fish had to be navigated by estimating its position relative to the ship. In other regions, where transponders were used so that Fish and ship positions were well known, the Fish has been seen to follow a track that was a smooth version of the ship's track, cutting corners and diminishing small excursions of the ship. Thus, to estimate the Fish track in this region we smoothed the ship track in a comparable way.

Given the Fish track thus derived, the position of the Fish on the track versus time must then be determined. This position can be determined whenever the distance of the Fish behind the ship is known, and that separation can occasionally be measured if first the ship and then the Fish passes over some distinctive high point in the topography. Eighty measurements of the separation made in this way ranged from 1 to 3 km, depending approximately upon the depth at which the Fish was being towed. From these measurements, an empirical relationship was calculated between ship-Fish separation and Fish depth, and this relationship was used in a first attempt to locate the Fish on the track. This approximation did not prove to be adequate when the Fish depth varied rapidly, in particular, along crossings of the central valley and ridges. Therefore the E-W positions along these lines were modified to fit topographic highs with those surveyed by *Heinrichs* [1970]. His data were taken along straight lines at a steady speed of about 17 km/hr, errors being estimated as less than 2 km. Where lines could not be compared to Heinrichs' survey, i.e., along N-S tracks and on tracks outside the central valley, locations were accepted as approximated by the relation of separation to Fish depth. On these tracks, Fish depths varied much less, so that the approximation is nearer the true case.

The probable errors in the Fish locations that were accepted can be summarized as follows. On the long flank tracks and on the N-S tracks in the central valley absolute location is known to within about 3 km, and separations of nearby points along the track are probably good to a few percent. On the E-W traverses of the central region absolute location is good to within 2 km, but separations of nearby points are only known to within 20 or 30%, so that quantitative measurements of slopes, for example, are not very reliable.

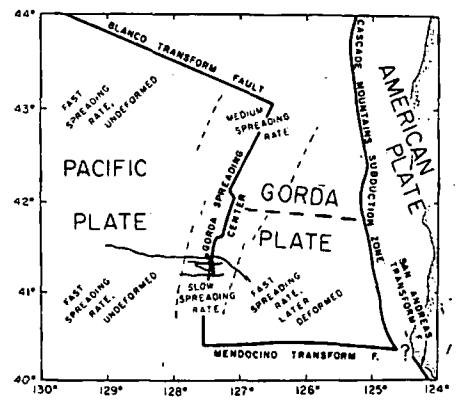

Fig. 2. Present plate configuration near the Gorda rise. Heavy lines show active plate boundaries. Heavy dashed line represents disruption of the Gorda plate. Light dashed line shows approximate boundary of crust formed at 37 mm/yr (fast) before the disruption. Since the disruption, the southern portion of the Gorda spreading center has spread at about 12 mm/yr (slow), and the southern portion of the Gorda plate has deformed internally. Survey tracks are shown. Only one track extends into the fast-spreading flank provinces.

REGIONAL SETTING AND SPREADING HISTORY

The Gorda rise lies off northern California and southern Oregon and has an active spreading center (Figures 1 and 2). Topographically, it consists of two linear ridges separated by a deep central rift valley. The inner sides of the ridges (the valley walls) are extremely steep, but the outer flanks descend much more gradually. The ridges terminate near the Mendocino and Blanco fracture zones, which serve as transform faults [*Tobin and Sykes*, 1968]. The ridges are also disrupted near their centers (about 42°N), where they are broken and offset and their trends change somewhat. This disruption appears to be a fundamental one, extending to the east into the Gorda plate as a deep in the topography, as a cross feature in the magnetic pattern, and as a slightly active seismic zone [*Northrop et al.*, 1968; *Bolt et al.*, 1968]. The tracks of our survey are shown on Figures 1 and 2, centered near 41°20′N, 127°30′W. They lie entirely within the region south of the disruption and sample only the more orderly middle part of that section.

The spreading history on the Gorda rise for the past 7 m.y. can be studied by using the magnetic anomalies mapped by *Raff and Mason* [1961] as interpreted by *Vine* [1968]. Anomalies west of the ridge (in the Pacific plate) are for the most part straight and orderly, indicating that this plate has remained intact since its formation at the ridge crest. If we assume that spreading was approximately symmetrical and perpendicular to the ridge crest, this magnetic pattern records the following history of spreading between the Pacific and Gorda plates.

Between 7 and 2.5 m.y. ago, the plates spread apart at a rate of about 37 mm/yr in a direction that gradually changed from N95°E to N100°E. Sometime between 2.5 and 1.8 m.y. ago, the discontinuity formed near 42°N, dividing the Gorda plate into two sections with very distinct behaviors. The motion of the northern section (north of 42°N) changed slightly to a trend of about N110°E and to a rate of about 30 mm/yr. The southern section of the plate, in contrast, slowed drastically. From sea surface magnetic anomalies, it cannot be determined whether the slowing was sudden or gradual. This history can be better delineated by using the near bottom magnetometer records in which the boundaries of the Jaramillo event (0.89–0.95 m.y. in age) can be distinguished. Figure 3 shows locations of magnetic reversals measured by the Fish along the long track across the western flank shown in Figures 1 and 2. The method for determination of these locations is discussed in a later section. When matched to the time scale of *Cox* [1969], the reversal locations indicate that the change in spreading rate occurred at 2.1 m.y., if it was abrupt, and has been constant at 12 mm/yr since 1.8 m.y. ago (perhaps since 2.1 m.y.). The apparent constancy in the slow spreading rate is important, because it implies that features in the central valley may be representative of slow spreading centers rather than being just transient features of a changing system.

Sea surface magnetic anomalies mapped over the Gorda plate, east of the ridge, clearly have been deformed. While those in the northern section are approximately parallel to their western counterparts, those in the south have been rotated 35° to 40°. *Silver* [1971] notes that most of the rotated anomalies are nearly parallel to one another, and the central anomaly is almost constant in width. Thus a major part of

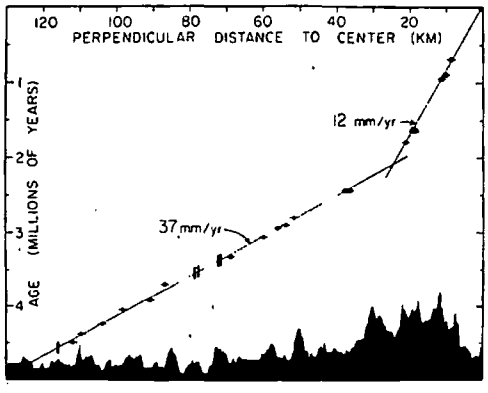

Fig. 3. Data establishing spreading rates and rate changes for the southern Gorda rise. Rectangles show locations of magnetic polarity reversals (listed in Table 1); the widths of the rectangles are estimates of the errors of the locations. The reversals are plotted versus their approximate ages, taken from the time scale of *Cox* [1969]; normal intervals in the time scale are shown as grey stripes. Black profile shows basement topography at 15× vertical exaggeration (see Figures 5, 9, and 11 for details). All data are from the western half of the long E-W track in Figures 1 and 2 (extension of line A, Figure 4) and are projected onto a line of trend N100°E perpendicular to the magnetic anomalies.

the rotation occurred
event during the Mat
From the discussion
region of our survey
different histories: (1)
ince, undisturbed ocea
37 mm/yr; (2) the
oceanic crust formed
later deformed; and
oceanic crust formed a
imate extent of these
tions of our survey li
Only one line extends
inces. Details of the
shown in Figure 4.

BATHYMETRY

Lineation and conti
rift valley. The str

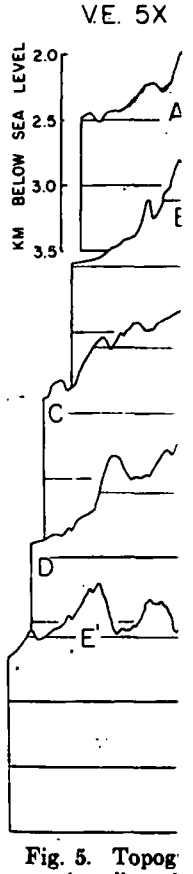

Fig. 5. Topog
central valley.
probable sedime
collected by the

the rotation occurred as a more or less discrete event during the Matuyama reversed epoch.

From the discussion above we can divide the region of our survey into three provinces of different histories: (1) the western flank province, undisturbed oceanic crust formed at about 37 mm/yr; (2) the eastern flank province, oceanic crust formed at about 37 mm/yr and later deformed; and (3) the central province, oceanic crust formed at 12 mm/yr. The approximate extent of these provinces and the locations of our survey lines are shown in Figure 2. Only one line extends well into the flank provinces. Details of the central survey lines are shown in Figure 4.

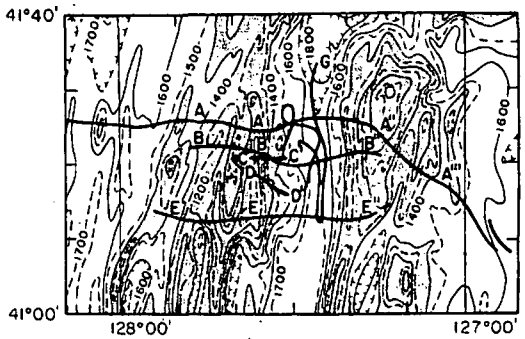

Fig. 4. Location and identification of deep tow survey tracks across the central valley, ridges, flanks of the southern Gorda rise. Bathymetry is the same as in Figure 1. Grey regions are shallower than 1400 fm (2.6 km).

BATHYMETRY AND STRUCTURE

Lineation and continuity of faulting in central rift valley. The structure of the Gorda rise appears to be completely dominated by faulting. The topographic features measured in and near the central valley are shown in Figure 5. While many small features appear to be vol-

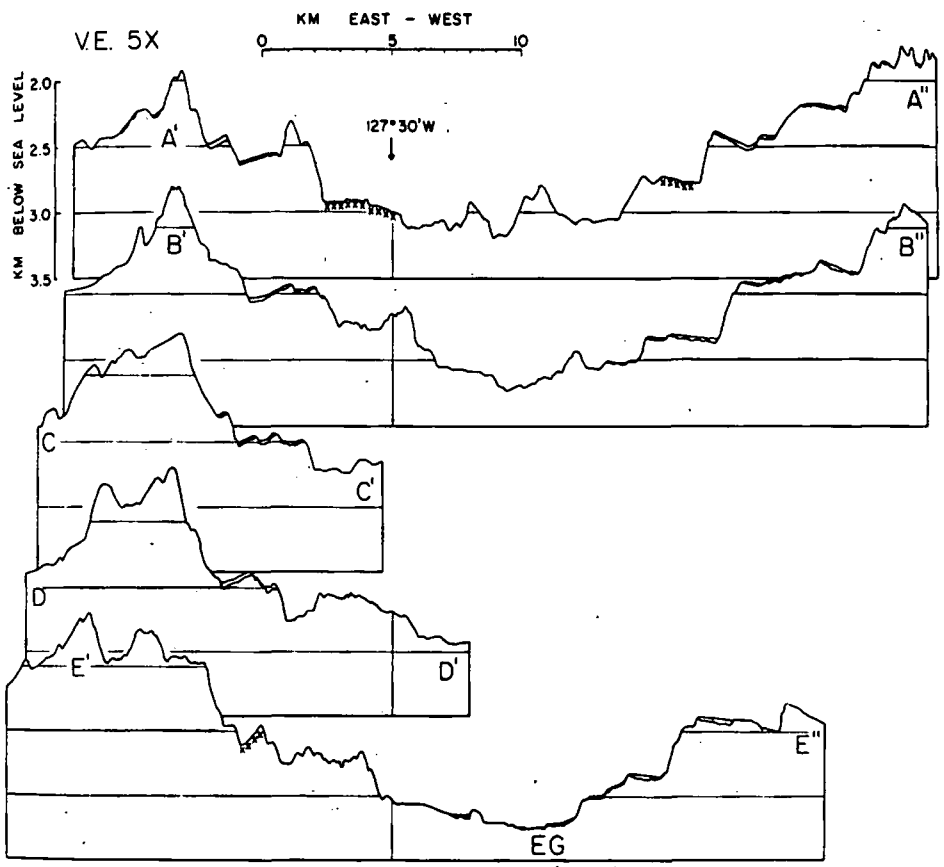

Fig. 5. Topographic profiles showing faulted, steplike topography in the walls of the central valley. Basement topography beneath sediments is shown where known. Other probable sediment-covered surfaces are marked by small crosses. The data shown were collected by the Fish along the tracks shown in Figure 4 and projected onto E-W lines.

canic in origin, most of the larger features have a blocky, faulted aspect [*Atwater and Mudie*, 1968]. The elevation of the two main ridges above the valley floor appears to be simply the result of normal faulting in the valley walls. Sediment distribution and magnetic evidence, to be discussed below, also require a faulting origin for the rift valley.

The faulting in the rift appears to be linear and parallel to the center of spreading. Large topographic features of the ocean floor tend to be elongated parallel to magnetic anomalies in this region [*Menard and Mammerickx*, 1967] and, on a more detailed scale, this lineation is seen in the major block faults within the rift valley, where the steplike features formed are very straight and continuous along the walls [*Heinrichs*, 1970]. The continuity of features can also be seen in our compilation in Figure 5, but this cannot be taken as independent confirmation of the linearity, since our sections were navigated by using Heinrichs' compilation. Our profiles do show that the larger steps are continuous in minor details of character; for example, the bare volcanic step near 127°30'W maintains its character for most of its length, a deeper trough always occurs just west of it, and a set of sediment-topped steps lies west of that.

Lineation of faults in the central rift valley is also shown in our side-looking sonar records. On E-W lines, scarplike features crossed by the down-looking sonars were recorded in the side-looking records as continuous linear features across the records, as is shown in Figure 6. During the N-S traverses, the side-looking sonars recorded numerous linear features paralleling the track or crossing it at small angles, as is shown in Figure 7. In order to compute the actual trends of the features seen in the side-looking sonar records, prominent points on the traces were digitized and were combined

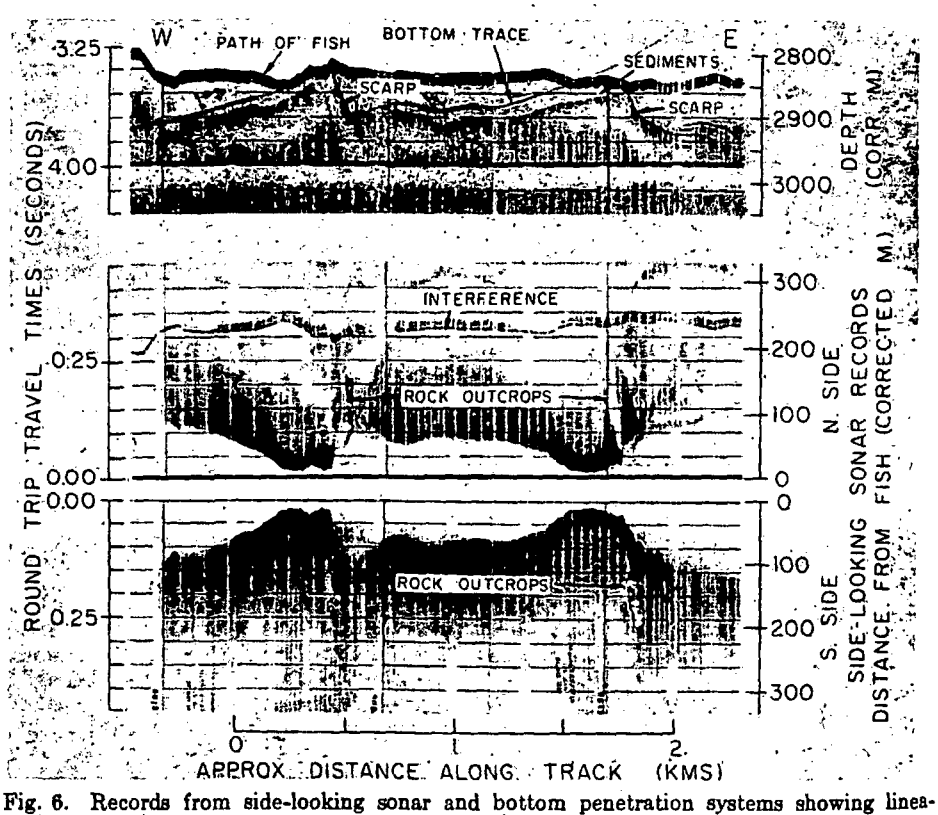

Fig. 6. Records from side-looking sonar and bottom penetration systems showing lineation of the scarps which bound sediment-covered steps high in the western valley wall. These data were collected along E-W track *B'B''*. A line has been drawn to clarify the location of the water-sediment interface, known from other records (see *Belderson et al.* [1972] for a discussion on the interpretation of side-looking sonar records).

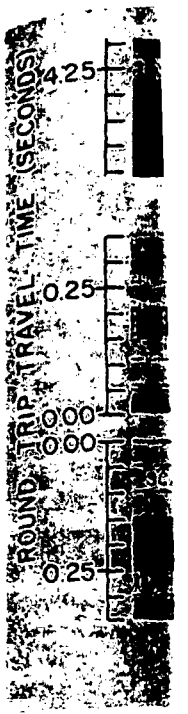

Fig. 7. F
scarp cuttin
These data
in Figure 5)

with Fish positi
velocity data. Si
poorly controlle
quite uncertain
responsible for
computed trend
8 shows the l
features in the
the rose diagran

The upper ro
rizes the trends
in the central
trends cluster s
central magnetic
topographic tre
appears to have
the last 2 m.y.,
valley may be
of slowly spread
pect to find sim
steplike feature
mid-Atlantic ri
[1968] and *Lon*

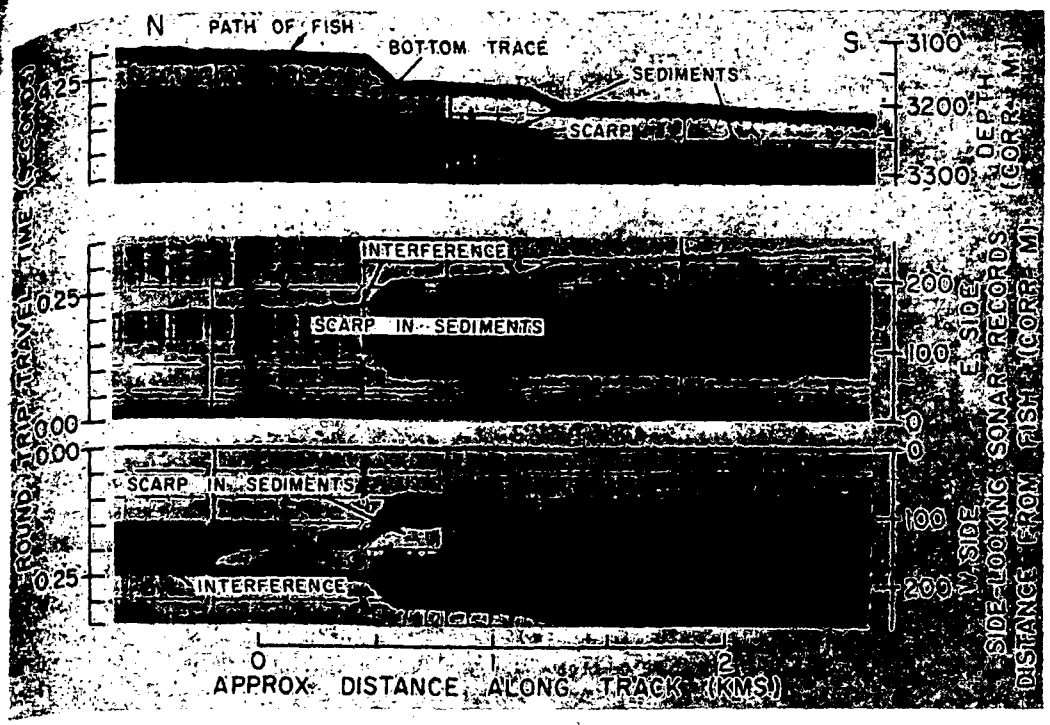

Fig. 7. Records from side-looking sonar and bottom penetration systems showing a small scarp cutting flat layered turbidite sediments at the eastern edge of the central valley floor. These data were collected along N-S track *G* near its crossing with track *E'E"* (marked *EG* in Figure 5).

with Fish position and height data and sound velocity data. Since the navigation of the Fish is poorly controlled, local velocities of the Fish are quite uncertain. These uncertainties may be responsible for errors of 10° to 20° in the computed trends of individual features. Figure 8 shows the locations of all detected linear features in the side-looking sonar records, and the rose diagrams summarize their trends.

The upper rose diagram in Figure 8 summarizes the trends computed for linear features in the central valley. Within the scatter, the trends cluster subparallel to the trend of the central magnetic anomaly and the central valley topographic trends. Since the spreading rate appears to have been constant at 12 mm/yr for the last 2 m.y., the linear faulting of the rift valley may be representative of the structure of slowly spreading centers, and we might expect to find similar features in others. A few steplike features have been reported in the mid-Atlantic rift by *van Andel and Bowin* [1968] and *Loncarevic et al.* [1966]. With more

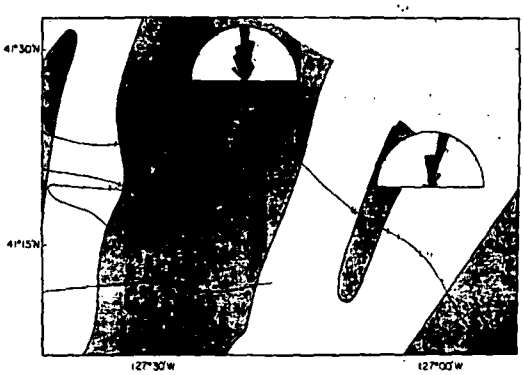

Fig. 8. Trends of linear features observed in side-looking sonar records. Dark marks indicate locations of features measured along the Fish tracks (light lines). Grey areas mark regions of positive magnetic anomaly as observed at the sea surface by *Raff and Mason* [1961]. The upper rose diagram summarizes trends of features measured in the central valley weighted by the length of feature measured. The lower rose diagram summarizes trends of features measured on the east flank weighted by the length of feature measured. The average trends lie subparallel to the magnetic anomaly (spreading center) trends.

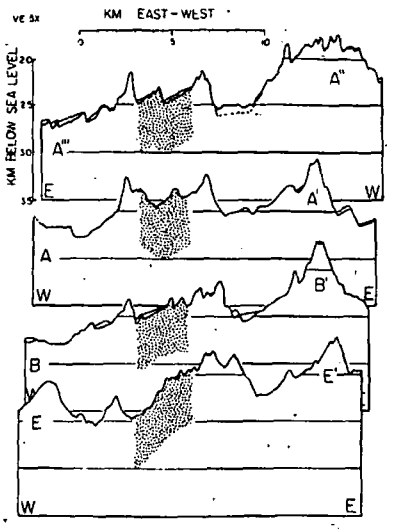

Fig. 9. Topographic lineation and symmetry in crust formed between 1 and 2.5 m.y. ago. Patterned regions indicate crust carrying the positive polarity magnetisation of anomaly 2 (1.6 to 1.8 m.y. old). The bottom three profiles were collected on the west flank; the top profile was collected on the east flank and is shown reversed. Letters identify positions on track lines in Figure 4.

detailed surveying, these might prove to be linear and continuous.

Lineation, continuity, and symmetry of features on inner flanks. On the flanks just outside the central valley, the geomorphology still appears to be dominated by faulting, although this is less striking. The topographic profiles can be divided by eye into sloping blocks a few kilometers in width with scarps facing inward toward the center. Within the meager control of our survey (three lines on the west, one on the east), the gross morphology appears to be linear and also symmetrical. In Figure 9 the bottom three profiles are from the west flank. They show that the crust formed between 1.6 and 1.8 m.y. ago (patterned sections) occupies the center of a sloping block between two lows in every profile. The top profile (*A'''A''*) is taken from the east flank and has been reversed for comparison. In this profile, crust that was formed between 1.6 and 1.8 m.y. occurs in the center of a block which is similar even in small detail to that in its western flank counterpart (*AA'*). This shows an amazing degree of symmetry in the sea floor generation and rifting process at the time that these features were formed. The symmetry is less pronounced in younger sections of the central province. They are symmetrical in a gross way; the highest peaks on the ridge crests occur in crust about 1 m.y. old and the valley center is approximately the center of anomaly 1, but features differ in detail (Figure 5).

The pervasive lineation of the features described above may be controlled by a basic grain of weakness built into the sea floor during its formation. This conclusion is suggested by the one profile that extends into the eastern flank province, the province formed at a fast spreading rate and later deformed. The seismic penetration and side-looking sonar records from this line in crust about 2.2 m.y. old are presented in Figure 10, which shows a number of small tilted blocks. The side-looking sonar record shows that the scarps are linear with a trend east of north. Figure 8 shows the location of all measured scarps in this region, and the lower rose diagram shows that their trends cluster well east of north, subparallel to the trend of magnetic anomalies in this region. This again shows that linear faulting occurs about parallel to the direction of the original emplacement of the crust. *Luyendyk* [1970] and *Larson* [1971] have also noted this relationship in deep tow studies of abyssal hills and of the East Pacific rise.

Distribution of Turbidite Sediments

The records from the seismic penetration system contain many examples of flat layered sediments that are interpreted to be turbidites of continental origin. While the distribution of these sediments is of interest for its own sake, it is also very important because of its tectonic implications. Since turbidity currents are not believed to flow uphill for any appreciable distance, it can be presumed that every terrigenous turbidite body was deposited at or below the shallowest contemporaneous channel between it and the continent. Turbidites presently found above the level must have been tectonically uplifted since their deposition.

The distribution and sources for turbidite sedimentation in the region around the Gorda rise can be inferred from the work of *Duncan* [1968] (reported by *Fowler and Kulm* [1970]) and from the topographic gradients mapped by

time that these features were
mmetry is less pronounced in
s of the central province. They
l in a gross way; the highest
dge crests occur in crust about
l the valley center is approxi-
ter of anomaly 1, but features
Figure 5).

e lineation of the features de-
may be controlled by a basic
ss built into the sea floor during
This conclusion is suggested by
that extends into the eastern
the province formed at a fast
ınd later deformed. The seismic
side-looking sonar records from
st about 2.2 m.y. old are pre-
e 10, which shows a number of
locks. The side-looking sonar
ıat the scarps are linear with a
rth. Figure 8 shows the location
scarps in this region, and the
gram shows that their trends
t of north, subparallel to the
ic anomalies in this region. This
ıt linear faulting occurs about
irection of the original emplace-
st. *Luyendyk* [1970] and *Larson*
) noted this relationship in deep
abyssal hills and of the East

N OF TURBIDITE SEDIMENTS

from the seismic penetration
many examples of flat layered
ıre interpreted to be turbidites
rigin. While the distribution of
is of interest for its own sake,
nportant because of its tectonic
ıce turbidity currents are not
uphill for any appreciable dis-
presumed that every terrigenous
was deposited at or below the
mporaneous channel between it
nt. Turbidites presently found
nust have been tectonically up-
deposition.

ion and sources for turbidite
the region around the Gorda
red from the work of *Duncan*
l by *Fowler and Kulm* [1970])
pographic gradients mapped by

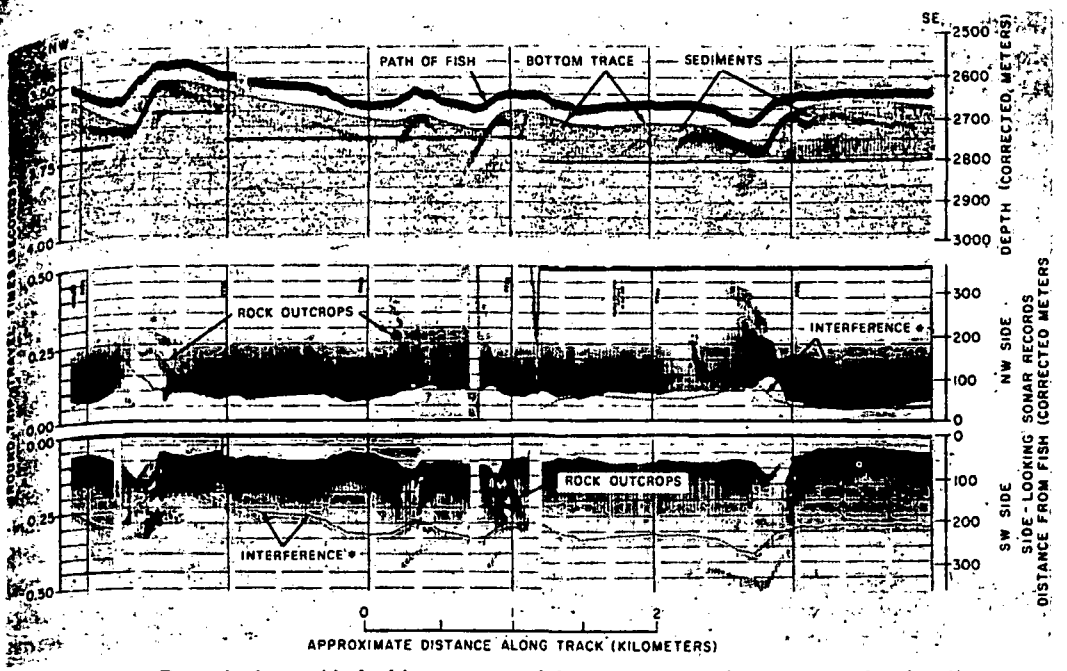

Fig. 10. Records from side-looking sonar and bottom penetration systems showing lineation of scarps that bound small faulted blocks on the eastern flank [from *Spiess and Mudie*, 1971]. These data were collected on NW-SE track near the point marked *A'''* in Figures 4 and 9.

McManus [1967] and by *Chase et al.* [1970]. The arrows in Figure 1 show probable paths for turbidity currents. Apparently some Columbia River sediments were carried southward through the Blanco Gap (Figure 1). Together with sediments of Klamath Mountain provenance (i.e., from southern Oregon and northern California), they filled the Gorda basin, and some flowed westward through the gap just north of the Mendocino ridge. Some of these mixed sediments flowed northward into the central valley of the Gorda rise [*Weser*, 1970], and some apparently continued eastward and then flowed northward up the axis of the linear valleys on the east flank of the Gorda rise.

Deep tow records taken in the central valley show flat, clearly bedded sediments in the valley floor in the south (e.g., Figure 7). Their northernmost detected occurrence in the valley floor was at about 41°16'N (at depth of 3.17 km, 1760 fm). From this point, the valley floor shallows northward to a saddle at 41°25'N, apparently forming an effective barrier, since the valley floor is bare of sediment there and farther north. Sediments are also found on the tops of the steps in the valley walls (Figure 5). These were also interpreted to be turbidites [*Atwater and Mudie*, 1968], since they are quite planar compared to the rough topography that they overlie and many show internal layering. Clayey sandstones have been dredged from the higher steps near 2200 meters (1200 fm) on the west wall and near 2000 meters (1100 fm) on the east wall. *Fowler and Kulm* [1970] report that these sandstones contain a sublittoral benthic foraminiferal assemblage in a matrix whose heavy minerals and clay content indicate continental sources. This confirms that these step-top sediments were deposited from turbidity currents originating on the continental shelf.

These step-top sediments are now found as shallow as 2.05 km (1010 fm), which is much shallower than the present level of turbidite sedimentation and much shallower than any possible path from the continent, and they are tilted. For these reasons we postulated [*Atwater and Mudie*, 1968] that the turbidites were deposited as a more continuous, nearly horizontal body at the time that the underlying crust occupied the valley floor, during and shortly after its formation. The sediments were subsequently broken, uplifted, and tilted along with

the underlying crust as it moved outward from the spreading center. This explanation for the perched location of the turbidites requires the hypothesis that the topographic configuration of the spreading center (a rift valley with flanking ridges) approximates a steady state configuration. If this hypothesis is valid, it puts strong constraints on models for the emplacement of oceanic lithosphere. *Deffeyes* [1970] discusses these constraints and concludes that the uplift of the steps must be accomplished by the addition of material in a zone as wide as the entire rift valley. Magnetic evidence discussed below shows that the near-surface material is emplaced in a much narrower zone, very near the center of the valley; therefore the material responsible for the uplifting must be weakly magnetized and mostly added at depth.

Figure 7 contains an example of the initiation of faulting and uplifting of sediments in the valley floor. It shows records taken along the N-S track *G* of Figure 4 (taken near its crossing with track *E'E''*; marked *EG* on Figure 5). The records show flat layered sediments near the eastern edge of the floor. A small scarp has broken the sediment layers and slightly uplifted those to the east. These sediments have begun their journey up the valley wall.

If we assume steady spreading and a steady state topographic configuration for the last million years, then the age of the crust of each step can be estimated, and the history of turbidite sedimentation in the valley floor can be determined from the present step-top sediment distribution. All our E-W crossings show probable turbidites on all east wall steps between about 0.3 and 0.7 m.y. of age, showing that the turbidite barrier in the valley floor is a young complication. Also it appears that the center of sedimentation has generally lain slightly east of the spreading center, since the steps in the eastern wall are more thickly and more consistently covered than those in the western wall. This could be a Coriolis effect similar to that which causes turbidity currents flowing down submarine fans to deposit sediment levees which are higher on the right-hand banks of their channels than on the left-hand ones in the northern hemisphere [*Menard*, 1955].

Probable recent turbidites were also found on the long track into the western flank province (westward extension of track *A* in Figure 4). The profile at the bottom of Figure 11 shows the ocean bottom trace and prominent subbottom reflectors that were recorded along that track. They have been digitized and plotted by computer at 15× vertical exaggeration. In the eastern portion, sediments drape the topography and are nearly devoid of internal reflectors. These are presumed to be pelagic sediments. This sea floor was formed by a fast spreading center, presumably on a high-standing riftless ridge so that it probably has never lain deep enough to receive turbidite sedimentation. West of km 70 nearly all the lows contain flat strongly layered sediments, but the highs are draped as before. The flat layered sediments are presumed to be terrigenous turbidites which recently passed westward through the gap north of the Mendocino ridge and then northward along the lineated valleys of this region (see Figure 1). The only other possible route of terrigenous turbidites to this region, through Cascadia Gap, seems to be ruled out, since the Gap is significantly deeper than this region and feeds directly into a well-developed channel that leads out of the area. The shallowest turbidities, in the basin at km 90, are 3.20 km deep (1720 fm). This appears to be very nearly the same as the depth of turbidite fill in the gap north of the Mendocino ridge, measured by profiles *B* and *C* of *Moore and Sharman* [1970].

Characteristics of Oceanic Magnetic Layer

Computer modeling system and its assumptions. The magnetic anomaly measured by the Fish is extremely complex, showing a strong complicated relationship to nearby topographic features and to variations of Fish height above the bottom. These data clearly could not be interpreted without taking the topography and Fish path into account; therefore we set up a computer modeling system to calculate the magnetic anomaly that would be expected along the actual path that the Fish followed over the actual basement topography that it measured. The models assume that the topography is two-dimensional parallel to the trend of the sea surface magnetic anomalies. The assumption is good if the distance from the Fish to the feature is much less than the length of the feature. Since topographic features in the region appear to be quite linear and continuous for kilometers

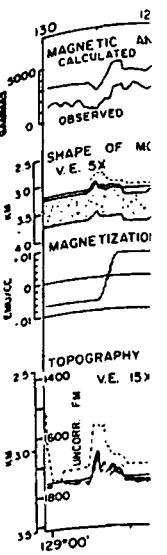

Fig. 11
were coll
flank pro
by the b
ments ar
where se
model la
to the di
the Fish

and the Fish
less than a fe
is realistic.

Since the g
region is the
its formatio
layer was mc
the top exce
forms. The
magnetized i
its present si
east flank pr
been rotated
lation the
vertically bo
zation, and
individual bl
along the Fis
Parker et a
the calculatic
netic layer
magnetizatio

Magnetizat
our first ex
grams, we sir

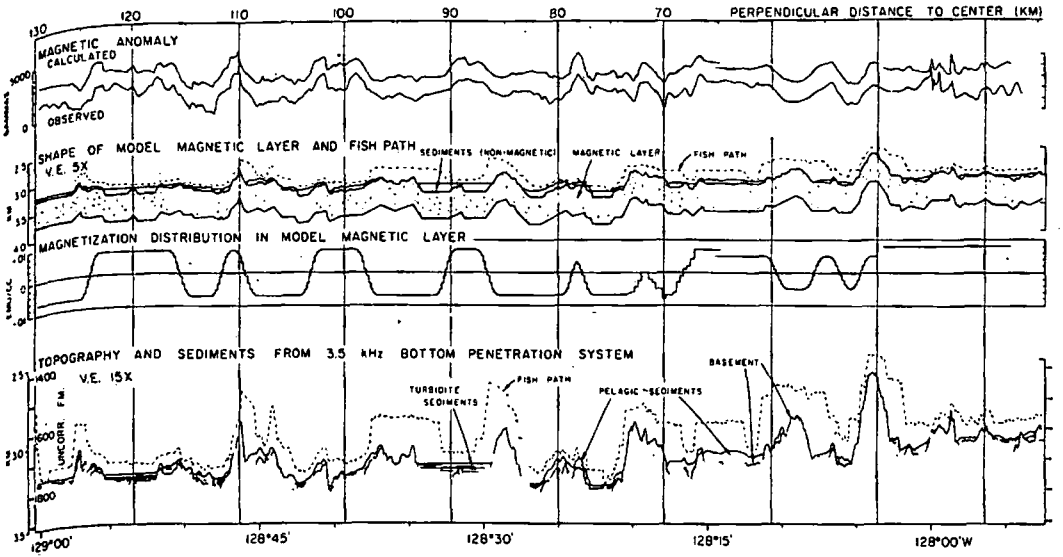

Fig. 11. Data collected by Fish on long west-flank track and magnetic model. The data were collected on the westward extension of track *A* in Figure 4 into the fast-spreading western flank province. The bottom profile shows digitized traces of features seen in records produced by the bottom penetration system, showing the distributions of opaque draped pelagic sediments and of layered ponded turbidite sediments. The basement trace in these records, where seen, was used to derive the model magnetic layer shown above (grey strip). This model layer was divided into narrow blocks of constant magnetization, magnetized according to the distribution shown ($W = 1.6$ km). Top traces show magnetic anomalies observed by the Fish and calculated from the model.

and the Fish height above the bottom is usually less than a few hundred meters, this assumption is realistic.

Since the gross form of the topography in this region is the result of faulting of the crust after its formation, the bottom of the magnetic layer was modeled as approximately parallel to the top except beneath some obvious volcanic forms. The layer was assumed to have been magnetized in a geocentric axial dipole field at its present situation except for material in the east flank province, which was assumed to have been rotated since its formation. In the calculation the magnetic layer was divided into vertically bounded blocks of constant magnetization, and the sum of anomalies due to the individual blocks was calculated at each point along the Fish path by the method described by *Parker et al.* [1973]. The only variables in the calculations were the thickness of the magnetic layer and the strength and polarity of magnetization of the blocks.

Magnetization of topographic features. For our first experiment with the modeling programs, we simply assumed that the entire ocean basement was uniformly normally magnetized to a depth of 1 km. We were pleased to find that this simple model predicted a very complex magnetic anomaly which in some regions simulated the shapes of the observed short-wavelength anomalies in considerable detail and in other regions simulated an inverse of the observed anomaly shapes. We conclude that much of the short-wavelength anomaly is simply the effect of magnetized topography and that the sections producing inverted anomalies are sections where the topography is magnetized with reverse polarity. The long-wavelength part of the observed deep tow magnetic anomaly contains the usual sea floor spreading pattern which was also observed at the sea surface and is conventionally interpreted to arise from normally and reversely polarized blocks in the sea floor. Without exception, normally polarized topography occurred on the tops of normal blocks, and reversely polarized topography occurred on reversed blocks, as is predicted by the sea floor spreading hypothesis.

Although the shapes of the observed anomalies were often approximately reproduced in the

first experiment, the amplitudes were not. The amplitudes could, however, be matched by simply increasing or decreasing the value of the constant magnetization assumed and by changing the polarity for the inverted cases, as shown in Figure 12. The majority of the regions in which the short-wavelength anomalies were not approximately simulated in this way either occurred where sediments obscured the basement so that the shape of the magnetized basement topography was not known (e.g., parts of section *B*, Figure 12) or else were located in transition zones between normal and reversely magnetized basement.

The values of magnetization used to obtain the fits just described are direct estimates of the magnitude of the bulk magnetization of the topographic features involved. The effects of varying the layer thickness or the shape of the layer bottom are small, since the Fish was towed very near the bottom. Among the geometrical assumptions built into the model, the assumption of perfect topographic linearity is the most troublesome. Nonlinearity will cause our estimates to be too low.

Figure 13 shows all the estimates of magnetization plotted with respect to their ages derived from the long-wavelength sea floor spreading anomalies as identified in Figure 3 and Table 1. The highest values in Figure 13 correspond to very young features of apparent volcanic construction, such as that shown in section *C*, Figure 12. The magnetizations of such features are plotted as triangles in Figure 13 and probably represent minimum values, since these volcanic features are unlikely to be very linear. The other estimates (rectangles) were obtained from sections of blocky fault-dominated topog-

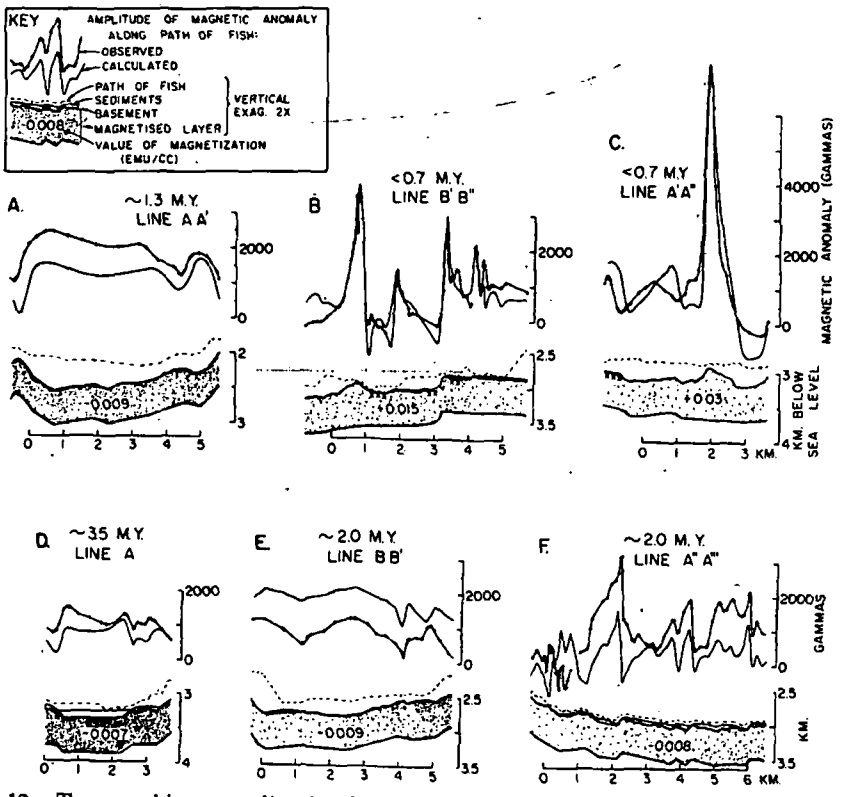

Fig. 12. Topographic anomalies in the magnetic field at the Fish, observed (line with crosses) and calculated (bare line). Calculations were made at points along the Fish path assuming a layer of constant magnetization (grey region, value of magnetization shown). Poor fits occur where basement below sediments is not known (*crosses at top of layer*) or only poorly known, e.g., parts of section *B*. Longer-wavelength variation in section *F* may be related to short events in the *Cox* [1969] reversal time scale.

mall, since the Fish was towed
tom. Among the geometrical
into the model, the assump-
ographic linearity is the most
linearity will cause our esti-
v.

all the estimates of magneti-
respect to their ages derived
velength sea floor spreading
ified in Figure 3 and Table 1.
s in Figure 13 correspond to
es of apparent volcanic con-
s that shown in section C,
gnetizations of such features
ngles in Figure 13 and proba-
mum values, since these vol-
unlikely to be very linear.
s (rectangles) were obtained
locky fault-dominated topog-

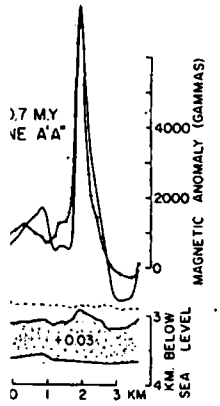

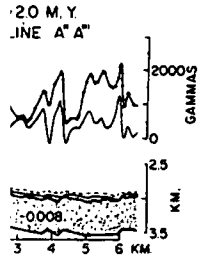

ish, observed (line with
nts along the Fish path
gnetization shown). Poor
t top of layer) or only
n in section F may be

raphy and therefore may be better measures of the magnetization of the fabric of the sea floor. However, many of the block tops also included peaks and irregular sections of constructional appearance. Their moderate magnetizations suggest that the bulk magnetization decreases quite rapidly during the first few hundred thousand years, similar to the rapid initial decrease noted by *Irving et al.* [1970] for surface samples. This decrease is presumably due to chemical alteration, as reported by *Marshall and Cox* [1972], although they expected the process to proceed more slowly.

The open rectangles in Figure 13 indicate magnetization of the sediment-covered steps in the central valley. These are the lowest values measured. These steps apparently received their sediments from turbidity currents while they still occupied the valley floor. Thus it seems quite likely that the volcanic rock forming the basement of these steps was at least partly intruded into the sediment, as it must be at the present time in the southern valley, where sediment drowns the spreading center. *Cox and Doell* [1962] and *Marshall and Cox* [1971] have shown that basalt bodies which cooled slowly have a much lower bulk magnetization than bodies which cooled quickly (in sea water, for instance). The blanket of sediment should slow the cooling process and thus cause a lower bulk magnetization. In this way, the turbidite flooding of the central valley may account for the unusually low value of average magnetization for the central anomaly rocks at the Gorda: in order to fit the central anomaly measured at the sea surface over most spreading centers, the magnetization of rocks in the center

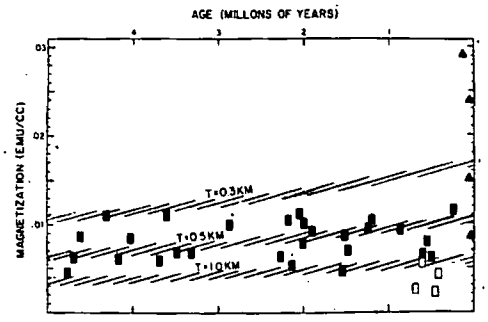

Fig. 13. Strength of bulk magnetization of topographic features, estimated by matching short-wavelength magnetic anomalies, as shown in Figure 12. Triangles are values for volcanic peaks; rectangles are for sections of fault-dominated topography; open rectangles are for sedimented steps. Ages were obtained from positions of reversal boundaries as identified in Figure 3. Slash lines show approximate magnetization required for the magnetic layer if it is assumed to be uniformly magnetized and to have a thickness T. Values best fit the line indicating a thickness of about 0.5 km.

TABLE 1. Locations and Widths of Boundaries of Normal Polarity Blocks Measured along Track *AA'* and its Westward Extension

Perpendicular Distance from Spreading Center, km		Epoch	Event	Anomaly Number
		Slow Spreading: 12 mm/yr		
0	8.8 (+0.2, - 0.5)	Brunhes	-	1
10.4 (+0.2, - 0.5)	11.4 (±0.2)	Matuyama	Jaramillo	
18.8 (±0.1)	21.2 (±0.1)	Matuyama	Gilsa	2
		Fast Spreading: 37 mm/yr		
37.0 (±1.0)	51.7 (±0.1)	Gauss		
53.9 (±0.1)	56.1 (±0.2)	Gauss	Kaena	
59.8 (±0.1)	68.8 (±0.3)	Gauss	Mammoth	
71.5 (±0.2)	72.2 (±0.2)	Gilbert	Possible new event	
77.6 (±0.2)	78.7 (±0.2)	Gilbert	Possible new event	
86.8 (±0.2)	90.7 (±0.3)	Gilbert	Cochiti	3.1
98.2 (±0.1)	103.8 (±0.2)	Gilbert	Nunivak	3.2
109.7 (±0.1)	111.9 (±0.1)	Gilbert		3.3
115.9 (±0.1)	124.6 (±0.1)	Gilbert		3.4

Anomaly names follow *Cox* [1969]; anomaly numbers follow *Pitman et al.* [1968] and *Klitgord et al.* [1972].

must be twice that of rocks in the flanks, while here it need only be about 50% higher. *Larson et al.* [1972] used this mechanism to account for the lack of magnetic anomalies in the sediment-filled basins of the Gulf of California.

Thickness of magnetic layer. Whereas the short-wavelength anomalies give the magnetization of individual topographic features, the long-wavelength anomalies give a measure of the total amount of magnetic material present in the normal and reversed blocks. In particular, the amplitude of the long-wavelength anomaly indicates the thickness of a uniformly magnetized magnetic layer, given the strength of magnetization or vice versa. We modeled the anomalies measured at the surface ship by assigning a layer thickness and then adjusting the magnitude of the magnetization to fit the observations. The slash lines in Figure 13 show the magnetizations required for various layer thicknesses. The figure shows that, if the entire magnetic layer can be assumed to be magnetized with the same strength as the topographic features, the layer is about 0.5 km thick. *Talwani et al.* [1971] used a similar method on sea surface anomalies at the Reykjanes ridge and reached a similar conclusion for the thickness.

This estimate of layer thickness is derived by assuming a single layer of constant magnitude magnetization overlying nonmagnetic material. In fact, in all but very young crust, magnetization may increase with depth near the top of the layer because of chemical weathering of surface materials by sea water. Furthermore, the magnetization probably decreases gradually below some depth as heat effects and percentage of intruded material increase. The value of 0.5 km derived above should be thought of as the thickness of an equivalent layer of constant magnitude magnetization.

Magnetic Polarity Reversals

The polarity of magnetization of the basement is clearly shown in the near bottom magnetic record both by the sign of the long-wavelength component of the anomaly and by the polarity of the magnetization of topographic features whenever a distinctive topographic anomaly was present. Models were made to locate the reversals and to study the transition zones between oppositely polarized blocks.

Locations of reversal boundaries. The long line across the western flank, partly shown in Figure 11, crossed crust from 0 to 5 m.y. in age. We modeled the magnetization by a set of uniformly magnetized normally and reversely polarized blocks connected by smooth transition zones, such as that shown in Figure 11.

The locations of the zero crossings of the transition zones were found by trial and error fitting of the calculated magnetic anomalies to those observed. The locations that give the best fit are listed in Table 1, along with estimates of the amounts by which they can be displaced before the fit obviously deteriorates. In Figure 3 the best fit reversal locations were plotted versus their age according to the Cox [1969] time scale, and two straight lines were drawn through them by eye. The deviation of points from the lines may indicate errors in navigation, minor spreading rate changes, or errors in the time scale ages. The last appears to be the case for the events in anomaly 3 (3.8 to 4.8 m.y.), where normal intervals in the Cox time scale are systematically too long in duration, but reversed intervals are too short.

Models for the reversal transition zones. In usual sea floor spreading models, blocks of oppositely polarized material are separated by abrupt boundaries. This model, when observed from near the ocean floor, would give rise to very large peaked edge effects at the reversal boundaries. The actual boundary anomalies observed were much wider and smoother, requiring a model with a gradual transition from one polarity to the other. We therefore modeled each reversal boundary as a set of narrow blocks, each with its own uniform magnetization, which changed from block to block in such a way as to approximate a smooth curve (a cosine curve from 0 to π). Examples of such models are shown in Figures 11 and 14. A transition width W was arbitrarily defined as the width of the narrowest zone in which 90% of the magnetization transition occurs.

Since the width of the transitions has very interesting implications for the spreading process, we wished to obtain an estimate of W. Preliminary comparisons with near-bottom models such as that in Figure 11 showed that W must be greater than 1 km and less than 5 km, but more precise estimates were difficult to obtain because of the domination of short-wave-

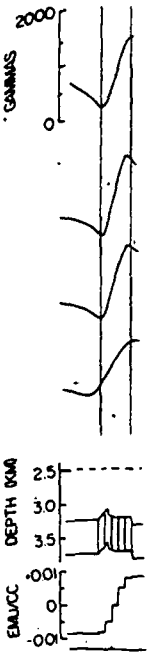

Fig. 14
were con
varying
tions in
anomalie

length topogr
lem we conti
of 2.5-km de
and Klitgord
data with an
varying W.
for $W = 1.4$,
also used). In
the effects of
to-trough widt
for a narrow
shape of the a
in its size with
A close study
differences in
2.1 km, altho
nitely require
discussion tha
2.1 km. Howe
about 1.5 to 3

Significance
The width of
studied above
tion of two eff

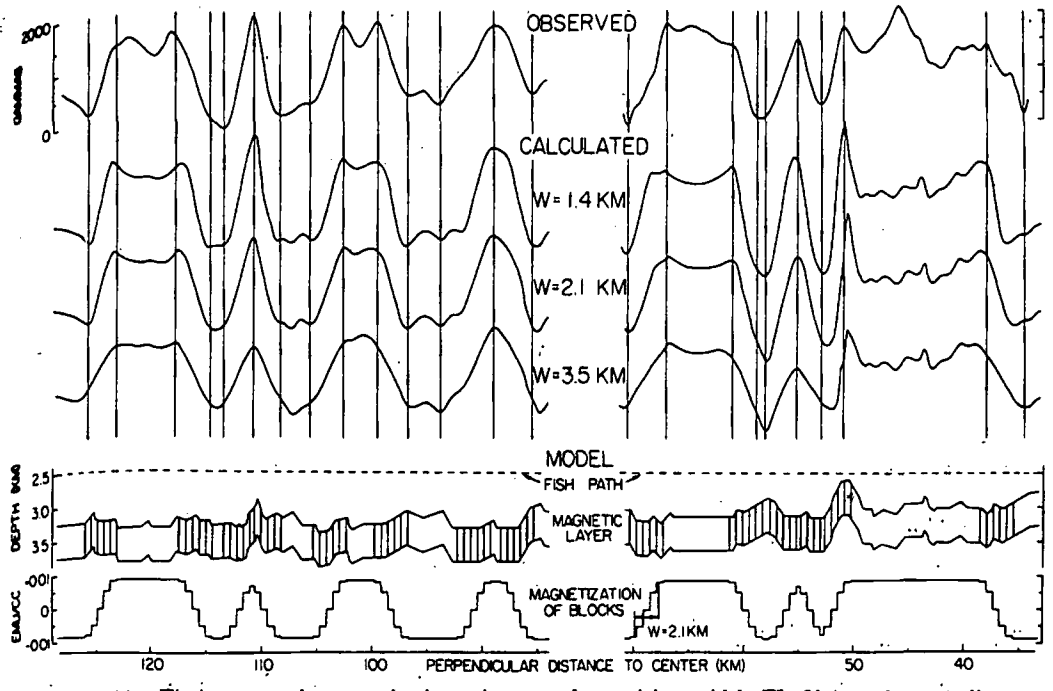

Fig. 14. Fitting procedure to obtain estimates of transition width W. Observed anomalies were continued upward to a plane at 2.5 km depth. Theoretical models were calculated for varying W. The model for $W = 2.1$ km is shown. Best fit widths are chosen from subtle variations in peak-to-trough width, shape, and for narrow anomalies, height relative to neighboring anomalies. Vertical lines are placed to help in peak and trough comparisons.

length topographic effects. To lessen this problem we continued the data upward to a plane of 2.5-km depth, using the method of *Parker and Klitgord* [1972]. We then compared the data with anomalies produced by models with varying W. Figure 14 shows this comparison for $W = 1.4$, 2.1, and 3.5 km ($W = 2.8$ km was also used). In regions of widely spaced reversals, the effects of varying W are best seen in peak-to-trough widths of individual transitions, while for a narrow event they are best seen in the shape of the anomaly (square or rounded) and in its size with respect to neighboring anomalies. A close study of Figure 14 with these subtle differences in mind suggest a best fit to $W = 2.1$ km, although some of the transitions definitely require greater or smaller values. In the discussion that follows, we shall assume $W = 2.1$ km. However, the range of real variation, about 1.5 to 3.5 km, should be kept in mind.

Significance of the polarity transition width. The width of the smooth reversal transitions studied above can be attributed to the combination of two effects: (1) the field takes a certain amount of time to complete a reversal, and (2) new material is emplaced over a finite zone around the center of spreading. Since the two effects add to give the final measured width, an estimate of either effect can only be made if the other is known from some independent study. A number of studies have been made of the transition time for reversals. Measuring the magnetization of deep sea sediment cores, *Ninkovich et al.* [1966] estimate that the transition time for the field to decrease in amplitude, reverse in polarity, and increase in amplitude again varies from 2000 to 20,000 years. *Harrison and Somayajulu* [1966], studying a reversal in a deep sea core, estimated that this transition time is about 10,000 years, whereas *Kent et al.* [1973] in a similar study estimated 3800 and 3500 years. *Dunn et al.* [1971] estimate about 10,000 years in a study of two reversals that were recorded by intrusive bodies as they cooled. The actual reversal of the direction of the field may be relatively quick, occurring when the intensity of the field is very low. However, the model used here idealizes the

transition as a smooth decrease to zero of the field intensity in one direction followed by a smooth increase in intensity in the opposite direction, so that the duration of the entire event is of interest.

From the discussion above, the intensity transition in the model should last 3000 to 20,000 years. At 37 mm/yr this accounts for 0.1 to 0.7 km of the transition width W measured above. The remainder of the transition width W_s, about 1.7 km, presumably reflects the process by which magnetic material is added at the ridge crest. It acts as a smearing or smoothing function for temporal changes in the magnetic field as they are recorded spatially in the crust. In particular, polarity reversal events of duration less than about 10,000 years and sinusoidal variations of period less than about 40,000 years will be greatly attenuated. Thus if this region is similar to other regions of similar spreading rate, it seems quite unlikely that the short-wavelength variations observed by *Larson and Spiess* [1970] record fluctuations in the field, as has been suggested.

Numerous crossings of reversals were available in the central slow-spreading province. However, an attempted study similar to that carried out on the flank reversals was not successful. The extremely rough topography, combined with a variable and daring Fish path, combined with the close proximity of the reversals in the Jaramillo–central anomaly section, made transition widths extremely difficult to model.

Models for the emplacement of the magnetic layer. The width of the smoothing function W_s derived above can be used to set limits for the widths over which various processes act at the spreading center. Figure 15 shows variations of a model for emplacement of magnetized crust. They are built on the assumption that, on the average, dikes are emplaced in a normal distribution with standard deviation σ_D about the spreading center and each dike feeds a flow that adds material in a normal distribution with standard deviation σ_F about its feeder. Idealizing the discussion of *Marshall and Cox* [1971], we assumed that all the magnetism is carried by pillow basalts that flowed onto the ocean floor. Thus, physically, the emplacement model includes a continual widening of the crust by dike intrusion, described by σ_D, and a continual addition of magnetized flow material at the surface, described by σ_C. The standard deviation σ_C is a combination of the others ($\sigma_C^2 = \sigma_F^2 + \sigma_D^2$) and reflects the fact that on a given patch of ground the amount of flow material added will depend on both the amount delivered to the vicinity by dikes and the way it is spread out by flows. Details of the model calculation are given in the Appendix.

In Figure 15 the first two models are extremes. The first is a dike model in which $\sigma_D \gg \sigma_F$; i.e., flows are very localized about their dikes. The second is a flow model in which $\sigma_F \gg \sigma_D$; i.e., dike material is added only at the very center and feeds very wide flows. The third model in Figure 15 shows combinations for varying ratios of σ_D/σ_C. The graphs show the transition of average magnetization of the magnetic layer that would be formed near the time of an instantaneous polarity transition.

The graphs contain some interesting phenomena that should be noted. For instance, all the polarity transitions are offset to the right so that the magnetization transition is centered about a location corresponding to a time that is older than the time of occurrence of the polarity reversal that it records. This effect would tend to displace all transitions outward from the center so that the central anomaly would always be too wide. For the pure dike model the effect is negligible, but for the pure flow model the central anomaly would be too wide by about W_s. Another point of interest is that the shapes of the magnetization transitions are not symmetrical; the steepest part of the transition occurs near its right-hand edge in the dike model and at its left-hand edge in the flow model. This effect may be important when skewness is studied or removed during the manipulation of magnetic anomalies; e.g., *Schouten and McCamy* [1972], *Blakely and Cox* [1972]. However, this parameter is very sensitive to the emplacement model chosen, and the most likely models, combinations with scattered dikes feeding moderate flows, are seen in the bottom graph to be nearly symmetrical.

Perhaps the most interesting phenomenon in the graphs in Figure 15 is the spreading effect of the dike injection model. While the first material emplaced with the new polarity is scattered with a normal distribution of given width, subsequent dike intrusion extends that

Fig. 15. and graph instantane during son wide scatt with a sta ranging flo The third standard d zero point given reve occurs.

region, so tha tained in the width of the in This is not th since in that m is accomplished center and, on out as a rigid b of requiring a for the dike m order to produ tion width. Fo sured above, requires that

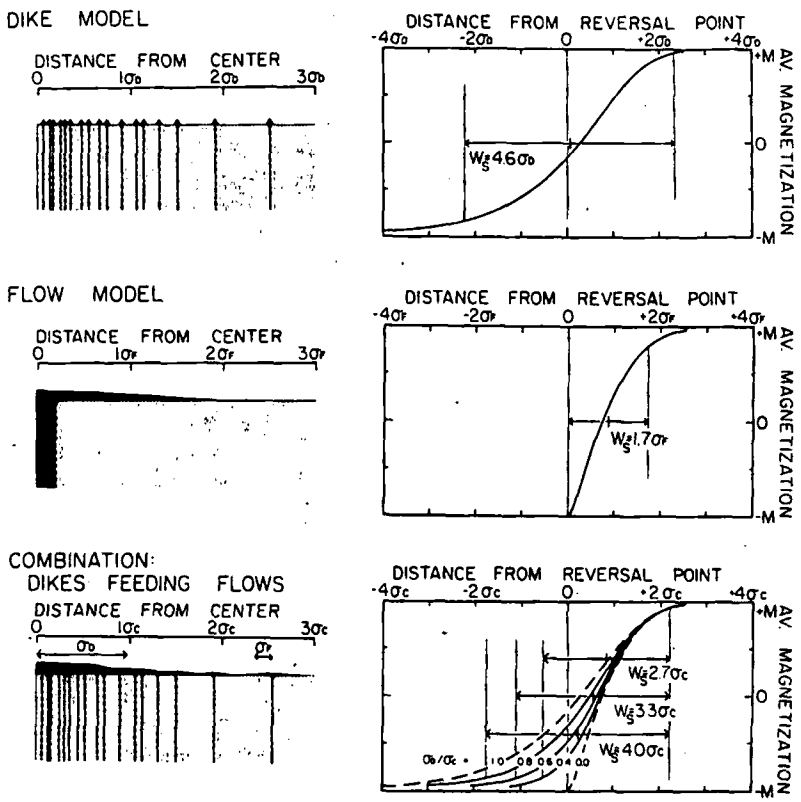

Fig. 15. Schematic models for the emplacement of magnetic material at a spreading center and graphs of the resulting average magnetization in crust formed around the time of an instantaneous polarity reversal. Black areas in models represent new material added to the crust during some interval of time. The top two models are extremes. The dike model assumes a wide scattering of dikes feeding very narrow flows (normally distributed about the center with a standard deviation σ_D). The flow model assumes centralized dikes feeding very wide-ranging flows (which distribute material normally about the center with standard deviation σ_F). The third model is a combination: a scattering of dikes feeding wide flows; σ_C is a combined standard deviation ($\sigma_C^2 = \sigma_F^2 + \sigma_D^2$), which describes the distribution of material added. The zero point in the graphs corresponds to the point where the reversal is expected to be found, given reversal age and spreading rate. W_s is the distance over which 90% of the transition occurs.

region, so that the final transition width contained in the sea floor is much wider than the width of the intrusion center which emplaced it. This is not the case for the pure flow model, since in that model all widening of the sea floor is accomplished by dikes emplaced exactly in the center and, once material is emplaced, it moves out as a rigid block. This difference has the effect of requiring a much narrower spreading region for the dike model than for the flow model in order to produce the same final observed transition width. For example, given the value measured above, $W_s \cong 1.7$ km, the flow model requires that most material was emplaced within 2.0 km of the center. This is a surprisingly narrow zone for such a gross process. However, the equivalent dike model predicts a still narrower zone, requiring that most of the material was emplaced within 0.7 km of the center. Details of these calculations are given at the end of the Appendix.

Our measurement of $W_s \cong 1.7$ km may be applicable to other regions of similar spreading rate. The Deep Tow survey of the East Pacific rise crest (30 mm/yr spreading rate) reported by *Larson* [1971] included two tracks very near the center of spreading. The surface near the center is broken by numerous small linear

rifts spaced 0.2 to 1.0 km apart. Any given flow probably cannot flow farther than the nearest rift in each direction, so that σ_r for the center is probably only about 0.2 km. If the results from the Gorda rise flanks are applicable here, $W_s = 1.7$ km and $\sigma_r = 0.2$ km require a combination model with σ_c about 0.4 km and the entire emplacement region is about 1.6 km wide, narrower than the width of the rifted zone.

It would also be interesting to apply the transition width results to the present Gorda rise spreading center. However, to do this the effect of spreading rate must be considered. *Harrison* [1968] and *Vine and Morgan* [1967], using observations made at the sea surface, reported that the transition width increases with decreasing spreading rate. In a personal communication reported by *Deffeyes* [1970], Vine quantified this relationship that the 'half width of the magnetic resolving power' is inversely proportional to the square root of the spreading rate. Assuming that Vine's half width is linearly proportional to W, and using $W = 2.1$ km for 37 mm/yr, this predicts $W = 3.8$ km for the central province (at 12 mm/yr), and $W_s \cong 3.3$ km. The valley floor topography shown in Figure 5 would probably limit most flows to a total width of 1 km or $\sigma_r \cong 0.3$ km. This fits with a combination model with $\sigma_c \cong 0.85$ km and most material being emplaced in the central 3.5 km, i.e., in the valley floor. This adds credibility to the conclusions reached earlier that each block of the basement that is now in the rift valley walls was originally emplaced in the valley floor and was then sedimented, faulted, moved outward, and uplifted to its present location.

Vertical distribution of magnetization in transition zones. The *Marshall and Cox* [1971] study carries interesting implications for the physical geometry of the transition zones. Their conclusions imply that most of the magnetization of the magnetic layer is carried by basalt that was extruded onto the sea floor and quenched in sea water. Therefore, after a polarity reversal occurs, material extruded and magnetized with the new polarity will overlie material magnetized with the old polarity. The graphs of average magnetization in Figure 15 might be better viewed as cross sections through the magnetic layer, the curves representing the surfaces that separate the new polarity material above from the old polarity below. In the calculated magnetic anomalies such as those in Figures 11 and 14, topographic effects within transitions were not reproduced very well. This misfit may arise because the transitions were modeled by using average magnetization so that a topographic feature on the sea floor at the center of the transition was assigned zero magnetization. The above discussion implies that it should have been assigned a magnetization with the new polarity. A cursory examination of the more obvious topographic anomalies observed within the transition zones indicates that they do generally carry the younger polarity.

Possible short polarity reversal events. In Figure 3 and Table 1, two small positive events are postulated to have occurred during the negative polarity interval 3.3 to 3.7 m.y. in age. These were needed in order to explain medium-wavelength features in the observed magnetics near km 72 and 78 in Figure 11. The older event is centered about 3.55 m.y. and could be modeled very well by superimposing two smooth transitions 1 km apart, implying that it was about 27,000 years in duration. The younger event could not be fitted as easily but appears to be centered about 3.4 m.y., and, judging from the amplitude of the magnetization peak (assuming constant smoothing width), it is of shorter duration than the older event.

The only other unexplained medium-wavelength events that are clearly detected in the magnetic records occurred near 2 m.y. on the east flank (shown in Figure 12F). These probably correspond to the short events in the *Cox* [1969] time scale. Unfortunately, these occur near the time of rotation of the Gorda plate and readjustments of spreading rate, so that their age and duration cannot be deduced.

CONCLUSIONS

In the preceding section we presented data and interpretations of a near-bottom survey made with the deep towed Fish over the Gorda rise. We now wish to reiterate and emphasize our major findings. The spreading on the Gorda slowed down 2 m.y. ago; our study therefore covers phenomena formed during the period of slow (12 mm/yr) spreading and older phenomena, now located on the flanks, that were formed during the period of fast (37 mm/yr) spreading.

The central region includes a deep axial

valley, a typical feature of slow spreading centers. Our detailed study shows that the rift valley topography is very lineated and blocky, suggesting the domination of block faulting during the formation of the gross topographic relief. Turbidite sediments of continental origin can flow into the region and have ponded in the rift valley floor. Similar sediments are also found perched on the tops of fault block steps high in the valley walls more than 1 km above the valley floor. As turbidity currents are unlikely to flow uphill any great distance, we believe that the perched sediments must have been tectonically uplifted by their underlying blocks. Our magnetic studies strengthen this conclusion as they imply that the surface of the oceanic basement was also emplaced primarily in the bottom of the rift valley. To account for these observations we envisage a steady-state model in which the new crust is continually emplaced in the center of the valley floor, is covered by turbidites, and then is faulted and carried outward and upward to form the valley walls.

In the fast-spreading flank regions, our most interesting results arose from our magnetic studies. Our profiles crossed many magnetic polarity reversals, recorded in the crust by the sea floor spreading process. The transition zones between regions of opposite polarity were found to be 1.5 to 3.5 km wide (average about 2.1). This transition width provides a measure of the width over which new material overlapped old during the spreading process. In particular, it implies that on the average most new magnetic material was added within 2 km of the spreading center or that the emplacement zone was about 4 km wide.

We studied some simple models for the emplacement of material at spreading centers, investigating the relationship of various dike and flow distributions to the width of magnetic polarity transition zones produced. We found that flow-dominated models produced transition zones of widths comparable to half the width of the emplacement zone. In contrast, dike-dominated models produced transition zones that were 2.5 times wider. Thus, if the polarity transitions that we measured were formed by a dike-dominated emplacement mechanism, the total emplacement zone may have been only 1.5 km wide, an extremely narrow zone for such a gross process. Geometrical observations at the east Pacific and Gorda rises suggest that the mechanism may well be dike dominated.

Since we were measuring the magnetic field very near the bottom, topographic features produced large distinctive short-wavelength anomalies in our magnetic profiles. We could match many of these anomalies using simple models and from the matches we could estimate the bulk magnetization of many individual topographic features. These values, plotted in Figure 13, show high values (0.02–0.03 emu/cm^3) only in the central, very young crust (age $<$200,000 years), and moderate values (0.005–0.01 emu/cm^3) elsewhere, decreasing slowly with age.

APPENDIX: MATHEMATICAL MODEL FOR EMPLACEMENT OF THE OCEANIC MAGNETIC LAYER

The model assumes that nonmagnetic dikes are intruded with a normal distribution (standard deviation σ_D) about the spreading center. These dikes serve two functions: they increase the width of the crust (i.e., they spread the sea floor), and they feed flows. The surface flows add magnetic material in a normal distribution (standard deviation σ_F) about their feeder dikes. The model is a continuum model, assuming a great many very small dikes, as opposed to other models in the literature that considered the random emplacement of individual large dikes.

The right-hand graphs in Figure 15 show the final distribution of average magnetization in the section of the magnetic layer that was emplaced by the model around the time of an instantaneous polarity reversal. The calculation of these distributions proceeded as follows: at time t_o (the moment of the reversal) a set of marker points $x_i(t_o)$ were identified in the sea floor. Advancing time in small steps, the points were followed as the sea floor spread, moving them outward from the center. The movement outward of a point at $x_i(t)$ during a short time interval Δt is proportional to the amount of dike material emplaced between it and the center during that time. Use $\Phi(x, \sigma)$ to represent the value of a normal distribution of standard deviation at a distance x from its center, $\Phi(x, \sigma) = (2\pi\sigma^2)^{-1/2} \exp -(x^2/2\sigma^2)$. Then the distance traveled by

a point at x_i during Δt is approximately given by

$$\Delta x_i(x_i(t)) \cong 2S\Delta t \int_0^{x_i(t)} \Phi(x, \sigma_D)dx$$

Note that at large distances from the center $\int_0^\infty \Phi dx = \frac{1}{2}$, so that the point moves away at the spreading rate S.

As the points in the sea floor move out from the center, the amount of new magnetic material added between each pair of points during each step in time is calculated and added to the amount collected there since the reversal. The amount added during Δt is calculated as follows: it is assumed that every dike delivers the same amount of material to the surface, so that the amount of material available to flows originating in a unit width source region at a given distance from the center x_s is controlled by the number of dikes emplaced in that region; i.e., it is proportional to $\Phi(x_s, \sigma_D)$. The thickness of new material added at another point x by flows originating in the source region at x_s depends upon the amount of material delivered by the feeder dikes to the source region $\Phi(x_s, \sigma_D)$ and upon the width of the flows that distribute this material, compared with the distance from the source region to the point $\Phi(x_s - x, \sigma_F)$. Thus the total thickness ΔH added during Δt to the point at x can be obtained by integrating over the entire source region:

$$\Delta H(x) = 2ST\,\Delta t \cdot \int_{-\infty}^{\infty} \Phi(x_s, \sigma_D)\Phi(x_s - x, \sigma_F)\,dx_s$$

By writing out the equations for the normal distributions and doing some algebraic shuffling and integration, this equation can be reduced to

$$\Delta H(x) = 2ST\Delta t\Phi(x, \sigma_c)$$

where $\sigma_c^2 = \sigma_D^2 + \sigma_F^2$. Note that the half rate at which cross-sectional area is added to the magnetic layer is ST, where T is the final thickness of the magnetic layer.

During Δt, the cross-sectional area of material added to the region between two points $x_i(t)$ and $x_{i+1}(t)$ centered about x_M is approximately given by $\Delta H(x_M)$ times the momentary distance between the points (this separation increases with time). For each step in time, this amount is added to that collected since the reversal.

The iteration continues until all points of interest leave the central region. The total cross-sectional area of magnetic material collected between each two points is then divided by their final separation distance to give the average thickness of new polarity material, a value that when compared to T gives the average magnetization between those points. The resulting magnetization distribution is plotted in the graphs in Figure 15 for various combinations of σ_F and σ_D.

In the graphs, the transition width of each distribution, W_s, is given in terms of the appropriate σ. Thus from our estimate that $W_s \cong 1.7$ km we can conclude the following for spreading rate 37 mm/yr: (1) If we assume the dike model (i.e., that the magnetic layer was predominantly formed by dikes feeding flows of negligible horizontal extent), the top graph shows that $W_s = 4.6\sigma_D$ and thus $\sigma_D \cong 0.37$ km; i.e., 95% of all material was emplaced within 0.74 km of the center. (2) If we assume the flow model (i.e., that the magnetic layer was predominantly formed by broad flows with dike intrusion only very near the center), the middle graph shows that $W_s = 1.7\sigma_F$ and thus $\sigma_F = 1.0$ km, i.e., 95% of the flow material was added within 2.0 km of the center. These are upper bounds for σ_D and σ_F; in combination models they must be even smaller. For example, when $W_s = 1.7$ km and $\sigma_D/\sigma_c = 0.6$, the bottom graph shows that $W_s = 3.3\sigma_c$ and thus $\sigma_c = 0.5$ km; or $\sigma_D = 0.3$ km and $\sigma_F = 0.4$ km. Since σ_c is the standard deviation of the total distribution of magnetized material, 95% of all material is emplaced within 0.8 km of the center. It is assumed that purely intrusive additions at any point in the formation of the crust will not be well detected magnetically. If important, their effect is to extend the crust, so that the widths given by the models are too large.

Acknowledgments. Barbara Faust, Peggy Larson, and Gordon Miller helped process the original data, and Gordon Miller helped develop many of the computer programs used. Many of the ideas were developed during discussions with Allan Cox, Kim Klitgord, Roger Larson, Monte Marshall, H. W. Menard, Peter Molnar, R. L. Parker, and Fred N. Spiess. Don Heinrichs and Jim Phipps at Oregon State University supplied help and en-

couragement in
ments. The manu
suggestions of All
W. Hawkins, Rog
W. Menard, Peter
assistance and co
M. D. Benson, J.
G. E. Forbes of t
Deep Tow Group
the crew of RV
during the collectic
This work was s
Research and the

Atwater, Tanya, faulting on the 731, 1968.
Belderson, R. H., and A. R. Stubb *a Picture Atlas*, Netherlands, 197
Blakely, R. J., a geomagnetic p Cenozoic, *J. Ge*
Bolt, B. A., C. Seismological central and nort cino escarpment 1725–1767, 1968.
Chase, T. E., H. Bathymetry of *Rep. Ser., TR-9* of Calif., San Di
Cox, Allan, Geon 237–245, 1969.
Cox, Allan, and F of the basalt in *Geophys. Res.*, 6
Deffeyes, K. S., T feature of the *Continents and* and B. L. Sm versity Press, N
Duncan, J. R., J glacial sedimen sea environme Oregon State
Dunn, J. R., M. F Paleomagnetic magnetic field,
Fowler, G. A., a and sedimentol deep-sea floor, *J. Mar. Res.*, 28,
Harrison, C. G. omaly patterns *Res.*, 73, 2137–21
Harrison, C. G. Behavior of t a reversal, *Nat*
Heinrichs, Donal

courgement in studies of the step-top sedi-ments. The manuscript was improved following suggestions of Allan Cox, C. G. A. Harrison, J. W. Hawkins, Roger Larson, Peter Lonsdale, H. W. Menard, Peter Molnar, and Fred Spiess. The assistance and cooperation of D. E. Boegeman, M. D. Benson, J. T. Donovan, G. Miller, and G. E. Forbes of the Marine Physical Laboratory Deep Tow Group and of Captain Hansen and the crew of RV *Thomas Washington* were vital during the collection of the data.

This work was supported by the Office of Naval Research and the National Science Foundation.

REFERENCES

Atwater, Tanya, and John D. Mudie, Block faulting on the Gorda rise, *Science, 159*, 729–731, 1968.

Belderson, R. H., N. H. Kenyon, A. H. Stride, and A. R. Stubbs, *Sonographs of the Sea Floor, a Picture Atlas*, 185 pp., Elsevier, Amsterdam, Netherlands, 1972.

Blakely, R. J., and A. Cox, Evidence for short geomagnetic polarity intervals in the early Cenozoic, *J. Geophys. Res., 77*, 7065–7072, 1972.

Bolt, B. A., C. Lomnitz, and T. V. McEvilly, Seismological evidence on the tectonics of central and northern California and the Mendocino escarpment, *Seismol. Soc. Amer. Bull., 58*, 1725–1767, 1968.

Chase, T. E., H. W. Menard, and J. Mammerickx, Bathymetry of the north Pacific, Chart 4, *Tech. Rep. Ser., TR-9*, Inst. of Marine Resour., Univ. of Calif., San Diego, 1970.

Cox, Allan, Geomagnetic reversals, *Science, 163*, 237–245, 1969.

Cox, Allan, and R. R. Doell, Magnetic properties of the basalt in hole EM7, Mohole project, *J. Geophys. Res., 67*, 3997–4004, 1962.

Deffeyes, K. S., The Axial valley: A steady-state feature of the terrain, in *The Megatectonics of Continents and Oceans*, edited by H. Johnson and B. L. Smith, pp. 194–222, Rutgers University Press, New Brunswick, N. J., 1970.

Duncan, J. R., Jr., Later Pleistocene and postglacial sedimentation and stratigraphy of deep-sea environments off Oregon, Ph.D. thesis, Oregon State Univ., Corvallis, 1968.

Dunn, J. R., M. Fuller, H. Ito, and V. A. Schmidt, Paleomagnetic study of a reversal of the earth's magnetic field, *Science, 172*, 840–845, 1971.

Fowler, G. A., and L. D. Kulm, Foraminiferal and sedimentological evidence for uplift of the deep-sea floor, Gorda rise, northeastern Pacific, *J. Mar. Res., 28*, 321–329, 1970.

Harrison, C. G. A., Formation of magnetic anomaly patterns by dyke injection, *J. Geophys. Res., 73*, 2137–2142, 1968.

Harrison, C. G. A., and B. L. K. Somayajulu, Behavior of the earth's magnetic field during a reversal, *Nature, 212*, 1193–1195, 1966.

Heinrichs, Donald F., More bathymetric evidence for block faulting on the Gorda rise, *J. Mar. Res., 28*, 330–335, 1970.

Irving, E., J. K. Park, S. E. Haggerty, F. Aumento, and B. Loncarevic, Magnetism and opaque mineralogy of basalts from the mid-Atlantic ridge at 45°N, *Nature, 223*, 974, 1970.

Kent, D. V., N. D. Opdyke, and W. Lowrie, Details of magnetic reversals recorded in a high deposition rate deep sea core (abstract), *Eos Trans. AGU, 54*, 254, 1973.

Klitgord, K. D., J. D. Mudie, and W. R. Normark, Magnetic lineations observed near the ocean floor and possible implications on the geomagnetic chronology of the Gilbert epoch, *Geophys. J. Roy. Astron. Soc., 28*, 35–48, 1972.

Larson, P. A., J. D. Mudie, and R. L. Larson, Magnetic anomalies and fracture-zone trends in the Gulf of California, *Geol. Soc. Amer. Bull., 83*, 3361–3368, 1972.

Larson, Roger L., Near-bottom geologic studies of the East Pacific Rise crest, *Geol. Soc. Amer. Bull., 82*, 823, 1971.

Larson, Roger L., and Fred N. Spiess, East Pacific Rise crest: A near-bottom geophysical profile, *Science, 163*, 68–71, 1969.

Loncarevic, B. D., C. S. Mason, and D. H. Matthews, Mid-Atlantic ridge near 45° north, 1, The Median Valley, *Can. J. Earth. Sci., 3*, 327–349, 1966.

Luyendyk, B. P., Origin and history of abyssal hills in the northeast Pacific Ocean, *Geol. Soc. Amer. Bull., 81*, 2237–2260, 1970.

Marshall, Monte, and Allan Cox, Magnetism of pillow basalts and their petrology, *Geol. Soc. Amer. Bull., 82*, 537–552, 1971.

Marshall, Monte, and Allan Cox, Magnetic changes in pillow basalt due to sea floor weathering, *J. Geophys. Res., 77*, 6459–6469, 1972.

Matthews, D. J., *Tables of the Velocity of Sound in Pure Water and Sea Water for Use in Echo Sounding and Sound-Ranging, H. D. 282*, The Hydrographic Department, Admiralty, London, 1939.

McManus, D. A., Physiography of Cobb and Gorda rises, northeast Pacific Ocean, *Geol. Soc. Amer. Bull., 78*, 527–546, 1967.

Menard, H. W., Jr., Deep-sea channels, topography and sedimentation, *Bull. Amer. Assoc. Petrol. Geol., 39*, 236–255, 1955.

Menard, H. W., and J. Mammerickx, Abyssal hills, magnetic anomalies and the East Pacific Rise, *Earth Planet. Sci. Lett., 2*, 465–472, 1967.

Moore, G. W., and G. F. Sharman, Summary of Scan Site 4, *Initial Reports of the Deep Sea Drilling Project*, vol. 5, pp. 761–773, U.S. Government Printing Office, Washington, D.C., 1970.

Ninkovich, Dragoslav, N. Opdyke, B. C. Heezen, and J. H. Foster, Paleomagnetic stratigraphy, rates of deposition and tephrachronology, in north Pacific deep-sea sediment, *Earth Planet. Sci. Lett., 1*, 476–492, 1966.

Northrop, J., H. W. Menard, and F. K. Duennebier, Seismic and bathymetric evidence of a fracture zone on Gorda ridge, *Science, 161*, 687–690, 1968.

Parker, R. L., and K. D. Klitgord, Magnetic upward continuation from an uneven track, *Geophysics, 37*, 662, 1972.

Parker, R. L., J. D. Mudie, and R. S. Howard, Another method for calculating magnetic anomalies, *Ref. 73-2*, 11 pp., Scripps Inst. of Oceanogr., Univ. of Calif., La Jolla, 1973.

Pitman, W. C., III, E. M. Herron, and J. R. Heirtzler, Magnetic anomalies in the Pacific and sea-floor spreading, *J. Geophys. Res., 73*, 2069–2086, 1968.

Raff, A. D., and R. G. Mason, Magnetic survey off the west coast of North America, 40°N latitude to 52°N latitude, *Geol. Soc. Amer. Bull., 72*, 1267–1270, 1961.

Reilly, W. I., Use of the international system of units (SI) in geophysical publications, *N. Z. J. Geol. Geophys., 15*, 148–156, 1972.

Shor, G. G., Jr., P. Dehlinger, H. K. Kirk, and W. S. French, Seismic refraction studies off Oregon and northern California, *J. Geophys. Res., 73*, 2175–2194, 1968.

Schouten, H., and K. McCamy, Filtering marine magnetic anomalies, *J. Geophys. Res., 77*, 7089–7100, 1972.

Silver, E. A., Tectonics of the Mendocino triple junction, *Geol. Soc. Amer. Bull., 82*, 2965–2978, 1971.

Spiess, F. N., and J. D. Mudie, Small scale topography and magnetic features, in *The Sea*, vol. 4, edited by A. E. Maxwell, pp. 205–250, Interscience, New York, 1971.

Talwani, M., C. C. Windisch, and M. G. Langseth, Jr., Reykjanes ridge crest: A detailed geophysical study, *J. Geophys. Res., 76*, 473–517, 1971.

Tobin, D. G., and L. R. Sykes, Seismicity and tectonics off the northeast Pacific Ocean, *J. Geophys. Res., 73*, 3821–3845, 1968.

van Andel, Tj. H., and C. O. Bowin, The Mid-Atlantic ridge between 22° and 23° north latitude and the tectonics of mid-ocean rises, *J. Geophys. Res., 73*, 1279–1298, 1968.

Vine, F. J., Spreading of the ocean floor: New evidence, *Science, 154*, 1405–1415, 1966.

Vine, F. J., Magnetic anomalies associated with mid-ocean ridges, in *The History of the Earth's Crust, A Symposium*, edited by R. H. Phinney, pp. 73–89, Princeton University Press, Princeton, N.J., 1968.

Vine, F. J., and W. J. Morgan, Simulation of mid-ocean ridge magnetic anomalies using a random injection model (abstract), in Abstracts for 1967, *Geol. Soc. Amer. Spec. Pap. 115*, p. 228, 1967.

Von Herzen, R. P., Ocean floor heat-flow measurements west of the United States and Baja California, *Marine Geol., 1*, 225–239, 1964.

Wesser, O. E., Lithologic summary, *Initial Reports of the Deep Sea Drilling Project*, vol. 5, pp. 569–620, U.S. Government Printing Office, Washington, D.C., 1970.

(Received May 4, 1973.)

28 March 1980, Volume 207, Number 4438 SCIENCE

important pages missing - need to get these copied

East Pacific Rise: Hot Springs and Geophysical Experiments

RISE Project Group:
F. N. Spiess, Ken C. Macdonald, T. Atwater, R. Ballard
A. Carranza, D. Cordoba, C. Cox, V. M. Diaz Garcia
J. Francheteau, J. Guerrero, J. Hawkins, R. Haymon
R. Hessler, T. Juteau, M. Kastner, R. Larson, B. Luyendyk
J. D. Macdougall, S. Miller, W. Normark, J. Orcutt, C. Rangin

Summary. Hydrothermal vents jetting out water at 380° ± 30°C have been discovered on the axis of the East Pacific Rise. The hottest waters issue from mineralized chimneys and are blackened by sulfide precipitates. These hydrothermal springs are the sites of actively forming massive sulfide mineral deposits. Cooler springs are clear to milky and support exotic benthic communities of giant tube worms, clams, and crabs similar to those found at the Galápagos spreading center. Four prototype geophysical experiments were successfully conducted in and near the vent area: seismic refraction measurements with both source (thumper) and receivers on the sea floor, on-bottom gravity measurements, in situ magnetic gradiometer measurements from the submersible *Alvin* over a sea-floor magnetic reversal boundary, and an active electrical sounding experiment. These high-resolution determinations of crustal properties along the spreading center were made to gain knowledge of the source of new oceanic crust and marine magnetic anomalies, the nature of the axial magma chamber, and the depth of hydrothermal circulation.

In April 1976 a group of ocean-oriented earth scientists gathered in La Jolla to discuss ways in which newly available capabilities for detailed studies of the sea floor, particularly manned small submersibles, might best be further developed and used in the Pacific Ocean (*1*). Although most of those at the meeting were from U.S. institutions, there were also representatives from France, which has operational deep submersibles, and Mexico, which has a number of potentially interesting offshore areas. An outcome of this meeting was the inception of the Rivera Submersible Experiments (RISE) program, whose results are the subject of this article.

The plate tectonic model of the earth's crust has focused the attention of marine geologists on the oceanic edges of the plates—the rise crests, transform faults, and trenches—as the regions in which investigations would be most likely to lead to an improved understanding of fundamental geological processes. The existence of exposed, small-scale phenomena at depths easily reached by today's submersibles led us to concentrate on the rise crests as particularly informative sites. Here one can observe the creation of new crust, phenomena relevant to the beginning of crustal motion, metallogenesis, hydrothermal effects, and new types of benthic biological communities. These regions have been the focus of fine-scale investigations with unmanned systems for many years (*2–5*) while more recently the FAMOUS project (*6–9*) and investigations of the Galápagos spreading center (*10*) have included major submersible programs as well.

The principal technical aspect in which the RISE program differed from the FAMOUS and Galápagos spreading center projects was a thrust to develop and exploit geophysical measurement capabilities which the submersibles and unmanned vehicles at that time did not possess. The result was a plan that emphasized physical measurements with complementary geological observations and sampling. Four geophysical experiments would be conducted to provide in situ measurements of rock magnetization; measurements of elastic (sound) wave propagation over short, shallow paths in the sea floor; very accurate gravity measurements (10 to 100 times as accurate as measurements made at the sea surface); and measurements of very low-frequency (0.2 to 2 hertz) electromagnetic propagation through the sea-floor material. The possibility of directly measuring crustal strain patterns was discussed initially but deferred in a later decision.

Our long-range goal is to investigate sites representative of the full range of known spreading rates (and related different morphologies) beyond the 20 to 40 millimeters per year characteristic of the Mid-Atlantic Ridge. The work reported here was carried out on the East Pacific Rise crest at 21°N (Fig. 1), where the Pacific and Rivera plates are separating at about 60 mm/year. This leaves for the fu-

F. N. Spiess, K. C. Macdonald, C. Cox, J. Hawkins, R. Haymon, R. Hessler, M. Kastner, J. D. Macdougall, S. Miller, and J. Orcutt, Scripps Institution of Oceanography, University of California, San Diego, La Jolla 92093; T. Atwater, Department of Earth and Planetary Sciences, Massachusetts Institute of Technology, Cambridge 02139; R. Ballard, Woods Hole Oceanographic Institution, Woods Hole, Massachusetts 02543; A. Carranza and V. M. Diaz Garcia, Centro de Ciencias del Mar y Limnología, Universidad Nacional Autónoma de México, México 20, D.F.; D. Cordoba and J. Guerrero, Instituto de Geología, Universidad Nacional Autónoma de México; J. Francheteau, Centre Océanologique de Bretagne, Centre National pour l'Exploitation des Océans, Brest 29N, France; T. Juteau, Laboratoire de Minéralogie-Pétrographie, Université Louis Pasteur, 67084 Strasbourg Cedex, France; R. Larson, Lamont-Doherty Geological Observatory, Palisades, New York 10964; B. Luyendyk, Geology Department, University of California, Santa Barbara 93106; W. Normark, Office of Marine Geology, U.S. Geological Survey, Menlo Park, California 94025; and C. Rangin, Institut de Géologie, Université de Paris, Paris, France.

0036-8075/80/0328-1421$02.00/0

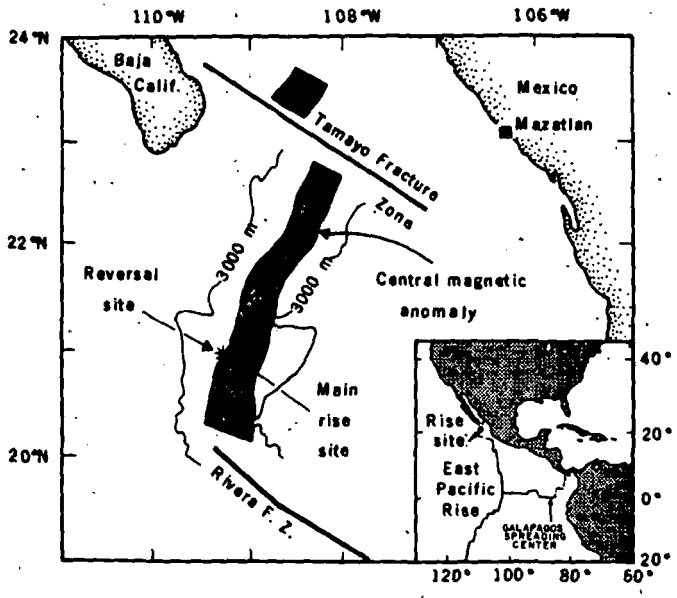

Fig. 1. Location of RISE program research sites in relation to the East Pacific Rise and Galápagos spreading center in the equatorial Pacific Ocean.

ture other locations in the faster range (up to 180 mm/year); they are perhaps more exciting because of their dynamics, but are far from shore, in the equatorial Pacific, and their study is barely feasible today in view of the lack of adequate tending facilities for *Alvin*.

Three previous investigations have been carried out at the 21°N site with an unmanned deep-tow system (*11*) to document fine-scale topography and magnetic field (*3, 12-15*), and as a companion to RISE there was a 1978 expedition, CYAMEX (*16-18*) with the French submersible *Cyana*.

RISE was carried out from late March to early May 1979, using the submersible *Alvin* (*19*), its catamaran-style tender *Lulu* (both operated by Woods Hole Oceanographic Institution), and the research vessels (R.V.) *Melville* and *New Horizon* operated by Scripps Institution of Oceanography. On the first leg, with *Melville*, we used the Scripps deep-tow system (*11*) and Woods Hole's versatile ANGUS camera sled (with temperature sensors). These systems were used to install the necessary transponder net, to carry out additional surveys for detailed dive site selection, and to reconnoiter for signs of hydrothermal activity and additional sulfide mounds of the type seen by the French workers (*17*) during CYAMEX. These preliminaries were all successful and sites suitable for the gravity profile, the short-range seismic experiment, and the sulfide mound studies were all located in an active hydrothermal region.

The principal diving leg was in the southwestern portion of the crestal area already mapped (Fig. 2). In 12 dives we carried out the planned short-range seismic and gravity measurements (with collateral geological observations and rock sampling). As hydrothermal activity was found, we investigated this phenomenon, observing vents with water as hot as 380° ± 30°C and their associated sulfide mounds, as well as cooler (20°C) springs with dense biological assemblages similar to those at the Galápagos spreading center (*10*). While the submersible work was in progress, the low-frequency electromagnetic work and further hot spring mapping with ANGUS were carried out from R.V. *Melville*. On the third leg we concentrated on the magnetic measurements program at the reversal area and performed additional observations and sampling in the sulfide mound-hot spring sites.

Geological Background

The crestal region discussed here, as defined by deep-tow studies (*13, 15*), is a 5-kilometer-wide axial block elevated about 80 meters above the adjacent rise flanks (Fig. 2). Based on the magnetic reversal time scale, the crust at this location formed within the last 100,000 years. The block is bounded by steep, discontinuous, elongate, constructional volcanic slopes which, taken together, show the most pronounced linearity of any features in this region. In the northeast part of the area the block is well defined on both sides, but to the southwest the relief increases to more than 100 m on the northwest side while the southeast boundary becomes indistinct.

Within the block most local relief is less than 75 m and consists of irregular volcanic peaks and ridges with some lineated fault-bounded ridges and troughs (Figs. 2 and 3). Its mean depth decreases from 2650 to 2600 m in 10 along the strike to the southwest, concurrent changes in local relief denced by the occurrence of fewer ear, steep-sided troughs.

On the basis of deep-tow work (*13*, augmented by observations from Cy (*16*), one can distinguish three volcan tectonic zones within the axial blo (Fig. 3). The innermost extrusion reg is flanked by a faulted and fissured exte sional zone, which is in turn bounded abyssal hills formed by back-tilted fau block terrane. These are referred to be as zones 1, 2, and 3, respectively (*16*).

The width of zone 1, which is the are of freshest lava flows and has at most light dusting of sediment, varies fro about 600 to a little over 1000 m. It is rel atively free of faults and fissures and characterized by a discontinuous axi ridge 20 to 80 m high. In the northea this terrane is largely formed of pillow la vas; to the southwest there are extensive lava lakes.

Although the flanking extensional zone (zone 2) is not symmetrical in width or relief on opposite sides of the ris axis, its morphology is distinctly linear. In contrast with the volcanic construc tional features of the extrusion zone, thi region is characterized by open fissure and horsts and grabens with relief of me ters to tens of meters, mostly aligned with the regional orientation of the ris crest. Sediment-free talus slopes here at test to quite recent displacements.

In zone 3, abyssal hill or tilted fault-block terrane, active fissuring appear less common and vertical offsets on a few faults produce linear ridges several kilometers long. The transition between zones 2 and 3, best defined by direct submersible observation, commonly occurs along axially facing fault scarps with large vertical displacements that form the ridges along the edges of the axial block.

Although the relief in zone 3—tens of meters here and at the Galápagos spreading center—contrasts dramatically with the hundreds of meters encountered in the FAMOUS area, the three zones at the different sites are remarkably similar.

Observations from *Cyana* in the adjacent northern (CYAMEX) area confirmed that most of zone 1 consists of pillow lava flows, with sheet flows limited to topographic lows. In the RISE area, however, sheet flows are more extensive and in places form most of the zone, although there is a low axial pillow ridge which is the site of most of the hydrothermal activity. CYAMEX work established that the sheet flows, especially

long the axis, are associated with "fos-" lava lakes that are commonly more than 5 m in depth and hundreds of meters across, including collapse areas that show pillars and lake margins with an apparent layering of alternating glass and crystalline basalt. This pseudolayering consists of chill-zone material and is thought to record lava levels within the lakes during drainback or lateral outflow from these inflation features (*20, 21*). The lava lakes may have been fed by vents that formed the pillow ridge.

The glassy surfaces of fresh submarine basalts and fragile glassy buds and projections on fresh pillow lavas are short-lived and provide an indication of relative age, as does the thickness of accumulated sediments. The extrusion zone is free of sediment cover; glassy surfaces on pillow and sheet flows and projections

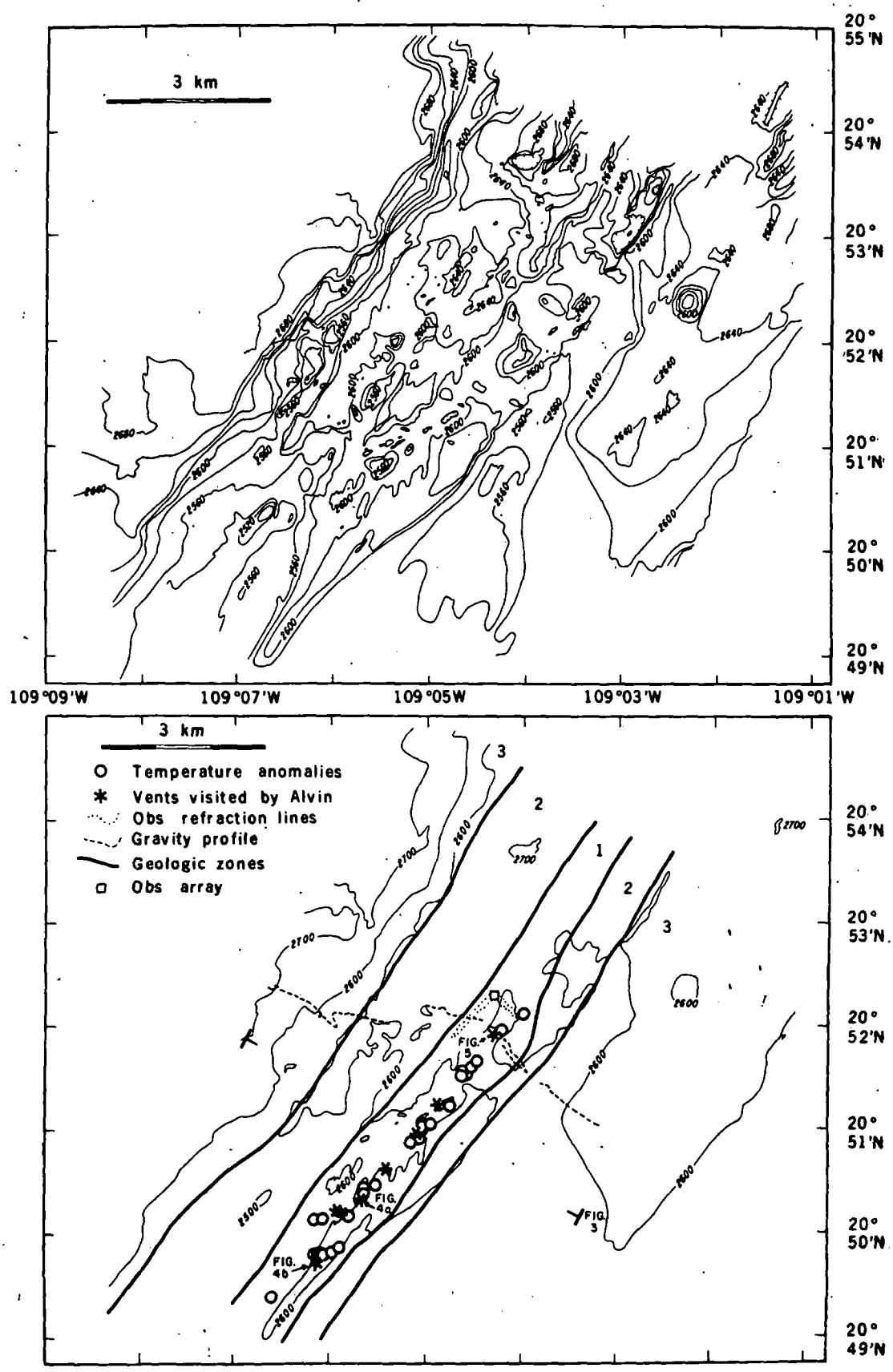

Fig. 2. Bathymetry of the RISE research area as determined with the deep-tow narrow-beam echo sounder with acoustic transponder position control. Depths are in meters, based on the sound velocity profile for the area. Lower section includes outlines of the geologic zones discussed in the text: extrusion region (zone 1), extensional zone (zone 2), and major block faulting (zone 3). Note that the vents occur in a linear zone only 200 to 300 m wide within zone 1. Eight of the 25 vents mapped were examined with *Alvin*.

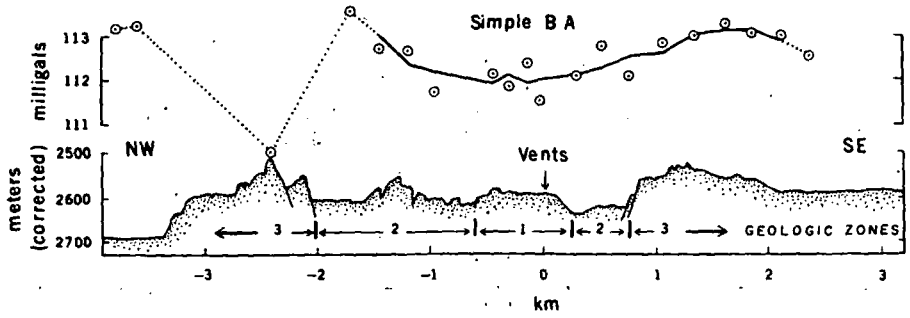

Fig. 3. Bathymetric and gravity profiles across the East Pacific Rise crest. Profile locations and zone designations are given in Fig. 2. Bathymetry is from the narrow-beam sounder of the deep-tow system. The plate boundary axis (0 km) is marked by a central volcano and active hydrothermal venting on this profile. Gravity anomaly (1 mgal = $10^{-6}g$) is derived from measurements made with *Alvin* firmly on the sea floor, corrected for gross topographic effects [Bouguer anomaly (*BA*)]. The solid line is a three-point running mean. The gravity minimum at −2.5 km is caused primarily by local topography, while that at the spreading center (zone 1) is caused by the presence of low-density material in the crust, possibly a shallow magma chamber.

on pillows are clearly observable even under light sediment dusting in the slightly older terrane within the zone. In the extension zone, glassy surfaces on the pillows are much less common, and the sediment thickness increases away from the axis. Near the outer edge of this zone, 40 to 50 percent of the pillow lava relief may be buried. Outside the extension zone, pillow lavas are nearly completely buried locally.

That the sea floor increases in age with distance from the axis is not true everywhere. Anomalously thin sediment cover and relatively fresh sheet flow basalts (which are more quickly buried than pillow flows) were observed in the extension zone and even off the axial block. The freshest flows observed on the westernmost dive, for example, were in the valley west of the axial block and not in the extension zone where the dive started. Apparently, large areas somewhat off-axis can occasionally be buried by extensive sheet flows whose source may be the same magma chamber that feeds zone 1.

Scattered evidence of past hydrothermal activity—primarily colored stain on rocks exposed at scarps—exists throughout the axial block, including one cluster of inactive sulfide mineral mounds (*17*) observed from *Cyana* on the boundary between zones 1 and 2.

Hydrothermal Vents

When this expedition began, the only major example of deep-sea hydrothermal activity was at the Galápagos spreading center, where vents were found in 1976 (*22–25*) characterized by temperature differences of 0.1°C. Subsequent submersible operations documented anomalies of 15° to 20°C and made the exciting discovery of associated dense faunal concentrations (*10, 26*). During RISE, our early measurements of temperature anomalies were quickly followed by submersible views of Galápagos-type vents (dense benthic populations and 20°C water in 2°C surroundings) and then by observations of spectacular hot-water jets with temperatures up to 380° ± 30°C precipitating metal sulfides onto the fresh basalt sea floor at the rise axis.

Twenty-five temperature anomalies indicating vents were documented with the ANGUS camera and temperature probe system, and eight of these were examined during submersible dives. The temperature spikes were confined to a band 100 to 200 m wide and about 6 km long, close to the rise axis in the southern part of the area. In spite of intense exploration with instruments towed near the bottom in the 2 by 10 km central portion of the region under study, no other sources have been located. In contrast to this very linear distribution, the vents at the Galápagos center, while still lying in the central extrusional zone, occur in groups along en echelon lines oriented about 15° to the axial direction.

The vents can be divided into two broad classes: Galápagos-type warm-water vents and sulfide mound hot-water vents, with the first type predominating in the northeast part of the band and the second type predominating at the southwest end (Figs. 2 and 4). That this along-axis zonation is probably transient is suggested by the weathered sulfide mounds found near some of our warm-water vents and found by the French (*17*) somewhat off-axis in the adjacent area to the northeast, where there no longer appears to be any concentrated hydrothermal activity. These two very different surficial manifestations of this phenomenon may be linked in evolutionary fashion, although not enough information is available yet to determine which form would be the older. The southernmost dive of *Alvin* and the lowering of ANGUS suggest that we may have defined the extent of this hydrothermal system to the southwest.

The Galápagos-type vents observed at 21°N emit warm water from hairline cracks and small fissures in the pillow ridge terrane over an area 10 to 30 m across. The venting water is generally clear and temperatures as high as 23°C were recorded close to major outlets. Mixing with the surrounding 1.8°C water is rapid. Directly above one vent of this type, the temperature was about 0.3°C above ambient at an elevation of 10 m, while at a corresponding distance away laterally the anomaly was less than 0.1°C. Inactive sulfide mounds were observed on one *Alvin* dive within a few tens of meters of a warm vent.

The fauna associated with these vent areas are their most visible feature (Fig. 5). On approaching a vent field one usually sees a number of galatheid crabs and then patches of large (25-centimeter long) conspicuous white clams (vesicomyid bivalve *Calyptogena*, tentatively *C. elongata*); the clams are mostly dead in the outlying areas, but, closer in, living animals predominate. The surfaces of the lava pillows usually bear white-tubed serpulid polychaetes, so abundant in some areas that the surfaces seem fully encrusted.

Most prominent in the field, usually clustered densely around a major warm-water vent, are giant tube worms, vestimentiferan pogonophorans (Fig. 5); these are 2 to 3 cm in diameter and up to 3 m tall and have red, gill-like crowns (the only part of the living animal exposed) that may be withdrawn quickly in response to a threat, as from one of the many brachyuran crabs in the vicinity. All of these organisms have also been found at the Galápagos vents. A small, lightly colored eel-like fish, possibly an ophidiid, was seen here for the first time but is more abundant near the hot vents. Two different archaeogastropod limpets seen at Galápagos were also collected here, and photographs show a third living on the shells of live vesicomyids. Some of the animals characteristic of Galápagos (*26*) were not observed here—for example, small anemones and mussels.

The similarity of the East Pacific Rise and Galápagos Rift fauna suggests that these vent communities are widespread and that their species are equipped with sophisticated dispersal mechanisms well suited for the detection of the discontin-

4 (top right). Sketches of hot-water vents locations indicated in Fig. 2, after sketches made by (A) T. Juteau and (B) C. Rangin during their observational dives. The black smoker is similar to that shown on the cover, from which 380° ± 30°C water temperatures were measured. The highest open-ocean hydrothermal temperature measured before this was 22°C at the Galápagos spreading center. Temperatures of water from "snowballs" were measured at ≈ 330°C. Specific rock and water samples discussed in the text are noted.

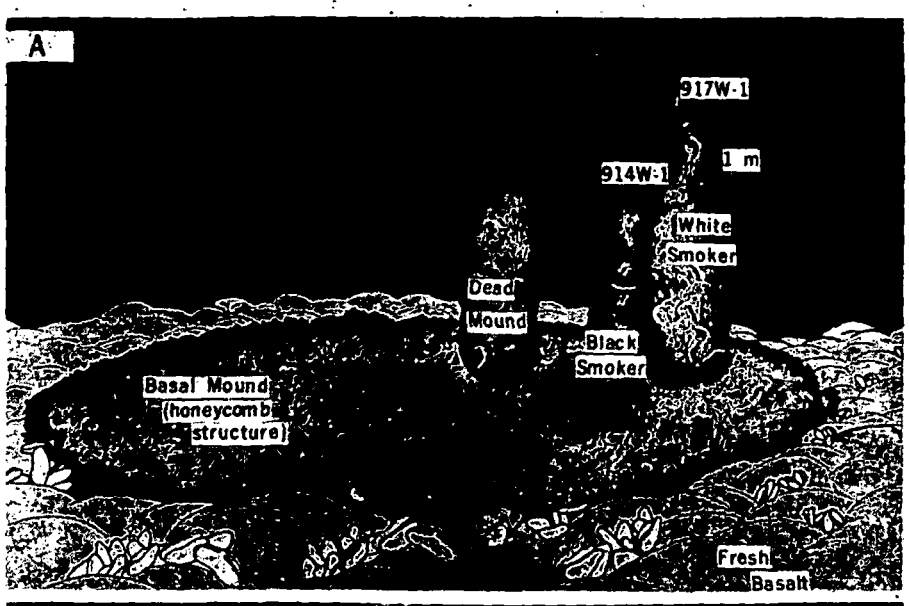

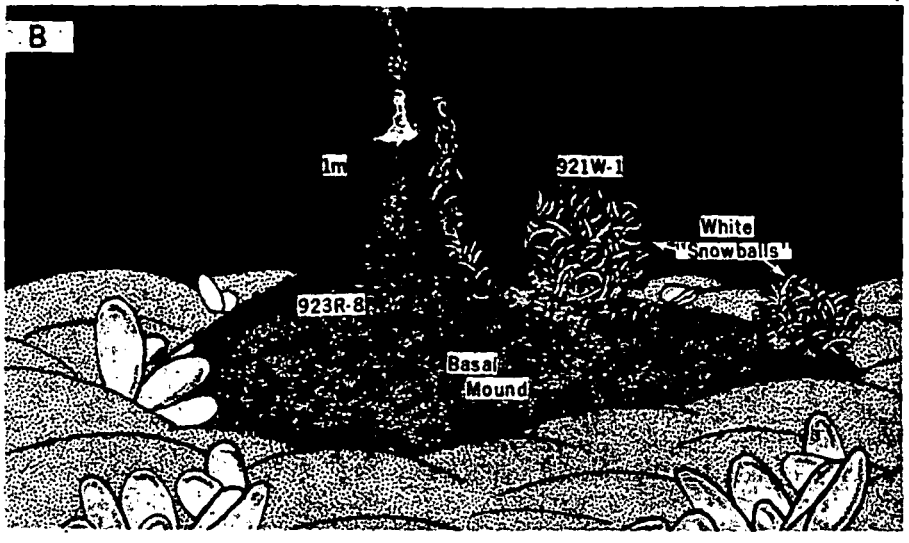

Fig. 5. Photograph of warm vent area at location shown in Fig. 2. Vents of this type emitted water at temperatures up to 23°C from fissues and hairline cracks in fresh pillow lava terrane. Clear vent water is present but not visible in this photograph. Animals in view are giant tube worms (vestimentiferan pogonophorans), clams (vesicomyid bivalve *Calyptogena*), and galatheid crabs. Limpets can be seen attached to some of the clam shells.

nough infor
o determine
older. The
in and one
est that we
it of this hy-
outhwest.
observed at
rom hairline
in the pillow
10 to 30 m
is generally
high as 23°C
ajor outlets.
g 1.8°C water
e vent of this
about 0.3°C
tion of 10 m,
istance away
is less than
nds were ob-
within a few
ent.
th these vent
feature (Fig.
ield one usu-
eid crabs and
25-centimeter
ams (vesico-
, tentatively
mostly dead
closer in, liv-
ne surfaces of
r white-tubed
abundant in
es seem fully

field, usually
major warm-
worms, vesti-
s (Fig. 5);
ter and up to
l-like crowns
g animal ex-
wn quickly in
m one of the
the vicinity.
ve also been
nts. A small,
possibly an
the first time
he hot vents.
opod limpets
so collected
v a third liv-
esicomyids.
acteristic of
t observed
emones and

Pacific Rise
uggests that
widespread
uipped with
anisms well
e discontin-

ous and ephemeral vent conditions. The cause of faunal differences is completely unknown, and biogeographic or ecological mechanisms are equally possible. Unfortunately, the Galápagos and East Pacific Rise are in the same ocean sector; therefore we must wait for more distant discoveries to demonstrate whether the community is worldwide.

In contrast to the biology-dominated Galápagos-type vents, the sulfide mound hot-water vents are most notable for their geological attributes. In these, the water flows out through a limited number of discrete chimneys or stacks, which are superposed on basal mounds built directly on fresh basalt pillows or flows (Fig. 4 and cover). The basal structures, similar to the CYAMEX sulfide mounds, are oxidized to Halloween colors of ocher, orange, and black and have overall lateral dimensions up to 15 by 30 m. They are honeycombed with a cross-cutting network of fossilized worm tubes. Vent constructions 1 to 5 m high rise above the base mound elevations of 2 m or more, and hydrothermal effects (staining, organisms, millimetric manganese coatings) extend tens of meters away from the vents (Fig. 4).

Edifices atop the mounds are classed as either black or white, and those venting particulates are dubbed smokers. The black chimneys are free of organisms. These "organ pipes" are as much as 30 cm in diameter and are occasionally fluted or capped by porous rock. High-temperature waters (> 350°C) spouting at high velocities (meters per second) from black chimneys are either clear or black with suspended particulates, which settle out to form a black sediment around the chimney structures (cover). The white chimneys are covered with worm tubes and thrive with worms and crabs. Structurally, they vary from chimneys to hummocky stacks to spherical "snowballs" (Fig. 4). Warm waters (32° to 330°C), clear to milky with white particulates, emanate gently from these features and deposit white sediment around the chimney bases.

The snowballs are the most striking biological feature associated with the hot

Table 1. Analyses of samples from hot-water vents (see Fig. 4) and deep East Pacific waters. Analyses were performed by J. Gieskes.

Sample	Cl* (per mil)	Ca* (m*M*)	Mg* (m*M*)	H_4SiO_4* (μM)	Li* (μM)	Mn† (ppm)
914W-1	19.17	13.60	52.81	234	31.2	0.320
917W-1	19.17	10.63	52.74	255	28.0	0.320
Deep East Pacific waters (2000 m)	19.17	10.53	53.40	180	27.0	< 0.04

*Analyzed by titration. †Analyzed by colorimetry.

vents. The sponge-like mass of tubes capping these vents is apparently formed by a pink terebillomorph polychaete (possibly a new family), which was observed to dart completely out into the water and then return to its tube. The slopes at the bases of the chimneys are populated with galatheids, brachyurans, and the eel-like ophidiid fish. A very primitive scalpellid barnacle of a new genus (*27*) was collected from such a site. Although the temperature of the exiting water is high (380° ± 30°C), the lateral gradients are so steep that even the chimney-top–dwelling polychaete is probably bathed in far cooler water.

The discovery of the high-temperature vents raises exciting questions for future biological research. This is apparently the first time water temperatures well in excess of the boiling point at 1 atmosphere have been found in open contact with the biosphere. Since high pressure, which permits these superheated conditions, counteracts some of the destructive effects of high temperature on biochemical systems, it is not unreasonable to wonder whether life may exist at higher temperatures here than elsewhere on the earth. A sample of 300°C water did not contain bacteria (*28*), but there is no other evidence on this point and this potentially important question must await further investigation.

Three water samples were taken from the vicinity of the vents (Fig. 4) with equipment originally designed for use from deep-tow (*11*). Since it was not possible to place the bottles exactly in the vents, there was considerable dilution; however, all samples have significantly elevated concentrations of ^3He and total He (*29*), implying a mantle contribution. Covariance of hydrogen and methane with helium in the vent water samples suggests that these gases are also mantle-derived (*30*). Analyses of filtered samples from adjacent black and white vent waters (Table 1) show similar enrichments (calcium, lithium, silicon, and manganese) and depletions (magnesium) relative to normal seawater. These are consistent with the trends observed in Galápagos hydrothermal fluids (*10*) and in basalt-seawater hydrothermal experiments (*31, 32*).

The black vent water precipitates consist primarily of pyrrhotite in hexagonal platelets (Fig. 6), plus pyrite, sphalerite, and Cu-Fe sulfides. Chemical composition of the pyrrhotite indicates a formation temperature of about 300°C, consistent with measured water temperatures. White vent particulates, apparently particles from worm tubes and chimney sulfides, are predominantly pyrite globules, barite rosettes, and ubiquitous amorphous silica.

In the heterogeneous mound and chimney materials the dominant solid phases, identified by x-ray diffraction, scanning electron microscopy, and electron microprobe studies, include sphalerite (ZnS), pyrite (FeS_2), and chalcopyrite ($CuFeS_2$). Other sulfides of zinc, iron, and copper are also present in minor quantities (wurtzite, pyrrhotite, marcasite, bornite, cubanite, and chalcocite). Calcium and barium sulfates (anhydrite, gypsum, and barite) and oxides of iron and silicon (goethite, and amorphous iron oxyhydroxide and silica) are quite common; native sulfur occurs often; and the magnesium silicate, talc, was found on one sample. The most significant vent minerals beyond those found in the CYAMEX inactive mounds (*17*) are pyrrhotite, anhydrite, barite, and talc. Cobalt, lead, silver, cadmium, and manganese were all detected in the CYAMEX samples at concentrations up to a few parts per thousand. The numerous and highly heterogeneous samples of the RISE collection are being analyzed for these and other elements.

The honeycomb rocks from basal mounds consist mainly of sphalerite and pyrite, lesser amounts of chalcopyrite, minor wurtzite and marcasite, amorphous silica and iron oxyhydroxides, and traces of native sulfur. Brittle, platy white precipitates coating the tube

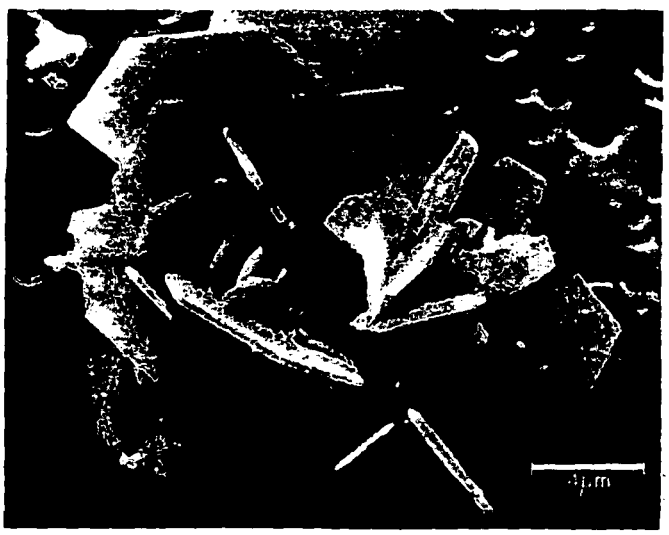

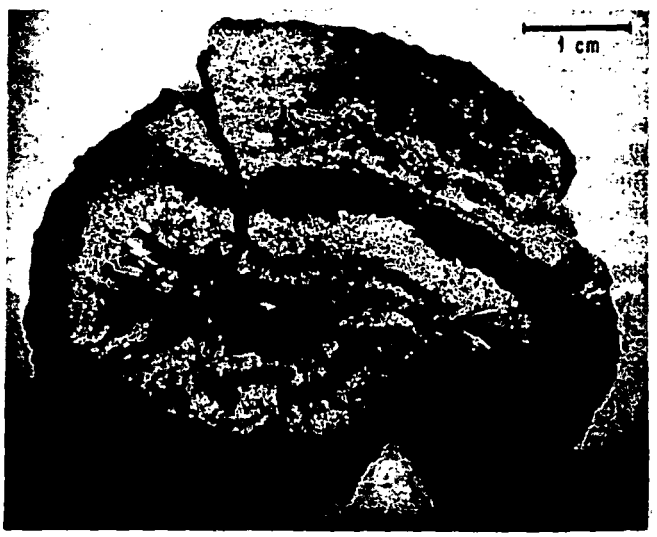

Fig. 6 (left). Scanning electron micrograph of filtered particulate pyrrhotite from hot (380° ± 30°C) waters from the black smoker shown in Fig. 4A and on the cover. Fig. 7 (right). Cross section of a small, typical chimney spire similar to those of Fig. 4A. Note concentric zonations of sphalerite, pyrite, and chalcopyrite. This zonation indicates changes in chemical and physical properties of the vents. Most zones are continuous, but the central zone of sphalerite cuts radially outward across the other zones. Both single-phase zones and zones created by intergrowth of several minerals occur in this sample.

walls of honeycomb samples are assemblages of barite and amorphous silica. Analyses to date have not fully elucidated the relationship between biogenic and inorganic mineral precipitation in the mounds.

Chimney spire samples all show radial changes in composition. Outer walls are often made of anhydrite, gypsum, and magnesium sulfate. Sulfur isotope analyses show that the anhydrite formed in equilibrium with seawater. In the innermost zones, in contact with the hot waters, are layers of coarsely crystalline chalcopyrite or pyrite. A typical small, partially closed spire (from the site shown in Fig. 4B) was studied, and a cross section of this construction revealed alternating bands of sphalerite, pyrite, and chalcopyrite (see Fig. 7). Outermost zones are enriched in amorphous silica. Cubic pyrite, the dominant phase in this sample, forms layers of different crystal sizes, which result in some of the observed banding. The three major phases are found as pure single-phase zones and as intergrowths with one other.

In addition to mound and chimney samples, near-vent sediments and basalt coatings were examined. Fine-grained black sediment scooped from the base of a black smoker contains sphalerite, pyrrhotite, pyrite, and traces of chalcopyrite, wurtzite, and sulfur. The chief phases match particulates suspended in the waters from the black smoker and represent fallout from exiting hot waters. Orange oxidized sediments collected near a dead mound exhibit a similar mineralogy. Mound fragments in these samples have higher pyrrhotite and lower pyrite concentrations than the associated sediments, indicating a rapid breakdown of unstable FeS_{1-x} to Fe-oxyhydroxide during physical disaggregation of mound materials. Rapid conversion of pyrrhotite to pyrite may explain the absence of pyrrhotite in most mound samples, or pyrrhotite may precipitate at higher temperatures within the basalt underneath the mounds. Manganese, which is largely absent from the hydrothermal mounds, precipitates hydrogenously, rather than hydrothermally, on basalt surfaces within a few meters of sulfide structures. Amorphous manganese oxyhydroxides create a dark-colored matting observed on glassy basalts around vents.

Sulfur isotope and petrographic evidence indicates that the concentric banding in active vent spires represents mineralization events that reflect changes in chemical and physical properties of the waters from which the spires precipitate. Fluctuations in temperature, pH, sulfur fugacity, and other physical and chemical parameters must occur as metal-laden solutions reach the basalt-seawater interface and traverse the lengths of the porous sulfide chimneys. These fluctuations, as well as temporal changes in the concentrations of dissolved species in the hydrothermal fluids, probably cause the observed concentric banding and may also produce vertical mineral zoning in chimneys (this possibility has not yet been investigated in detail). Considerable vent-to-vent variation in temperature was observed over relatively short distances, and seawater is undoubtedly drawn under the influence of a pressure gradient through the porous materials of mounds and chimneys to mix with rising low-density hydrothermal fluids. This inward flow of seawater allows organisms to live and grow on some chimneys and accounts for the precipitation of anhydrite in outer chimney zones.

The hydrothermal constructions sampled during the RISE program are mechanically fragile and chemically unstable in the sea floor, and they are therefore presumably ephemeral features. The iron-rich layers commonly overlying basaltic basement in Deep Sea Drilling Project (DSDP) holes (*33, 34*) may contain a component of reworked degradation products from similar vent structures. Sulfides deposited in hydrothermal conduits within the basalt layer may become sealed off from further interaction with seawater and be less susceptible to oxidation; such deposits could be the precursors of ophiolite sulfides.

Petrology of Basalts

The data presented here are based on microprobe and x-ray fluorescence analyses of glass samples collected from *Alvin* in zone 1 and along the gravity profile track of Fig. 2 and samples collected by transponder-navigated dredge hauls in zones 1, 2, and 3. This set of samples constitutes a geochemical profile across the axial region for a distance of about 3 km on each side of the axis of spreading. We wished to look for spatial and temporal variations in magma chemistry and microphenocrysts as well as any variation in magma chemistry that might be related to the morphology of the units sampled.

The glasses are fresh tan sideromelane (basalt glass) with only minor amounts of microphenocrysts of calcium plagioclase, magnesium olivine, and, in a few samples, clinopyroxene. We assume that the glass analyses represent original liquid compositions because of the apparent freshness of the samples and the small size and scarcity of the microphenocrysts. The data suggest that all of the samples experienced minor amounts of crystal fractionation (5 to 20 percent) before their eruption.

Data for the glass samples (vitrophyres) from pillow rinds, sheet flow plates, and pillow buds, as well as microphenocrysts, are summarized in Table 2. Element abundances and ratios are in Figs. 8 and 9. Samples from within about 500 m of the presumed axis of active spreading are all bright fresh glass with little or no Fe-Mn coating. Samples from greater distances have Fe-Mn coatings ranging from thin films to thicknesses of about 0.5 mm. Those with the thicker coatings (for example, > 0.1 mm) typically also have a palagonite rind of about the same thickness as the Fe-Mn crust. The palagonite and Fe-Mn crusts were removed from the glass samples that were analyzed by x-ray fluorescence. Plagioclase is the most common microphenocryst (3 to 10 percent); olivine forms 1 to 5 percent. Clinopyroxene is rare. The plagioclase forms small euhedral unzoned crystals. There is a range in plagioclase composition in individual samples which suggests that some grains are xenocrysts. The olivine is commonly irregular and skeletal in form, apparently the result of crystallization during rapid cooling. On the basis of FeO/MgO ratios of coexisting glass and olivine, the olivine appears to be in equilibrium with the enclosing glass.

Vesicles are rare, but in a few samples there are microvesicles (< 0.5 mm) which may amount to a few tenths of a percent by volume. The vesicles are decorated with sulfides, pyroxene (?), and phyllosilicates.

The samples are olivine tholeiites; all of them plot close to the presumed cotectic in the olivine-plagioclase-pyroxene diagram (Fig. 8). Abundances of K, Ti, P, Ba, Rb, Sr, Ni, and Zr are all typical of ocean ridge tholeiites (*35–37*). The samples are similar to glass samples from the FAMOUS area on the Mid-Atlantic Ridge (Fig. 9) (*37, 38*) and to other East Pacific Rise samples such as those from the CYAMEX area (*39*). The RISE samples have slightly higher values of TiO_2 and FeO*/MgO (FeO* is total iron oxides) and a smaller range of these values than many of the glasses collected on the Mid-Atlantic Ridge (Fig. 9). The limited composition range for the RISE samples collected on the 6-km-long transect suggests that the samples are derived from a common parent magma by fractional crystallization of olivine

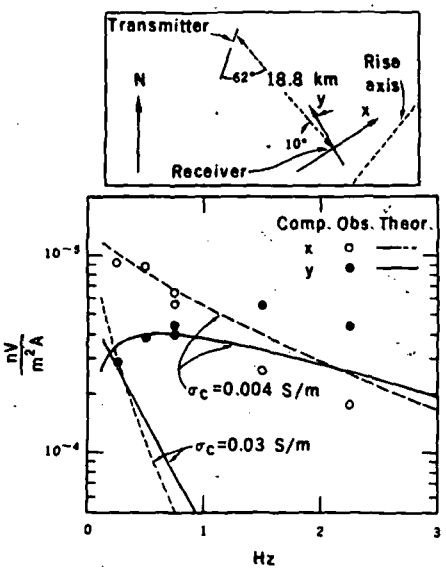

Fig. 11 (left). Ratio of received signal amplitudes (nanovolts per meter) to source dipole amplitude (ampere-meters) as a function of frequency (hertz). The open and closed circles were obtained from a preliminary analysis of the x and y components, as defined in the plan view above. The broken and solid lines represent theoretical values for a model in which the crustal conductivity, σ_c, is homogeneous and isotropic. Fig. 12 (right). *Alvin* magnetometer crossing of two negatively magnetized pillow basalts. Top three curves are the components of the field as noted; bottom curve is the vertical gradient. More than 250 clear measurements were made on either side of the polarity boundary, and all measurements showed the "correct" polarity. The boundary is very narrow, implying a narrow zone of crustal formation.

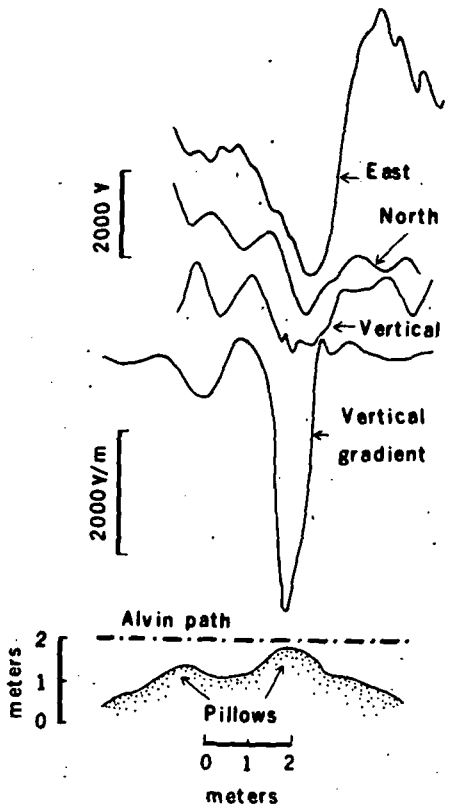

due to a shallow magma chamber or to localized pervasive fracturing of the upper ocean crust associated with hydrothermal vents and (ii) to obtain an estimate of the density of the upper crust.

The primary instrument used was a LaCoste & Romberg geodetic land meter, modified after use on the Mid-Atlantic Ridge last year (*51*), with variable damping and capacitance readout. All measurements were made with the submersible resting solidly on the sea floor. Replicate measurements were made at each station and the resulting observed precision was about 0.05 milligal ($5 \times 10^{-8} g$, where g is the gravitational acceleration).

Position control was from the transponder navigation net used for the RISE project, which is precise to about 10 or 15 m. This gives a negligible error in the latitude correction. Depth of *Alvin* (meter depth) was taken from an up-looking echo sounder transducer, which is accurate to a few meters in any region but precise to about 1 m. This could affect the precision of the gravity measurements by ± 0.2 to 0.3 mgal. Instrument drift was negligible and was not corrected for, nor was a correction attempted for earth tides. Gravity measurements were corrected to a sea-floor datum at 2556 m (uncorrected depth of the shallowest station) with the aim of enhancing local residual anomalies. For sea-floor gravity stations three corrections are needed to find the simple Bouguer anomaly relative to the sea-floor datum (*52*):

1) + 0.3086h for the decrease in g in bringing the meter up to the datum (h is datum depth minus station depth and is negative).

2) + 0.04319z for the subtractive effect of the water layer above the meter for a density of 1.03 grams per cubic centimeter (z is the water depth).

3) −0.04193 σh to replace the crust between the station and the datum (σ is the Bouguer density).

The simple Bouguer anomaly needs to be corrected for the subtractive effects of the sea-floor terrane in regions surrounding each station (*53*). At this writing, the bathymetric data have not been compiled in sufficient detail to calculate these corrections fully.

A profile plot of the simple Bouguer anomaly shows it has a range of about 2 mgal (Fig. 3). However, 10 or 12 stations define a gravity low of up to 1.5 mgal with a half-width (*53*) of approximately 1.0 km. This negative anomaly is centered about the central volcanic ridge and occupies zones 1 and 2 (Fig. 2). Another gravity low appears near −2.4 km (Fig. 3), but this will be largely removed with topographic corrections.

The size and width of the central negative anomaly can be quickly analyzed in terms of a two-dimensional horizontal cylinder source. The total mass deficiency is 9×10^7 kilograms per meter of ridge. The cylinder center is at 1.0 km below the datum. If the cylinder's top edge reaches up to the datum, a minimum density contrast of 0.03 g/cm³ is indicated. If the maximum density contrast is 0.21 g/cm³ (rock-melt contrast), then the cylinder's top edge is 0.63 km below the datum. The density contrast in this ideal case could be due to a shallow magma chamber or crustal fracturing, or both. Further work on the *Alvin* crustal seismic travel-time data in this region may give an independent crustal density estimate to aid in resolving this question.

Crustal density was estimated by studying the correlation between observed gravity and bathymetry. The increase in observed gravity, Δg, for a station h m below the datum is $h(0.04193 \Delta\sigma - 0.2222)$, where h is negative. A graph of Δg against h has a slope of 0.155 mgal/m. The density contrast is then 1.60, giving a rock density of 2.63 g/cm³ between the shallowest and deepest stations.

Electromagnetic Sounding

An electromagnetic sounding technique was used during RISE to study the structure of electrical conductivity in the basement rocks near the spreading center of the East Pacific Rise. The study will provide information on the presence of conducting fluids within the upper crustal rocks.

The method of sounding involved two elements. A transmitter and a horizontal electrical dipole antenna 800 m long were dragged behind R.V. *Melville*. The antenna injected electromagnetic signals into the ocean and underlying crust at frequencies of 0.25 to 2.25 hertz. Because the signals were at relatively high frequencies, the signal in the ocean was rapidly absorbed, so that long-range signals could only have propagated within the crust. The second element consisted of three receivers that had been dropped to the sea floor from the ship before the transmissions were started. To our knowledge, no similar measurements have been attempted before, nor have any other techniques been able to provide estimates of the conductivity of the shallower crust under the oceans.

The most distant receiver was 18.8 km

way from the transmitter antenna. At this receiver the signal was clearly above noise at all the frequencies transmitted. Figure 11 shows preliminary results of the analysis of data from this receiver. The observed amplitude of the two horizontal components of the electric field normalized by the dipole strength of the transmitter antenna is shown as a function of frequency. The observed data are compared in Fig. 11 with theoretical curves derived from a simple model in which a horizontal electric dipole antenna is mounted at the plane interface between two uniform conductors representing the ocean (conductivity, 3.2 siemens per meter) and the crust (conductivity, σ_c). The comparison shows that the effective conductivity of the crust approximates 0.004 S/m. The electromagnetic skin depth of a uniform material of conductivity 0.004 S/m is 8 km for a frequency of 1 Hz. We believe this is about the effective depth of our sounding.

Previously, the conductivity of the igneous part of the oceanic crust was estimated from dredged and drilled samples (*44*) and by logging of holes drilled into basement rocks as part of the Deep Sea Drilling Project (*54*). The drilling showed that the upper part of the oceanic crust consists of basalt in many forms: pillows, massive but cracked flows, and highly fragmented pieces. The only successful deep drillings into solid rock have been in the older parts of the crust, where alteration products have plugged many fractures and vesicles. Nevertheless, the logs of electrical conductivity indicate that seawater is the dominant carrier of electricity. The results from drilling logs are widely scattered but give a geometric mean of 0.03 S/m.

The fact that our observations show an effective conductivity lower than 0.03 S/m at high frequencies may indicate that cracks and fractures are less prevalent and therefore the ability of seawater to provide conductive paths is reduced in parts of the crust below those so far drilled. The difference between the theoretically modeled and observed fields at 1.5 and 2.25 Hz is suggestive of anisotropic conductance in the upper crust, where water-filled cracks parallel to the spreading axis are expected to warp the electric field.

Magnetic Reversal Experiment

One can glean information about the earth's interior by examining the effects of naturally occurring boundaries, edges, or discontinuities on the magnetic and gravity fields. Therefore we studied the magnetic field over the Brunhes-Matuyama reversal boundary, the most recent major reversal recorded in the oceanic crust. Our goals were to determine in detail how sharp and linear the polarity transition is, and to use this information (i) to infer the width of the zone of crustal formation at the spreading center and (ii) to determine how important deep (layer 3) magnetic sources are in generating marine magnetic anomalies.

The reversal that we studied occurs 20 km west of the main RISE dive site in crust 0.7 million years old (Fig. 1). Surface ship surveys show the reversal here to be clear and linear but not unusually so (*55*). In 1977 Macdonald *et al.* (*14*) conducted a near-bottom magnetic survey over a 4 by 6 km area straddling the reversal boundary. Magnetic measurements were made on a level plane approximately 200 m above the bathymetry, using the deep-tow vehicle of the Marine Physical Laboratory (Scripps Institution of Oceanography) with precise transponder navigation. Three-dimensional modeling of the field by a Fourier inversion technique (*56*) shows that the polarity transition boundary is extremely straight and sharp and is very close to two-dimensional even on a scale of hundreds of meters. The polarity transition width is narrow, only 1000 to 1400 m throughout the study area, which suggests a zone of crustal emplacement only 600 to 1000 m wide at the spreading center (*14*).

With these results in hand, we returned to the same area with *Alvin* as part of RISE to conduct even finer scale magnetic measurements aimed at the volcanic extrusive component of the reversal boundary. A fluxgate magnetic gradiometer and three-component magnetometer were mounted in *Alvin*'s sample basket and used to make rapid, in situ determinations of crustal magnetic polarity (*57*). Typical magnetic targets were individual basalt pillows, wrinkled sheet flow ridges, and the sharp edges of fault scarps. During five geologic traverses in the reversal area, more than 250 clear in situ polarity determinations were made across the reversal boundary (Fig. 12).

In comparing the *Alvin* polarity measurements with the deep-tow inversion solution, we had several surprises. Even on long traverses (total of 4 km) to either side of the polarity boundary, every magnetic target had the correct polarity (positive or negative)—that is, a polarity that agreed with the magnetic stripes. This is not too surprising for the young side of the reversal boundary, since the newer polarity material should overlie the older. However, it is surprising that there were no outliers of newer polarity material or volcanoes on the older side of the boundary.

The reversal transition zone is very narrow. On one dive the boundary was traversed several times along a linear zone only tens of meters wide. Along strike, the reversal transition zone was actually a geologic contact; a flow (+) butted up against an axially dipping fault scarp (−), and a pillow flow front (+) facing west forming a narrow valley with a pillow flow front (−) facing east. In other places where sediment cover obscured any possible contacts, the transition from positive to negative polarity could be defined by our measurements to a zone less than 150 m wide.

The reversal boundary based on *Alvin* in situ measurements is displaced approximately 500 m away from (west of) the spreading center relative to the boundary in the deep-tow inversion solution. This offset is precisely known since the *Alvin* navigation net was linked with long-life transponders used in the deep-tow work.

When combined with the deep-tow inversion solution, the *Alvin* measurements suggest that the zone of formation of magnetic crust is very narrow. After allowing for the effects of crustal dilatation by faulting and the finite period required for the earth's field to reverse, the resultant zone of crustal emplacement is only 500 to 1000 m wide. This is in excellent agreement with geologic determinations from *Alvin* and *Cyana* for the width of zone 1, which varies from 400 to 1200 m at the present spreading axis. Thus the zone of crustal formation today and about 0.7 million years ago has been very sharply defined in space, generally less than 1 km in width.

The 500-m westward displacement of the *Alvin* determination of the reversal boundary relative to the potential field location represents spillover of basalt flows away from axial vents over older, negative-polarity crust. The width of this overlap when combined with the potential field data provides valuable information that may constrain the role of deeper sources in generating marine magnetic anomalies.

The focus of current work is to combine the *Alvin* polarity determinations with both surface-tow and deep-tow magnetic inversion solutions to sort out the extrusive and intrusive contributions to the finite width of the field reversal recorded in the crust. From this we hope to place bounds on the width of volcanism,

the width of dike intrusion, and the importance of layer 3 sources such as gabbro in generating marine magnetic anomalies.

Summary of Geophysical Experiments

All four geophysical experiments were prototypes, and it is difficult this soon after the cruise to have complete results or to merge them with the geological and hydrothermal observations. However, the combined research efforts are taking several interesting directions. Combination of the seismic and gravity results should resolve the question of whether the axial gravity anomaly is caused by a shallow magma chamber or surficial fissuring (we suspect the former). These results in turn will be combined with inferences about the magma chamber from the petrologic studies. While the gravity and seismic studies may indicate the presence and depth of a magma chamber near the axis, the electrical studies may indicate its width by sensing high conductivity at depth off-axis. The seismic and electrical studies should place bounds on the depth of fissuring of the crust and, combined with the hydrothermal observations, be used to determine the depth of hydrothermal circulation along the axis. The magnetic studies in the reversal area already suggest a narrow zone of crustal formation that has been stable for some time and agree well with the geological observations. The magnetic studies should also indicate how important deeper layer 3 sources and cumulate settling portions of the magma chamber are as sources of lineated magnetic anomalies.

Conclusions

The axis of the East Pacific Rise is marked by a zone of recent volcanism approximately 1000 m wide. Near the center of the volcanic zone, there is a very narrow band of active hydrothermal vents—at least 25 vents along a strip 7 km long and only 200 to 300 m wide. In the northeast, vents are characterized by water temperatures of 5° to 20°C, flow rates of centimeters per second, clear vent waters, and exotic biological communities similar to those at the Galápagos vents (giant tube worms, clams, galatheid crabs). These communities, independent of photosynthesis for survival, must have unusual dispersal systems that allow them to populate various areas of the world rift system as hydrothermal vents evolve and die out. To the southwest, vent waters contain more particulate matter, often dark in color (black smokers); the exit temperatures reach 380° ± 30°C; flow rates are on the order of several meters per second; and conditions appear less inviting for the biological communities near the vents, except for a new polychaete, which may live at very high temperatures. The marked along-strike variation may indicate an evolutionary cycle in the development of the vent system. Actively forming massive sulfide deposits occur within the vent chimneys at high-temperature springs, while inactive sulfide mound deposits occur slightly off-axis from the cooler vents. Mineral deposits include sphalerite, pyrite, chalcopyrite (and other Fe, Cu, and Zn sulfides), anhydrite, sulfur, barite, opal, and talc. Chimneys exhibit a distinct concentric zoning of sulfide minerals, which suggests episodicity in the physical and chemical properties of the vents. The hydrothermal waters contain the first such occurrences of pyrrhotite and other sulfide compounds as well as methane. Covariance of methane with ^3He indicates a mantle source for both. There is substantial evidence for biological influence on the mineral deposits; for example, worm-tube honeycomb structures form the foundations for many sulfide mounds.

Basalt samples from the spreading center have a narrow range of chemical composition and are extremely primitive. They probably formed by fractional crystallization from a shallow magma chamber, possibly from a single parent magma.

Alvin has been used for the first time as a geophysical tool. The on-bottom gravity and seismic measurements have yielded the first in situ determinations of shallow crustal seismic velocity and density. Further analysis of the gravity, seismic, and electrical data should place bounds on the depth of hydrothermal activity and crustal fissuring, and determine the extent of the axial magma chamber. Magnetic measurements at the reversal boundary indicate a narrow (500 to 1000 m) zone of crustal formation, and may place bounds on the role of deep crustal sources in generating marine magnetic anomalies.

References and Notes

1. K. C. Macdonald and F. N. Spiess, *Scripps Inst. Oceanogr. Ref. 76-18* (1976).
2. T. Atwater and J. D. Mudie, *J. Geophys. Res.* **78**, 8665 (1973).
3. R. L. Larson and F. N. Spiess, *Science* **163**, 68 (1969).
4. K. C. Macdonald and B. P. Luyendyk, *Geol. Soc. Am. Bull.* **88**, 621 (1977).
5. K. D. Klitgord and J. D. Mudie, *Geophys. J. R. Astron. Soc.* **38**, 563 (1974).
6. FAMOUS was the French-American Mid-Ocean Undersea Study carried out in 1971 to 1974 on the Mid-Atlantic Ridge rift valley and adjacent fracture zones near 36°50'N.
7. J. R. Heirtzler and Tj. H. van Andel, *Geol. Soc. Am. Bull.* **88**, 481 (1977).
8. ARCYANA, *Science* **190**, 108 (1975).
9. R. D. Ballard, W. B. Bryan, J. R. Heirtzler, G. Keller, J. G. Moore, Tj. H. van Andel, *ibid.*, p. 103.
10. J. B. Corliss *et al.*, *ibid.* **203**, 1073 (1979).
11. F. N. Spiess, C. D. Lowenstein, D. E. Boegeman, J. D. Mudie, in *Oceans '76* (Institute of Electrical and Electronics Engineers and Marine Technology Society, Washington, D.C., 1976).
12. R. L. Larson, *Geol. Soc. Am. Bull.* **82**, 801 (1971).
13. W. R. Normark, *Geology* **4**, 681 (1976).
14. K. C. Macdonald, S. P. Miller, S. P. Huestis, F. N. Spiess, *J. Geophys. Res.*, in press.
15. W. R. Normark, T. R. Alpha, G. R. Hess, G. S. Lichtman, C. E. Gutmacher, *U.S. Geol. Surv. Open-File Rep. 78-350* (1978); W. R. Normark, *Mar. Geod.* **3**, 29 (1979).
16. CYAMEX Science Team, *Mar. Geophys. Res.*, in press.
17. ———, *Nature (London)* **277**, 523 (1979).
18. The two submersible operations, CYAMEX and RISE, plus a third scheduled for the Tamayo Fracture Zone in October 1979 have been linked together as a Mexican-French-U.S. program designated RITA (Rivera-Tamayo). Although the first was primarily supported by France and the second by the United States, there has been full participation in planning, sea operations, and reporting by scientists from all three countries.
19. *Woods Hole Notes* **1**, 2 (1979).
20. R. D. Ballard, R. T. Holcomb, Tj. H. van Andel, *J. Geophys. Res.*, in press.
21. J. Francheteau, T. Juteau, C. Rangin, in preparation.
22. R. F. Weiss, P. F. Lonsdale, J. E. Lupton, A. E. Bainbridge, H. Craig, *Nature (London)* **267**, 600 (1977).
23. P. F. Lonsdale, *Earth Planet. Sci. Lett.* **36**, 91 (1977).
24. ———, *Deep-Sea Res.* **24**, 857 (1977).
25. J. B. Corliss, J. Dymond, M. Lyle, K. Crane, *Earth Planet. Sci. Lett.* **40**, 12 (1978).
26. Galápagos Biology Expedition Participants, *Oceanus* **22**, 2 (1979).
27. W. A. Newman, *Trans. San Diego Soc. Nat. Hist.*, in press.
28. H. W. Jannasch and C. O. Wirsen, *BioScience*, in press.
29. J. Lupton, G. Klinkhammer, W. Normark, R. Haymon, K. Macdonald, R. Weiss, H. Craig, in preparation.
30. J. A. Welhan and H. Craig, *Geophys. Res. Lett.*, in press.
31. W. Seyfried and J. Bischoff, *Earth Planet. Sci. Lett.* **34**, 71 (1977).
32. M. J. Mottl and H. D. Holland, *Geochim. Cosmochim. Acta* **42**, 1103 (1978).
33. C. C. von der Borsch and R. W. Rex, in *Initial Reports of the Deep Sea Drilling Project*, D. A. McManus *et al.*, Eds. (Government Printing Office, Washington, D.C., 1970), vol. 5, p. 541.
34. D. S. Cronan *et al.*, *Science* **175**, 61 (1972).
35. A. E. J. Engel, C. G. Engel, R. G. Havens, *Geol. Soc. Am. Bull.* **76**, 719 (1965).
36. W. G. Melson, T. L. Vallier, T. L. Wright, G. Byerly, J. Nelen, in *The Geophysics of the Pacific Ocean Basin and Its Margin* (American Geophysical Union, Washington, D.C., 1976), p. 351.
37. W. B. Bryan and J. G. Moore, *Geol. Soc. Am. Bull.* **88**, 556 (1977).
38. W. B. Bryan, *J. Petrol.* **20**, 293 (1979).
39. CYAMEX Science Team, in preparation.
40. T. L. Wright and P. C. Doherty, *Geol. Soc. Am. Bull.* **81**, 1995 (1970).
41. P. L. Roeder and P. F. Emslie, *Contrib. Mineral. Petrol.* **29**, 275 (1970).
42. E. Schreiber and P. J. Fox, *J. Geophys. Res.* **81**, 4071 (1976).
43. ———, *Geol. Soc. Am. Bull.* **88**, 600 (1977).
44. R. D. Hyndman and M. J. Drury, *J. Geophys. Res.* **81**, 4042 (1976).
45. N. I. Christensen and M. H. Salisbury, *Earth Planet. Sci. Lett.* **19**, 461 (1973).
46. N. Warren and B. Rosendahl, in *Initial Reports of the Deep Sea Drilling Project* (Government Printing Office, Washington, D.C., in press), vol. 54.
47. P. J. Fox, E. Schreiber, J. J. Peterson, *J. Geophys. Res.* **78**, 5155 (1973).
48. P. Spudich and J. Orcutt, *ibid.*, in press.
49. R. E. Houtz, *ibid.* **81**, 6321 (1976).
50. M. Henry, L. Dorman, J. Orcutt, *Eos* **59**, 1138 (1978).
51. B. P. Luyendyk, in preparation.
52. L. L. Nettleton, *Gravity and Magnetics in Oil Prospecting* (McGraw-Hill, New York, 1976).

S. Hammer, *Geophysics* 4, 184 (1939).
R. J. Kirkpatrick, in *Initial Reports of the Deep Sea Drilling Project*, L. Dmitriev *et al.*, Eds. (Government Printing Office, Washington, D.C., 1979), vol. 46, p. 401.
R. L. Larson, *Scripps Inst. Oceanogr. Ref. 70-2* (1970).
R. L. Parker and S. P. Huestis, *J. Geophys. Res.* 79, 1587 (1974).
T. M. Atwater and K. C. Macdonald, *Eos* 59, 1198 (1978).

58. We acknowledge the highly competent support provided by *Alvin*'s operators, led by pilots D. Foster, R. Hollis, and G. Ellis; the crews of R.V. *Lulu* (J. Boord, master), R.V. *Melville* (A. Arsenault, master), and R.V. *New Horizon* (A. Phinney, master); and the members of the several hardworking scientific parties. F. Grassle and J. Kerridge made substantial contributions through analyses and descriptions of biological and mineralogical samples. L. Shure aided in the collection and analysis of the magnetic data. The expedition was funded by the Seabed Assessment Program of the National Science Foundation International Decade of Ocean Exploration office under grants NSF/OCE 78-01664, 78-21082, and 79-09984. Funds for mineralogical and geochemical analyses were provided by a grant from the Academic Senate, University of California, San Diego. Support for the electrical measurements was provided by the National Science Foundation and the Office of Naval Research (Earth Physics Branch).

Sulfide Deposits from the East Pacific Rise Near 21°N

R. Hekinian, M. Fevrier, J. L. Bischoff, P. Picot, W. C. Shanks

Summary. Massive sulfide deposits were discovered from the diving saucer *Cyana* on the accreting plate boundary region of the East Pacific Rise near 21°N. The deposits form conical and tubular structures lying on a basaltic basement. Mineralogical and geochemical analyses showed two main types of intimately associated products: a polymetallic sulfide-rich material composed of pyrite and marcasite in association, zinc-rich phases, and copper-rich compounds, and an iron-rich oxide and hydroxide material (also called gossan) composed largely of goethite and limonite. Silicate phases such as opaline, silica, iron-silicon clay, and trace amounts of mica and zeolite are encountered in both types of material. Possible mechanisms for the formation of the sulfide deposits on the East Pacific Rise are discussed.

The early discoveries of hydrothermal products at accreting plate boundaries were sediments rich in iron and manganese (*1*). More recent findings of strongly fractionated iron-manganese concretions, material rich in silicon-iron clay, and hydrous iron oxides have been collected from the Galápagos spreading center (*2*, *3*), from the Mid-Atlantic Ridge near 26°N (*4*, *5*) and 37°N (*6*), and from the Gulf of Aden (*7*). Direct visual observations of thermal springs were made during a submersible study on the rift valley of the Galápagos spreading center (*8*).

The first discovery of a sizable submarine polymetallic sulfide deposit on a ridge system was made in the Red Sea during the international Indian Ocean expedition (1963 to 1965). In addition, many ancient massive sulfide deposits found in ophiolites are thought to have been formed on the sea floor in large oceans or marginal basins. These deposits consist primarily of pyrite, chalcopyrite, and sphalerite (*9*–*12*). The ophiolitic massive sulfide deposits, such as those in the Troodos complex in Cyprus (*13*), Semail in Oman (*14*), and Betts Cove and York Harbor in Newfoundland (*12*, *15*), appear to represent ancient oceanic crust formed at mid-oceanic spreading ridges. A summary of the ophiolite complexes containing sizable ore deposits around the world is given by Coleman (*16*).

A recently formed massive sulfide deposit with similarities to the ophiolitic deposits was recently discovered by a manned submersible on the East Pacific Rise at 21°N during a French-American-Mexican joint project (project RITA) on rapidly spreading ridges (*17*, *18*) (Fig. 1). The East Pacific Rise deposit occurs at a spreading ridge at 21°N. The rate of separation at the site, 3 centimeters a year, appears to have been constant during the last 4 million years (*18*). As indicated by deep-tow studies (*19*), the ridge crest in the area is dominated by a central zone of volcanic hills about 2 to 5 kilometers wide flanked on either side by a zone of open fissures.

More recent dives in the region by the submersible *Alvin* have discovered other massive sulfide mounds and actively discharging hydrothermal vents and solid particles with fluid temperatures of 375° ± 25°C (*20*, *21*). Conical plumes discharging sulfide minerals on the sea floor were recently predicted by Solomon and Walshe (*22*) from experimental studies of deposits of the Cyrpus and Kuroko type. We present here the results of mineralogical and geochemical studies of sulfide deposits during dives of the submersible *Cyana* at 21°N (*23*).

Geologic Setting of the Sulfide Deposit

The deposits were sampled at two sites (Cy 78-08 and Cy 78-12) located on the flanks of steep-sided structural depressions about 20 to 30 meters deep and 20 to 30 meters wide, situated 700 to 800 meters west of the axis of the East Pacific Rise (Fig. 1) (*17*). The general area consists of a 1.5-km-wide band of fissured and faulted terrane associated with a horst and graben zone (*17*, *24*). The massive sulfide deposits form roughly cylindrical hills ranging up to 10 m high and averaging 5 m in diameter (*23*). In an area visited during dive Cy 78-8, at least three vertical hills aligned in an approximately north-south direction (025°) were seen over a distance of about 50 m. The hills are about 3 to 4 m apart and the flanks of two different hills could be seen from the porthole of the submersible when it passed between them. The edifices are variegated with ocher, red, white, and dark gray colors and appear to be extremely porous. The first sample (8-14A) was taken on a tall hill (approximately 10 m high) and consists of a brownish-red ocher-like material. The second sample was taken about 10 m away from the first on the same hill.

The authors' affiliations are: R. Hekinian, Centre Océanologique de Bretagne, Brest Cédex 29273, France; M. Fevrier, Centre Océanologique de Bretagne and Université de Bretagne Occidentale, Brest Cédex 29200; J. L. Bischoff, U.S. Geological Survey, Menlo Park, California 94025; P. Picot, Bureau de Recherche Géologique et Minière, Orleans Cédex 45018; and W. C. Shanks, Department of Geology and Geophysics, University of Wisconsin, Madison 53706.

0036-8075/80/0328-1433$02.00/0

JOURNAL OF GEOPHYSICAL RESEARCH, VOL. 87, NO. B10, PAGES 8477–8489, OCTOBER 10, 1982

Geophysical Evidence for the Absence of a Crustal Magma Chamber Under the Northern Juan de Fuca Ridge: A Contrast With ROSE Results

KEVIN J. MCCLAIN AND BRIAN T. R. LEWIS

Geophysics Program and School of Oceanography, University of Washington, Seattle, Washington 98195

Deep-tow reflection data, seismic refraction data to ocean bottom seismometers, and gravity interpretations of the northern Juan de Fuca Ridge all suggest a very narrow or absent crustal magma chamber under this portion of the rise axis. The seismic features that have been suggested as indicating crustal magma chambers on other parts of the East Pacific Rise, such as travel time delays and reflections from the top of a shallow magma reservoir, are not found on the northern part of this ridge. These results indicate that at spreading rates of 3 cm/yr crustal cooling (probably by water penetration) is sufficiently rapid to prevent the existence of a steady state crustal magma chamber and therefore crustal accretion may be episodic.

INTRODUCTION

The Juan de Fuca plate off the Washington-Oregon coast has long been cited as an example of seafloor spreading. *Raff and Mason* [1961] published the magnetic lineation map of the region, which gave early evidence for plate tectonic concepts.

Detailed magnetic anomaly analysis by *Riddihough* [1977] shows that for the past several million years the half spreading rate at the ridge has been 3 cm/yr. Examination of the magnetic anomalies and topography across this ridge also show that spreading has continued to the present.

Shor et al. [1968] undertook seismic refraction measurements on the Juan de Fuca Ridge, and their results indicated normal ocean crustal velocities and thicknesses. Assuming that this ridge is the result of processes typical of accretion at 3 cm/yr, our goal was to study in detail the structure of this ridge axis to define better the processes of accretion. For this study we selected the simplest part of this ridge system, located between 46° and 47°N latitude.

Figure 1 shows the location of the experiment area, and Figure 2 shows typical reflection profiles on the east side of the ridge in the study area verifying the two-dimensionality of this area.

During September 1978 the University of Washington completed a seismic refraction survey of the northern end of the Juan de Fuca Ridge near 47°N latitude. In June 1980 the southern end of our original survey area was profiled with a deep-towed reflection system and a shipboard gravity meter.

This paper presents data from these experiments with the analysis being directed toward determining the presence or absence of a magma chamber under the rise axis. Evidence either for or against the existence of a magma chamber under the axis would provide strong constraints on the question of whether accretion is continuous or episodic. Comparison is made, where possible, with similar data obtained during Project ROSE.

DEEP-TOW REFLECTION DATA

The University of Washington deep-towed array was deployed across the segment of rise crest shown in Figure 1 to determine if reflections from the top of a magma chamber could be detected. This system telemeters digital data from a subsurface package to a shipboard data logger and is normally used with a 20-element 2-km-long hydrophone array. For this experiment the multichannel array was replaced by a single-channel streamer, and the sampling rate was increased from 200 to 4000 S^{-1}. This was done because the horizontal dimensions of the problem under investigation were expected to be of the order of tens to hundreds of meters, and the greatest possible time resolution was desired. The source during this experiment was a 0.049 m^3 (300 $in.^3$) air gun, used with and without a bubble suppressor.

During the deployment we attempted to fly the system at a constant depth of about 2100 m, or about 100 m above the highest point of the topography. Figure 3 shows a reflection profile across the ridge with a surface-towed system, and Figure 4 shows a shipboard monitor record of a deep-tow line at the rise axis. Some of the apparent depth variations in the deep-tow line are caused by variations in streamer height, but it is clear even from this monitor record that one is getting greatly increased resolution of topography and an indication of subsurface reflections. Diffraction off topography is also clearly seen.

To improve the resolution of the axial topography, the data along two lines were plotted at an expanded scale (Figure 5), and these show an axial graben morphology with indications of faulting at the edges of the graben. The total relief of the graben is about 75 m, and the width is about 1.5 km. The variable reflectivity of the seafloor within the graben may be indicative of the distribution of sheet flows and pillow basalts.

To search for deep reflectors under the axis that might be indicative of magma reservoirs, some computer processing of the data was undertaken. This consisted of pie-slice filtering in frequency wave number space to subdue the topographically diffracted energy, applying time-varying gain to accentuate the deep reflectors and dynamic range compression to reveal low-amplitude signals. A section of processed data under the axis is shown in Figure 6. From these data one can clearly see subsurface reflections or diffractions off subsurface interfaces but no well-defined reflections from an interface one might identify as a magma chamber roof. To convince the reader that we are in fact observing subsurface events and not just side reflections off

Paper number 1B1905.
0148-0227/82/001B-1905$05.00

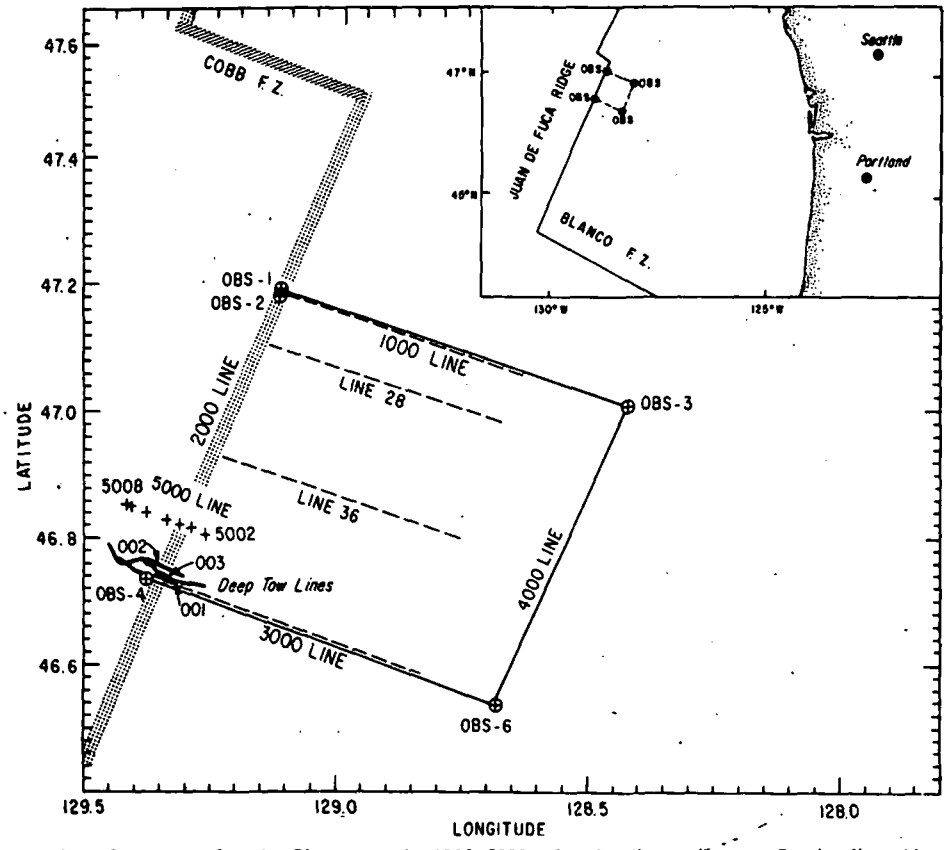

Fig. 1. Location of the area of study. Shown are the 1000–5000 refraction lines, air gun reflection lines (dotted lines), and the deep-towed reflection lines 001–003.

seafloor topography, we computed theoretical diffraction curves assuming point source topography located at several distances to the side of the streamer's path. These are shown in Figure 7 superimposed on the data and indicate that most of the reflections are too narrow to be explained by seafloor topography and must therefore be due to subsurface reflections or diffractions.

We conclude therefore that there is no convincing seismic reflection evidence for a magma chamber with a well-defined upper surface presently under the axis, at least to depths of about 5 or 6 km. There is a hint in the data at about 2 s subbottom (approximately 6 km) of a diapiric structure under the axis. This may indicate upwelling mantle material, but at this point the inference is tenuous. Further processing of these data is planned to resolve the fine structure, but we do not expect that this will substantially change our conclusions regarding the lack of a well-defined magma chamber containing molten rock.

Seismic Refraction Results

The location of the seismic refraction experiment is shown in Figure 1. Ocean bottom seismometers (OBS) [*Lister and Lewis*, 1976] were placed along the ridge axis and 55 km to the east of the axis on 2-m.y.-old oceanic crust to form a square grid. Refraction lines were then shot between these instruments forming four reversed seismic lines both parallel and perpendicular to the ridge crest.

In addition, another line of shots, the 5000 line, was fired across the ridge crest to investigate lateral inhomogeneity across the ridge for rays bottoming at different depths.

Shots Across the Ridge—The 5000 Line

The 5000 line consisted of eight shots fired from east to west across the ridge (Figure 1), with shot sizes ranging from 120 to 240 pounds of Tovex explosive. The shots were located with Loran C navigation, accurate to several hundred meters. The shot break time for shot 5001 was missed, and so this shot is not included in this data analysis. To correct for the ridge topography, the shots were corrected to a depth of 2620 m, with water and rock travel time above this depth removed. This was done by using the appropriate apparent velocity values for the ranges from shots to OBS's based upon the four refraction lines. Two sets of corrections were computed, assuming rock velocities of 3.0 and 4.5 km/s for the basement topography. This choice of velocity made little difference in the pattern of corrected arrival times to the OBS's. For Figures 8, 10, and 11, the 5000 line topographic correction was computed assuming a rock velocity of 3 km/s. All seismic traces were also band-pass filtered from 2 to 18 Hz.

The two off axis OBS's, 55 km east of the ridge, OBS-3 and OBS-6, both show a similar pattern of arrivals after correction for topography (Figure 8). From a comparison with other shot lines in this experiment, we believe the predominant energy in Figure 8 is from wide-angle mantle reflections. These show no significant time offsets as the shots cross the ridge axis.

A very similar set of shots across the East Pacific Rise was recorded during Project ROSE by the University of Washington OBS's [*Lewis and Garmany*, this issue]. Figure 9

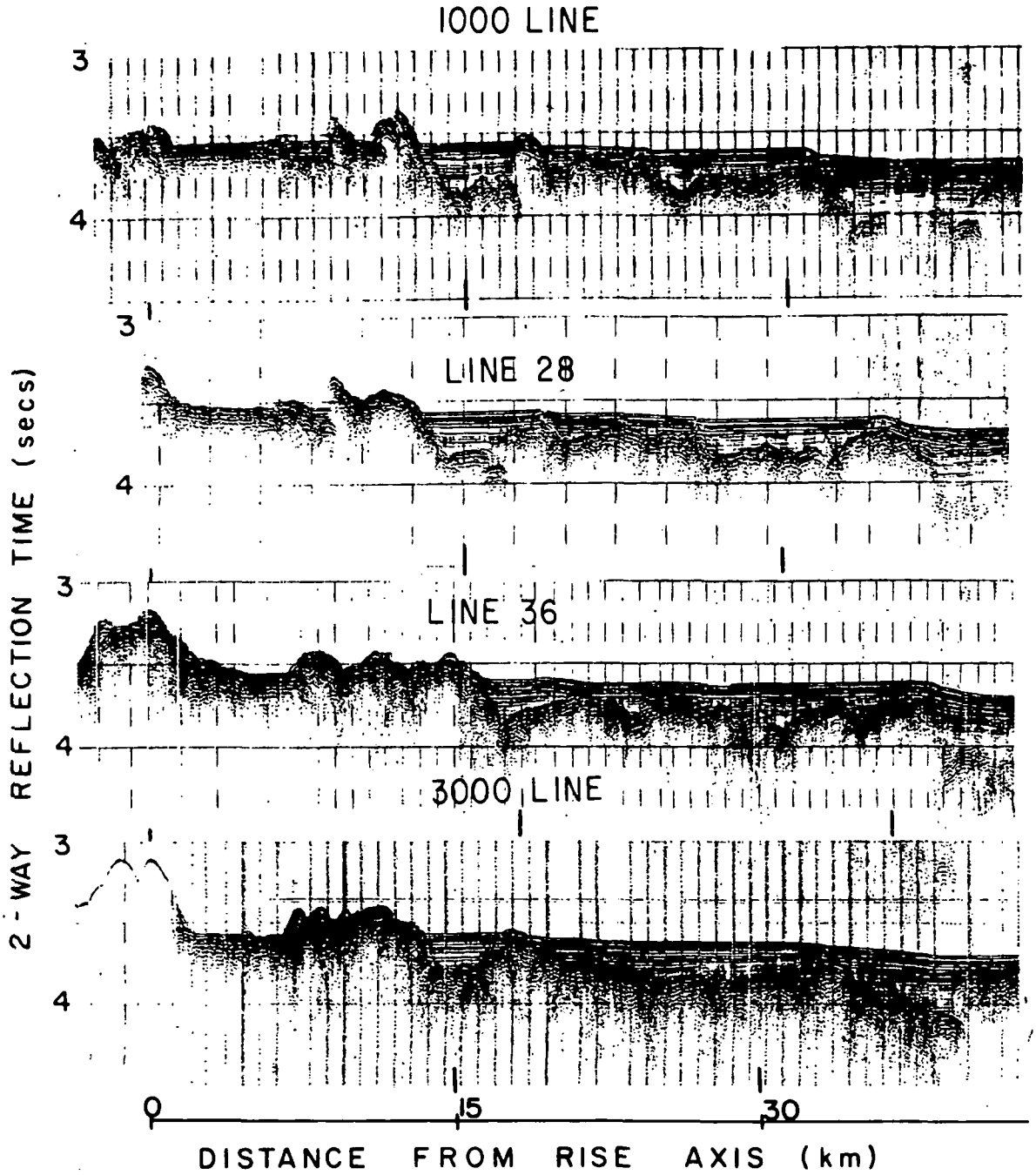

Fig. 2. Four air gun reflection lines on the east side of the ridge showing the two-dimensional nature of the topography. Lines on the profiles indicate distances of 0, 15, and 30 km from the rise axis. Profile locations are shown as dotted lines in Figure 1.

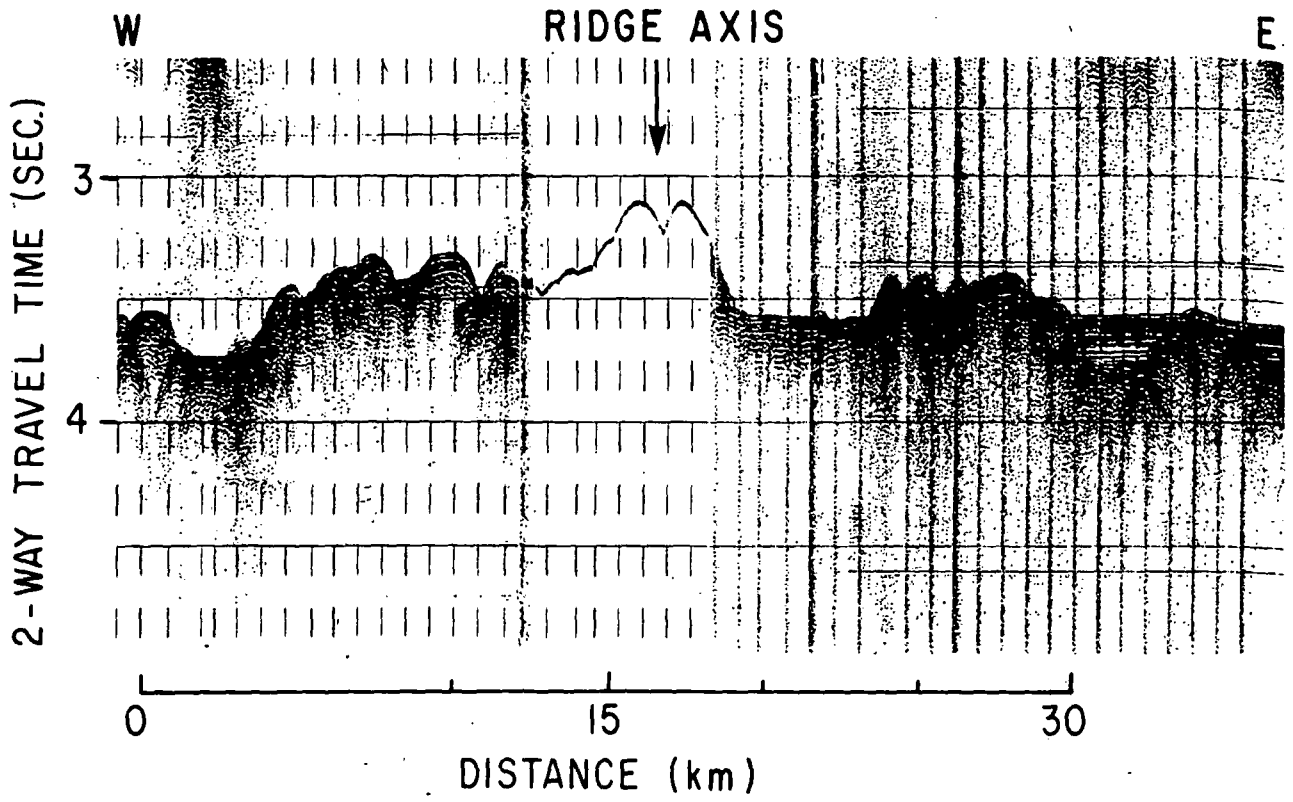

Fig. 3. An example of a reflection record across the ridge axis using a surface towed streamer and a 40 in.^{3} air gun.

(right) shows the 5000 line shots recorded by OBS-3 from this study with no corrections for water depth or topography. Figure 9 (left) shows line 6L from Project ROSE as recorded by OBS 403 and OBS 407 with no corrections applied. Corresponding shot-receiver geometries for these two experiments are plotted beneath the seismic data in Figure 9 and are nearly identical.

Yet one sees a dramatic difference in the propagation of energy across the ridge in these two areas. Little or no energy propagates across the 12°N axis, whereas shots across the Juan de Fuca Ridge show little or no attenuation of energy.

Lewis and Garmany [this issue] modeled several sets of refraction data from the ROSE area. In their models, the ridge is underlain by a narrow zone of low-velocity material. The effect of the low velocity is to cause time delays in crustal arrivals at ranges of about 15 km and to attenuate severely and delay crustal multiple paths at ranges of 60–80 km. This low-velocity material extends to within 1 or 2 km of the seafloor and is about 1 km wide at depths of 2 km.

From a comparison of the two data sets in Figure 9, we infer that the northern Juan de Fuca Ridge does not have an axial low-velocity zone similar to the faster spreading East Pacific Rise at 12°N.

Record sections for the on-axis instruments, OBS-1 to the north and OBS-4 to the south of the 5000 line, are shown in Figure 10. OBS-1 is approximately 44 km from the shots, and OBS-4 is approximately 12 km from the shots. These instruments recorded the 5000 line shots as a fan pattern across the ridge. To interpret these arrivals, an average velocity from each shot to the two OBS's was computed. This was done by taking the distance from shot to receiver and dividing by the topographically corrected total travel time. A plot of this average velocity of the shots for OBS-1 and OBS-4 is shown in Figure 11. OBS-4 shows an average velocity of 5.7 km/s over the ridge axis and velocities about 0.4 km/s slower off-axis. OBS-1 shows an opposite trend with velocities over the ridge of 6.1 km/s as compared with velocities of 6.4 km/s off-axis. OBS-4 at an average distance of 11 km from the shots is recording rays that bottom in the crust, whereas OBS-1 at a distance of 44 km is recording rays that normally bottom at mantle depths. We infer from the average velocity pattern that the upper crust under the ridge is of slightly higher velocity than off-axis. The lower crust or mantle under the ridge is of slightly lower velocity than at similar depths off-axis. These variations are small and support the hypothesis of no crustal magma chamber under the ridge.

Reversed Refraction Lines

The four reversed refraction lines consist of two reversed lines perpendicular to the ridge, one reversed line along the ridge axis, and one reversed line on 2-m.y.-old crust 55 km east of the axis. Shot sizes along the lines ranged from 5 to 180 pounds. No corrections for topography or sediment thickness have been applied to the data presented in Figures 12 and 13.

The 2000 line was shot along the axis of the ridge from north to south (Figure 12, top). One can see from the bathymetric profile that depth along the axis decreases toward the south. There is no clear mantle arrival on either of the reversed lines nor an indication of a caustic related to a velocity increase at the crust-mantle boundary. At distances where mantle arrivals are normally recorded (greater

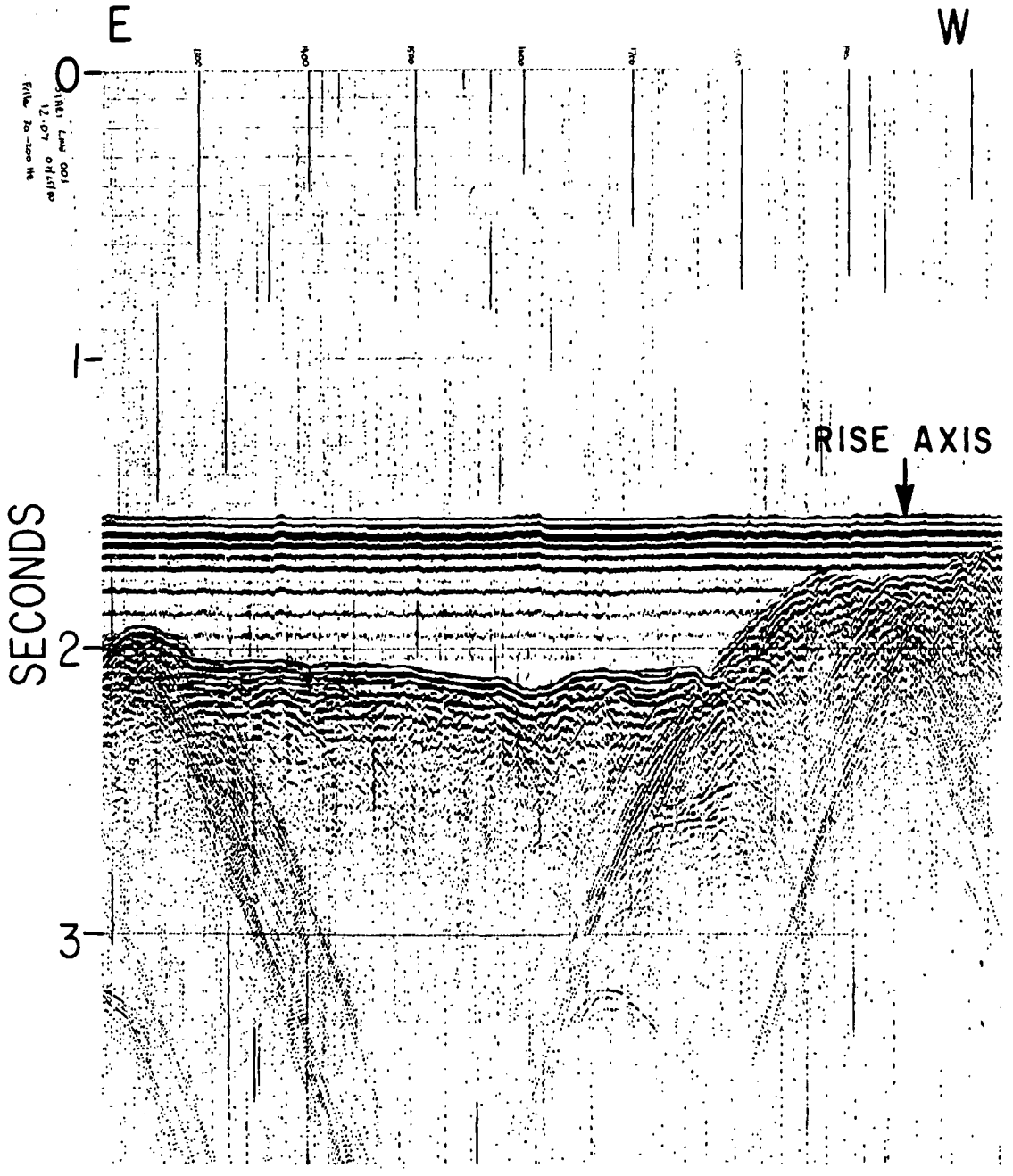

Fig. 4. An example of a shipboard monitor record with the deep-towed streamer at a depth of 2300 m and an air gun source at the surface. The rise axis is on the right of the figure. The total length of the profile is about 8 km.

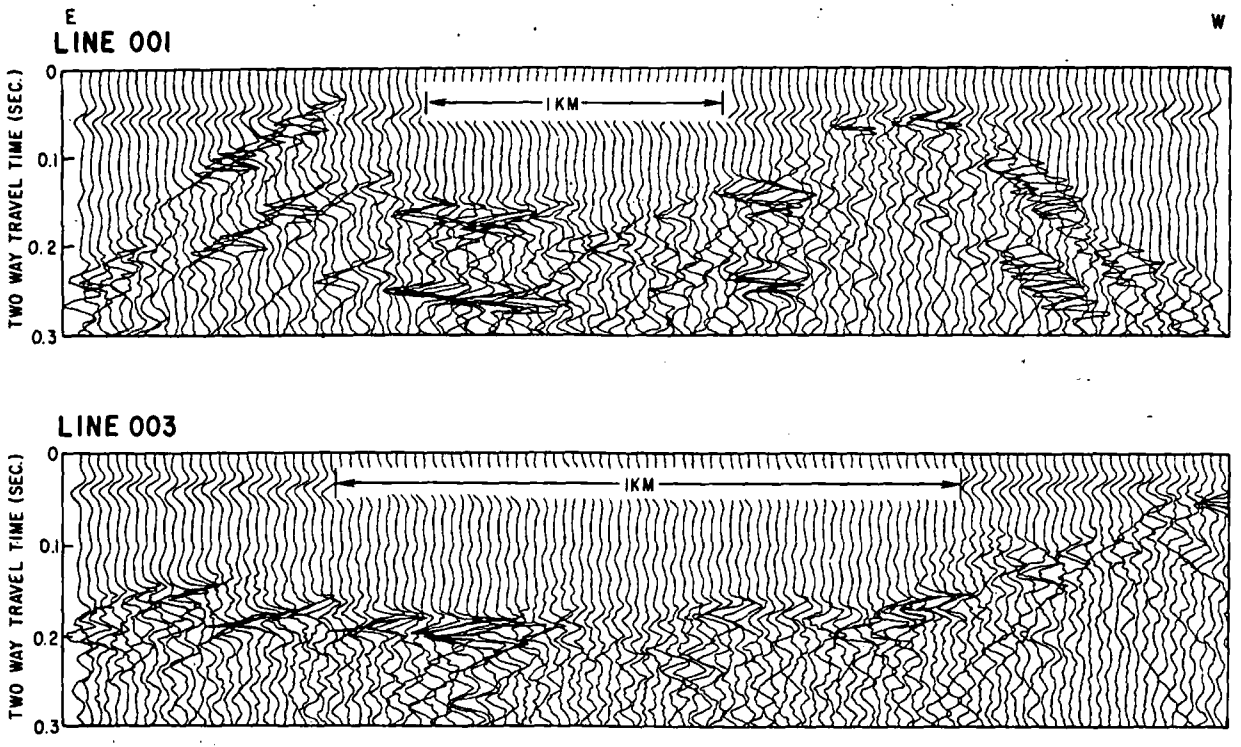

Fig. 5. Expanded plots of the deep-towed reflection data across the rise axis for lines 001 and 003. Note the small axial valley and the indications of faulting within the axial valley.

than 30 km), the apparent velocity across the shots is ~6.8 km/s.

The 4000 line is located 55 km from the ridge axis and parallel to it (Figure 12, bottom). The age of the ocean crust here is ~2 m.y. based on magnetic anomalies. This line was shot over a small basement high that can be seen in the reflection profile. This basement high makes interpretation difficult since it affected crustal arrivals on one OBS and mantle arrivals on the other. Mantle velocity as seen from OBS-3 is ~7.2 km/s. Such a low mantle velocity could be the result of mantle anisotropy, with slow *Pn* velocity parallel to the ridge [*Morris et al.*, 1969], or high temperatures or both.

The 1000 and 3000 lines are perpendicular to the rise axis, and both run east from the ridge to a distance of ~55 km (Figure 13). A mantle caustic and clear mantle refracted arrivals with an average velocity of ~7.8 km/s is observed on both lines. Both of these reversed lines show close agreement in their reversed times, indicating a velocity structure that is well behaved. A velocity model based on the 3000 and 5000 lines is discussed in the next section.

Two-Dimensional Ray Trace Modeling

To model in some detail the structure perpendicular to and across the ridge, we used a two-dimensional ray tracing technique described by *McMechan and Mooney* [1980]. Data modeled were the reversed 3000 line and the combined 3000 and 5000 lines as seen from OBS-6. Since we directly input the observed basement topography, it was unnecessary to make topographic corrections to the observed data. Sediment thickness was accounted for assuming a sediment velocity of 1.5 km/s.

First, a model was constructed to match the observed travel times for the reversed 3000 line. A structure with crustal thickness of 5 km and a mantle depth of 8 km below sea level fit the data well. No variation in crustal properties near the ridge were needed to fit the travel times for OBS-4, which was on the ridge.

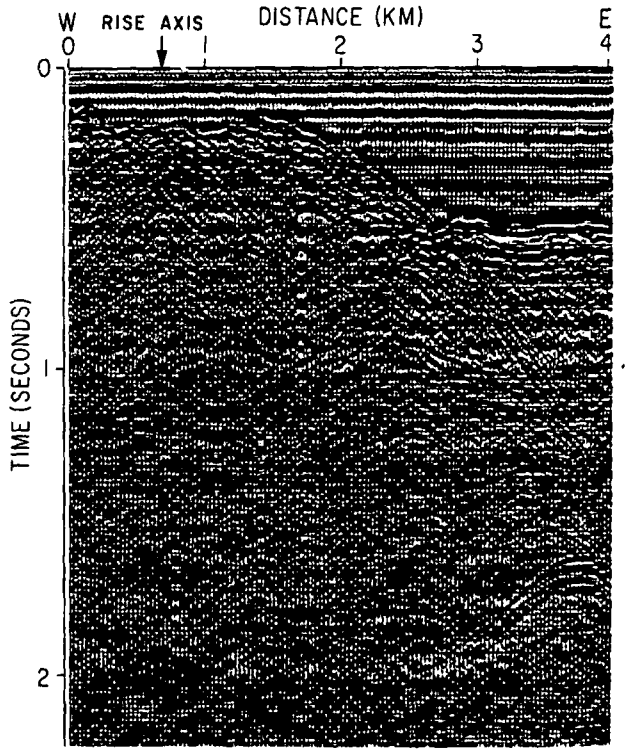

Fig. 6. Processed (see text) deep-towed reflection data across the rise axis. The ridge axial valley is on the left of the figure.

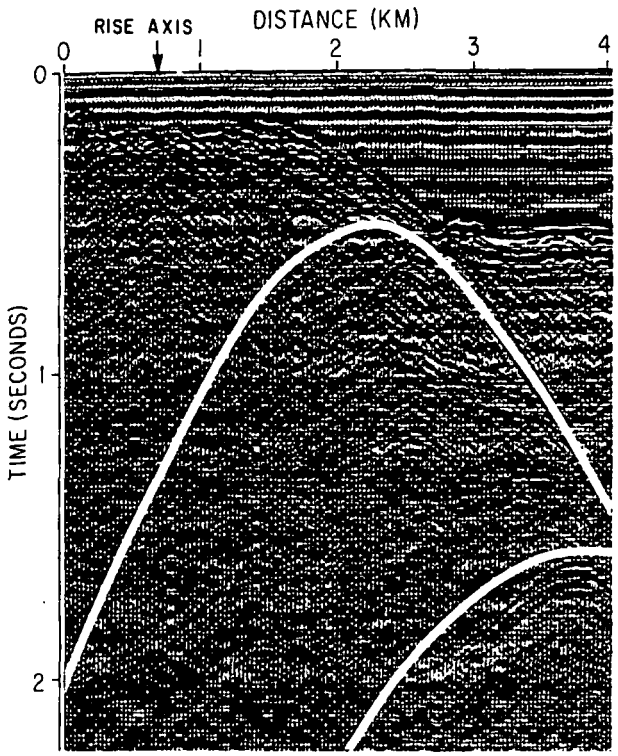

Fig. 7. Diffraction curves superimposed on the deep-towed data that were calculated from the assumption of side reflections off point source topography located to the side of the deep-towed array at two distances. This comparison is to show that many of the features in this record are too narrow to be due to seafloor topography and therefore represent subsurface reflections and diffractions.

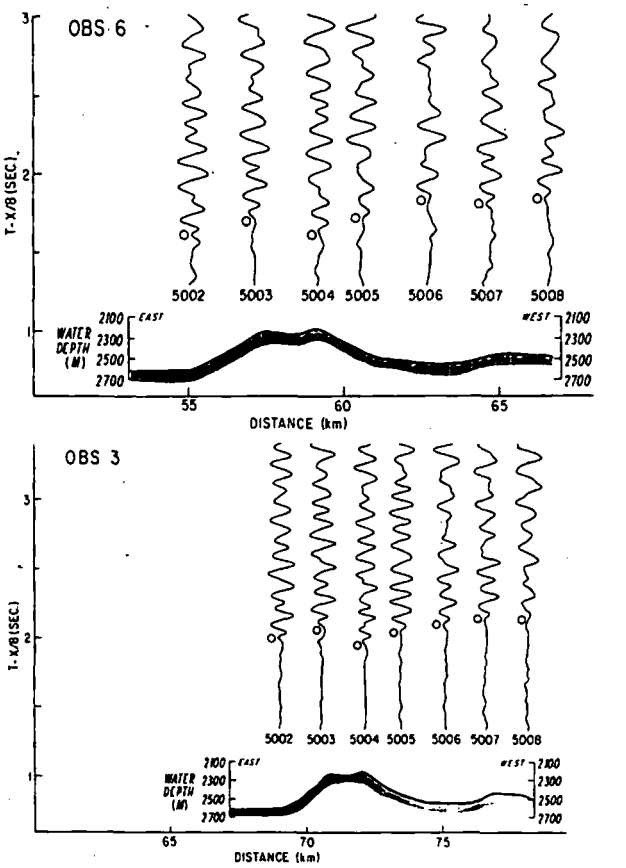

Fig. 8. The 5000 line shots across the ridge to OBS-6 and OBS-3. These instruments were located about 55 km east of the ridge. Corrections for seafloor topography have been applied to the seismograms. Mantle reflection (*PmP*) picks are indicated by circles. The mantle reflections show little or no offset as the shots cross the ridge.

First arrival times computed from the model for OBS-6 are shown as arrows in Figure 14 (top). The combination of the 3000 and 5000 lines as recorded by OBS-6 are shown in Figure 14 (top). The data do not show clear *Pn* arrivals across the ridge, but *PmP* arrivals are clear and do not appear attenuated by propagation through the ridge. The model used to fit the 3000 line reversal was extended across the ridge, and ray paths for *PmP* arrivals to OBS-6 for shots crossing the ridge were computed.

Ray paths for the computed *PmP* arrivals and their fit to the observed data are shown in Figure 14 as circles. These travel times fit the observed data well. One can see from the model that for shots near the ridge, these *PmP* rays sample the upper and middle crust under the axis. If there were a low-velocity region under the axis, these rays should be retarded and refracted with respect to normal crust. Yet their match with the observed data supports the hypothesis of no low-velocity material and therefore no magma chamber under the ridge.

Synthetic Seismogram Model

To confirm this high degree of lateral homogeneity across the ridge, synthetic seismograms were computed for the combined 3000 and 5000 lines as recorded by OBS-6, using the *Fuchs and Müller* [1971] reflectivity method incorporating Filon's integration method [*Frazer and Gettrust*, 1981]. This method assumes a laterally homogeneous velocity structure, and so the match of the synthetic seismograms to the observed data across the ridge can test the hypothesis of no large velocity variations under the ridge axis.

The observed data, computed synthetic data, and the corresponding velocity-depth model are shown in Figure 15. The model used is similar to the two-dimensional ray trace model and has a crustal thickness of 4.8 km with a mantle depth of 7.6 km.

The match to the observed data is good considering that no topographic corrections have been applied to the observed data. Later arrivals in the observed data for shots across the ridge match well with later arrivals in the synthetic data. *Pn* arrivals are of larger amplitude in the synthetic seismograms than in the observed data for shots crossing the ridge. This could easily be accounted for by a negative gradient in the mantle under the ridge.

Interpretation of Gravity Data

Shipboard gravity data were also collected along the three deep-towed reflection lines over the ridge crest. Instrumentation was a LaCoste and Romberg Air-Sea Gravity Meter, and corrections were applied for instrument drift, latitude variation, and the Eötvös correction. Ship speeds on all

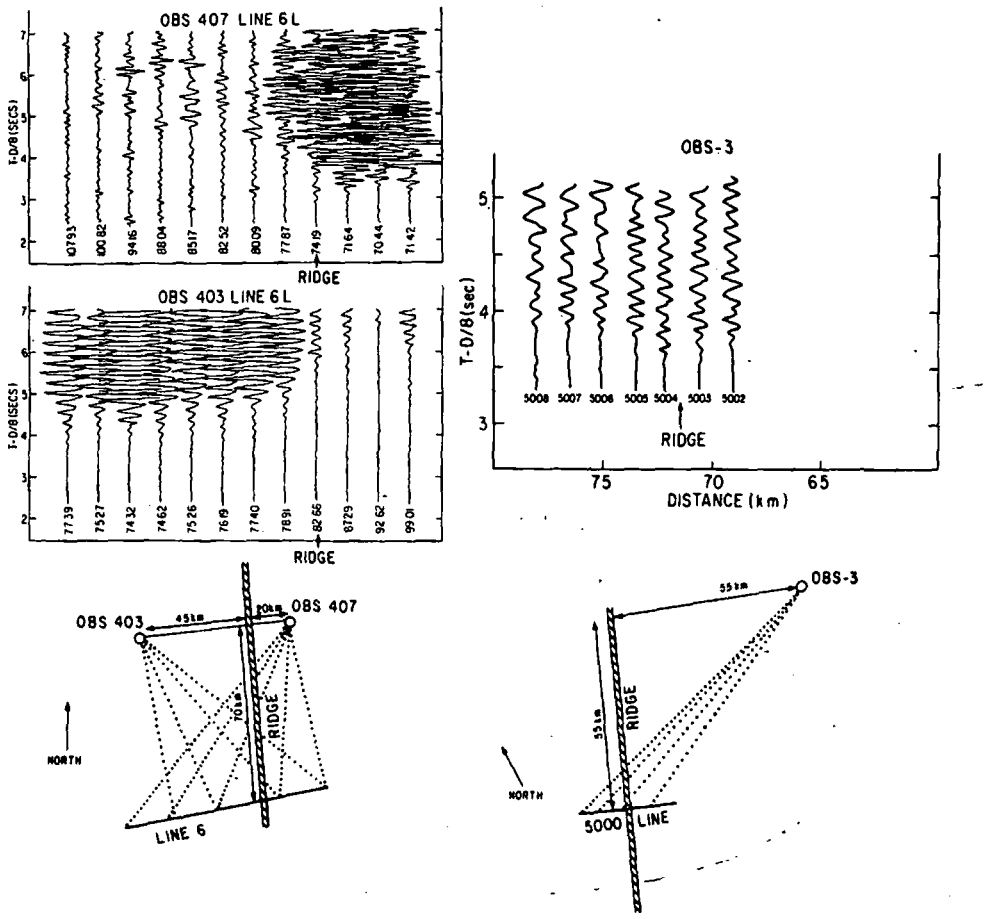

Fig. 9. A comparison of similar data sets from the ROSE area (left) and the northern Juan de Fuca Ridge (right). The two record sections on the left side of the figure are from line 6 shots across the East Pacific Rise as recorded by OBS 403 and OBS 407. Shot and receiver geometry are shown beneath the data. Note the poor energy propagation as shots cross the rise axis. The record section on the right side of the figure is from the 5000 line (this study) across the Juan de Fuca Ridge as recorded by OBS-3. Shot and receiver geometry are shown beneath the data. Note the excellent energy propagation as shots cross the ridge. All record sections have no topographic corrections.

three lines were less than 2 knots, and the latitude variation was very minor. At this slow speed, many data points could be collected along each of the profiles, providing a more accurate sampling of the gravity variations than is usually obtained.

To use the gravity anomaly to imply density variations under the ridge, one must understand the various factors that can affect the anomaly. Obviously, the topographic variation will affect the gravity anomaly. There may also be density variations in the upper crust due to fracturing and cooling as one moves away from the ridge. The presence of a magma chamber in the lower crust and partial melt in the mantle will also affect the gravity anomaly.

Assuming the fairly simplistic model that lateral density variations in the upper crust are responsible for the gravity anomaly, one can solve for this lateral density variation. Using the technique of *Parker* [1972] and *Oldenburg* [1974], one can invert for a lateral density variation which produces the gravity anomaly. From *Parker* [1972],

$$F[\Delta g(x)] = -2\pi G e^{-|k|Z_0} \sum_{n=1}^{\infty} \frac{|k|^{n-1}}{n!} F[\rho(x)h^n(x)]$$

Here, $g(x)$ is the gravity anomaly, $\rho(x)$ is the lateral density variation, k is the horizontal wave number, G is the gravitational constant, $h(x)$ is the topography, and Z_0 is the depth below the surface from which one measures $h(x)$. We define $g = -dU/dz$, which is the opposite of Parker's sign convention. Following a procedure similar to *Oldenburg* [1974], by transposing the $n = 1$ term from the above summation and rearranging, one has

$$F[\rho(x)h(x)] = \frac{F[\Delta g(x)]e^{|k|Z_0}}{2\pi G} - \sum_{n=2}^{\infty} \frac{|k|^{n-1}}{n!} F[\rho(x)h^n(x)]$$

One can use this equation, given Z_0, $h(x)$, and $g(x)$, with an initial guess of $\rho(x) = 0$ to solve iteratively for $\rho(x)$. This inversion assumes a flat bottom layer and a lateral density variation. The gravity and topography were smoothed by using a high-pass filter. The data were then sampled at evenly spaced points, extended to 2^n points so the Fast Fourier transform algorithm could be used and windowed to reduce wrap around discontinuities.

The ridge crest topography and free-air anomaly for line 001 are shown in Figure 16. The ridge rises 300 m above the

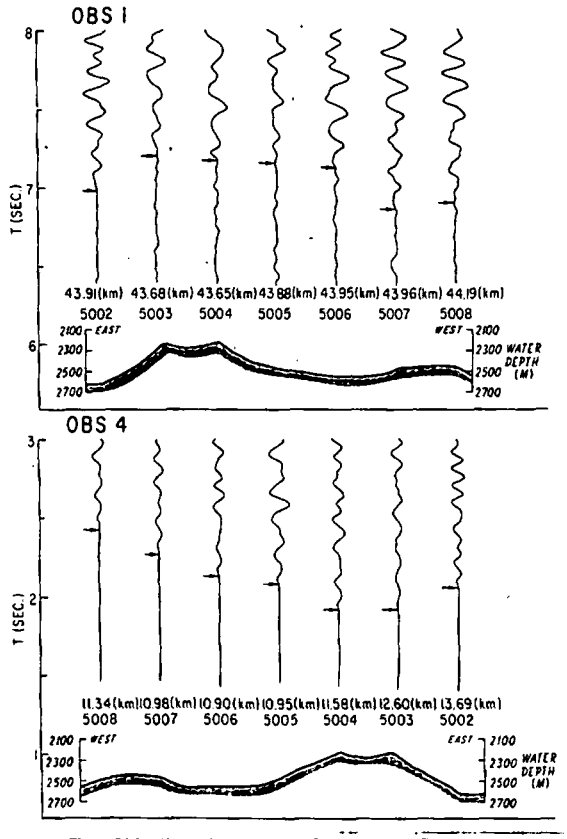

Fig. 10. The 5000 line shots to OBS-1 and OBS-4, both located on the ridge axis (see Figure 1). The first arrival picks are indicated by arrows.

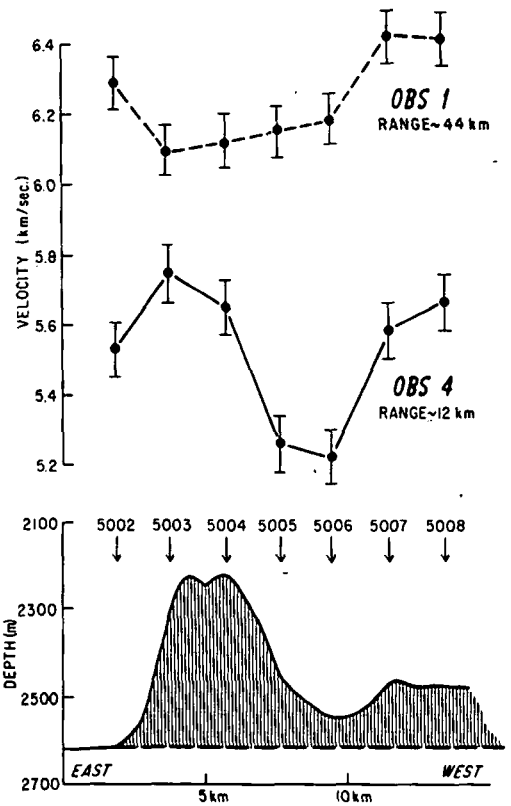

Fig. 11. Average velocity (travel time/range) plots for the 5000 line shots to OBS-1 and OBS-4. Corrections have been applied to remove the shaded topography.

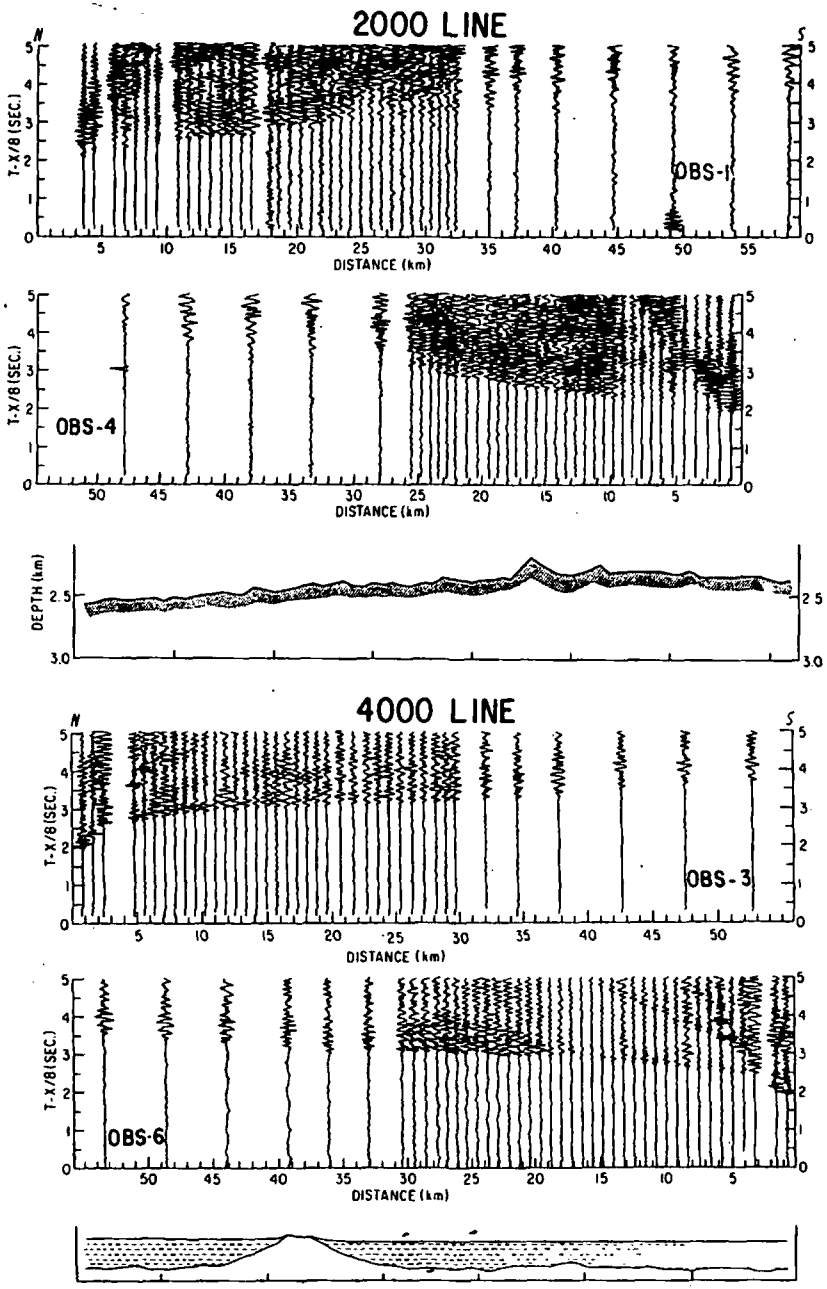

Fig. 12. Reversed record sections for the 2000 lines along the ridge axis (top) and the 4000 line parallel to and 55 km east of the ridge (bottom). Sediment cover is indicated by dashed horizontal lines.

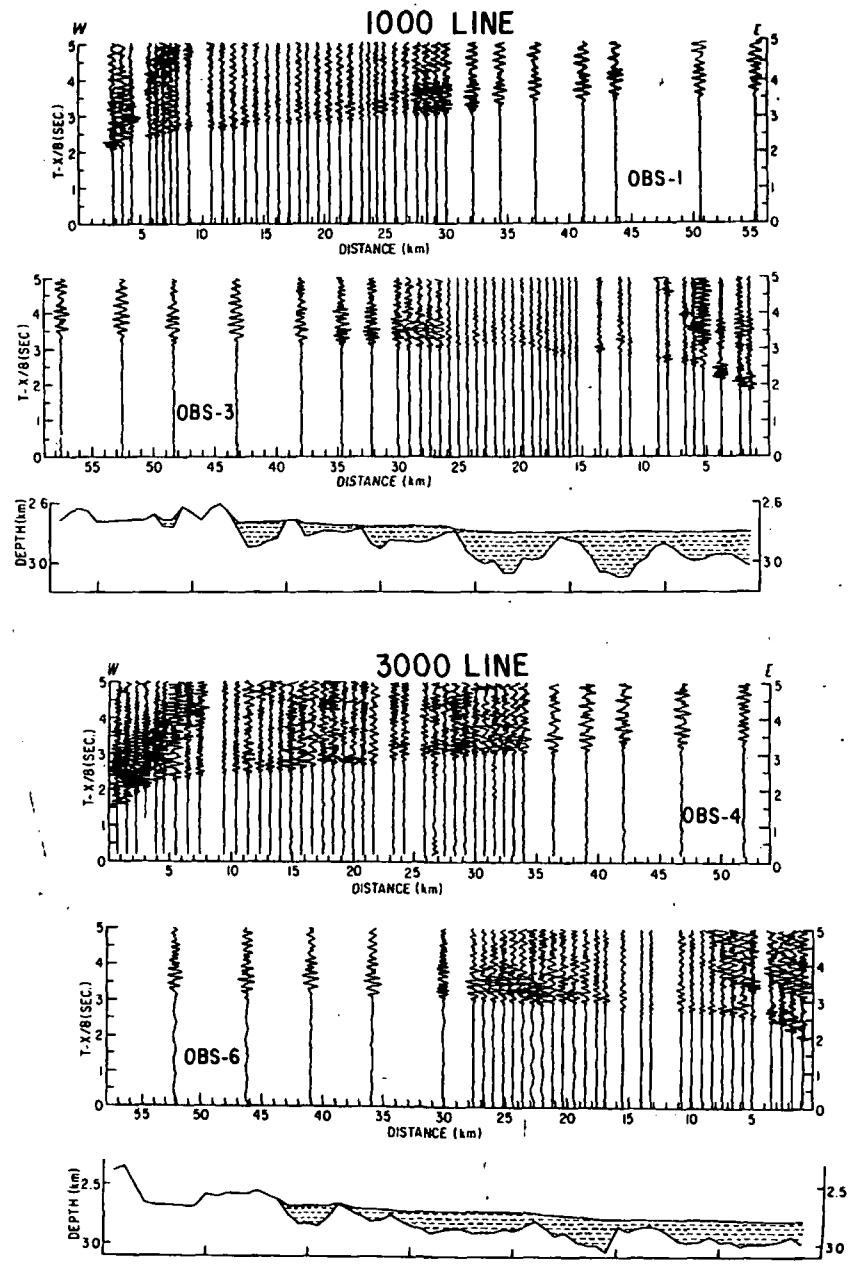

Fig. 13. Reversed record sections for the 1000 line (top) and the 3000 line (bottom) shot perpendicular to the ridge. Sediment cover is indicated by dashed lines.

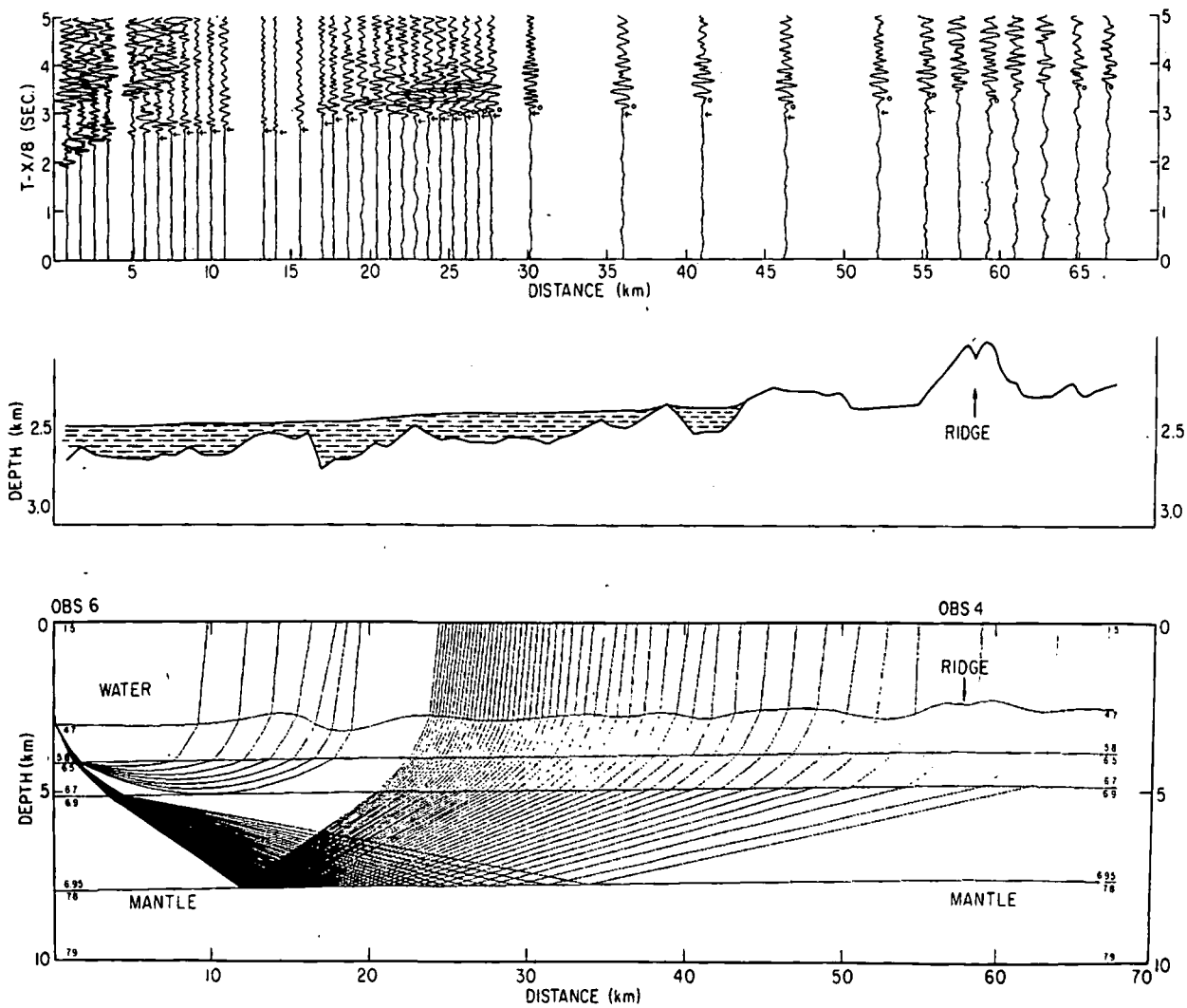

Fig. 14. Record section for the 3000 and 5000 lines as recorded by OBS-6 (top), bathymetry and sediment cover for these lines (center), and two-dimensional ray trace model (bottom). Shown in the ray trace model are ray paths for crustal refractions and wide-angle mantle reflections. Arrows on the top record section indicate computed times for crustal and mantle refractions as computed from the model. Mantle refracted ray paths are not shown on the bottom model. Circles on the data indicate *PmP* arrivals for ray paths shown in the model.

surrounding topography, and the gravity anomaly has a peak to peak amplitude of 4 mGal. Results of the density inversion for line 1 are also presented in Figure 16 for several values of Z_0. All inversions at different Z_0's fit the data within 1 mGal accuracy. The inversion became unstable for Z_0 larger than 3.7 km. Convergence occurred when either 50 iterations were performed or if the maximum difference between the old and new solution was less than 10^{-12} times the maximum of the new solution. The different density contrast profiles obtained with different Z_0's represent the nonuniqueness of the gravity inversion. However, we note that for $Z_0 = 3$ km the density contrast fluctuates by 1 g/cm^3, which is probably unreasonable. For larger Z_0's, the fluctuations are smaller, and no statistically discernible difference can be seen in the density under the rise axis.

We infer from this that the profile can be adequately explained by a two-dimensional topography with a roughly constant density of about 2.4 g/cm^3 (allowing for the rock-water contrast).

In the ROSE area, *Lewis* [this issue] has shown by a similar density inversion that the gravity cannot be explained by two-dimensional topography of constant density. Inversion results for the ROSE area suggest a mass excess under the ridge as compared with the adjacent lithosphere. Inversion results from the northern Juan de Fuca Ridge require no such mass variation, which suggests a different crustal density structure for the two areas.

Plotted at the same scale in Figure 17 are the bathymetric and free-air profiles for both the northern Juan de Fuca Ridge and the East Pacific Rise near 12°N in the ROSE area [*Lewis*, this issue]. The Juan de Fuca data are an east-west profile at 46°50'N taken from line 8 of the N.O.S. *Surveyor* data.

From the bathymetry, one sees that the East Pacific Rise near 12°N has a broader ridge crest than does the northern Juan de Fuca Ridge. The bathymetry near the Juan de Fuca Ridge is about 400 m higher in mean elevation than the East Pacific Rise, and each ridge rises about 300 m above the surrounding topography.

The corresponding free-air anomalies for these two ridges

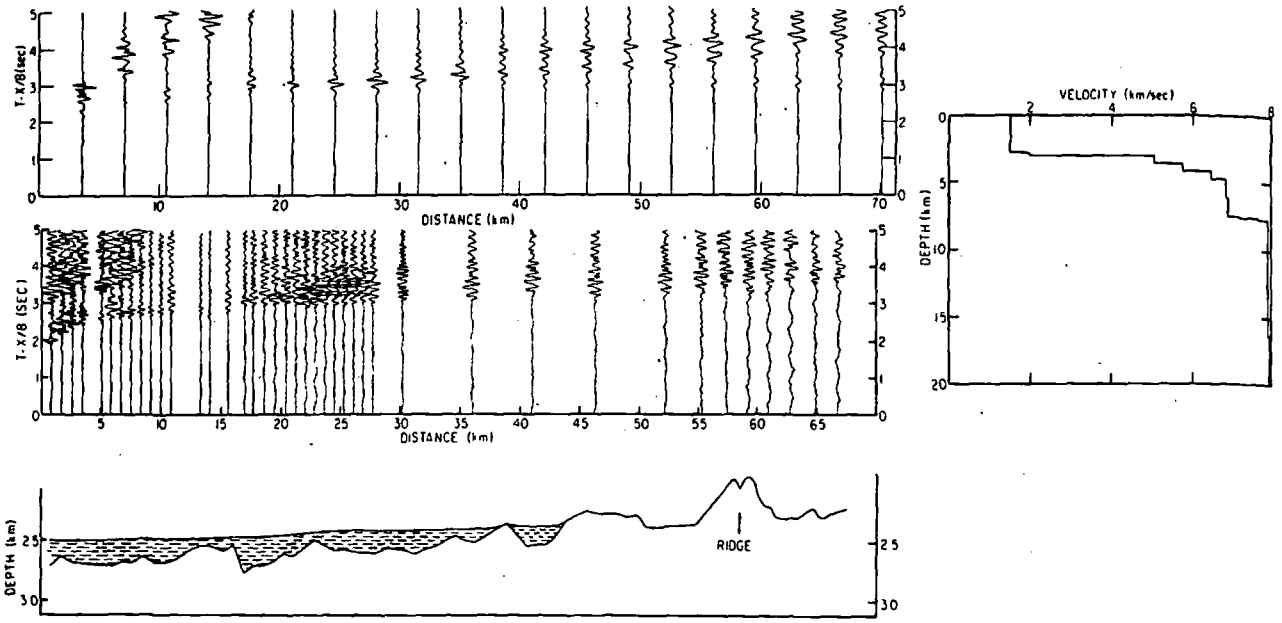

Fig. 15. Comparison of the observed 3000 and 5000 line data and synthetic seismograms computed from the laterally homogeneous model shown on the right.

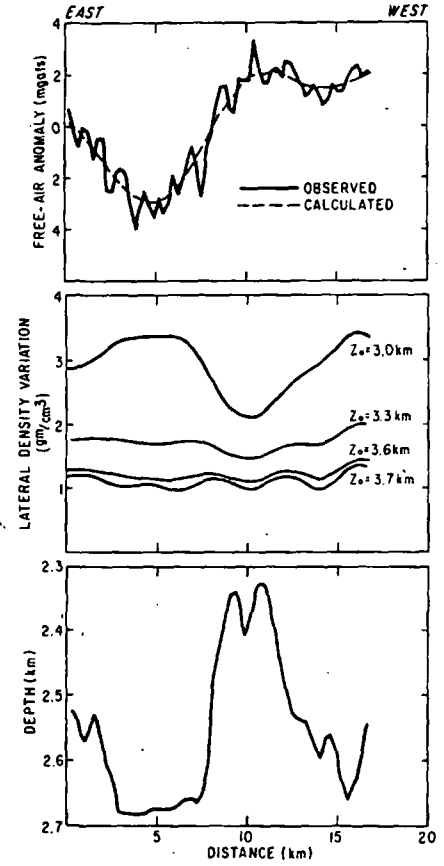

Fig. 16. Bathymetry, density inversion results, and observed and computed gravity anomalies across the ridge. The ridge axis is at 10 km on the distance scale. Z_0 is the depth below the surface from which the topography $h(x)$ is measured in the inversion. See text for discussion of results.

are very different. The free-air anomaly across the East Pacific Rise near 12°N has a peak-to-peak amplitude of about 12 mGal. Across the Juan de Fuca Ridge, the free-air anomaly is only about 5 mGal. These differences reflect different density structures with depth under each of these ridges.

CONCLUSIONS

We have shown that neither the seismic refraction, seismic reflection, nor gravity data support the existence of a zone under the axis of the northern Juan de Fuca Ridge having low velocity or abnormal density. Since we expect partial melt to exhibit abnormally low velocity [*Murase and McBirney*, 1973], we infer that there is no extensive zone of partial melt in the crust, particularly to the extent predicted by thermal models that do not include the effects of water cooling [*Sleep*, 1975]. Comparison with the fast spreading East Pacific Rise at 12°N shows significant differences in both the propagation of seismic waves across the axis and in the density structure under the axis.

The absence of a well-defined crustal magma chamber under the northern part of the Juan de Fuca Ridge places strong constraints on the processes of crustal accretion. First, it suggests that at this spreading rate, accretion may be episodic rather than continuous. Second, it implies that crustal cooling is far more rapid than predicted by conductive thermal models and that the rapid cooling probably extends to the base of the crust. An obvious mechanism for cooling is circulation of sea water through the crust by means of cracks [*Lister*, 1972]. A third implication relates to the petrology of the crust. We note that areas that may have steady state crustal magma chambers, such as the 12°N area, and areas with possible episodic accretion, such as the northern Juan de Fuca, produce crust of the same seismic

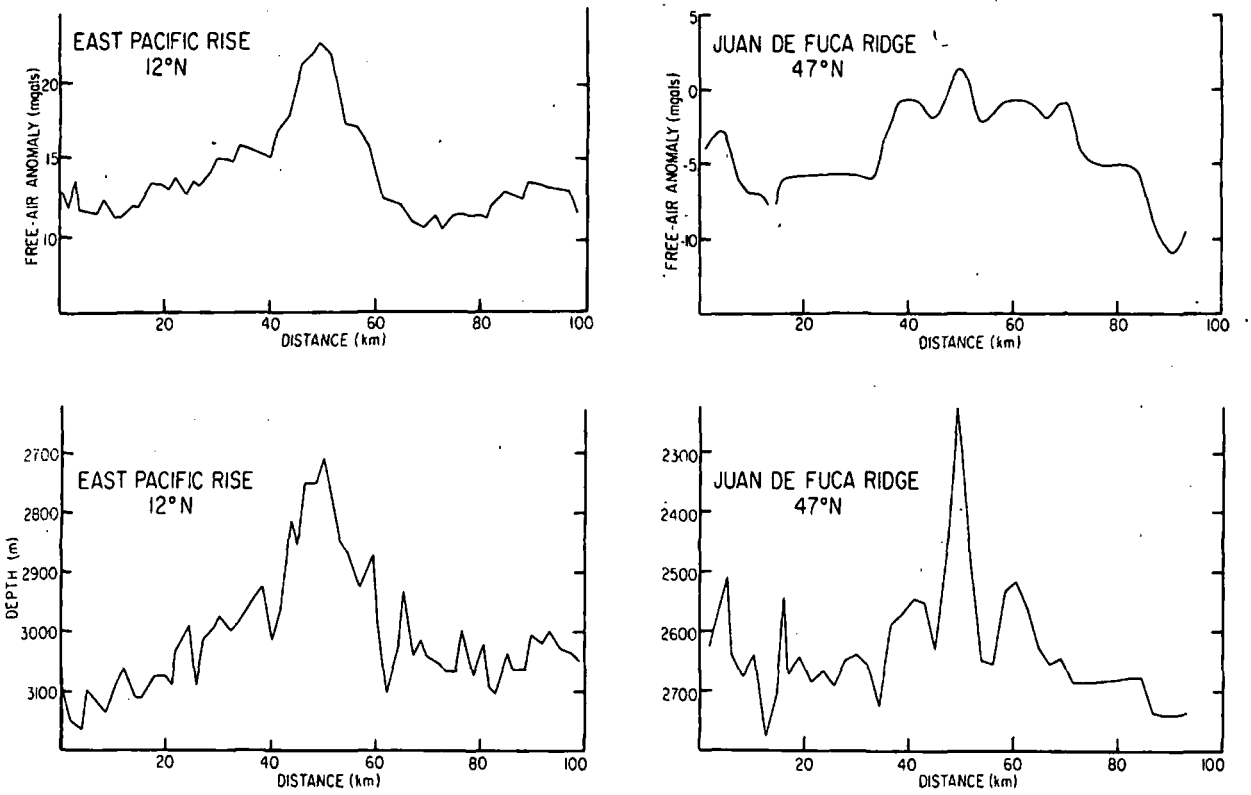

Fig. 17. A comparison of free-air anomalies and topography across the East Pacific Rise at 12°N (left) and the northern Juan de Fuca Ridge (right).

thickness (6 ± 1 km). If the crust mantle boundary were a petrologic boundary, it is unlikely that such different accretion mechanisms would produce such similar seismic thicknesses and velocities. An alternative explanation is that the crust-mantle transition represents the maximum depth to which water penetrates and the lower crust consists of hydrothermally altered ultramafics [*Clague and Straley*, 1977]. In this case it would not be surprising that different accretion processes give similar crustal thicknesses.

Acknowledgments. This work was done with support from the National Science Foundation (grant OCE 7621528) and the Office of Naval Research (contract N00014-80-C-0252). We also acknowledge the help of J. Taber with the two-dimensional ray tracing and W. Mooney and G. McMechan for providing this program. This is contribution number 1265, School of Oceanography, University of Washington.

REFERENCES

Clague, D. A., and P. F. Straley, Petrologic nature of the oceanic Moho, *Geology, 5*, 133–136, 1977.

Frazer, L. N., and J. F. Gettrust, On a generalization of Filon's method and its use in the computation of synthetic seismograms, submitted to *Geophys. J. R. Astron Soc.*, 1981.

Fuchs, K., and G. Müller, Computation of synthetic seismograms with the reflectivity method and comparison of observations, *Geophys. J. R. Astron. Soc., 23*, 417–433, 1971.

Lewis, B. T. R., Constraints on the structure of the East Pacific Rise from gravity data, *J. Geophys. Res.*, this issue.

Lewis, B. T. R., and J. D. Garmany, Constraints on the structure of the East Pacific Rise from seismic refraction data, *J. Geophys. Res.*, this issue.

Lister, C. R. B., On the thermal balance of a mid-ocean ridge, *Geophys. J. R. Astron. Soc., 26*, 515–535, 1972.

Lister, C. R. B., and B. T. R. Lewis, An ocean bottom seismometer suitable for arrays, *Deep Sea Res., 23*, 113–124, 1976.

McMechan, G. A., and W. D. Mooney, Asymptotic ray theory and synthetic seismograms for laterally varying structures: Theory and application to the Imperial Valley, California, *Bull. Seismol. Soc. Am., 70*, 2021–2035, 1980.

Morris, G. B., R. W. Raitt, and G. C. Shor, Velocity anisotropy and delay time maps of the mantle near Hawaii, *J. Geophys. Res., 74*, 4300–4316, 1969.

Murase, T., and A. R. McBirney, Properties of some common igneous rocks and their melts at high temperatures, *Geol. Soc. Am. Bull., 84*, 3563–3592, 1973.

Oldenburg, D. W., The inversion and interpretation of gravity anomalies, *Geophysics, 39*, 526–536, 1974.

Parker, R. L., The rapid calculation of potential anomalies, *Geophys. J. R. Astron. Soc., 31*, 447–455, 1972.

Raff, A. D., and R. G. Mason, Magnetic survey off the west coast of North America, 40°N to 52°N, *Geol. Soc. Am. Bull., 72*, 1267–1270, 1961.

Riddihough, R. P., A model for recent plate interactions off Canada's west coast, *Can. J. Earth Sci., 14*, 384–396, 1977.

Shor, G. G., Jr., P. Dehlinger, H. K. Kirk, and W. S. French, Seismic refraction studies off Oregon and northern California, *J. Geophys. Res., 73*, 2175–2194, 1968.

Sleep, N. H., Formation of oceanic crust: Some thermal constraints, *J. Geophys. Res., 80*, 4037–4042, 1975.

(Received June 8, 1981;
revised December 2, 1981;
accepted December 18, 1981.)

Geophysical measurements in the region of the Explorer ridge off western Canada[1,2]

R. D. HYNDMAN, G. C. ROGERS, AND M. N. BONE

Earth Physics Branch, Department of Energy, Mines and Resources, Pacific Geoscience Centre, Patricia Bay Institute of Ocean Sciences, P.O. Box 6000, Sidney, B.C., Canada V8L 4B2

C. R. B. LISTER AND U. S. WADE

Department of Oceanography, University of Washington, Seattle, WA 98195, U.S.A.

D. L. BARRETT

Geological Survey of Canada, Department of Energy, Mines and Resources, Atlantic Geoscience Centre, Bedford Institute, Dartmouth, N.S., Canada B2Y 4A2

E. E. DAVIS

Department of Earth and Planetary Sciences, Massachusetts Institute of Technology, Cambridge, MA 02139, U.S.A.

T. LEWIS

Division of Seismology and Geothermal Studies, Earth Physics Branch, Department of Energy, Mines and Resources, Ottawa, Ont., Canada K1A 0Y3

S. LYNCH

Department of Geophysics and Astronomy, University of British Columbia, Vancouver, B.C., Canada V6T 1W5

AND

D. SEEMANN

Geological Survey of Canada, Department of Energy, Mines and Resources, Pacific Geoscience Centre, Sidney, B.C., Canada V8L 4B2

Received February 8, 1978

Revision accepted April 27, 1978

The region of the Explorer spreading centre off Vancouver Island, British Columbia, has been studied through a marine geophysical survey. Earthquake epicentres located by three ocean bottom seismometers confirm that the boundary between the Pacific plate and the Explorer plate (the northern extension of the Juan de Fuca plate) at present lies along the Sovanco fracture zone, the Explorer ridge, and the Dellwood Knolls. The epicentres of earthquakes in this area as determined by the onshore seismic network are found to be subject to significant errors. The ocean bottom seismometers also have been used for a detailed seismic refraction line just to the north of the Explorer spreading centre employing explosives and a large airgun as sources. A preliminary analysis of the data indicates a fairly typical crustal structure but a shallow and low velocity mantle near the ridge crest, and illustrates the value of ocean bottom seismometers in oceanic refraction studies. A new geothermal heat flux probe was employed in this study that permitted repeated 'pogostick' penetrations without raising the instrument to the surface. Six profiles with a total of 112 penetrations provided valuable data on the nature of hydrothermal circulation in the oceanic crust. Eleven standard heat probe stations provided some restraints on the poorly known age of the oceanic crust along the margin. Seismic reflection profiles using a 3.5 kHz system, a high resolution pulser profiler, and a large airgun were used as aids in the interpretation of the seismic and heat flow data.

On a étudié la région du centre d'expansion Explorer au large de l'Ile de Vancouver en Colombie-Britannique à l'aide d'un levé géophysique marin. Les épicentres de séismes localisés par trois sismomètres installés dans le fond de l'océan confirment le fait que la limite entre la plaque du Pacifique et la plaque Explorer (l'extension au nord de la plaque Juan de Fuca) se trouve à présent le long de la zone de fracture de Sovanco, de la crête d'Explorer et des monticules de Dellwood. Les épicentres des séismes dans cette région tels que déterminés par le réseau sismique côtier semblent être entachés d'erreurs significatives. On a aussi utilisé les sismomètres

Can. J. Earth Sci., 15, 1508–1525 (1978)

[1]Earth Physics Branch Contribution No. 723.

[2]Contribution of Bedford Institute of Oceanography No. BI 679.

sur le fond océanique pour un profil détaillé de sismique-réfraction juste au nord du centre d'expansion Explorer en utilisant des explosifs et de gros fusils à air comme sources. Une analyse préliminaire des données indique une structure de la croûte assez typique mais un manteau à faible profondeur et à basse vitesse près du sommet de la crête et illustre l'utilité des sismomètres de fond dans les études de réfraction océaniques. On a utilisé dans cette étude une nouvelle sonde pour le flux de chaleur géothermique qui permet des pénétrations répétées sans ramener l'instrument en surface. Six profils avec un total de 112 pénétrations ont fourni des données précieuses sur la nature de la circulation hydrothermale dans la croûte océanique. Onze stations de sondes thermiques standard ont fourni quelques limites aux âges mal connus de la croûte océanique le long de la bordure. On a utilisé des profils de sismique-réflexion avec un système de 3.5 kHz, un profileur à pulsation de grande résolution et un gros fusil à air pour aider à l'interprétation des données sismiques et thermiques.

[Traduit par le journal]

Introduction

This article presents data and preliminary analyses of seismicity, seismic refraction, seismic reflection profiling, and heat flow from a cruise on C.F.A.V. *Endeavour* in the area of the Explorer spreading centre off Vancouver Island, British Columbia (Fig. 1). The area is one of considerable tectonic complexity with interaction between a number of lithospheric plates (e.g., Wilson 1965). The triple point junction between the Explorer plate (the northern extension of the Juan de Fuca plate), the Pacific plate, and the North America plate is located at or near the edge of the continental shelf between the northern end of Vancouver Island and the southern end of the Queen Charlotte Islands (e.g., Riddihough 1977). In this region the zone of convergence or subduction off Vancouver Island meets the Queen Charlotte transform fault system which extends to the northwest and the Juan de Fuca – Explorer ridge system which extends to the southwest.

In addition to collecting data important to the detailed understanding of this particular area, we have attempted to make use of a special feature of the region, that a spreading ridge system approaches a continental margin subduction zone, to examine several fundamental tectonic and geophysical processes.

The first important consequence of a spreading centre obliquely approaching a convergent continental margin is that the lithosphere produced at the ridge is subducted after reaching an age of only a few million years. The age and the thickness of the oceanic lithosphere being subducted decreases to the north toward the triple point. It is of fundamental importance to know, if at less than some limiting age, the lithosphere will not have sufficient strength or rigidity to remain a coherent unit thrusting beneath the continent. The small plates may deform or break up, defining the limit to plate tectonics. In addition, the rapid changes in the motions of the small plates (e.g., Riddihough 1977) probably depends primarily on the forces along their boundaries. If the changes in motion and in the boundaries can be outlined in detail, basic information on plate driving forces may be obtained.

One part of the study was directed to better outlining the location of the Pacific–Explorer plate boundary from earthquakes recorded on ocean bottom seismometers and from seismic profiling. The exact location of the boundary and triple point has been difficult to determine because of the complicated and rapidly developing series of en-echelon spreading centres and connecting transform faults extending from the north end of the Juan de Fuca ridge. The boundary is probably defined by a spreading centre along the Explorer ridge with a bifurcation at its northern end, a transform fault following the Revere–Dellwood fracture zone, a spreading centre at the Dellwood Knolls, and possibly a further transform fault to a short spreading centre just south of the Queen Charlotte Islands (e.g., Srivastava *et al.* 1971; Bertrand 1972; Tiffin 1973; Barr and Chase 1974; Chase *et al.* 1975; Riddihough and Hyndman 1976; Chase 1977). The short segments are not clearly resolved by previous seismic profiles, by magnetic anomalies, or by earthquake epicentres located by land stations. A

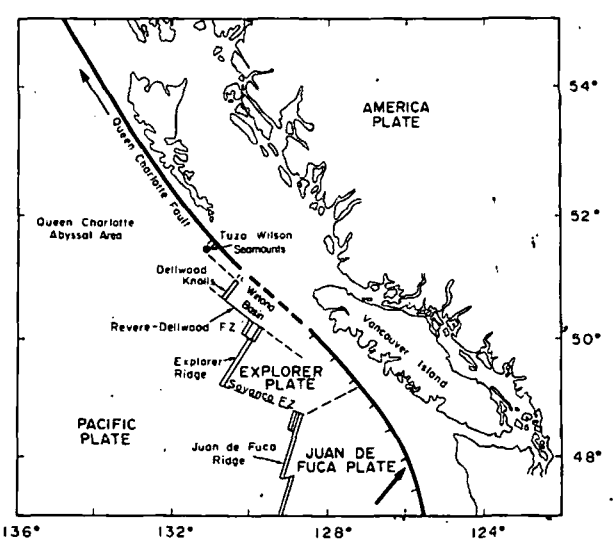

FIG. 1. Location map of study area.

related part of the study was to use seismic refraction measurements to examine the crustal structure in the area which previous work had shown to be complex and variable, perhaps in response to the plate interactions (e.g., Clowes and Malecek 1976).

The second important aspect of the fact that the ridge system approaches the continent is the rapid terrigenous sedimentation over the spreading centre, the sediment cover being a critical factor in the thermal regime of the young crust. Previous geothermal heat flow measurements in this area had first demonstrated that hydrothermal circulation dominated the thermal regime of young oceanic crust (e.g., Lister 1972). A thick impermeable sediment cover appears to seal off the crust from convective exchange with the ocean so that the total heat flux from the cooling lithosphere may be measured by a heat flux probe. The Juan de Fuca – Explorer ridge system is one of the few areas where the sedimentation rate is sufficiently high to seal off the crust very close to the spreading axis. This study employed a large number of closely spaced heat flow measurements to outline the thermal regime of oceanic crust of various ages and sediment covers.

Ocean Bottom Seismometer Instruments and Operation

Two types of free fall, pop-up ocean bottom seismometers were employed in this study: the first type of design essentially as described by Lister and Lewis (1976) and Johnson *et al.* (1977) (two units, designated PGC instruments) and the second type of design similar to that described by Sutton *et al.* (1977) (two units, designated AGC instruments). The PGC instruments consist of a 60 cm diameter buoyant aluminum sphere instrument package that fits into a large 400 kg flowerpot-shaped concrete anchor, attached by a magnetic link. One vertical and two horizontal 4.5 Hz seismometers and a time code are direct recorded on magnetic tape for up to 300 h. A square root signal compression permits an 80 dB effective dynamic range over a frequency band of 2–100 Hz.

The AGC instruments consist of an 18 cm diameter cylindrical instrument housing with a 33 cm diameter glass sphere for flotation. A 50 kg concrete anchor is attached by an evacuated clamshell release (see Barrett *et al.* 1977; Heffler and Locke 1978). Recording is continuous direct on standard magnetic tape cassettes for up to 300 h, with a frequency band from 2–20 Hz. High frequency direct waves through the water are detected by superimposing a rectified and smoothed signal on the clock tape channel. The output from one vertical and one horizontal 4.5 Hz geophone and a hydrophone are recorded with a dynamic range of 40 dB.

The four seismometers were first employed in a 70 km line for seismic refraction (Figs. 2 and 6). One AGC instrument deployed several kilometres from OBS site 3 failed to return to the surface and was lost. We now think that sediment may have sealed the tube before sea water completely filled the evacuated space. An external rubber water reservoir is now used to fill the evacuated space. After the refraction experiment the remaining AGC instrument was redeployed at OBS site 5 to form a 30 km triangular array for 6 days of earthquake recording. The location of the deployments was determined by satellite and Loran A to within about 0.5 km.

All of the three recovered instruments performed well, the only important failure being the hydrophone of the AGC instrument which operated only for a short period on the first deployment and not at all on the second. This was a significant loss as the hydrophone signal appears to be very valuable for the identification of some phases not clearly defined on the geophone records. Examples of records obtained from earthquakes and explosive charges are shown in Figs. 3 and 4. Profiles of airgun shots on the vertical seismometer of OBS site 2 PGC instrument and explosive shots on the AGC instrument at site 3 are shown in Fig. 8 *a*, *b*. The quality of the data from the two instrument types is generally good, both for shots and for earthquakes. The AGC instrument record appeared to exhibit considerable ringing. However this ringing may reflect crustal resonances that characterize ridge crests (Prothero 1977), rather than instrument response.

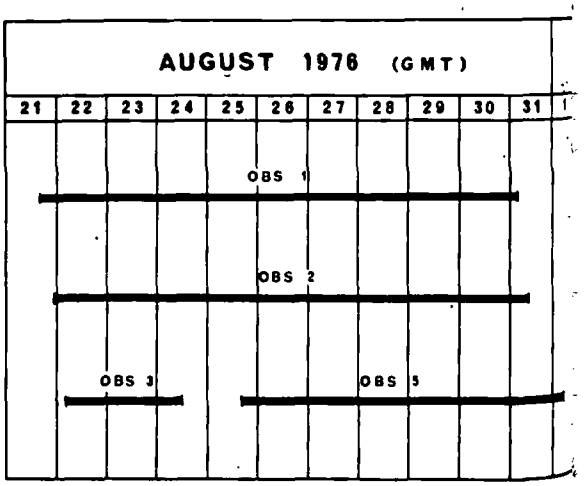

FIG. 2. Recording periods of ocean bottom seismometers.

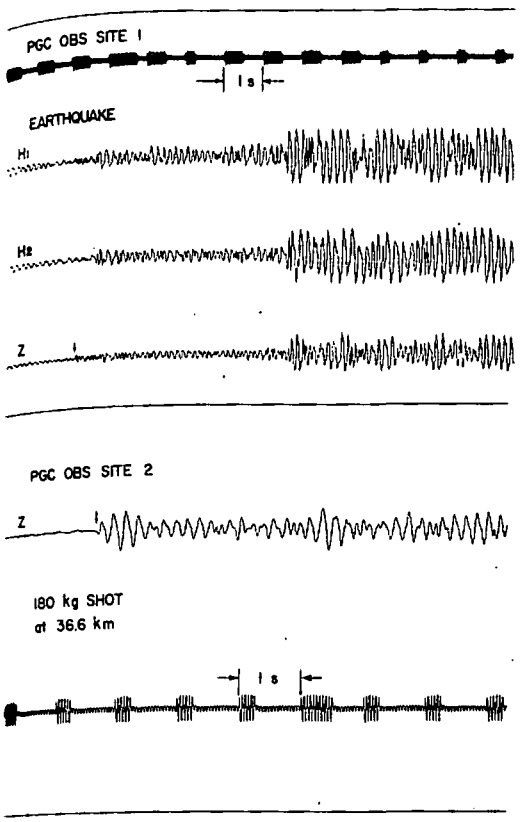

FIG. 3. Examples of an earthquake and an explosion recorded on a PGC ocean bottom seismometer.

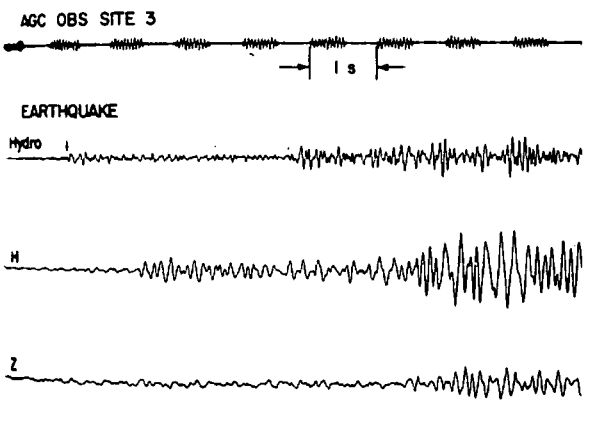

FIG. 4. Example of an earthquake recorded on an AGC ocean bottom seismometer.

Seismicity of the Explorer Ridge Area

Earthquake epicentres west of northern Vancouver Island located by land stations show a large scatter that in a general way follows the Pacific – Juan de Fuca plate boundary as defined by marine geophysical data. But in detail there is rather poor coincidence of epicenters and the ridge transform segments (Milne *et al.* 1978) (Fig. 5). As pointed out by Barr and Chase (1974), most of the epicentres lie to the east of the Explorer ridge. They have suggested that the apparent trend of events represents a new plate boundary, the Queen Charlotte transform extending south to the northern end of the Juan de Fuca ridge cutting off the Explorer spreading centre (see also Wilson 1965). The Explorer spreading centre is quite well defined by the magnetic anomaly pattern, bathymetry, seismic reflection profiles, and heat flow measurements so such a new plate configuration would necessarily be very recent (e.g., Hyndman and Riddihough 1977).

However, the locations of most offshore events determined by the land seismic station network as given in seismicity maps (e.g., the map of Barr and Chase 1974) probably have uncertainties of 50–100 km (very recent events are better located as the network has expanded). Some systematic biases also exist because all of the stations are to

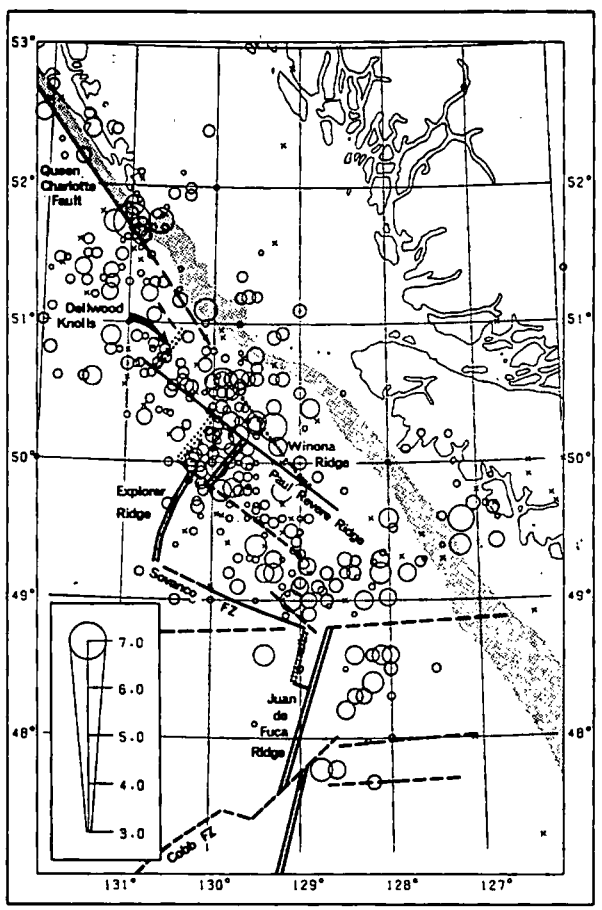

FIG. 5. Earthquake epicentres in the Explorer plate region from the Canadian land seismic network (after Milne *et al.* 1978).

one side of the events and because of the complex and poorly known velocity structure across this converging continental margin. Careful relocation of selected offshore earthquakes in this area using land network data with more exact velocity models (Tobin and Sykes 1968; Wetmiller 1971; Lee 1978) suggests that most of the events probably are along the spreading centres and transform fault boundaries as defined by marine geophysical data. The few fault plane solutions available for the region indicate predominantly strike-slip faulting in agreement with the accepted trend and motions of the transform fault segments (see summary in Milne *et al.* 1978). Some of the earthquakes located to the east of the ridge system are not mislocations but appear to be associated with a plate boundary extending perpendicular to the margin to the north end of the Juan de Fuca ridge (Figs. 1 and 5) (called here the Nootka fault zone) that separates the main Juan de Fuca plate from the small Explorer plate to the north. Magnetic data (Riddihough 1977) suggests left lateral motion of about 2 cm year^{-1} and two fault plane solutions (Rogers 1976; Lee 1978) are consistent with this interpretation.

The primary intent of the ocean bottom seismometer earthquake recording was to see if the microseismicity confirmed motions along the main plate boundaries rather than a recent break up of the Explorer plate that would give general seismicity, and to better define the boundaries. A summary of the results is given here.

Several hundred earthquakes were recorded at one or more of the seismometers during the 10 day recording period, with magnitudes from less than 1 to one event of magnitude about 4 that was also recorded on a number of land stations. Of these events, 34 were well recorded by all three seismometers and could be located reliably. The velocity model was taken from the seismic refraction experiments in the area and both P and S first arrivals were used in the epicentre location. The depths were restricted to 3 km on the basis of the depths obtained in other similar spreading ridge areas (e.g., Reichle *et al.* 1976). The few events in our study for which, using shear wave arrivals, depth could be estimated are consistent with such shallow depth. The estimated accuracy of the epicentres ranges from less than 5 km near the array to about 15 km for the most distant events located (Fig. 6).

The epicentres lie in three distinct groups that clearly follow and substantiate the Pacific–Explorer plate boundary as defined by previous geophysical studies: along the Explorer spreading centre, the Revere–Dellwood transform fault, and

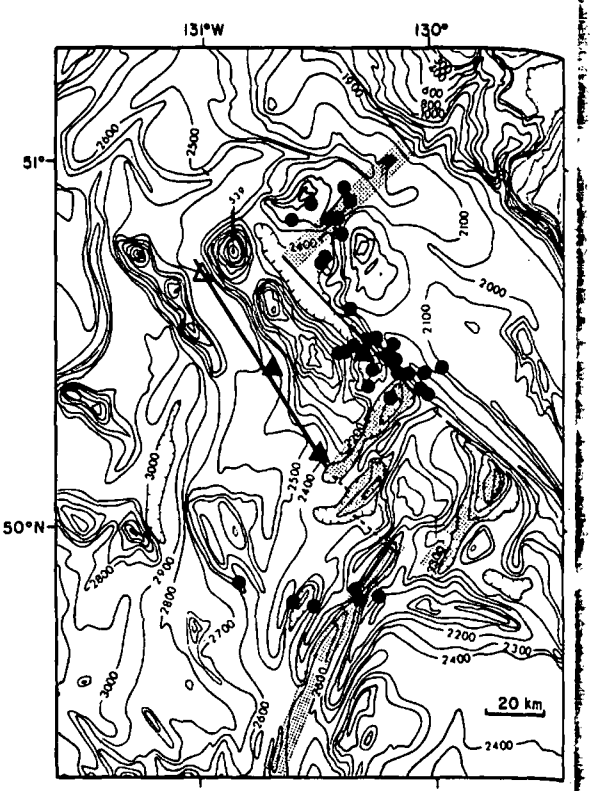

FIG. 6. Earthquake epicentres in the area of the Explorer and Dellwood spreading centres located by the ocean bottom seismometers. The solid triangles mark the sites of the seismometers used to locate the events. The open triangle is the location of the additional site used in the refraction line. The bathymetric contours are in metres from Tiffin and Seemann (1975).

the Dellwood spreading centre. No events were located in the Winona basin to the south and east that would indicate deformation or breaking up of the Explorer plate. There also were no events that might be associated with the bending of the oceanic lithosphere into the subduction zone, as found off Japan (Nagumo *et al.* 1976). The epicentres suggest that spreading is primarily on the northwest of the two branches at the northern end of the Explorer spreading centre, but several poorly located smaller events (not plotted) may be on the southeast branch. The seismicity substantiates the Dellwood Knolls being a spreading centre. The concentration of events on the Revere–Dellwood fracture zone, particularly near its intersection with the Explorer spreading centre (see also Wetmiller 1971), is consistent with previous ocean ridge microearthquake studies that found most events to occur on transform offsets of ridges, and to be most frequently located in the central trough of the fracture zone (e.g., Prothero *et al.* 1976; Reid *et al.* 1973; Spindel *et al.* 1974; Francis *et al.* 1977; Reichle *et al.* 1976). The events associated with the Dellwood spreading

e area of the Explorer and
by the ocean bottom seis-
he sites of the seismome-
n triangle is the location of
ion line. The bathymetric
l Seemann (1975).

re. No events were
o the south and east
on or breaking up of
) were no events that
ending of the oceanic
)n zone, as found off
he epicentres suggest
the northwest of the
end of the Explorer
poorly located smal-
be on the southeast
ntiates the Dellwood
e. The concentration
wood fracture zone.
on with the Explorer
tmiller 1971), is con-
lge microearthquake
ts to occur on trans-
) be most frequently
of the fracture zone
d *et al.* 1973; Spindel
; Reichle *et al.* 1976).
: Dellwood spreading

centre are scattered rather uniformly over the apparent zone of accretion in contrast to results from the mid-Atlantic ridge which show most events on one wall of the median valley some distance from the apparent zone of accretion (e.g., Spindel *et al.* 1974; Francis *et al.* 1977).

One event of magnitude M_L = 3.8 (m_b = 4.4) occurred on the Revere–Dellwood transform fault and was well recorded at a number of land stations (Fig. 7). The epicentre from the ocean bottom seismometers should have an accuracy of about 2 km. The U.S. Geological Survey P.D.E. epicentre for this event (using P first arrivals only) is some 60 km to the east of its actual location as determined by the ocean bottom seismometers. The epicentre from the routine location of earthquakes by the Canadian Seismological Service (EPB) (using P and S arrivals) has a smaller but still significant error, lying 20 km north of the actual location. We emphasize that more stations were employed for this latter epicentre than were available for locating most previous events, particularly prior to 1964 (see Milne *et al.* 1978). Thus, the location uncertainty for most previously located events is larger than 20 km. These errors suggest that a significant systematic location bias is responsible for the large number of epicentres located to the east of the actual plate boundary, from land station data. This large event will permit a travel time calibration for the western Canada land network that will result in more accurate location of offshore events in the general area.

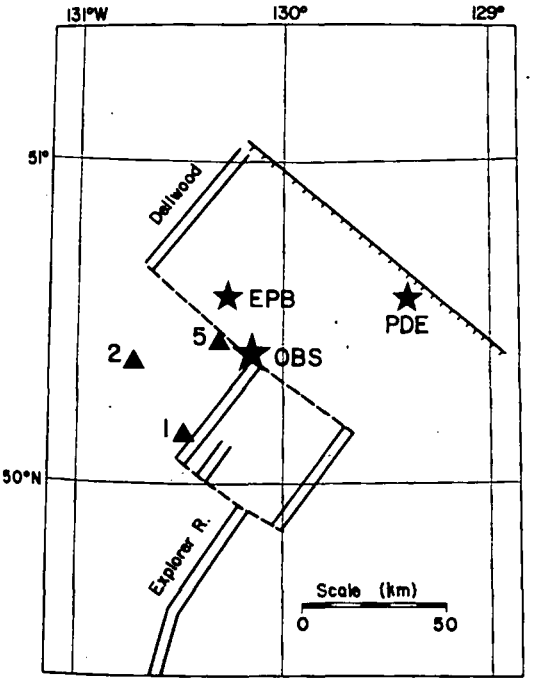

FIG. 7. Various epicentres for the largest earthquake recorded by the ocean bottom seismometers. PDE is the U.S. Geological Survey preliminary determination; EPB is the Candian Seismological Service, Earth Physics Branch, epicentre.

Seismic Refraction

Ocean bottom seismometers have been a significant technical advance in explosion seismology providing fixed location high sensitivity detectors that can record S as well as P arrivals. Some previous studies near the crests of spreading ridges have outlined a variety of special crustal structures ranging from nearly normal crustal structure (e.g., Whitmarsh 1973; Snydsman *et al.* 1975; Davis *et al.* 1976) to a narrow zone of partial melting under the zone of acretion (Reid *et al.* 1977) and a low velocity layer at the base of the crust (Lewis and Snydsman 1977).

In this study a detailed 70 km long seismic refraction line was undertaken, to the northwest of, and perpendicular to the Explorer spreading centre near the Revere–Dellwood fracture zone (Fig. 6). PGC ocean bottom seismometers were deployed about 5 and 35 km from the spreading centre (0.2 and 1.2 Ma old crust) and an AGC instrument at about 75 km from the spreading centre (about 2.5 Ma old crust). A total of 2300 kg of high velocity explosive was detonated in 80 shots ranging from 4.5–180 kg, in a general pattern of alternating large and small shots (Fig. 8*a*). The large shots provided sufficient energy for arrivals at distant seismometers while the small charges provided arrivals that did not overload nearby seismometers. The charges were deployed and fuse detonated while the ship was moving at 8 kn. The fuse time was adjusted to give the optimum shot depth (e.g., Shor 1963) using estimates of the charge sinking rates. Shot times were obtained from comparison of WWV time signals and arrivals both at a towed hydrophone and at a low sensitivity geophone on the ship's deck, correcting for the shot to ship travel time. In addition to the explosive charges, a 1000 in.^{3} (16 L) airgun firing at 2 min intervals was traversed over each seismometer both parallel and perpendicular to the profile to obtain detailed information at short ranges, i.e., to about 15 km (Fig. 8*b*).

To obtain travel times to the ocean bottom seismometers, the following time corrections were applied: (1) OBS clock drift — the clocks were rated in a cold room for several days before and after deployment and interpolated corrections applied. (2) The shot depths were corrected to be effectively at the surface. (3) A standard water

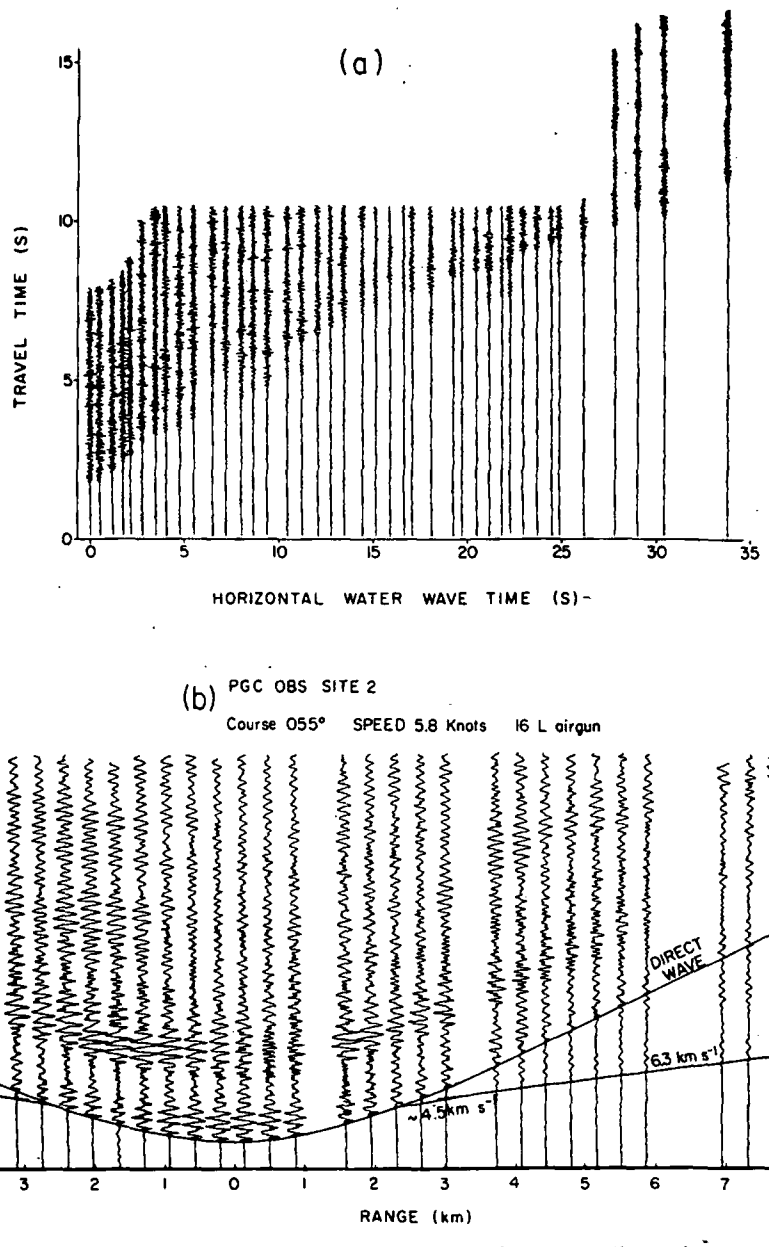

FIG. 8. (*a*) Explosion seismic section across AGC OBS at site 3, vertical seismometer. (*b*) A seismic section across the PGC seismometer at site 2 with the large airgun. The traces are vertical seismometer, 15 Hz low pass filtered.

depth of 1.74 s and sediment thickness of 0.36 s were used, differences being corrected with 4.7 km s^{-1} material. Uncertainties in these corrections and in the shot instants may result in travel time errors of up to 0.050 s.

Shot to receiver horizontal distances were obtained from the direct water wave arrivals. The direct one segment path, the three segment path (one reflection off the bottom and one off the surface), and the five segment path were all used at different ranges. The travel time – distance relation for each path was determined using ray tracing and an average water velocity – depth profile from measurements in the area. Synthetic seismograms were used as an aid in the identification of the different water wave arrivals (McMechan 1978). The conditions of nearly constant ship speed during the shooting and that the distances between shots as computed for the different seismometers should be the same were used as constraints. The estimated distances should be accurate to within 0.3 km.

The analysis of marine seismic refraction data

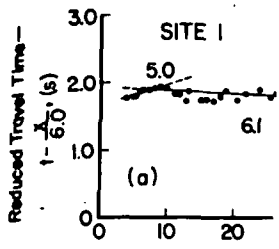

has recently advanced
travel time inversion
amplitude and wavefor
Kennett 1977). But in
only the first arrival ti
nent seismometers hav
simple layered solutio
zontal seismometer d
amplitude information
interpretation, althou
were not normalized t
distance, and the effe
compression on the PC
rected. Examples of re
a, *b*. The section for on
OBS site 2 shown in F
the record from a simil
Whitmarsh (1977).

The reduced first arr
site 1 near the axis
centre, with shots to th
9*a*. The travel time plo
in Fig. 9*b*. The latter
profiles. Site 1 exhibit
7.3 km s^{-1} and a somew
crustal layer 3 velocit
horizontal, layered int
10. For comparison, al
locity structure from
mid-Atlantic ridge by
by Kennett (1977) and t
of the Explorer sprea
Malecek (1976) (mean
low mantle velocity is
and Malecek (1976) m
(not plotted) but is m
s^{-1}, like our line, for pe
10) (see also Malecek a
profile is partly revers
site 2 which give a si
ity–depth structure. T
simple dip of the struc
resents a general chan
from the spreading cen

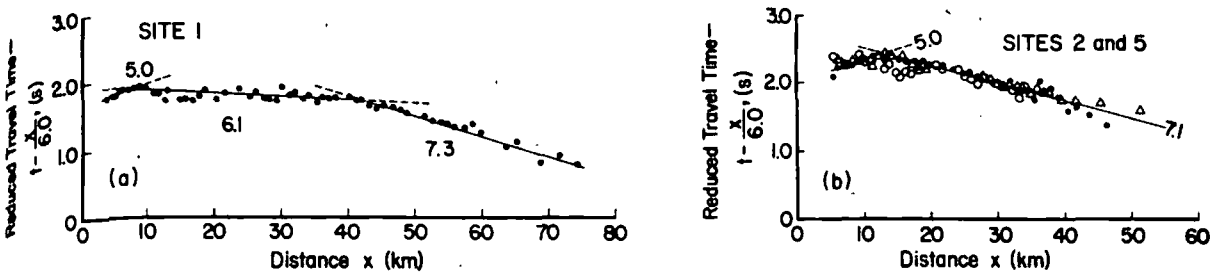

FIG. 9. Composite travel time plots for seismic refraction line.

has recently advanced considerably through new travel time inversion techniques and through amplitude and waveform techniques (see review by Kennett 1977). But in this preliminary analysis, only the first arrival times on the vertical component seismometers have been employed to obtain a simple layered solution (e.g., Ewing 1963). Horizontal seismometer data for a few shots and amplitude information were examined to aid in the interpretation, although the record amplitudes were not normalized to constant charge size or to distance, and the effect of the square root signal compression on the PGC instruments was not corrected. Examples of records are shown in Figs. 4, 8 *a, b*. The section for one profile of the airgun across OBS site 2 shown in Fig. 8*b*, may be compared to the record from a similar source from Langford and Whitmarsh (1977).

The reduced first arrival travel time plot for OBS site 1 near the axis of the Explorer spreading centre, with shots to the northwest, is shown in Fig. 9*a*. The travel time plots for sites 2 and 3 are shown in Fig. 9*b*. The latter two sites have very similar profiles. Site 1 exhibits a low mantle velocity of 7.3 km s^{-1} and a somewhat lower than normal lower crustal layer 3 velocity of 6.1 km s^{-1}. A simple horizontal, layered interpretation is shown in Fig. 10. For comparison, also plotted are a detailed velocity structure from the median valley of the mid-Atlantic ridge by Fowler (1976) as interpreted by Kennett (1977) and the structure just to the south of the Explorer spreading centre by Clowes and Malecek (1976) (mean of their 72-2 and 72-2R). The low mantle velocity is similar to that of the Clowes and Malecek (1976) model for parallel to the ridge (not plotted) but is much lower than their 7.8 km s^{-1}, like our line, for perpendicular to the ridge (Fig. 10) (see also Malecek and Clowes 1977). The site 1 profile is partly reversed by the southeast shots to site 2 which give a significantly different velocity–depth structure. The difference may reflect a simple dip of the structure but more probably represents a general change in structure going away from the spreading centre, in particular with layer 3 velocity increasing. The profiles to sites 2 and 5 were not sufficiently long to clearly record mantle arrivals, but all of the profiles have a layer 3 velocity of about 7.1 km s^{-1}. This velocity and the depth are similar to the Kennett–Fowler model.

The previous seismic refraction studies in the area by Clowes and Malecek (1976) and Malecek and Clowes (1977) suggest a complex variable structure to the south of the Explorer ridge. Their data require major vertical faulting or possibly some rather special velocity anisotropy. The different travel time plots among our sites may have a similar origin. Another nearby profile on the Juan de Fuca plate near the northern end of the Juan de Fuca ridge has given a normal crustal structure except that the crust is slightly thicker than average (Davis *et al.* 1976).

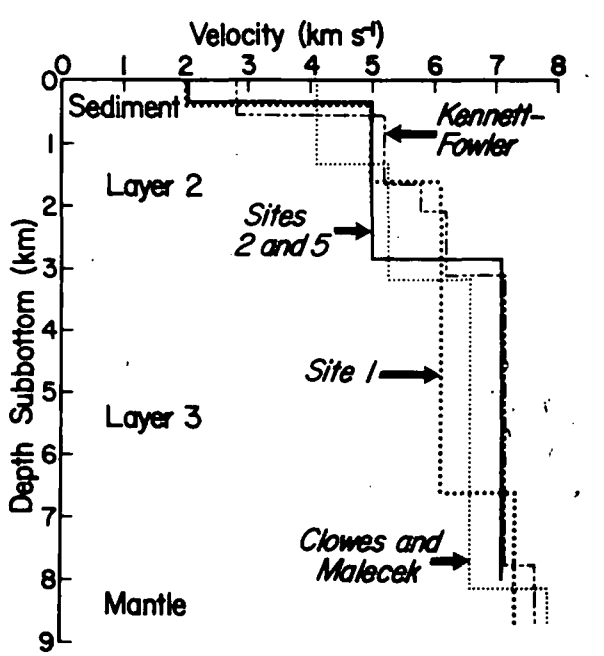

FIG. 10. Simple layered structure interpretation of seismic refraction line with crustal structure from a mid-Atlantic ridge profile by Fowler (1976), as interpreted by Kennett (1977), and the results of a reversed line in the area by Clowes and Malecek (1976).

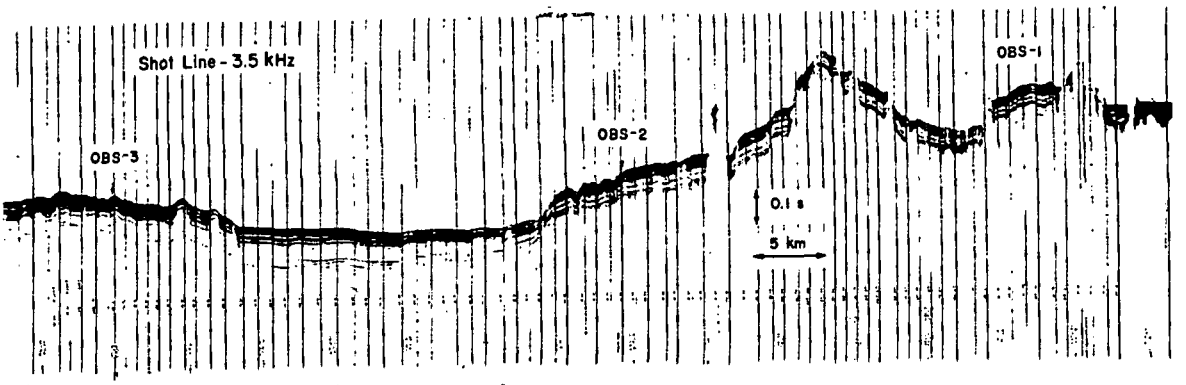

FIG. 11. Sediment profile from 3.5 kHz sounder system along refraction line.

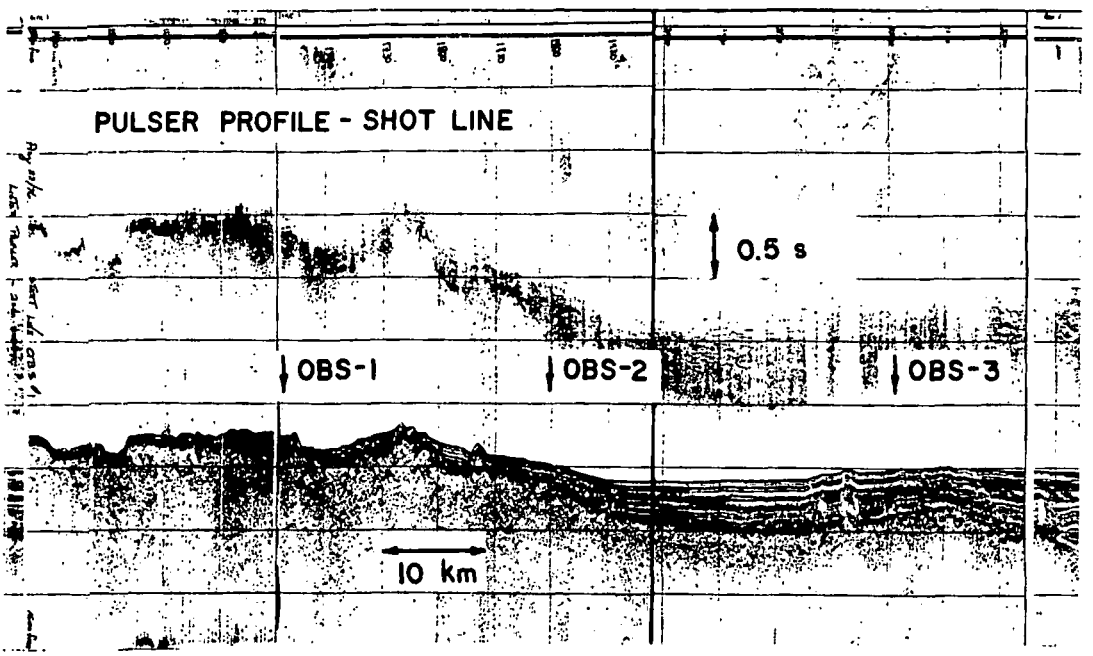

FIG. 12. Sediment profile along refraction line from pulser system.

In addition to the first arrival data several other features are noted in the records. (1) At short distances a clear arrival is apparent at a nearly constant time after the bottom reflection which we interpret to be the P to S conversion at the base of the sediments beneath the seismometers. For example, it is about 1 s after the first arrival at site 2 (Fig. 8*b*). (2) The horizontal seismometers have an arrival beyond about 15 km distance with a velocity of about 4.0 km s^{-1} which appears to be a layer 3 refracted shear wave. More careful analysis should permit quite accurate estimates of the velocity ratio of P to S waves and Poisson's ratio. (3) There is a region of very low amplitude arrivals at distances between 20 and 25 km, close to the change in velocity from 6.3–6.9 km s^{-1} which suggests a shadow zone produced by a low velocity zone. Synthetic seismograms are required to determine in detail the velocity structure responsible for this feature.

Seismic Profiling

Three systems were employed to profile the bottom sediments: (1) a 3.5 kHz Ocean Research Equipment sounding system, (2) a high resolution pulser system using an attraction type electromagnetic transducer operating at 150–300 Hz (see Davis and Lister 1977*b*), (3) a large 1000 in.^{3} (16 L) Bolt airgun. The three systems permitted a complete range of resolution and penetration. The 3.5 kHz system with penetration of a few 10's of metres was operated over a large number of profiles to examine the fine structure of the sediments near

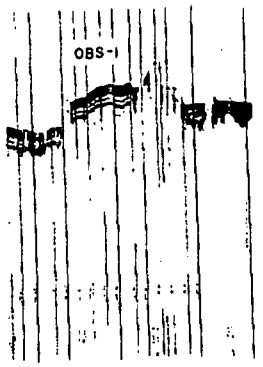

line.

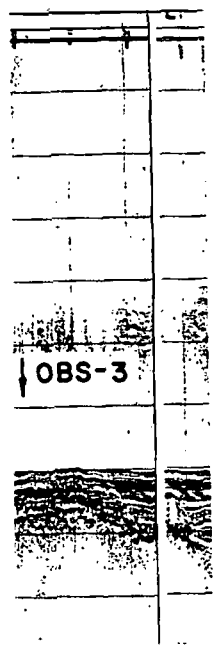

velocity zone. Synthetic
to determine in detail the
ible for this feature.

Profiling

ployed to profile the bot-
.5 kHz Ocean Research
em, (2) a high resolution
attraction type elec-
operating at 150–300 Hz
7*b*), (3) a large 1000 in.³
ree systems permitted a
ion and penetration. The
etration of a few 10's of
a large number of profiles
ure of the sediments near

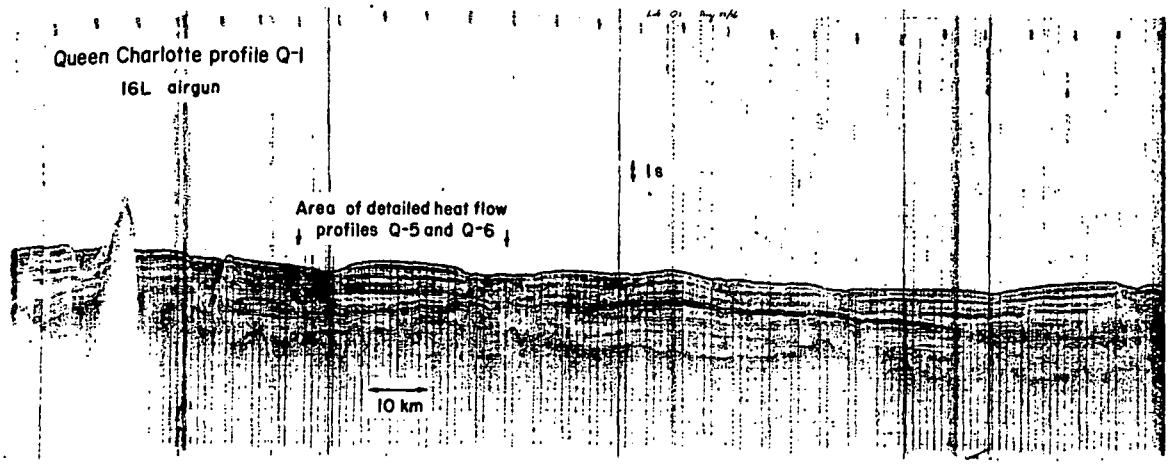

FIG. 13. Sediment profile on Queen Charlotte abyssal fan from large airgun.

the ridge crests and proved particularly valuable for determining the detailed surface sediment structure along the heat flow profiles. An example is shown in Fig. 11. The pulser system outlined sediment structure with very high resolution to thicknesses of at least 500 m and was particularly important for the seismic refraction line (Fig. 12), and for the heat flow profiles. The large low frequency airgun provided consistent penetration to over 1 km of sediments and demonstrated the smooth basement under the abyssal area off the Queen Charlotte Islands (Fig. 13). These latter data were important for the heat flow profiles and for the analysis of previously recorded seismic refraction data.

A few pulser and 3.5 kHz profiles are of particular interest. They show unusual sedimentary mounds that could be hydrothermal deposits occurring where crustal hydrothermal circulation vents to the seafloor. Such deposits have recently received considerable attention near the Galapagos spreading centre (e.g., Williams *et al.* 1974; Corliss *et al.* 1977).

Heat Flow Measurements

Geothermal heat flux measurements are the most important source of information on the thermal structure of the ocean crust and uppermost mantle. The Juan de Fuca ridge system is one of the best studied spreading centres, the region being covered by over 200 previous measurements. The most recent study involved a detailed survey with 112 measurements on a grid over a 100 km square area at the intersection of the Juan de Fuca ridge and the Sovanco fracture zone, that provided some of the clearest evidence for the high permeability and extensive hydrothermal circulation in the crust (Davis and Lister 1977*a*). The east side of the Juan de Fuca ridge also provides one of the best areas in the world to attempt to measure the total heat flux from young oceanic lithosphere, because in that area, very thick impermeable turbidite sediments prevent convective hydrothermal heat loss to the ocean.

To outline the details of crustal hydrothermal circulation, very closely spaced heat flow stations

FIG. 14. Photograph of multi-penetration, digital telemetering heat probe.

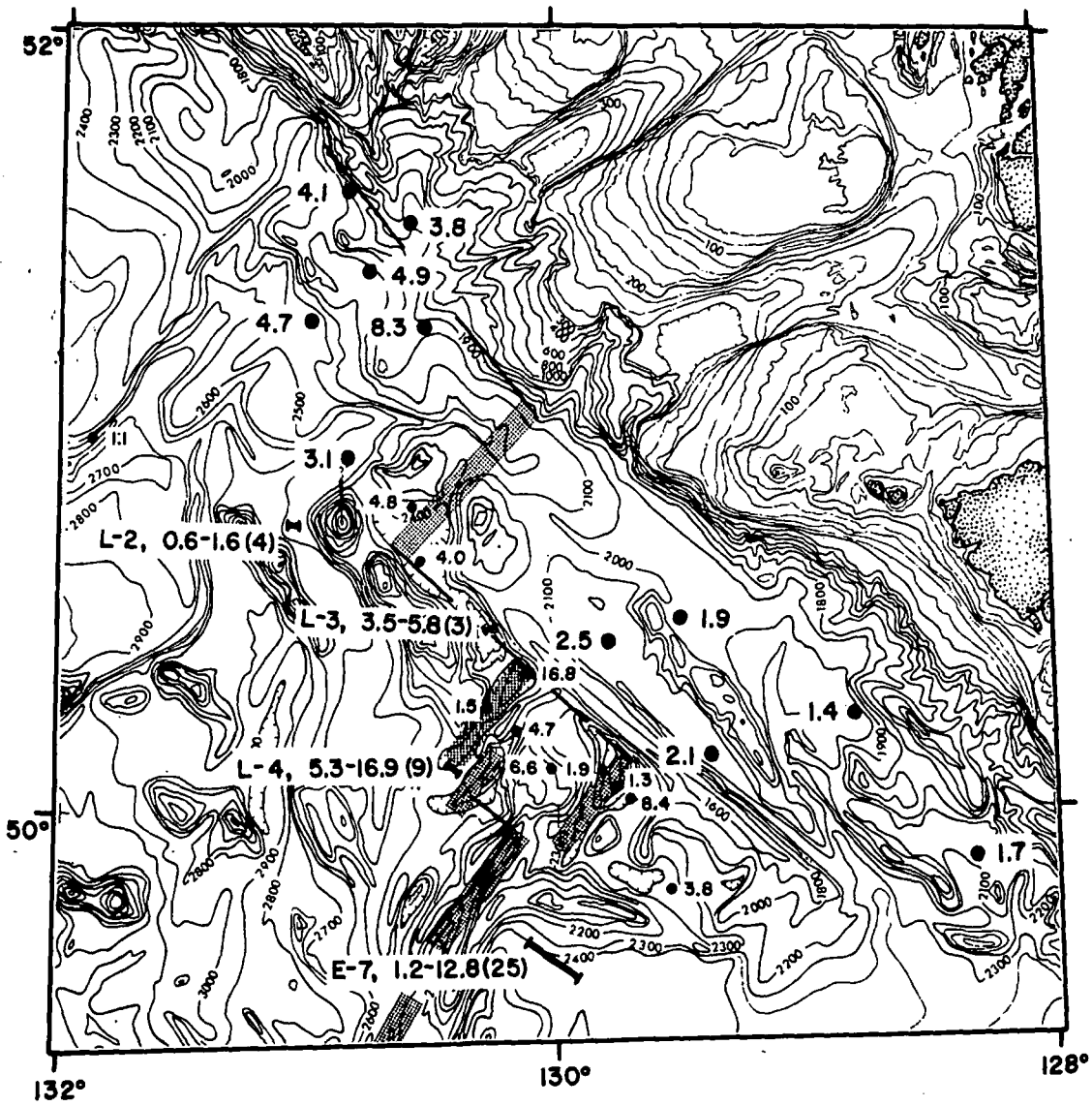

FIG. 15. Heat flow measurements in Explorer–Dellwood area. The multi-penetration profiles are shown with short lines and the range of measured heat flux given.

are required. In this study a new heat probe was employed that permitted repeated 'pogostick' penetrations without raising the instrument to the surface. In addition, 10 standard heat probe measurements are reported, in the Winona basin along the margin of northern Vancouver Island and near the Tuzo Wilson seamounts. The origin of the seafloor in these areas is not clear and since there generally is a thick sediment cover, the measured heat flows may give useful restraints on the crustal age.

Multiple Penetration Heat Flow Measurements

Several profiles of closely spaced heat flow measurements were made by the 'drift station' technique, using a new multi-penetration telemetering instrument (Fig. 14). The ship is set up to drift slowly across the features of interest, and the probe is dropped into the bottom at suitable intervals. The minimum interval depends on the on-bottom time, drift speed, instrument and wire weight, depth, and wire drag parameters. We found that with a drift speed of about $\frac{1}{2}$ m s^{-1} (1 kn) and an on-bottom time of 4 min, a station spacing of about 0.7 km was possible in 3 km of water. The advantage of this technique is that the ship can move consistently enough in one direction for several satellite fixes to delineate the track over the ocean floor. With the aid of on-profile recording of acoustic reflection data, precisely located heat flow measurements can

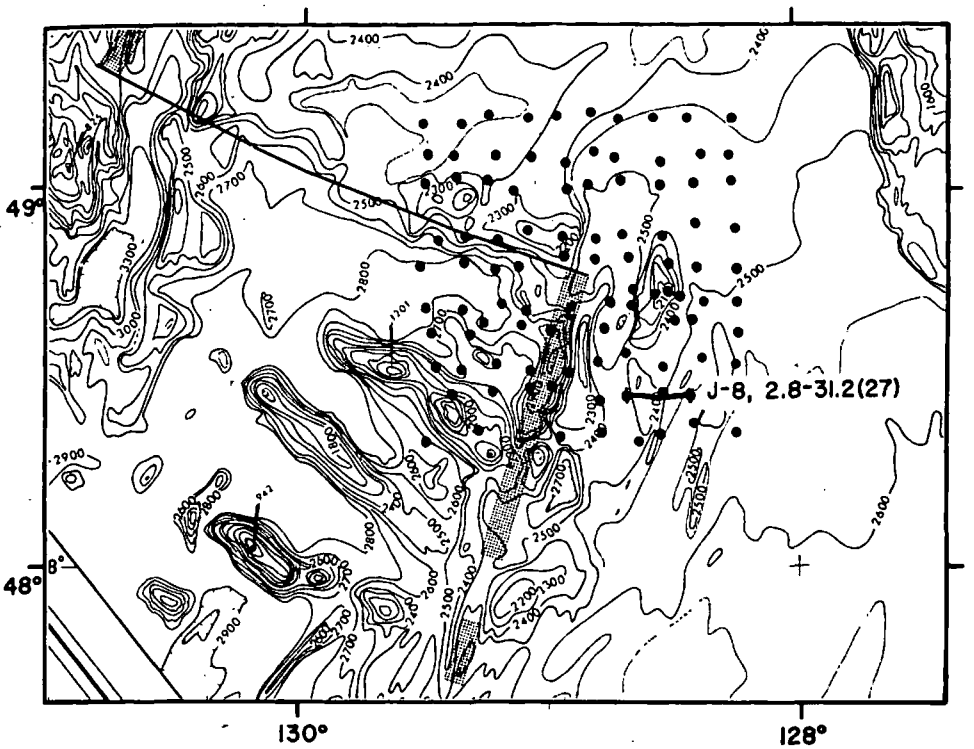

FIG. 16. Location of detailed heat flow profile on Juan de Fuca ridge. Dots mark the heat flow grid of Davis and Lister (1977*a*).

then be made over features of interest without the expense and operating complexity of acoustic navigation networks with bottom transponders.

The instrument was designed to meet the critical requirements for drift-station work. Temperature information is digitized and telemetered in real time to the ship via an acoustic link. The link employs frequency-shift keying and operates at 11.5 kHz so that standard ship's transducers can be used as receivers. A narrow-bandwidth encoding technique was devised that requires minimal encoding logic in the instrument and allows the receiver to re-synchronize rapidly after any signal dropouts. The probe itself uses a 'violin bow' design, placing the thermistors in a thin steel tube held under tension by a heavy strength member (Fig. 14). The latter is strong enough to resist bending during skew pullouts from the drifting ship, while the sensors are in a tube small enough to equilibrate rapidly with the sediment. The sensor string consists of three single thermistors for gradient measurement, interspersed by two groups of nine series–parallel thermistors to determine mean thermal resistivities for the gradient intervals. A resistance wire heater runs the full active length of the sensor tube to provide a calibrated heat pulse for the resistivity determination. When the measured thermal gradients are fairly high, as in the area of investigation, a gradient can be determined in 3–5 min on the bottom, and the sediment conductivity in a total of about 14 min. The mechanical design of the probe proved highly satisfactory, achieving 120 penetrations without significant damage. Some multipath acoustic interference was observed when the instrument was oscillating freely on the wire, but disappeared when it was in the bottom. Now that the form of the deep-sea signal has been determined, it is expected that the receiver can be modified to be less sensitive to this type of interference.

A total of 112 successful penetrations were made on eight profiles in a variety of areas (Figs. 15, 16, and 17; Table 1). Measurements in an intermontane trough on the northwest flank of Explorer ridge (near the track of the reversed OBS seismic refraction line) were low and variable as predicted by theories of hydrothermal circulation for regions with nearby permeable outcrops (Lister 1972; Sclater *et al.* 1976) (Stations L-1, L-2). The sediment-filled fracture-zone trough northwest of Explorer ridge yielded relatively high values also consistent with hydrothermal circulation under a sealing sediment fill where the lithosphere is young (L-3). A short multi-penetration profile very near the crest of Explorer ridge, near where the seismic refraction line intersects the spreading centre on the north

TABLE 1. Multi-penetration probe heat flow data

Penetration	Gradient ($m°C\ m^{-1}$)	Conductivity† ($mcal\ °C^{-1}\ cm^{-1}\ s^{-1}$)	Heat flow† ($\mu cal\ cm^{-2}\ s^{-1}$)
Station L-1: 50°41.0′N, 131°00.5′W Northwest flank, northern Explorer ridge (base of seamount)			
1	0.21	1.80	0.39
Station L-2: 50°44.0′N, 131°07.0′W to 50°43.8′N, 131°04.7′W Northwest flank, northern Explorer ridge (base of seamount)			
1	33	1.80	0.59
2	31	1.80	0.56
3	54	1.80	0.97
4	86	1.80	1.55
Station L-3: 50°28.3′N, 130°17.0′W to 50°28.5′N, 130°15.5′W Intersection of Explorer ridge with northern fracture zone			
1	328	1.77*	5.81
2	198	1.77	3.50
3	206	1.77	3.65
Station L-4: 50°08.1′N, 130°26.9′W to 50°06.6′N, 130°24.1′W Northwest flank, Explorer ridge (near crest)			
1	4.57	2.30	10.51
2	7.51	2.30	17.28
3	4.01	2.30	9.22
4	7.68	2.30	17.66
5	7.31	2.30	16.81
7	3.98	2.30	9.11
8	2.68	2.30	6.16
9	2.26	2.30	5.20
10	2.80	2.30*	6.43
Station E-7: 50°40.5′N, 130°06.5′W to 50°35.9′N, 129°56.9′W Southeast flank, Explorer ridge			
1	104	2.21*	2.30
2	54	2.21	1.18
3	164	2.21	3.62
5	173	2.21	3.82
6	114	2.21	2.52
8	576	2.21	12.73
9	303	2.21	6.70
10	353	2.21	7.80
11	370	2.21	8.18
12	424	2.21	9.37
13	296	2.21	6.54
14	315	2.21	6.96
15	371	2.21	8.20
16	346	2.21	7.65
18	289	2.21	6.39
19	203	2.21	4.49
20	88	2.21	1.94
21	255	2.21	5.64
22	396	2.21	8.75
23	209	2.21	4.62
24	108	2.21	2.39
25	134	2.21	2.96
26	294	2.21	6.50
27	413	2.21	9.13
28	421	2.21	9.30

TABLE 1 (*Continued*)

Penetration	Gradient ($m°C\ m^{-1}$)	Conductivity† ($mcal\ °C^{-1}\ cm^{-1}\ s^{-1}$)	Heat flow† ($\mu cal\ cm^{-2}\ s^{-1}$)
Station J-8: 48°27.8′N, 128°40.8′W to 48°27.9′N, 128°27.5′W East flank, Juan de Fuca ridge			
1	353	2.35*	8.30
2	176	2.30	4.05
3	192	2.30	4.42
4	391	2.30	8.99
5	238	2.30	5.47
6	546	2.30	12.56
7	531	2.30	12.21
8	217	2.30	4.99
9	315	2.30	7.24
10	475	2.30	10.92
11	1410	2.30	32.43
13	411	2.30	9.45
14	161	2.30	3.70
15	346	2.30	7.95
16	151	2.30	3.47
17	161	2.30	3.70
18	139	2.30	3.19
19	242	2.30	5.56
22	180	2.30	4.14
23	347	2.30	7.98
24	404	2.30	9.29
25	142	2.30	3.26
26	150	2.30	3.45
27	160	2.30	3.68
28	178	2.30	4.39
29	191	2.30	4.39
30	351	2.30	8.07
Station Q-5: 51°23.81′N, 134°24.58′W to 51°23.74′N, 134°07.06′W Queen Charlotte abyssal fan			
1	24	2.10*	0.50
2	24	2.10	0.50
3	25	2.10	0.53
4	26	2.10	0.55
6	28	2.10	0.58
8	28	2.10	0.59
9	58	2.10	1.22
11	57	2.10	1.20
12	64	2.10	1.34
13	74	2.10	1.56
14	94	2.10	1.98
15	102	2.10	2.14
16	96	2.10	2.01
17	105	2.10	2.21
18	109	2.10	2.28
19	101	2.10	2.12
20	106	2.10	2.22
21	102	2.10	2.14
22	81	2.10	1.71
23	82	2.10	1.73
24	88	2.10	1.85
25	61	2.10	1.29
26	54	2.10	1.13
27	41	2.10	0.86
28	28	2.10	0.60
29	28	2.10	0.60
30	29	2.10	0.62

Pene- tration	Gradient ($m°C\ m^{-1}$)
Station Q-6: 5	
	Qu
1	49
2	43
3	47
4	49
5	70
6	26
7	79
9	83
10	100
11	97
12	90
13	107
14	106
15	99
16	107

*Measured conductivi
†1 $m°C\ m^{-1}$ = 1 mK
1 $\mu cal\ cm^{-2}\ s^{-1}$ = 41.9

side, shows high
a general tenden
northwest end of
and two nearby
simultaneous se
the south flank
values that rang
distance of 4 kr
variation, all
raphy.[3] It appea
circulation, alth
are not entirely
confirmed by a
Juan de Fuca
occur even wh
ment cover is e
high value (31.2
fault zone.

A pair of profi
each other wer
ronment: the ab
lotte Islands (
sediment appea
oceanic basem
mounts, which
proximately ½ s
The heat flow
models is 3.5 μ
12 Ma, but the

[3] 1 $\mu cal\ cm^{-2}\ s^{-1}$

TABLE 1 (*Concluded*)

Penetration	Gradient (m°C m^{-1})	Conductivity† (mcal °C^{-1} cm^{-1} s^{-1})	Heat flow† (μcal cm^{-2} s^{-1})
Station Q-6: 55°22.1′N, 134°14.1′W to 51°26.91′N, 134°15.80′W			
Queen Charlotte abyssal fan			
1	49	2.28*	1.12
2	43	2.28	0.98
3	47	2.28	1.07
4	49	2.28	1.11
5	70	2.28	1.60
6	26	2.28	0.59
7	79	2.28	1.81
9	83	2.28	1.89
10	100	2.28	2.28
11	97	2.28	2.21
12	90	2.28	2.05
13	107	2.28	2.44
14	106	2.28	2.41
15	99	2.28	2.26
16	107	2.28	2.44

*Measured conductivity value.
†1 m°C m^{-1} = 1 mK m^{-1}, 1 mcal cm^{-1} s^{-1} °C^{-1} = 0.419 W m^{-1} K^{-1}
1 μcal cm^{-2} s^{-1} = 41.9 mW m^{-2}.

side, shows high and variable values (L-4). There is a general tendency for high values to occur near the northwest end of the profile, where a 15 m fault step and two nearby volcanic outcrops are visible on the simultaneous seismic profile. A longer profile on the south flank of Explorer ridge (E-7) contains values that range from 1.2–12.8 μcal cm^{-2} s^{-1} in a distance of 4 km, and two more cycles of large variation, all largely uncorrelated with topography.[3] It appears as if the patterns of hydrothermal circulation, although influenced by tectonic faults, are not entirely controlled by them, and this is confirmed by a long profile on the east flank of the Juan de Fuca ridge (J-8). Substantial variations occur even where basement is smooth and sediment cover is even, although the one exceptionally high value (31.2 μcal cm^{-2} s^{-1}) is associated with a fault zone.

A pair of profiles approximately at right angles to each other were run in an entirely different environment: the abyssal area west of the Queen Charlotte Islands (Q-5, Q-6). This is a region where sediment appears to have flooded over a smooth oceanic basement with occasional small seamounts, which frequently project above the approximately ½ s (two-way travel time) of sediment. The heat flow predicted by cooling lithosphere models is 3.5 μcal cm^{-2} s^{-1} for the local age of 12 Ma, but the measured values peak at about 2.4 μcal cm^{-2} s^{-1}. The 19 km long east–west profile (Q-5) contains a single peak of heat flow, and the cross profile confirms that the variation is three dimensional. If the oceanic crust is permeable, with fair uniformity in this area, the presence of discrete ventilation points at outcropping seamounts could force the convection into cells with the long horizontal scales observed. The sediment cover is so even that the heat flow variations must represent variations in the basement temperature from about 4°C to 20°C above local ocean-floor temperature. This implies remarkably efficient ventilation and horizontal transport of heat, since more than half of the lithospheric heat flux appears to be advected through the ventilating outcrops.

[3] 1 μcal cm^{-2} s^{-1} = 41.9 mW m^{-2}.

Standard Heat Probe Measurements

Six heat flow measurements were made on this cruise in the Winona basin using conventional marine heat probe techniques. Five additional values reported here were measured on an earlier *Endeavour* cruise of the Department of Geological Sciences, Univeristy of B.C., in the region off the southern end of the Queen Charlotte Islands (Fig. 15) (Table 2). The temperature gradient was measured with a 1.3 cm diameter, 2.5 m long solid probe containing four thermistor sensors. The temperature resolution is ±10 m°C at a full scale range of 1°C. All of the temperature–depth profiles are linear to the measurement accuracy, the gradient accuracy being about ±10%. Langseth and Von Herzen (1970) discuss the operation and sources of error of this type of instrument in detail.

The thermal conductivity of the sediments penetrated by the gradient probe was estimated from measurements on gravity core samples taken within 20 km of each gradient measurement. The sediment cores are olive green hemi-pelagic material that appears very homogeneous. Most cores were only 70–130 cm in length so represent only half the depth of penetration of the gradient probe. The observed nearly linear increase of conductivity with depth was used to estimate the mean conductivity for the depth interval of probe penetration. The conductivity was measured every 15 cm along the cores using the transient needle probe technique (Von Herzen and Maxwell 1959). Fused silica was employed as a reference (Ratcliffe 1959) and the conductivities were corrected by +5% for the difference between laboratory and seafloor temperature and pressure (Ratcliffe 1960; MacDonald and Simmons 1972). The conductivities are all very similar, with an average increase with depth of 0.01 mcal cm^{-1} s^{-1} °C^{-1} (0.004 W m^{-1} K^{-1}) per

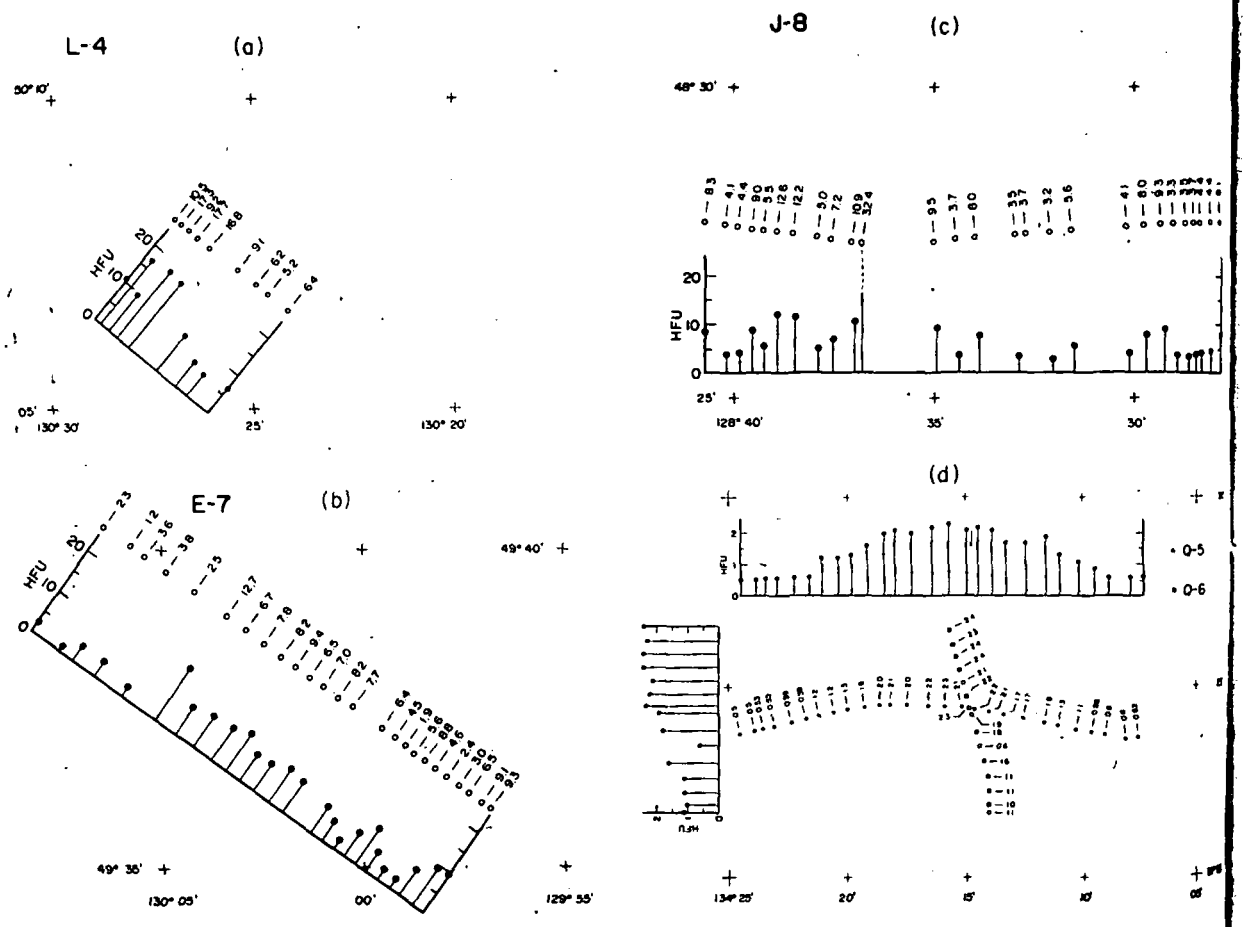

FIG. 17. Detailed locations and values of heat flow measurements with plots of heat flow versus distance along profiles.

metre, with the exception of station 9 which had both a much higher conductivity and a more rapid increase with depth (Fig. 18). The heat flux values have an estimated accuracy of ±15%, the main sources of error being the lack of coincidence of the gradient measurement and conductivity cores, and in the uncertainty in the gradient probe readings for zero temperature difference between sensors. The zero gradient reference was difficult to obtain at some of the shallower sites where there are significant gradients in the near bottom water. The errors given in Table 2 are subjective estimates, the statistical estimates generally being considerably smaller.

We have applied no correction for the reduction in heat flow produced by sediment deposition. The effect may be significant in the Winona basin where both the crust is relatively old and the sedimentation rates are high. No evidence is seen in the gradients for time variations in bottom water temperature but we point out that they could be important particularly for the shallower sites. Thermal refraction by sediment ponding and basement topography also could be important.

The five values near the Tuzo Wilson seamounts are all high, with an average of 5.2 μcal cm^{-2} s^{-1} (220 mW m^{-2}) (Figs. 1 and 15). This average is the rate to be expected from crust about 5 Ma old (Lister 1975; Davis and Lister 1977*a*), an age appropriate for lithosphere produced at an old northeasterly extension of the Explorer spreading centre at a half rate of 3 cm $year^{-1}$ (Fig. 19). There is a thick sediment cover in the measurement area which should reduce the effect of advective hydrothermal cooling but ventilation of circulation may occur at the outcropping seamounts themselves. A small amount of cooling by hydrothermal ventilation and from sedimentation would make the data compatible with the crust being produced at the Dellwood Knolls. That the crust was produced from a spreading centre at the Tuzo Wilson seamounts is less probable but cannot be discounted because of the unknown effect on the heat flow measured of hydrothermal circulation in the crust.

TABLE 2. Standard probe heat flow data

Station	Location Long. (°N)	Location Lat. (°W)	Water depth (m)	Gradient* (m°C m^{-1})	Conductivity* (mcal cm^{-1} s^{-1} °C^{-1})	Heat flux* (μcal cm^{-2} s^{-1})
EPB76-1-1	49°53.4′	128°18.1′	1990	98±3	1.7±0.1	1.7±0.3
EPB76-1-2	50°15.3′	128°49.3′	2030	79±2	1.8±0.1	1.4±0.3
EPB76-1-3	50°28.6′	129°31.7′	1960	103±3	1.8±0.1	1.9±0.4
EPB76-1-4	50°10.5′	129°22.8′	2150	119±4	1.8±0.1	2.1±0.4
EPB76-1-6	50°27.0′	129°48.4′	2140	139±1	1.8±0.1	2.5±0.4
EPB76-1-9	50°53.8′	130°52.0′	2460	141±5	2.2±0.1	3.1±0.6
UBC76-10-3	51°16.3′	131°00.3′	2286	245±5	1.9±0.1	4.7±0.7
UBC76-10-4	51°36.3′	130°50.8′	1947	210±5	1.9±0.1	4.1±0.6
UBC76-10-6	51°23.0′	130°45.8′	2057	255±5	1.9±0.1	4.9±0.7
UBC76-10-7	51°30.2′	130°36.8′	1338	197±5	1.9±0.1	3.8±0.6
UBC76-10-8	51°13.9′	130°32.4′	2002	432±10	1.9±0.1	8.3±1.0

*1 m°C m^{-1} = 1 mK m^{-1}, 1 mcal cm^{-1} s^{-1} °C^{-1} = 0.419 W m^{-1} K^{-1}, 1 μcal cm^{-2} s^{-1} = 41.9 mW m^{-2}.

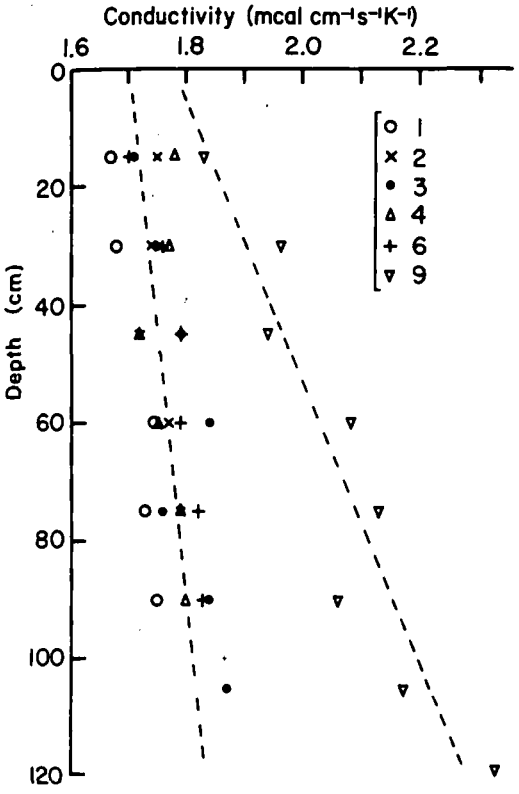

FIG. 18. Thermal conductivity as a function of depth along cores measured by needle probe.

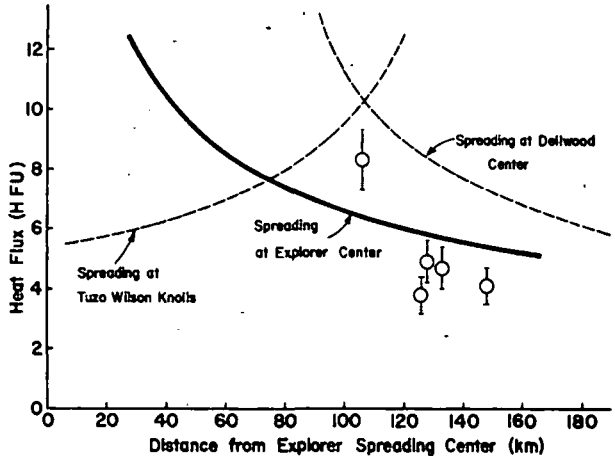

FIG. 19. Heat flux versus distance perpendicular to the Dellwood and Explorer spreading centres for the five heat flow values in the region of the Tuzo Wilson seamounts. The theoretical curves are $12\sqrt{t}$, where t is the crustal age (Lister 1975). A half spreading rate of 3 cm year^{-1} is assumed. The best fit is for lithosphere produced by an old extension of the Explorer spreading centre or by spreading at the Dellwood Knolls.

The five values in the Winona basin are quite uniform and much lower, the average being 1.8 μcal cm^{-2} s^{-1}. The higher values occur in the western part of the basin. The sediment cover is thick (up to 2 km) and continuous over a large horizontal scale (greater than 50 km) so advective hydrothermal cooling is probably not important. However, sediment deposition in the basin is rapid which will significantly reduce the measured heat flow. A rough estimate of the reduction is about by a quarter, giving an implied crustal age of roughly 20 Ma with the crust being younger in the western part of the basin compared to the eastern part.

Acknowledgements

We wish to acknowledge the able assistance and cooperation of the master and crew of C.N.A.V. *Endeavour* in carrying out this study. D. L. Tiffin and R. M. Clowes were of major assistance in the organization of the cruise and in providing equipment and facilities. R. L. Chase organized and was chief scientist for the cruise on which five of the heat flow values reported were obtained. Very helpful discussions were held with R. P. Riddihough, C. E. Keen, G. A. McMechan, and W. G.

Milne. H. J. Bennetts provided invaluable assistance in the equipment and cruise preparation.

BARR, S. M., and CHASE, R. L. 1974. Geology of the northern end of Juan de Fuca ridge and sea-floor spreading. Canadian Journal of Earth Sciences, **11**, pp. 1384–1406.

BARRETT, D. L., HEFFLER, D. E., and KEEN, C. E. 1977. Ocean bottom seismometer developments. Geological Survey of Canada, Report of Activities, Part B, pp. 129–132.

BERTRAND, W. G. 1972. A geological reconnaissance of the Dellwood seamount area, northeast Pacific Ocean, and its relation to plate tectonics. M.Sc. thesis, University of British Columbia, Vancouver, B.C.

CHASE, R. L. 1977. J. Tuzo Wilson Knolls: Canadian hotspot. Nature, **266**, pp. 344–346.

CHASE, R. L., TIFFIN, D. L., and MURRAY, J. W. 1975. The western Canadian continental margin. *In* Canada's continental margins and offshore petroleum exploration. *Edited by* C. J. Yorath, E. R. Parker and D. J. Glass. Canadian Society of Petroleum Geologists, Memoir 4, pp. 701–721.

CLOWES, R. M., and MALECEK, S. J. 1976. Preliminary interpretation of a marine deep seismic sounding survey in the region of Explorer ridge. Canadian Journal of Earth Sciences, **13**, pp. 1545–1555.

CORLISS, J., DYMOND, J., GORDON, L., VON HERZEN, R. P., BALLARD, R., GREEN, K., EDMOND, J., WILLIAMS, D., CRANE, K., BAINBRIDGE, A., and VAN ANDEL, J. 1977. Alvin diving program on the Galapagos rift. American Geophysical Union, Annual Meeting, June, 1977, Washington, DC.

DAVIS, E. E., and LISTER, C. R. B. 1977*a*. Heat flow measured over the Juan de Fuca ridge: evidence for widespread hydrothermal circulation in a highly heat transportive crust. Journal of Geophysical Research, **82**, pp. 4845–4860.

——— 1977*b*. Tectonic structures on the Juan de Fuca ridge. Geological Society of America Bulletin, **88**, pp. 346–363.

DAVIS, E. E., LISTER, C. R. B., and LEWIS, B. T. R. 1976. Seismic structure on Juan de Fuca ridge: ocean bottom seismometer results from the Median Valley. Journal of Geophysical Research, **81**, pp. 3541–3555.

EWING, J. I. 1963. Elementary theory of seismic refraction and reflection measurements. *In* The sea. Vol. 3. *Edited by* M. N. Hill. Interscience, New York, NY. pp. 1–19.

FOWLER, C. M. R. 1976. Crustal structure of the mid-Atlantic ridge crest at 37°N. Geophysical Journal of the Royal Astronomical Society, **47**, pp. 459–491.

FRANCIS, T. J. G., PORTER, I. T., and MCGRATH, J. R. 1977. Ocean bottom seismograph observations on the mid-Atlantic ridge near lat. 37°N. Geological Society of America Bulletin, **88**, pp. 664–677.

HEFFLER, D. E., and LOCKE, D. L. 1978. An OBS release mechanism. Marine Geophysical Researches. In press.

HYNDMAN, R. D., and RIDDIHOUGH, R. P. 1977. Canada's active western margin—the recent interaction of continent and ocean floor (Abstract). *In* Program with abstracts. Geological Association of Canada Annual Meeting, Vancouver, B.C., April 1977.

JOHNSON, R. V., II, LISTER, C. R. B., and LEWIS, B. T. R. 1977. A direct recording ocean bottom seismometer. Marine Geophysical Researches, **3**, pp. 65–85.

KENNETT, B. L. N. 1977. Towards a more detailed seismic picture of the ocean crust and mantle. Marine Geophysical Researches, **3**, pp. 7–42.

LANGFORD, J. J., and WHITMARSH, R. B. 1977. Pop-up bottom seismic recorder (PUBS) of the Institute of Oceanographic Sciences, U.K. Marine Geophysical Researches, **3**, pp. 43–63.

LANGSETH, M. G., JR., and VON HERZEN, R. P. 1970. Heat flow through the world oceans. *In* The sea. Vol. 4, Pt. 1. *Edited by* A. E. Maxwell. Interscience, New York, NY. pp. 299–352.

LEE, K. 1978. An earthquake swarm near the northern end of Juan de Fuca ridge. Submitted to Canadian Journal of Earth Sciences.

LEWIS, B. T. R., and SNYDSMAN, W. E. 1977. Evidence for a low velocity layer at the base of the oceanic crust. Nature, **266**, pp. 340–344.

LISTER, C. R. B. 1972. On the thermal balance of a mid-ocean ridge. Geophysical Journal of the Royal Astronomical Society, **26**, pp. 515–535.

——— 1975. The heat flow consequences of the square root law of ridge topography (Abstract). International Union of Geodesy and Geophysics, 16th General Assembly, Grenoble, France, 1975.

LISTER, C. R. B., and LEWIS, B. T. R. 1976. An ocean bottom seismometer suitable for arrays. Deep-Sea Research, **23**, pp. 113–124.

MACDONALD, K., and SIMMONS, G. 1972. Temperature coefficient of the thermal conductivity of ocean sediments. Deep-Sea Research, **19**, pp. 669–671.

MCMECHAN, G. A. 1978. Multiple water reflections recorded at the ocean bottom. Canadian Journal of Earth Sciences, **15**, pp. 78–85.

MALECEK, S. J., and CLOWES, R. M. 1977. Crustal structure near Explorer ridge from a marine deep seismic sounding survey. Journal of Geophysical Research. In press.

MILNE, W. G., ROGERS, G. C., RIDDIHOUGH, R. P., MCMECHAN, G. A., and HYNDMAN, R. D. 1978. Seismicity of western Canada. Canadian Journal of Earth Sciences, **15**, pp. 1170–1193.

NAGUMO, S., KASAHARA, J., and KORESAWA, S. 1976. Structure of microearthquake activity around Japan trench. off Sanriku, obtained by ocean-bottom seismographic network observation. Journal of Physics of the Earth, **24**, pp. 215–225.

PROTHERO, W. A., JR. 1977. Anomalous S wave propagation below the East Pacific Rise at 21°N (Abstract). Proceedings of the International Association of Seismology and Physics of the Earth's Interior, Durham, August, 1977. p. 58.

PROTHERO, W. A., REID, I., REICHLE, M. S., and BRUNE, J. A. 1976. Ocean bottom seismic measurements on the East Pacific Rise and Rivera Fracture Zone. Nature, **262**, pp. 121–124.

RATCLIFFE, E. H. 1959. Thermal conductivities of fused and crystalline quartz. British Journal of Applied Physics, **10**, pp. 22–25.

——— 1960. The thermal conductivities of ocean sediments. Journal of Geophysical Research, **65**, pp. 1535–1541.

REICHLE, M. S., SHARMAN, G. F., and BRUNE, J. N. 1976. Sonobuoy and teleseismic study of Gulf of California transform fault earthquake sequences. Bulletin of the Seismological Society of America, **66**, pp. 1623–1641.

REID, I., and MACDONALD, K. C. 1973. Microearthquake study of the mid-Atlantic ridge near 37°N, using sonobuoys. Nature, **246**, pp. 88–90.

REID, I., ORCUTT, J., and PROTHERO, W. A. 1977. Seismic evidence for a narrow zone of partial melting underlying the East Pacific Rise at 21°N. Geological Society of America Bulletin, **88**, pp. 678–682.

RIDDIHOUGH, R. P. 1977. A model for recent plate interactions off Canada's west coast. Canadian Journal of Earth Sciences, **14**, pp. 384–396.

RIDDIHOUGH, R. P., and HYNDMAN, R. D. 1978. Canada's active western margin—the case for subduction. Geoscience Canada, **3**, pp. 269–278.

ROGERS, G. C. 1976. The Vancouver Island earthquake of 5 July, 1972. Canadian Journal of Earth Sciences, **13**, pp. 92–101.

SCLATER, J. G., CROWE, J., reliability of oceanic heat cal Research, **81**, pp. 2997

SHOR, G. G., JR. 1963. Refra procedure. *In* The sea. Vo ence, New York, NY. pp.

SNYDSMAN, W. E., LEWIS, Upper mantle velocities c and Planetary Science Le

SPINDEL, R. C., DAVIS, S. R. P., and PHILLIPS, J. D median valley of the mid- **248**, pp. 577–579.

SRIVASTAVA, S. P., BARRE TER, K. S., SHIH, K. G TOMLINSON, A. G., DAVI Preliminary analysis of g Juan de Fuca ridge. Cana pp. 1265–1281.

SUTTON, G. H., KASAHARA D. A. 1977. Ocean bot Hawaii Institute of Geo searches, **3**, pp. 153–177.

TIFFIN, D. L. 1973. Marine margin. Report of Activi Canada, Paper 73-1A. 127

SCLATER, J. G., CROWE, J., and ANDERSON, R. N. 1976. On the reliability of oceanic heat flow averages. Journal of Geophysical Research, **81**, pp. 2997–3006.

SHOR, G. G., JR. 1963. Refraction and reflection techniques and procedure. *In* The sea. Vol. 3. *Edited by* M. N. Hill. Interscience, New York, NY. pp. 30–38.

SNYDSMAN, W. E., LEWIS, B. T. R., and MCCLAIN, J. 1975. Upper mantle velocities on the Northern Cocos Plate: Earth and Planetary Science Letters, **28**, pp. 46–50.

SPINDEL, R. C., DAVIS, S. B., MACDONALD, K. C., PORTER, R. P., and PHILLIPS, J. D. 1974. Microearthquake survey of median valley of the mid-Atlantic ridge at 36°30′N. Nature, **248**, pp. 577–579.

SRIVASTAVA, S. P., BARRETT, D. L., KEEN, C. E., MANCHESTER, K. S., SHIH, K. G., TIFFIN, D. L., CHASE, R. L., TOMLINSON, A. G., DAVIS, E. E., and LISTER, C. R. B. 1971. Preliminary analysis of geophysical measurements north of Juan de Fuca ridge. Canadian Journal of Earth Sciences, **8**, pp. 1265–1281.

SUTTON, G. H., KASAHARA, J., ICHINOSE, W. N., and BYRNE, D. A. 1977. Ocean bottom seismograph development at Hawaii Institute of Geophysics. Marine Geophysical Researches, **3**, pp. 153–177.

TIFFIN, D. L. 1973. Marine geophysical activities on the Pacific margin. Report of Activities, Part A. Geological Survey of Canada, Paper 73-1A. 127 p.

TIFFIN, D. L., and SEEMANN, D. 1975. Bathymetric map of the continental margin of western Canada. Geological Survey of Canada, Open File 75–301.

TOBIN, P. G., and SYKES, L. R. 1968. Seismicity and tectonics of the north-east Pacific Ocean. Journal of Geophysical Research, **72**, pp. 3821–3846.

VON HERZEN, R. P., and MAXWELL, A. E. 1959. The measurement of thermal conductivity of deep-sea sediments by a needle-probe method. Journal of Geophysical Research, **64**, pp. 1557–1563.

WETMILLER, R. J. 1971. An earthquake swarm on the Queen Charlotte Island fracture zone. Bulletin of the Seismological Society of America, **61**, pp. 1489–1505.

WHITMARSH, R. B. 1973. Median valley refraction line, mid-Atlantic ridge at 37°N. Nature, **246**, pp. 297–299.

WILLIAMS, D. L., VON HERZEN, R. P., SCLATER, J. G., and ANDERSON, R. N. 1974. The Galapagos spreading center: lithospheric cooling and hydrothermal circulation. Geophysical Journal of the Royal Astronomical Society, **38**, pp. 587–608.

WILSON, J. T. 1965. Transform faults, ocean ridges and magnetic anomalies southwest of Vancouver Island. Science, **150**, pp. 482–485.

JOURNAL OF GEOPHYSICAL RESEARCH, VOL. 85, NO. B7, PAGES XXXX_XXXX, JULY 10, 1980

THE INTERRELATION BETWEEN VARIATIONS IN MAGNETIC ANOMALY AMPLITUDES AND BASALT MAGNETIZATION AND CHEMISTRY ALONG THE SOUTHEAST INDIAN RIDGE

Roger N. Anderson,[1] Dann J. Sparlosu,[1] Jeffrey K. Weissel, and Dennis E. Hayes[1]

Lamont-Doherty Geological Observatory of Columbia University
Palisades, New York 10964

Abstract. Magnetic model studies, rock magnetization, and major element chemical analyses show that unusually large amplitude magnetic anomalies found along the easternmost segment of the Southeast Indian Ridge [zone A] are caused by the high intensities of magnetization of basalts intruded at the ridge axis. In turn, these high magnetizations are caused by a threefold increase in weight percent of titanomagnetites from normal midocean ridge basalts intruded in the west [zones B and C] to ferrobasalts intruded in the high magnetic anomaly zone to the east. The Fe-Ti increase in the opaques reflects a major elemental enrichment in Fe and Ti caused by extensive shallow fractionation of plagioclase, clinopyroxene, and olivine. This shallow fractionation appears related to unusually cold magma crystallization temperatures, perhaps caused by proximity to a postulated downwelling zone in the asthenosphere south of Australia. However, examination of these correlations in greater detail points to several ambiguities: although the entire region is deep, and therefore the lithosphere is integrally colder than normal plates, zone A is shallower than zones B and C, but geothermometrically, its axial magmas are colder. We do not know how cold magmas directly relate to ferrobasalt generation. Also, plumelike geochemical signatures are also seen in some of the analyses. It appears that plume mantle sources are mixing with MORB sources and then undergoing extensive shallow fractional crystallization in zone A.

Introduction

The Southeast Indian Ocean has been investigated in a systematic reconnaissance fashion mainly through the programs of the USNS Eltanin. The sea floor spreading pattern of magnetic lineations and fracture zones has been recognized [Weissel and Hayes, 1971, 1972], the general bathymetry [Hayes and Conolly, 1972], and sediment distribution [Houtz and Markl, 1972] have been mapped, and a first-order plate tectonic description of the region has been made [Weissel and Hayes, 1972; Weissel et al., 1977] (Figure 1). The plate kinematics for the Cenozoic are relatively well understood in this region. Furthermore, the geophysical data delineate several important features that are anomalous in relation to observations in other parts of the world midocean ridge system and also with regard to widely accepted models for accretion and subsequent cooling and contraction of the oceanic lithosphere [e.g., Sclater et al., 1971]. These observations, which may reflect unusual dynamic conditions in the asthenosphere, are as follows:

1. A 'boomerang'-shaped regional depression running north-south across both the Indian and Antarctic plates has been defined by computing 'depth anomalies' from the comparison of Southeast Indian Ocean bathymetric, seismic reflection, and magnetic lineation data and the worldwide oceanic subsidence curve of Sclater et al. [1971] [Weissel and Hayes, 1974]. The maximum depth anomaly of this feature is about 1 km, and its 'wavelength' is about 1500 km. This large depression is superimposed upon ridge flanks which are about 400 m deeper than the global average. Weissel and Hayes [1974] suggested that the depth anomaly is related to downwelling in the mantle.

2. Since 40 m.y. B.P., long episodes of highly asymmetric sea floor spreading have taken place within discrete longitudinal zones along the Southeast Indian Ridge (Figure 2). From about 40 to 15 m.y. B.P., asymmetric accretion occurred between 128° and 139°E, but about 15-10 m.y. ago the locus of asymmetric spreading shifted westward and presently coincides with the deepest and most morphologically complicated section of ridge crest, known as the Australian-Antarctic Discordance. Elsewhere along the Southeast Indian Ridge during the past 40 m.y., crust was accreted approximately symmetrically [Weissel and Hayes, 1971, 1972].

3. Major variations in teleseismic activity along the ridge crest are observed. The section comprising the Australian-Antarctic Discordance (Figure 1) is associated with a broad band of diffuse seismicity, whereas the 700-km-long section of ridge crest immediately to the east is essentially aseismic at the teleseismic level.

4. Large and sometimes abrupt changes in the amplitudes of near-crestal magnetic anomalies occur along the strike of the Southeast Indian Ridge (Figure 2).

This paper is primarily concerned with an attempt to determine (1) the mechanism by which the variation in magnetic anomaly amplitudes occurs and (2) its possible interrelationship with the depth anomalies. Vogt and Johnson [1973] previously suggested that such large variations in magnetic anomaly amplitudes along strike at midocean ridges reflect geochemical changes in the basalts making up layer 2A. Their 'telechemistry' idea of using the amplitude of magnetic anomalies to infer Fe and Ti contents (and, in turn, an array of light-ion lithophile (LIL) elements and Pb and Sr concentration in oceanic basalts is directly testable on the Southeast Indian Ridge. The telechemistry prediction is that anomalously high magnetic anomaly amplitudes correspond to high natural remanent magnetization, susceptibility, titanomagnetite concentration, and thus high FeO* and TiO_2 in basalts which form the oceanic crustal magnetic layering. While Vogt and Johnson [1973] suggested that such magnetic and geochemi-

[1] Also at Department of Geological Sciences, Columbia University, New York, N.Y. 10027.

Paper number 80B0312.
0148-0227/80/080B-0312$01.00

Interesting - precise ocean locations given

JOURNAL OF GEOPHYSICAL RESEARCH, VOL. 87, NO. B10, PAGES 8379–8388, OCTOBER 10, 1982

Location of Instruments on the Seafloor by Joint Adjustment of Instrument and Ship Positions

KENNETH C. CREAGER AND LEROY M. DORMAN

Geological Research Division, Scripps Institution of Oceanography
University of California, San Diego, La Jolla, California 92093

The problem of determining accurate locations for arrays of underwater instruments is similar to the problem of locating local earthquakes by utilizing a limited number of receivers but is complicated by the fact that estimated errors in longitude and latitude of a given receiver (ship) position are nonzero and are typically correlated. Estimates of ship positions at sea are commonly determined by fixes from the Navy Transit navigation satellite system. This system calculates position error ellipses which vary in size and orientation from fix to fix. Deviations in the orientations of the principal axes of the error ellipses from north-south and east-west result in the introduction of off-diagonal elements in the ship position variance matrix. Tying each ship fix to a stationary array of ocean bottom seismometers (OBS's) using acoustic ranging allows averaging of fixes, thus solving simultaneously for ship and OBS positions, puts tight constraints on the system as a whole and especially on the relative positions of the OBS's. In addition to ship positions, the data required to locate the instruments are two-way travel times between the ship and transponders on the instruments, and initial depth estimates of OBS's read from the bathymetry. The parameters which we solve for are the locations of the instruments (including depth) and of the ship at each fix. The forward problem, calculating acoustic travel times from distances between ship fixes and OBS's, is solved by a ray shooting algorithm. This system of equations is linearized and transformed to diagonalize the covariances; it is then solved iteratively by inverting the data jointly using singular value decomposition and step-length damping. The solution includes the covariances of the parameters. We show calculations of positions of four OBS's for deployments during three experiments including the Rivera oceanic seismic experiment (ROSE). Typical fix error ellipses (1 σ) are 300 m by 200 m and resulting instrument position uncertainties are approximately 100 m. Relative instrument positions are accurate to about 50 m. Relative errors can be decreased to 10 to 20 m by using simultaneous rather than sequential ranging.

INTRODUCTION

A problem common to nearly every scientist who does experiments at sea is the determination of position with respect to fixed earth coordinates or position relative to other positions in the experiment. In ocean bottom seismology the seismologist generally lets the seismograph package free-fall through the water until it rests on the ocean bottom. The location of the instrument is often assumed to be at the point of deployment which is typically not precisely known. However, it is advantageous to know the precise location of the instrument. There are two kinds of experiments for which ocean bottom seismometers (OBS's) are commonly used: (1) determining earth structure by seismic refraction studies, and (2) locating local earthquakes. Examples of both types will be shown.

In refraction studies it can be advantageous to shoot to an array of OBS's instead of just one OBS. The advantages of an array are that the apparent velocity or ray parameter can be measured directly and that seismograms can be stacked to increase signal-to-noise ratio of seismic waves. If relative positions of the OBS's are not known precisely, then the advantages of an array over one OBS are minimal.

Because OBS's are sensitive instruments with good high-frequency response and can be emplaced nearly anywhere on the seafloor, they are useful for monitoring small local events which cannot be observed or located from land. Ocean bottom earthquake studies are typically done on mid-ocean ridges or trenches. In each of these settings it is important to know precisely where the instruments are relative to the geologic features and relative to each other. A major, but yet unachieved, goal of microearthquake studies at sea is the use of the locations and characteristics of earthquakes to map the depth dependence of the physical properties of the crust. The success of this work is currently limited by the inaccuracy of the depth determinations. The marine problem is more severe than the land problem because the crust is thinner and instrument location accuracy is poorer. The effects on the shape of the earthquake travel time curve due to a change in source depth are relatively subtle in comparison to those resulting from change in origin time or epicenter location; and hence, depth accuracy is easily degraded by inaccuracy in instrument location.

There are many ways of determining the positions of the OBS's, but they all depend upon first determining the deploying ship's position. With the current Navy Transit navigation satellite system we can get ship fixes on the average of about one an hour with a few hundred meter to 1-km accuracy. A rough estimate of the position of the OBS can be obtained by getting a ship fix (from dead reckoning between satellite fixes or whatever method is available) when the OBS is dropped, assuming the currents are not strong enough to cause appreciable drift as the OBS falls. An OBS typically falls 1-km every 10 min. This method will give position uncertainties of the

Paper number 2B0223.
0148-0227/82/002B-0223$05.00

$$\mathbf{x}_R = \mathbf{D}\,\mathbf{x} \tag{37}$$

The marginal distribution for the vector $\mathbf{x}$ is the appropriate 3 times number of OBS's by 3 times number of OBS's partition of $\mathbf{V}_p$, and is written $< (\mathbf{x} - <\mathbf{x}>)\,(\mathbf{x} - <\mathbf{x}>)^T >$. We can calculate the covariance matrix of the positions of the OBS's relative to each other

$$< (\mathbf{x}_R - <\mathbf{x}_R>)\,(\mathbf{x}_R - <\mathbf{x}_R>)^T >$$

$$= \mathbf{D} < (\mathbf{x} - <\mathbf{x}>)\,(\mathbf{x} - <\mathbf{x}>)^T > \mathbf{D}^T \tag{38}$$

We find that we often know the relative positions of the OBS's much better than we know their absolute positions, especially when travel time uncertainties are small. Thus, in agreement with our intuition, precise relative distances between OBS's can be measured by ranging to several OBS's simultaneously, even if inaccurate fixes must be used.

EXAMPLES

DPSN2. The DPSN2 expedition carried out in 1976 on the R/V *Thomas Washington* near the East Pacific Rise at 9°N included refraction lines shot to an array of four OBS's only a few kilometers apart from each other [*Rosendahl and Dorman*, 1980]. The seismograms from the four OBS's can be stacked to increase the signal-to-noise ratio if the relative positions of the OBS's are known. The angle of incidence of a seismic wave approaching the array can be calculated if the relative OBS positions in the array are known precisely. Many of the advantages of an array of OBS's over one OBS are lost if the shape of the array is not known. The water temperature was measured to a depth of 250 m with an expendable bathythermograph (XBT). Hydrocast data from previous cruises were used to calculate acoustic velocity in the depth range from 250 m to the ocean bottom at 3200 m.

Figure 2*a* shows the satellite ship fixes and the error ellipses calculated for them using the Matzke algorithm. Because the ellipses have a wide range of shapes and orientations, a lot of pertinent information would be lost if covariance in the observations were not accounted for. Remember that covariance is introduced by rotating an error ellipse away from a north-south or east-west orientation. A good example of this is the error ellipse for the initial ship fix in the upper right-hand corner of Figure 2*a*. The pertinent information is the distance between the ship and the OBS array; in this case the distance is measured in the direction of the semiminor axis of the ellipse which is oriented with its semimajor axis at an azimuth of 140°, measured clockwise from north. If the covariant errors are not considered here (i.e., if the ellipse is oriented with an axis pointing north-south), then the position uncertainty along the pertinent direction (50° clockwise from north) would be doubled. At the other extreme, the initial ship fix ellipse on the far left-hand side of Figure 2*a* is long and narrow and oriented with its long axis in a line with the OBS array. This is unfortunate from the standpoint of locating the OBS's because it puts little constraint on the OBS's positions. However, because the OBS positions are constrained by the other data and because the distance to this fix from each OBS position is well constrained by acoustic ranging, the ship's position becomes extremely well constrained. That the distance between the OBS and each ship fix is well constrained (especially for the ship fixes farthest away from the array) can be seen by the orientation of the adjusted ship position error ellipses in Figure 2*a*. They are each oriented with their semimajor axes approximately normal to the line between the fix and the OBS array.

Figure 2*a* also shows the solution for the OBS positions and adjusted ship positions with their error ellipses. This solution is consistent with the statistical assumptions in that (1) the theoretical value of chi squared equals the observed misfit ($\hat{\mathbf{e}}^{0T}\,\hat{\mathbf{e}}^0$), and (2) the adjusted ship positions lie within the 1 standard deviation ellipses for the initial fixes 75% of the time. They are expected to be within the 1 standard deviation ellipses 66% of the time. This solution is obtained when the standard deviation for the travel times is 50 ms. The 1 standard deviation error ellipses for the OBS positions are about 100 m, whereas these position solutions put each of the OBS's about 1-km away from their positions as estimated from the positions of their deployments. The shapes of the array as determined by deployment locations and by acoustic ranging are quite different.

The geometry associated with a tight array of OBS's surrounded by many ship fixes is ideal for getting good relative positions of the OBS's. The relative positions are known to within about 50 m but could be much better if the travel times could be determined more precisely, as is discussed below.

VENT1. The VENT1 experiment in July and August 1980 on the R/V *Melville* was a look at seismic activity on the East Pacific Rise at 21°N. Previously, as part of the RISE experiment, the ridge area was thoroughly surveyed with the DEEP TOW instrument from Scripps Institution of Oceanography, and with the ALVIN from Woods Hole Oceanographic Institution. The bathymetry was well mapped, and three long-lived navigation transponders (with 5-year life expectancies) were left on the bottom with their relative positions known to within 10 m. The water depth is about 2600 m. Using these transponders and two more which were deployed and located at the beginning of the VENT1 cruise, ship fixes could be obtained continuously with up to 20-m precision. The water velocity was calculated from conductivity-temperature-depth observations made on a previous cruise.

Some of the OBS's were lowered to the ocean bottom on the end of a wire. Near the end of the wire just above the OBS was a transponder of the type used on the DEEP TOW sled which got continuous fixes with a 20-m accuracy from the navigation transponders fixed on the ocean bottom. When the OBS got near the ocean bottom it was released, so its position could be known very accurately. There is one problem with this method. The latch connecting the wire to the OBS takes about 30 min to burn and thus release the OBS. There is no way of knowing when the OBS was actually dropped, so depending upon the rate at which the ship and OBS were drifting, this error could be sizable (perhaps 200 m).

As an independent check on the position of the OBS, we applied the technique described in this paper. We used the transponders fixed on the ocean bottom for ship navigation, but unfortunately, the uncertainty in the times when we were ranging to the OBS's was up to 5 min, so the ship fix uncertainties were ellipses oriented with their semimajor axes aligned with the track line of the ship. The length of the semimajor axis is the ship's speed multiplied by the uncertainty in the time of the ranging to the OBS's. The length of the semiminor axis is determined by the accuracy of the ship fixes.

Figure 4 shows the initial ship fixes (triangles), solutions for the ship fixes (crosses), and the solutions for OBS positions (solid circles). The stability of this solution is demonstrated by plotting the iterative steps in acquiring the solution. For the initial iteration all OBS positions were set at the location indicated by the star near the bottom right-hand corner of Figure 4. The OBS solutions for each iteration are shown by a dot. The final solution is very close (within 200 m for all OBS's) to the locations determined by the method of deploying the OBS's on the ends of wires.

Because we had continuous ship position fixes, we did not have to interpolate acoustic travel times to the time of ship fixes. This advantage greatly improved the reliability of the acoustic travel time estimates. The solution which is consistent with the chi squared test is obtained when the travel time errors are estimated to be on the order of 5 ms. The OBS's were all located to a 1 standard deviation accuracy of about 100 m. Due to the geometry of the OBS's and ship fixes the semimajor axes of the relative error estimates are not much lower than the absolute error estimates, but the semiminor axes of the relative error estimates are about 25 m. The reason for this is that three of the OBS's are constrained by data from only one direction.

ROSE. The active phase of the ROSE experiment carried out in January and February 1979 included an array of instruments at the crest of the East Pacific Rise at about 12°N. The water depth is about 2800 m. The sound velocity in water was calculated from conductivity-temperature-depth observations made during the experiment. In this case the satellite navigation program in the Magnavox receiver did not provide any statistical estimates of uncertainty, so we generated them using relations derived from the geometry of the satellite passes. These are $\sigma_{\text{latitude}} = 0.3$ nautical miles and $\sigma_{\text{longitude}} = 0.3$ nautical miles $\div \cos(\theta)$, where θ is the altitude of the satellite pass at the closest point of approach. These error estimates, in conjunction with estimated errors of 50 ms for the acoustic travel times, produced a satisfactory chi squared value of 11 for 10 degrees of freedom. However, five out of the seven adjusted ship positions are outside their initial ship fix standard deviations, as can be seen in Figure 5. This is not a serious problem because none of the adjusted ship positions are far outside the error ellipses.

Due to inadequacies in the ship fixes and in the geometry (i.e., not ranging to each OBS from all directions) we were only able to locate the OBS's to an accuracy of 250 m in their semiminor axes and to as much as 500 m in their semimajor axes. Our solution for the position of each OBS is roughly 1 km away from its position as estimated from the location of its deployment. In fact, the solution puts the OBS 'DOE' about 2 km closer to both 'INEZ' and 'GWEN' than was thought from their locations as determined by the estimates of where they were deployed.

SUMMARY AND CONCLUSIONS

We have demonstrated the ability to locate a tight array of ocean bottom instrument packages to within a standard deviation of slightly over 100 m using Navy Transit navigation satellite fixes and acoustic ranging between ship and OBS, even though the 1 standard deviation satellite error ellipses are typically about 300 m. This solution has relative OBS position uncertainties of 50 m. Solving jointly for better estimates of ship positions as well as for OBS positions, we can tie the ship positions into the fixed OBS array to put tight constraints on both ship positions and OBS positions. The skewnesses of the satellite error ellipses are incorporated in the solution by using covariant statistics.

The problem is set up as a 'generalized inverse' problem with OBS depths, ship positions, and acoustic ranges as data, and OBS positions and ship positions as parameters. The matrix equation corresponding to the linearized forward problem is transformed to make the errors in the transformed data space isotropic. Singular value decomposition is used to calculate the 'generalized inverse.' Step-length damping was added when it became clear that an iterative solution to the nonlinear problem often did not converge. Covariance matrices for the parameters and for relative positions of the OBS's are calculated. Error ellipses for the ship and OBS positions are plotted.

Further improvements can be made when ship fixes are improved and when travel time errors are decreased by ranging to all OBS's simultaneously instead of sequentially. We try to range to the OBS's when the ship is moving slowly, but sometimes we range to the OBS's when the ship is moving at 5 knots relative to the OBS's. In this case the one-way travel time from the OBS to the ship will change by 0.1 s every minute. Because of the length of time required to obtain each travel time and the fact that we must interpolate between ranges to get travel time to the OBS's at the time of a satellite fix, we often assign errors in travel times of 0.05 s. In the DPSN2 example these error estimates along with the satellite fix position error estimates give the appropriate value for χ^2.

In a problem like this one where there is a tight array of OBS's surrounded by a dozen ship positions, the relative positions in the array can be very tightly constrained if the travel times are well known. This is easily demonstrated. We use the final solution which is shown in Figure 2*a* as the original guess for the parameters $\mathbf{p}_0$. This assures us that $\Delta\mathbf{p}$ will be small so that the linear approximation (equation (2)) is good. Then the estimate for travel time errors can be reduced to any small value and the solution is obtained after one iteration. When the travel time error estimates are small the χ^2 measure of misfit is large, indicating that the solution is unrealistic. However, the parameter error estimates will be the estimates which are appropriate to the estimated errors in the data. In other words, we have a way of calculating what the parameter uncertainties would be if the experiment were identical

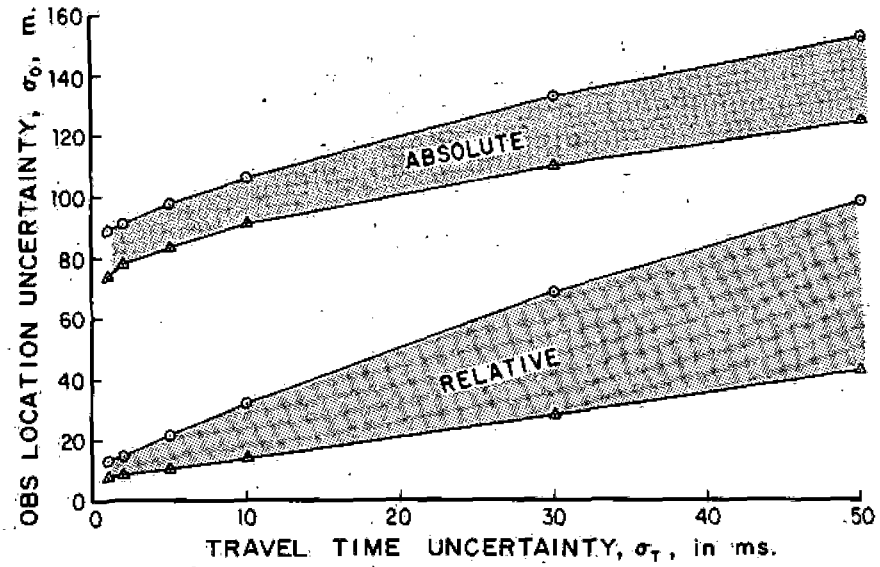

Fig. 6. Plot of absolute and relative OBS uncertainties as a function of uncertainties in acoustic travel times in the DPSN2 experiment. See text for detailed explanation.

except for a reduction in the travel time errors. Figure 2*b* shows the error ellipses for the OBS and adjusted ship positions under the assumption that the errors in the travel times are 2 ms. We can see that there is a significant improvement in the sizes of the error ellipses when we compare this solution to the solution in Figure 2*a*, but the greatest improvement is in the reduction of relative errors in the OBS positions.

If the travel times were perfect we would expect the absolute errors in OBS locations to be proportional to $\sigma\ n^{-1/2}$, where σ is the size of the ship fix errors and n is the number of fixes. We would also expect the relative errors to go to zero as the travel time errors go to zero. Figure 6 shows that although the relative errors do not go to zero as travel time errors go to zero, they do go close to zero. The computer program was run 6 times on the DPSN2 problem with travel time uncertainty estimates of 1, 2, 5, 10, 30, and 50 ms. In Figure 6 the circles are averages of the lengths of the semimajor axes of the error ellipses for the four OBS's in the DPSN2 example. The triangles are averages of the lengths of the semiminor axes for the four OBS's. The relative positions of the OBS's in the DPSN2 experiment could have been estimated to within 10 or 20 meters if travel times could be measured to within 2 to 5 ms. The repeatability of the travel time measurements is within 1 ms. We are developing the hardware to range to all OBS's simultaneously, so travel time measurements with precisions of 2 to 5 ms may soon be possible.

We have thus far used this method to locate small arrays of instruments using two-way travel times from transponders. The same algorithm can be used with water wave travel times from shots to perform a global adjustment of shot positions and instrument locations. In a large-scale experiment such as ROSE, this may be valuable but we have not done this yet.

Acknowledgements. J.L. Abott implemented that Matzke algorithm on the IBM 1800 and suggested the way to simulate fix statistics. J. Orcutt contributed to a previous version of the program. K. Sverdrup programmed the plotting. This work was supported by the Office of Naval Research and the National Science Foundation and the Naval Ocean Research and Development Activity.

REFERENCES

Buland, R., The mechanics of locating earthquakes, *Bull. Seismol. Soc. Am.*, *66*, 173-187, 1976.

Dorman, L. M., A linear relationship between earth models and seismic body wave data, *Geophys. Res. Lett.*, 6, 132-134, 1979.

Flatte', S. M., R. Dashen, W. Munk, K. Watson, and F. Zaharaisen, *Sound Transmission Through a Fluctuating Ocean*, Cambridge University Press, Cambridge, 1979.

Golub, G. H., and C. Reinsch, Singular value decomposition and least squares solutions, in *Linear Algebra*, edited by J. H. Wilkinson and C. Reinsch, pp. 134-151, Springer-Verlag, New York, 1971.

Hoffman, K., and R. Kunze, *Linear Algebra*, 332 pp., Prentice-Hall, Englewood Cliffs, N. J., 1961.

Jackson, D. D., Interpretation of inaccurate, insufficient and inconsistent data, *Geophys. J. R. Astron. Soc.*, *28*, 97-109, 1972.

Jenkins, G. M., and D. G. Watts, *Spectral Analysis and Its Applications*, 525 pp., Holden-Day, San Francisco, Calif., 1968.

Jordan, T. H., and K. A. Sverdrup, Teleseismic location techniques and their application to earthquake clusters in the south-central Pacific, *Bull. Seismol. Soc. Am.*, *71*, 1105-1130, 1981.

Lanczos, C., *Linear Differential Operators*, 546 pp., Van Nostrand, London, 1961.

Matzke, D. E., An optimum six parameter estimation process for navigation satellite (SRN-9) data, *Mar. Tech. Soc. J.*, *5*(2), 37-42, 1971.

Moore, R. D., L. M. Dorman, C.-Y. Huang, and D. L. Berliner, An ocean bottom, microprocessor based seismometer, *Mar. Geophys. Res.*, *4*, 451-477, 1981.

Penrose, R., A generalized inverse for matrices, *Proc. Cambridge Philos. Soc.*, *51*, 406-415, 1955.

Prothero, W. A., A free fall seismic capsule for seismicity and refraction work, in *Proceedings of the Offshore Technology Conference*, pp. 181-195, Offshore Technology Conference, Dallas, Texas, 1976.

Rao, C. R., *Linear Statistical Inference and Its Applications*, 625 pp., 2nd ed., John Wiley, New York, 1973.

Rosendahl, B. R., and L. M. Dorman, Summary of the geology and geophysics of the East Pacific Rise in the vicinity of the Siqueiros Fracture Zone, *Initial Rep. Deep Sea Drill. Proj. 54*, 23-36, 1980.

Wiggins, R. A., The generalized inverse problem: Implications of surface waves and free oscillations for earth structure, *Rev. Geophys. Space Phys.*, *10*, 251-285, 1972.

(Received June 4, 1981;
revised January 28, 1982;
accepted February 5, 1982.)

GEOPHYSICAL RESEARCH LETTERS, VOL. 7, NO. 11, PAGES 989-992, NOVEMBER 1980

MAGMA CHAMBER AND MANTLE REFLECTIONS - EAST PACIFIC RISE

Thomas J. Herron[1], Paul L. Stoffa and Peter Buhl

Lamont-Doherty Geological Observatory of Columbia University, Palisades, New York 10964

Abstract. A multichannel seismic reflection profile of stacked and migrated common depth point data across the East Pacific Rise near the Siqueiros Fracture Zone supports and extends previous observations (at two crossings 27 to 50 km to the south) of reflections assumed to be from the top of a magma chamber and of reflections from the M-discontinuity. The reflection assumed to be associated with the top of the magma chamber is 1-1/2 to 2 km below the sea floor. The combined results of the three crossings suggest that the chamber is continuous along the Rise crest and that its width, which varies from 2 to 8 km, correlates with the width of the Rise crest as indicated by the bathymetric contours. The reflections from the crust-mantle boundary can be detected beneath the raised axial block of the East Pacific Rise and although weak, can be detected beneath the magma chamber.

Introduction

For several years, Lamont-Doherty Geological Observatory has acquired digitally-recorded marine seismic reflection data aboard the R/V CONRAD through the use of a 24-group hydrophone streamer, 2400 m long, and four, 466 in.^{3} (7.64 l) air guns towed behind the ship. The air guns, at a pressure of 2000 psi (13.8×10^6 N/m^2), are fired simultaneously once every 20 s (approximately every 50 m when a ship's speed of 5 knots (9.3 km/h) is assumed). Computer processing of the data includes common depth point gather, semblance velocity analysis, normal moveout correction, stack deconvolution and, when necessary, wave equation migration. Herron et al. (1978) and Stoffa et al. (1980) showed examples of seismic reflections from within the oceanic crust and from the crust-mantle boundary on two, 24-fold, common-depth point profiles across the East Pacific Rise near the Siqueiros Fracture Zone. The two profiles (lines 17 and 19, Figure 1) were separated by about 23 km along the Rise crest. On line 17 we observed a reflection (identified as R4) about 2 km below the sea floor at the Rise crest which we assume originates from the top of the seismic low-velocity zone detected at this site by Orcutt et al. (1975, 1976). This low-velocity zone most likely indicates the presence of a magma chamber from which new oceanic crust develops (Cann, 1974; Sleep, 1975, 1979; Rosendahl, 1976). After processing the data from the two lines, Stoffa et al. (1980) made the important observation that reflections from the M-discontinuity can be traced almost continuously under the 10 to 20 km wide raised axial block of the East Pacific Rise, indicating that the M-discontinuity is formed immediately under the magma chamber, at about 6 km below the sea floor, presumably by gravity settling of crystals from the melt. In this present paper we show further examples of what we believe are reflections from the top of the magma chamber and from the M-discontinuity on MCS line 20 which crosses the Rise crest about 27 km north of line 19.

Observations

Figure 2 shows a 100 km section of stacked and migrated seismic data from line 20. A mantle reflection at about 6 s of two-way traveltime can be followed across most of Figure 2. The reflection is particularly strong under the western flank of the Rise crest. It can also be traced with considerable confidence for about 60 km east of the Rise crest.

Figure 3 shows only the Rise crest portion of the line with an expanded horizontal scale. This profile shows a reflection at about 4.1 s which we associate with that identified by Herron et al. (1978) as R4 on line 17. Reflection R4 can be traced across the Rise crest and down the eastern flank for a distance of about 4 km.

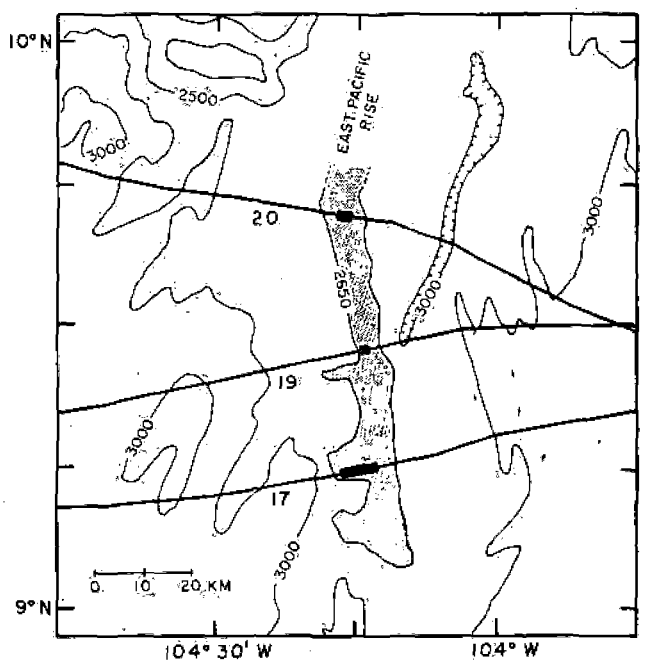

Fig. 1. Track chart showing location of MCS lines 17, 19 and 20. Bathymetry taken from Rosendahl et al. (1976) and Batiza et al. (1977). The extent along the ship's track of the reflection R4, assumed to be related to the top of a magma chamber, is shown by the thickened track lines. Note that the magma chamber width is related to the width of the Rise crest as measured by the 2650 m contour.

[1] Also at Rutgers University, Dept. of Geology, Newark, New Jersey 07104.

Paper number 80L1434.

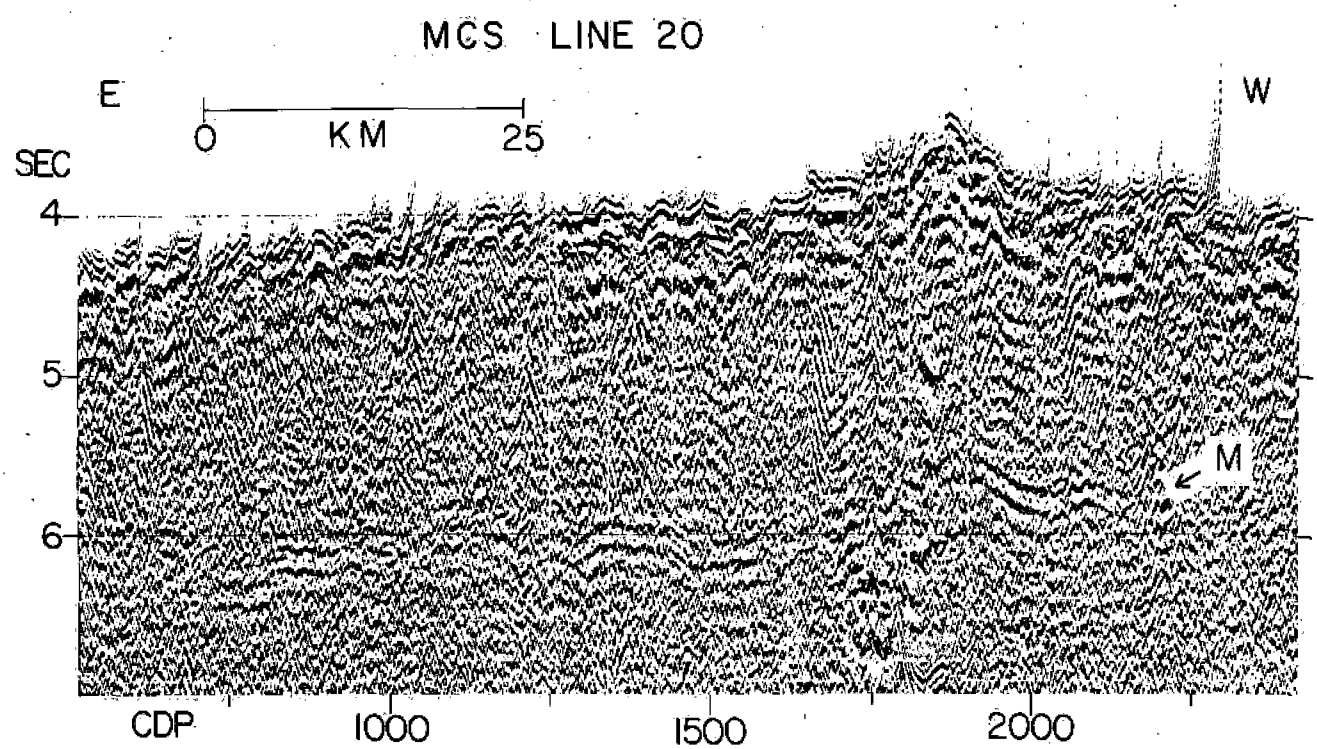

Fig. 2. Line 20 crossing of the East Pacific Rise. 24-fold common depth point, stacked section. Band-pass 2-15 Hz. Wave equation migration using a velocity of 1500 m/s was applied to the stacked data. Note the strong mantle reflection approximately paralleling the sea floor under the western flank of the Rise crest. The mantle reflection can be followed for about 60 km east of the Rise crest. The vertical exaggeration of the sea floor is 16.7 to 1.

A comparison of the seismic structure observed on line 17, 19 and 20 is given by the line drawings in Figure 4 which shows the sea floor, R4, and M-discontinuity reflections on the three crossings of the Rise crest. The time and depth below the sea floor of reflection R4 and the interval velocity between the sea floor and R4 are summarized in Figure 4. The reflection time below sea floor of R4 decreases from 0.8 s at line 17 to 0.65 s at line 20. The interval velocities were

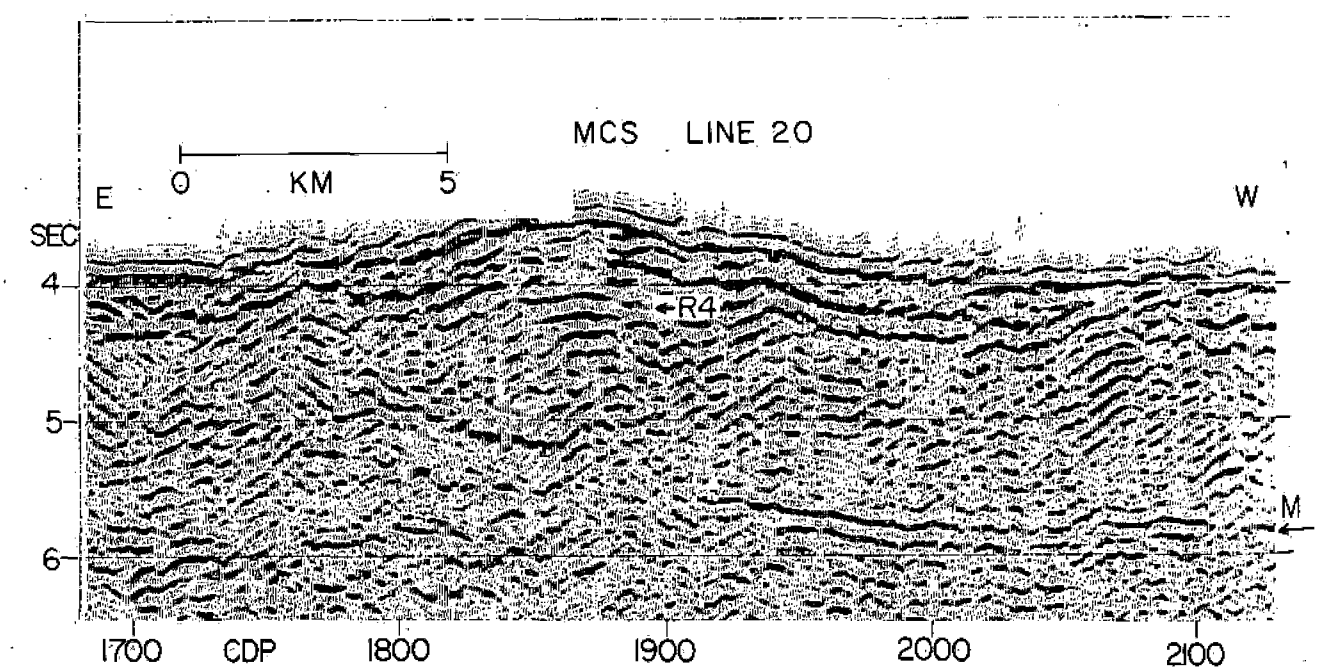

Fig. 3. Migrated section. Band-pass 0-10 Hz. Mantle reflection M and assumed magma chamber reflection R4 are identified. Vertical exaggeration is 3.3 to 1.

determined by semblance velocity analysis. As indicated by Herron et al. (1978) these measurements could be in error by ±0.5 km/s which corresponds to about a 0.2 km error in depth to reflection R4.

Using the mean velocities shown in Figure 4, the depth below sea floor of R4 decreases from about 2 km at line 17 to 1.5 km at line 20. Even allowing for errors in velocity this is probably a real decrease in depth to R4 over the approximately 50 km distance from line 17 to line 20.

Discussion

In our seismic cross sections of the East Pacific Rise, we observe only three prominent reflections: the sea floor and the M-discontinuity reflections, defining the top and bottom of the oceanic crust, and reflection R4, which we assume defines the top of a magma chamber within the crust. We do not detect reflections that would delineate the sides of the magma chamber. Either the sides of the chamber are too steep for detection by vertical-incidence seismic profiling or are too gradational to provide the sufficiently rapid change in acoustic impedance necessary for reflection of seismic energy. The bottom of the magma chamber may coincide with the mantle reflection which we can trace almost continuously under the Rise crest or, if it is above the mantle reflector, it is too gradational to be detected. If, as suggested by Rosendahl (1976), the chamber is only about 30% molten on the average, it is understandable that we would detect only the top of the chamber in our seismic reflection experiments.

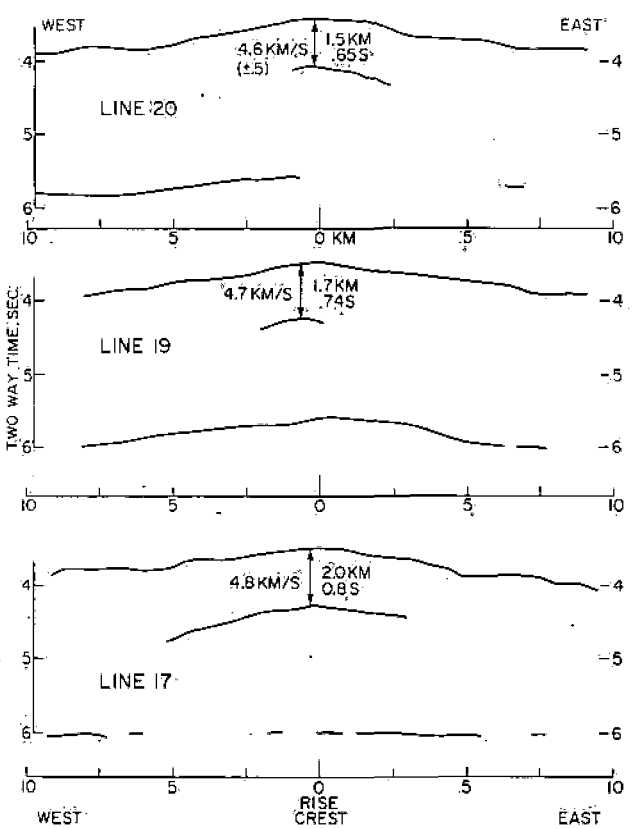

Fig. 4. Seismic structure on MCS lines 17, 19 and 20. The mantle reflection on lines 19 and 20 roughly parallels the sea floor, but on line 17 it remains at about 6 sec of traveltime. The magma chamber is broader and deeper on line 17 as compared to lines 19 and 20.

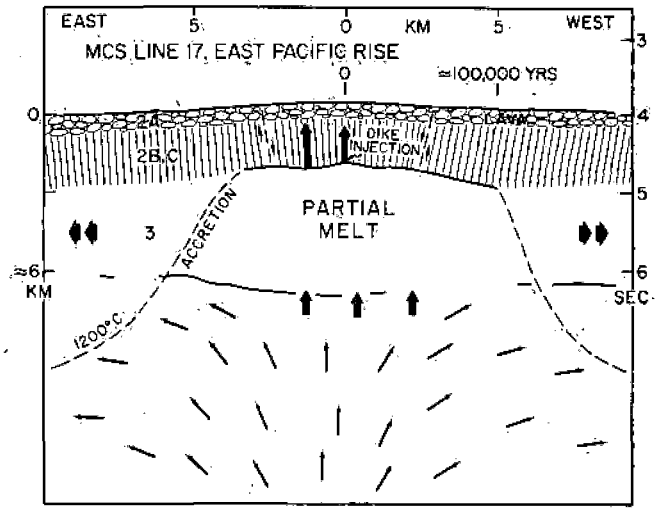

Fig. 5. Schematic diagram illustrating how our seismic observations may fit with present ideas on the genesis of oceanic crust. The sea floor was plotted with no vertical exaggeration and the magma chamber and mantle reflections were plotted at their observed times below the sea floor. The half-spreading rate near line 17 is about 5 cm/yr.

As discussed by Stoffa et al. (1980), the mantle reflection on line 17 is not parallel to the sea floor under the Rise crest but remains at about 6 seconds of total two-way traveltime. Although Stoffa et al. describe the mantle reflection on line 19 as "paralleling" the sea floor under the Rise crest, this is only accurate in comparison to the large and obvious increased time of mantle below sea floor on line 17. In fact, both lines 19 and 20 show an increased time to mantle at the Rise crest of 0.1 s or more, but this is difficult to measure accurately because of roughness of the sea floor and the very low frequency of the mantle reflection which makes its onset uncertain. The large increase of mantle time below sea floor on line 17 at the Rise crest and the slight increase on lines 19 and 20 imply either a thickening of the crust or a decrease in the average velocity between the sea floor and mantle in the axial zone.

Figure 4 shows that the top of the magma chamber on line 17 is about 8 km wide. On lines 19 and 20 the top is apparently only about 2 and 4 km wide, respectively. Because there is enough energy to reflect from the mantle beneath and beyond the magma chamber on these lines, it is likely that the full width of the top of the chamber was detected. If line 17 then crosses a magma chamber several times wider than at lines 19 and 20, it is possible that the greater volume of the chamber is accompanied by a greater average percent of melt within the chamber. This would explain the much increased reflection time below sea floor at the line 17 Rise crest as due to a more depressed velocity within the magma chamber, relative to lines 19 and 20, rather than due to a thicker crust in the axial zone.

Figure 1 shows the location of the top of the magma chamber under each MCS line relative to the

2650 m bathymetric contour. Where the contour shows the Rise crest to be broad, the magma chamber is wide (line 17) and where the crest is narrow the magma chamber is narrow (line 19). Based on these three crossings we suggest that the bathymetric contours at the very top of the Rise crest indicate the width of the underlying magma chamber. Also, unless our detection of reflection R4 on three crossings was fortuitous, the results suggest that this 50 km section of Rise crest is underlain by a continuous magma chamber.

While we do not have adequate velocity information to convert our seismic time sections to depth sections we can plot a time section to approximate a depth section. By choosing the appropriate expanded horizontal scale we can show a section without much distortion. Figure 5 is an approximate "depth" section of the line 17 data. The sea floor reflection has been plotted with no vertical exaggeration and reflection R4 and the mantle reflection have been plotted at their observed times below sea floor. The downward bulge of the mantle reflection does not necessarily imply a thickening of the crust under the Rise crest, but as noted above is probably due to the depressed velocity within the magma chamber. If, as suggested by Cann (1974), Sleep (1975), and Rosendahl (1976), layer 2 of the crust is formed by volcanic action and dike injection from the top of the magma chamber and layer 3 grows by crystallization out of the sides of the chamber, then our seismic information fits with the geologic ideas as shown in Figure 5.

On our three crossings of the Rise crest the sea floor was observed to be very smooth for several km on either side of the crest. At points farther from the crest the sea floor is broken up quite severely by block faulting. The evidence of faulting is seen in our seismic sections in the many diffraction hyperbolas originating from scattering points at the sea floor outside the smooth central region (see Figure 3, Herron et al., 1978). Except for this smooth region we find it necessary to apply wave equation migration to our data to remove diffracted energy and thereby to detect reflections from below the sea floor. Figure 5 shows inferred faults that bound the smooth sea floor on line 17. The smooth central block which is entirely underlain by the magma chamber (that is, by reflection R4) may drop down as spreading of the oceanic crust occurs, but there is no seismic evidence that the displacement of the fault surface offsets reflection R4. However, because the wavelength of the seismic waves in layer 2 is several hundred meters, fault displacements of less than 100 meters would be difficult to detect.

Figure 5 suggests that the top of the magma chamber may be preserved on much older crust as the layer 2 - layer 3 boundary of seismic refraction studies. Whether this is true or not, we do not detect any continuous reflections extending outward from the axial block of the East Pacific Rise that could be attributed to the top of layer 3. The layer 2 - layer 3 boundary must, therefore, be too gradational to detect by vertical-incidence seismic reflections, at least in this geographic area.

The arrows directed upward through the mantle reflection in Figure 5 indicate the possibility that magma ascends from sources within the upper mantle to replenish the magma chamber as spreading occurs. The optimum spatial resolution of our data is, on average, 50 m along a reflecting surface below the array. Thus, even on line 19 where we detect a mantle reflection on almost every common depth point gather, and certainly on lines 17 and 20 where gaps occur in the mantle reflection, the seismic data do not preclude the possibility of ascending magma.

In conclusion, we emphasize that seismic reflection profiling with our 2.4 km hydrophone array does not provide adequate velocity resolution to determine unambiguously whether there is a low-velocity zone below reflection R4. The discussion of our results in terms of a magma chamber hypothesis rests upon our observation of increased mantle reflection time below sea floor under the Rise crest, which can imply a low-velocity zone, also upon the detection by seismic refraction methods of a low-velocity zone under the line 17 section of the Rise crest (Orcutt et al., 1975, 1976), and the assumption that the depressed seismic velocity is due to a region of full or partial melt.

Acknowledgments. This work was supported by the Office of Naval Research under Contract N00014-80-C-0098. We appreciate the assistance of R.E. Houtz and J.W. Ladd who critically reviewed the manuscript. LDGO Contribution No. 3051.

References

Batiza, R., B.R. Rosendahl, and R.L. Fisher, Evolution of oceanic crust, 3, petrology and chemistry of basalts from the East Pacific Rise and the Siqueiros transform fault, J. Geophys. Res., 82, 265-276, 1977.

Cann, J.R., A model for oceanic crustal structure developed, Geophys. J. Roy. Astron. Soc., 39, 169-187, 1974.

Herron, T.J., W.J. Ludwig, P.L. Stoffa, T.K. Kan, and P. Buhl, Structure of the East Pacific Rise crest from multichannel seismic reflection data, J. Geophys. Res., 83, 798-804, 1978.

Orcutt, J.A., B. Kennett, L. Dorman, and W. Prothero, A low velocity zone underlying a fast-spreading rise crest, Nature, 256, 475-476, 1975.

Orcutt, J.A., B.L.N. Kennett, and L.M. Dorman, Structure of the East Pacific Rise from an ocean bottom seismometer survey, Geophys. J. Roy Astron. Soc., 45, 305-320, 1976.

Rosendahl, B.R., R.W. Raitt, L.M. Dorman, L.D. Bibee, D.M. Hussong, and G.H. Sutton, Evolution of oceanic crust, 1. A physical model of the East Pacific Rise crest derived from seismic refraction data, J. Geophys. Res., 81, 5294-5304, 1976.

Sleep, N.H., Formation of oceanic crust: Some thermal constraints, J. Geophys. Res., 80, 4037-4042, 1975.

Sleep, N.H., and B.R. Rosendahl, Topography and tectonics of mid-oceanic ridge axes, J. Geophys. Res., 84, 6831-6839, 1979.

Stoffa, P.L., P. Buhl, T.J. Herron, T.K. Kan and W.J. Ludwig, Mantle reflections beneath the crestal zone of the East Pacific Rise from multichannel reflection data, Marine Geology, 35, 83-97, 1980.

(Received July 21, 1980;
accepted September 9, 1980.)

JOURNAL OF GEOPHYSICAL RESEARCH, VOL. 87, NO. B10, PAGES 8364–8378, OCTOBER 10, 1982

Magnetotelluric Experiment Over the ROSE Area

J. H. FILLOUX

Scripps Institution of Oceanography, La Jolla, California 92093

Seafloor observations of natural electromagnetic fluctuations diffusing into the earth have been made in the vicinity of the Pacific Rise at 12°N and 21°N to gather information on the electrical conductivity structure of the oceanic basement near a spreading ridge. At 21°N the close proximity of land (Baja California) introduces a noticeable distortion of the EM fields, and consequently the magnetotelluric sounding for this area must be interpreted with caution. At both locations the conductance of the upper 200 km appears exceptionally high and the conductivity rises rapidly below, reaching 1 S m^{-1} or more at 350 km. The statistical significance of a prominent conductivity increase near a depth of 22.5 km detected in the inverted data from 12°N and of a less developed one at 30 km in the case of 21°N is discussed. Records of the magnetic variations at 21°N taken above the spreading center, compared to records from 40 and 120 km to the west, reveal a conspicuous enhancement of the high-frequency horizontal variations in a direction slightly west of magnetic north. We interpret this distinctive feature as the signature of an electric current sheet concentrated in an extremely high conductance, relatively shallow layer electrically bridging the two seafloor areas adjacent to the spreading center. An approximate calculation suggests a conductance in excess of 3000 S per meter of ridge crest in the close vicinity of the accretion center, equivalent to 1 to 8 km of molten basalt, depending on temperature (1000°–1200°C?) and depth (2–10 km?). This structure is consistent with seismic refraction information for the same area and with stratigraphic reconstruction of a fossil accretion center in Samail ophiolite. An interpretation in terms of a well-developed magma chamber is irresistible, although confirmation of the existence of this feature as well as improvement of its resolution by means of additional EM data would be of major interest.

INTRODUCTION

The seafloor magnetotelluric experiment (SFMT) associated with project ROSE was designed to complement a series of geophysical investigations in the close vicinity of the spreading center of the Pacific Rise at 21°N. The strategy was to deploy a linear array of seafloor electric and magnetic recorders across the rise crest to observe over a period of 3 months the diffusion into crust and mantle of low-frequency natural electromagnetic (EM) signals originating in the ionosphere and above. A successful interpretation of such data was expected to lead to information on the electrical conductivity structure with depth and, hopefully, laterally as well. With equipment available to occupy seven stations, including one set of instruments to spare, this SFMT experiment was to be the most extensive in coverage and in observational duration attempted to date.

The field work began in mid-January 1979 and the instrumentation to occupy four of the seven sites had been deployed when the anticipated clearance to operate in Mexican waters appeared in jeopardy. Deployment of further equipment was postponed and a new location at 12°N, also adjacent to the Pacific Rise but in international waters, was selected as an alternate experimental area. Because of the extensive delay, as well as of the necessary crowding of several experiments within a restricted time period, the balance of the MT instruments (four pairs) was used in a modest two-station array that remained on the seafloor for only 3 weeks.

The experiment covered here, therefore, involves two independent clusters (see map of Figure 1): one at 21°N, not too distant from the tip of Baja California; the second at 12°N, roughly 500 km off the coast of southern Mexico. A preliminary analysis of the data collected during the second short experiment has already been published [*Filloux*, 1981]. This same article also contains a progress report on a series of experiments conducted to date under nearly identical experimental conditions, in particular with the same self-contained free-fall electric and magnetic recorders (described in the work of *Filloux* [1980*b*]). The data processed and analyzed so far appear consistent with each other and also with present concepts of plate tectonics. A low conductivity zone, possibly related to plate thickness seems to prevail near the surface, followed by a rapid conductivity rise that is encountered at a depth increasing with plate age [*Filloux*, 1980*a*]. It should be emphasized that the resolution of magnetotelluric techniques is inherently low, increases only slowly with the length of the time series collected and that no data inversion methodology is yet widely accepted by the community of geophysicists involved with MT methods. We believe that under these conditions it is the consistency among a growing number of conductivity profiles, probably somewhat optimistically interpreted if taken individually, that best supports the usefulness of seafloor magnetotellurics in submarine geophysical research.

It will be seen that the experiment reviewed here, somewhat mutilated from the very start, produced fewer specific and somewhat different results than those expected. Nevertheless, the limited new information on lithosphere and mantle structure in the vicinity of the Pacific Rise is sufficient to allow suggestive comparisons with the structure of other deep seafloor basements. Furthermore, the unanticipated enhancement of the high-frequency horizontal magnetic variations at the spreading center is interpreted as the signature of an extremely shallow layer with an exceptionally high conductance, best explained by the existence of a substantial melt cross section: i.e., a fully developed magma chamber, or effectively connected, magma-impregnated matrix, with a thickness of several kilometers. Ultimately, the simultaneous coverage of two areas of the Pacific Rise relatively distant from each other and the peculiarity of the

Paper number 2B0133.
0148-0227/82/002B-0133$05.00

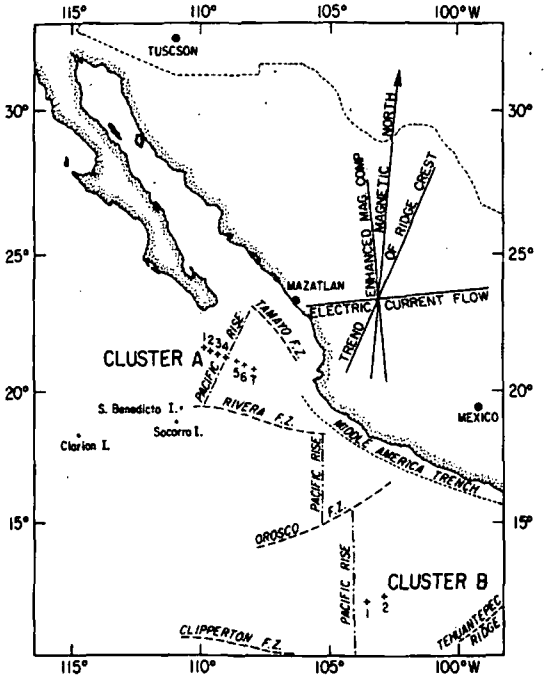

Fig. 1. Map of the area covering the EM observations referred to in the text. The initial plan was to deploy a single, linear array of seven stations, 1 to 7, across the Pacific Rise spreading area at 21°N. However, only four sites, 1 to 4, were occupied, constituting the instrument cluster A. The balance of instruments was deployed for a short time as cluster B around 12°N, on the Coco's side of the ridge crest. Note the position of the magnetic observatory of Tucson and an azimuth diagram referring to various orientations discussed in the text.

setting with respect to the continental borderline contribute a solid, if unintended, guidance in planning future programs of magnetotelluric exploration of the ocean basins.

EXPERIMENTAL SETTING

It was initially assumed that the induction processes from ionospheric sources taking place in oceanic crust and mantle across a typical spreading center would uncover a clearly two-dimensional anomaly with a strike matching closely the spreading axis. The model suggesting this geometry is supported by our present understanding of the mechanisms of ocean floor spreading which involve (1) the supply along the spreading axis of very hot magma rising from the deep, then moving and solidifying laterally to form new lithosphere, and (2) the progressive decrease of the cross section of partly melted and highly conducting material away from the accretion center [*Oxburgh and Turcotte*, 1968; *Parker and Oldenburg*, 1973; *Presnall et al.*, 1979].

For the above reasons, a linear array extending perpendicularly across the spreading center, with a central station located as close as possible to the ridge axis appeared optimum. The separation between the stations was determined largely by the scale and geometry of local tectonic features, namely, the tip of Baja California as well as the Tamayo fracture zone to the north, and the Rivera fracture zone and adjacent island cluster (Islas Socorro and San Benedicto) to the south. It was anticipated from previous experience that the assumption of two dimensionality could hardly apply beyond a fraction of the length of this segment of the rise crest, on both sides. These circumstances, taken together with the number of instruments available, resulted in an average spacing of 40 km, but the search for adequately flat topography also played a determinant role. The location of the crossing of the spreading axis by the MT traverse was chosen at 21°10'N so as to be sufficiently removed from the area of concurrent dense experiments of the RISE program centered at 20°52'N, 109°05'W [*Spiess et al.*, 1980]. Because the precise bathymetry available to RISE did not extend far enough to the north, the position of the central station, Station 4A, with respect to the spreading axis is known only to within ±1 km. (A location to the south of the main center of research activity was given some consideration at first to lessen the possibility of coastal interference; however, this alternate location would have brought the array too close to the ridge offset adjacent to the Rivera fracture zone.) The array is shown in Figure 1, cluster A, although only the first four of the seven stations initially projected were occupied.

The deployment operation was carried out proceeding from the west-northwest, our attention being concentrated on a search for sediment pockets among an extremely rough bottom. Although occasionally encountered, these sediment patches were so restricted in size that the Omega navigation was not sufficiently stable to permit us to find them again should we decide to return, or if we drifted away. As a result, the instrumentation deployed at cluster A included a high proportion of substantially tilted instruments (see Table 1 for informative data on the deployment). Although we had gained considerable experience before reaching the ridge axis and in spite of finding a promising spot (albeit one surrounded by rather chaotic relief), both electric and magnetic recorders at this particularly strategic position landed with exceptionally high tilt. See Table 1 and map, Figure 1. We were surprised to encounter the shallowest seafloor somewhat to the west of the accepted location of the spreading axis, as shown in Table 1.

Following the decision to curtail further instrument installation after completing the deployment at Station 4A and unable to immediately retrieve instruments already in place because of our reliance on preset timers for recovery, the question arose as to whether a 3-week experiment carried out with four sets of instruments only, and with ship time restricted to the daylight portion of two days, was justifiable. Our decision to proceed was based in part on the high expenses irreversibly incurred and also on the anticipation that the new location, farther removed from the shoreline, might prove to be more favorable on account of the reduced influence of the coastal anomaly.

The cluster B experiment at 12°N unfolded with exceptional smoothness, and it provided redundant data from two stations east of the ridge crest (*Filloux* [1981]; see map of Figure 1). The usability of these data was unfortunately limited by the short duration of the experiment and by the very modest level of ionospheric activity that characterized this period.

INSPECTION OF DATA

Although subject to drastic alterations during its execution, the experiment reported in this article resulted in the most extensive set of seafloor magnetotelluric data collected to date. Inasmuch as a large MT data set of oceanic origin has never been described in detail as yet, a valuable insight into the applicability of SFMT to submarine geophysical research can be gained directly from a thorough and critical inspection of the ROSE MT data prior to analysis. However,

TABLE 1. Description of the Data Sets

Station	Signal	Position		Depth, m	Tilt, deg	Data Return
		North	West			
1A	E	21°38.8′	109°56.1′	3194	0.5	both components
1A	M	21°32.3′	109°56.0′	3194	6.5	all 3 components
2A	E	21°25.7′	109°37.0′	2996	1.5	both components
2A	M	21°25.8′	109°37.4′	3010		lost instrument
3A	E	21°16.7	109°16.6′	2748	5.2	only one component (A_z = 168°)
3A	M	21°16.5	109°16.9′	2770	2.6	all 3 components
4A	E	21°09.4′	108°50.9′	3029	13.	only one component (A_z = 213°)
4A	M	21°09.7′	108°51.1′	3025	8.2	all 3 components
1B	E	12°06.0′	103°30.5′	3004	4.	both components
1B	E	12°05.5′	103°30.0′	2952	2.	both components (noisy)
1B	M	12°07.5′	103°30.2′	3011	1.6	all 3 components
1B	M	12°08.2′	103°30.1′	3033	0.1	all 3 components
2B	E	12°19.6′	102°46.7′	3077	1.8	both components
2B	E	12°19.4′	102°47.3′	3128	0.5	occasionally very noisy
2B	M	12°20.3′	102°47.5′	3128	1.3	all 3 components
2B	M	12°20.0′	102°47.2′	3113	0.	all 3 components (noisy)

For both cluster A and cluster B: station number, recorded signals (E, electric; M, magnetic), geographic position, depth, instrument tilt and field components successfully recorded.

to achieve this objective, the large dynamic range and wide frequency band characteristic of such recordings require four illustrations with time scales successively expanded by factors of 4 (see Figures 2–5). In examining these illustrations it is helpful to know that the sampling rate of our instrumentation is a selectable binary number of data points per hour. This choice facilitates comparison with the standard hourly time series derived from permanent magnetic observatories.

The data set collected during the ROSE program is described in Table 1 and the position of the various SFMT stations are indicated on the map of Figure 1. The data from cluster A span approximately 96 days, with 92 days of simultaneous coverage at a sampling rate of $2^6 = 64$ per hour. The data of cluster B, at $2^7 = 128$ samples per hour, last only 19 days. They are included in Figure 4 only. Since it is instructive to compare the seafloor data to continental data from a not too distant area, the magnetic variations from Tucson's observatory are also included in Figure 4.

One may notice in Table 1 that the ROSE MT data return includes several gaps: magnetic data from Station 2A are missing as a result of a lost magnetometer and one horizontal electric field component is missing at Station 3A as well as Station 4A. At the latter two locations the orientation of the single successfully recorded electric field component is toward azimuth 168° for Station 3A and 213° for Station 4A, with respect to magnetic north. Although both instruments landed on the seafloor with a strong tilt, the direction of this tilt was fortunately such that the single electric field component properly recorded was nearly horizontal at both stations. Since the magnetometers record the three components of the magnetic variation, tilt information was used for a precise correction of the magnetograms.

Most of the data from cluster A ($85\frac{1}{3}$ days, that is 2^{11} data points at 1 per hour for each time series) are plotted in Figure 2. The purpose of the plots at odd azimuths is to make possible an intercomparison of all data, including those from Stations 3A and 4A where one of two E field components is missing.

In all traces the solar daily variation is conspicuous as well as the episodic bursts of active high-frequency signals associated with magnetic storms. The high coherence between these features in all traces is obvious. At lower frequencies (periods of weeks and over) this coherence is less perfect. Nevertheless, the slow modulation of the magnetic storms is tracked very closely by all three H components. In the case of D and Z, however, while 1A and 3A follow each other very closely, 4A does not. This sustained, smooth wandering drift is not a common feature of our previous magnetic records, and therefore we have no reason in the present case to incriminate instrumental behavior. Our tentative explanation is that the instrument at Station 4A was subjected to a slow tilting and possibly also to rotation. We return to this subject later.

In the case of the electric signals, the long-period undulations are only weakly correlated with those in the magnetic signals. This behavior is attributed to the superimposition onto the electric fields of ionospheric origin of electric fields induced by the interaction of mesoscale oceanic motions with the earth's main magnetic field [*Cox et al.*, 1976].

A selected $21\frac{1}{3}$-days segment of the data (sampling interval 1/4 hour) is illustrated in Figure 3, including the most conspicuous feature visible in Figure 2. The quality of the coherence between all traces is more readily appreciated from the finer resolution of the new scale. Also, the enhanced induction of electric signals at higher frequencies is overwhelming, providing a nice illustration of Faraday's law (that electric induction varies as the time derivative of the magnetic field). The quality of the tracking between the same components is also noteworthy.

A $5\frac{1}{3}$-days segment, including also the magnetic variations at Tucson and the data from cluster B at 12°N, is shown in Figure 4 (sampling rate 16 per hour). One immediately notes considerable differences in the magnetic variations over the three areas: Tucson, Pacific Rise at 21°N, and Pacific Rise at 12°N. The horizontal variations at Tucson are characterized by active high-frequency pulsations and rather rapid jumps that are greatly attenuated in the seafloor records as a result of oceanic shielding. One also notices that while the various components of cluster 1A track each other quite well (and similarly for cluster B), the traces of cluster A do not closely track those of cluster B, a fact that illustrates the spatial variability of the ionospheric fields. Another important remark which will be of use later is that the Z variations in the

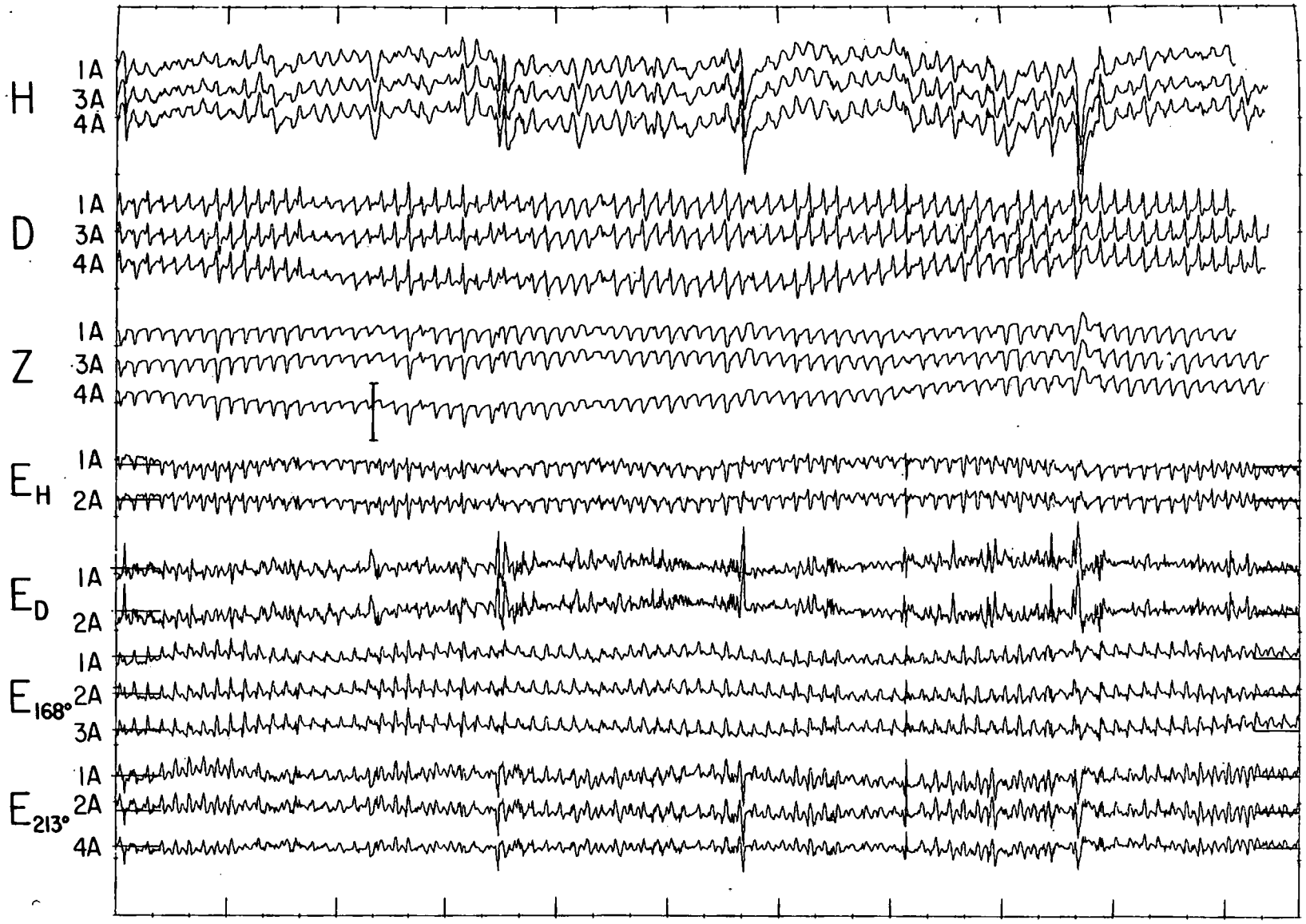

Fig. 2. Data from cluster A for a period of 85⅓ days starting at 1200 UT on January 24, 1979. Time scale: the large ticks (horizontal axis) are separated by 8 days. The vertical scale reference segment corresponds to 100 nanoteslas(nT) and 10 microvolts per meter. H, D, and Z refer to the magnetic variations toward the magnetic north, magnetic east, and downward, respectively. E_H and E_D are the horizontal electric and magnetic components to the magnetic north and east. $E_{168°}$ and $E_{213°}$ are the horizontal electric field components corresponding to the azimuths 168° and 213° with respect to magnetic north. The symbols 1A to 4A identify the observation sites by their number and cluster letter reference. The dark horizontal segments at each end of the electric records indicate the position of the $E = 0$ reference level.

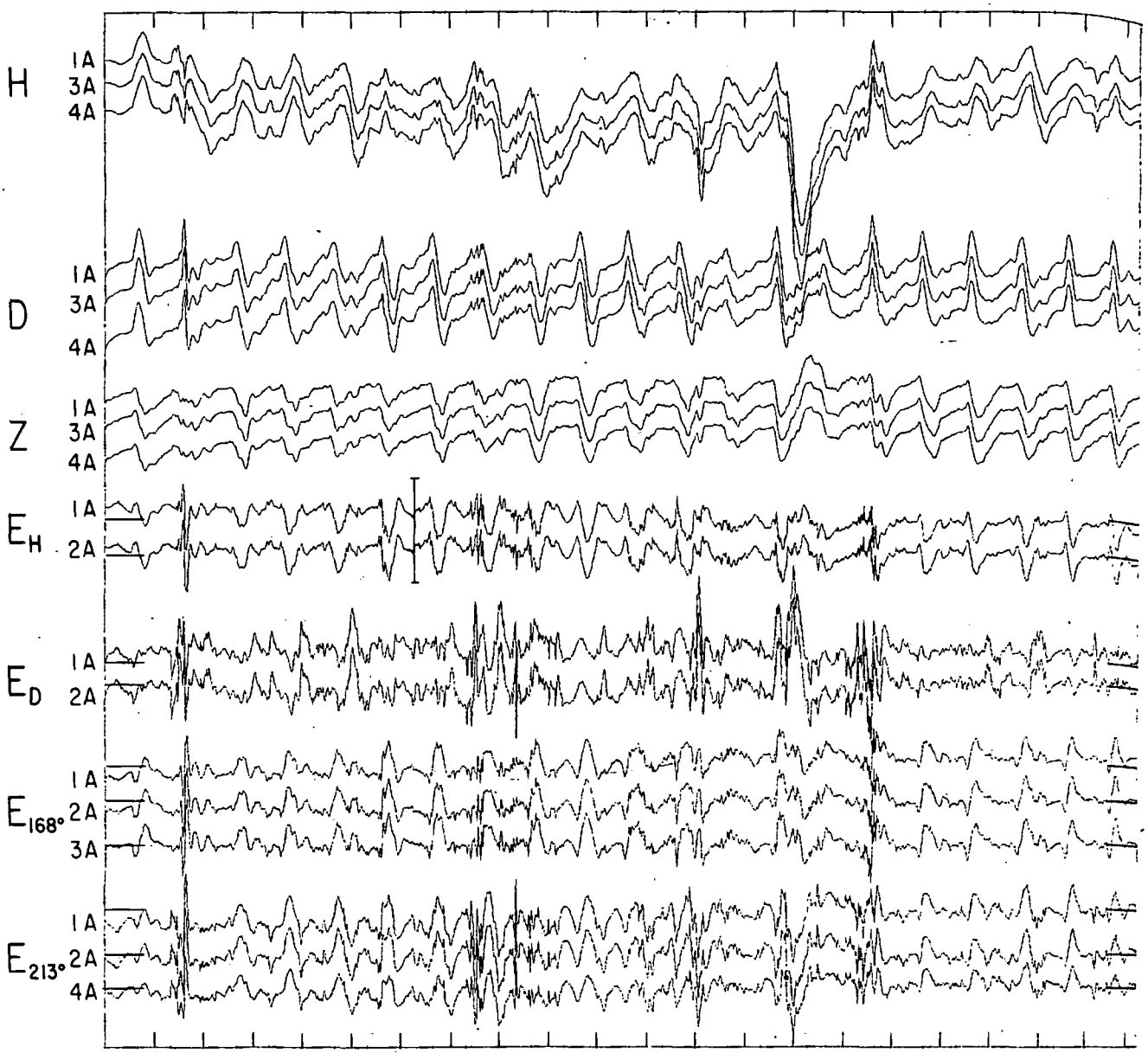

Fig. 3. Data from cluster A for a period of 21⅓ days starting at 0000 UT on March 21, 1979. Time scale: the larger ticks (horizontal axis) correspond to 24 hours. The scale reference segment corresponds to 100 nT and 10 μV/m. Other information is identical to that in legend for Figure 2.

data from cluster A are greater than those of cluster B where at medium frequencies they are essentially nonexistent (the very high frequency ripples in Z for 1B are due to instrumental noise). Again a remarkable coherence exists between all electric traces, and the coherence with magnetic fluctuations can be appreciated to be high at all frequencies including the highest ones by referring to the variations at Tucson that do not suffer oceanic shielding and therefore that retain unattenuated high-frequency signals.

Finally, Figure 5 exemplifies the highest resolution sustained by the data (64 samples per hour). The reader may verify that the smallest ripples in the magnetic traces have a strong expression in the electric ones. Furthermore, at the highest frequencies, coherent, very active signals are often visible in the electric records, particularly intense during the most active, longer-period magnetic excursions, although the magnetic pulsations that cause these high-frequency ripples are too faint to have been recorded. This observation is important, for it points out a great advantage to be derived from an increase in the sensitivity of the magnetic recorders. We should also point out that correspondent electric or magnetic components for the various stations of cluster A still track each other remarkably well at these higher frequencies. There is, however, one notorious exception, not easily noticed in the previous illustrations because the lower sampling rate and the resulting longer record segments emphasize lower frequency: the horizontal variations to the magnetic north, H, at Station 4A are considerably enhanced. In fact, some events in this latter record of unquestionable reality as proven by their clear counterpart in electric fields are not even perceptible in the correspondent records from Stations 1A and 3A. There is no indication that a similar remark holds for the other two components D and Z. However, a more precise analysis has shown that the observed horizontal magnetic enhancement of high frequencies is maximized for an orientation slightly west of exact

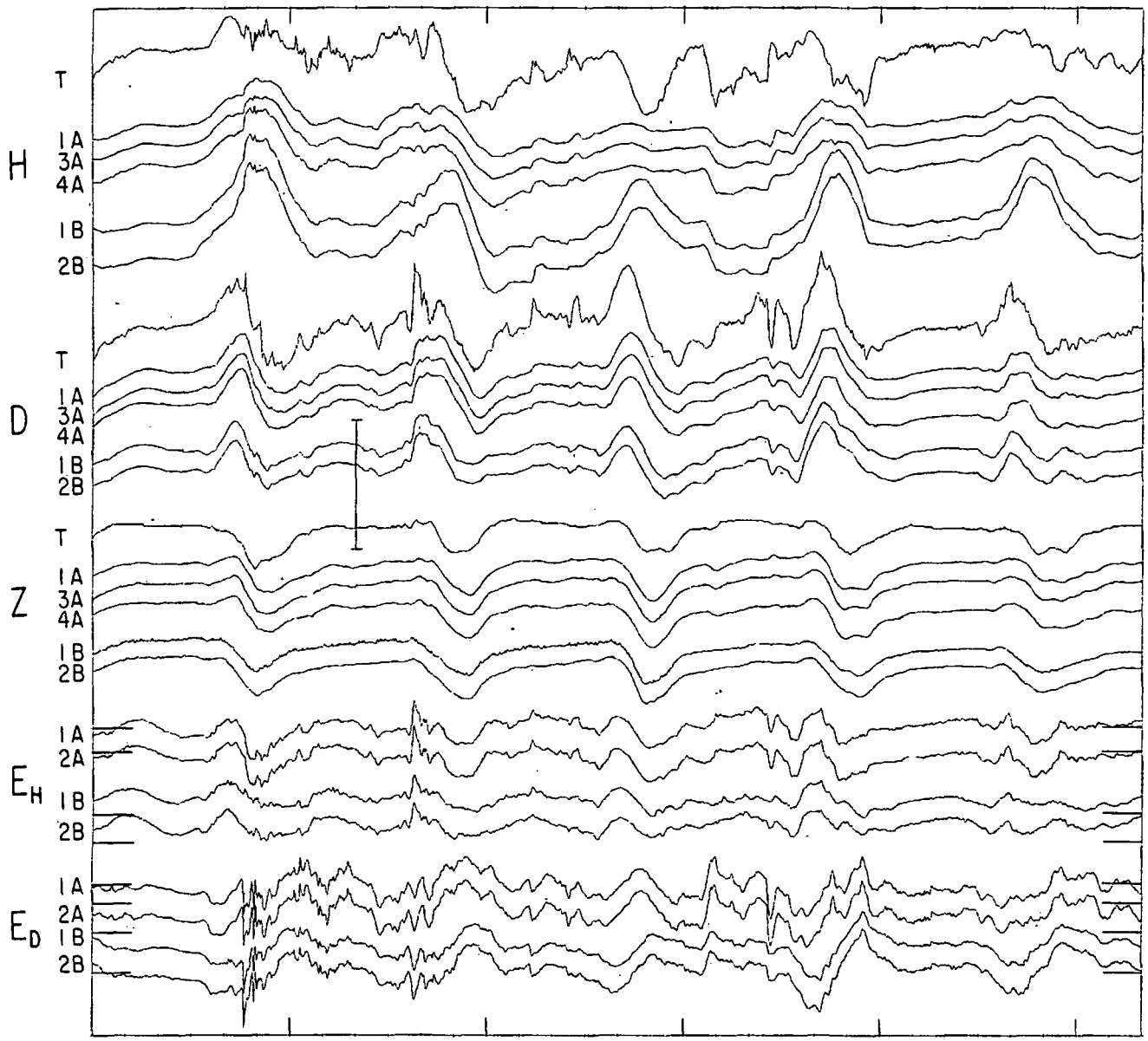

Fig. 4. Data from cluster A, cluster B and from Tucson magnetic observatory for a period of $5\frac{1}{3}$ days starting at 0000 UT on February 3, 1979. Time scale: the large ticks (horizontal axis) correspond to 2-hours separation, the small ones to 4 hours. The vertical scale reference segment corresponds to 10 nT and 100 μV/m. Other information is identical to that in legend for Figure 2 except that data from Tucson (T) and cluster B are also included.

magnetic north (approximate rotation required: 10°). We suggest in a later section that the high-frequency enhancement observed at Station 4A constitutes the magnetic expression of a localized electric current sheet crossing the spreading center at a relatively shallow depth, channeled by a high conductance layer that must result from some form of magma accumulation.

MAGNETOTELLURIC SOUNDINGS

Inasmuch as MT profiling requires availability of both horizontal components of electric and magnetic fields the summary of Table 1 indicates that appropriate data exist only for the two stations of cluster B and for Station 1A of cluster A.

A preliminary interpretation of the data from cluster B has been made earlier [*Filloux*, 1981]. It was shown that the seafloor response functions (seafloor impedances) were very similar at both locations, with nearly the same frequency dependence but with a slightly larger modulus for Station 2B, most distant from the ridge crest but also closest to land. It was also shown that the impedance tensor Z in

$$\mathbf{E} = Z\,\mathbf{F} \qquad (1)$$

($\mathbf{E}$ is horizontal electric field; $\mathbf{F}$ is horizontal magnetic variations) was moderately anisotropic with a ratio between principal axes around 2.5 at both stations. Some arguments were presented to suggest that the distance from the coastline (500 km) ruled out the determinant influence of the coastal effect in justifying the observed stretching of Z. Some of these arguments were derived from earlier studies of this effect off the coast of California [*Filloux*, 1967; *Cox and Filloux*, 1974]. A more thorough justification, however, would require additional data spanning the spreading ridge, extending eastward to the coast and preferably beyond, and also some distance westward.

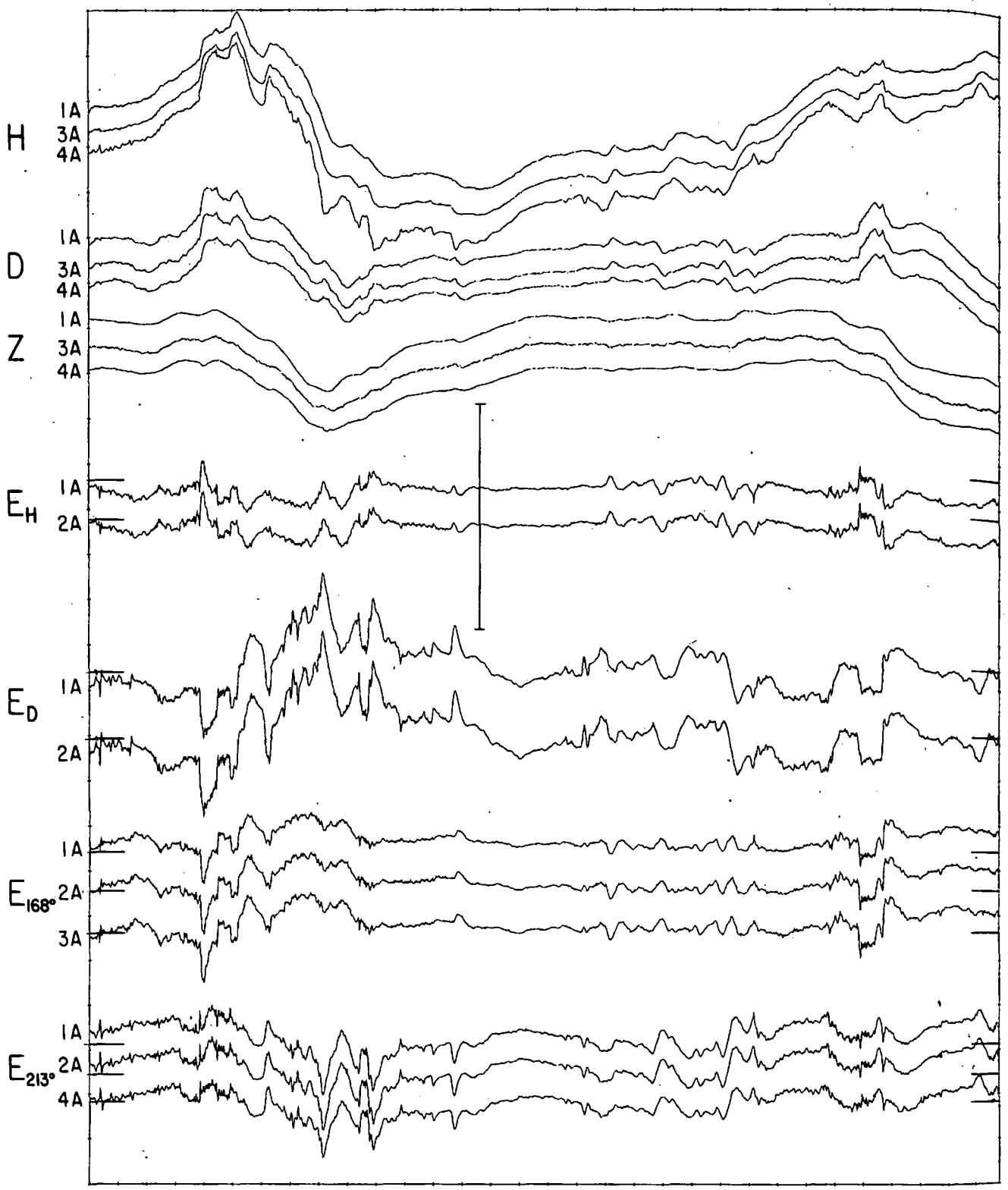

Fig. 5. Data from cluster A for 1½ days starting at 1200 UT on February 21, 1979. Time scale: the ticks (horizontal axis) are 1 hour apart. The scale reference segment corresponds to 100 nT and 20 μV/m. Other information is identical to that in the legend of Figure 2.

The data were interpreted in terms of a horizontally layered isotropic structure following a procedure already used in the treatment of earlier data [see *Filloux*, 1977, 1980*a*]. The impedance tensor to be inverted, Z^{inv}, was chosen according to an extension of Berdichevskiy's approach for minimizing the influence of anisotropy associated with surface anomalies [*Berdichevskiy and Dmitriev*, 1976]: namely,

$$Z^{inv} = (Z_m \cdot Z_M \cdot A_m^{-1} \cdot A_M^{-1})^{1/4} \quad (2)$$

where Z_m, Z_M, A_m, and A_M are the off-diagonal terms of the

optimally rotated Z and A tensors in the expressions

$$\mathbf{E} = Z\,\mathbf{F} + \mathbf{N}_E \tag{3}$$

$$\mathbf{F} = A\,\mathbf{E} + \mathbf{N}_F \tag{4}$$

and where $\mathbf{N}_E$ and $\mathbf{N}_F$ represent the residual uncorrelated noise in electric and magnetic signals, respectively. The conductivity profile retained was one that preserved the principal features of an initial 12-layer model as the number of layers was progressively reduced. The optimizing scheme consisted in minimizing the relative variance V between the model predicted impedances, $Z^m(f)$, and the observed ones, $Z^o(f)$, according to

$$V = \frac{1}{N}\sum_{n=1}^{N} w_n \frac{|Z_n^m - Z_n^o|^2}{|Z_n^o|^2} \tag{5}$$

with

$$\sum_{n=1}^{N} w_n = N$$

where w_n were weight factors intended to de-emphasize, in earlier interpretations, the importance of the high- and low-frequency estimates most affected by noise (N is the number of impedance estimates, centered at frequencies f). However, in the preliminary report on the Pacific Rise soundings at 12°N [*Filloux*, 1981] the weight factors were taken to equal unity.

The resulting optimum model was characterized by rapid conductivity rises around 22, 80, and 290 km, with the possibility of intermediate zones of reduced conductivity. Because this model matched surprisingly well Presnall's predicted 'double partial melt zone in the mantle beneath mid-ocean ridges' [*Presnall*, 1980], we reassessed the original data, trying to improve them, and we reinverted them according to a more stringent criterion.

We found no ground to change the initial impedance estimates which are listed for Station 1B in Table 2, together with the compound coherence, number of degrees of freedom and accepted relative errors $\pm\varepsilon$.

For model optimization criterion we followed an alternate approach which minimizes χ^2 instead of V (see, for instance, *Parker* [1980]) with

$$\chi^2 = \sum_{n=1}^{N} \frac{|Z_n^m - Z_n^o|^2}{\varepsilon_n |Z_n^o|^2} \tag{6}$$

Clearly, this optimization scheme achieves in a systematic manner the function of the weights, w_n, in (5). It also lends itself to a formal model validity study based on the statistical properties of χ^2 distributions.

The new inversion produced an optimum conductivity profile that departs from the one initially published only very slightly (compare Figure 6, profile A, with *Filloux* [1981]). For this optimum profile, $\chi^2 = 7.3$. With the number of (complex) impedance estimates $N = 12$ the expected value of χ^2 is $M = 2N = 24$ and the 95% confidence level lies at $\chi^2 = M + 2(2M)^{1/2} = 38$. The existence of inverse solutions to the set of observed impedances is therefore supported by the low χ^2 value achieved by the optimum model. This value however is so low that it indicates an excessive overfit of the set of observed impedances. In other words the specificity of this model exceeds in a statistical sense the information contained in the data. Therefore other simpler models may have to take precedence.

A variety of discretely layered models have been considered, those with most instructive behavior being represented in the diagrams of Figure 6. From our rather extensive survey we conclude (1) that an optimum two-layer model is not acceptable, (2) that all optimum models, no matter how layered require a very large conductivity rise around 250- to 300-km depth, and (3) that all satisfactory layered patterns—those leading to $\chi^2 \leq 38$—are characterized by an unusually high integrated conductivity in the upper 250 km. As a consequence of 1 above, some structure is required in the upper layer of an optimum twin layer model such as model E in Figure 6. As a consequence of 3 above, any reduction of the conductivity in the lithosphere and upper mantle requires a correspondent conductivity increase below (see, for instance, models D and E of Figure 6). More specific statements are not permitted with confidence if solely based on the χ^2 criterion. This conclusion, however, should not be taken in an overly pessimistic sense. There are other criteria helping to reduce the nonuniqueness ambiguity. For instance, at equal χ^2 values those models producing a predicted impedance function that let the observed values fall randomly on one side or the other must be preferred to those resulting in more organized distributions of the individual frequency contributions to χ^2. In that sense model A is superior to B and C, although the latter are also characterized by low χ^2 values. Furthermore, the optimistic acceptance of a structured model such as model A becomes less

TABLE 2. Seafloor Impedance Z at Station 1B for 12 Frequencies, in Modulus $|Z|$ and Phase ϕ_z

Frequency, cph	$\lvert Z\rvert$	ϕ_z, deg	ν	R_c^2	ε	θ, deg
0.0605	0.0309	76.7	22	0.646	0.437	25.9
0.1064	0.0517	63.1	24	0.909	0.176	10.1
0.1552	0.0645	62.5	40	0.934	0.109	6.2
0.2627	0.0926	57.5	100	0.859	0.101	5.8
0.3896	0.1067	57.5	160	0.821	0.090	5.2
0.5039	0.1177	58.8	200	0.826	0.079	4.5
0.7773	0.1560	58.6	300	0.837	0.062	3.6
1.168	0.1910	59.1	300	0.740	0.083	4.7
1.715	0.2591	57.7	300	0.728	0.086	4.9
2.328	0.5297	59.2	100	0.656	0.177	10.2
5.45	0.7250	58.0	100	0.452	0.269	15.6
8.58	0.7615	57.5	100	0.410	0.350	19.3

The number of degrees of freedom (ν), the coherence squared (R_c^2), the relative error on modulus (ε), and the phase error (θ) are also tabulated. Units: Z, μV/m/nT; phase: lead of electric with respect to magnetic.

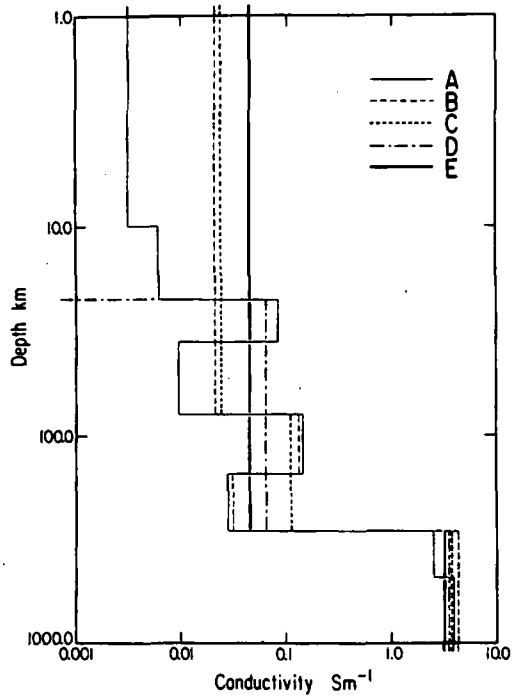

Fig. 6. Various horizontally layered models for Station 1B with different geometries and layer numbers but all with low χ^2 values; see text. All these models are obtained from schematization of the more complex model A, by selecting the layer geometry and minimizing χ^2 with respect to the conductivity in these layers: (*a*) seven layers and half space, $\chi^2 = 7.3$; (*b*) three layers, $\chi^2 = 9.0$; (*c*) two layers, $\chi^2 = 10.5$; (*d*) also two layers, $\chi^2 = 18.7$; (*e*) one layer (and half space) $\chi^2 = 67.1$.

heuristic when its predictions are closely reflected by other independent but relevant MT soundings. This is the case for the autonomous soundings at Stations 1B and 2B [*Filloux*, 1981]. These remarks illustrate the importance of dense SFMT arrays because an improved data coverage may greatly enhance the credibility of the interpretations of MT experiments. Furthermore, improvements in structural resolution can be achieved in at least two ways: (1) by means of constraints derived from other geophysical information and (2) by approaches that will reduce estimated as well as actual errors in the response functions. Much can be done in both instances, and we will come back to this exceedingly important subject.

Even since the planning stage we had feared the possibility that the closeness of land at 21°N could degrade MT exploration over this area. In the preceding section we have pointed out the existence of residual vertical magnetic fluctuations in the records obtained there, fluctuations often revealing the influence of the coast as pointed out initially by *Parkinson* [1962]. Since the coastal effect is largely due to the intensification of electric current circulation along the coast as a result of the conductivity contrast between land and ocean [*Filloux*, 1967; *Cox and Filloux*, 1974], we have investigated the relationship between these vertical magnetic variations Z and both the local electric currents (represented by their associated electric field components E_H and E_D) and the magnetic components H and D. In the first case we have estimated the transfer function T^Z with constituents $T_x{}^Z$ and $T_y{}^Z$ in the relation

$$Z = T_x{}^Z E_x + T_y{}^Z E_y \tag{7}$$

and in the second the transfer functions S^Z in

$$Z = S_x{}^Z \mathrm{H} + S_y{}^Z \mathrm{D} \tag{8}$$

where the frequency dependence is omitted and where x and y refer to magnetic north and east orientations, respectively. The results of this inquiry are presented in Table 3. In spite of a relatively high coherence even in the case of S^Z considering the low signal level in magnetic variations, the behavior of both T^Z and S^Z rules out a simple interpretation in terms of a reasonably two-dimensional coastal interference [*Filloux*, 1967]. This is particularly clear from the considerble difference between the phases of the two constituents of either T^Z and S^Z, but also from the rapid dependence on frequency of the azimuth that maximizes the correlation between Z and either the horizontal electric or the horizontal magnetic variations.

In attempting a MT interpretation of the conductivity structure beneath Station 1A the properties of the tensors Z and A in (3) and (4) also revealed a definitely three-dimensional character. In particular, Z and A were not convertible by rotation to a form with simultaneously small diagonal terms, even by applying preliminary deskewing [*Larsen*, 1975]. However, it was found that a 10° rotation (trigonometric direction on a chart) to the new orientation $x'y'$ resulted in a subjectively smooth and normal behavior of the tensor components $Z_{x'x'}$ and $A_{y'y'}$. A MT interpretation restricted to the use of the electric field component $E_{x'}$ and the horizontal

TABLE 3. Relationship, at Station 1A, Between the Vertical Magnetic Variations Z and (1) the Horizontal Electric Field (Transfer Function T^z, With Components $T_x{}^z$ and $T_y{}^z$) and (2) the Horizontal Magnetic Variations (Transfer Function S^z)

Frequency, cph	$R_c{}^2$	Mod.	$T_x{}^z$ Phase	Mod.	$T_y{}^z$ Phase	$R_c{}^2$	Mod.	$S_x{}^z$ Phase	Mod.	$S_y{}^z$ Phase
0.061	0.594	6.40	31	3.03	−177	0.521	0.029	106	0.012	70
0.102	0.663	4.21	14	2.59	−136	0.529	0.029	35	0.027	86
0.144	0.705	3.71	29	2.75	−146	0.576	0.037	77	0.032	59
0.187	0.799	2.96	27	2.21	−144	0.669	0.038	57	0.022	43
0.221	0.745	1.20	12	1.57	−133	0.685	0.055	60	0.009	−13
0.312	0.833	2.04	42	1.97	−124	0.535	0.053	45	0.017	12
0.355	0.811	1.08	41	2.06	−134	0.687	0.060	68	0.017	−84
0.462	0.763	2.04	76	1.27	−129	0.535	0.041	53	0.023	−105
0.696	0.783	0.11	−162	1.14	−113	0.467	0.045	63	0.026	−124
1.02	0.764	0.27	−152	0.73	−96	0.252	0.023	62	0.018	−136
1.42	0.688	0.18	−91	0.56	−89	0.059	0.008	118	0.004	68

Note that the magnetic variations Z are dominantly dependent on the north electric component at low frequency and on the east electric component at high frequency. Note also that the ratio vertical to horizontal magnetic variations remains significant at all frequencies. Units: T, nT/μV/m; S, dimensionless.

TABLE 4. Seafloor Impedance Z at Station 1A for 12 Frequencies, in Modulus $|Z|$ and Phase Φ_z

Frequency, cph	$\|Z\|$	ϕ_z, deg	ν	R_c^2	ε	θ, deg
0.0281	0.0322	81.3	44	0.641	0.293	17.
0.0565	0.0425	70.0	84	0.805	0.136	7.8
0.1226	0.0710	69.9	62	0.946	0.078	4.5
0.2085	0.0925	65.3	64	0.956	0.069	4.0
0.2915	0.1368	64.6	64	0.960	0.065	3.7
0.3755	0.1679	63.7	86	0.968	0.051	2.9
0.5107	0.1910	59.6	200	0.951	0.040	2.3
0.7744	0.2502	57.4	320	0.945	0.033	1.9
1.118	0.3027	50.1	400	0.950	0.028	1.6
1.929	0.386	44.9	240	0.910	0.047	2.8
5.062	0.636	47.7	260	0.765	0.083	4.7
10.453	0.845	47.6	400	0.650	0.090	5.2

The number of degrees of freedom (ν), the coherence squared (R_c^2), the relative error on modulus (ε), and the phase error (θ) are also tabulated. Units: Z, μV/m/nT; phase: lead of electric with respect to magnetic.

magnetic component F_y was therefore attempted. The resulting response function estimates are presented in Table 4 for 12 frequency bands.

Because of the extended duration of the simultaneous time series available, the estimates at frequencies above 0.1 cph were strictly based on the record sections with sustained ionospheric activity and at the very highest frequencies we used only the most energetic record segments. This resulted in a particularly extended usable frequency range since coherent high-frequency signals persisted on occasions up to 15 cph. This also led to coherencies considerably above those achieved for the cluster B data at 12°N. Nevertheless, when inverting the response functions of Table 4, one estimate at each end of the tabulated frequency band was discarded on account of the reduced coherence ($R^2 < 0.7$), which resulted in 10 retained values. Thus the significant levels for χ^2 became 20 for the expected value and 31.5 for the 95% confidence limit.

Following our previous approach, an overresolved starting conductivity profile using eight layers was obtained (profile A on Figure 7) leading to $\chi^2 = 10.2$. This profile is remarkably unstructured, featuring a rather uniform though relatively high conductivity down to 250 km, with a modest intermediate increase in the range 35–80 km, followed by a rapid rise between 250 and 400 km. Two simplified versions of this initial model, profiles B and C with $\chi^2 = 10.7$ and 12.7 are also shown on Figure 7, both overfit (in a χ^2 sense) in spite of their extreme simplicity.

Because of the questionable legitimacy of using data known to be affected by a well-demonstrated coastal distortion, we have not invested an extended effort in the interpretation of the MT response at Station 1A. Taken at its face value the sounding at Station 1A suggests a relatively high conductance for the upper 250 km, though smaller by a factor of 2 compared to that at Station 1B. If the shallow conductivity rise in the two profiles has an acceptable significance, it occurs slightly deeper in profile 1A, 30 km against 22.5 km, but additional support is necessary to strengthen the real importance of this feature. Finally a 2-decade increase in conductivity around 250-km depth constitutes a definite common feature of the two soundings and in both cases this is a particularly resilient feature under the χ^2 criterion.

It should be noted that the two soundings result from situations that are extremely different in two aspects, namely, (1) the two original data sets (the time series of EM variations) differ in length by a factor of 4, leading to a large difference in the error bars on the response functions as shown in Tables 2 and 4, and (2) the information from Station 1A is contaminated in a manner difficult to appraise by a particularly complex expression of the coastal effect.

MT SIGNATURE OF THE RIDGE CREST

In the case of a postulated accumulation of magma below a ridge crest, one may expect that electric current channeling through the conduction belt formed by juvenile accreting materials will be revealed by magnetic variations associated with the electric current confined in it. Such a channeling effect is often detected on land where it is particularly conspicuous in the induced vertical variations, Z. No such effect was noticeable near the ridge crest at 12°N, and in

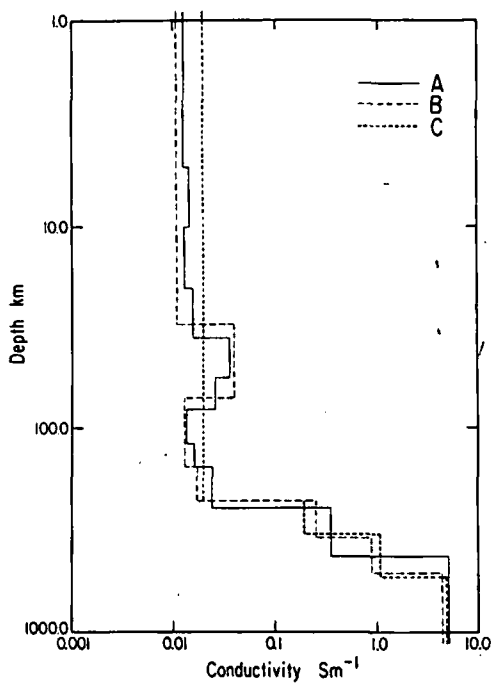

Fig. 7. Various horizontally layered models for Station 1A with different geometries and layer numbers, all derived from an initial 10 layers optimum model displaying a notable initial smoothness: (*a*) ten layers (and half space), $\chi^2 = 10.2$; (*b*) six layers, $\chi^2 = 10.7$; (*c*) three layers, $\chi^2 = 12.7$.

spite of a much more complete set of stations at 21°N, including station 4A in the immediate vicinity of the spreading axis, no conspicuous enhancement of the vertical magnetic variation is observed there. We have qualitatively explained this difference of behavior between land and ocean [*Filloux*, 1981] by the fact that vertical magnetic variations from electric channeling in the oceanic basement can induce efficient systems of horizontal electric currents in the overlying ocean capable of cancelling out these vertical magnetic variations to a high degree. There are too many gaps, however, in our data set to verify this explanation by proving from the electric field distribution the existence of an electric current circulation with the necessary configuration. Alternatively, such a channeling of electric currents along the ridge crest may be absent because the geometry of the ionospheric fields and the overall conductivity structure of the basement prevent it. In any case, the lack of conspicuous enhancement of the vertical magnetic variations in the vicinity of the Pacific Rise at 21°N, with polarity reversed on the axis, is consistent with the observations of *Law and Greenhouse* [1981] over the Juan de Fuca Ridge.

Even in the absence of information to the east of the ridge crest, the rapid disappearance westward of the enhanced magnetic variations in H must be attributed to a cause other than the nonuniformity of the source field, since this effect is too localized in space and too permanent in time (see Figure 5). Thus an explanation involving electrical current channeling through a heterogeneous spreading system is compelling. Although quite limited, the following facts point to a rather specific model.

The enhancement of the horizontal variations at Station 4A is not apparent at low frequencies (see Figures 2 and 3). It becomes noticeable around 1 cph and it is particularly obvious around 5 cph. It is lost at high frequency—above 15 cph—but this is probably a simple consequence of an insufficient magnetic sensitivity coupled with the very rapid decrease of ionospheric energy at these frequencies as can be implied by rare occasional high-frequency bursts in H, well correlated with similar impulses in the electric field, and with no counterpart in either D or Z. A more precise scrutiny of the data indicates that the actual preferential enhancement axis is not exactly to the magnetic north (component H) but roughly 10° west of due magnetic north. A data segment sufficiently enlarged to take advantage of the full resolution of the data is illustrated in Figure 8 to provide the reader with a way to verify directly from the data many of the features pointed out. It can be seen that there is a very slight enhancement of D at Station 4A with polarity opposed to that of H, illustrating the required slight westward rotation referred to above (see also map of Figure 1 for various orientation parameters). The magnetic enhancement at Station 4A has essentially disappeared at Station 3A, 40 km to the west, and no other significant feature can be distinguished from the way the magnetic variations track each other at the three stations (1A, 3A, 4A).

The observed effect is consistent with a current sheet concentrated below Station 4A and flowing roughly east-west in a direction principally normal to the trend of spreading and thus involving minimally the type of axial channeling mentioned earlier. Because of the negligible expression of the observed effect not only at Station 1A but also at Station 3A, the following conclusions must apply: (1) the postulated pinching of electric currents in the vicinity of Station 4A must disappear rapidly westward, and (2) the depth of current concentration into a current sheet below Station 4A must be very shallow in comparison with the distance separating Stations 3A and 4A, namely, 40 km. We therefore visualize the existence of a conductor at a relatively small depth below Station 4A providing a preferential passage of electric currents across the spreading system, currents driven by ionospheric induction away from the ridge and following a path of least impedance from one side to the other. If hot and conducting magma does exist to great depths below the axis of the ridge, then some form of conducting bridge must extend laterally to collect an electric current intense enough at shallow depth to account for the observed magnetic anomaly. The schematic representation of such a configuration is shown in Figure 9. In the absence of data to the east of the spreading axis we assume that the spreading system is roughly symmetric. The degree to which this assumption is

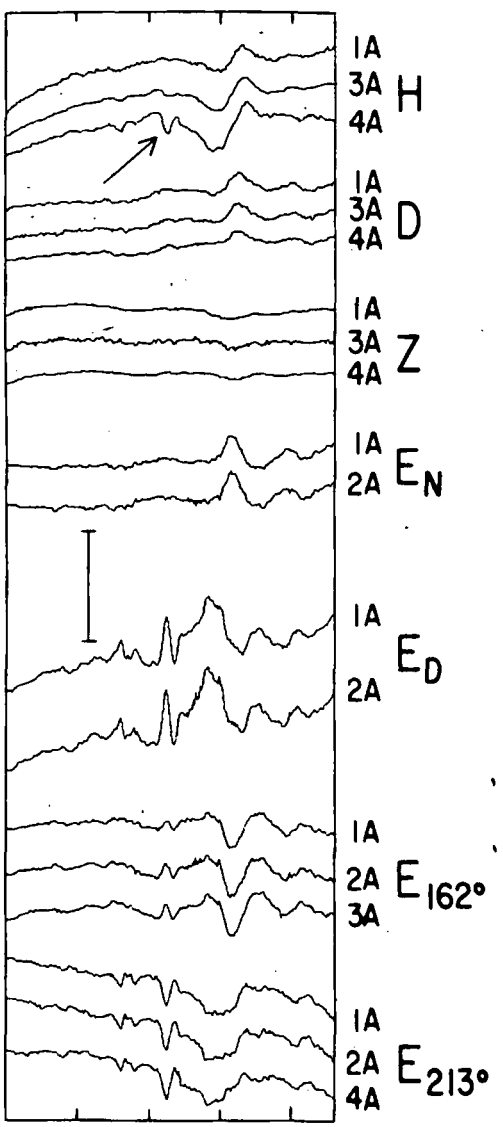

Fig. 8. Detailed data from cluster A (enlarged from Figure 5) illustrating the horizontal magnetic variations enhancement discussed in the text. The time ticks are 1 hour apart. The scale reference segment represents 20 nT or 4 μV/m. The arrow points to a feature of horizontal magnetic variations toward the magnetic north that is conspicuous in most, though not all, EM components (see text). Its simple shape makes it suitable to illustrate the observed enhancement effect.

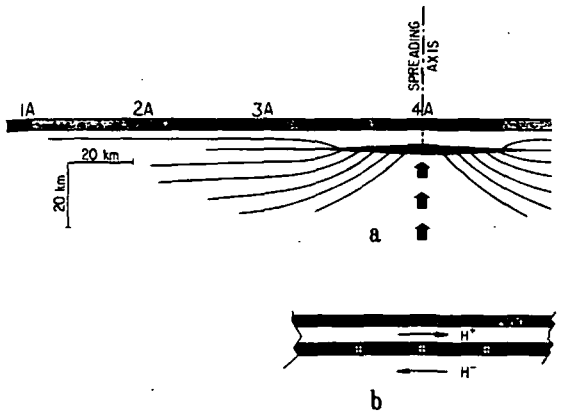

Fig. 9. Schematic representation of the postulated conductivity structure of the spreading system that can explain the enhancement of horizontal magnetic variations at Station 4A. (*a*) Section normal to the spreading system. The dark arrows symbolize rising magma. The fine line pattern represents electric current flow. (*b*) Longitudinal section along the spreading axis. Depth, lateral extent, and geometry could be of slightly different proportions. Continuity along the ridge crest for long distances is not implied.

satisfied does not affect the conclusions drawn later. In Figure 9 we have used a horizontal layer thinning away from the axis to symbolize the progressive rather than a less realistic abrupt reduction of conductance. Note that this tapering is not really required and also that the wings of the conductor-collector do not need to be exactly horizontal. Note also that the electric current bridging capability of the system is frequency dependent and favors currents induced by high-frequency variations which have a shallower penetration depth.

Although a quantitative appraisal is difficult with the scant data available, an approximate calculation can be made of the conductance of the postulated current collector in the vicinity of Station 4A and in turn of the magma cross section required.

The relationship between magnetic field at the seafloor and the current I in the collector per unit of ridge crest can be estimated starting with the first Maxwell equation in the absence of displacement current (Ampere's law) according to

$$\nabla \times \mathbf{H} = \mu_0 \mathbf{J} \tag{9}$$

where **H** refers to the magnetic induction vector (unit: weber m^{-2} = tesla), **J** is the current density (unit: ampere m^{-2}), and μ_0 is the permeability of free space, $\mu_0 = 4\pi \times 10^{-7}$ henry m^{-1}. In the present text, magnetic vectors and their components are always defined as above.

We have seen earlier that at sufficiently high frequencies (>3 cph) the horizontal magnetic variations toward 10° west of due magnetic north are overwhelmingly enhanced on the spreading axis by comparison with their expression at a modest distance away from it. We therefore conclude that the horizontal variations at Station 4A due to the currents locally concentrated below dominate the natural ionospheric contribution. In such a case the values of **H** above and below the current sheet, H^+ and H^- (see Figure 9), must be nearly equal, that is

$$|H^-| \cong |H^+| = H \tag{10}$$

Integrating (9) around the closed contour of Figure 9 and taking (10) into account lead to

$$I = \frac{2}{\mu_0} H \tag{11}$$

The conductance Σ per unit ridge crest below Station 4A could be calculated from knowledge of the electric field E using Ohm's law rewritten according to

$$\sigma = \mathbf{J}/\mathbf{E}$$

and integrated through the conductor to give

$$\Sigma = \frac{2}{\mu_0} \frac{H}{E} \tag{12}$$

We do not unfortunately have direct knowledge of **E** in the conductor. This is so for two reasons, namely: (1) only one component of the electric field on the seafloor was successfully recorded at Station 4A, and (2) we do not know to what extent the continuity of the horizontal component of **E** is conserved between conductor and seafloor. We may notice, however, that all electric field evidence favors its relative uniformity over the entire cluster A, a fact strengthened by the following observation: the component of **E** recorded at Station 4A, oriented toward 213°, includes a substantial contribution from the component of **E** significant in our calculations, which is oriented toward 80°. Thus an appreciable change in the magnitude of the latter at Station 4A would disrupt the near-perfect tracking of the horizontal field components plotted for Stations 1A, 3A, and 4A which is not the case, as particularly obvious in Figure 5. We have therefore proceeded with our calculation confident that taking the electric field value at Station 1A would not lead to an alarmingly adverse estimate.

In order to establish the value of H/E in (12) we have expressed H as a function of E according to

$$H = A_{x'} E_{x'} + A_{y'} E_{y'} \tag{13}$$

where $A_{x'}$ and $A_{y'}$ are appropriate transfer functions. The values of $A_{x'}$, $A_{y'}$ are given in Table 5 for four frequencies of interest (units: H in nanoteslas and E in $\mu V\ m^{-1}$). We have selected for $A_{y'}$ the 4-cph estimate, namely, 2.2×10^{-3} mks units, which retains a high coherence at the highest frequency. This choice leads from (12) to $\Sigma = 3500$ S per meter of ridge crest, which is a considerable conductance, equivalent to 1.2 km of seawater.

We are quite aware of the simplistic nature of our approach to the previous conductance estimates. Nevertheless, in spite of the crudeness of both method and model the existence of a very shallow, laterally restricted zone with exceptionally high conductivity below the ridge crest appears difficult to reject. It is true that assuming the ionospheric contribution at 4A to be negligible may result in an overestimate of H and hence of Σ as well. There are, however, factors playing in the opposite direction. In estimating H/E from $A_{y'}$ we have assumed all noise to be in H, which would correspond to an underestimate of H/E in (12). Furthermore, if the current concentration below the ridge crest results from distant induction processes, and flows through a preferential zone of reduced resistivity, the field could be reduced there if this zone were not sufficiently well connected electrically to its surroundings. Given the considerable conductivity contrasts possibly existing between solid and liquid basaltic materials, this situation is plausible.

TABLE 5. Relationship Between the Horizontal Magnetic Variations at Station 4A and the Horizontal Electric Field at Station 1A at High Frequencies: Transfer Functions $A_{x'}$ and $A_{y'}$ in Equation (13) (See Text)

Frequency, cph	R_c^2	$A_{x'}$		$A_{y'}$	
		Mod.	Phase	Mod.	Phase
1.55	0.958	1.03	121	2.54	25
2.64	0.958	0.834	149	2.52	35
4.05	0.935	0.766	163	2.24	48
6.08	0.895	0.723	171	1.89	61

Clearly, the interpretation attempted here is one of great complexity, where two- or three-dimensional approaches supported by appropriate additional data would be extremely useful.

Without undue speculation the most compelling explanation of the magnetic anomaly at Station 4A is that a considerable cross section of magma is present beneath that station. It is not possible, however, to conclude from the EM data alone whether this magma concentration exists in the form of an open magma chamber or of an efficiently connected solid matrix with a high melt concentration. It is likewise not possible to qualify the depth of its occurrence except to say that it must be very small in comparison with 40 km.

Observations capable of revealing the feature discussed above are unfortunately difficult to carry out because of the extremely rough bottom topography in the very restricted area of interest. A second attempt to deploy EM instrumentation on the axis of the ridge during the second part of the experiment at 12°N failed, the closest practical location being found 35 km to the east [*Filloux*, 1981]. At this distance the effect would not have been recognizable at 21°N. With less energetic magnetic activity in the 12°N data the lack of detectable enhancement of high-frequency EM variations at 35 km from the crest compared with those at 120 km (second occupied site) can only be taken as inconclusive. However, the data of *Law and Greenhouse* [1981] support an enhancement of horizontal variations to the magnetic north at a station 20 km from the Juan De Fuca Ridge compared to those at a station 40 km away, on the opposite side. With the ridge trend oriented roughly 25° east of true north and the magnetic declination 15° east, an effect similar to that observed on the Pacific Rise may also exist there. If so, it would probably be more readily observable at stations closer to the spreading axis. If this feature constitutes a distinctive magnetic anomaly associated with spreading processes, a detailed investigation of its geometry and permanence along ridge crests should prove to be quite rewarding.

Using plausible values for the conductivity of melted basalts at relatively low pressure in function of temperature [*Shankland and Waff*, 1974, 1977; *Shankland*, 1979; *Waff and Weill*, 1975; *Rai and Manghnani*, 1977] and using plausible mid-ocean ridge geotherms [*Oxburgh and Turcotte*, 1968; *Presnall*, 1980], we arrive at an estimate for conductivity of 0.5 to 4 S m^{-1} and for temperature of 1000° to 1200°C. These values correspond to thickness bounds of 1 and 8 km of unobstructed melt in the vicinity of the spreading axis. If the postulated liquid basalt cross section were to occur within a porous solid matrix, the thickness of the conductive layer would be correspondingly increased. Under these conditions it is highly probable that a magma reservoir sufficiently developed to deserve the name of 'magma chamber' does exist below Station 4A. Direct and indirect support of such a feature is provided by the following independent inquiries.

A seismic refraction profile with three ocean bottom seismographs located near the Pacific Rise axis, 30 km to the south-southwest of Station 4A, reveals the existence of a pronounced low-velocity layer with an upper interface at a depth 2.5 km below the seafloor in the immediate vicinity of the spreading axis [*Reid et al.*, 1977]. This low-velocity zone, roughly 3 km thick on the axis, fades away within approximately 10 km. Below this layer the velocity rises only slowly for another 3 km. The authors interpret the anomaly in terms of shear attenutation due to partial melting. The dimension and the proportions of the involved cross section match well those of our postulated magma accumulation.

Recent investigations concerning the nature of ophiolites strongly support a spreading seafloor origin of these geological formations. *Pallister and Hopson* [1981] in particular recognize in Samail Ophiolite the evidence of a once operative magma chamber astride a now exposed fossil spreading center. Through stratigraphic reconstruction of processes and dimensions, they visualize a single, large, long-lived magma chamber with dimensions and shape quite consistent with the one we propose, namely, a cross section 5 km thick on the spreading axis, tapering away over a distance of roughly 18 km, i.e., in one direction (see their Figures 18 and 19).

DISCUSSION

The seafloor magnetotelluric program of the ROSE experiment was executed along lines that departed considerably from those initially planned. As a result, the contributions of this experiment are somewhat disconnected, falling into three principal categories: (1) MT soundings at various locations in the vicinity of the Pacific Rise; (2) the discovery of an unanticipated EM signature of the spreading system, a finding which has been tentatively interpreted in term of the conductance and thickness of liquid basalt in the lithosphere adjacent to the accretion axis (leaving little doubt as to the existence there of a sizeable magma chamber); and (3) the acquisition of a broad range of information as a result of a series of unexpected situations that required on the spot modifications of methods and/or objectives. From our point of view, a special merit of the experiment results from the guidance it may provide in planning future research projects in submarine geophysics which intend to include seafloor magnetotellurics.

The MT soundings at both locations suffer from serious deficiencies: at 21°N on account of the complex coastal influence and perhaps of other interfering inhomogeneities, at 12°N because of the extremely short data sets. When compared, these data sets demonstrate a fact of great significance, namely, that a considerable reduction of the error in seafloor response functions does result from an increased duration of observation (see Tables 2 and 4). With respect to the confidence we should ascribe to the inverted data, we realize that, considering the low resolution of EM techniques, we tend to give an optimistic weight to the models proposed. In the past we have stressed the self-consistency of an ensemble of SFMT results in justifying the validity of the geophysical message. In the present work we have tried to be more cautious by testing plausible models

against the χ^2 misfit criterion. Although we value the objectivity of this criterion, we tend to consider it austere. It seems that a preference established upon a single number may lean toward excessive rigidity. As pointed out earlier, there are features of the misfit which deserve consideration as does, for instance, the degree of randomness of its various contributions with frequency. All arguments considered, we believe that it would be a dangerous strategy to reject, upon an overfit result from the χ^2 test, the possible existence of the two high-conductance layers suggested for the structure of the Cocos plate. The χ^2 test should be seen as inconclusive, not as negative, with respect to the existence of these layers. The similarity of results for the two soundings at 12°N [*Filloux*, 1981] and their compatibility with the model of *Presnall* [1980] add credibility to the findings, certainly enough so to make it extremely desirable to pursue such MT investigation of a spreading zone with improved coverage in time and space.

In spite of definite advances, data inversion of SFMT data continues to suffer a double handicap, namely, the inherent complexity of the theoretical problem and the scarcity of the necessary data. In particular, the estimation of errors in the response functions relies too often, but with little other choice, on a number of important assumptions concerning signal statistic and field geometries that are in fact not satisfied. In such a case, a solid experimental attack which maximizes the EM information by means of dense observational arrays active for long durations and which seeks guidance from alternate geophysical evidence appears to be most realistic. We believe that this is a hopeful and perhaps the only approach, in spite of many uncertainties.

The detection of a very specific and conspicuous anomaly in the horizontal, high-frequency magnetic variations just above the rise crest is a rewarding aspect of this difficult experiment because the limited data are sufficient to identify an intense, high-conductivity disturbance within the young lithosphere. The manifestation of this effect in the magnetic variations with little or no counterpart in the electric fields is vitally important because, in an area as extreme in seafloor irregularity as an accretion center, magnetometers that record all three components will provide the necessary information whatever their rest position on the seafloor. This situation is not true for electric field recorders of practical design which record the two electric components parallel to their resting plane. This is not to say that E field measurements are not useful. Nevertheless the three electric field components are more costly to obtain than their magnetic counterparts and the electric field is perhaps also less determinant in the resolution of heterogeneous features. Inasmuch as free-fall, self-contained, three-component magnetometers can be constructed with the necessary precision and at a moderate cost, magnetic variation surveys may constitute a technique well adapted to the investigation of the oceanic basement in a ridge crest area.

Among all EM observations obtained during the SFMT ROSE experiment, those from Station 4A are the only ones from the close vicinity of the spreading axis. They are also the only ones among the five successful sets of magnetic variations that display the specific anomaly of horizontal variations interpreted earlier in terms of an extensive magmatic activity. In addition to this behavior, the magnetic records at Station 4A are the only ones affected by very long term undulations as pointed out earlier. We believe that it is at least conceivable that these slow, ample fluctuations reflect tectonic motions of the local seafloor, generated by internal magma activity associated with spreading processes, motions which in turn tilt and possibly rotate the instrument with respect to the main earth field. If it is so, the angular amplitudes involved approach 10^{-4} radians per month.

The SFMT experiment at the ROSE site also draws importance from the diversity of its teaching. The splitting of the SFMT experiment of ROSE into two subexperiments points out the considerable degree of ionospheric nonuniformity we must face. It also stresses forcefully the need to take into account the importance of coastal influences. On the positive side the often questioned validity of MT research at low latitudes on account of reduced ionospheric signals cannot be taken too seriously if one compares the data from 12°N and 21°N. MT research on the continent has revealed widespread inhomogeneity and has pointed out the effectiveness of vertical magnetic variations to reveal anomalous structures. While vertical magnetic variations are greatly reduced on the seafloor, the data from Station 4A indicate, nevertheless, that magnetic variations in other components may also constitute important clues in SFMT exploration. Along with these findings various SFMT design parameters have become more specific—for instance, those related to array geometry. Linear arrays along the spreading axis are needed to tell us about the degree of continuity of magma concentrations while transverse arrays can establish their scales. We know now that the station separation initially selected for the present experiment would have been more favorable if reduced.

Finally, and marginal to the objectives of the experiment, we are reminded that tilt measurements in the vicinity of the spreading center should be able to help us quantify magmatic activity. This is so because the instrumental sensitivity and stability required in such tectonically active areas can be readily achieved.

CONCLUSION

The magnetotelluric experiment at the ROSE site suggests that important information about seafloor structure and active tectonic processes related to a spreading system is contained in observable natural electric and magnetic variations associated with magnetospheric and ionopsheric perturbations. Over such a tectonically complex area the selection and the correct deployment of an optimum array is made difficult by the exceptionally rough topography of the ocean floor. Consequently, field work must be carried out with care, with the best possible navigational assistance and, if possible, with duplication of instruments at each site. Classic, one-dimensional MT interpretations of the data are not well adapted to the complex tectonic setting of a ridge area, but specific anomalies of the EM field resulting from heterogeneities with high-conductivity contrasts in the seafloor over such areas may provide alternate opportunities for interpretation. The evidence for the existence of a magma chamber along the spreading axis illustrates this fact and the consistency of the predicted size and proportions with those suggested by other research approaches is encouraging. Given the status of SFMT observational techniques, particularly with respect to observation of magnetic variations, it seems that time has come when a series of SFMT experiments of one-half to a full year's duration could be meaning-

fully undertaken, proceeding from an appropriate ridge crest and, over several years, covering adjacent plates to their subduction boundaries.

Acknowledgments. This work has been supported by the National Science Foundation: grants OCE78 14524 and OCE79 18382. The Scripps Institution of Oceanography scientists greatly appreciated the hospitality and spirit of participation demonstrated by the staff and crew of the University of Washington aboard their R/V *Thomas Thompson*.

REFERENCES

Berdichevskiy, M. N., and V. I. Dmitriev, Distortion of magnetic and electrical fields by near surface lateral inhomogeneities, *Acta Geodaet. Geophys. Montanist Acad. Sci. Hung.*, *11*(3–4), 447–483, 1976.

Cox, C. S., and J. H. Filloux, Two-dimensional numerical models of the California E. M. coastal anomaly, *J. Geomagn. Geoelectr.*, *26*, 257–267, 1974.

Cox, C. S., J. H. Filloux, and D. Cayan, Electromagnetic observations during MODE I: Sea floor electric field and transport, *Polymode News*, *14*, 6–21, 1976.

Filloux, J. H., Oceanic electric currents, geomagnetic variations and the deep electrical conductivity structure of ocean-continent transition of central California, Ph.D. thesis, 166 pp., Univ. of Calif., San Diego, La Jolla, 1967.

Filloux, J. H., Ocean floor magnetotelluric sounding over the north central Pacific, *Nature*, *269*(5626), 297–301, 1977.

Filloux, J. H., Magnetotelluric soundings over the northeast Pacific may reveal spacial dependence of depth and conductance of the atmosphere, *Earth Planet. Sci. Lett.*, *46*, 244–252, 1980*a*.

Filloux, J. H., Observation of very low frequency electromagnetic signals in the ocean, *J. Geomagn. Geoelectr.*, *32*, SII–SII2, 1980*b*.

Filloux, J. G., Magnetotelluric exploration of the North Pacific: Progress report and preliminary soundings near a spreading ridge, *Phys. Earth Planet. Inter.*, *25*(3), 187–195, 1981.

Larsen, J. C., Low frequency (0.–1.6 cpd) electromagnetic study of deep mantle electrical conductivity beneath the Hawaiian Islands, *Geophys. J. R. Astron. Soc.*, *43*, 14–56, 1975.

Law, L. K., and J. P. Greenhouse, Geomagnetic variation sounding of the asthenosphere beneath the Juan de Fuca Ridge, *J. Geophys. Res.*, *86*(B2), 967–978, 1981.

Oxburgh, E. R., and D. L. Turcotte, Mid-ocean ridges and geotherm distribution during mantle convection, *J. Geophys. Res.*, *73*, 2643–2661, 1968.

Pallister, J. S., and C. A. Hopson, Samail ophiolite plutonic suite: Field relations, phase variation, cryptic variation and layering, and a model of a spreading ridge magma chamber, *J. Geophys. Res.*, *86*(B4), 2593–2644, 1981.

Parker, R. L., The inverse problem of electromagnetic induction: Existence and construction of solution based on incomplete data, *J. Geophys. Res.*, *85*(B8), 4421–4428, 1980.

Parker, R. L., and D. W. Oldenburg, Thermal model of ocean ridges, *Nature Phys. Sci.*, *242*, 137–139, 1973.

Parkinson, W. D., The influence of continents and oceans on geomagnetic variations, *Geophys. J. R. Astron. Soc.*, *6*, 441–449, 1962.

Presnall, D. C., A double partial melt zone in the mantle beneath mid-ocean ridges, *Phys. Earth Planet. Inter.*, *23*, 103–111, 1980.

Presnall, D. C., J. R. Dixon, Jr., T. H. O'Donnell, and S. A. Dixon, Generation of mid-ocean ridge tholeiites, *J. Petrol.*, *20*, 3–35, 1979.

Rai, C. S., and M. H. Manghnani, Electrical conductivity of basalts to 1550°C, Magma Genesis, edited by H. J. B. Dick, *Bull. Oreg. Dep. Geol. Miner. Ind.*, *96*, 219–232, 1977.

Reid, I., J. A. Orcutt, and W. A. Prothero, Seismic evidence for a narrow zone of partial melting underlying the East Pacific Rise at 21°N, *Geophys. Soc. Am. Bull.*, *88*, 678–682, 1977.

Shankland, T. J., Physical properties of minerals and melts, *Rev. Geophys. Space Phys.*, *17*(4), 792–802, 1979.

Shankland, T. J., and H. S. Waff, Conductivity in fluid-bearing rocks, *J. Geophys. Res.*, *79*(32), 4863–4868, 1974.

Shakland, T. J., and H. S. Waff, Partial melting and electrical conductivity anomalies in the upper mantle, *J. Geophys. Res.*, *82*(33), 5409–5417, 1977.

Spiess, F. N., K. C. Macdonald, T. Atwater, R. Ballard, A. Carranza, D. Cordoba, C. Cox, V. M. DiazGarcia, J. Francheteau, J. Guerrero, J. Hawkins, R. Haymon, R. Hessler, T. Juteau, M. Kastner, R. Larson, B. Luyendyk, J. D. Macdougall, S. Miller, W. Normack, J. Orcutt, and C. Rangin, East Pacific Rise: Hot springs and geophysical experiments, *Science*, *207*(4438), 1421–1433, 1980.

(Received May 27, 1981;
revised November 3, 1981;
accepted January 22, 1982.)

rra Madre del Sur de Mexico,
ol. Inst. Geol. Univ. Nac. Auton.

and structure. Geol. Soc. Am.

C.A. Burk and C.L. Drake
ger, New York, N.Y., pp.25—44.
ol. Asoc. Mex. Geol. Pet.,

c refraction observations in
2.
anet. Sci. Lett., 21: 209—212.
d accretion in trenches. Geol.

., 1978. Late Cenozoic subduc-
hern Middle America Trench.

uthern Mexico. Geol. Soc. Am.

, Von Huene, R.E., Watkins, J.S.,
Middle America Trench. In: Int.
cess, Feb. 4th, 1976, 2.
f the Pacific, North American,
Planet. Sci. Lett., 7:425—428.
Ladd, J.W. and Worzel, J.L.,
ff Oaxaca, Mexico, and Guatemala.

bean and Middle America
oc. Am. Bull., 80:1639—1684.
nd Lewis, B.T.R., 1975. Refracted
ots in southern Mexico. Am.

in shallow and deep water
es of compressional waves,

northern part of the Cocos plate.

iment subduction and offscraping
I (Editors), Island Arcs, Deep
on, Washington, D.C., pp.199—

lope model. In: C.A. Burk and
rgins. Springer, New York, N.Y.,

, McMillen, K.J., Ladd, J.W. and
e widespread occurrence of
d rises. Am. Assoc. Pet. Geol.

rench: seismic-refraction studies.

ydrate horizons detected in
Am. Assoc. Pet. Geol. Bull.,

s on the Cocos Plate. Earth Planet.

Marine Geology, 35 (1980) 83—97

MANTLE REFLECTIONS BENEATH THE CRESTAL ZONE OF THE EAST PACIFIC RISE FROM MULTI-CHANNEL SEISMIC DATA*

P.L. STOFFA[1], P. BUHL[1], T.J. HERRON[1], T.K. KAN[2] and W.J. LUDWIG[1]

[1] *Lamont-Doherty Geological Observatory of Columbia University, Palisades, New York 10964 (U.S.A.)*
[2] *Atlantic Richfield Co., Dallas, Texas 75221 (U.S.A.)*

(Received June 13, 1979)

ABSTRACT

Stoffa, P.L., Buhl, P., Herron, T.J., Kan, T.K. and Ludwig, W.J., 1980. Mantle reflections beneath the crestal zone of the East Pacific Rise from multi-channel seismic data. Mar. Geol., 35: 83—97.

Two 24-fold, stacked multi-channel seismic-reflection profiles show the position of the M-discontinuity nearly continuously across the East Pacific Rise near 9°N. In the past, the position of this important boundary in the oceans has been determined almost exclusively by seismic-refraction measurements. The mantle reflection events are enhanced by the process of migration which diminishes the masking effect of the sea-floor diffractions. In one crossing of the Rise crest, the mantle reflections do not parallel the topographic relief in the time section, while in the other the mantle reflections follow the sea-floor topography. The presence of mantle reflections beneath the axial zone of an active spreading center indicates that the M-discontinuity is a feature which forms nearly contemporaneously with the oceanic crust.

INTRODUCTION

During June, 1976, scientists aboard R/V "Conrad" acquired three lines of 24-fold, multi-channel seismic (MCS) data across the East Pacific Rise using four, 466 cubic-inch air guns, see Fig.1. After basic processing, i.e., demultiplex and CDP (Common Depth Point) gather, normal move-out correction and stack, shallow reflection events were observed in the data which appear to correspond to the top of the low-velocity zone predicted by Orcutt et al. (1976), from ocean bottom seismic refraction measurements (see Herron et al., 1978). In one crossing MCS Line 17, time-varying predictive deconvolution and wave equation migration of the axial portion further confirmed the presence of these reflection events. Subsequent migration, after stack of Lines 17 and 19 using the Split-Step Fourier algorithm (see Stoffa et al., 1977), followed by a 0—10 Hz zero phase band-pass filter, time-varying gain and trace scaling of 2—1, indicated the presence of a reflection

*L-DGO Contribution No.2861.

event at about 2 sec of two-way travel time below the sea floor (Figs.2 and 3). This reflector which corresponds to the M-discontinuity can be traced from the flanks through the crest of the East Pacific Rise. In a 3 km wide zone under the crest, this reflector is weak or absent, see Fig.3c. This region may correspond to a zone of injection for new crustal material.

In a topographically rough region such as a mid-ocean ridge, one would expect that mantle reflections would be difficult to obtain. We have found that we must satisfy three requirements in order to observe reflections from mantle:

(1) a repetitive, high-energy, low-frequency sound source fired frequently along the ship's track which provides sufficient signal level to detect weak reflection events;

(2) multi-channel data recording and subsequent CDP stacking to improve the signal-to-noise ratio;

(3) wave-equation migration to remove the sea-floor diffractions which obscure the mantle reflections.

Ideally, the data should be migrated before the correction for normal move-out is applied and prior to the CDP stack. This is a time-consuming process, since each of 24-constant offset sections must be individually migrated, regrouped into CDP gathers, corrected for normal move-out and then stacked. We have migrated a considerable part of Line 19 before stack and this has resulted in a significantly improved mantle reflection profile (see Fig.3c). In both cases (migration before and after stack), a constant velocity of 1500 m/sec was used since most of the energy, even deep in the

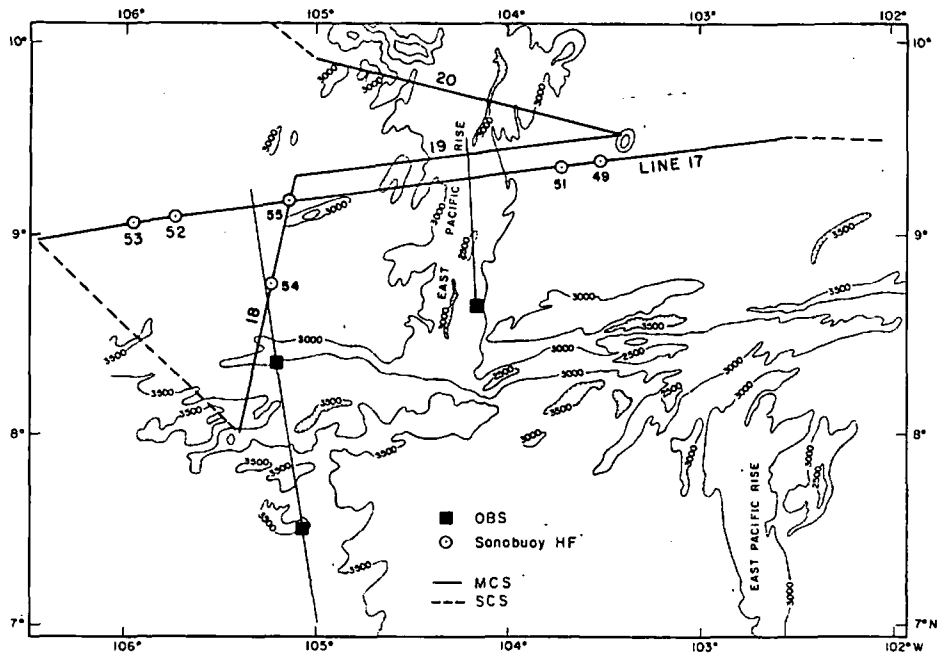

Fig.1. Track chart indicating the location of multi-channel lines 17 and 19. Circles with dots indicate sonobuoy locations; black squares indicate OBS refraction profiles.

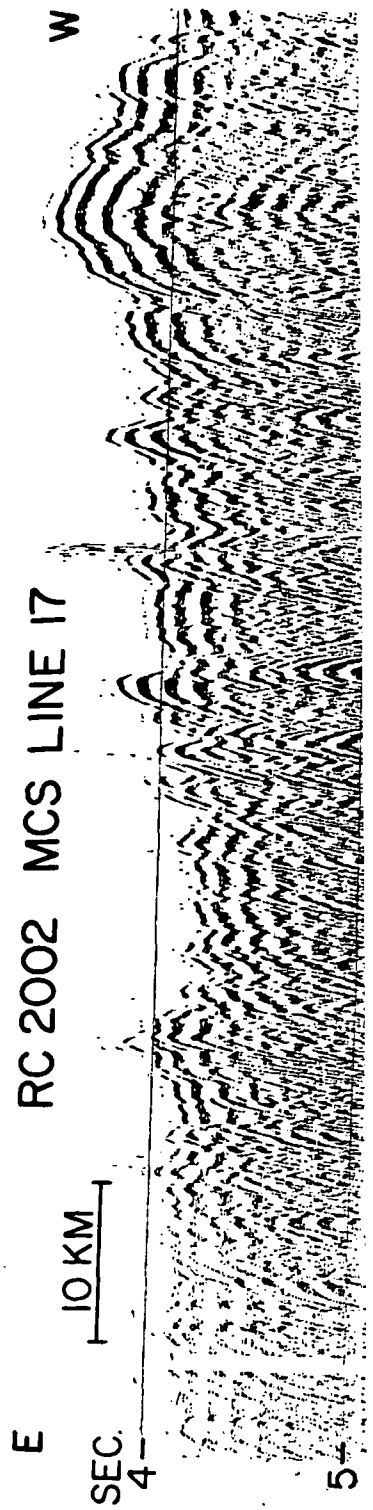

ne below the sea floor (Figs.2 and 3).
l-discontinuity can be traced from
acific Rise. In a 3 km wide zone
ıbsent, see Fig.3c. This region may
crustal material.
as a mid-ocean ridge, one would
lifficult to obtain. We have found
n order to observe reflections from

ency sound source fired frequently
icient signal level to detect weak

ıbsequent CDP stacking to improve

the sea-floor diffractions which

fore the correction for normal
stack. This is a time-consuming
sections must be individually
rrected for normal move-out and
rable part of Line 19 before stack
proved mantle reflection profile
ore and after stack), a constant
st of the energy, even deep in the

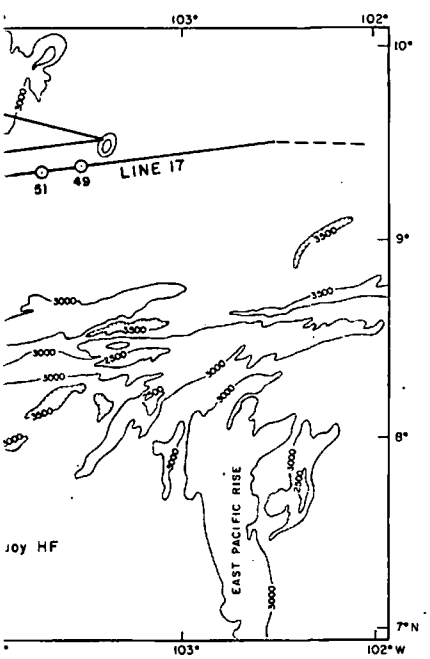

ti-channel lines 17 and 19. Circles with
indicate OBS refraction profiles.

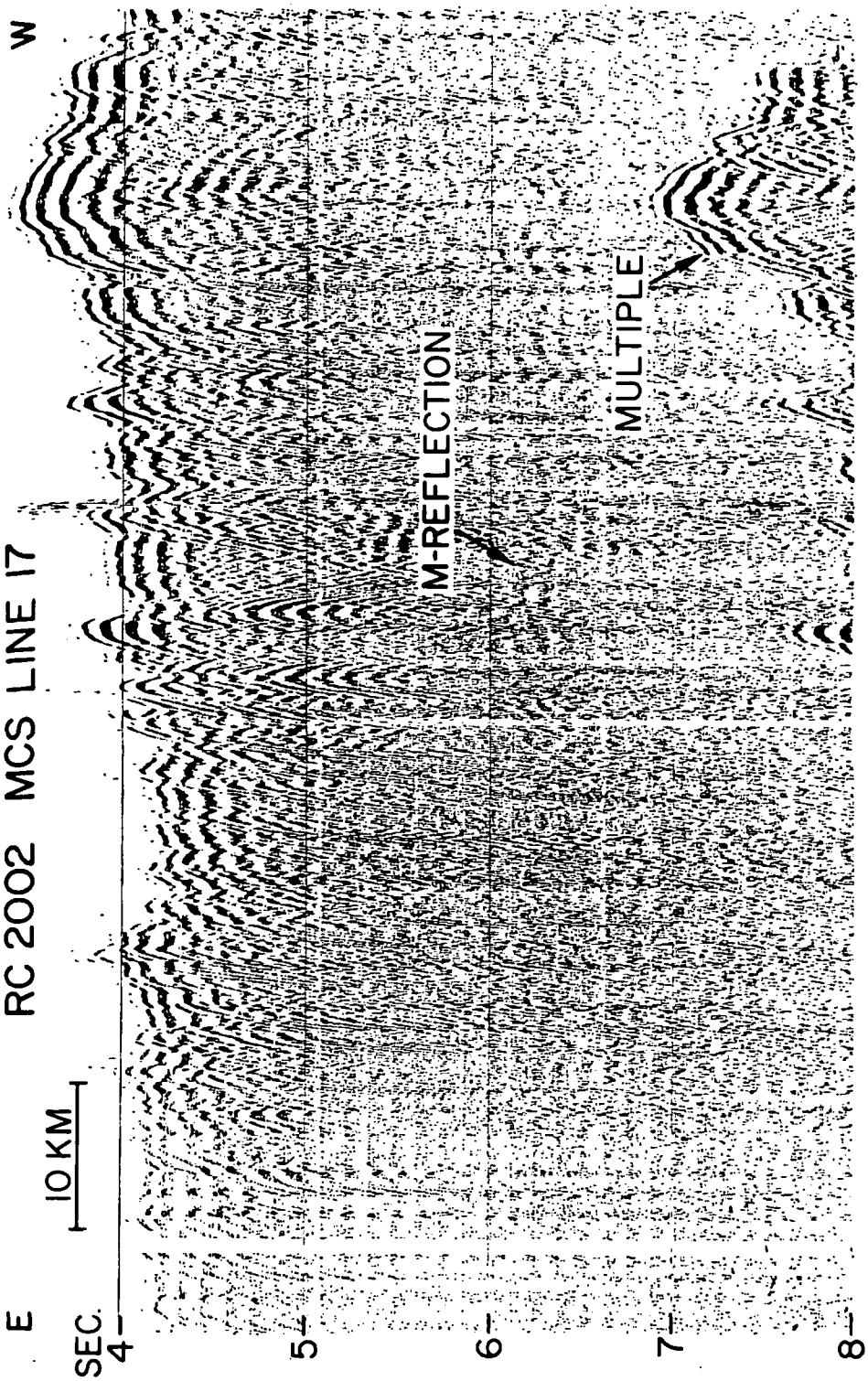

Fig. 2a. For caption see p. 87.

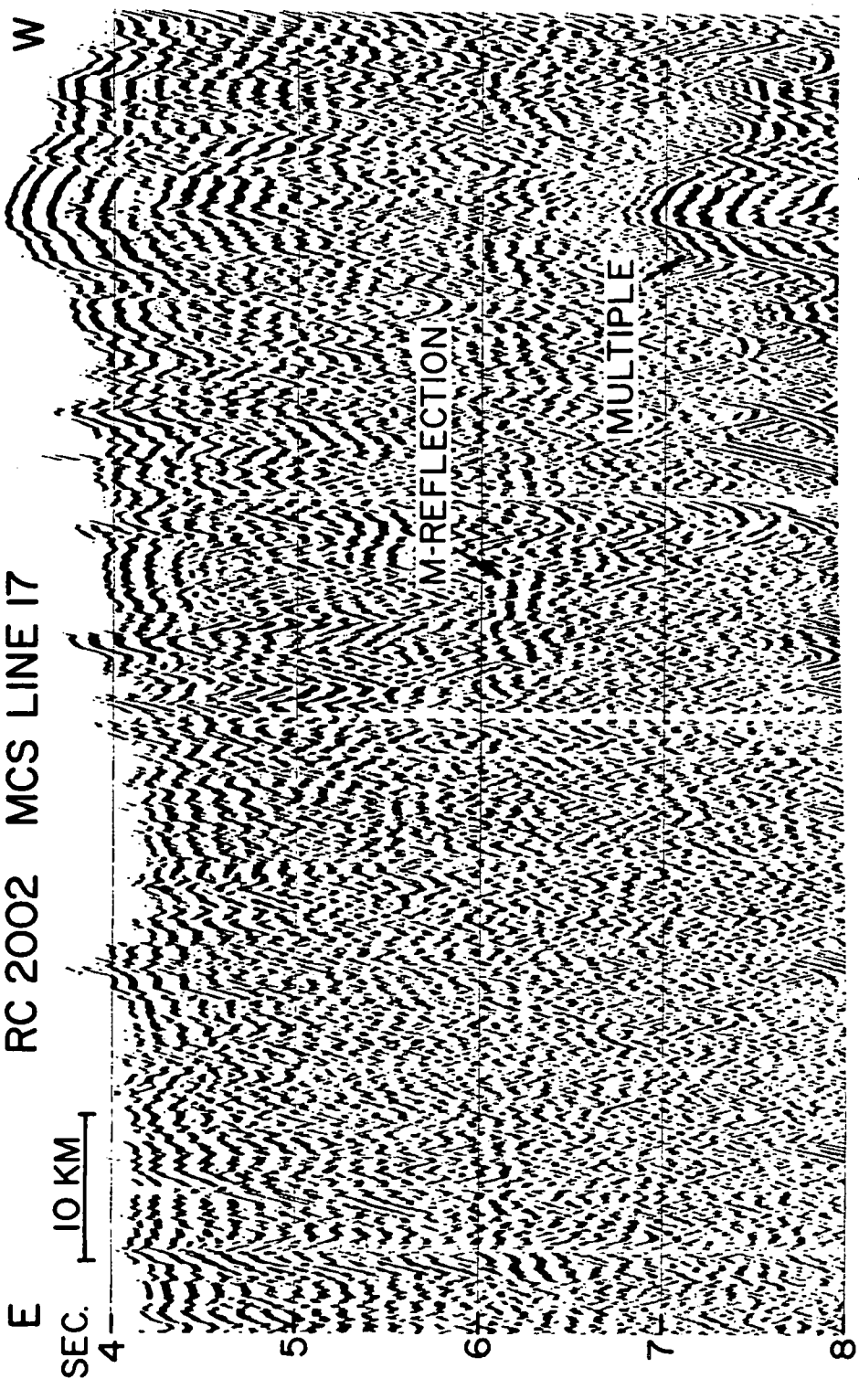

Fig. 2b. For caption see p. 87.

section, comes from s
reflections appear to
fore, do not require m
primary benefit from
set is to remove the u

We have also acquir
in the Western Pacific,
continuous deep crust
beneath the sea-floor i
reflector has been con
correlation with sonob
Fig.4). The observatio
Pacific and the new cr
tinuity is an ocean-wid
Both these data sets su
impedance contrast pe
oceanic basement.

EVENT IDENTIFICATIO

The principal charac
content sharply peaked
travel time of about 2 s
normal move-out of th
average velocity for the

Because of absorptio
from mantle should be
on Lines 17 and 19 (Fi
have this characteristic.
(this is the bubble pulse
the bottom return and
from the M-discontinui
since the higher frequer

Numerous two-ship r
studies over ocean crust
about 2 sec below baser
reflections 2 sec below
strongly confirmed by s
(Buhl et al., 1978; Hout

Fig.2.a,b. Line 17 crossing c
pass 0—10 Hz. b. migrated,
Fig.2a were migrated using
and under the Rise axis appe
et al. (1976). Note the mant
but can be traced laterally th
cating a thickening of the cr
and mantle in the axial zone

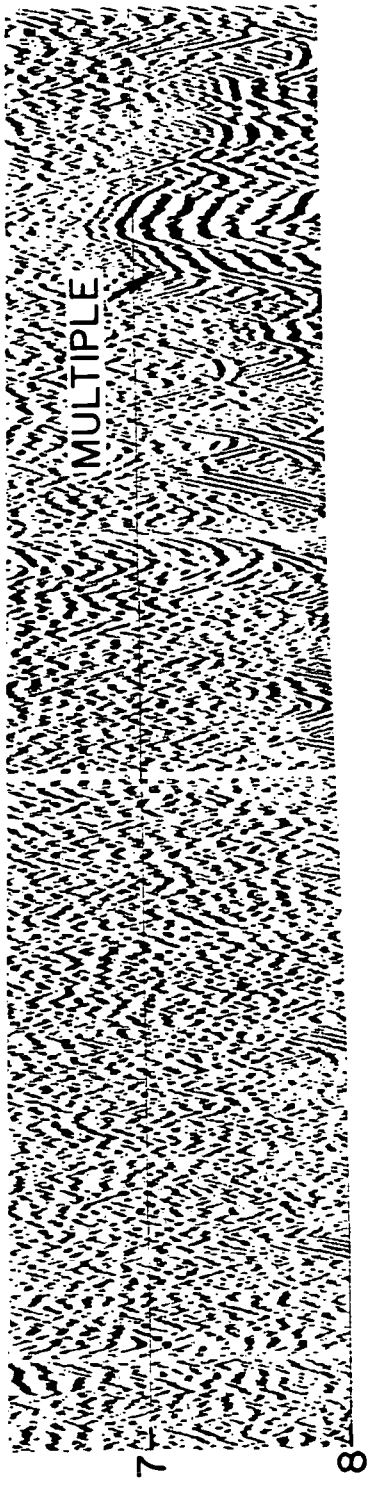

Fig. 2b. For caption see p. 87.

section, comes from sea-floor diffractions, (see Fig.5). Also, the mantle reflections appear to originate from a laterally smooth surface and, therefore, do not require migration as do the sea-floor reflections. Thus, the primary benefit from migration (either before or after stack) for this data set is to remove the unwanted energy from the region of mantle reflections.

We have also acquired and processed multi-channel seismic reflection data in the Western Pacific, just seaward of the Japan Trench. In this data, a continuous deep crustal reflection is observed at about 2 sec of travel time beneath the sea-floor in over 2,000 nm of multi-channel seismic track. This reflector has been confirmed as a reflection from the M-discontinuity through correlation with sonobuoy reflection and refraction data (Buhl et al., 1978; Fig.4). The observation of mantle reflections in the old crust of the Western Pacific and the new crust of the East Pacific Rise indicates that the M-discontinuity is an ocean-wide first-order velocity discontinuity, at least at 8 Hz. Both these data sets suggest that no other discontinuity with as much impedance contrast persists in the crust to any great lateral extent below oceanic basement.

EVENT IDENTIFICATION

The principal characteristics of the mantle reflections are: (1) low-frequency content sharply peaked at the 8-Hz bubble pulse frequency; (2) two-way travel time of about 2 sec below the top of oceanic basement, and (3) small normal move-out of the event across the receiving array indicating a high average velocity for the overlying section.

Because of absorption of high frequencies in the earth's crust, reflections from mantle should be dominantly low-frequency. Mantle reflections observed on Lines 17 and 19 (Figs.2 and 3), and those in the Western Pacific (Fig.4), have this characteristic. Although the air gun spectrum is rich in 8-Hz energy, (this is the bubble pulse period) higher frequencies do exist as can be seen in the bottom return and its water column multiples. But, the energy detected from the M-discontinuity is dominated primarily by the bubble pulse period since the higher frequencies are attenuated.

Numerous two-ship refraction and sonobuoy reflection and refraction studies over ocean crust indicate a vertical two-way travel time to mantle of about 2 sec below basement. In the Western Pacific, identification of the reflections 2 sec below basement as originating from the M-discontinuity is strongly confirmed by sonobuoys along 2,000 nm of multi-channel profiles, (Buhl et al., 1978; Houtz et al., 1978).

Fig.2.a,b. Line 17 crossing of the East Pacific Rise crest: a. 24-fold stacked section; band-pass 0—10 Hz. b. migrated, stacked section; band-pass 0—10 Hz. The stacked data of Fig.2a were migrated using a velocity of 1,500 m/sec. The reflection at about 4.2 sec and under the Rise axis appears to correspond to the top of the low-velocity zone of Orcutt et al. (1976). Note the mantle reflection which is strongest in the middle of the section, but can be traced laterally through the axial block. It does not parallel the sea floor indicating a thickening of the crust or a decrease in interval velocity between the sea-floor and mantle in the axial zone. The vertical exaggeration is 17.5 to 1.

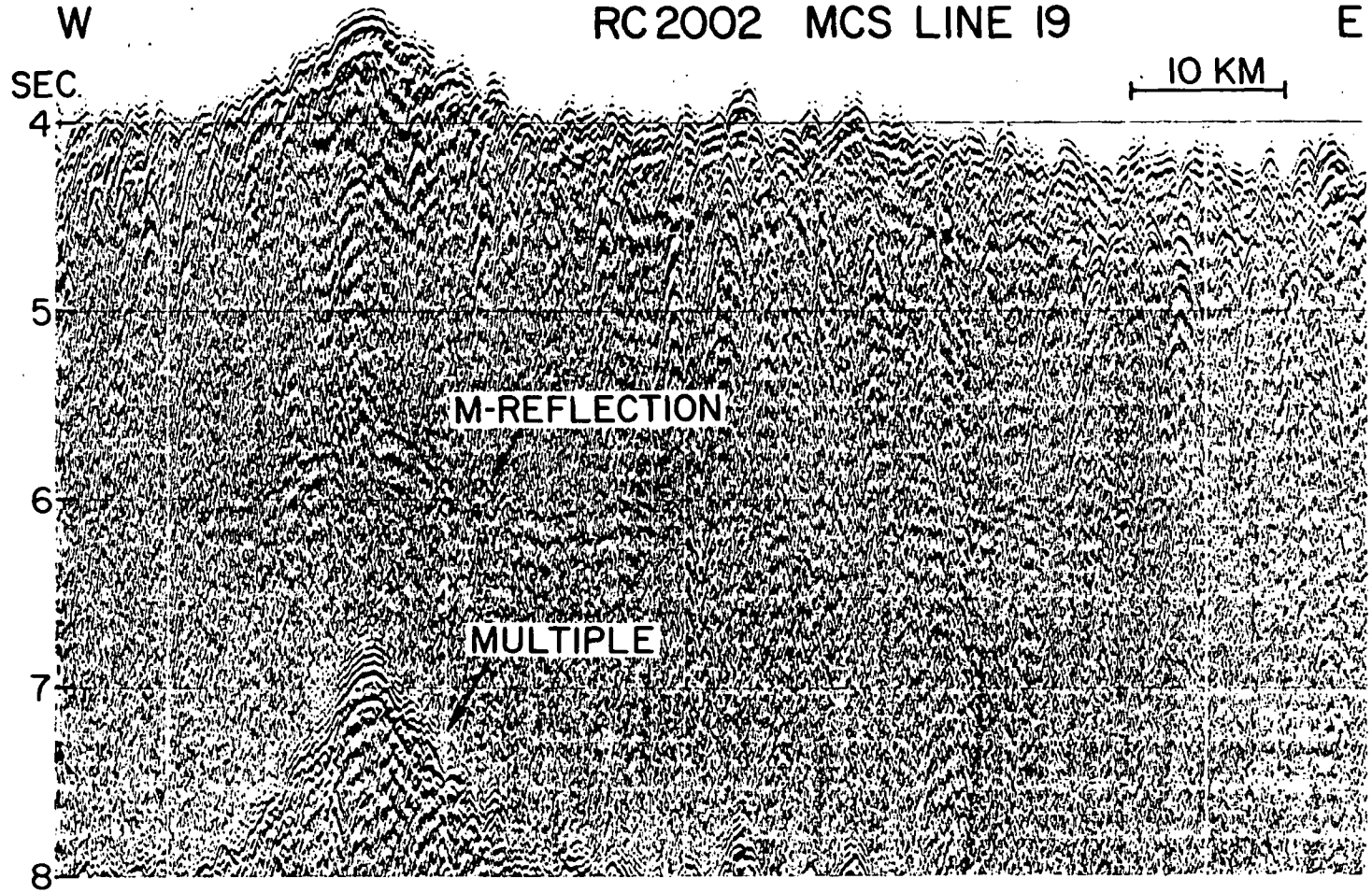

Fig. 3a. For caption see p. 90.

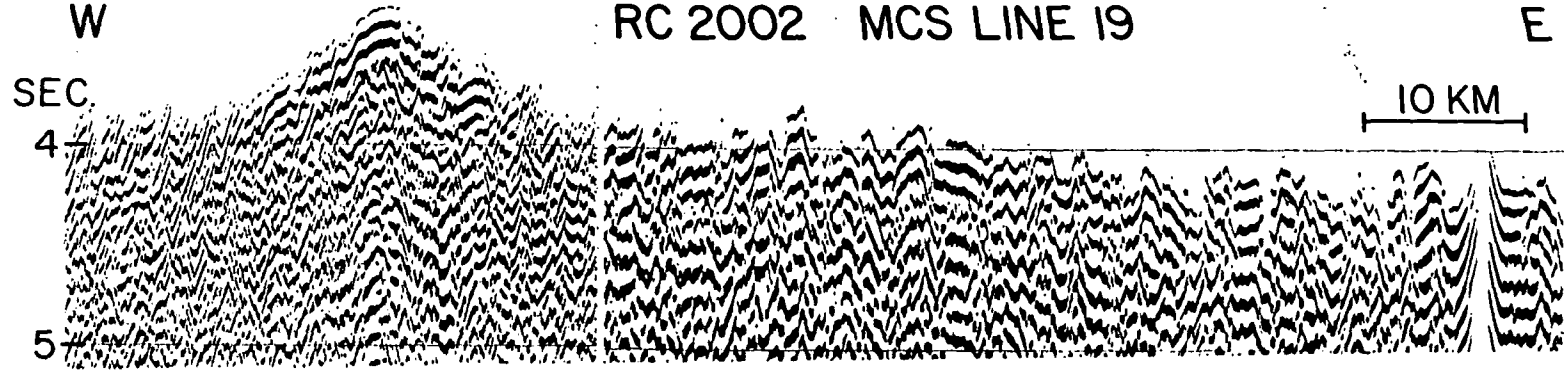

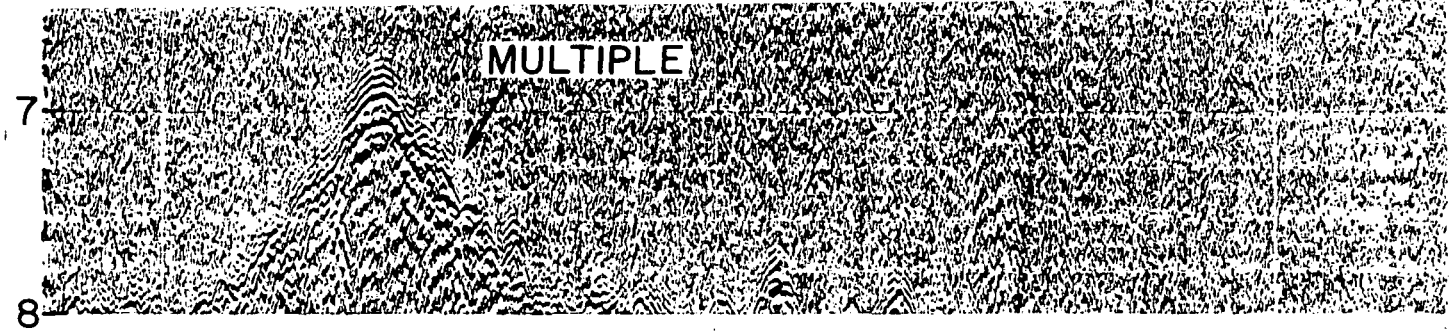

Fig. 3a. For caption see p. 90.

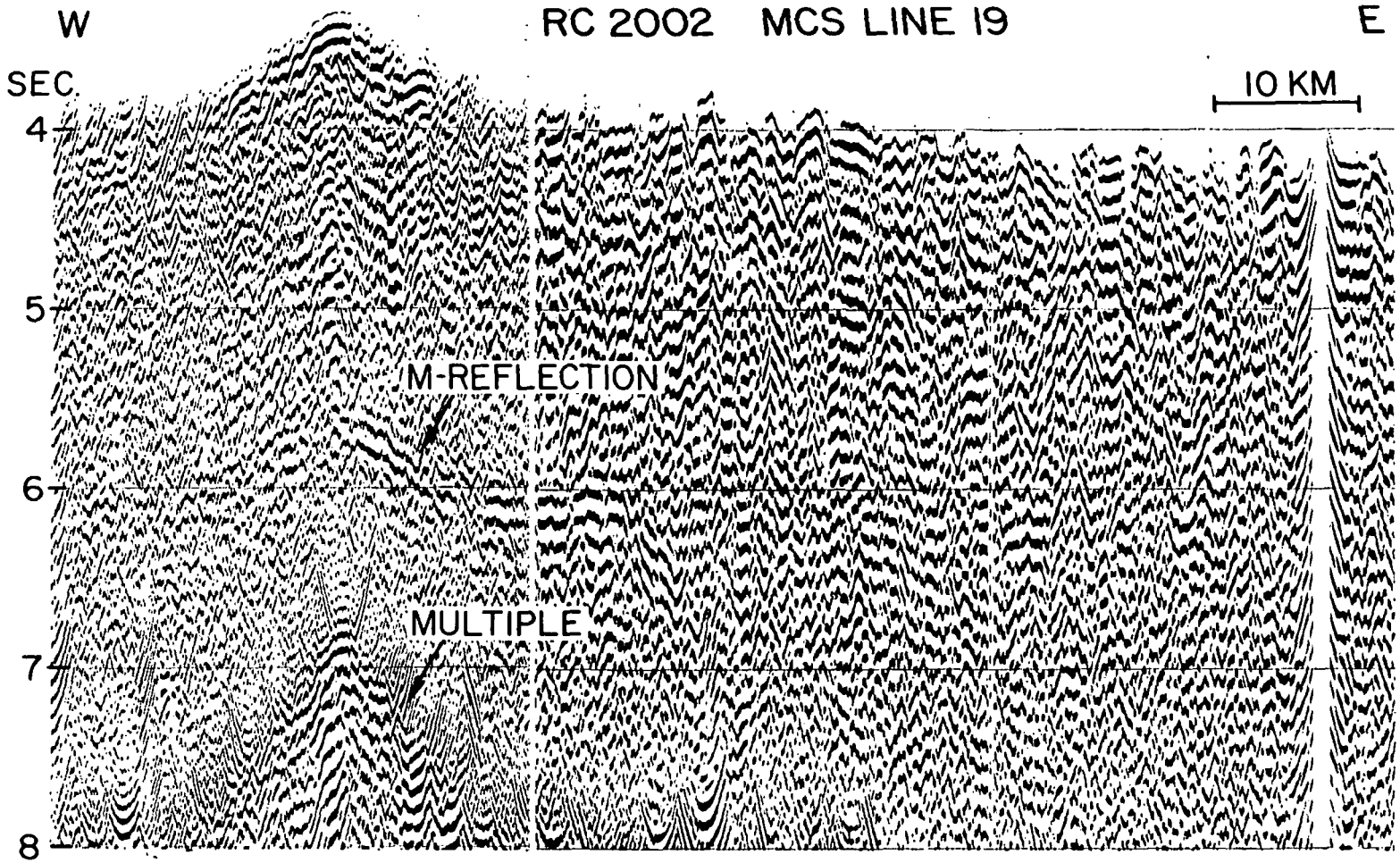

Fig. 3b. For caption see p. 90.

Fig. 3c.

Fig.3.a,b,c. Line 19 crossing of East Pacific Rise crest: a. stacked, and b. migrated sections. The same processing as in Fig.2. Note the strong mantle reflection just to the east of the axis which continues under the Ridge crest. Unlike line 17, the mantle reflection parallels the sea floor suggesting a constant crustal thickness and velocity; c. Migration before stack: The 24 constant offset sections were migrated using a velocity of 1500 m/sec. These sections were then combined to make CDP gathers, corrected for normal move-out and then stacked. In addition, the amplitudes were corrected for spreading loss and attenuation. Note the well-defined mantle reflection, except in a 3-km zone slightly to the west of the Rise crest.

Examination of the CDP gathers s
with small normal move-out, see Fig
gathers are contaminated by the pre
high amplitude events obscure the w
events. In the migrated CDP gathers
attenuated and weak mantle reflecti
semblance velocity scans for two of
gathers show the mantle reflection a
indicating a high average velocity bet
This confirms our identification of t
because of poor resolution, does not
velocities from the data. Examinatio
alternative identification of the crust
at the sea floor and reflected from a
shear waves would have a much lowe
normal move-out across the gather. T
in the gathers shown. A similar argu
and the apparent absence of shallow,
ates the possibility of these reflectio
clearly are not water-column multipl
furthermore, they are not multiples
such multiples, the air guns were "ra
$20 + \tau$ sec, where τ is a random fract
from previous shots would not appea
This means that they would appear a
sections. Even if the air guns were no
acquisition, in 4 sec of water multipl
at 3.5 sec (24—20.5) and 7.5 sec (28-
~ 6 sec. Such multiples would also fo
vertical exaggeration of 6 or 7. This i
surface under the Rise crest on Line
does follow the sea-floor topography
the first sea-floor multiple.

Of the six sonobuoys deployed, o
the ridge on Line 17 gives a critical a
range and arrival time of this event a
crustal-velocity section with a vertica
The sonobuoy stations do show the p
7.4 km/sec) in the crust well above t
Table I, we show the velocities and la
buoy data along Line 17 and the arri
reflection.

Examination of the CDP gathers shows low-frequency coherent arrivals with small normal move-out, see Figs.5 and 6. In Fig.5, the original CDP gathers are contaminated by the presence of sea floor diffractions. These high amplitude events obscure the weak, underlying primary reflection events. In the migrated CDP gathers the sea-floor diffractions have been attenuated and weak mantle reflection hyperbolas can be seen. In Fig.6, the semblance velocity scans for two of the migrated Common Depth Point gathers show the mantle reflection as an arrival with a high apparent velocity, indicating a high average velocity between the sea-floor and this reflector. This confirms our identification of these events as primary reflections, but because of poor resolution, does not allow us to calculate accurate crustal velocities from the data. Examination of the CDP gather also eliminates an alternative identification of the crustal reflections — shear waves converted at the sea floor and reflected from an interface above mantle. Converted shear waves would have a much lower apparent velocity and hence a larger normal move-out across the gather. This difference would be detectable even in the gathers shown. A similar argument based on the small normal move-out and the apparent absence of shallow, laterally persistent reflections eliminates the possibility of these reflections being internal multiples. The events clearly are not water-column multiples produced by the current shot and, furthermore, they are not multiples from previous shots. In order to eliminate such multiples, the air guns were "randomly" fired. The shot spacing was $20 + \tau$ sec, where τ is a random fraction between 0 and 1. Thus, multiples from previous shots would not appear as coherent events in the CDP gathers. This means that they would appear as weak incoherent arrivals in the stacked sections. Even if the air guns were not "randomly" fired during the data acquisition, in 4 sec of water multiples from the previous shot would appear at 3.5 sec (24—20.5) and 7.5 sec (28—20.5). The mantle reflections occur at ~6 sec. Such multiples would also follow the sea-floor topography with a vertical exaggeration of 6 or 7. This is clearly not the case for the flat mantle surface under the Rise crest on Line 17. On Line 19, the mantle reflection does follow the sea-floor topography, but its vertical exaggeration is less than the first sea-floor multiple.

Of the six sonobuoys deployed, only sonobuoy station 52 on the flank of the ridge on Line 17 gives a critical angle reflection from the mantle. The range and arrival time of this event agrees with that predicted from a typical crustal-velocity section with a vertical reflection time to mantle of 6.5 sec. The sonobuoy stations do show the presence of high-velocity layers (up to 7.4 km/sec) in the crust well above the mantle reflections. In Fig.7 and in Table I, we show the velocities and layer thicknesses derived from the sonobuoy data along Line 17 and the arrival time of the vertical-incidence mantle reflection.

Fig.3.a,b,c. Line 19 crossing of East Pacific Rise crest: a. stacked, and b. migrated sections. The same processing as in Fig.2. Note the strong mantle reflection just to the east of the axis which continues under the Ridge crest. Unlike line 17, the mantle reflection parallels the sea floor suggesting a constant crustal thickness and velocity; c. Migration before stack: The 24 constant offset sections were migrated using a velocity of 1500 m/sec. These sections were then combined to make CDP gathers, corrected for normal move-out and then stacked. In addition, the amplitudes were corrected for spreading loss and attenuation. Note the well-defined mantle reflection, except in a 3-km zone slightly to the west of the Rise crest.

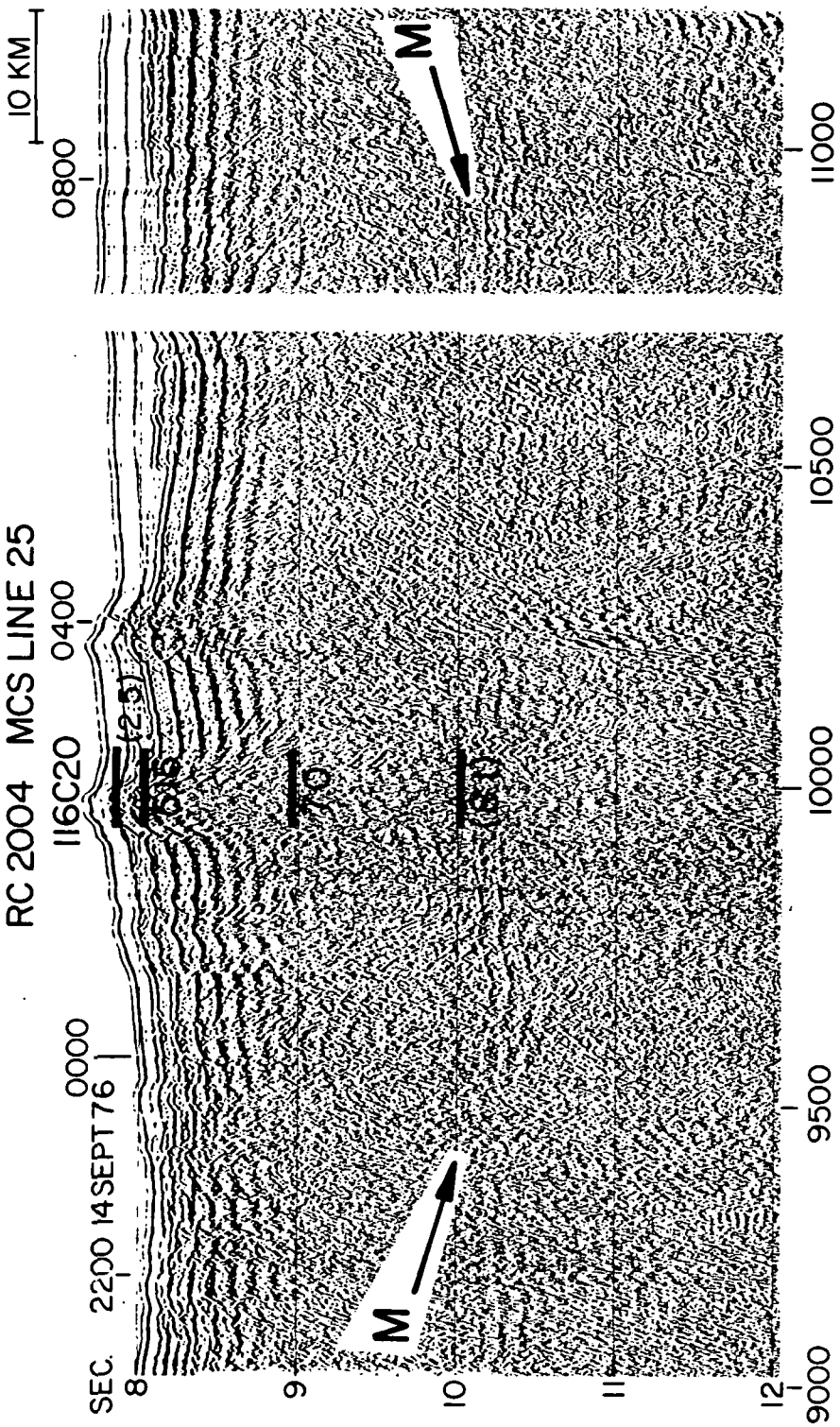

Fig.4. 24-fold, stacked section of line 25 in the western Pacific, seaward of the Japan Trench, (After Buhl et al, 1978). The numbers drafted on the section are the velocities in km/sec, derived from Sonobuoy 116 C20. The lines are the vertical reflection times. Note the very good agreement between the depth of the observed mantle reflection at 10.0 secs and that calculated from the sonobuoy station.

CONCLUSIONS

The observation of continu
the crestal zone of the East P
indicates that the M-discontin
crust is generated and that re
discontinuity appear to be th
old and new oceanic crust. La
not generate strong reflection
correspond to reflection R4 c
Layer 2—Layer 3 boundary n
and not a velocity discontinu
about velocities immediately
existence of these reflections
indicates that there is a signif

In Fig.3c, where the data w
stacked, we have also applied
velocity function derived fro
decrease in mantle reflectivity
the topographic crest of the I
crustal material. While increa
reflection is almost continuo
decreased. Mantle reflections
of the profiles. These could b
that further processing, (i.e.,
show mantle reflections in th
mantle may be incoherent du
both of these lines before sta

Reflection R4 of Herron e
lines at 0.8 sec below the sea-
sea-floor at the Rise crest, wh
constant (2.1 sec) two-way tr
might indicate a laterally con
velocity of approximately 6.5
0.5-sec time anomaly on Line
a velocity decrease to 4.7 km
The contrast between these t
crustal structure, below R4, i
angle reflection/refraction ex
vertical-incidence control. Th
such as that postulated by Or

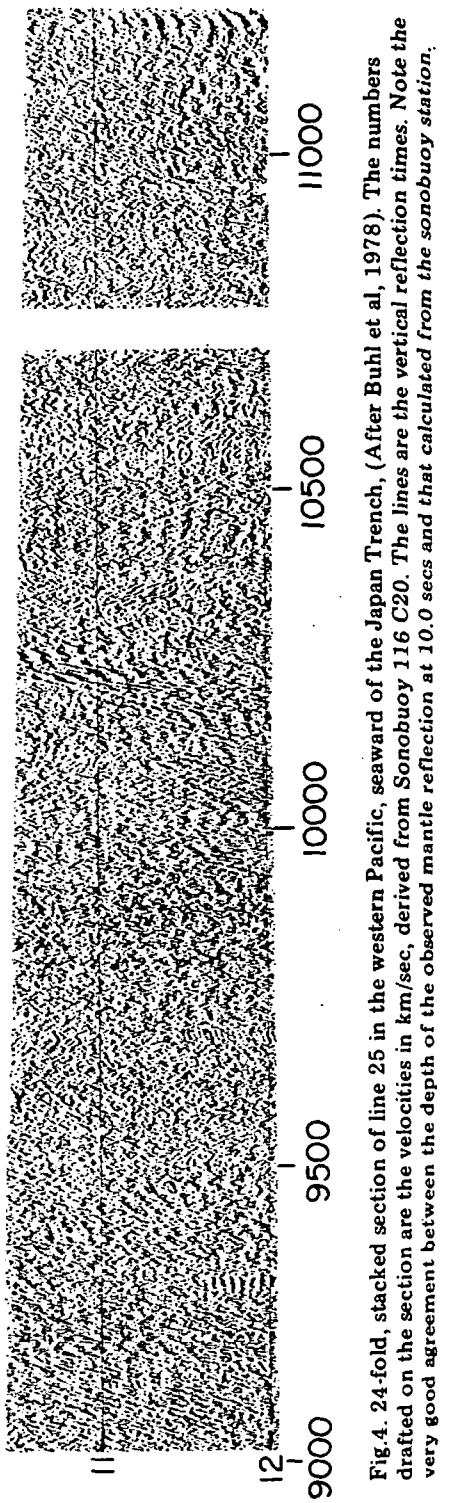

Fig.4. 24-fold, stacked section of line 25 in the western Pacific, seaward of the Japan Trench, (After Buhl et al, 1978). The numbers drafted on the section are the velocities in km/sec, derived from Sonobuoy 116 C20. The lines are the vertical reflection times. Note the very good agreement between the depth of the observed mantle reflection at 10.0 secs and that calculated from the sonobuoy station.

CONCLUSIONS

The observation of continuous reflections from the M-discontinuity across the crestal zone of the East Pacific Rise, except for a 3 km wide zone, indicates that the M-discontinuity is formed immediately when new oceanic crust is generated and that reflections from oceanic basement and the M-discontinuity appear to be the principal reflection events recorded in both old and new oceanic crust. Layer 3 identified in most refraction stations does not generate strong reflections except perhaps near the Rise crest where it may correspond to reflection R4 of Herron et al. (1978). This suggests that the Layer 2—Layer 3 boundary may be marked by a change in velocity gradient and not a velocity discontinuity. While our data give no direct information about velocities immediately above and below the M-discontinuity, the existence of these reflections both under the flanks and under the crestal zone indicates that there is a significant impedance contrast across this boundary.

In Fig.3c, where the data were migrated before the CDP gather and then stacked, we have also applied a correction for spreading loss using an average velocity function derived from the sonobuoy solutions. The apparent decrease in mantle reflectivity in this 3 km wide zone slightly to the west of the topographic crest of the Rise may indicate a zone of injection for new crustal material. While increasing the display gain shows that the mantle reflection is almost continuous across this zone, its reflectivity is definitely decreased. Mantle reflections are also difficult to discern along other portions of the profiles. These could be additional zones of injection, but we feel that further processing, (i.e., wave-equation migration before stack) may show mantle reflections in these areas. Since the energy returning from mantle may be incoherent due to scattering by the rough sea-floor, migrating both of these lines before stacking would help answer this question.

Reflection R4 of Herron et al. (1978) is seen at the Rise crest on both lines at 0.8 sec below the sea-floor. On Line 19, mantle is 2.1 sec below the sea-floor at the Rise crest, while on Line 17 it is 2.6 sec. The approximately constant (2.1 sec) two-way travel time through the crust along profile 19 might indicate a laterally constant velocity. Sonobuoy solutions indicate a velocity of approximately 6.5 km/sec between R4 and mantle. Thus, the 0.5-sec time anomaly on Line 17 arises either from a thickening of 1.6 km, a velocity decrease to 4.7 km/sec, or some combination of these extremes. The contrast between these two profiles 10 km apart indicates that the deep crustal structure, below R4, is not constant along the crest and that wide-angle reflection/refraction experiments would be difficult to interpret without vertical-incidence control. This variability indicates that low-velocity zones such as that postulated by Orcutt et al. (1976) are most likely localized.

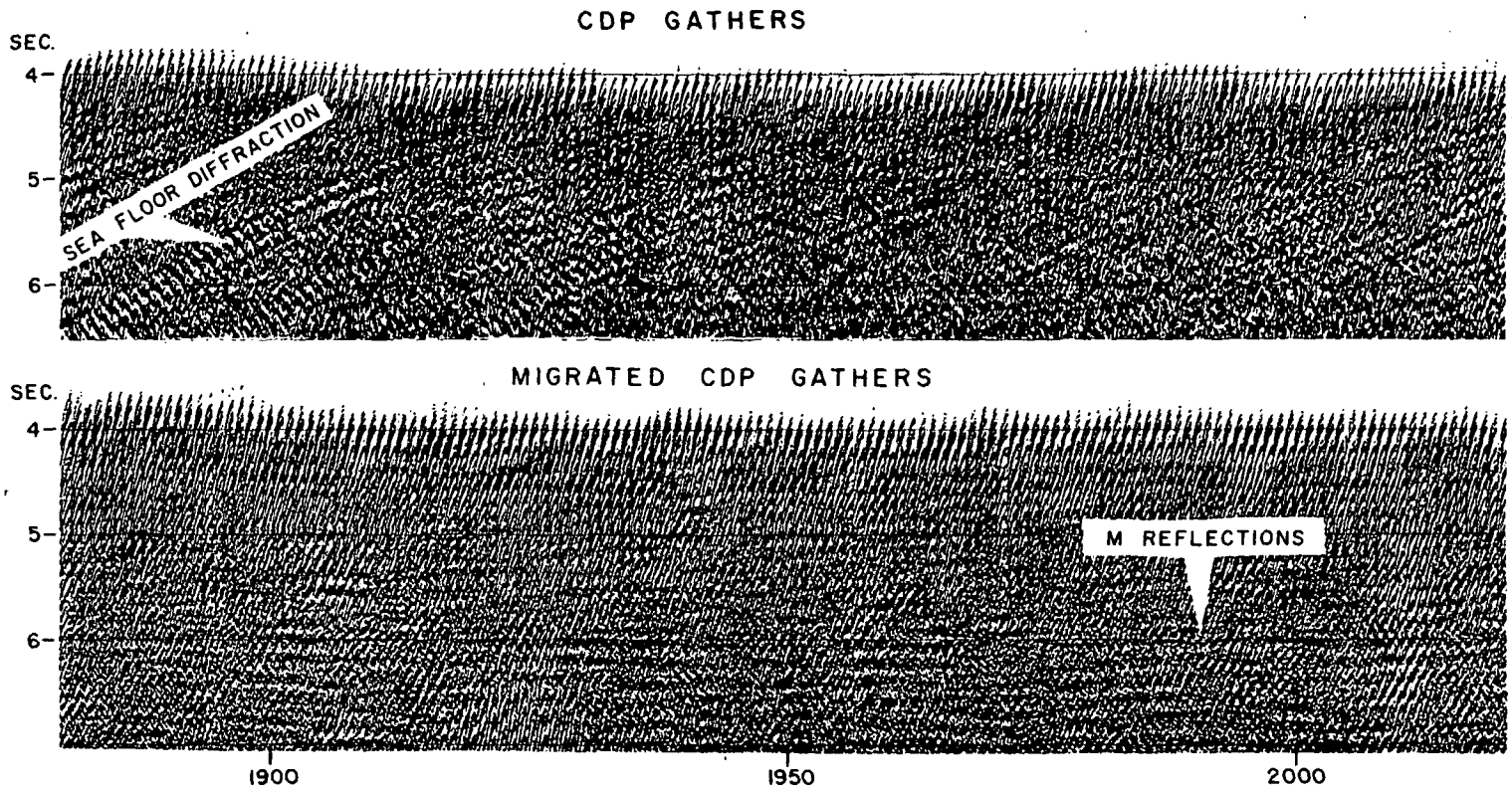

Fig.5. A comparison of CDP gathers before (a) and after (b), migration of constant offset sections. Note that the very strong sea-floor diffractions in (a) have been attenuated in (b), which now show the mantle reflections at 6 secs.

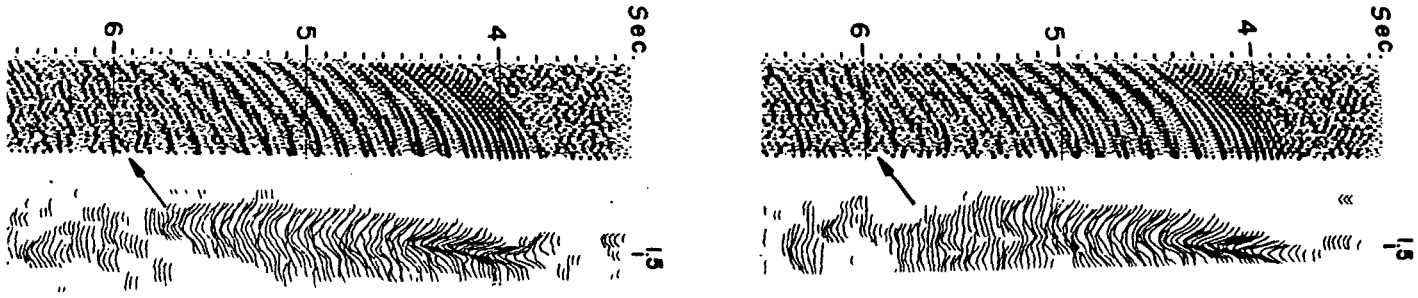

Fig.6. Two migrated CDP g
scans on the right. Note the
velocity scans indicate an R
event as a primary P-wave r

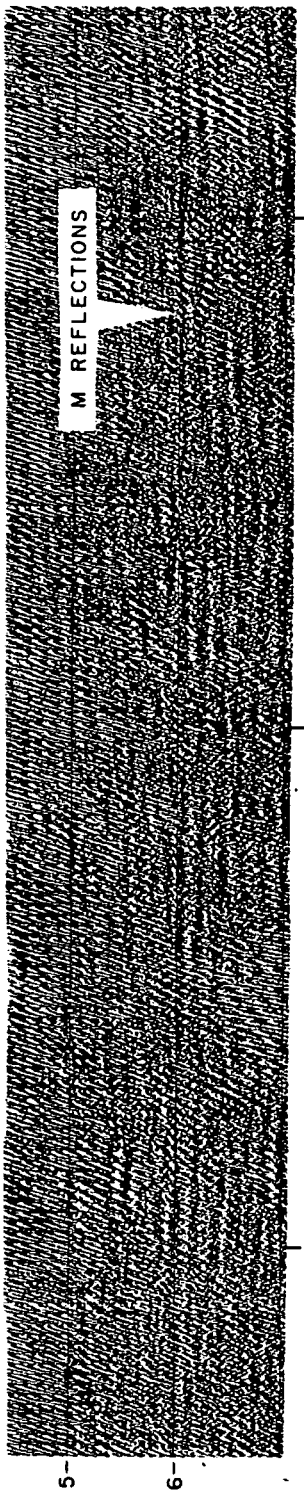

Fig.5. A comparison of CDP gathers before (a) and after (b), migration of constant offset sections. Note that the very strong sea-floor diffractions in (a) have been attenuated in (b), which now show the mantle reflections at 6 secs.

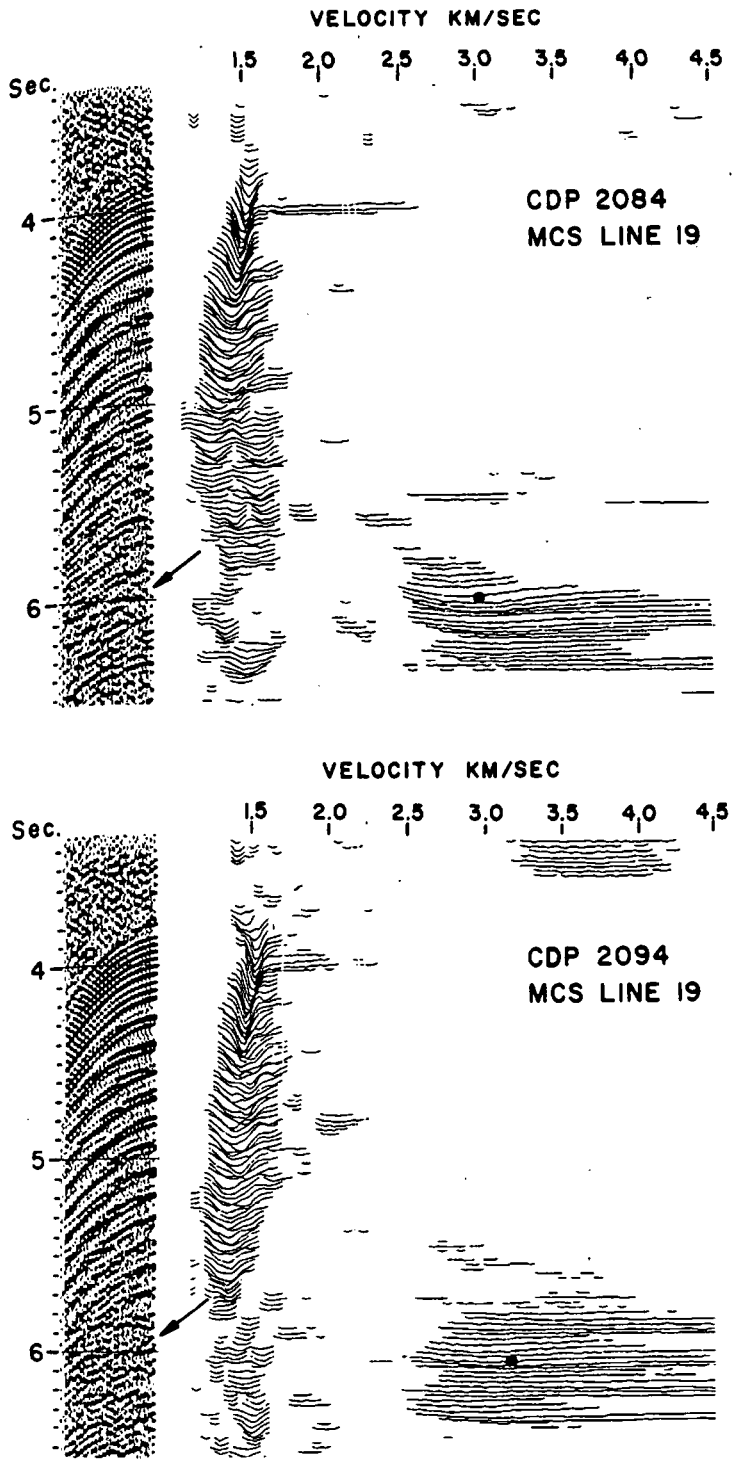

Fig.6. Two migrated CDP gathers on the left, and the corresponding semblance velocity scans on the right. Note the relatively flat reflection hyperbolas at about 6 sec. The velocity scans indicate an RMS velocity of 3 km/sec. This confirms identification of this event as a primary P-wave reflection.

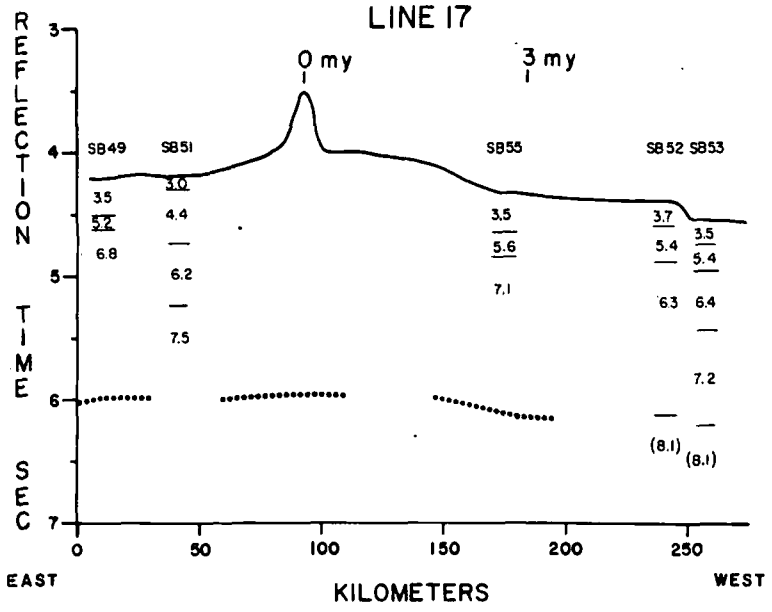

Fig.7. Schematic cross-section of line 17 showing the sea floor at 4 sec and mantle at 6 sec. Also shown are the sonobuoy solutions.

TABLE I

Results of sonobuoy stations, "Conrad" cruise 20-02 survey of PAC-4

Sonobuoy	Velocity (km/sec)					Water	Thicknesses (km)				Location	
	V_2	V_3	V_4	V_5	V_6		h_2	h_3	h_4	h_5	latitude(N)	longitude(W)
49	3.5*	5.2	6.8			3.16	0.51	0.30			09°23.0'	103°30.7'
51	3.0*	4.4	6.2	7.4		3.13	0.19	0.94	1.58		09°20.8'	103°43.8'
52	3.7*	5.4	6.3		8.1	3.29	0.37	0.77	3.91		09°05.0'	105°43.7'
53	3.5*	5.4	6.4	7.3	8.1	3.41	0.36	0.55	1.54	2.86	09°02.2'	105°57.5'
54	3.7*	5.7	6.9			3.14	0.83	0.68			08°44.6'	105°19.6'
55	3.5*	5.6	7.1			3.24	0.56	0.60			09°08.9'	105°16.1'

Asterisks denote assumed velocities; all velocities are unreversed refraction velocities.

ACKNOWLEDGEMENTS

The IPOD Site Survey Management, under subcontract with DSDP (UC-NSF-C-482-2) supported the data acquisition and N00014-75-C-0210 supported the data processing and interpretation. We thank Dr. Manik Talwani and Dr. Philip D. Rabinowitz for critical reviews of the manuscript.

REFERENCES

Buhl, P., Stoffa, P.L., Kan, T.K., Talwani, M. and Ewing, J., 1978. Observation of reflections from the M-discontinuity in the Western Pacific by near-vertical incidence multichannel profiling. Trans. Am. Geophys. Union, 59(4).

Herron, T.J., Ludwig, W.J., Stoffa
East Pacific Rise crest from mu
83(B2):798—804.

Houtz, R.E., Buhl, P., Stoffa, P., W
the decrease in upper mantle se
Am. Geophys. Union, 59(4).

Orcutt, J.A., Kennett, B.L.N. and
from an ocean bottom seismom

Stoffa, P.L., Kan, T.K., Buhl, P. an
Step" algorithm to the migratio
Annual International Meeting o
Alberta, Canada, September 21,

Herron, T.J., Ludwig, W.J., Stoffa, P.L., Kan, T.K. and Buhl, P., 1978. Structure of the East Pacific Rise crest from multi-channel seismic-reflection data. J. Geophys. Res., 83(B2):798–804.

Houtz, R.E., Buhl, P., Stoffa, P., Windisch, C. and Murauchi, S., 1978. Observations of the decrease in upper mantle seismic velocity beneath the Japan-Bonin trench. Trans. Am. Geophys. Union, 59(4).

Orcutt, J.A., Kennett, B.L.N. and Dorman, L.M., 1976. Structure of the East Pacific Rise from an ocean bottom seismometer survey. Geophys. J. R. Astron. Soc., 45:305–320

Stoffa, P.L., Kan, T.K., Buhl, P. and Kutschale, H., 1977. The application of the "Split-Step" algorithm to the migration of marine seismic data. Paper presented at the 47th Annual International Meeting of the Society of Exploration Geophysicists, Calgary, Alberta, Canada, September 21, 1977; Geophysics, 42(7).

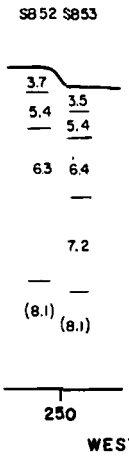

floor at 4 sec and mantle at

\C-4

)		Location	
	h_3	latitude(N)	longitude(W)
		09°23.0′	103°30.7′
58		09°20.8′	103°43.8′
91		09°05.0′	105°43.7′
54	2.86	09°02.2′	105°57.5′
		08°44.6′	105°19.6′
		09°08.9′	105°16.1′

efraction velocities.

)contract with DSDP (UC-
d N00014-75-C-0210
. We thank Dr. Manik
l reviews of the manuscript.

. J., 1978. Observation of reflec-
by near-vertical incidence multi-

interesting - limited use

JOURNAL OF GEOPHYSICAL RESEARCH, VOL. 86, NO. B12, PAGES 11,609-11,615, DECEMBER 10, 1981

ON MEASURING THE ELECTRICAL CONDUCTIVITY OF THE OCEANIC CRUST BY A MODIFIED MAGNETOMETRIC RESISTIVITY METHOD

R. N. Edwards

Department of Physics, University of Toronto, Toronto, Ontario, Canada, M5S 1A7

L. K. Law and J. M. DeLaurier

Pacific Geoscience Centre, Department of Energy, Mines and Resources
Sidney, British Columbia, Canada V8L 4B2

Abstract. Magnetotelluric sounding reveals a conductive zone beneath the Pacific Ocean at depths in excess of 60 km but does not resolve the resistivity of the lithosphere above this zone. Further resolution can be obtained by controlled source electrical methods. The simplest of these are the galvanic techniques. Dipole-dipole resistivity sounding is not suitable because dipole separations of thousands of kilometers would be required to obtain values of the resistivity. A viable alternative is to measure on the ocean floor the magnetic field of a vertical bipolar source extending from the sea surface to the seafloor. Magnetometer transmitter separations of only a few kilometers are sufficient to determine the resistivity of a half space beneath the ocean. Sounding curves similar to those of the resistivity method may be constructed to resolve the resistivity of a layered lithosphere. The curves constructed are valid at alternating frequencies which are small compared with a skin frequency not in the ocean but in the lithosphere. The depth of penetration is of the order of half the transmitter-receiver separation. Magnetic field amplitudes are in the range of picotesla for reasonable lithospheric resistivities and separations up to 10 times the length of the bipole. Modern instrumentation, modified for the ocean floor, can detect such signals at a range of 20 km at a frequency of about 0.02 Hz averaged over several hours.

Introduction

Recent innovative developments in instrumentation and technology enable electromagnetic data to be collected on the floor of the deep ocean. Natural field variations were measured by Filloux [1977, 1980] and by Law and Greenhouse [1981] at three points beneath the Pacific Ocean. Their analyses of the data revealed the presence of a region of high conductivity beneath the lithosphere. The depth to the conductor increases with lithospheric age. Oldenburg [1981] reanalyzed all three data sets and determined that the maximum value of the conductivity is about 0.1 S m^{-1} at depths of 60-80, 125-150, and 180-225 km for ages 1, 30 and 72 Ma, respectively. Our own inversions of the data, using simple layered models and the generalized inversion technique of Jupp and Vozoff [1975], by and large agree with this analysis. We find that the simplest layered model, fitting the data as well as a conductive continuum at all three locations, is three layers (resistive, conductive, resistive) over a conductive half space. Uniformly, of the seven degrees of freedom in our model, only two are well determined by the data. These are the thickness t_1 of the first layer (resistive) and the conductivity-thickness product S_2 of the second layer (conductive). The parameter S_2 varies little from site to site and has a value of 6000 $\pm$ 600 S, while the thickness t_1 is determined to about 10% and increases with lithospheric age as described by Oldenburg. The data do not provide independent estimates of the resistivity and thickness of the second layer nor values of the resistivity of the oceanic lithosphere and oceanic crust above the conductor.

In view of the relevance of the electrical sounding of the upper mantle in the determination of temperature, percent partial melt, and by extension, a description of the physical processes inside the earth, it is important to expand the available data. Magnetic fields originating above earth's surface are screened by the conductive ocean and temporal variations of periods shorter than a few minutes cannot be observed. Consequently, magnetotelluric data from the ocean floor are band limited. The electrical structure of the lithosphere may never be resolved with the technique.

Controlled source electromagnetic techniques are the obvious solution to this problem. They enable the resistivity of at least the uppermost parts of the first layer to be quantified. Further, they can map the electrical anisotropy of the ocean floor, which has two benefits. Electrically isotropic areas are suitable for siting seafloor instruments for magnetotelluric deep sounding. Electrical anisotropy, likely to be present because of the correlation between the axis of a spreading ridge and the crystal orientation in the lithosphere [Raitt et al., 1969; Keen and Tramontini, 1970] clearly has a tectonic significance.

It is the purpose of this paper to investigate one of the possible approaches to controlled source sounding beneath a layer of sea water. In contrast to the inductive techniques which have been proposed theoretically [Bannister, 1968; Coggon and Morrison, 1970] and which are starting to be used experimentally [Cox, 1980; Cox et al., 1981], we describe a straightforward galvanic technique, a modification of the magnetometric resistivity (MMR) method [Edwards, 1974; Edwards et al., 1978].

Conventional galvanic techniques such as the dipole-dipole resistivity method are not practical for sounding the oceanic crust. Take the case of determining the resistivity of a resistive half space beneath a sea layer 3 km thick. If the resistivity of the space is 500 times that of sea water, dipole separations of up to 3000 km would be required, a formidable logistical problem. An alternative method is to measure the magnetic field on the seafloor due to the galvanic current flowing from a vertical bipolar transmitter extending from the sea surface to the seafloor.

We show in the following theory that this method is very sensitive to seafloor resistivity even when the transmitter-receiver separation is short, of the order of the length of the bipole, i.e., the depth of the sea. We further show that both an intermediate resistive zone and an intermediate conductive zone within the crust may be delineated by expanding the transmitter-receiver separation to distances comparable with the depth to the zone.

All 'galvanic' techniques assume a static or dc approximation, whereas experimentally alternating

Paper number 1B0749.
0148-0227/81/001B-0749$01.00

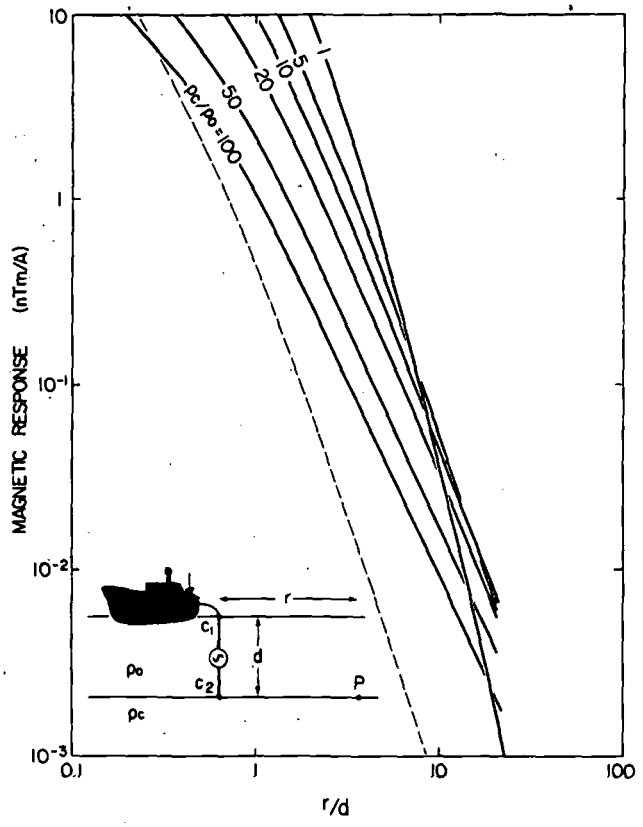

Fig. 1. The magnetic field on the seafloor of a vertical bipole source. The values are in nanoteslas per ampere of current flow for a bipole length of 1 m. The crustal to oceanic resistivity ratio varies from 1 to 100. The dashed line is the perturbation field if the transmitter is bent into the form of a circular arc.

currents are transmitted. The higher the frequency of the alternating current, the quicker an accurate measurement may be made. We have elected to present a quasi-static theory which includes the effects of electromagnetic induction. The mathematical reduction of the quasi-static expression for the magnetic field to the static solution yields the frequency range for which the static solution is valid. Preempting our conclusions, the upper frequency of the range depends not on the electromagnetic skin effect in the ocean but on the skin effect in the crust, a consequence of the large contrast in resistivity between the crust and the ocean. The magnetic fields predicted theoretically are very small, but similar fields have been measured accurately over the appropriate range of frequencies by Duncan et al. [1980]. Consequently, from the practical standpoint the method is feasible but does require the adaptation of available instrumentation to a deep ocean environment.

Theory

The ocean and subjacent oceanic crust are represented by a layer of resistivity ρ_o and a lower half space of resistivity ρ_c, respectively. The planes $z = -d$ and $z = 0$ represent the ocean surface and the ocean floor. Two current poles, a current sink labeled C_1 of strength $-I(t)$ and a current source C_2 of strength $I(t)$, are located at (0, 0, -d) and at the origin (0, 0, 0) of a cylindrical coordinate system (r, ϕ, z), respectively, as shown in Figure 1. The poles C_1 and C_2 are joined by a straight insulated conductor which carries a current I(t) from C_1 to C_2 in the positive z direction. Let I(t) vary as $I\exp(i\omega t)$.

The electric current flow everywhere has axial symmetry about the z-axis. Consequently, the time varying magnetic field $\underset{\sim}{B}$ may be written as

$$\underset{\sim}{B} = B(r;z)\exp(i\omega t)\,\underset{\sim}{\hat{\phi}} \qquad (1)$$

In regions of constant resistivity ρ, the field $\underset{\sim}{B}$, neglecting the effect of displacement currents, obeys the Helmholtz differential equation

$$\underset{\sim}{\nabla} \times \underset{\sim}{\nabla} \times \underset{\sim}{B} = -(\mu/\rho)\,\partial \underset{\sim}{B}/\partial t \qquad (2)$$

which reduces to

$$\frac{\partial^2 B}{\partial r^2} + \frac{1}{r}\frac{\partial B}{\partial r} - \frac{B}{r^2} + \frac{\partial^2 B}{\partial z^2} = \alpha^2 B \qquad (3)$$

where

$$\alpha^2 = i\omega\mu/\rho \qquad (4)$$

The magnetic field in the ocean close to the wire is independent of z and from (3) is given by

$$B = \left(\frac{\mu I \alpha_o}{2\pi}\right) K_1(\alpha_o r) \qquad (5)$$

where $\alpha_o^2 = i\omega\mu/\rho_o$ and K_1 is the modified Bessel function of the second kind of order 1. Expression (5) reduces to

$$B = \mu I/2\pi r \qquad (6)$$

as α_o tends to zero, the low frequency static limit.

A Hankel transform pair relating any function A(r;z) and its transform $A(\lambda;z)$ may be defined as

$$A(\lambda;z) = \int_0^\infty rA(r;z)\,J_1(\lambda r)\,dr \qquad (7)$$

$$A(r;z) = \int_0^\infty \lambda A(\lambda;z)\,J_1(\lambda r)\,d\lambda \qquad (8)$$

where the Bessel function $J_1(\lambda r)$ satisfies the differential equation

$$J_1''(\lambda r) + \left(\frac{1}{\lambda r}\right) J_1'(\lambda r) + \left(1 - \left(\frac{1}{\lambda r}\right)^2\right) J_1(\lambda r) = 0 \qquad (9)$$

The Hankel transform of (3), obtained from (8) and its first and second derivatives and through the use of (9), is

$$\frac{d^2 B}{dz^2} - \lambda^2 B = \alpha^2 B \qquad (10)$$

The trivial general solutions of (10) in the ocean and in the crust are, respectively,

$$B_o(\lambda;z) = (\mu I/2\pi)\,\{F\exp(-\theta_o z) + G\exp(\theta_o z)\} \qquad (11)$$

and

$$B_c(\lambda;z) = (\mu I/2\pi)\,\{H\exp(-\theta_c z)\} \qquad (12)$$

where F, G, and H are arbitrary constants, and

$$\theta^2 = \lambda^2 + \alpha^2$$

The Hankel transform of the particular integral; (5) is

$$(\mu I \alpha_o/2\pi)\int_o^\infty r K_1(\alpha_o r)J_1(\lambda r)dr = \mu I \lambda/2\pi\theta_o^2 \quad (13)$$

by standard integral 6.565/4 of Gradshteyn and Ryzhik [1965]. Consequently the complete solution of (10) in the ocean is

$$B_o(\lambda;z) = (\mu I/2\pi)\{F\exp(-\theta_o z) + G\exp(\theta_o z) + \lambda/\theta_o^2\} \quad (14)$$

The electric field $\underset{\sim}{E}$ in the earth has two components in $\hat{r}$ and $\hat{z}$ directions related to $\underset{\sim}{B}(r;z)$ by Ampere's law

$$\nabla \times B\hat{\phi} = (\mu/\rho)(E_r \hat{r} + E_z \hat{z})$$

In particular,

$$(\mu/\rho)E_r(r;z) = -\partial B(r;z)/\partial z$$

and, equivalently,

$$(\mu/\rho)E_r(\lambda;z) = -dB(\lambda;z)/dz \quad (15)$$

The arbitrary constants may be determined from the boundary conditions on z = -d and z = 0. The magnetic field B is zero on z = -d and is continuous across z = 0. Also, the electric field component E_r is continuous across z = 0.

The boundary equations reduce to

$$\begin{pmatrix} \exp(\theta_o d) & \exp(-\theta_o d) & 0 \\ 1 & 1 & -1 \\ -\rho_o\theta_o & \rho_o\theta_o & \rho_c\theta_c \end{pmatrix}\begin{pmatrix} \lambda F \\ \lambda G \\ \lambda H \end{pmatrix} = \begin{pmatrix} -\lambda^2/\theta_o^2 \\ -\lambda^2/\theta_o^2 \\ 0 \end{pmatrix}$$

and the solution for H, in particular, is

$$\lambda H = \left(\frac{1-K}{2}\right)\left[\frac{1 - 2\exp(-\theta_o d) + \exp(-2\theta_o d)}{(1 - K\exp(-2\theta_o d)}\right]\cdot\left(\frac{\lambda^2}{\theta_o^2}\right) \quad (16)$$

where the reflexion coefficient K is

$$(\rho_c\theta_c - \rho_o\theta_o)/(\rho_o\theta_o + \rho_c\theta_c)$$

The inverse Hankel transform

$$(\mu I/2\pi)\int_o^\infty H J_1(\lambda r)d\lambda \quad (17)$$

is the final expression for the magnetic field on the seafloor.

The Low-Frequency Static MMR Limit

At the low frequency limit, $\theta_o = \theta_c = \lambda$. The integral (17) may be evaluated by expanding its denominator by the binomial theorem. Then, by employing the standard integral.

$$\int_o^\infty \exp(-\lambda s)J_1(\lambda r)d\lambda = \frac{1}{r}\left[1 - \frac{s}{(r^2+s^2)^{1/2}}\right]$$

$$B(r;0) = (\mu I/4\pi r)\,[2f(d) - f(2d) + \sum_{m=1}^{\infty} K^m\, f(2(m-1)d) - f(2(m+1)d)\,] - 2\sum_{m=1}^{\infty} K^m\,[f((2m-1)d) - f((2m+1)d)] \quad (18)$$

where f(x) is an abbreviation for $x/(r^2+x^2)^{1/2}$.

The correctness of expression (18) may be partly confirmed by examining the two obvious limits. If K is unity, no current can penetrate the lower half space, no current crosses a horizontal Ampere circuit radius r, and consequently, B (r;0) must be zero. For this case, the only term in the first power series is f(2d), while the only term in the second power series is -2f(d). Consequently, the field B does indeed vanish. The second limit occurs if $\rho_c = \rho_o$; the uniform each case for which K=0. The magnetic field is

$$B(r;0) = (\mu I/4\pi r)\left[\frac{2d}{(r^2+d^2)^{1/2}} - \frac{2d}{(r^2+4d^2)^{1/2}}\right] \quad (19)$$

This expression may be derived independently in the following manner. First, replace the effect of the sea surface, the plane z = -d by a second current system in the region z<-d (the air) such that the total current flow is symmetrical about the earth/air interface. Next, compute the total current flowing through the aforementioned circular Ampere circuit. Assume that the combined current system is in a whole space and that current anywhere within the earth is the superposition of radial flow from each of the four current poles. Finally, calculate the magnetic field by Ampere's law. The result is expression (19).

The Effect of Frequency

An interesting, relevant asymptotic solution illustrating the effect of frequency may be obtained. The contrast in resistivity between the ocean and the oceanic crust is large, i.e., $\rho_o << \rho_c$. Consequently, $\theta_o\rho_o$ is in practice much smaller than $\theta_c\rho_c$ even though $\theta_o \geq \theta_c$. The reflexion coefficient K can therefore be approximated by $1 - \varepsilon$, where ε is $2\theta_o\rho_o/\theta_c\rho_c$.

At distances r large compared with d, λd is small compared with unity for all λ contributing to the Hankel transform (17).

With the above two approximations and the further weaker condition that the 'current channelling number', $d\rho_o\theta_c/2\rho_o$ is large compared with unity, expression (16) reduces to

$$\lambda H = \rho_o\lambda^2/2d\rho_c\theta_c \quad (20)$$

which is independent of α_o, i.e., of the skin effect of the ocean. The Hankel transform (17) becomes

$$(\mu I\rho_o d/4\pi\rho_c)\int_o^\infty \frac{\lambda^2}{(\lambda^2+\alpha_c^2)^{1/2}} J_1(\lambda r)d\lambda \quad (21)$$

or

$$(\mu I\rho_o d/4\pi\rho_c r^2)\,[e^{-\alpha_c r}(1+\alpha_c r)] \quad (22)$$

by standard integral 6.554/1 of Gradshtyen and Ryzhik [1965]. If r is small compared with a skin depth in the oceanic crust, expression (22) reduces to

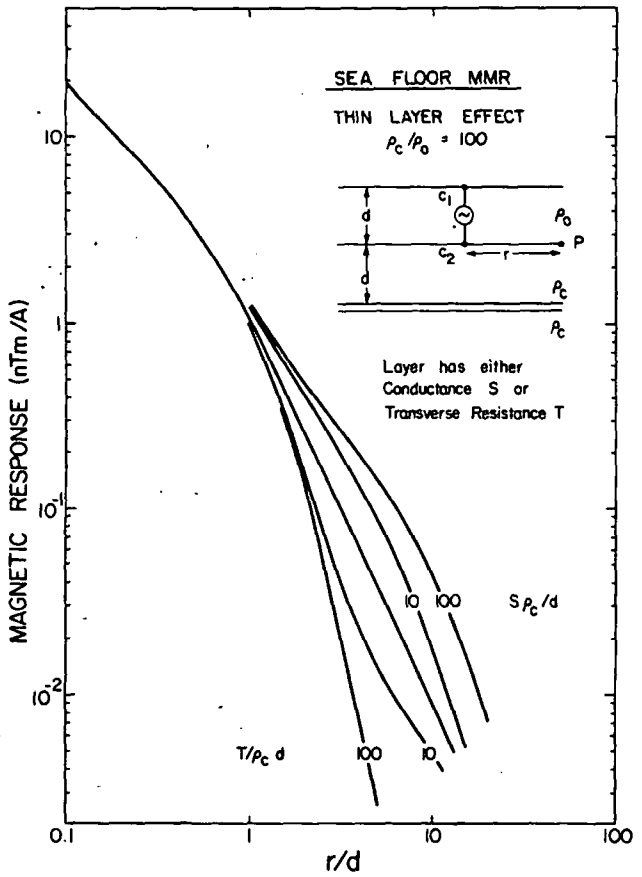

Fig. 2. The effect on the magnetic field of an intermediate crustal layer. The oceanic resistivity is one hundredth of the crustal resistivity.

$$(\mu I \rho_o d/4\pi\rho_c r^2)(1 - \alpha_c{}^2 r^2) \qquad (23)$$

The amplitude of the magnetic field is to first order independent of frequency, and the phase of the field for small angles is simply $\omega\mu r^2/\rho_c$.

The Effect of a Thin Intermediate Crustal Layer

We can show that both a conductive and a resistive thin intermediate layer may be detected by its MMR response. Let the layer have resistivity-thickness product T, conductivity-thickness produce S, finite small thickness t, and lie between $z = h_1$ and $z = h_2$. To a first approximation, let the horizontal fields within the layer obey a Taylor expansion of the form

$$B|_{h_2} = B|_{h_1} + t \cdot \frac{\partial B}{\partial z}\Big|_{h_1} \qquad (24)$$

$$E_r|_{h_2} = E_r|_{h_1} + t \cdot \frac{\partial E_r}{\partial z}\Big|_{h_1} \qquad (25)$$

Equations (24) and (25) may be modified using Maxwell's equations so that they correct the regions $0 < z < h_1$ and $h_2 < z < \infty$ directly. The fields or the field derivatives used must be continuous either across h_1 or across h_2. In this way, the Helmholtz differential equation (3) in the two regions may be solved without explicitly finding a solution to the equation within the layer. The resulting boundary conditions are

$$B|_{h_2} = B|_{h_1} - \mu S E_r|_{h_1} \qquad (26)$$

$$E_r|_{h_2} = E_r|_{h_1} + (T/\mu)\frac{\partial}{\partial r}\left(\frac{1}{r}\frac{\partial}{\partial r}(rB)\right)\Big|_{h_1} - i\omega t B|_{h_1} \qquad (27)$$

and they must describe the physics of the interaction of the layer with its environment. At the MMR static limit, if the layer is conductive, the electric component E_r is continuous through it and the conductivity-thickness product S may be found. In contrast, if the layer is resistive, the magnetic field B is continuous though it and the resistivity-thickness product T may be found.

The method of obtaining the magnetic field is a continuation of the theory already described. General solutions to the Helmholtz equation have to be assigned in the two crustal regions outside the layer and the arbitrary constants determined by applying the standard boundary conditions on z = 0 and the special boundary conditions (26) and (27) across the layer.

Results

The MMR-Type Curves

The magnetic fields at the low frequency static limit given in expressions (18) and (19) have been plotted as a function of r/d in Figure 1. The contrast in resistivity ρ_c/ρ_o between the oceanic crust and the sea water ranges from 1 to 100. The vertical axis is in nanotesla

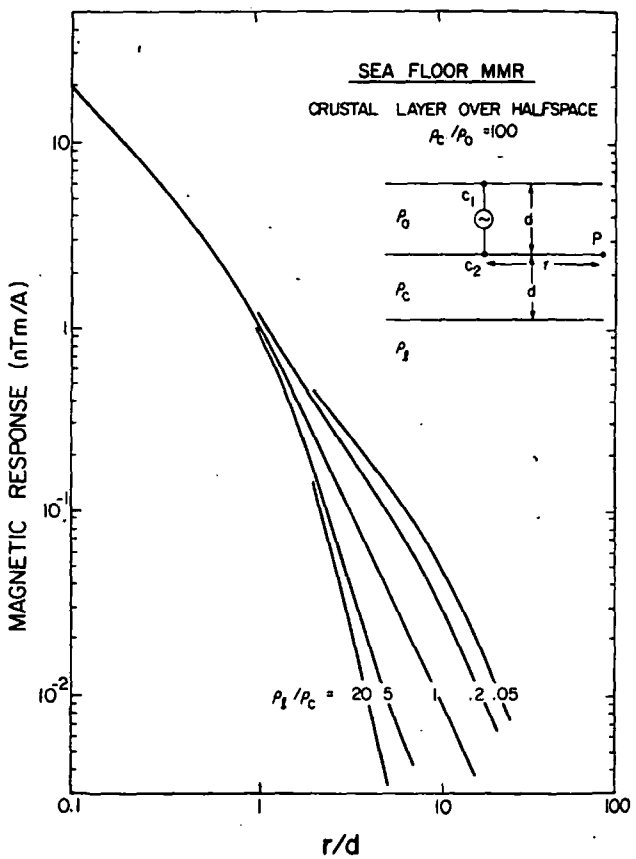

Fig. 3. The effect on the magnetic field of a conductive or resistive lower half space of resistivity different from that of the crust. The oceanic resistivity is one hundredth of the crustal resistivity.

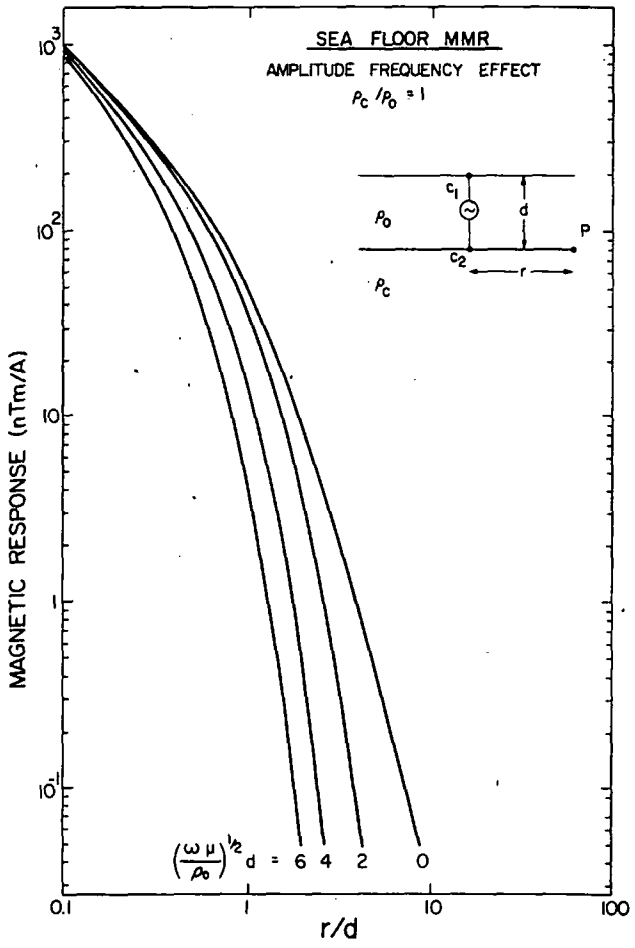

Fig. 4a. The effect of frequency on the MMR sounding curve. The crustal and oceanic resistivities are equal.

(gamma) per ampere of current flow for a value of d of 1 m. If d is larger by a factor m than 1 m, then the fields shown should be reduced by m.

As the ratio ρ_c/ρ_o increases, the rate at which the field falls off with r/d changes from an inverse fourth power to an inverse square law as predicted by expressions (19) and (23). For r/d and ρ_c/ρ_o large, the field is almost proportional to ρ_c/ρ_o, again as predicted by expression (23). This lack of any asymptotic behavior is the most striking and promising feature of the curves. Assuming that the resistivity of the sea water is known, it is sufficient to measure the magnetic field to an accuracy of 10% to obtain the resistivity of the crust to the same degree of accuracy. It is also clear that estimates of ρ_c/ρ_o may be made at relatively short separations between the transmitter and the receiver.

The effect of a thin conductive or resistive intermediate layer is illustrated in Figure 2. Shown is one of the set of many possible type curves, the one for a principal contrast in resistivity between the sea water and the crust of 100. The layer is at a depth d and its conductivity-thickness product S and resistivity-thickness product T have been normalized by the scale length d and the resistivity of the crust ρ_c. The dimensionless channelling numbers produced, $T/\rho_c d$ and $S\rho_c/d$, have values of 10 and 100. To a first approximation, the gross distortion of the basic central sounding curve for a channelling number N should be confined to the range $1 < r/d < N$.

The effect of a conductive or a resistive lower half space located at a depth d of resistivity ρ_ℓ different from ρ_c is illustrated in Figure 3. The type curves are complementary to those of Figure 2, the principal ratio ρ_c/ρ_o being again 100. Unlike the curves for the thin layer, these sounding curves remain offset from and appear to parallel the basic central sounding curve for all large values of r/d.

Overall, Figures 2 and 3 leave the impression that schemes of interpretation of a layered earth could be developed akin to those of the standard resistivity method. The attractive feature of the MMR sounding technique is that both a layer and a lower half space buried at a depth d are clearly visible at values of r/d not much greater than 2. Tentatively, the 'depth of exploration' of the system is about one half the transmitter-receiver horizontal separation.

The Effect of Frequency

In computing the MMR curves, we have assumed a static dc approximation. In practice, it is most desirable to use an alternating current of as high a frequency as possible in order to minimize the time required to stack the magnetic field signal and obtain an adequate signal to noise ratio. The effect of frequency on the MMR curves was outlined earlier. The curves are distorted not by skin effects in the ocean but by skin effects in the crust, provided there is a large contrast in resistivity between the ocean and the crust. This is illustrated in Figure 4 by adding to the MMR sounding curves, transcribed from Figure 1 for resistivity contrasts ρ_c/ρ_o of 1 and 100, respectively, additional curves for which the oceanic electromagnetic response number

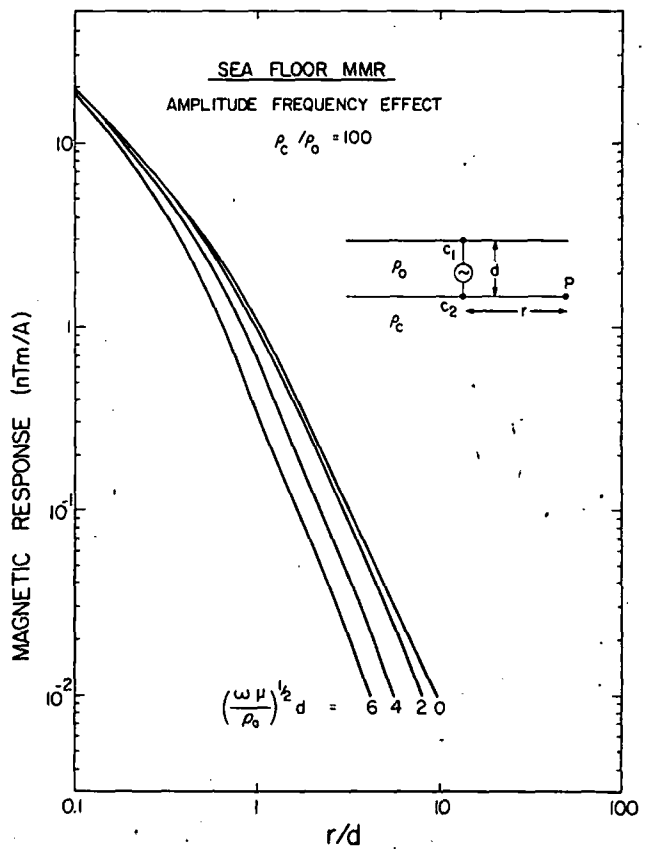

Fig. 4b. The effect of frequency on the MMR sounding curve. The oceanic resistivity is one hundredth of the crustal resistivity.

$(\omega\mu/\rho_o)^{1/2}$ d is varied from 2 to 6. When the ratio of resistivities is only 1 (Figure 4a), a severe depression of the type curves is evident as the response number, and the ratio r/d increases. The MMR approximation is not appropriate over the range of r/d shown unless the response number is very small compared with unity. However, when the ratio of resistivities is 100 (Figure 4b), a considerable improvement is apparent. The MMR approximation is valid to a few percent for r/d less than 10 provided that the oceanic response number is no greater than unity. A more complete picture of the effect is of course obtained by inspecting expression (22). The crustal electromagnetic response number controls the validity of the MMR curves. It is only one tenth of the oceanic number for this case.

The curves of Figures 1, 2, 3, and 4 are given primarily as an aid to experimental design. They provide estimates of magnetic field strength, of the effects of frequency and of suitable ranges for the separation r/d. In practice, where frequencies are pushed upward to the limit of MMR validity, we would include inductive effects in a numerical generalized inverse analysis. The additional computer time involved is minimal, and as demonstrated by expression (23), the inclusion of phase data provides independent absolute estimates of crustal conductivity.

Systematic Experimental Error

The MMR method described is a null method. The magnetic field on the seafloor is sensitive to the current entering the crust, and hence the crustal resistivity, because the magnetic field of the current in the wire and the return current in the ocean almost cancel each other. The null is maintained provided the current flow in the ocean has axial symmetry. A systematic deviation from this symmetry is experimentally possible. Unknown ocean currents could deflect the current carrying wire from the vertical for the duration of an experiment. The resulting erroneous or perturbation current flow is the difference between the current flowing downwards in a straight wire and that in a bent wire. In Figure 1 the dashed line is the perturbation field of one such flow. The wire is bent into a circular arc with a maximum deviation at half depth of 1% of the depth. The measurement point P is in the plane of the arc. Notice that the rate falls off with r/d as an inverse cube. (The perturbation current can be considered the superposition of many current loops or magnetic dipoles stretched between the sea surface and the seafloor.) In contrast, the fall off with r/d of the magnetic field of the current in the crust at large resistivity contrast is as an inverse square law. It is at large resistivity contrast that small magnetic fields are to be expected and the effect of systematic error most visible. Luckily, the effect is not as disturbing as it might be because of its greater rate of decline with distance.

Experimental

The implementation of the method is principally a problem in logistics. An overnight period of about 8 hours is a sensible upper limit for the time to take a single measurement. A ship can keep station to a few tens of meters for this length of time for reasonable sea states. On successive nights, other transmitter locations are occupied, at progressively increasing horizontal distance away from a preprogramed recording seafloor magnetometer. In this way, the sounding curve may be obtained.

What is the maximum range? It is instructive to calculate a typical value. Let us select reasonable values for the parameters I, d, ρ_o, and ρ_c of 20 A, 2 km, 0.25 Ωm, and 25 Ωm, respectively. The ratio ρ_c/ρ_o is 100. From Figure 4b, the MMR sounding curves are applicable for a maximum angular frequency ω given by $d\sqrt{\omega\mu/\rho_o} = 2$, provided the range r is not greater than 20 km. The corresponding minimum period $2\pi/\omega$ is 32 s. Commercial flux gate magnetometers capable of just distinguishing a square 1-pT input signal of this period from intrinsic instrumental noise are available. They can be modified and launched in conventional ocean floor pressure vessels. Synchronous detection over a period of 8 hours would enable the same signal to be measured to an accuracy of 3.3%. Referring to Figure 1, the 1 pT level for the parameters given is crossed at a range of about 6 km. A relatively accurate sounding can be obtained to this range. At larger ranges, the accuracy deteriorates, but it is adequate to ranges of 20 km. The calculation of a maximum range is again only a guide to experimental design. In practice, a single period would not be used: The period and averaging time increase with range. The calculation also ignores natural geomagnetic noise. Our knowledge of this noise on the ocean floor at periods shorter than a few minutes at the 1-pT level is sparse. Whether it can be overcome remains to be seen. It does have a different spatial character from the controlled signal so that it could be removed by differential measurements.

Conclusions

Our aim in this short thesis was to put forward a logistically-simple method of determining the resistivity of the lithosphere beneath the ocean. The magnetic field on the seafloor of a vertical bipole source was determined using the full quasi-static theory including the effects of electromagnetic induction. The reduction to the static MMR approximation revealed the importance of the skin effect in the crust rather than in the ocean. Type curves for simple layered structure resembled those for the resistivity method. They enabled a theoretical depth of penetration to be obtained as about one half the transmitter-receiver separation. Signal to instrumental noise considerations set the penetration into the lithosphere at about 10 km with readily adaptable apparatus. The penetration can be increased with larger transmitter currents and improved receiver instrumentation. The unknown factor is the electromagnetic noise level at the seafloor which may limit extension to greater depths.

Acknowledgements. The importance of seafloor electromagnetic measurements was stressed by Sir Edward Bullard to his graduate students in the late 1960s. At that time, many seafloor magnetometers were constructed; several were deployed, few were recovered. Only recently have advances in technology made such measurements routinely possible. It was Teddy's overriding enthusiasm that encouraged some of us to persevere. One of the authors (R.N.E.) would like to thank the staff of the Pacific Geoscience Centre for the hospitality accorded him during a brief sabbatical leave. The work was supported in part by a grant from the Natural Science and Engineering Research Council of Canada. Earth Physics Branch contribution 953.

References

Bannister, P. R., Determination of the electrical conductivity of the sea bed in shallow waters, Geophysics, 33, 995-1002, 1968.

Coggon, J. H., and H. F. Morrison, Electromagnetic investigation of the sea floor, Geophysics, 35, 476-489, 1970.

Cox, C., Electromagnetic induction in the oceans and inferences on the constitution of the earth, Geophys. Surv., 4, 137-156, 1980.

Cox, C. S., T. K. Deaton, and P. Pistek, An active source E-M method for the seafloor, submitted to Radio Sci., 1981.

Duncan, P. M., A. Hwang, R. N. Edwards, R. C. Bailey, and G. D. Garland, The development and applications of a wide-band electromagnetic sounding system using a pseudo-noise source, Geophysics, 45, 1276-1296, 1980.

Edwards, R. N., The magnetometric resistivity (MMR) method and its application to the mapping of a fault, Can. J. Earth Sci., 11, 1136-1156, 1974.

Edwards, R. N., H. Lee, and M. N. Nabighian, On the theory of magnetometric resistivity (MMR) methods, Geophysics, 43, 1176-1203, 1978.

Filloux, J. H., Ocean floor magnetotelluric sounding over the north-central Pacific, Nature, 269, 297-301, 1977.

Filloux, J. H., Magnetotelluric soundings over the northeast Pacific may reveal spatial dependence of depth and conductance of the asthenosphere, Earth Planet. Sci. Lett., 46, 244-252, 1980.

Gradshteyn, I. S., and I. M. Ryshik, Tables of Integrals, Series, Products, Academic, New York, 1965.

Jupp, D.L. B., and K. Vozoff, Stable iterative method for the inversion of geophysical data, Geophys. J. R. Astron. Soc., 42, 957-976, 1975.

Keen, C., and C. Tramontini, A seismic refraction survey on the Mid-Atlantic Ridge, Geophys. J. R. Astron. Soc., 20, 473-492, 1970.

Law, L. K., and J. P. Greenhouse, Geomagnetic variation sounding of the asthenosphere beneath the Juan de Fuca Ridge, J. Geophys. Res., 86, 967-978, 1981.

Oldenburg, D. W., Conductivity structure of the upper mantle beneath the Pacific plate, Geophys. J. R. Astron. Soc., 65, 359-394, 1981.

Raitt, R. W., G. G. Shor, T. J. G. Francis, and G. B. Morris, Anisotropy of the Pacific upper mantle, J. Geophys. Res., 74, 3095-3109, 1969.

(Received September 2, 1980;
revised January 6, 1981;
accepted March 24, 1981.)

JOURNAL OF GEOPHYSICAL RESEARCH, VOL. 86, NO. B5, PAGES 3783–3790, MAY 10, 1981

Microearthquake Activity on the Orozco Fracture Zone: Preliminary Results From Project ROSE

PROJECT ROSE SCIENTISTS[1]

We present preliminary hypocenter determinations for 52 earthquakes recorded by a large multi-institutional network of ocean bottom seismometers and ocean bottom hydrophones in the Orozco Fracture Zone in the eastern Pacific during late February to mid-March 1979. The network was deployed as part of the Rivera Ocean Seismic Experiment, also known as Project ROSE. The Orozco Fracture Zone is physiographically complex, and the pattern of microearthquake hypocenters at least partly reflects this complexity. All of the well-located epicenters lie within the active transform fault segment of the fracture zone. About half of the recorded earthquakes were aligned along a narrow trough that extends eastward from the northern rise crest intersection in the approximate direction of the Cocos-Pacific relative plate motion; these events appear to be characterized by strike-slip faulting. The second major group of activity occurred in the central portion of the transform fault; the microearthquakes in this group do not display a preferred alignment parallel to the direction of spreading, and several are not obviously associated with distinct topographic features. Hypocentral depth was well resolved for many of the earthquakes reported here. Nominal depths range from 0 to 17 km below the seafloor.

INTRODUCTION

The Rivera Ocean Seismic Experiment (ROSE) is a multi-institutional study of the structural evolution of young oceanic crust and mantle and of the structure and tectonics of an active transform fault [*Wilson*, 1965] using a large network of ocean bottom seismometers (OBS) and ocean bottom hydrophones (OBH) [*Ewing*, 1979]. The field work for Project ROSE consisted of two phases during January to March 1979. In Phase I a number of seismic refraction lines were shot both parallel and perpendicular to isochrons on 0- to 4-m.y.-old seafloor near the East Pacific Rise at 11° to 13°N latitude. Phase II consisted of a predominantly passive survey of microearthquake activity on the Orozco transform fault and adjacent rise axis areas. Groups from 12 institutions, including the University of California at San Diego and at Santa Barbara, University of Hawaii, Instituto Oceanográphico at Manzanillo, Lamont-Doherty Geological Observatory, Massachusetts Institute of Technology (MIT), Naval Ocean Research and Development Activity, Naval Research Laboratory, Oregon State University, University of Texas, University of Washington, and Woods Hole Oceanographic Institution (WHOI), participated in the field work, conducted from five research vessels (R/V *Robert Conrad*, R/V *Kana Keoki*, R/V *Thomas Thompson*, USNS *De Steiguer*, USNS *Hayes*). A total of 67 ocean bottom seismometers and hydrophones as well as several hydrophone arrays were deployed, and several multichannel seismic lines were also run. This paper presents the preliminary locations of the largest microearthquakes recorded by the OBS and OBH array in the Orozco Fracture Zone during phase II of ROSE.

The Orozco transform fault, at approximately 15.25°N latitude, offsets the East Pacific Rise left laterally by about 90 km (Figure 1). The local spreading rate is 49 mm/yr (half-rate) with an azimuth of N85°E, based on the Cocos-Pacific pole of *Minster and Jordan* [1978]. Thus the maximum age contrast across the transform is about 2 m.y. at present. The large-scale topographic manifestation of the Orozco Fracture Zone (Figure 1) belies this modest offset and is a reflection of a past tectonic configuration. The complicated bathymetry to the west of the current spreading center has been interpreted to contain the signature of a number of eastward jumps of the spreading center [*Sclater et al.*, 1971; *Lynn and Lewis*, 1976]. Before a proposed jump 4–5 m.y. ago, the Orozco Fracture Zone may have marked the boundary between the Rivera and Pacific plates, a role currently played by the Rivera Fracture Zone [*Klitgord and Mammerickx*, 1979].

A number of microearthquake surveys in oceanic transform fault and ridge crest areas have been conducted with sonobuoys and with ocean bottom seismometers [*Francis and Porter*, 1973; *Reid et al.*, 1973, 1977; *Reid and Macdonald*, 1973; *Spindel et al.*, 1974; *Macdonald and Mudie*, 1974; *Prothero et al.*, 1976; *Reichle et al.*, 1976; *Reichle and Reid*, 1977; *Solomon et al.*, 1977; *Francis et al.*, 1977, 1978; *Lilwall et al.*, 1977, 1978; *Johnson and Jones*, 1978; *Jones and Johnson*, 1978]. Because all such previous studies have been conducted with at most a few stations, the epicentral location capabilities have been quite limited, and the focal depth resolution generally poor. Thus the detailed relationship between epicenter locations and specific physiographic features has often been suspect, and the important information from focal depths on deep thermal and mechanical structure has typically been absent in such surveys. Project ROSE is unprecedented in the large number of ocean bottom stations deployed in concert for a dedicated experiment of oceanic earthquake characterization. Because of the large OBS and OBH network the epi-

[1] Project ROSE scientists providing data for this study include J. I. Ewing and G. M. Purdy at the Department of Geology and Geophysics, Woods Hole Oceanographic Institution, Woods Hole, Massachusetts 02543; A. M. Tréhu and S. C. Solomon at the Department of Earth and Planetary Sciences, Massachusetts Institute of Technology, Cambridge, Massachusetts 02139; T. Ouchi and A. K. Ibrahim at the Marine Science Institute, University of Texas, Galveston, Texas 77550; J. F. Gettrust and K. Furukawa at the Hawaii Institute of Geophysics, University of Hawaii, Honolulu, Hawaii 96822; S. P. Nishenko and P. W. Pomeroy at Lamont-Doherty Geological Observatory, Columbia University, Palisades, New York 10964; W. A. Prothero at the Department of Geological Sciences, University of California at Santa Barbara, Santa Barbara, California 93106; J. D. Garmany and B. T. R. Lewis at the Department of Oceanography, University of Washington, Seattle, Washington 98195; and S. H. Johnson and L. D. Bibee at the School of Oceanography, Oregon State University, Corvallis, Oregon 97331. Epicenter locations were calculated by A. M. Tréhu.

Paper number 80B1528.
0148-0227/81/080B-1528$01.00

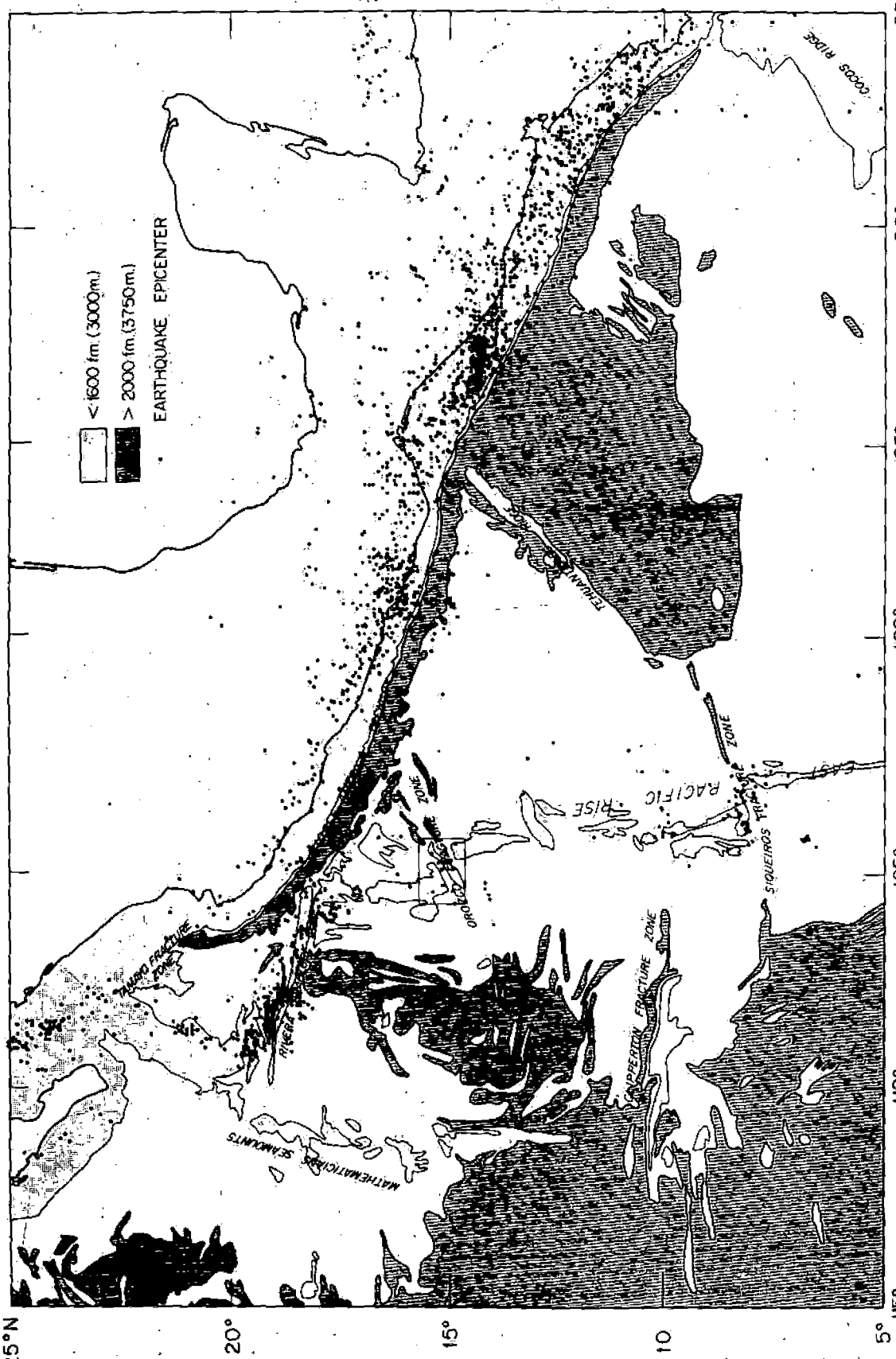

Fig. 1. Bathymetry and seismicity within the general region of the ROSE experiment. Bathymetric contours adapted from *Chase et al.* [1969]. The 1600-fm (3000 m) and 2000-fm (3750 m) contours are adequate to illustrate the major physiographic features of the region; depths less than 1600 fm are lightly shaded, and depths greater than 2000 fathoms are darkly shaded (*small isolated seamounts are not included*). Earthquake epicenters are from the U.S. Geological Survey *Preliminary Determination of Epicenters* and include teleseismically recorded events with focal depth less than 70 km during the time period 1964–1977. *The box centered at 15°N, 105°W delimits the area of Figure 3.*

central locations, focal depths, and other source parameters of the earthquakes recorded during ROSE phase II are unusually well constrained.

Fifty-two earthquakes which occurred during the 2-week period from February 27 to March 13 have been located using arrival times from the OBS and OBH network during the second phase of ROSE. All of the well-located events are within what one would expect to be the active portion of the transform, and many are clearly associated with topographic features. More detailed analysis of our data and discussions of the tectonic significance of our findings will be presented in later publications.

DATA

Data from 26 instruments belonging to 8 institutions were used for the locations. The important features of these instruments and their geographic coordinates during deployment are summarized in Tables 1*a* and 1*b*. This data set represents approximately two thirds of the instruments operating during the second phase of the ROSE project. Figure 2 shows histograms of the number of events per 12-hour period observed by these instruments. *P*-wave arrival time readings were obtained from all stations; *S*-wave arrival times could only be picked to the desired accuracy from those stations equipped with two horizontal components.

Depth corrections were calculated to normalize all stations to a water depth of 3000 m. A *P*-wave velocity of 6.5 km/s was assumed in making this correction, and *S*-wave arrival times were corrected by assuming a ratio of *P*-wave to *S*-wave velocity of 1.75. All times were also corrected for clock drift assuming a constant drift rate during the time of deployment. Total clock drift over a period of a month was on the order of 0.25 seconds for most instruments.

Reading errors in picking the arrival times were less than 0.04 s for most of the events and most of the instruments. Possible nonsteady clock drift and errors in the instrument location, however, increase the effective arrival time errors to about 0.08 s when the whole network is considered.

LOCATION METHOD

Earthquakes were located using the computer program HYPOINVERSE developed by the U.S. Geological Survey [*Klein*, 1978]. The nonlinear nature of the earthquake location problem is well known, as is its linear approximation in the form $[A] \cdot [x] = [b]$, where $[A]$ is an $n \times 4$ matrix of the travel time derivatives, $[x]$ is a 4-dimensional vector of adjustments to an assumed hypocenter and origin time, and $[b]$ is an n-dimensional vector of differences between the observed arrival times and those calculated for the assumed hypocenter. Because HYPOINVERSE solves for $[x]$ by doing a singular value decomposition on $[A]$ and calculating the generalized inverse of $[A]$, the method provides the resolution, covariance and data importance matrices. Moreover, by explicitly calculating the singular values and singular vectors of $[A]$, the method points out small singular values representing directions in which the hypocentral adjustment vector is poorly constrained by the data. The capacity to truncate small singular values and to damp adjustments in such directions increases the stability of the inversion. A reading error of 0.08 was assumed for the calculation of the covariance matrix.

Another important feature of the location algorithm is that it assigns weights to the observed arrival times as a function of

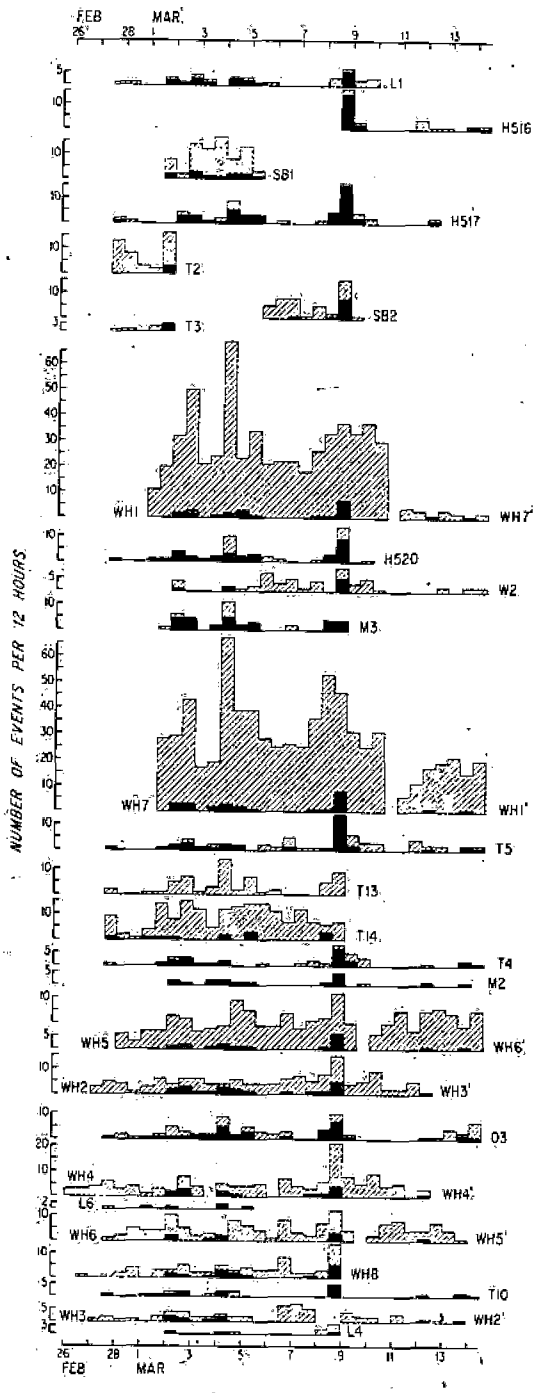

Fig. 2. Histograms of earthquake activity per half day observed during phase II of ROSE. The instrument identification codes are given in Table 1. Histograms for all instruments providing readings for this study are included and are stacked from top to bottom in order of decreasing latitude. The hatched area represents all events reported for the instrument, whereas the solid area represents only those earthquakes located in this study and listed in Table 3. No arrival times from T13 were used for the locations. The great number of events reported from the WHOI instruments is partly an artifact of the method of defining an 'event.' For the continuously recording WHOI instruments, any discrete event with a maximum amplitude of at least twice the background noise level was defined as an event; for many of these it is impossible to pick a first arrival. For the other instruments, only those events whose arrival time had been determined were included. Note also that instruments SB1, SB2, T2, and T14 recorded many, presumably very nearby events which were not recorded by enough instruments to permit a location to be calculated.

Earthquake epicenters are from the U.S. Geological Survey Preliminary Determination of Epicenters and include teleseismically recorded events with focal depth less than 70 km during the time period 1964–1977. The box centered at 15°N, 105°W delimits the area of Figure 3.

TABLE 1*a*. Characteristics of Ocean Bottom Seismometers and Hydrophones Used for This Study

Institution	Institution Abbreviation	Components*	Recording†	Reference
University of California at Santa Barbara	SB	V, H, H	D, E	*Prothero* [1979]
University of Hawaii	H	V, H, P	A, C	*Sutton et al.* [1977]
Lamont-Doherty Geological Observatory	L	V, P	A, C	*Bookbinder et al.* [1978]
Massachusetts Institute of Technology	M	V, H, H	D, E	*Mattaboni and Solomon* [1977]
Oregon State University	O	V, P	A, C	*S. H. Johnson et al.* [1977]
University of Texas at Galveston	T	V	A, E	*Latham et al.* [1978]
University of Washington	W	V, H, H	A, C	*R. V. Johnson et al.* [1977]
Woods Hole Oceanographic Institution	WH	P	A, C	*Koelsch and Purdy* [1979]

*V, vertical geophone; H, horizontal geophone; P, hydrophone.
†D, digital; A, analog; E, event detection; C, continuous.

the residual from the previous iteration. This provision is useful for pointing out arrival time readings which are grossly in error, such as in the case of a misidentification of phase. For the first iteration, *P*-wave arrival times were assigned a weight of 1. To compensate for larger arrival time reading errors combined with the inherently greater importance of these readings toward the solution, *S*-wave arrival times were weighted by a factor of 0.75. A complete description of the location program is given by *Klein* [1978].

The assumption that [*A*] is known implies that the velocity structure is known. We assumed that the *P*-wave velocity structure was a stack of 9 homogeneous, flat layers approxi-

TABLE 1*b*. Geographic Coordinates of Instruments During Phase II of ROSE

Instrument	Latitude		Longitude		Depth (Corrected Meters)
	Degrees	Minutes	Degrees	Minutes	
L1	15	30.30	105	25.98	2800
H516	15	29.60	105	5.30	2842
SB1	15	26.20	105	4.40	2801
H517	15	25.40	104	56.60	3883
T2	15	25.20	105	15.10	3010
SB2	15	21.70	105	2.00	3032
T3	15	18.16	105	12.76	3041
WH1	15	13.98	104	54.72	2678
WH7′	15	13.98	104	54.48	2740
H520	15	12.70	104	55.10	2725
W2	15	10.50	105	18.50	3388
M3	15	9.30	104	55.32	2855
WH7	15	9.18	104	50.58	2863
WH1′	15	9.12	104	52.38	2890
T5	15	8.70	105	11.30	3572
T13	15	6.92	104	38.73	3214
T14	15	6.67	104	31.27	2791
T4	15	6.10	105	27.10	3090
M2	15	5.58	104	56.22	2856
WH6′	15	3.42	104	45.18	2203
WH5	15	1.98	104	44.88	2517
WH3′	14	59.88	105	16.50	3013
WH2	14	59.10	105	16.98	2996
O3	14	58.43	104	50.14	4068
WH4	14	54.90	105	8.52	3098
WH4′	14	53.82	105	8.01	3090
L6	14	52.38	104	30.00	2966
WH5′	14	51.00	104	44.40	2678
WH6	14	50.52	104	44.40	2715
WH8	14	49.68	105	22.62	3184
T10	14	48.43	104	59.43	3347
WH2′	14	40.80	105	15.00	3311
WH3	14	40.38	105	15.72	3329
L4	14	31.32	105	15.35	3203

In the instrument identifications the letters refer to the institution abbreviations of Table 1*a*, and the numbers to each institution's numbering scheme. The 'primed' WHOI identifications correspond to the position of each instrument after being redeployed. Because the tape capacity of the WHOI instruments is about 8 days, most were retrieved and redeployed midway through phase II.

mating a two-layer crust with velocity gradients in each layer (Table 2). This structure was based on the results obtained from line B of *Orcutt et al.* [1976] and line 57 of *Lewis and Snydsman* [1979], refraction profiles shot parallel to the spreading center to the south of the ROSE study area at 9°N and 13.5°N on crust with ages of 2.9 and 0.4 m.y., respectively. The *S*-wave velocity model was obtained from the *P*-wave model assuming a *P*-wave to *S*-wave velocity ratio of 1.75.

EARTHQUAKE LOCATIONS

The hypocentral parameters of the earthquakes located during phase II of ROSE are presented in Table 3. All events located with a root-mean-squared residual of less than 0.25 s are included. Although data from 26 stations were used, no event was recorded by all stations. Thirteen earthquakes were located using at least 15 arrival time readings. Most locations calculated from only four or five readings are supported by temporal and spatial association with a larger, well-located earthquake and by a *P-S* arrival time interval in agreement with that measured on the MIT instruments. An initial hypocenter close to the station reporting the earliest arrival was assumed. The locations were calculated twice, starting from initial depths of 5 and 12 km. For most events the two initial hypocenters converged to the same solution. For a few events, however, two different depths were obtained. An examination of the behavior of the root-mean-squared residual with depth when locations were calculated for a series of fixed depths from 2 to 20 km indicated that this behavior could be attributed to a constant residual with depth over an interval around one of the initial depths. In these cases the solution giving the smaller residual was chosen; with the exception of four events (March 2, 1300 hours; March 2, 1721 hours; March 3, 1724 hours; March 4, 2010 hours) this was the shallower solution.

The axes of the covariance matrix of the hypocentral solution define the 32% confidence ellipse of the solution to the linearized problem. The 95% confidence ellipse can be obtained by multiplying the axis lengths by 2.4. Because the problem is not linear, these ellipses provide only a qualitative measure of the precision of the location. The projections of these axes onto horizontal and vertical planes through the hypocenter are listed in Table 3 as measures of the horizontal and vertical errors in the solution. Only the larger of the two horizontal errors is listed. These formal errors suggest that most of the earthquake locations are precise to within 1 or 2 km in the horizontal direction and point out those events for which the geometry of the available data provides little constraint on the hypocentral depth.

Locating events with other layered crustal models or with different subsets of the data did not change the absolute or relative locations significantly. For example, substitution of the 'average oceanic crust' of *Raitt* [1963] resulted in a change in the calculated hypocenter of less than 1 km horizontally and less than 2 km vertically for most events.

Although most of the earthquakes were not detected by all of the instruments, the large number of instruments deployed during ROSE was useful for two reasons. It obviously extended the spatial extent of the area of good hypocentral resolving power of the network compared to the much smaller networks of instruments used in earlier studies. Equally importantly, however, the large number of stations led to the detection of errors in data processing which might otherwise have been undetected and would have therefore led to erroneous locations. An examination of the residuals at each station for those events located using 18 or more arrivals revealed systematic trends which could be traced to errors in the clock drift correction for a few instruments. Small events located using only 4–6 arrival times including these erroneous data often seemed to be well located (as indicated by small root-mean-squared residuals and covariance ellipses) when actually their locations were in error by several kilometers.

The calculated epicenters are superimposed on a map of the local bathymetry in Figure 3. The bathymetric map includes data obtained during Project ROSE and indicates a complex tectonic environment. The transform fault is marked by a 90-km² area of dramatic topography. Most of the earthquake activity was localized in two areas and is visibly related to topographic features.

About one half of the earthquakes located occurred in the northwestern portion of the transform area and were aligned along a long, narrow trough with a strike of N80°E. That this trend probably represents the current spreading direction is supported by the predicted Cocos-Pacific spreading direction [*Minster and Jordan*, 1978], by nearby magnetic anomalies [*Klitgord and Mammerickx*, 1979], by a teleseismic study of a large ($m_b = 5.1$) event from the transform (A. M. Tréhu, work in progress, 1981), and by the trend of anisotropy beneath a possible low-velocity zone in the upper mantle (G. M. Purdy, work in progress, 1981). During the period of the experiment, activity was distributed along the length of the trough. During March 1–4, activity occurred at the eastern and western extremities of the trough. Following a period of quiet during March 5–7, a main shock–aftershock sequence occurred near the center of the trough on the afternoon of March 8.

These events seem to have occurred over a broad range of depths. The calculated locations of many of the events from the westernmost end of the trough indicate a source in the upper mantle, whereas the events of the March 8 sequence seem to have been very shallow, within the upper crust. This interpretation is supported by the observation on the seismograms obtained by the MIT instruments of what is interpreted to be a mantle refraction as the first arrival from the largest events of March 8. This phase cannot be observed from the events at the westernmost end of the trough. Confirmation of these depth determinations will require a reexamination of the records in an attempt to identify characteristics diagnostic of the source depth. The calculated depths might also be a consequence of the simple layered velocity model. The polarity of the first motion observed on the MIT, WHOI, Lamont, Ha-

TABLE 2. Layered *P*-Wave Velocity Model Used for Earthquake Locations

Layer	Velocity, km/s	Depth, km	Thickness, km
1	4.38	0.00	0.40
2	5.00	0.40	0.40
3	5.62	0.80	0.40
4	6.05	1.20	0.80
5	6.39	2.00	1.00
6	6.73	3.00	1.00
7	7.07	4.00	1.00
8	7.42	5.00	1.00
9	7.72	6.00	0.65
10	7.84	6.65	

TABLE 3. Hypocentral Parameters of Earthquakes Recorded During the Second Phase of ROSE

Orgin Time		Latitude		Longitude		Depth,	nor		mag,	dcs,	rmsr,	erh,	erd,
Date 1979	UT	Degrees	Minutes	Degrees	Minutes	km	P	S	deg	km	s	km	km
Feb. 27	2238:36.31	15	13.17	104	47.71	0.85	7	0	147	13.3	0.24	1.3	4.5
March 1	1150:7.12	15	4.68	104	38.14	3.56	4	2	191	12.8	0.07	0.8	pdc
March 1	1216:23.12	15	21.54	105	17.84	5.20	2	3	271	8.3	0.02	0.8	1.2
March 1	1457:51.17	15	22.52	105	14.40	0.10	6	2	90	5.1	0.19	0.7	2.0
March 1	1506:34.58	15	23.14	105	13.79	8.52	3	2	199	4.4	0.01	2.2	0.8
March 2	0523:10.70	15	14.97	104	44.13	11.47	19	2	218	15.8	0.14	1.0	1.7
March 2	0718:4.85	15	24.90	104	57.76	3.00	13	2	144	2.2	0.08	1.1	1.1
March 2	0854:5.74	15	6.88	104	49.14	10.04	3	1	323	4.9	0.00	2.4	1.4
March 2	1300:20.92	15	24.18	105	12.82	17.05	13	2	140	15.5	0.09	0.5	1.5
March 2	1335:1.57	15	6.47	104	49.22	10.15	3	1	322	5.5	0.00	2.6	1.5
March 2	1645:8.41	15	23.38	105	12.40	0.00	8	1	131	15.2	0.12	0.5	1.4
March 2	1721:9.48	15	24.24	105	11.96	14.18	15	2	139	14.0	0.09	0.5	2.2
March 3	1724:58.03	15	24.72	105	13.16	12.48	16	2	224	15.9	0.09	0.7	2.5
March 3	2311:59.89	15	10.94	104	49.17	5.22	4	2	290	4.1	0.12	1.2	2.2
March 4	0919:23.83	15	12.35	104	47.19	3.35	18	3	144	8.5	0.15	0.6	1.1
March 4	0937:47.56	15	12.73	104	48.75	11.99	4	1	216	11.3	0.11	1.0	pdc
March 4	0942:18.27	15	12.49	104	47.32	7.80	19	1	144	8.5	0.14	0.6	2.0
March 4	1001:7.85	15	12.00	104	47.27	6.16	4	1	226	14.0	0.13	1.1	pdc
March 4	1012:53.66	15	12.48	104	47.83	8.19	4	1	223	13.0	0.12	1.1	pdc
March 4	1037:12.09	15	9.50	104	50.83	5.77	4	0	199	0.8	0.00	1.4	0.7
March 4	1053:8.26	15	9.47	104	49.79	11.64	4	1	204	9.9	0.05	1.5	pdc
March 4	1121:17.06	15	25.62	104	59.15	0.46	8	0	174	4.6	0.11	1.1	3.7
March 4	1459:45.84	15	18.92	104	45.95	1.84	7	1	233	18.1	0.08	0.8	1.7
March 4	1856:5.16	15	25.24	105	0.22	2.55	15	2	163	6.4	0.10	1.0	13
March 4	2010:37.27	15	23.80	105	12.44	15.04	8	1	135	15.0	0.07	0.6	1.6
March 5	0058:14.75	15	44.28	104	44.18	18.18	6	0	297	41.4	0.15	3.6	6.5
March 5	0219:4.28	15	13.08	104	47.88	8.82	9	2	145	12.9	0.10	0.6	2.1
March 5	1010:27.31	15	18.58	104	44.46	17.21	9	1	192	20.2	0.10	0.9	3.6
March 6	2305:13.10	15	23.65	105	0.51	8.13	3	1	356	4.5	0.09	2.7	pdc
March 7	1643:31.65	15	26.55	105	12.41	0.78	8	1	259	20.6	0.07	1.9	2.7
March 8	0002:35.97	15	13.05	104	47.67	8.81	6	1	145	8.9	0.09	0.6	2.7
March 8	0023:55.33	15	12.87	104	48.46	0.08	4	1	178	7.8	0.14	2.6	2.8
March 8	0058:5.39	15	13.33	104	47.23	4.17	14	2	149	9.8	0.14	0.6	1.5
March 8	0131:55.08	15	13.81	104	47.54	0.12	4	1	151	16.3	0.03	0.4	1.2
March 8	1214:26.42	15	24.06	105	7.06	0.00	18	1	88	10.1	0.08	0.3	1.0
March 8	1219:0.53	15	24.04	105	6.43	0.11	16	2	82	9.0	0.11	0.4	1.0
March 8	1238:22.63	15	24.06	105	6.90	0.30	16	3	147	9.0	0.12	0.4	1.0
March 8	1250:17.03	15	25.63	105	7.41	8.56	4	1	187	8.3	0.03	1.0	2.9
March 8	1258:1.94	15	6.30	104	45.38	0.93	3	1	286	18.6	0.18	1.8	5.3
March 8	1339:26.56	15	23.87	105	6.08	0.18	6	0	86	8.4	0.10	0.5	pdc
March 8	1432:18.41	15	24.49	105	5.32	0.06	7	0	83	7.8	0.13	0.9	6.9
March 8	1445:54.67	15	24.31	105	5.50	0.79	6	0	87	7.9	0.03	0.6	3.4
March 8	1451:59.77	15	24.02	105	6.29	0.22	7	0	91	8.8	0.10	0.7	5.6
March 8	1452:16.69	15	24.58	105	6.60	1.41	10	1	207	30.6	0.09	0.9	2.1
March 8	1514:9.56	15	24.38	105	5.43	0.37	4	1	161	7.9	0.10	0.7	2.0
March 8	1601:29.79	15	24.46	105	5.88	0.06	16	0	79	8.6	0.12	0.4	1.3
March 8	1832:44.68	15	16.64	104	31.57	5.01	7	0	276	36.2	0.09	4.0	pdc
March 8	2044:39.14	15	25.04	105	16.43	2.00	6	1	239	26.6	0.07	1.4	pdc
March 12	1101:54.18	15	11.53	104	45.88	4.46	13	1	211	12.5	0.08	0.6	1.0
March 13	1849:17.42	15	8.81	104	39.07	4.15	6	1	295	14.8	0.03	1.0	1.3
March 13	2342:10.64	15	9.07	104	48.09	16.15	5	0	229	20.0	0.14	2.4	7.1
March 14	1107:53.31	15	51.83	104	7.25	14.93	5	0	329	111.4	0.22	3.4	pdc

Latitudes and longitudes are in degrees and minutes N and W, respectively; nor, number of readings; mag, maximum azimuthal gap; dcs, distance to closest station; rmsr, root mean square residual; erh, horizontal error (from projection of error ellipse onto horizontal plane); erd, depth error; pcd, poor depth control (as indicated by an eigenvalue of [A] less than 0.016, corresponding primarily to the hypocentral adjustment in depth); the error ellipses are at 32% confidence.

waii, and Texas instruments for the events from this northern area are consistent with right lateral strike slip motion along faults parallel to the trough.

The second concentration of microearthquake activity is southeast of the first and is associated with two topographic troughs, one trending approximately east-west and the other trending north-south. The distribution of epicenters displays a broad north-south trend. Most of the events were clustered at the intersection of the two troughs. The southern, deepest part of the north-south trending trough did not manifest any seismic activity during the experiment. Several of the events from this area do not bear any obvious relationship to the topography (e.g., March 2, 0523 hours; March 5, 1010 hours). The depths indicated for these earthquakes are quite scattered and some events may have been subcrustal. One event in particular (March 2, 0523 hours) was recorded throughout the array and consistently yields an apparently well constrained depth of about 12 km below seafloor. The first-motion radiation patterns from the largest of these events do not permit a simple determination of the source mechanism, at least not with the

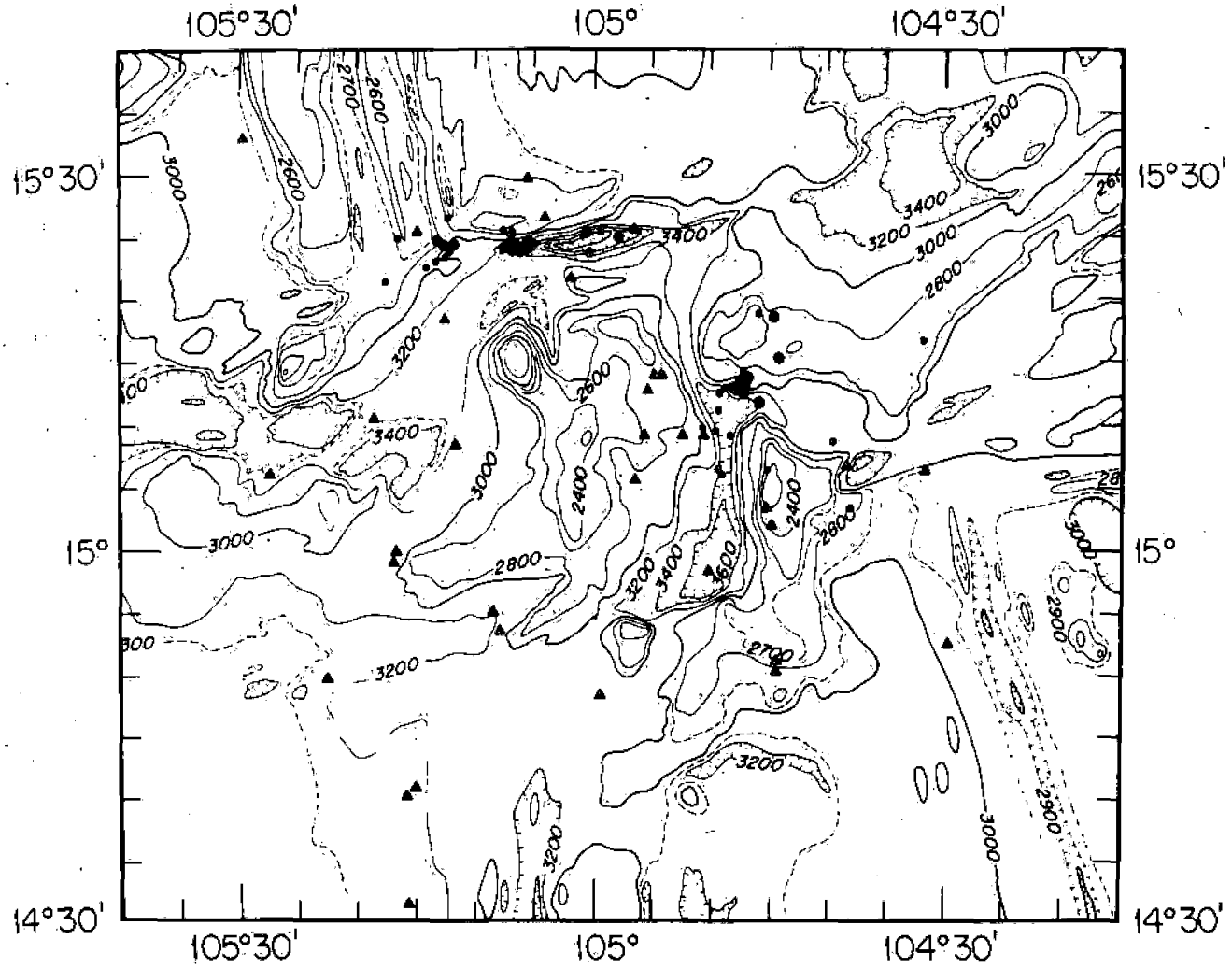

Fig. 3. Stations (triangles) and earthquakes (large dots represent events located using at least 10 readings; small dots represent events located using fewer than 10 readings) from phase II of ROSE superimposed on the local bathymetry of the active portion of the Orozco Fracture Zone. Geographical coordinates of the instruments are listed in Table 1, and hypocentral parameters of the earthquakes are given in Table 3. The bathymetric map is a preliminary map constructed by J. Mammerickx including data obtained by the R/V *Conrad* and R/V *Kana Keoki* during phase II of ROSE. Contours are in corrected meters; the contour interval is 100 m. The axis of the East Pacific Rise to the north and south of the fracture zone is at longitudes of 105°20′ and 104°20′, respectively. The main shock–aftershock sequence of March 8 was located at approximately 15°24′N, 105°06′W.

data currently available. They do not, however, appear to be consistent with simple strike-slip motion.

Of the events for which arrival times are presently available from four or more instruments, only two (March 5, 0058 hours; March 14, 1107 hours) seem to have been outside of the active transform zone. Because these two events occurred well outside of the station network, errors on the hypocentral coordinates are probably larger than those listed in Table 3, and we cannot say whether or not these events were associated with the Orozco Fracture Zone. Station T14, located near the axis of the East Pacific Rise, recorded many near earthquakes (with *S-P* times less than 2 s), but none of these events were large enough to have been located by the network.

CONCLUSIONS

1. Project ROSE has yielded a data set on oceanic microearthquakes unique in the number of independent recordings of the larger events and in the extent to which epicentral locations, focal depth, and other source parameters may be quantitatively characterized. The experiment has also demonstrated the power of redundancy in an OBS and OBH network.

2. In the Orozco Fracture Zone during the period February 27 to March 14, 1979, some 50 microearthquakes were recorded by enough stations in the ROSE network to determine preliminary hypocentral locations and origin times. Of the well-located epicenters, all lie within the active portion of the Orozco transform fault.

3. Roughly one-half of the earthquakes were aligned along a long narrow trough that extends at N80°E azimuth from the northern rise crest intersection. The strike of the trough and first motions from these events support the hypothesis that these earthquakes occurred by strike-slip faulting with slip in the direction of relative motion of the Cocos and Pacific plates. Well-constrained focal depths for these events range from very shallow to subcrustal; the nominal depth range is 0 to 17 km.

4. Most of the remaining earthquakes occurred in a topographically complicated region in the central transform, an

area that may owe its complexity to one or more spreading pole changes and ridge jumps in this part of the Pacific in the last few million years. While some of these events are closely associated with topographic features, others are not, and there is no clear lineation of epicenters in the direction of predicted plate motion. Well-constrained focal depths for this second group of earthquakes also range from 0 to 17 km.

5. The preliminary hypocentral locations of Orozco fracture zone microearthquakes reported here will form the basis for further, more detailed studies by ROSE investigators of earthquake source properties and of the propagation characteristics of earthquake-generated phases.

Acknowledgments. We thank the captains and crews of the R/V *Conrad*, R/V *Kana Keoki*, R/V *Thomas Thompson*, and USNS *De Steiguer* and the other scientists and technical personnel who participated in phase II of ROSE. We also thank J. Mammerickx for providing the bathymetric map used in Figure 3. Financial support for this experiment was provided by the Office of Naval Research, under contract N00014-80-C-0273 to MIT, N00014-79-C-0071 and NR-083-004 to WHOI, N00014-78-C-0570 to the University of Texas, NRO7-456 to the University of Calif. at Santa Barbara, N00014-80-C-0252 to the University of Washington, N00014-79-C-0004 to Oregon State University, N00014-80-C-0098 to Lamont-Doherty Geological Observatory, N00014-75-C-0209 to the University of Hawaii, and by the National Science Foundation, under grant EAR78-23849 to Lamont-Doherty Geological Observatory.

REFERENCES

Bookbinder, R. G., A. C. Hubbard, W. G. MacDonald, and P. W. Pomeroy, Design of an ocean bottom seismometer with response from 25 Hz to 100 sec, in *Proceedings of the 4th Annual Conference: Oceans 78*, pp. 510–515, Marine Technology Society/IEEE, New York, 1978.

Chase, T. E., H. W. Menard, and J. Mammerickx, Bathymetry of the north Pacific, maps 9, 10, Scripps Inst. of Oceanogr., La Jolla, Calif., 1969.

Ewing, J. I., ROSE project overview and general results (abstract), *Eos Trans. AGU, 60*, 887, 1979.

Francis, T. J. G., and I. T. Porter, Median valley seismology: The mid-Atlantic ridge near 45°N, *Geophys. J. R. Astron. Soc., 34*, 279–311, 1973.

Francis, T. J. G., I. T. Porter, and J. R. McGrath, Ocean-bottom seismograph observations on the mid-Atlantic ridge near lat. 37°N, *Geol. Soc. Amer. Bull., 88*, 664–677, 1977.

Francis, T. J. G., I. T. Porter, and R. C. Lilwall, Microearthquakes near the eastern end of St. Paul's Fracture Zone, *Geophys. J. R. Astron. Soc., 53*, 201–217, 1978.

Johnson, R. V., II, C. R. B. Lister, and B. T. R. Lewis, A direct recording ocean bottom seismometer, *Mar. Geophys. Res., 3*, 65–85, 1977.

Johnson, S. H., and P. R. Jones, Microearthquakes located on the Blanco fracture zone with sonobuoy arrays, *J. Geophys. Res., 83*, 255–261, 1978.

Johnson, S. H., M. D. Cranford, B. T. Brown, J. E. Bowers, and R. E. McAllister, A free-fall direct recording ocean bottom seismograph, *Mar. Geophys. Res., 3*, 103–117, 1977.

Jones, P. R., and S. H. Johnson, Sonobuoy array measurements of active faulting on the Gorda ridge, *J. Geophys. Res., 83*, 3435–3440, 1978.

Klein, F. W., Hypocenter location program HYPOINVERSE, 1, User's guide to versions 1, 2, 3, 4, *Geol. Surv. Open File Rep. U.S., 78-694*, 1978.

Klitgord, K. D., and J. Mammerickx, Bathymetric, magnetic and tectonic trends of the East Pacific Rise, 8°–21°N (abstract), *Eos Trans. AGU, 60*, 888, 1979.

Koelsch, D. E., and G. M. Purdy, An ocean bottom hydrophone instrument for seismic refraction experiments in the deep ocean, *Mar. Geophys. Res., 4*, 115–125, 1979.

Latham, G., P. Donoho, K. Griffiths, A. Roberts, and A. K. Ibrahim, The Texas ocean bottom seismograph, paper presented at the Offshore Technology Conference, Soc. of Explor. Geophys., Houston, Tex., 1978.

Lewis, B. T. R., and W. E. Snydsman, Fine structure of the lower oceanic crust on the Cocos plate, *Tectonophysics, 55*, 87–105, 1979.

Lilwall, R. C., T. J. G. Francis, and I. T. Porter, Ocean-bottom seismograph observations on the mid-Atlantic ridge near 45° N, *Geophys. J. R. Astron. Soc., 51*, 357–370, 1977.

Lilwall, R. C., T. J. G. Francis, and I. T. Porter, Ocean-bottom seismograph observations on the mid-Atlantic ridge near 45°N—Further results, *Geophys. J. R. Astron. Soc., 55*, 255–262, 1978.

Lynn, W. S., and B. T. R. Lewis, Tectonic evolution of the northern Cocos plate, *Geology, 4*, 718–722, 1976.

Macdonald, K. C., and J. D. Mudie, Microearthquakes on the Galapagos spreading center and the seismicity of fast-spreading ridges, *Geophys. J. R. Astron. Soc., 36*, 245–257, 1974.

Mattaboni, P. J., and S. C. Solomon, MITOBS: A seismometer system for ocean-bottom earthquake studies, *Mar. Geophys. Res., 3*, 87–102, 1977.

Minster, J. B., and T. H. Jordan, Present-day plate motions, *J. Geophys. Res., 83*, 5331–5354, 1978.

Orcutt, J. A., B. L. N. Kennett, and L. M. Dorman, Structure of the East Pacific Rise from an ocean bottom seismometer survey, *Geophys. J. R. Astron. Soc., 45*, 305–320, 1976.

Prothero, W. A., Jr., An operationally optimized ocean-bottom seismometer capsule, *Phys. Earth Planet. Inter., 18*, 71–77, 1979.

Prothero, W. A., I. Reid, M. S. Reichle, and J. N. Brune, Ocean bottom seismic measurements on the East Pacific Rise and Rivera Fracture Zone, *Nature, 262*, 121–124, 1976.

Raitt, R. W., The crustal rocks, in *The Sea*, vol. 3, edited by M. N. Hill, pp. 85–102, Interscience, New York, 1963.

Reichle, M. S., and I. Reid, Detailed study of earthquake swarms from the Gulf of California, *Bull. Seismol. Soc. Am., 67*, 159–171, 1977.

Reichle, M. S., G. F. Sharman, and J. N. Brune, Sonobuoy and teleseismic study of Gulf of California transform fault earthquake sequences, *Bull. Seismol. Soc. Am., 66*, 1623–1641, 1976.

Reid, I., and K. Macdonald, Microearthquake study of the mid-Atlantic ridge near 37°N, using sonobuoys, *Nature, 246*, 88–89, 1973.

Reid, I., M. Reichle, J. Brune, and H. Bradner, Microearthquake studies using sonobuoys, preliminary results from the Gulf of California, *Geophys. J. R. Astron. Soc., 34*, 365–379, 1973.

Reid, I., J. A. Orcutt, and W. A. Prothero, Seismic evidence for a narrow zone of partial melting underlying the East Pacific rise at 21°N, *Geol. Soc. Am. Bull., 88*, 678–682, 1977.

Sclater, J. G., R. N. Anderson, and M. L. Bell, Elevation of ridges and evolution of the central eastern Pacific, *J. Geophys. Res., 76*, 7888–7914, 1971.

Solomon, S. C., P. J. Mattaboni, and R. L. Hester, Microseismicity near the Indian Ocean triple junction, *Geophys. Res. Lett., 4*, 597–600, 1977.

Spindel, R. C., S. B. Davis, K. C. Macdonald, R. P. Porter, and J. D. Phillips, Microearthquake survey of median valley of the mid-Atlantic ridge at 36°30'N, *Nature, 248*, 577–579, 1974.

Sutton, G. H., J. Kasahhara, W. N. Ichinose, and D. A. Byrne, Ocean bottom seismograph development at Hawaii Institute of Geophysics, *Mar. Geophys. Res., 3*, 153–177, 1977.

Wilson, J. T., A new class of faults and their bearing on continental drift, *Nature, 207*, 343–347, 1965.

(Received June 13, 1980;
revised October 27, 1980;
accepted October 30, 1980.)

Mod Important

JOURNAL OF GEOPHYSICAL RESEARCH, VOL. 87, NO. B10, PAGES 8509-8518, OCTOBER 10, 1982

MICROEARTHQUAKES ON THE EAST PACIFIC RISE AT 21°N AND THE RIVERA FRACTURE ZONE

William A. Prothero, Jr.

Department of Geological Sciences, University of California, Santa Barbara
Santa Barbara, California 93106

Ian D. Reid

Department of Geology, Dalhousie University
Halifax, Nova Scotia, Canada B3H 3J5

Abstract. During March and April of 1974, three ocean bottom seismometer (OBS) capsules were deployed in arrays on the East Pacific Rise (EPR) at 21°N for 8 days, on the Rivera Fraction Zone (RFZ) for 9 days, and at the EPR/RFZ intersection for 12 days. Seismicity on the EPR is characterized by extremely small events, none large enough to trigger all of the instruments simultaneously. A weak 24-hour periodicity in OBS event trigger rate is observed. This could be related to earth strain tides or a modulation in the trigger sensitivity due to a varying noise level. On the Rivera Fracture Zone, an en echelon pattern of earthquakes with a maximum depth of 10 km was observed. Seismic activity at the junction of the EPR and RFZ becomes more diffuse and terminates abruptly at the EPR. The junction array was slightly offset from the active zone of seismicity, and the depth of only one event is reliably determined at 5.4 ± 2 km. The S wave spectra of microearthquakes at the junction and on the RFZ are computed, and seismic moments and corner frequencies determined. Stress drops are between 0.1 and 10 bars and show no systematic difference at the two deployment sites. Larger earthquakes observed at teleseismic distances do show markedly lower stress drops when they originate near to spreading centers, but these differences are not observed at the microearthquake level in this study. It is suggested that this is due to a natural tendency for small earthquakes to have small stress drops and a lack of large earthquakes during the RFZ deployment.

Introduction

During March and April of 1975, a microearthquake experiment (ELENERTH Expedition), using arrays of three ocean bottom seismometers (OBS), was conducted on the East Pacific Rise at 21°N, on the Rivera Fracture Zone and at the junction of these features. Various aspects of this experiment have been discussed by Prothero et al. [1976], Reid et al. [1977], and Reid and Prothero [1981]. In this paper, we review the published work and present previously unpublished results, including rise crest seismicity and measurements of S wave spectra. This material is of current interest in view of the recent RISE and ROSE experiments in this and similar areas.

The schematic tectonics of the region are shown in Figure 1. The northernmost segment of the East Pacific Rise (EPR) lies between the Tamayo and Rivera fracture zones, which link it to the Gulf of California spreading system and to the main East Pacific Rise, respectively [Larson, 1972a, b]. The EPR at 21°N has been extensively studied; surveys using the Scripps Institution of Oceanography 'Deep-Tow' system were done by Larson [1971] and Normark [1976], and microearthquake and refraction studies took place during ELENERTH Expedition [Reid et al., 1977]. More recently, this was the area studied by the project RISE [Rise Team, 1980].

This section of the EPR is spreading at the intermediate half rate of 30 mm yr^{-1} [Larson, 1972 a, b], but has the basic characteristics of fast spreading: smooth topography and low seismicity. An axial high is present at 21°N [Larson, 1971; Normark, 1976] but is much less pronounced than that on the faster parts of the EPR system [Rosendahl et al., 1976]. Seismic refraction [Reid et al., 1977] indicates a narrow low-velocity region beneath the rise crest, which may be due to a crustal melt zone. Close to the axis the crust is intensely fissured, and on-axis fresh basalt is evidence of recent and ongoing volcanic activity. Recent studies using the submersible Alvin have identified numerous centers of biological activity near zones of active hydrothermal circulation [Rise Team, 1980]. At teleseismic distances, a small number of earthquakes with magnitudes up to m_b = 5.0 are reported in the PDE listings for this section of the EPR. Preliminary work indicates that these events are strike slip in nature and occur on a small transform offset within the ridgecrest (K. Macdonald, personal communication, 1981). However, the ridge is nearly aseismic compared to the Rivera Fracture Zone, which generates a large number of events with body wave magnitudes up to 5.7.

The Rivera Fracture Zone (RFZ) is an active transform between this section of the EPR and a triple junction with the main EPR system and the Middle America Trench (Figure 1). Physiographic and seismological data indicate a change in tectonic regime midway along the RFZ. The western half, from the junction with the EPR at 20°N, 109°30'W to about 18°45'N, 107°30'W, is delineated by two parallel ridges, of average elevation 500-1000 m, separated by a deep, steep-sided depression reaching 2000 m below the regional seafloor [Mammerickx, 1978]. Along the eastern half of the RFZ, to the triple junction, this depression disappears, and a single ridge is present. The change coincides with a change in strike to a more east-west direction.

There is also a marked contrast in the nature of the seismicity [Meyers and von Hake, 1976] on these two parts of the RFZ. The western half is characterized by a relatively large number of small

Paper number 1B1613.
0148-0227/82/001B-1613$05.00

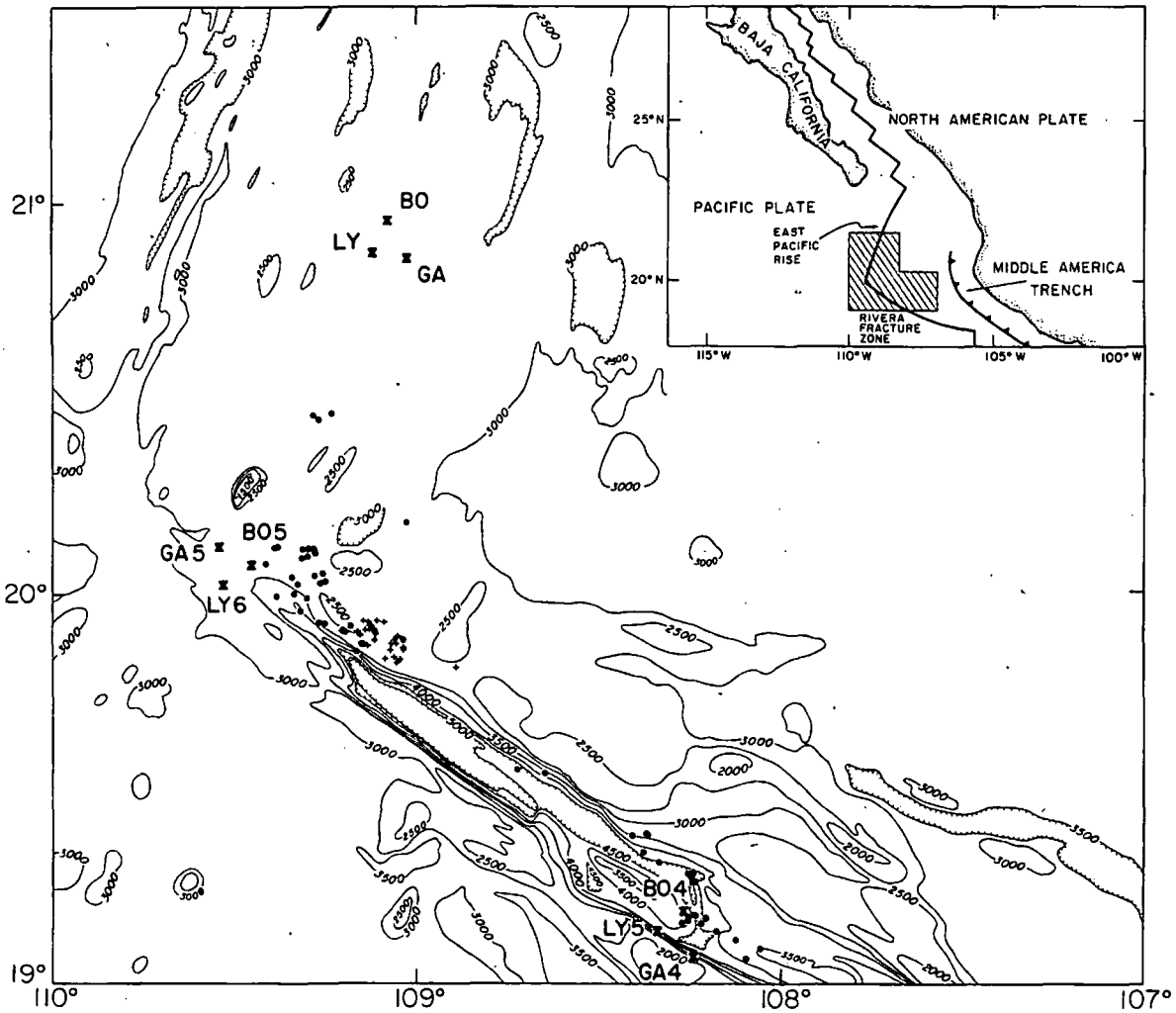

Fig. 1. Location of ELENERTH Expedition, OBS deployment sites, and earthquake epicenters. Each of the three instrument arrays is a separate deployment. The GA5, B05, LY6 array is at the junction of the EPR and Rivera Fracture Zone. The crosses are epicenters of a swarm sequence observed during this deployment.

to medium size earthquakes, with a maximum magnitude of m_b = 5.2, which tend to cluster in time and space, giving rise to swarm sequences. A typical sequence of this kind, observed during the experiment near the EPR-RFZ junction, is described in detail by Reid and Prothero [1981]. Along the eastern length there are fewer and larger earthquakes, with a general mainshock-aftershock character.

Microearthquakes on the western length suggest an en echelon pattern of faulting within the central depression, suggesting that this feature is a rift produced by a component of spreading along this part of the RFZ. This hypothesis is supported by the character of the seismicity and by fault plane solutions [Molnar, 1973], which indicate an oblique component of motion. If this interpretation is correct, it implies some relative motion between the Rivera and North American plates [Larson, 1972a, b; Molnar, 1973].

Instrumentation

The OBS design included a single vertical short-period seismometer with event-triggered digital recording [Prothero, 1977]. Data from a single 2-Hz vertical geophone were sampled at 128 Hz with a 12 bit (1:4096) resolution, and recorded on magnetic tape. An acoustic transpond and command system was fitted to all capsules but had to be removed from GA after the first deployment. Navigation and capsule location used satellite positioning and (except for GA) acoustic ranging. The location accuracies of OBS capsules BO and LY are estimated at better than 50 m, while the GA location error is estimated at less than 200 m [Reid, 1976]. Figure 2 shows relevant recording statistics for the three array deployments. The principal technical problem occurred during the ridgecrest deployment. It was a large 'ground loop' induced transient which, when the recorder was turned on, caused spurious triggering, rapid use of recording tape on LY, and a large transient signal. This fault was rectified for subsequent deployments.

Microseismicity Studies

This work, on the ELENERTH Expedition, was the first scientific use of the Scripps Institution ocean bottom seismometer (OBS) system. The cap-

Elenerth Capsule Deployments

RIDGE CREST

Site	Array 1	Time Set to 0 1974	Recording (days)	No. of Events	Simultaneous Events
3	GA3	13 Mar. 2343Z	8.2	563 (.5)	GA–LYD 33
2	LYD4	13 Mar. 1129Z	15 hrs.	7007 (all)	LYD–BO 18
1	BO3	13 Mar. 0053Z	8.8	377 (.4)	GA–BO 39; GA–LYD 17; LYD–BO

FRACTURE ZONE

Site	Array 2	Zero Time	Recording (days)	Events	Simultaneous Events
6	GA4	26 Mar. 0110Z	8.9	105 (~.4)	GA–LYD 67
5	LYD5	24 Mar. 0642Z	10.3	680 (.8)	LYD–BO 57
4	BO4	25 Mar. 0812Z	9.8	155 (.25)	GA–BO 37; GA–LYD 31; LYD–BO

JUNCTION

Site	Array 3	Zero Time	Recording (days)	Events	Simultaneous Events
3	GA5	7 Apr. 0934Z	12.0	254 (.5)	GA–LYD 196
2	LYD6	6 Apr. 2317Z	12.6	304 (.8)	LYD–BO 213
1	BO5	6 Apr. 0920Z	13.5	409 (.8)	GA–BO 209; GA–LYD 183; LYD–BO

Fig. 2. Event-recorded statistics for the three array deployments. The quantity in parentheses in the column titled "No. of events" is the fraction of the tape capacity used for that deployment.

sules, designated BO, LY, and GA, were deployed in three separate arrays (Figure 1). The first, on the EPR at 21°N, was designed to detect microearthquake activity, tectonic or volcanic in origin, associated with the spreading process. The others, on the RFZ and at the EPR-RFZ intersection known to be seismically active areas, were intended to provide an accurate delineation of the active faults relative to the topography and to study the general nature of oceanic microearthquakes: such features as depth, stress drop, etc.

The array on the spreading axis was deployed for 8 days. Shots from a seismic refraction experiment along the ridgecrest [Reid et al., 1977] were responsible for the simultaneous triggering shown in Figure 2 for this array. Apart from these, no events occurred large enough to trigger more than one OBS, so no positive microearthquake identification and location were possible. However, there were a number of interesting events of probable seismic origin recorded on individual capsules. Representative records from some of these are shown in Figure 3. The signals are partly obscured by the low-frequency recorder turn-on transient pulse. We see on BO particularly though, a sharp initial onset, apparent later phases, and a coda, all suggestive of seismic origin. Event A has a sharp onset, with several impulsive arrivals almost 2s later. However, events B and C are of quite different character, with a more emergent onset of a quite monochromatic character.

The largest event recorded had an approximate local magnitude of 0.5, based on the magnitude scale developed by Reid [1976]. The high-frequency signal impressed on the turnon transient is the source of the trigger. A biological origin for some events of this kind has also been proposed [Buskirk et al., 1980] and is certainly a possible explanation for many of the events. Since BO is on the center of the ridge crest, it is tempting to associate this with harmonic tremor from volcanic activity or to a waveguide propagation mode in the axial crustal structure [Macdonald et al., 1980]. The frequency of the harmonic signal in Figure 3c is approximately 25 Hz, which is higher than observed on land volcanoes [Kubotera, 1974], but the character of the ridge crest magma and hydrothermal circulation systems may produce quite different effects from land analogies. Both LY and GA were off-axis by about 8 km. A similar harmonic signal is also observed on LY on Figure 3e, with a frequency of

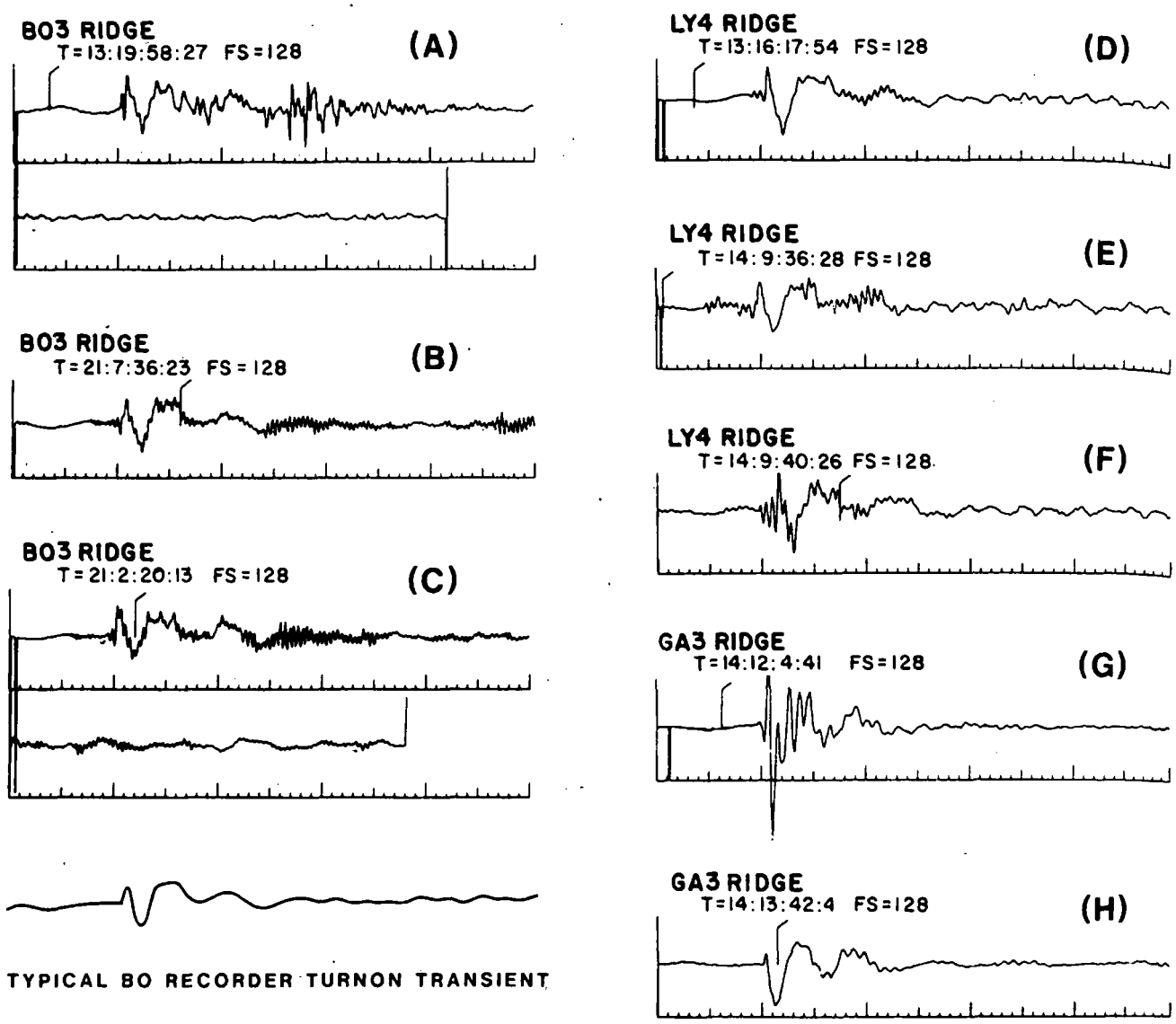

Fig. 3. Representative events recorded on the EPR array. Each event is contaminated by a tape recorder turnon transient, but their general character can be seen. OBS BO is on the center of the EPR, while LY and GA are off axis by approximately 10 km.

approximately 17 Hz. The triggers on GA were mostly impulsive and could be explained by an impulsive source followed by a ringdown due to the seafloor instrument interaction. Another possibly important sound source is associated with hydrothermal circulation. While circulation through vents is probably rather constant on the time scale of this experiment, there is a great deal of kinetic energy in the process that could serve as a source of seismic energy associated with the intermittent spreading process.

Figure 4 is a plot of number of events recorded versus time for each of the three instruments. LY is not shown since it used all of its tape in 24 hours and also had a more sensitive trigger and so recorded small events at a greater rate. Both BO and GA appear to trigger uniformly through the deployment, with GA having slightly fewer in the last half but increasing near the end.

The theoretical horizontal strain tide (E-W component) has been plotted in the BO seismicity figure. A possible, rather weak clustering of events at 24-hour periods suggest a possible correlation between earth rotation effects and earthquake activity. Possible explanations include seismicity induced by earth strain tides (with the peaks in activity at the end removed, the correlation coefficient is -0.3), changes in trigger sensitivity due to 24-hour variations in bottom noise induced by ocean currents, or changes in biologically induced triggers with ocean currents.

Rivera Fracture Zone Results

The principal results from the fracture zone array deployment are reported by Prothero et al. [1976]. Two capsules (LY and GA) were located on top of the southern wall of the rift and the third (BO) on the rift floor. Thirty-nine earthquakes triggered all three recorders (most of these could be located) and are plotted in Figure

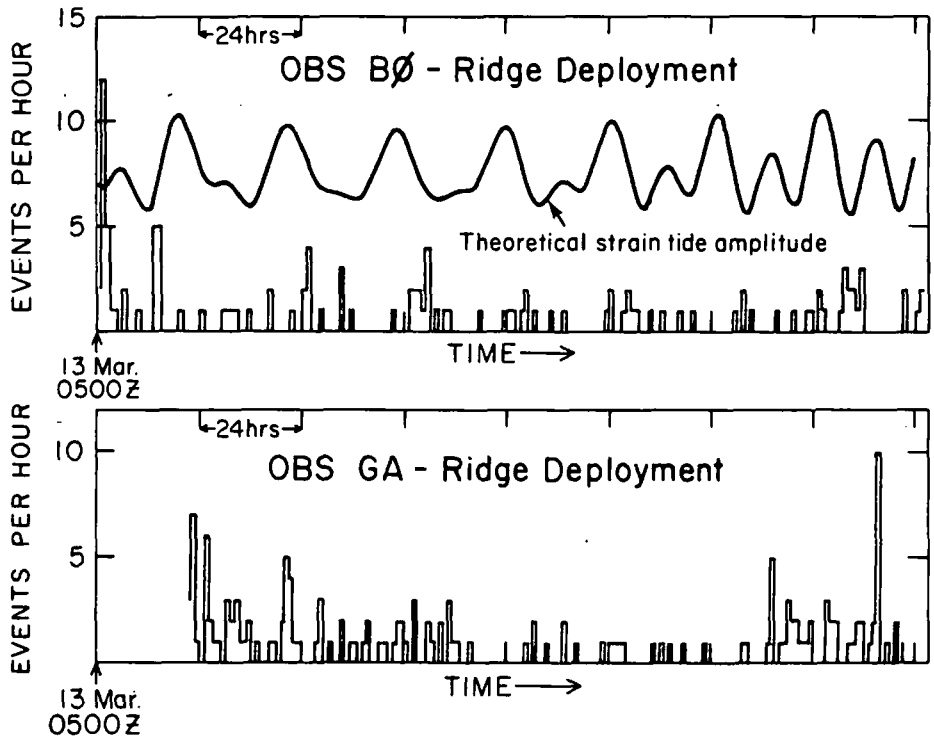

Fig. 4. Number of events recorded per hour on capsules BO and GA. A theoretical horizontal strain tide component is plotted with BO events.

5. Locations were computed using a half-space program written by Buland [1976]. Given the sparseness of the array and the probable heterogeneity of the velocity structure in the region, the use of a layered velocity model was not warranted. A compressional velocity of 6.5 km/s and shear velocity of 3.75 km/s were used. Depending on the distance of the event from the array, errors in the choice of a half-space velocity make relatively small changes in the epicenter locations and do not change the overall pattern of seismicity significantly. The label for each event (Figure 5) is the relative time of the event, to the nearest minute, and the depth, in kilometers. The depths of the cluster of epicenters within the array can be determined with fairly good confidence. Fractional errors in depth for these events should be comparable to fractional errors in the velocity model. The six earthquakes for which we feel depth determinations

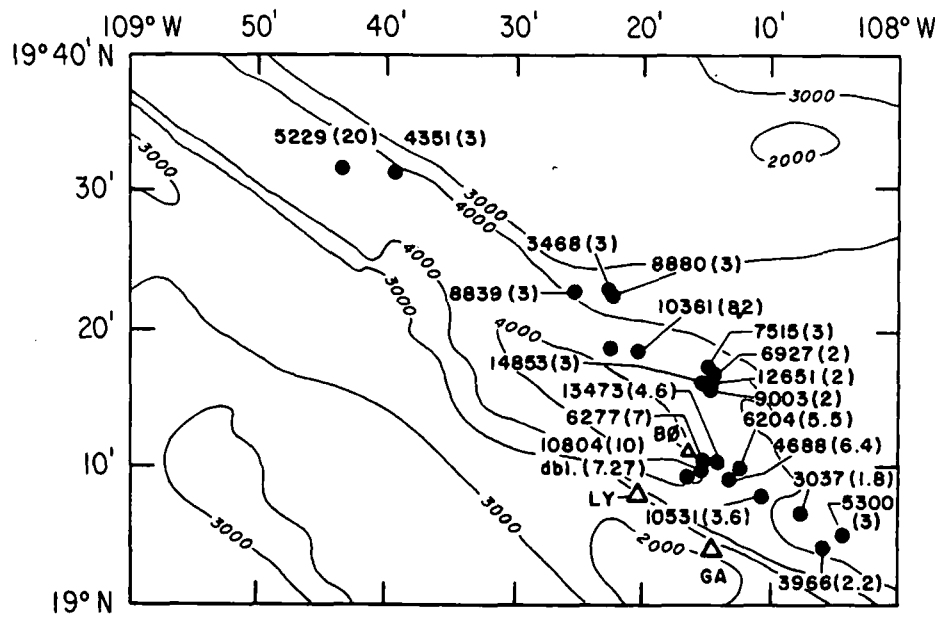

Fig. 5. Detail of events recorded at the the fracture zone site B04, GA4, LY4 shown in Figure 1. The label for each epicenter is the relative time in minutes and the depth in kilometers.

are reliable lie between 4 and 9 km [Prothero et al., 1976; Reid, 1976]. Thus we infer that the zone of brittle fracture which can generate earthquakes is at least 9 km thick. Given the short time scale involved in the deployment, these results are not significantly different from what would be expected on the San Andreas Fault in California [Hileman et al., 1973].

The epicenters appear to delineate at least two en echelon faults with azimuth about 330° within the rift. There is no evident depth/epicenter variation which would indicate a non-vertical fault plane. First motions are generally consistent with right-lateral strike slip along these faults. Prothero et al. [1976] suggest that this pattern indicates active seafloor spreading within the rift, with transform segments offset by short spreading centers, an interpretation supported by the other evidence mentioned above.

Reid [1976] developed two magnitude scales. The first scale is approximately consistent with the Richter magnitude for microearthquakes with peak frequencies between 10 and 20 Hz. It is given by $M_L' = \log A + 0.037D + 4.2$, where A is the peak amplitude of the seismic signal, in millimeters of ground motion, and D is the distance, in kilometers. A coda magnitude scale was also developed. This is computed by plotting the log of the amplitude of the coda versus time, which is approximated by $A(t) = A_0 t^{-2.4}$. The logarithm of the amplitude at 10 s (or the extrapolation of the plot to 10 s for smaller events) is used in the magnitude formula, which is given by $M_C' = \log A_C + 5.3$, where A_C is the coda amplitude at 10 s, measured in millimeters of ground motion. The two magnitude scales are consistent to within a fraction of a magnitude unit and appear to be grossly independent of distance. It must be noted that these magnitude scales were developed for earthquakes in the 0 to 3 magnitude range for rather short distances (<50 km). Direct correlations with Richter magnitude may be dubious because of differences in the response of the Wood-Anderson torsion seismometer, which defines the Richter magnitude, and the response of the OBS system. However, the developed magnitude scales are self-consistent and provide a useful basis for oceanic microearthquake studies. Reid [1976] also computes b values based on these magnitude scales and arrives at a b value of 0.95, a typical value in land-based studies. The spectra of events recorded at this site will be discussed in a later section.

EPR-RFZ Intersection

This array (Figure 6) was deployed for 12 days, and was the most successful in terms of numbers of events recorded. The main objective here was to study the termination of active transform faulting at the rise crest. Of particular interest was the sharpness of this termination, with its implications for the position and width of the spreading zone, and in the depth of seismicity in very young crust.

Most of the activity recorded was due to a large earthquake sequence nearby on the RFZ (crosses on Figure 1), which has been discussed in detail by Reid and Prothero [1981]. All earthquakes recorded were outside the array, and only one reliable depth was obtained for an event near the junction (event 15780 in Figure 6), with a fairly, but not unusually, small value of 5.4 ± 2 km. Figure 6 shows epicenter locations. It appears that the line of earthquakes along the RFZ does not in fact reach the junction, at about 20°N, 109°30'W, but becomes offset to the northeast. This might reflect a weakness at the corner of the plate boundary or simply a continuation of the en echelon fault pattern seen farther down the RFZ. The activity ends abruptly near the spreading axis. Reid et al. [1977] used observed S wave attenuation to support the existence of a shallow zone of attenuation, probably involving

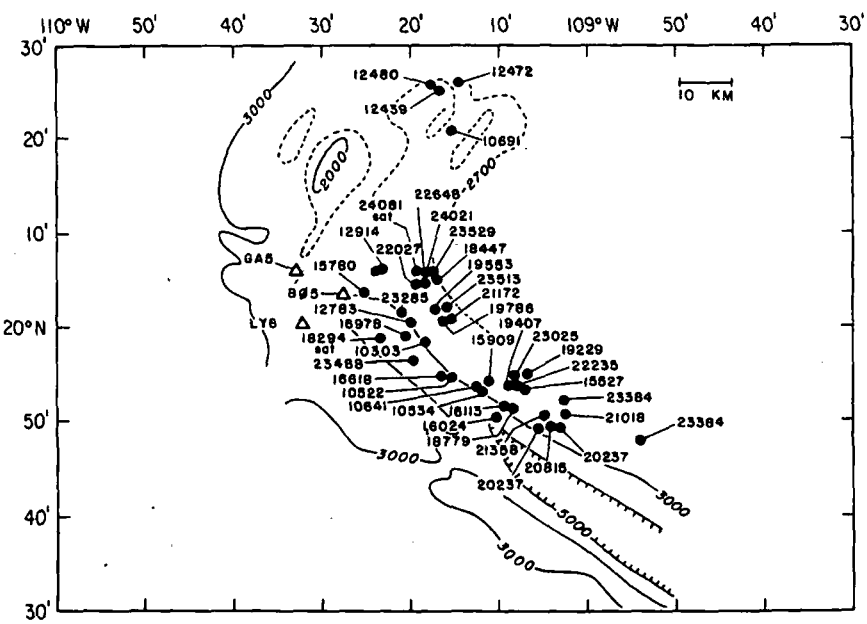

Fig. 6. Detail of events recorded at the junction of the EPR and the RFZ. Some, but not all of the aftershocks of the large three-event sequence are also plotted.

melting, near the spreading axis. P and S first motions and amplitudes are again consistent with right lateral strike slip on faults parallel to the RFZ.

Microearthquakes at the junction showed more tendency than those on the RFZ to cluster into sequences of several events, probably reflecting the association of earthquake swarms with ridge crests and other volcanic regimes.

Spectra

The OBS system was specifically designed with digital recording at 128 samples/s, to provide adequate data for microearthquake spectral analysis. According to the theory of Brune [1970, 1971], the seismic moment, fault dimension, and stress drop of earthquakes can be determined from S wave spectrum. In practice, crustal structure and site-dependent resonances can introduce complications, but microearthquake spectra provide useful results if the source is within one source depth of the receiving stations [Helmberger and Johnson, 1977].

In the Brune [1970, 1971] model, the seismic moment M_o and stress drop $\Delta\sigma$ are given by

$$M_o = \frac{4\pi\rho R^3 \Omega_o}{K R_{\theta\phi}}$$

and

$$\Delta\sigma = \frac{0.27\pi^3 M_o f_c^3}{\beta^3}$$

where Ω_o is the low-frequency spectral amplitude, f_c is the corner frequency, β is the shear velocity, R is the distance, ρ is the density, $R_{\theta\phi}$ is the radiation pattern factor, and K is the surface correction factor taken as 2.

Figure 7 shows one of the better displacement spectra from BO at the RFZ deployment. The portion of the seismogram indicated by the horizontal line is Fourier-transformed and corrected for instrument response and attenuation, assuming a frequency-independent Q factor of 250. The seismic moments and corner frequencies found with this method are relatively insensitive to the Q chosen and length of the S wave sample that is transformed. The rise in values at both low and high frequencies is due to the instrument response and Q corrections, which divide the signal plus noise by an increasingly small number. A good discussion of the application of this theory can be found in the work by Tucker and Brune [1973]. Figure 8 shows spectra computed from seismograms recorded at BO, LY, and GA at the fracture zone deployments. They are plotted, with event number to the right, for northernmost events at top and southernmost at the bottom. Each spectra is adjusted vertically in the figure so the amplitude scale only applies to individual spectra. Capsule BO spectra show rather classic behavior with a relatively flat low-frequency portion and a normal high-frequency falloff. There are no obvious persistent resonances (peaks in the spectra). LY however shows a strong resonance at about 28-Hz throughout. A resonance at 7-8 Hz appears for several of the more northern events but not for others. It would seem that the 28-Hz resonance is either an internal instrument resonance or a bottom coupling effect. The same peak does not occur on junction deployment spectra, so it could be dependent on the instrument orientation, bottom coupling, or a local structure effect. A 28-Hz coupling frequency would indicate a very stiff bottom [Sutton et al., 1980]. A stiff hard bottom is also consistent with the location of the instrument on a structural high, which would probably be relatively clear of a more compliant sediment cover, resulting in a higher bottom coupling frequency. GA shows a persistent resonance at 18-20 Hz. Again, the resonance does not appear in junction deployment spectra, so it must be a feature of the particular site. These resonance peaks may be ignored, by interpolating through them, except where they occur close to the corner frequency. This is a valid procedure for an isolated peak which does not occur at a critical part of the spectrum. However, the 20-Hz peak in GA spectra makes corner frequency picks extremely speculative in many cases since the high-frequency asymptote cannot be easily identified. Interestingly, capsules LY and GA, which have strong spectral resonances, are located on the west of the Rivera Fracture Zone at the top of the large fault scarp, while BO, which has little obvious resonance behavior, is on the east on a deep valley floor.

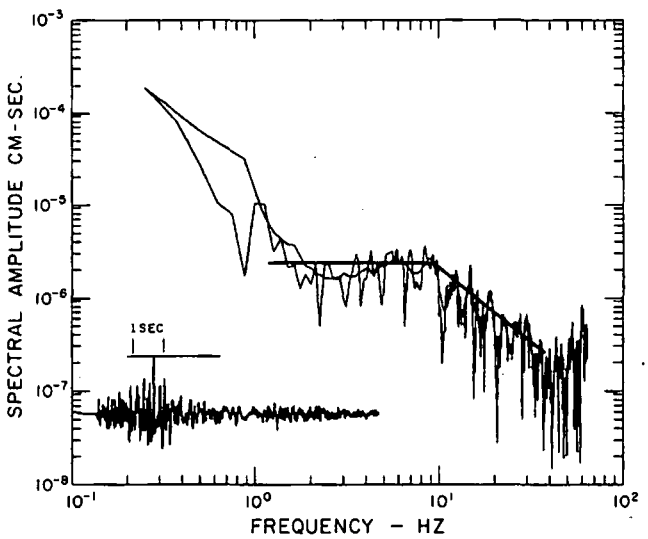

Fig. 7. Example of S wave spectra recorded by BO at the fracture zone site. The line over the seismogram is the portion which is transformed. The lines over the spectrum show the low-frequency asymptote and high-frequency falloff. The corner frequency is at the intersection of these two lines.

Figure 9 shows the seismic moment plotted versus corner frequency for spectra without large peaks in the region of the corner frequency for both fracture zone and junction deployments. Symbols connected by lines indicate results from spectra of the same earthquake recorded on different instruments and give an idea of the noise inherent in the measurements. Only BO was used for junction deployment spectra studies, since only events closer than 6 km were used, and few of these recorded on GA and LY, which were farther away. The inset of Figure 9 shows stress drops reported in other studies of earthquakes in northern Baja and the Gulf of California [Thatcher,

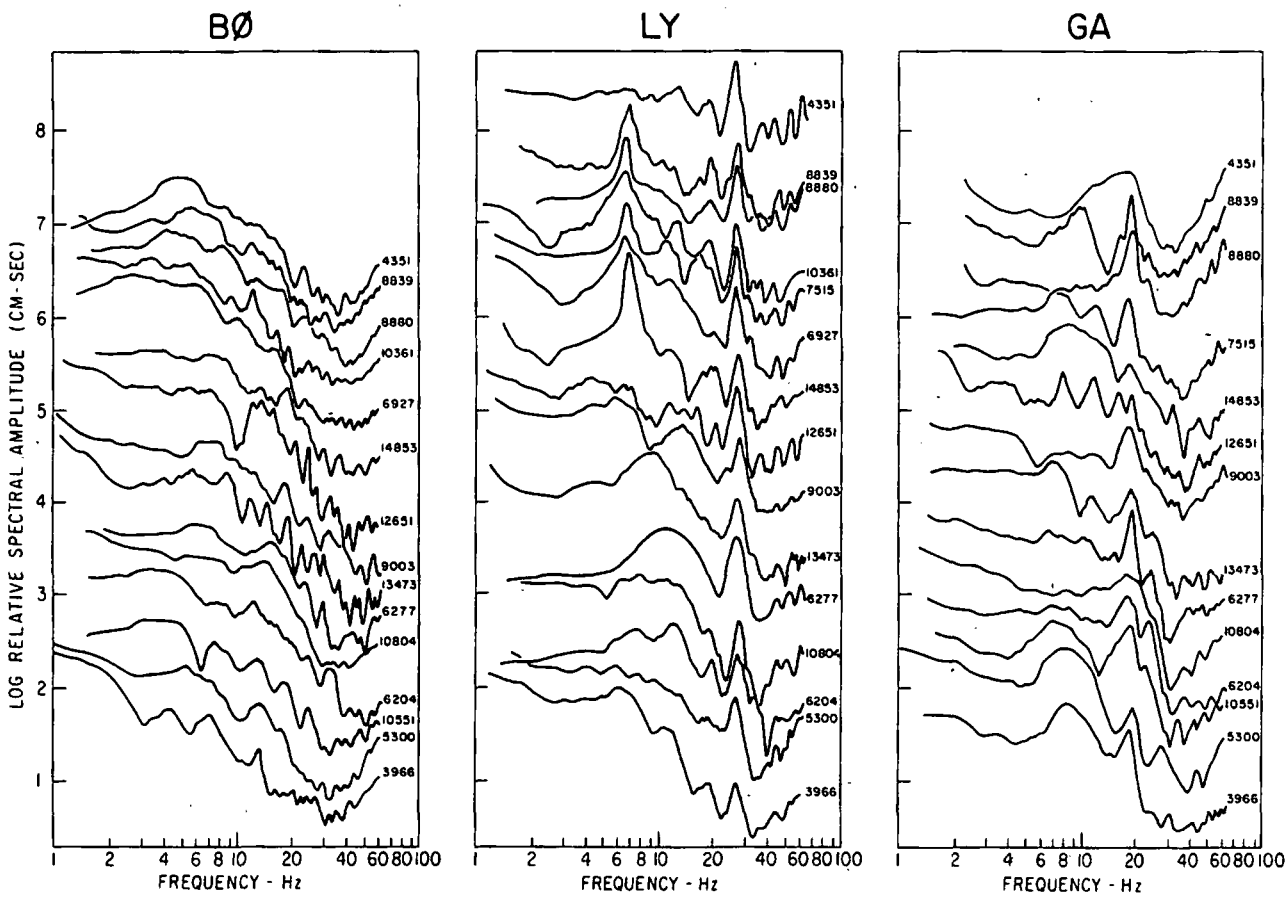

Fig. 8. Spectra from fracture zone site events. Each spectrum is keyed to its epicenter by the number at the right. They are sorted from northernmost events at the top to southernmost events at the bottom. The spectra have been adjusted vertically, so the amplitude scale applies only to individual spectra.

1972], the 1966 Imperial Valley Earthquake [Brune and Allen, 1967], and from Reid and Prothero [1981] from the three event sequence observed during the experiment under discussion in this paper.

Interestingly, there is little significant difference between stress drops measured at the junction and fracture zone sites. They are both quite low and, on the average, junction stress drops are slightly higher than fracture zone stress drops for these small events. A comparison may be made to a study of the S wave spectra of the San Fernando earthquake aftershocks [Tucker and Brune, 1973]. Aftershocks show stress drops ranging from a high of 300 bars to a low of 0.5 bar. (J. N. Brune, personal communication, 1976). Higher stress drops occurred for larger events. It would be expected, from the well-known frequency-magnitude relation then, that the vast majority of events above some minimum magnitude threshold would have low stress drops. Thus, if the microearthquakes observed during this experiment had a similar statistical distribution of stress drops as the aftershocks of the San Fernando earthquake, higher stress drop events might have an extremely low probability of being observed, even though the stress regime of the region might be capable of producing high stress drop events. Studies of larger events at teleseismic distances do show a trend toward low stress drops for earthquakes generated near to spreading centers in young crust. This is most clearly shown in Figure 9 where the results of Thatcher [1972] are plotted for Gulf of California earthquakes. The transform fault through the Gulf of California is composed of numerous small spreading offsets so it might be expected to have a similar thermal regime as the young portion of the Rivera Fracture Zone. The Gulf of California events have much lower average stress drops than Northern Baja events, as do stress drops from earthquakes recorded in this study, including the sequence of three larger earthquakes observed during the junction deployment. So, it seems likely that the low stress drops observed at the two sites merely reflect the general tendency of small earthquakes to have low stress drops. Following this logic further, the lack of larger earthquakes observed at the RFZ site would then explain the lack of higher stress drop events there. A longer or luckier deployment time during which larger earthquakes were recorded would have a better chance of higher stress drops than those observed at the EPR-RFZ intersection. It might be noted that an extremely high dynamic range instrument would be necessary to avoid saturation on the larger events which would be of interest.

It is likely, and these data support this hypothesis, that it will be very difficult to find a systematic dependence on the age of the generating structure in background microearthquake spectra. Statistics favoring low stress drop events, intrinsic propagation path effects, and

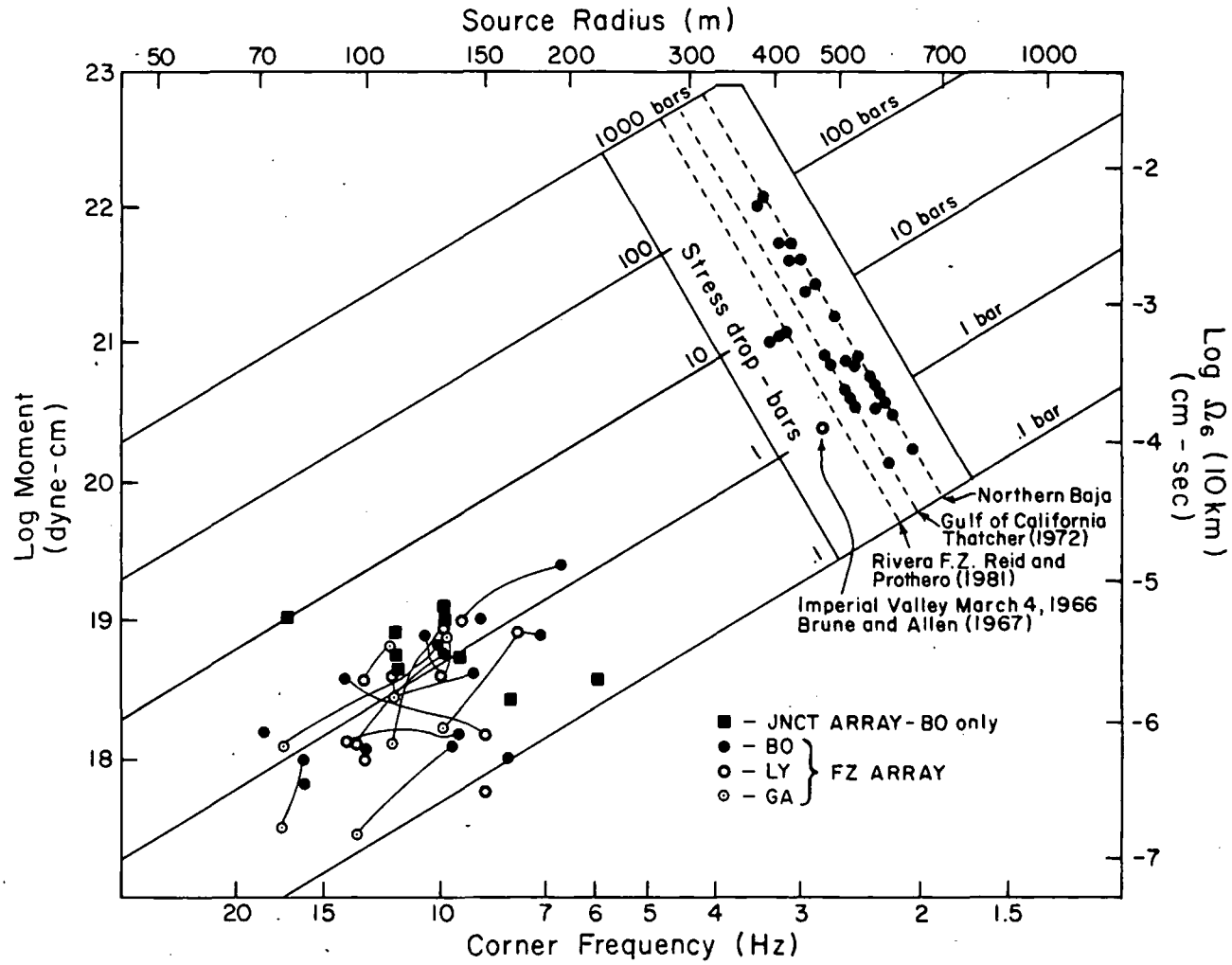

Fig. 9. Moment versus corner frequency plotted for S wave spectra of events recorded at both the junction and fracture zone sites. Points connnected by solid lines are from a single event but were recorded on different instruments. The inset plots stress drops for earthquakes reported in the literature for selected regions, showing that low stress drops are observed in areas of young crust, near to spreading centers, while higher stress drops are observed elsewhere.

source directivity will probably mask any small thermal effects that might be present.

Summary and Conclusions

The data reviewed and reported here have provided valuable information on the seismicity and tectonics of this and similar oceanic regions. On the EPR axis, no earthquakes occurred which were large enough to trigger more than one OBS capsule. The most interesting aspect of the events that were recorded is their anomalous, harmonic character suggestive of harmonic tremor or a waveguide propagation mode in the axial crustal structure. Events showed a weak clustering at 24-hour intervals, which could be caused by strain tides or a 24-hour modulation of the trigger sensitivity by changes in the background noise level.

On the Rivera Fracture Zone, microearthquakes showed an en echelon pattern within the rift valley. If its interpretation as a spreading transform system is correct, this has implications for processes along other leaky transform faults, which might also have discrete spreading centers. There seems to be no seismic activity deeper than 10 km, in agreement with other oceanic microearthquake studies and with results from seismic moment summing [Brune, 1968] and surface waves [Weidner and Aki, 1973], but this result should be considered in the context of a leaky, not a simple, tranform.

At the EPR-RFZ intersection, earthquake activity was mostly outside the three-station array, so it was not possible to constrain the depths of most of the events. One event nearly beneath one of the OBS's had a depth of 5.4 ± 2 km. Activity was offset from the RFZ near the spreading axis, indicating an unexpected complexity in the plate boundary near the junction. This may reflect a continuation of the en echelon spreading transform pattern of the western RFZ, or possibly be a boundary effect at the corner of the plate. The seismicity appears to terminate sharply at the rise crest, confirming the position and narrowness of the spreading zone. Earthquakes in this region also tend to cluster in swarmlike sequences, probably reflecting the association of earthquake

swarms with ridge crests and other volcanic regimes.

Stress drops, computed from S wave spectra for nearby events at the RFZ deployment, were compared to stress drops determined for EPR-RFZ intersection events. All of the stress drops were low (between 0.1 and 10 bars), and no systematic difference between the two sites was observed. Larger earthquakes observed at teleseismic distances [Thatcher, 1972] do show relatively lower stress drops near to ridge crests. If small earthquakes in these regions tend to have low stress drops, as observed for the aftershocks of the San Fernando Earthquake of 1971 (J. N. Brune, personal communication, 1976), then the low stress drops observed at the RFZ deployment site may simply reflect the lack of larger events recorded and a natural tentency for small events to have low stress drops.

Acknowledgments. Mike Reichle, Dave Willoughby, Dorothy Darling, Georgeanne Ray, John Orcutt, Paul Spudich, and Captain Newbegin and the crew of the Ellen B. Scripps contributed in an important way to this research. The authors would also like to thank J. Berger and D. Agnew for providing us with a theoretical earthtide generating program. Ken Macdonald and two anonymous reviewers also made comments which improved this paper substantially. This work was sponsored by the National Science Foundation.

References

Brune, J. N., Seismic movement, a seismicity, and rate of slip along major fault zones, J. Geophys. Res., 73, 777-784, 1968.

Brune, J. N., Tectonic stress and the spectra of seismic shear waves from earthquakes, J. Geophys. Res., 75, 4997-5009, 1970.

Brune, J. N., Corrections, J. Geophys. Res., 76, 5002, 1971.

Brune, J. N., and C. R. Allen, Low stress drop, low magnitude earthquake with surface faulting: The Imperial California, earthquake of March 4, 1966, Bull. Seismol. Soc. Am., 57, 501-514, 1967.

Buland, R., The mechanics of locating earthquakes, Bull. Seismol. Soc. Am., 66, 173-187, 1976.

Buskirk, R. E., C. Frohlich, and G. Latham, Evidence that biological activity affects ocean bottom seismograph recordings (abstract), Eos Trans. AGU, 61, 309, 1980.

Helmberger, D., and L. R. Johnson, Source parameters of moderate size earthquakes and the importance of receiver crustal structure in interpreting observations of local earthquakes, Bull. Seismol. Soc. Am., 67, 301-313, 1977.

Hileman, J. A., C. R. Allen, and J. M. Nordquist, Seismicity of the southern California region 1 January 1932 to 31 December 1972, Calif. Inst. of Technol., Contrib. 2385, Pasadena, 1973.

Kubotera, A., Volcanic tremors at Aso Volcano, in Physical Volcanology, edited by L. Civetla, P. Gasparini, G. Luongo, and A. Rupolla, pp. 29-48, Elsevier, New York, 1974.

Larson, R. L., Near-bottom geologic studies of the East Pacific Rise Crest, Geol. Soc. Am. Bull., 82, 823-842, 1971.

Larson, R., Near-bottom studies of the East Pacific Rise Crest and tectonics of the mouth of the Gulf of California, Ph.D. dissertation, Univ. of Calif. at San Diego, La Jolla, 1972a.

Larson, R., Bathymetry, magnetic anomalies, and plate tectonic history of the mouth of the Gulf of California, Geol. Soc. Am. Bull., 82, 3345-3360, 1972b.

Macdonald, K., J. A. Orcutt, and J. S. McClain, Ocean bottom microearthquake studies of the RISE hydrothermal field (abstract), Eos Trans. AGU, 61, 1048, 1980.

Mammerickx, J., M. S. Reichle, and I. D. Reid, Bathymetry of the Rivera Fracture Zone, IMR, Tech. Rep. TR62, Scripps Inst. of Oceanogr., San Diego, Calif., 1978.

Meyers, H., and C. A. von Hake, Earthquake data file summary, Natl. Geophys. and Solar-Terr. Data Cent., Boulder, Colo., 1976.

Molnar, P., Fault plane solutions of earthquakes and direction of motion in the Gulf of California and on the Rivera Fracture Zone, Geol. Soc. Am. Bull., 84, 1651, 1973.

Normark, W. R., Delineation of the main extrusion zone of the East Pacific Rise at lat. 21°N., Geology, 4, 681-685, 1976.

Prothero, W. A., A digital event-recording ocean bottom seismometer capsule, Mar. Geophys. Res., 3, 119-141, 1977.

Prothero, W. A., I. Reid, M. S. Reichle, and J. N. Brune, Ocean bottom seismic measurements on the East Pacific Rise and Rivera Fracture Zone, Nature, 262, 121-124, 1976.

Reid, I., The Rivera plate: A study in seismology and plate tectonics, Ph.D. thesis, Univ. of Calif. at San Diego, La Jolla, 1976.

Reid, I., and W. A. Prothero, An earthquake sequence studied with ocean-bottom seismographs, Geophys. J. R. Astron. Soc., 64, 381-391, 1981.

Reid, I., J. Orcutt, and W. Prothero, Seismic evidence for a narrow zone of partial melting underlying the East Pacific Rise at 21°N., Geol. Soc. Am. Bull., 88, 679-682, 1977.

Rise Team, East Pacific Rise: hot springs and geophysical experiments, Science, 207, 1421-1433, 1980.

Rosendahl, B. R., R. W. Raitt, L. M. Dorman, L. D. Bibee, D. M. Hussong, and G. H. Sutton, Evolution of the oceanic crust, 1, A physical model of the East Pacific rise crest derived from seismic refraction data, J. Geophys. Res., 81, 5294-5304, 1976.

Sutton, G., et al., Lopez Island ocean bottom seismometer intercomparison experiment, Geophys. Rep. HIG-80-4, Hawaii Inst. of Geophys., Honolulu, 1980.

Thatcher, W., Regional variations of seismic source parameters in the Northern Baja California area, J. Geophys. Res., 77, 1549-1565, 1972.

Tucker, B., and J. N. Brune, Seismograms, S wave spectra, and source parameters for aftershocks of San Fernando earthquake: San Fernando, California, Earthquake of February 9, 1971, Publ. 3, pp. 69-121, NOAA, Washington, D.C., 1973.

Weidner, D., and K. Aki, Focal depth and mechanism of mid-ocean ridge earthquakes, J. Geophys. Res., 78, 1818, 1973.

(Received June 11, 1981;
revised October 14, 1981;
accepted October 16, 1981.)

JOURNAL OF GEOPHYSICAL RESEARCH, VOL. 87, NO. B8, PAGES 6725–6750, AUGUST 10, 1982

Northern East Pacific Rise: Magnetic Anomaly and Bathymetric Framework

KIM D. KLITGORD

U.S. Geological Survey, Woods Hole, Massachusetts 02543

JACQUELINE MAMMERICKX

Geologic Research Division, Scripps Institution of Oceanography, La Jolla, California 92093

The oceanic crust in the eastern Pacific between 7°N and 30°N and east of 127°W contains a fairly complete history of the spreading centers associated with the East Pacific Rise since 25 m.y. B.P. (late Oligocene). In this paper, we have summarized the seafloor spreading magnetic-anomaly data and the bathymetric data that reflect the record of this tectonic history. The well-defined magnetic lineations north of the Clarion fracture zone, in the mouth of the Gulf of California, and on the east flank of the East Pacific Rise (EPR) are carefully examined and used to provide a guide for interpreting the spreading pattern between the Clarion and Clipperton fracture zones, southward of the Rivera fracture zone over the Mathematician Ridge, and over the entire EPR east of the Mathematician Ridge between the Rivera and Siqueiros fracture zones. The bathymetric data provide a trace of the fracture zone pattern in each of the above mentioned areas. The fracture zone bathymetry and the seafloor spreading magnetic lineations on the EPR south of the Rivera fracture zone have a distinctive fanning pattern caused by close poles of rotation and plate boundary reorganizations. All these data provide a good record of the plate reorganizations in the middle Miocene at magnetic anomaly 5A time (12.5 to 11 m.y. B.P.), in the late Miocene at magnetic anomaly 3'–4 time (6.5 m.y. B.P.), and in the Pliocene at magnetic anomaly 2'–3 time (3.5 m.y. B.P.). Several abandoned spreading centers, including the Mathematician Ridge, were left behind as a result of these reorganizations. The Mathematician Ridge is shown to be a set of ridges and trough whose origin is related to the tectonic activity associated with each of the above mentioned reorganizations since anomaly 5A.

INTRODUCTION

The crest of the East Pacific Rise (EPR) is the youngest point on the tape recording of the eastern Pacific tectonic history. North of the equator, the crest of the EPR forms the present plate boundary between the Pacific and Cocos plates (Pacific-Cocos spreading center) and Pacific and Rivera plates (Pacific-Rivera spreading center) (Figure 1). The four plates involved in the post-Oligocene history of the EPR between the Galapagos and Murray fracture zones are the Pacific, Guadalupe, Rivera, and Cocos. The Guadalupe plate evolved into the Rivera and Cocos plates, and the transform boundary between the Rivera and Cocos plates shifted as the spreading center between them and the Pacific plate shifted.

Reorganizations of plate motions altered spreading center trends and shifted plate boundaries. This history of plate motions and plate boundaries is recorded in the tectonic fabric of the region (Figure 2): the bathymetric structure and magnetic anomaly patterns. Fracture zones trace the motion of the plates away from the spreading center, and the seafloor spreading magnetic lineations allow the crustal ages to be mapped. In addition to the long periods of relatively uniform plate motion, the magnetic and bathymetric data record plate reorganizations, including changes in spreading direction, spreading center jumps, and other shifts in plate boundaries (the breakup or joining of plates). Although these dramatic reorganizations are recorded in the oceanic crust [*Sclater et al.*, 1971], the resultant complex pattern of magnetic lineations requires detailed identification of the magnetic anomalies that are younger and older than the tectonic event.

Paper number 2B0274.

In this paper we examine the available magnetic anomaly (Figure 3) and bathymetric data [*Mammerickx and Smith*, 1981] for the EPR north of 7°N. These data provide the basis for constructing a more comprehensive plate tectonic model for the eastern equatorial Pacific [*Mammerickx and Klitgord*, this issue]. Previous regional studies have concentrated on the tectonics north of the Clarion fracture zone (near 20°N) [*Hayes and Pitman*, 1970; *Menard*, 1978; *Morton and Lowrie*, 1978] or south of the Galapagos fracture zone (near the equator) [*Pitman et al.*, 1968; *Herron*, 1972; *Molnar et al.*, 1975; *Mammerickx et al.*, 1975; *Handschumacher*, 1976] and have made general inferences on the tectonic structure between the equator and 20°N. Detailed areal or topical studies have provided evidence for most of the basic tectonic structures for the EPR north of the equator [*Larson et al.*, 1968; *Chase et al.*, 1970*b*; *Sclater et al.*, 1971; *Larson*, 1972; *Herron*, 1972; *Lynn and Lewis*, 1976], and these results have been incorporated into our regional study.

PREVIOUS WORK

The eastern equatorial Pacific north of the equator (Figure 2) has been the site of many geophysical surveys, some dating back to the 1950's [*Menard*, 1960, 1964]. The relatively shallow depths associated with the EPR (Plate 1*a*) are evident on the regional bathymetric charts [e.g., *Menard*, 1960, 1964; *Heezen*, 1962; *Chase et al.*, 1970*b*; *Mammerickx and Smith*, 1981] and many detailed investigations have been made of the ridge crest [e.g., *Menard*, 1964; *Menard and Mammerickx*, 1967; *Sclater et al.*, 1971; *Larson*, 1972; *Crane*, 1976; *Lonsdale*, 1977; *Lonsdale and Spiess*, 1980; *Mammerickx*, 1980; *Normark*, 1980]. The major Pacific fracture zones, which have large topographic expressions (Plates 1*b* and 1*c*), have been traced into the eastern Pacific [*Menard and Fisher*, 1958; *Menard*, 1964; *Menard and*

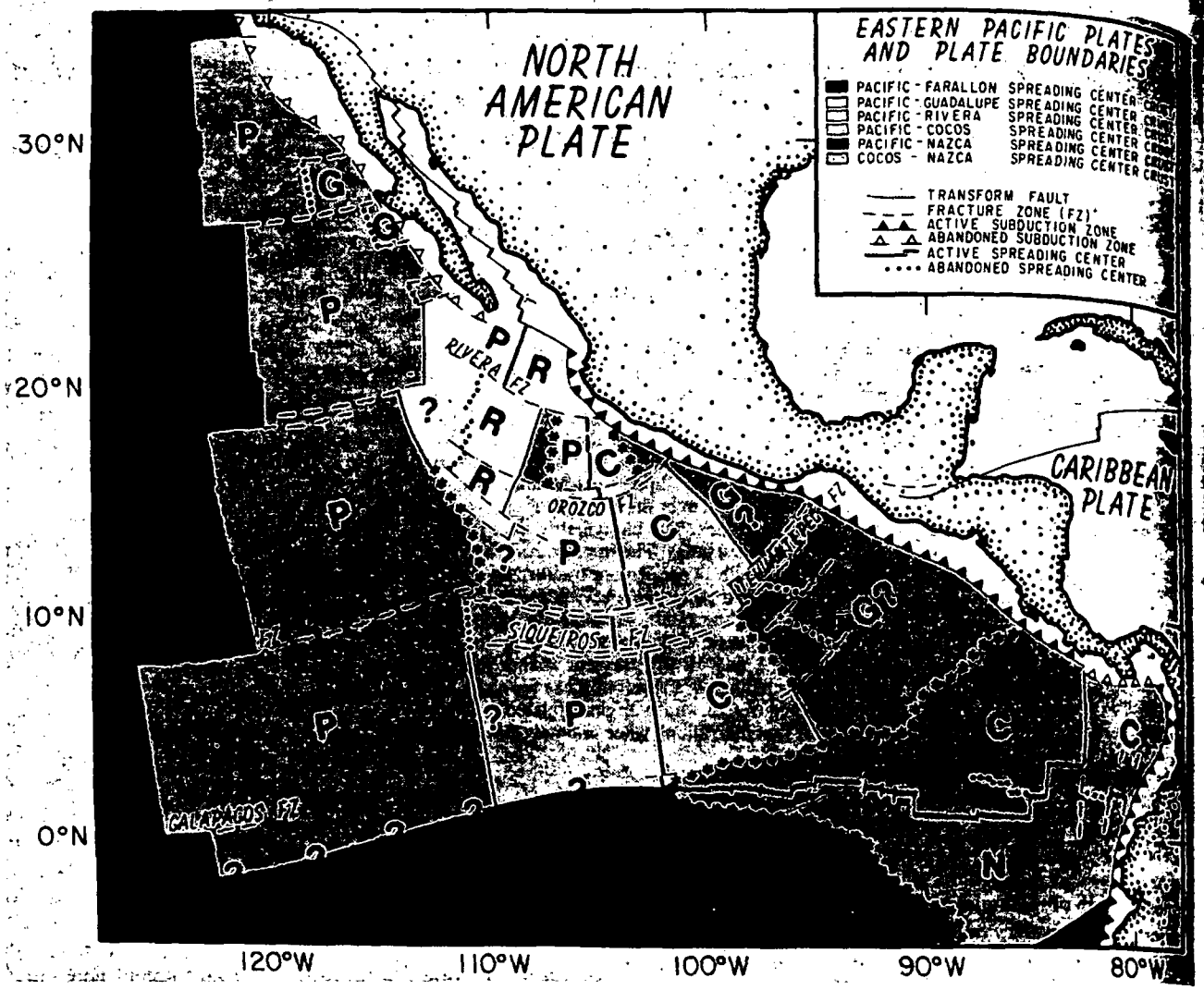

Fig. 1. Plates and plate boundaries in the eastern equatorial Pacific. Shading indicates the spreading center origin for various parts of the Pacific (P), Rivera (R), Cocos (C), and Nazca (N) plates. Abandoned parts of the Guadalupe (G) plate that are now part of the Pacific plate off Baja and part of the Cocos plate off the Middle America trench are also indicated.

Chase, 1970] and provide considerable control on the possible interpretations of the evolution of the Pacific-Farallon spreading center [*Menard*, 1978]. Some of the fracture zones and transform faults in the mouth of the Gulf of California and east of the Mathematician Ridge (Plate 1) have been studied in detail. These include the Tamayo fracture zone [*Kastens et al.*, 1979], the Rivera fracture zone [*Larson*, 1972; *Prothero et al.*, 1976; *Mammerickx et al.*, 1978], the Orozco fracture zone [*Project ROSE Scientists*, 1981; *Ewing and Meyer*, 1982], the Siqueiros fracture zone [*Crane*, 1976; *Rosendahl and Dorman*, 1980], and the Tehuantepec Ridge [*Truchan and Larson*, 1973; *Couch and Woodcock*, 1981]. However, the connection between these fracture zones and the major Pacific fracture zones (Clarion, Clipperton, Galapagos) has been uncertain. The Mathematician Ridge [*Sclater et al.*, 1971] and the Clipperton Ridge [*Menard and Fisher*, 1958; *van Andel et al.*, 1975] have been interpreted as abandoned spreading centers [*Menard*, 1969; *Sclater et al.*, 1971; *Herron*, 1972; *Anderson and Davis*, 1973; *van Andel et al.*, 1975]. These abandoned spreading centers probably are related to the system of fossil spreading centers found south of the equator [*Anderson and Sclater*, 1972; *Herron*, 1972; *Handschumacher*, 1976; *Mammerickx et al.*, 1980; *Rea*, 1978, 1981].

Only certain segments of the seafloor spreading magnetic anomaly lineation pattern associated with the EPR have been examined in detail. The magnetic lineations north of the Clarion fracture zone west of Baja California (Plate 2b) [*Atwater and Menard*, 1970; *Chase et al.*, 1970a; *Taylor et al.*, 1971; *Theberge*, 1971; *Morton and Lowrie*, 1978] are from the western flank of the Pacific-Farallon spreading center (PFSC) and the Pacific-Guadalupe spreading center (PGSC) [*Atwater*, 1970; *Menard*, 1978] (Figure 1). These lineations are easily correlated with the geomagnetic time scale [*Heirtzler et al.*, 1968; *Ness et al.*, 1980] and with the magnetic lineations west of Washington, Oregon, and California [*Mason and Raff*, 1961; *Raff and Mason*, 1961; *Atwater and Menard*, 1970; *Theberge*, 1971; *Elvers et al.*, 1973], which are some of the best examples of seafloor spreading magnetic lineations. South of the Clarion fracture zone and west of the Mathematician Ridge the approximate locations of magnetic anomalies 6 and 7 have been indicated [*Herron*, 1972; *Handschumacher*, 1976; *Menard*, 1978] on the basis of only a couple of profiles, but examination of the

entire anomaly pattern (Plate 2c) for crust younger than anomaly 7 (25 m.y. B.P.) is necessary to develop the tectonic history of the Mathematician Ridge. South of the Gulf of California, the last 11 m.y. of seafloor spreading history has been faithfully recorded in the magnetic anomalies over the Pacific-Rivera spreading center (PRSC) between Tamayo and Rivera fracture zones (Plate 2a) [*Larson et al.*, 1968; *Atwater*, 1970; *Larson*, 1972]. The magnetic lineation pattern over the Mathematician Ridge south of the Rivera fracture zone is associated with the PRSC until anomaly 2' time [*Sclater et al.*, 1971; *Handschumacher*, 1976; *Menard*, 1978]. Although we agree with the symmetrical set of magnetic lineation correlations presented by *Handschumacher* [1976], the correlations are fairly tenuous, and the magnetic anomaly pattern south of the Orozco fracture zone is even more complex.

The magnetic anomaly pattern about the present EPR (Plate 2a) between the Rivera and Siqueiros fracture zones has been partially identified out to anomaly 5. Between the Rivera and Orozco fracture zones, the lineations can be found on both flanks of the EPR to just past anomaly 2', where a major bathymetric and tectonic discontinuity exists [*Sclater et al.*, 1971; *Lynn and Lewis*, 1976]. Between the Orozco and Siqueiros fracture zones the magnetic lineations on the northern part of the eastern flank of the EPR have been identified out to anomaly 5 [*Larson and Chase*, 1970; *Sclater et al.*, 1971; *Lynn and Lewis*, 1976; *Schilt et al.*, 1982]. On the western flank of this same ridge segment, the lineations have been mapped on the basis of only two or three profiles [*Larson and Chase*, 1970; *Sclater et al.*, 1971; *Herron*, 1972]. South of the Siqueiros fracture zone (Plates 1a and 2a), the rise crest has been charted, but the published identification of magnetic lineations consists of a tenuous interpretation of one profile by *Herron* [1972].

METHOD OF STUDY

A new bathymetric contour map for the equatorial Pacific (Plate 1) [*Mammerickx and Smith*, 1981] provides the essential framework upon which we have located and identified the seafloor spreading magnetic anomaly lineations (Plate 2). Besides delineating major fracture zone trends and anomalous structural features (e.g., the Mathematician Ridge), the

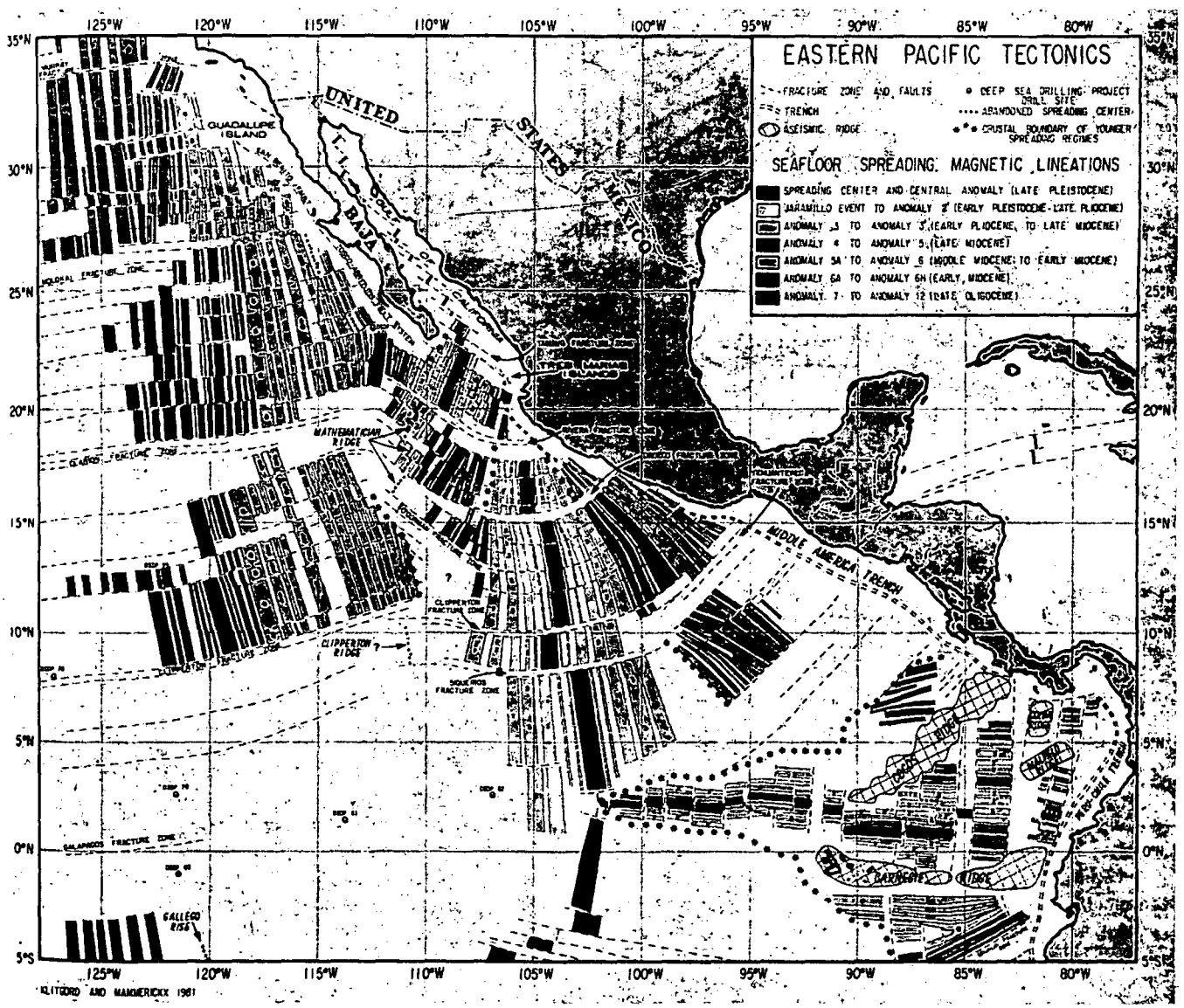

Fig. 2. Tectonic fabric for the eastern equatorial Pacific. The locations of the most important bathymetric features, such as fracture zones, trenches and aseismic ridges, and many of the seafloor spreading magnetic lineations are shown. Boundaries between oceanic crust generated at different spreading centers are indicated.

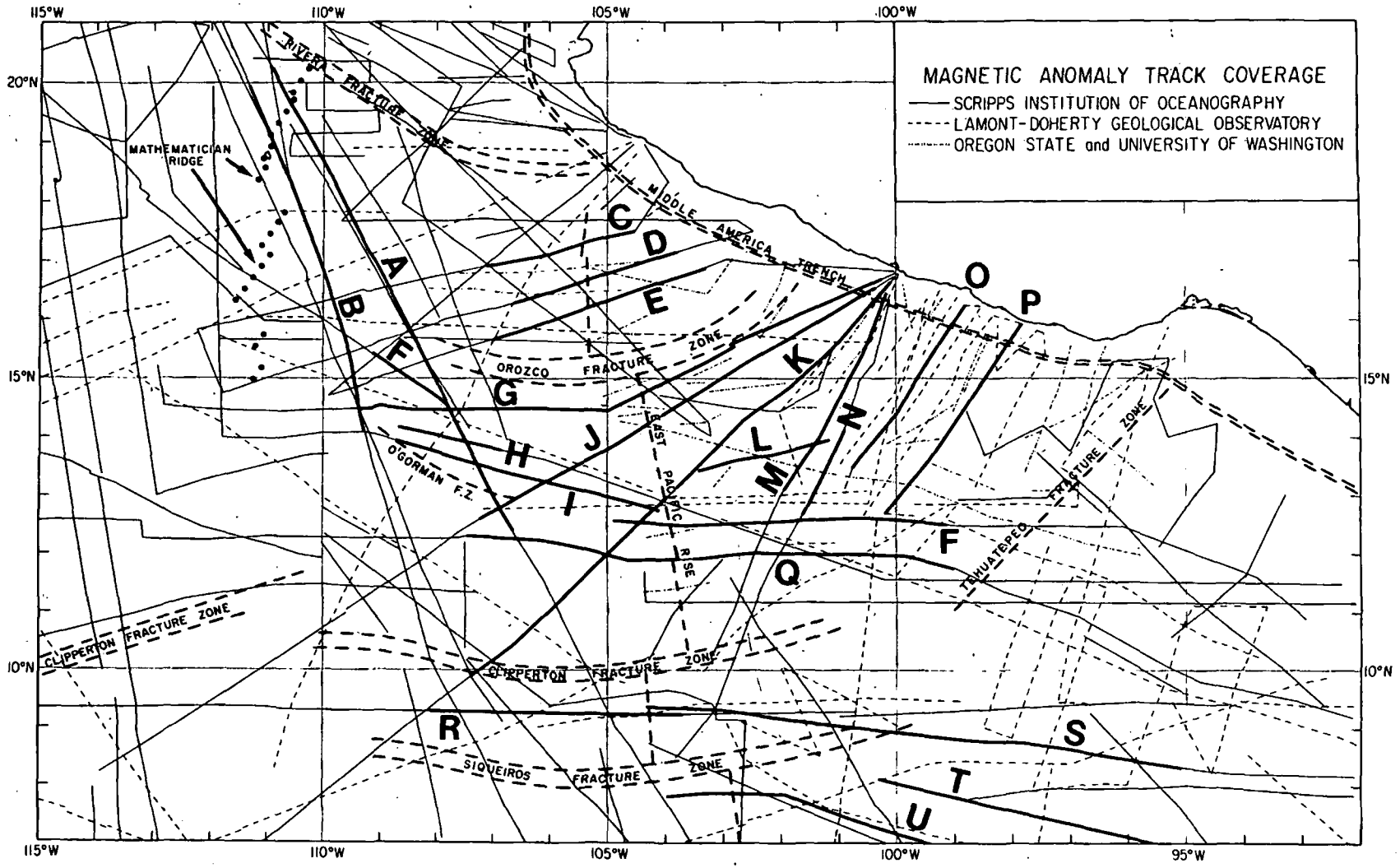

Fig. 3*a*

Fig. 3. Track line locations used in the compilation of the magnetic anomaly lineation maps. The track lines for Plate 2a are shown in Figure 3a, those for Plates 2b and 2c are shown in Figure 3b. The profiles are labeled according to the institution source. The heavier lines on Figure 3a are locations for profiles shown in Figures 4, 6, 7, 10, and 11; the profiles are labeled as follows: Pleiades (A), F. Drake 77 (B), Scan 11 (C, D, E), Explorer 60 (F), Tripod 3 (G), T. Washington (H), Siqueiros (I), Scan 10 (J), Swansong (K), OSU/UW (L), Cocotow 1 (M), Cocotow 2 (N), LDGO (O, P), *Glomar Challenger* 16 (Q), Papagayo 1 (R), *Glomar Challenger* 54 (S, U), and Indomed (T). The heavier lines on Figure 3b are locations for profiles shown in Figures 5, 8, and 9; the profiles are labeled as follows: Gam 1 (A, B, C, D, E), Gam 2 (K, L, M, N, O), LDGO (F, G), *Conrad* 10.5 (I), Tripod (H), *Glomar Challenger* 16 (J), Cocotow 1 (P), Dolphin 2 (Q), Pleiades 1 (R), and F. Drake 77 (S).

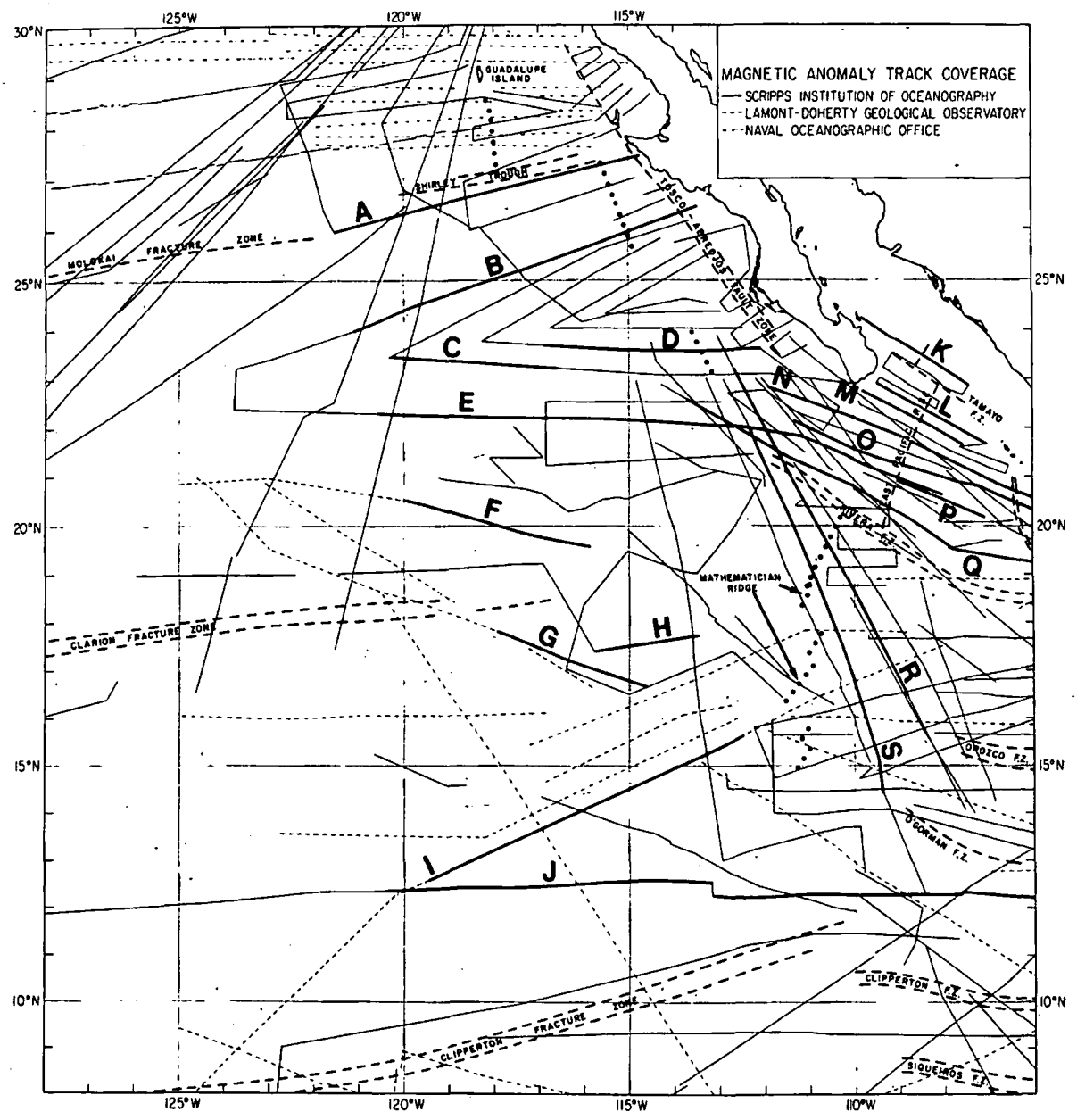

Fig. 3*b*

Scan 11 (C, D, E), Explorer 60 (F), Tripod 3 (G), T. Washington (H), Siqueiros (I), Scan 10 (J), Swansong (K), OSU/UW (L), Cocotow 1 (M), Cocotow 2 (N), LDGO (O, P), *Glomar Challenger* 16 (Q), Papagayo 1 (R), *Glomar Challenger* 54 (S, U), and Indomed (T). The heavier lines on Figure 3b are locations for profiles shown in Figures 5, 8, and 9; the profiles are labeled as follows: Gam 1 (A, B, C, D, E), Gam 2 (K, L, M, N, O), LDGO (F; G), *Conrad* 10.5 (I), Tripod (H), *Glomar Challenger* 16 (J), Cocotow 1 (P), Dolphin 2 (Q), Pleiades 1 (R), and F. Drake 77 (S).

bathymetric data indicate the possible locations of minor fracture zones that might affect the magnetic anomaly pattern. The present crest of the EPR is delineated in the bathymetry as a regional basement high, whereas spreading centers that were abandoned during plate reorganizations are seen as a combination of regional swells [*Sclater et al.*, 1971] and narrow median troughs [*Anderson et al.*, 1976, 1978; *Lonsdale and Klitgord*, 1978].

The correlation of magnetic anomaly lineations with the geomagnetic time scale is difficult in equatorial regions, and we have used both modeling and extrapolation techniques to facilitate the lineation identifications. The low-amplitude seafloor spreading magnetic anomalies associated with a north trending ridge in the equatorial region [*Raff*, 1968; *Schouten*, 1971] are often masked by short-period time variation anomalies and by anomalies caused by variations in the depth to the magnetized layer. The shape distortion in the magnetic anomaly pattern, which is used to determine the phase shifting and thus the remanent magnetization parameters of the oceanic crust [*Schouten and McCamy*, 1972], is often obscured in a region of low magnetic signal-to-noise ratio. This makes the task of comparing observed anomalies with synthetic anomalies produced by means of the geomagnetic time scale [*Heirtzler et al.*, 1968] very difficult. In this study, the magnetic anomaly pattern in regions where the lineations are well established were carefully analyzed and compared with synthetic magnetic anomaly profiles. The geomagnetic time scale of *Ness et al.* [1980] is used here to date magnetic lineations and to calculate model magnetic anomaly profiles. These results were then extrapolated into regions where sparse data density and low-amplitude anomalies make the identification of lineations uncertain. The comparison of anomaly patterns with nearby anomalies that have been identified is often easier than attempting to correlate anomalies with the geomagnetic time scale.

The regions of our extrapolated interpretations are as follows: (1) lineations west of the Mathematician Ridge

between the Clarion and Clipperton fracture zones extrapolated from the lineations north of the Clarion fracture zone [*Atwater and Menard*, 1970; *Chase et al.*, 1970*a*; *Morton and Lowrie*, 1978], (2) lineations associated with the Mathematician Ridge extrapolated southward from the Gulf of California lineations [*Larson et al.*, 1968], and (3) lineations east of the Mathematician Ridge between the Orozco and Siqueiros fracture zones extrapolated to the south and to the west flank of the EPR from the lineation pattern on the eastern flank of the EPR just south of the Orozco fracture zone [*Lynn and Lewis*, 1976; *Schilt et al.*, 1982].

Data Bases

Bathymetric Data

The bathymetric contours used in our study (Plates 1*a*–1*c*) are derived from available data in the eastern Pacific [*Mammerickx et al.*, 1978; *Mammerickx*, 1980; *Mammerickx and Smith*, 1981]. The density of ship track coverage used in this recompilation [see *Mammerickx and Smith*, 1981] is quite variable; the densest coverage is found in the Gulf of California, along the crestal region and on the eastern flank of the EPR and north of the Clarion fracture zone west of Baja California. The region encompassing the Mathematician and Clipperton ridges and the region west of these ridges has a fairly sparse track coverage. In this region of sparse coverage, there is considerable freedom in the closure patterns chosen for the various bathymetric features. In such regions the contours were oriented to be in agreement with the trends of adjacent structural features that are better delineated and to be consistent with our basic tectonic model constructed from both the magnetic and bathymetric data. This technique has proven useful in other regions of sparse data coverage, such as the southeastern Pacific [*Molnar et al.*, 1975; *Mammerickx et al.*, 1975]. It does result, however, in a certain amount of interpretative bias in the contouring. Because the contours are not allowed to disagree with the bathymetric values along any given ship track, the track coverage map [see *Mammerickx and Smith*, 1981] provides a means for estimating the amount of interpretation in the contouring for any given region and thus the reliability of the trends of individual bathymetric features.

Magnetic Anomaly Data

Much of the available magnetic data (Figure 3) has been incorporated into our study, including profiles from the Scripps Institution of Oceanography (SIO), Oregon State University (OSU), Lamont-Doherty Geological Observatory (LDGO), University of Washington, (UW), U.S. Naval Oceanographic Office (USNOO), and the data archives of the National Geophysical and Solar-Terrestrial Data Center (NGSDC). Some of the data were available on magnetic tape, although most of the profiles were taken from existing plots. The magnetic anomalies plotted along track in Plates 2*a*–2*c* were compiled at 1.2-in./deg longitude on a Mercator Projection, but the magnetic anomalies are not all at the same vertical scale. The bulk of the data was taken from the SIO Geologic Data Center Track charts of SIO magnetic data [*Chase et al.*, 1972], updated to 1978. For most of these profiles, the data north of 15°N were compiled at 1000 nT (1 nanotesla = 1 gamma) per inch, whereas south of 15°N, they were compiled at 500 nT/in. The OSU and UW data were taken directly from *Lynn and Lewis* [1976, Figure 2] and are at a vertical scale of about 1000 nT/in. The LDGO data were recompiled at 1000 nT/in. and come from various *Conrad* and *Vema* cruises [see, e.g., *Herron*, 1972; *Ludwig and Rabinowitz*, 1980]. The aeromagnetic data of the USNOO between 28°N and 32°N were taken directly from *Taylor et al.* [1971, Figure 3] and were recompiled at 650 nT/in. on our 1.2-in./deg compilation. Other USNOO data were taken from *Morton and Lowrie* [1978, Plate 10] and were recompiled at 800 nT/in.

The regional field removed from the profiles varies considerably, and we have not attempted to preserve a standard baseline value (such as a zero value at the ship track) for the anomalies plotted along track. We generally removed an arbitrary value from the anomaly values for each cruise in an attempt to center the plotted anomaly about the ship track. Because the primary interpretation of the magnetic lineations is based upon anomaly shapes and spacing and not on absolute values, this arbitrary shift does not affect our interpretation but does facilitate the graphic display of the data.

Bathymetric Features

Fracture Zones

Fracture zone topography is one of the most distinctive features of the eastern Pacific [*Menard*, 1964, 1966]. The fracture zone marks the path of a spreading center [*Le Pichon*, 1968; *Morgan*, 1968] and provides important information for determining poles of rotation [*Harrison*, 1972]. Three different sets of fracture zones are found in the eastern equatorial Pacific: (1) fracture zones west of Baja California and the Mathematician Ridge, (2) fracture zones in the mouth of the Gulf of California and associated with the Mathematician Ridge, and (3) fracture zones east of the Mathematician ridge and related to the EPR south of the Rivera fracture zone.

Fracture zones west of the Mathematician-Clipperton Ridge and those north of the Clarion fracture zone (Plate 1), follow the same general trend as the major Pacific fracture zones. East of magnetic anomaly 7, the fracture zone trend swings more northeast, the ridge crest orientation becoming nearly parallel to the coastline and presumably to the subduction zone [*Mammerickx and Klitgord*, this issue]. Paralleling the major fracture zones are many isolated seamounts, narrow ridges, and troughs that may be the topographic expressions of additional fracture zones.

Three of the major Pacific fracture zones (Figure 1)—the Molokai, Clarion, and Clipperton—cross our study area. The bathymetric expression of the Molokai fracture zone is substantially diminished as it enters the survey area near 25°N (Plate 1*b*), the prominent bathymetric lineament shifting 100 km northward to form the Shirley Trough [*Menard*, 1978]. The Clarion fracture zone (Plate 1*c*) is a set of parallel features west of anomaly 7 that splay to the east. Bathymetric features along the northern side of the fracture zone follow the trend of the fracture zones to the north, whereas the southern side follows a more easterly trend along 18°N. The Clipperton fracture zone is also a broad zone of parallel structures that swings slowly northeast until it reaches the Mathematician Ridge. Between the Molokai and Clarion fracture zones, the general fracture zone trend swings slowly from 085° near anomaly 7 to 073° near anomaly 5B. The fracture zone trend between the Clarion and Clipperton fracture zones swings slowly from 080° near anomaly 7 to 073° near anomaly 5B. Because of the sparse track density in

the western part of our study area, the small difference in the fracture zone trends for similar age crust north and south of the Clarion fracture zone is not considered significant.

The fracture zones in the mouth of the Gulf of California (Plate 1*b*) have a variety of trends that reflect past changes in the motion of the Rivera plate. The present southeast trend of the Tamayo and Rivera fracture zones (about 124°) [*Larson*, 1972; *Kastens et al.*, 1979; *Mammerickx*, 1980] has existed only since anomaly 2′ time [*Klitgord et al.*, 1975]. During the formation of anomaly 2′, the fracture zones had a slightly more easterly trend, and between anomaly 2′ and anomaly 4 time, the trend was even more southeasterly (about 130°) than at present. This fracture zone trend of about 130° is clearly recorded in the bathymetric relief [*Mammerickx*, 1980] and follows the trend of the Tres Marias Islands and their adjacent southern scarp. South of the Tres Marias fracture zone [*Mammerickx*, 1980], the fracture zone trends swing slowly to a more easterly direction between anomalies 4 and 5 on the east flank of the Pacific-Rivera spreading center, whereas the fracture zone trends on the western flank swing around to the west until they merge into the older Pacific-Guadalupe system trends.

The fracture zones associated with the Mathematician Ridge (Plate 1*a*) are nearly parallel to the fracture zones associated with magnetic anomalies 3 to 4 in the Gulf of California. Several deep troughs, which we interpret as the expression of fracture zones, are well defined east of the Mathematician Ridge (Plate 1*a*), the most prominent of these troughs being associated with the O'Gorman fracture zone [*Mammerickx and Smith*, 1981]. South of the O'Gorman fracture zone, this same southeast trend is mapped as offsetting the Mathematician Ridge, but the trends are very uncertain just east of 110°W because of the sparse data. The large east trending bathymetric peak and trough near 10°N forms the southernmost boundary of these southeast trending features. This large east trending bathymetric feature has been considered part of the Clipperton fracture zone and intersects the northeast trending older part of the Clipperton fracture zone near 112°W. This large ridge and trough extends from 112°W to 107°W, where it merges into the younger part of the Clipperton fracture zone that is parallel to the Siqueiros fracture zone and offsets the present EPR at 10°N. The bathymetric features south of this east trending ridge and trough, in the vicinity of the Clipperton Ridge (near 111°W), appear to change gradually from a northeast trend that parallels the older Clipperton fracture zone to a more easterly trend parallel to the Siqueiros fracture zone.

The fracture zones associated with the EPR between the Rivera and Siqueiros fracture zones (Plate 1*a*) sweep in an arc, concave to the north, away from the EPR. On crust younger than anomaly 4 are four prominent fracture zones: Rivera, Orozco, Clipperton, and Siqueiros. Each of these fracture zones is a broad topographic structure consisting of several parallel deep troughs and large ridges. Each of these fracture zones coincides with a large offset in the EPR. The largest of the fracture zones that do not offset the EPR is the O'Gorman fracture zone, which has a deep trough that can be traced into anomaly 3 on both flanks. A large ridge on the south side of the fracture zone on the eastern flank of the EPR continues from anomaly 2′ to the edge of the central anomaly.

Between these major fracture zones are narrow troughs and small chains of seamounts, which we have interpreted as additional fracture zones that offset the magnetic lineations in places. Among these latter features, those at 17.8°N, 17°N, 12°N, and 9°N offset the present EPR. Other smaller troughs parallel to these features also may be the expressions of fracture zones. As in the Atlantic, the amount of offset on any transform fault may change, or even become negligible, forming 'zero offset' transform faults [*Schouten and White*, 1980; *Schouten and Klitgord*, 1982], while the topographic and crustal structure of the transform fault often remains. The bathymetric features interpreted as fracture zones on the eastern flank of the EPR on crust older than anomaly 3′ (6.5 m.y. B.P.) are parallel to the Tehuantepec Ridge and trend more steeply to the northeast than does the younger set of fracture zones. Although the arcuate shape of the EPR fracture zone pattern is caused primarily by a close pole of rotation for the EPR since 11 m.y. B.P., some contribution to this arclike trend has been made by the change in spreading direction prior to 6.5 m.y. B.P. [*Lynn and Lewis*, 1976] and the intersection of the Mathematician system with the western flank of the EPR.

The Tehuantepec Ridge on the north side of the Tehuantepec fracture zone (Plate 1*a*) is the largest linear bathymetric feature on the east flank of the EPR. This ridge has such large relief because it is the morphologic expression of a fracture zone that separates crust of significantly different ages, the younger shallower crust being to the north [*Truchan and Larson*, 1973]. Like the other major Pacific fracture zones, the Tehuantepec fracture zone is a broad bathymetric structure. The trend of the northern ridge (the Tehuantepec Ridge) parallels the fracture zones north of the Tehuantepec fracture zone and the structural trends along the south side of the fracture zone are parallel to the features to the southeast. Although it may look like the Tehuantepec fracture zone connects to the younger Clipperton fracture zone at 10°N [*Truchan and Larson*, 1973], it actually terminates in the vicinity of 11°N, 99°W. Near this point, the structures along the north side of the Tehuantepec fracture zone swing around to a more westerly trend, whereas the structures on the south side remain on the same southwest trend for the entire length of the fracture zone. The southwest trending lineaments on the southeast side of the Tehuantepec fracture zone also do not change trend and they terminate rather than continuing around to meet the EPR fracture zones.

Spreading Centers and Plate Boundaries

A distinctive bathymetric relief is associated with both the present and the abandoned spreading centers. The rise crest of the present EPR (Figure 4) [*Menard*, 1964; *Sclater et al.*, 1971] can be traced across our study area from 7°N, 102.8°W to 18°N, 105.5°W (Plate 1*a*), where it is offset by the Rivera fracture zone into the mouth of the Gulf of California. North of the Rivera fracture zone, the broad bathymetric high (Plate 1*b* and Figure 5) continued northeastward from 20°N, 109°W to the Tamayo fracture zone near 23°N, 108°W. Within the Gulf of California the spreading center is a series of narrow troughs connected by long transform faults. The crest of the EPR is a bathymetric peak south of the Rivera fracture zone (Figure 4) [*Sclater et al.*, 1971; *Anderson and Noltimier*, 1973], whereas it often has a small axial depression north of the Rivera fracture zone [*Mammerickx*, 1980]. The bathymetric relief generated at the EPR does not vary much along its length (Figure 4), the changes in the scale of

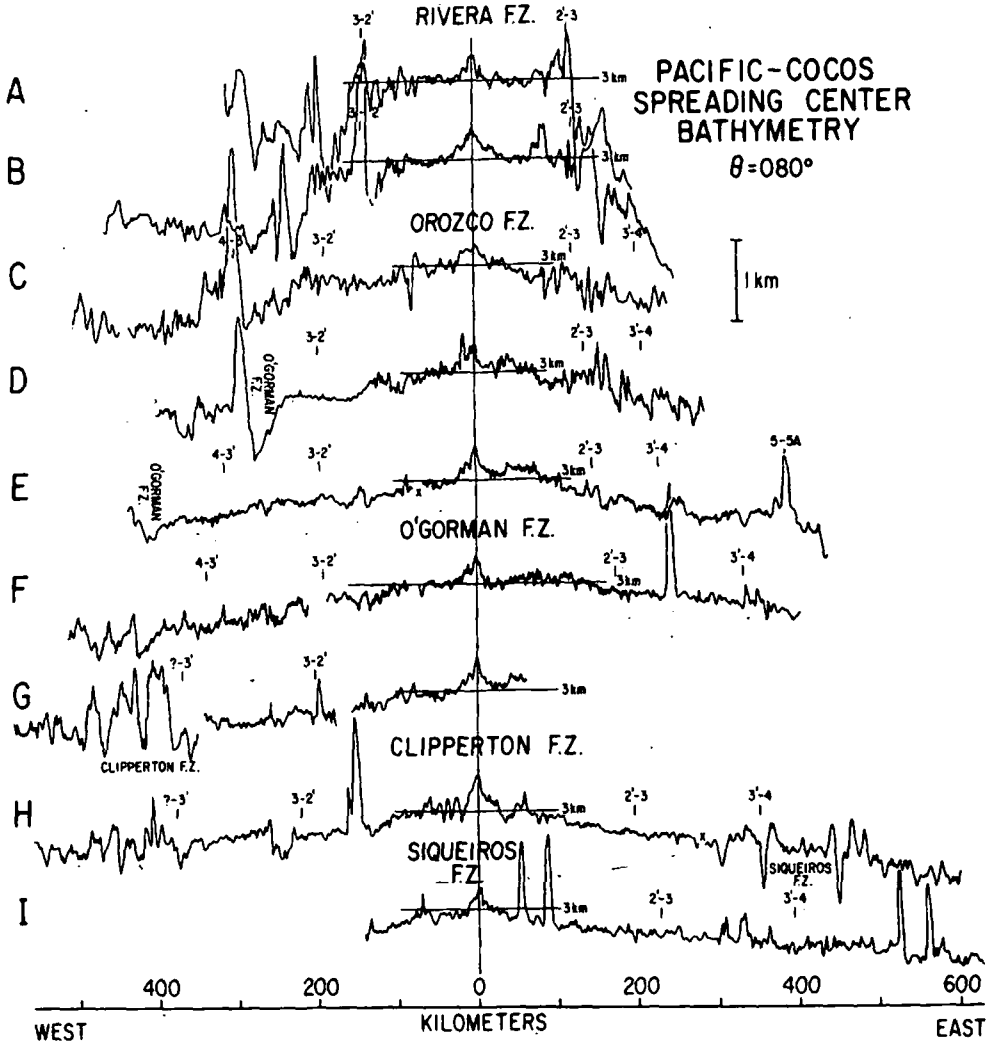

Fig. 4. Bathymetric cross sections of the Pacific-Cocos spreading center. The location of magnetic anomaly boundaries are indicated (e.g., 3–2′ is the boundary between anomaly 3 and anomaly 2′). The profiles are from Scan 11 (A and B), Tripod 3 (C), Scan 10 (D), Siqueiros and Swansong (E), *Glomar Challenger* 16 (F), Swansong (G), Papagayo 1 and *Glomar Challenger* 54 (H), and *Glomar Challenger* 54 (I). Where two ship profiles were composited to make a single profile, the join is indicated with a cross. The profiles have been projected along the azimuth (θ) of 080°. See Figure 3*a* for track locations.

relief taking place at the time of plate motion changes. The relief becomes very rough on the western flank of the EPR to the west of anomaly 3′.

The plate boundary reorganizations left behind several abandoned spreading centers in the eastern Pacific [*Sclater et al.*, 1971; *Handschumacher*, 1976; *Rea*, 1978]. These abandoned spreading centers are reflected in the bathymetry as narrow ridges and troughs. The most obvious examples of abandoned spreading centers, where symmetrical sets of magnetic lineations have been identified, are all narrow troughs with flanking ridges (e.g., the Malpelo Rift [*Lonsdale and Klitgord*, 1978, Figure 3], just north of the Galapagos Rift [*Anderson et al.*, 1976, Figure 3], the Galapagos Rise [*Anderson et al.*, 1978, Figure 11], the Coral Sea [*Weissel and Watts*, 1979, Figure 4], and the Magellan Trough [*Tamaki et al.*, 1979, Figure 6]. The morphology of the abandoned PGSC at 28°N, 118°W (Plate 1*b*) [*Batiza and Chase*, 1981] closely resembles these examples. The large ridge on which Guadalupe Island sits is just north of and along the same trend as the narrow trough, but the magnetic anomaly pattern associated with it is much more chaotic.

In many ways, the Mathematician Ridge resembles the abandoned segment of the PGSC near Guadalupe Island. The Mathematician Ridge is a group of bathymetric features that includes both ridges and narrow troughs (Plate 1*a* and Figure 5). These features are oriented roughly northeast and have offsets to the southeast, giving an overall northward trend to the gross structure. As with the abandoned PGSC, the northern end of the Mathematician Ridge is a large ridge with islands that extends from about 18°N to 19.5°N at 111°W. Between 16°N and 18°N, the structure is that of a trough with flanking ridges. A pair of very large ridges is located between 15°N and 16°N. The southern end of the Mathematician Ridge is a series of southeast trending peaks and troughs between 12°N and 15°N just west of 110°W. The increasing seafloor depth away from the crest of the Mathematician Ridge (Figures 5 and 6) is the characteristic originally used to identify this abandoned spreading center [*Sclater et al.*, 1971].

There are two other possible segments of abandoned spreading centers reflected in the bathymetric data. Just south of the Clipperton fracture zone near 111°W, the Clipperton Ridge has been interpreted as part of the abandoned Mathematician Ridge–Galapagos Rise spreading sys-

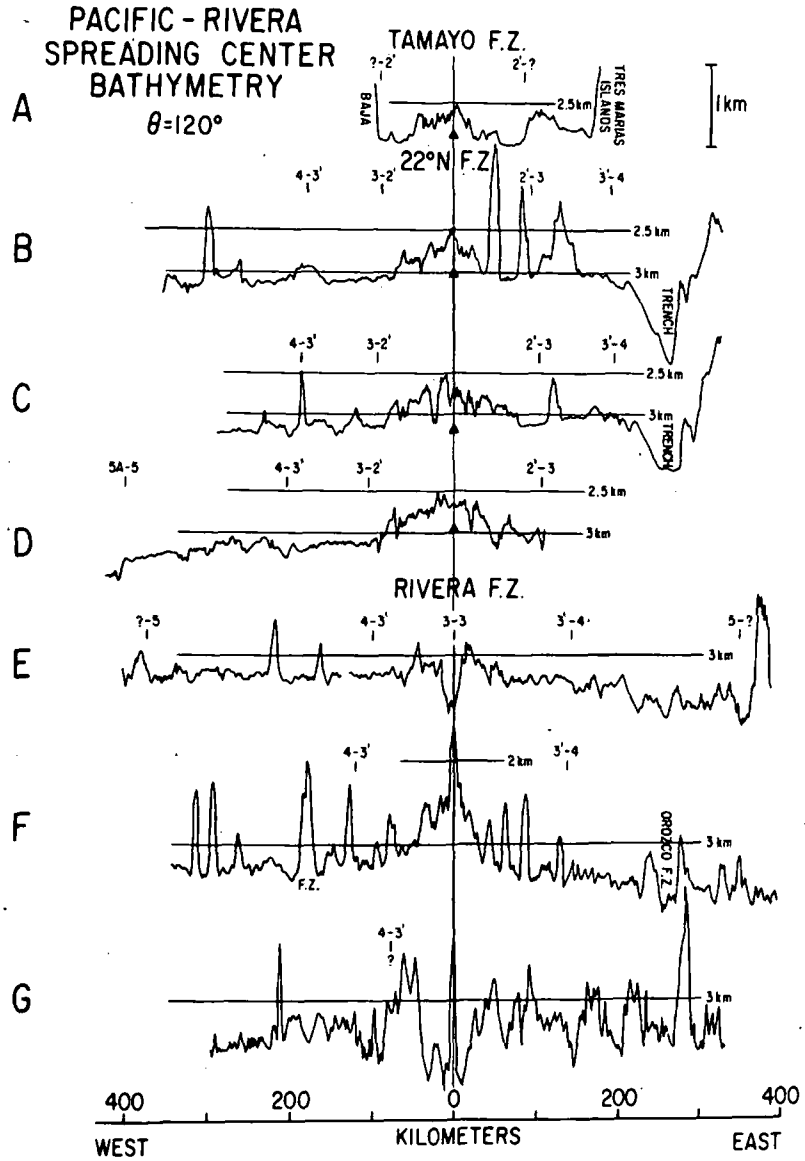

Fig. 5. Bathymetric cross sections of the Pacific-Rivera spreading center. The profiles are from Gam 2 (A, B, C), Gam 1 (D), Pleiades 1 (E), F. Drake 77 (F), and *Glomar Challenger* 16 (G). Projection azimuth is 120°. See Figure 4 for explanations and Figure 3*b* for track locations.

tem [*Anderson and Davis*, 1973; *van Andel et al.*, 1975; *Rea*, 1978]. The Clipperton Ridge is a minor bathymetric feature (Plate 1*a*) that does not closely resemble the other abandoned spreading centers. However, the large relief associated with the Clipperton and Siqueiros fracture zones and the sparse data coverage around the feature preclude us from ruling out the Clipperton Ridge as a segment of an abandoned spreading center. On the eastern flank of the EPR, south of the Tehuantepec Ridge, is an east trending tough with flanking ridges near 11°N (Plate 1*a*). Seafloor deepens away from this feature on its western flank (Figure 7), suggesting that it also is an abandoned spreading center.

Other ancient plate boundaries are engrained into the bathymetric relief as deep troughs or narrow zones of rugged relief. The western edge of the Mathematician Ridge is marked by a narrow trough (Plate 1*a*) from 16°N, 112.5°W to 12°N, 111°W. This bathymetric trough separates the smooth bathymetric relief to the west on PGSC crust from the series of large ridges and troughs that comprise the Mathematician Ridge. The youngest of the magnetic lineations from the PGSC terminates at this trough. Between the Rivera and Orozco fracture zones a deep trough, surrounded by rough relief, is observed at 107°W (Plate 1*a*). It lies on the boundary between crust generated at the Mathematician Ridge part of the PRSC and the EPR-generated crust [*Sclater et al.*, 1971]. A similar structure is found on the eastern flank of the EPR between 16°N and 18°N at 104°W.

The gradual deepening of the seafloor away from a spreading center [*Sclater et al.*, 1971] provides a means for distinguishing between crust generated at different spreading centers. Between the Orozco and O'Gorman fracture zones, the seafloor deepens westward from the EPR to past anomaly 5 and then shallows as it approaches the Mathematician Ridge (Figure 6). Similar bathymetric trends, first deepening and then shallowing, are found between the EPR and the Galapagos Rise [*Anderson and Sclater*, 1972, Figure 4] and between the Pacific-Antarctic Ridge and the Chile Rise [*Mudie et al.*, 1972, Figure 2D; *Klitgord et al.*, 1973, Figure 1]. The low point in the seafloor marks the boundary between crust generated at the two different spreading

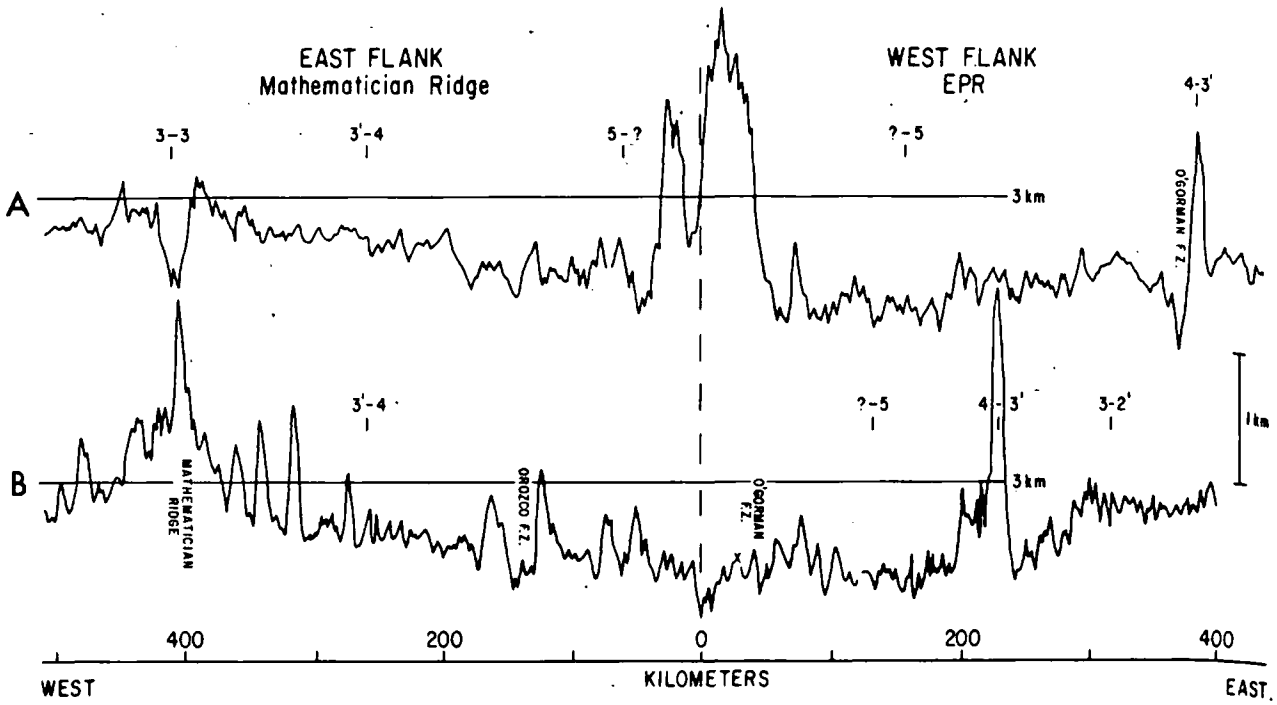

Fig. 6. Bathymetric profiles from SIO expeditions Pleiades 1 (A), and F. Drake 77 and Tripod 3 (B) across the boundary between Pacific-Rivera spreading center (Mathematician Ridge) and the Pacific-Cocos spreading center (EPR). See Figure 4 for explanation and Figure 3*a* for locations.

centers. South of the Tehuantepec Ridge, a similar pattern is observed (Figure 7); a low point in the seafloor is found between 10°N, 99°W and 7°N, 96.5°W (Plate 1*a*), shallowing to the west toward the EPR and to the east toward the east trending trough with flanking ridges mentioned above.

Seafloor Spreading Magnetic Lineations

Pacific-Guadalupe Spreading Center

With the exception of the small piece of the Guadalupe plate just north of the Shirley Trough, all the clearly identified seafloor spreading magnetic lineations generated at the Pacific-Guadalupe spreading center (PGSC) are from the western flank. The magnetic lineations east of anomaly 5 on the Cocos plate may be on a remnant of the PGSC eastern flank [*Lynn and Lewis*, 1976], but they are not readily correlated with the geomagnetic time scale. The magnetic lineations on the PGSC and PFSC western flank within our study area (Plates 2*b* and 2*c*) are as old as anomaly 12 (32 m.y. B.P. in the late Oligocene) and as young as anomaly 5A (11 m.y. B.P.) south of the Clarion fracture zone, and as young as between anomalies 5A to 5B time (12.5 m.y. B.P.) north of the Clarion fracture zone.

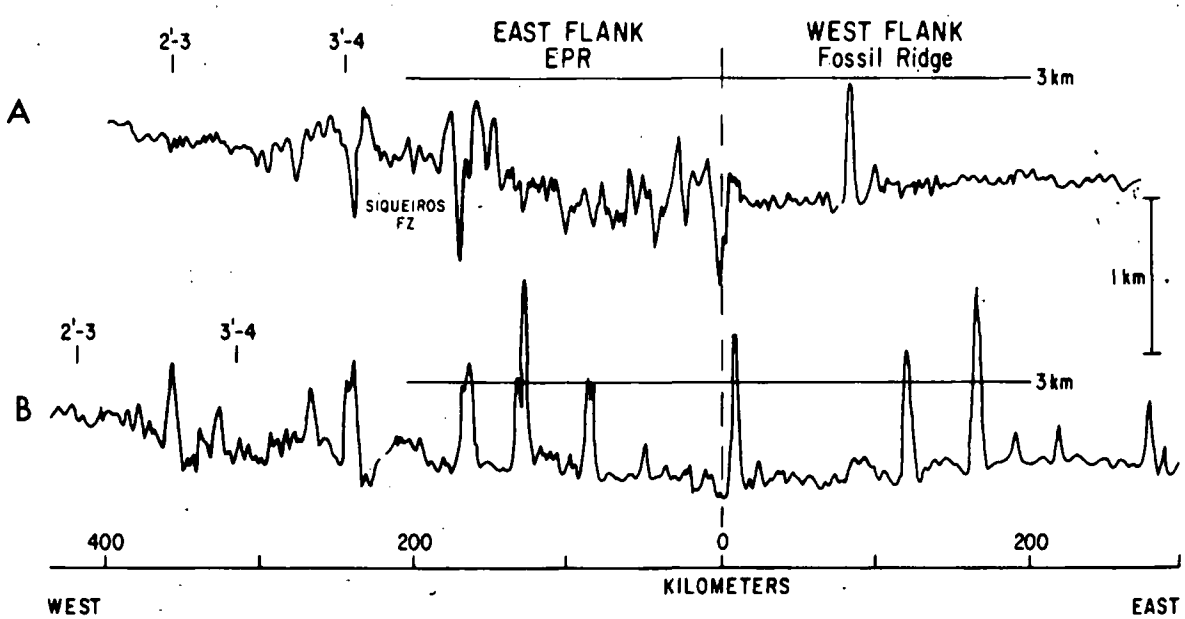

Fig. 7. Bathymetric profiles from the *Glomar Challenger* leg 54 (A) and SIO expedition Indomed (B) across the boundary between the Pacific-Cocos spreading center and the abandoned spreading center south of the Tehuantepec Ridge. See Figure 4 for explanation and Figure 3*a* for locations.

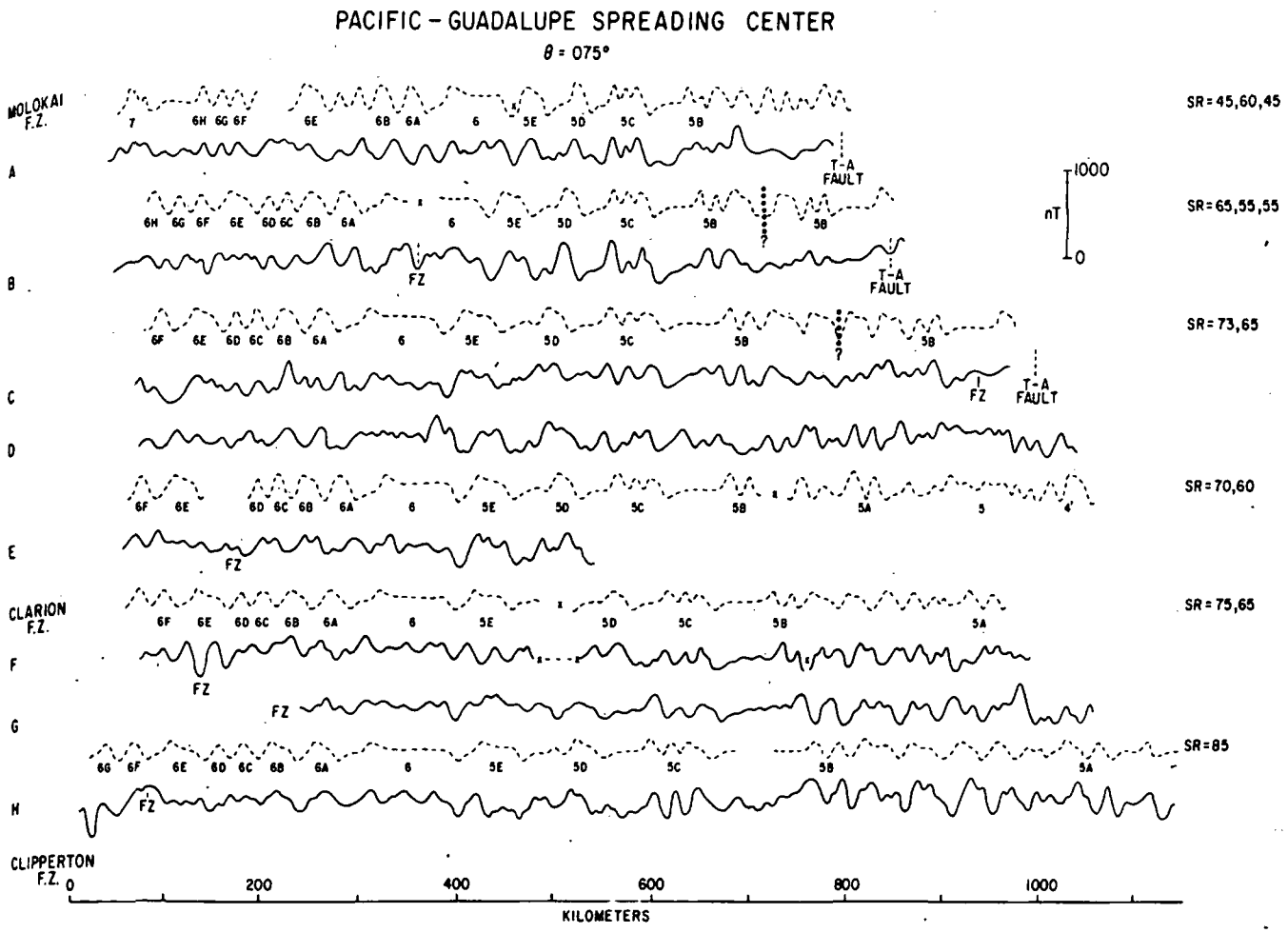

Fig. 8. Observed (solid curves) and synthetic (dashed curves) magnetic anomaly profiles for the west flank of the Pacific-Guadalupe spreading center. The spreading rates (SR) used in the model profiles are half rates in mm/yr. The profiles have been projected along the azimuth (θ) of 075°. Where more than one SR or ship track was used, the join is indicated with a cross. T-A is the Tosco-Abreojos fault zone. A magnetization of 10 A/M in a 0.5-km thick layer was used. The profiles were taken from the SIO and LDGO cruises Gam I (A, B, C, D), LDGO (E), LDGO and Tripod (F), *Conrad* 10.5 (G), and *Glomar Challenger* 16 (H). See Figure 3*b* for track locations.

The magnetic lineations between the Molokai and Clarion fracture zones [*Atwater and Menard*, 1970; *Chase et al.*, 1970*a*] are readily correlated with the geomagnetic time scale (Figure 8). Most of the reversals between magnetic anomalies 5, 6, and 7 are recorded in the oceanic crust. The anomalies between anomalies 5 and 6 were assigned letters A-E [*Elvers et al.*, 1973; *Blakely*, 1974] and are used here. We have used the letters A-H for the eight normal magnetization blocks between anomalies 6 and 7 [*Ness et al.*, 1980] for ease of discussion and labeling. Anomaly 6E provides a good marker along the entire length of our study area, and our comparison with the geomagnetic time scale (Figure 8) indicates that the reversal probably was longer than the duration given by *Ness et al.* [1980]. Most of the disturbances in this pattern of lineations are just north of the Clarion fracture (Plate 2*b*). Part of the sequence between anomaly 6E and anomaly 7 is missing, and between anomalies 5B and 6 there appears to be a duplication of anomaly 5E and a disturbance at anomaly 5C. The orientation of the magnetic lineations is well controlled east of anomaly 6 and is nearly orthogonal to the fracture zones. The lineation offsets indicated at the fracture zones are well defined by the data density. The sparse track coverage west of anomaly 6 provides only a minimum control on the lineation trends. Some or all of the indicated lineation offsets west of anomaly 6 (Plates 1*b* and 2*b*) may be the result of small navigation errors. We have drawn these lineations orthogonal to the fracture zones, but even if we had assumed that there were no small offsets due to fracture zones, the orientation would only change by about 5°.

The only basic differences between our interpretation and that of *Atwater and Menard* [1970] are our addition of several fracture zones and the availability of a more detailed geomagnetic time scale [*Ness et al.*, 1980] with which to correlate the magnetic data between anomalies 5 and 7. The youngest magnetic lineation that we can confidently identify north of the Clarion fracture zone is the anomaly just older than anomaly 5A (12.5 m.y. B.P.). The basement age of 14.5 m.y. at DSDP site 471 (Plate 2*b*, 23.48°N, 112.50°W) [*Haq et al.*, 1979] and the suggestion of an abandoned spreading center just west of DSDP site 471 [*Ness et al.*, 1981] fit quite well into our proposed lineation pattern (Plate 2*b*). We have suggested another abandoned spreading center just south of the Shirley trough, and the magnetic anomaly correlation with synthetic anomalies (Figure 8) is plausible but not convincing. South of DSDP site 471, the magnetic lineations

swing around into the mouth of the Gulf of California [*Chase et al.*, 1970*a*] where there are well-preserved lineations from anomaly 5 to the central anomaly (Figure 9).

The magnetic anomalies south of the Clarion fracture zone (Plate 2*c*) are lower in amplitude but are as easily recognized as the lineations to the north (Plate 2*b*). Anomalies 6E through 5A can be identified between the Clarion and Clipperton fracture zones, and indications of lineations as old as anomaly 12 are found on a couple of profiles that go west of anomaly 6E. Anomaly 5A is just west of the trough that bounds the western limit of the disturbed bathymetric zone associated with the Mathematician Ridge. There is a small difference between our anomaly interpretation and that of *Herron* [1972], but the basic story is the same, the youngest crust west of the Mathematician Ridge has an age of 11 m.y. Small offset fracture zones have been used to coincide with a few of the linear bathymetric feature that cross the area (Plate 1*c*) and to account for the few disruptions found in the anomaly lineation pattern (Plate 2*c*). Some of these offsets could be the result of navigational errors.

Pacific-Rivera Spreading Center

The magnetic anomalies in the mouth of the Gulf of California [*Larson et al.*, 1968] include the lineation sets on both flanks of the Pacific-Rivera spreading center (PRSC) (Plate 2*b* and Figure 9). Between the Rivera fracture zone and the transform fault at 22°N, the magnetic lineations include the central anomaly through anomaly 5. This is the segment of the PRSC that was always outside the Gulf of California, bound to the north by the fracture zone along the southwest tip of Baja California that connected with the Tosco-Abreojos fault zone [*Spencer and Normark*, 1980]. Between the 22°N transform fault and the Tres Marias fracture zone [*Mammerickx*, 1980], magnetic anomaly 2′ on the western flank of the PRSC abuts continental crust of Baja California [*Curray et al.*, 1979] and is the oldest identifiable magnetic lineation on the eastern flank. The parallel trend of the Tres Marias fracture zone and the fracture zones to the south in crust generated between 3.5 and 6.5 m.y. B.P. (anomalies 3 and 3′) suggest that the Tres Marias fracture zone may have been an active transform fault during this early period [*Mammerickx*, 1980] and that the Middle America trench consumed most of the newly generated crust. North of the Tres Marias fracture zone, the oldest identifiable lineation is magnetic anomaly 2 (2 m.y. B.P.).

Prior to anomaly 2′, the PRSC extended south of the Rivera fracture zone along the Mathematician Ridge [*Sclater*

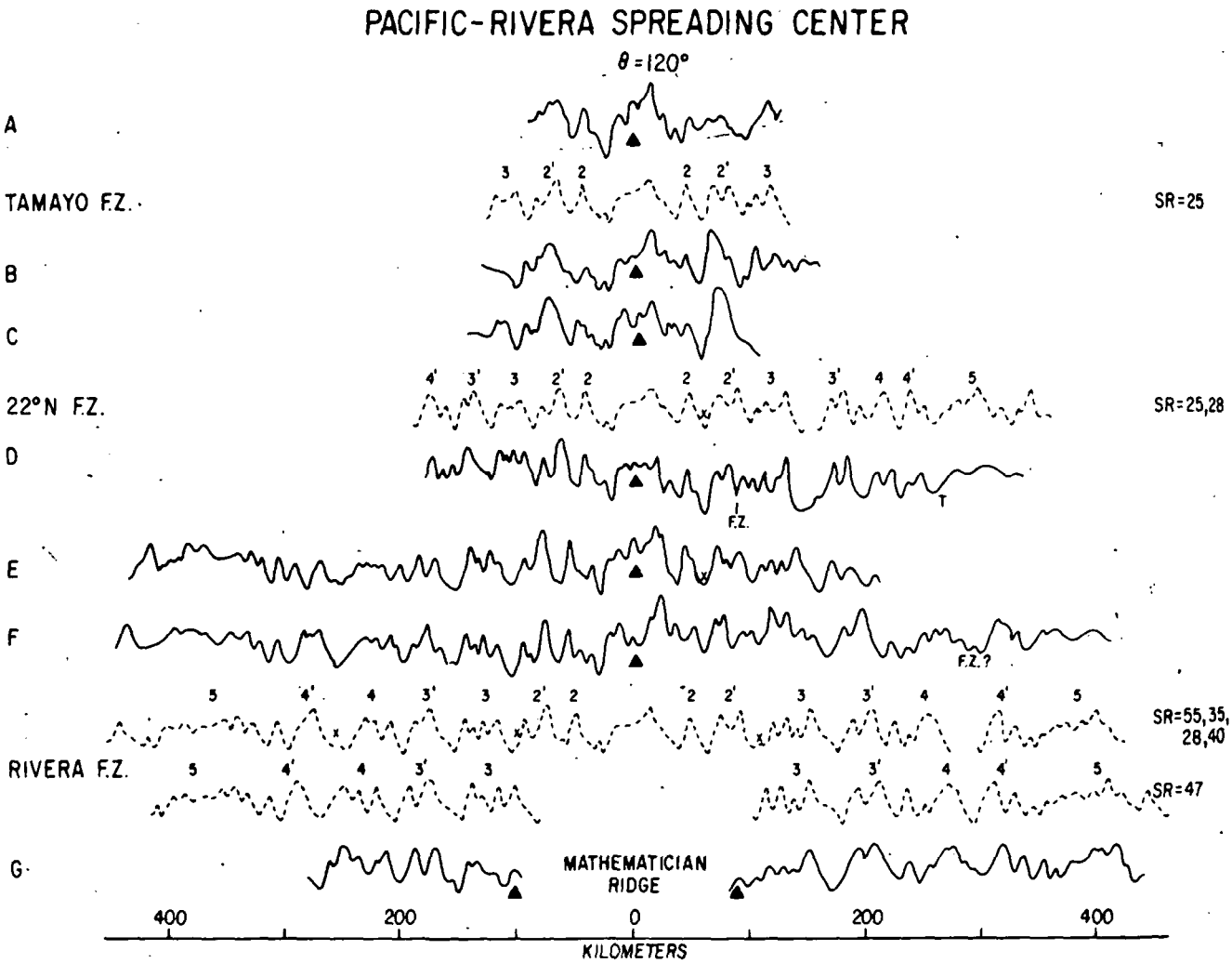

Fig. 9. Observed and synthetic magnetic anomaly profile for the Pacific-Rivera spreading center. The profiles are from SIO cruises Gam 2 (A, B, C, D), Gam 1 and Cocotow 1 (E), Dolphin 2 (F), and Pleiades 1 (G). Projection azimuth is 120°. See Figure 8 for explanations and Figure 3b for track locations. Trench axis (T) is indicated at right side of profile D.

et al., 1971; *Handschumacher*, 1976; *Menard*, 1978]. The magnetic anomalies associated with the Mathematician Ridge are not as easily correlated with the seafloor magnetic reversal sequence as those lineations north of the Rivera fracture zone (Figure 9), but anomaly 3 to anomaly 4′ can be identified on both flanks of the ridge, from 19°N to the Rivera fracture zone. The location of anomaly 3 on the western flank of the Mathematician Ridge lines up with the location of anomaly 3 north of the Rivera fracture zone, consistent with the PRSC having been a continuous ridge from Baja California to at least 19°N, the rise crest and eastern flank migrating toward the Middle America trench. Between 17°N and 18.5°N the youngest lineation on either side of the Mathematician Ridge is anomaly 3′, indicating that this part of the PRSC was abandoned earlier than the segments to the north. The adjacent segment of the EPR, between the Orozco fracture zone and a fracture zone near 16.5°N, contains magnetic lineations as old as anomaly 3 (Plate 2*a*), whereas the anomalies on the EPR just north of 16.5°N are only as old as anomaly 2′. The offset in the Mathematician Ridge at 18.5°N corresponds to offsets near 16.5°N in the two north trending narrow troughs that bound the EPR between the Rivera and Orozco fracture zones (Plate 1*a*), with a much wider zone of EPR-generated crust to the south. Along the Mathematician Ridge, south of 17°N, a few magnetic lineations were found but could not be correlated with the geomagnetic time scale.

Pacific-Cocos Spreading Center

A fanlike pattern characterizes the magnetic anomaly lineations for the EPR south of the Rivera fracture zone (Plate 2*a*) [*Lynn and Lewis*, 1976]. These magnetic anomalies reflect at least three episodes of spreading: (1) the central anomaly to anomaly 2′ (0 to 3.5 m.y. B.P.), (2) anomaly 3 to anomaly 3′ (3.5 to 6.5 m.y. B.P.), and (3) anomaly 4 to anomaly 5A (6.5 to 11 m.y. B.P.). There is sufficient data coverage to map reliably the lineations associated with the two younger episodes on both flanks of the EPR (Plate 2*a* and Figure 10). The oldest episode is found on the eastern flank between the Orozco fracture zone and the Tehuantepec Ridge [*Lynn and Lewis*, 1976] and on the western flank between the Orozco fracture zone and the O'Gorman fracture zone (Plate 2*a* and Figure 11). The data are insufficient to identify the anomaly pattern for crust older than anomaly 3′ south of the Clipperton fracture zone or on the western flank of the EPR between the O'Gorman and Clipperton fracture zones.

Since just before anomaly 2′ time (3.5 m.y. B.P.), the Pacific-Cocos spreading center (PCSC) has stretched southward from the Rivera fracture zone to the Galapagos triple junction. The Rivera fracture zone is the active transform fault that connects the EPR with the Middle America trench [*Larson*, 1972; *Prothero et al.*, 1976], and it has formed the northern end of the Cocos plate since 3.5 m.y. B.P. A well-defined magnetic anomaly pattern, with anomaly widths continuously increasing southward, characterizes this youngest part of the EPR (Plate 2*a*, Figure 10, and Table 1). Large offsets in the anomaly pattern occur at the Orozco, Clipperton, and Siqueiros fracture zones. There are several small offsets in the lineations between the major fracture zones: two are found between the Rivera and Orozco fracture zones, and three are found between the Orozco and Clipperton fracture zones. Of these latter three fracture zones, only the one at 12°N offsets the crest of the EPR (Plate 1*a*).

Between anomaly 3′ to 2′ time, the northern boundary of the PCSC jumped northward from Orozco to the Rivera fracture zones. PCSC-generated magnetic anomalies older than anomaly 3 are found only south of the Orozco fracture zone. Anomalies 3 and 3′ are well defined on both flanks of the EPR (Plate 2*a* and Figure 10), although anomaly 3′ becomes difficult to delineate south of the Clipperton fracture zone. By anomaly 3 time the PCSC had extended as far north as 16.5°N, accounting for the wider section of EPR crust between the Orozco and 16.5°N fracture zones than between the 16.5°N and Rivera fracture zones.

The magnetic lineation pattern for anomalies 3 and 3′ has large offsets at the Orozco, Clipperton, and Siqueiros fracture zones, but some of the smaller offsets found in the younger lineation pattern are not present. The fracture zones between the Orozco and Clipperton fracture zones are marked by bathymetric ridges and troughs (Plate 1*a*), although there is no apparent magnetic lineation offset (Plate 2*a*). A similar pattern of zero-offset fracture zones has been identified in the Atlantic [*Schouten and White*, 1980] and only closely spaced track spacing (about 10 km) reveals the narrow zones of disturbance in the magnetic pattern [*Schouten and Klitgord*, 1982]. The sparse track coverage on the western flank precludes a determination of lineation trends south of the O'Gorman fracture zone, but the existing data are consistent with the pattern found on the eastern flank.

The anomaly pattern beyond anomaly 3′ on the eastern flank of the EPR between the Orozco fracture zone and the Tehuantepec Ridge provides a clear record of plate motion back to the time of the reorganization at about 11 m.y. B.P. [*Lynn and Lewis*, 1976]. The anomaly widths increase rapidly to the south (Plate 2*a* and Figure 11), resulting in the more distinct separation of individual anomalies (such as the three magnetic events that make up anomaly 4). The matching anomalies on the western flank can be identified only as far south as the O'Gorman fracture zone. The anomalies on the west flank south of the O'Gorman fracture zone could swing around to the northeast, parallel to the Pacific-Rivera lineations, or swing to a more northward orientation and finally northwest trend, parallel to the Pacific-Guadalupe lineations.

A clear set of magnetic anomalies east of anomaly 5A on the eastern flank of the EPR has not been correlated with the geomagnetic time scale. These anomalies probably were generated on the eastern flank of the PGSC between the Clarion and Clipperton fracture zones [*Lynn and Lewis*, 1976], but the large number of short field reversals between anomalies 5A and 5B hinders a convincing correlation of the anomalies with the geomagnetic time scale [*Schilt et al.*, 1982]. These anomalies clearly persist east of the Middle America trench axis, reflecting oceanic crust of the downgoing Cocos plate at the subduction zone. The detailed study of the trench between 100°W and 101°W by *Karig et al.* [1978] shows these same anomalies. The northeast trending magnetic anomaly near 16.8°N, 100.5°W, reported by *Karig et al.* [1978], coincides with one of our fracture zone locations.

South of the Tehuantepec Ridge, in the Guatemala Basin, the magnetic lineations are parallel to the anomalies older than anomaly 3′ north of the ridge. Although we have not been able to correlate these anomalies with the geomagnetic time scale, the bathymetric data (Plate 1*a* and Figure 7)

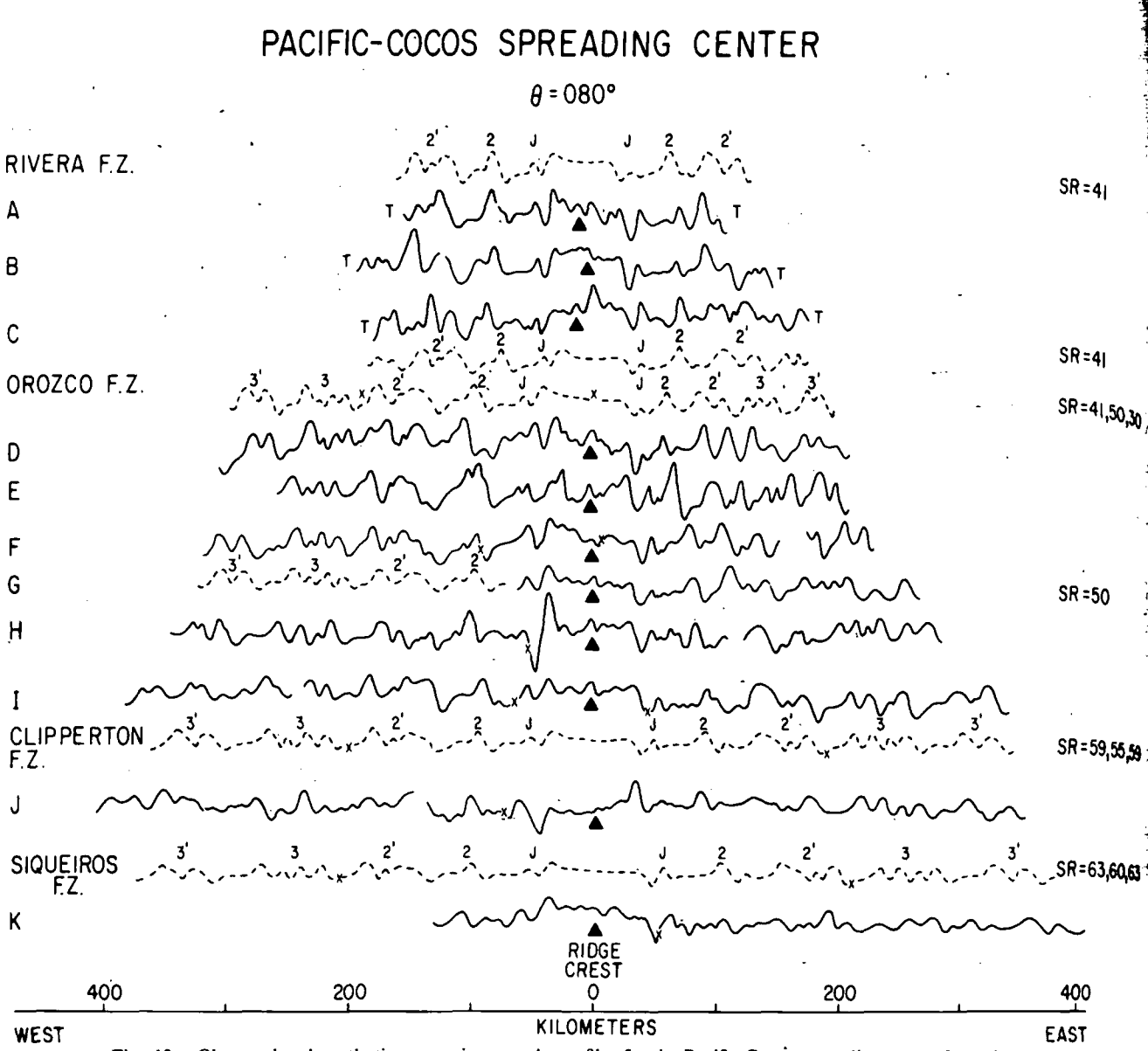

Fig. 10. Observed and synthetic magnetic anomaly profiles for the Pacific-Cocos spreading center from the central magnetic anomaly to magnetic anomaly 3'. The profiles are from the cruises Scan 11 (A, B, C); Tripod 3 (D); Scan 10 (E); Siqueiros, *T. Washington*, and Swansong (F); OSU/UW (G); *Glomar Challenger* 16 (I); Papagayo 1 and *Glomar Challenger* 54 (J); and *Glomar Challenger* 54 (K). Project azimuth is 080°: See Figure 8 for explanations and Figure 3*a* for track locations. Trench axis (T) is indicated at right side of profiles A, B, C.

suggest that the basin contains the rise crest and the eastern flank of the PGSC. The crustal age of early Miocene at DSDP site 495 (12.5°N, 91.02°W) [*von Huene et al.*, 1980] northeast of our postulated abandoned spreading center is consistent with the crust being generated at the PGSC (Figure 1). The magnetic anomalies in the vicinity of 11°N, 97°W are at an angle to the other magnetic lineations and are parallel to the deep bathymetric trough mentioned previously as a possible abandoned spreading center. This narrow zone is clearly a region of anomalous tectonic activity, even if it is not an abandoned spreading center.

Poles of Rotation and Spreading Rates

The present plate motions in the eastern equatorial Pacific can be described in terms of the poles of rotation and angular spreading rates (Table 1). These parameters, which can be determined from the magnetic lineation (Plates 2*a* and 2*b*) and fracture zone (Plates 1*a* and 1*b*) data [*Harrison*, 1972], enable one to determine the present spreading rate at any place on the EPR (Table 1). The width of the central magnetic anomaly along the Pacific-Rivera and Pacific-Cocos spreading centers was used to provide the spreading rate data, and bathymetric trends at the rise crest were used to determine transform fault azimuths. The theoretical spreading rates and transform fault azimuths were determined along the length of the EPR, using the instantaneous pole of rotations determined for both spreading centers (Tables 1 and 2). The data base and length of the rise crest for the PCSC are suitable for accurately determining the present instantaneous pole of rotation (37.15°N, 107.88°W with an angular spreading rate of 2.21°/m.y.). There is always some uncertainty in determining poles of rotation [*Harrison*, 1972], and the reliability of our pole for the PCSC can be seen by comparing observed and predicted spreading rates and transform fault azimuths (Table 1). A similar comparison for the data in the mouth of the Gulf of Califor-

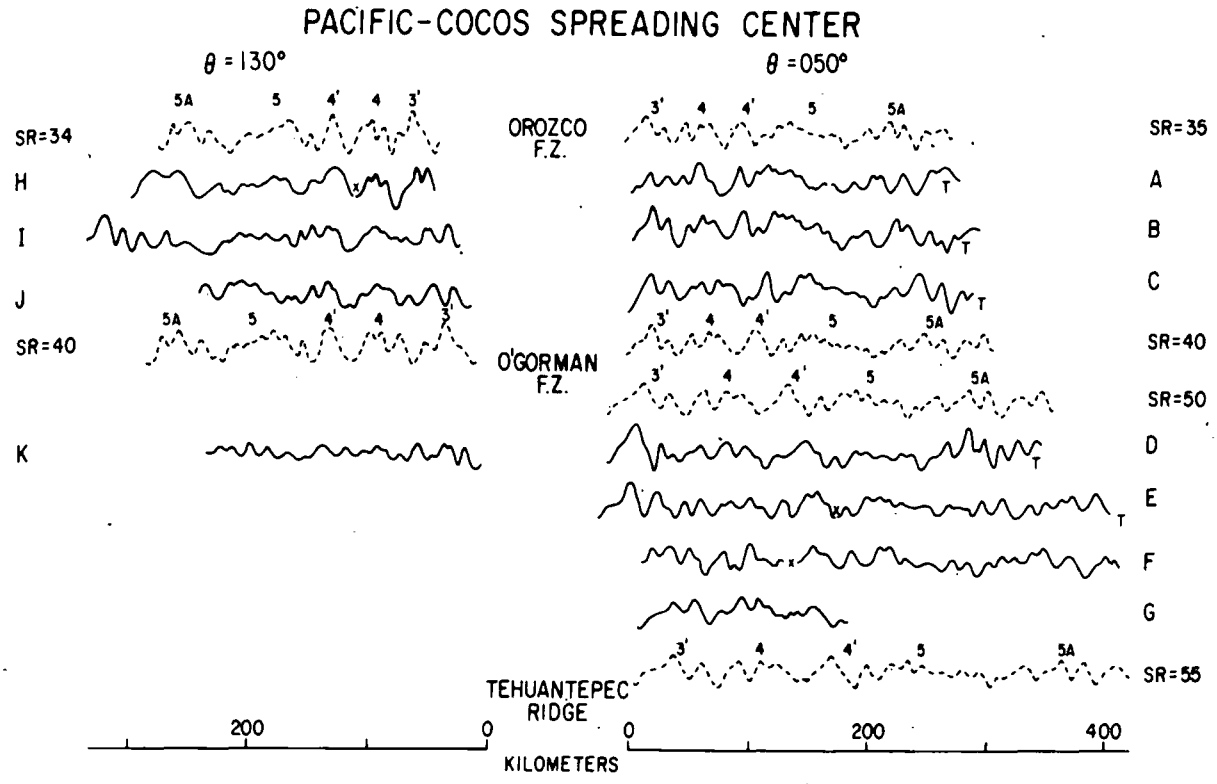

Fig. 11. Observed and synthetic magnetic anomaly profiles for the Pacific-Cocos spreading center from magnetic anomaly 3' to magnetic anomaly 5A. The profiles are from the cruises Tripod 3 (A), Scan 10 (B), Swansong (C), Cocotow 1 (D); Cocotow 2 and LDGO (E), Explorer 60 and LDGO (F), *Glomar Challenger* 16 (G), Explorer 60 (H), *T. Washington* (I), and Siqueiros (J). Projection azimuths are 130° and 050°. See Figure 8 for explanations and Figure 3*a* for track locations. Trench axis (T) is indicated at right side of profiles A, B, C; D, E.

nia using the PRSC pole of rotation (27.7°N, 104.7°W, 4.7°/m.y.) indicates a good agreement between calculated and observed spreading rates but only modest agreement for the azimuths (Table 2). Considering the short segment of spreading center between the Tamayo and Rivera fracture zones and the lack of large rise crest offsets, except at the two ends of the spreading center, these results are not unreasonable.

The instantaneous poles of rotations indicate the independent nature of the Pacific-Rivera and Pacific-Cocos spreading centers at the present time. The PCSC pole would require a transform azimuth of 090° north of the Rivera fracture zone and a rate significantly different from the observed spreading rate in the mouth of the Gulf of California. The Pacific-Cocos pole is quite close to the pole determined by *Chase* [1972] (36°N, 108°W, 2.37°/m.y.). The difference between our PCSC pole and that of *Minster et al.*

TABLE 1. Pacific-Cocos Spreading Center Pole-of-Rotation Data: Instantaneous Pole-of-Rotation Parameters 37.15°N, 107.88°W With an Angular Rate of 2.21°/m.y.

	W_c, km	SR_{obs}, mm/yr	SR_{calc}, mm/yr	TF_{obs}	TF_{calc}
Rivera fracture zone					
17.75°N	56	81	82	85°	84.0°
17.04°N	58	84	85	85°	84.2°
15.38°N	64	93	92	85°	84.5°
Orozco fracture zone					
15.07°N	64	93	93	80°	82.8°
14.06°N	67	97	97	80°	82.7°
12.88°N	72	104	102	80°	82.5°
11.90°N	74	107	106	80°	82.6°
10.27°N	76	110	112	80°	82.5°
Clipperton fracture zone					
9.95°N	77	111	113	83°	83.9°
9.12°N	80	116	116	84°	83.9°
8.40°N	83	120	119	84°	84.0°
Siqueiros fracture zone					
8.28°N	83	120	120	82°	81.8°
2.70°N	—	—	141	—	81.8°
Galapagos triple junction					

W_c, width of the central magnetic anomaly; SR_{obs}, measured total spreading rate; SR_{calc}, calculated total spreading rate; TF_{obs}, measured transform fault trends, and TF_{calc}, calculated transform fault trends, are in degrees from north.

TABLE 2. Pacific-Rivera Spreading Center Pole-of-Rotation Data Instantaneous Pole-of-Rotation Parameters 27.74°N, 104.67°W With an Angular Rate of 4.73°/m.y.

	W_c, km	SR_{obs}, mm/yr	SR_{calc}, mm/yr	TF_{obs}	TF_{calc}
Tamayo fracture zone					
23.22°N	35	51	52	124°	127.3°
22.90°N	36	52	52	124°	121.6°
22.60°N	38	55	55	124°	121.3°
21.96°N	42	61	62	124°	120.6°
20.95°N	50	72	72	124°	119.1°
19.98°N	54	78	77	124°	112.7°
Rivera fracture zone					

[1974] (41.3°N, 108.1°W, 2.02°/m.y.) is caused by the longer time record over which Minster et al. averaged their rotation data.

Seismic activity provides one of the best indicators of present-day plate boundaries [*Isacks et al.*, 1968]. Aside from those associated with the Middle America trench, most of the earthquake epicenters are located on the transform faults [*Sykes*, 1967]. The locations of earthquakes along the Tamayo and Rivera fracture zones define the transform faults that bound the Rivera plate [*Reichle et al.*, 1976; *Prothero et al.*, 1976]. The earthquakes on the Orozco fracture zone were monitored during the passive phase of Project ROSE [*Project ROSE Scientists*, 1981]; the main bands of earthquakes are along the north side of the Orozco fracture zone (near 15.5°N) and on what may be a spreading segment near the center of the broad fracture zone (near 15.2°N). Teleseismic locations indicate that these seismic zones are also found along the southern side of the Orozco and on the Clipperton and Siqueiros fracture zones. Most of the other earthquakes are along the axis of the EPR [*Project ROSE Scientists*, 1981, Figure 1] but are too poorly located to properly define small transforms. In general, these seismic markers of transform faults along the PRSC and PCSC systems are consistent with our pole of rotation determinations and the pattern of fracture zones (Plates 1*a* and 1*b*) that intersect the rise crest.

Poles of rotation for older crust generated at the Pacific-Cocos spreading center are not calculated here, but the anomaly pattern (Plate 2*a*) does indicate some qualitative estimations concerning the poles. The fanning pattern for the lineations younger than anomaly 4, with data available from both flanks of the EPR, was generated by a close pole of rotation [*Lynn and Lewis*, 1976]. For the lineations older than anomaly 4 only the set on the eastern flank set of the EPR is available, and it could result from a close pole of rotation or from a more distant pole that was migrating eastward between anomalies 5A and 4. The close pole could generate lineations on the western flank that continue to sweep around to the northwest, having a northeast orientation. The O'Gorman fracture zone trend suggests this possibility, but it is part of the PRSC system and may not have any bearing on the older PCSC system tectonic pattern. The reconstruction at anomaly 5A time using such a close pole for the PCSC system would not make the older lineations east of anomaly 5A and south of the Tehuantepec ridge, on the eastern flank of the EPR, parallel to the Pacific-Guadalupe lineations. The pole of rotation migrating eastward would generate a set of lineations on the western flank that fan around from the Pacific-Guadalupe lineation trend to a northeast trend, while at the same time it generated the observed pattern on the eastern flank. This migrating pole hypothesis would make the crust south of the O'Gorman fracture zone on the EPR west flank part of the PCSC and suggests that the southern extension of the PRSC could not have been active for very long after the anomaly 5A reorganization.

PLATES AND PLATE BOUNDARIES

The magnetic anomaly and bathymetric data in the eastern equatorial Pacific outline a series of rigid plates and shifting plate boundaries (Figures 1 and 12) [*Mammerickx and Klitgord*, this issue]. Prior to 11 m.y. B.P., the ocean basin in our study area north of the Galapagos triple junction was dominated by two plates, the Pacific and the Guadalupe, which were separated from the North American plate by a subduction zone (Figure 12*a*). A major change in the Pacific-Guadalupe spreading system took place in the middle Miocene about magnetic anomaly 5A time (at 12.5 m.y. B.P. north of the Clarion fracture zone [*Chase et al.*, 1970*a*; *Menard*, 1978; *Batiza and Chase*, 1981] and at 11 m.y. B.P. south of the Clarion fracture zone [*Herron*, 1972]), as the Guadalupe plate fragmented.

The two plates that evolved from the breakup of the Guadalupe plate, the Rivera and Cocos plates, gradually changed in size as the southern end of the Pacific-Rivera spreading center and the northern end of the Pacific-Cocos spreading center shifted northward. The bathymetric evidence suggests that the PRSC originially extended southward along the entire length of the Mathematician Ridge to the Clipperton fracture zone (Figure 12*b*). The magnetic lineation evidence for such a spreading center is very poor south of the O'Gorman fracture zone. The magnetic data on the eastern flank of the EPR are fairly convincing that the PCSC extended as far north as the Orozco fracture zone at this time. A plausible tectonic interpretation (Figure 12*b*) suggests that a microplate would have existed for a while south of the Orozco fracture zone between two spreading centers. The large east trending bathymetric feature at the southern end of the Mathematician Ridge, joining the old Clipperton fracture zone with the new Clipperton fracture zone, would have formed the southern boundary of this microplate and may have been a compressional feature. This western spreading center would have pushed the Cocos Plate southeast of its original position, with Tehuantepec fracture zone originally corresponding to the Clipperton fracture zone (Figure 12*a*). The Mathematician Ridge south of O'Gorman fracture zone abuts anomaly 5A to the west (Plate 2*c*) which would make the Mathematician Ridge appear to be an abandoned spreading center that died about 11 m.y. B.P. [*Herron*, 1972]. The postulated set of fracture

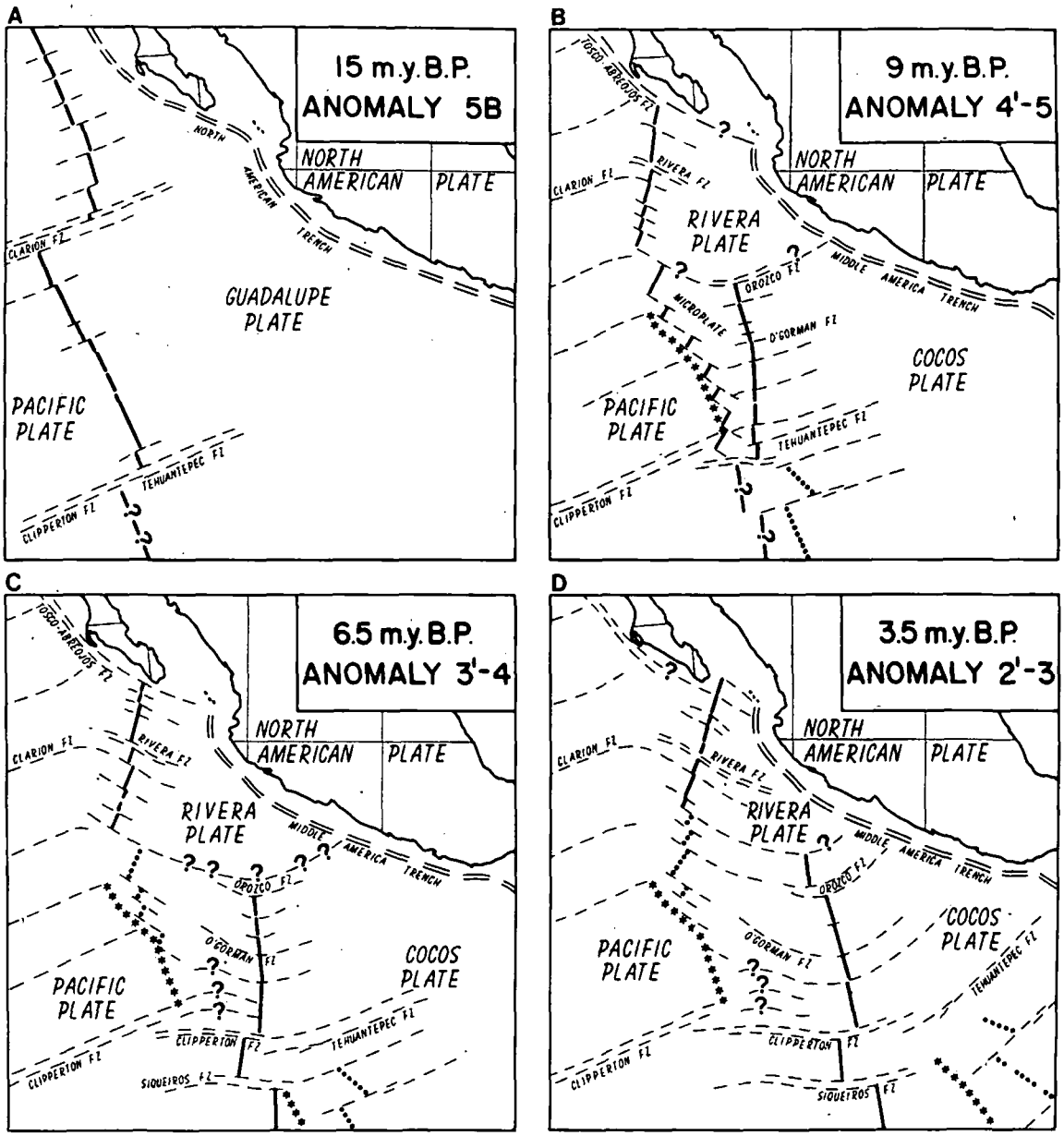

Fig. 12. Plates and plate boundaries for the eastern equatorial Pacific at magnetic anomaly 5B time (early Miocene) (Figure 12*a*), anomaly 4'–5 time (late Miocene) (Figure 12*b*), anomaly 3'–4 time (late Miocene) (Figure 12*c*), and anomaly 2'–3 time (Pliocene) (Figure 12*d*).

zones that curve to the west on the western flank of the EPR west of anomaly 3' (Figures 12*c* and 12*d*) are parallel to the Clipperton fracture zone. The plate motion associated with this postulated trend is necessary to bring the magnetic lineations east of anomaly 5 on the eastern flank of the EPR and the lineations south of Tehuantepec Ridge parallel with the magnetic lineations west of the Mathematician Ridge. The southern end of the PRSC was abandoned shortly after it became active, with the O'Gorman fracture zone next forming the southern boundary of the microplate [*Mammerickx and Klitgord*, this issue]. By 6.5 m.y. B.P. there was a simple three-plate system with the Orozco fracture zone forming the southern boundary of the Rivera plate and the PRSC and the northern boundary of the Cocos plate and the PCSC (Figure 12*c*). This boundary continued to shift northward (Figure 12*d*), and since 3.5 m.y. B.P. (Figure 1) the Rivera fracture zone has linked the PRSC to the PCSC and the Middle America trench.

The Mathematician Ridge is a bathymetric feature that was left in the oceanic crust as a result of the northward retreat of the PRSC. The magnetic anomaly data are consistent with the progressively younger ages for this feature in a northward direction. The southernmost part of the ridge has magnetic anomaly 5A against its western edge and a postulated age of 11 m.y. B.P. [*Herron*, 1972]. The central part of the feature was abandoned about 6.5 m.y. B.P., while the northern section ceased spreading about 3.5 m.y. B.P. [*Sclater et al.*, 1971]. The magnetic anomalies just south of the Clipperton fracture zone (Plate 2*a*) can only be identified on crust as old as anomaly 3', consistent with the 6.5 m.y. B.P. age for the Clipperton Ridge [*Anderson and Davis*, 1973]. Thus one finds that different parts of the Mathematician-Clipperton Ridge system are associated with three different tectonic events [*Menard*, 1978] and that there is no inconsistency between the data sets used by *Sclater et al.* [1971], *Herron* [1972], and *Anderson and Davis* [1973] and

between their different age interpretations for the tectonic event producing the ridge system.

SUMMARY

The complicated tectonic history of the East Pacific Rise north of the Galapagos triple junction (near the equator) is recorded in the magnetic anomaly patterns and bathymetric grain of the oceanic crust. These data record the activity of three different spreading centers: the Pacific-Guadalupe, Pacific-Rivera, and Pacific-Cocos as well as the shifting plate boundaries of the four plates in the region. The bathymetric structure and magnetic anomaly lineations have been carefully examined for all three of these spreading centers between 7°N and 30°N. Three plate motion reorganizations are documented: (1) the breakup of the Guadalupe plate at anomaly 5A time (11 to 12.5 m.y. B.P.) into the Rivera and Cocos plates and a spreading center reorientation from a northwest to northeast trend, (2) small reorientation of the Pacific-Cocos spreading center and northward migration of the Pacific-Rivera spreading center just before anomaly 3' time (6.5 m.y. B.P.), and (3) the abandonment of the Pacific-Rivera spreading center south of the Rivera fracture zone (the Mathematician Ridge) just before anomaly 2' time (2.5 m.y. B.P.), when the Pacific-Cocos spreading center jumped northward to the Rivera fracture zone.

The bathymetric expressions of several abandoned spreading centers are located in the eastern Pacific. The Mathematician Ridge is shown to be a series of bathymetric structures that are associated with each of the above mentioned tectonic events and becomes progressively younger from south to north. Segments of the abandoned Pacific-Guadalupe spreading center are found along the west coast of Baja. An abandoned spreading center in the Guatemala Basin, just south of the Tehuantepec Ridge, can be identified by means of bathymetric data and also may be a segment of the abandoned Pacific-Guadalupe spreading center. A common characteristic of all of these sections of abandoned spreading centers is a narrow trough with flanking bathymetric peaks superimposed on a regional swell.

Fracture zones in the eastern Pacific belong to three distinct tectonic regimes: the Pacific-Guadalupe spreading center, Pacific-Rivera spreading center, and Pacific-Cocos spreading center. The PGSC fracture zones include the major Pacific fracture zones (Molokai, Clarion, and Clipperton) and perhaps the Tehuantepec fracture zone and others parallel to it on the older part of the Cocos plate. With the breakup of the Guadalupe plate the PGSC transform zones disappear and the PRSC fracture zones (Tamayo, Rivera, and O'Gorman) and PCSC fracture faults (Orozco, Clipperton, and Siqueiros) take their places. As a result of the major plate reorganization at about anomaly 5A time (11 to 12.5 m.y. B.P.), there is no clear one-to-one correspondence between the old fracture zone pattern (PGSC) and the new one (PRSC and PCSC).

Acknowledgments. We wish to thank M. McNutt, G. Mountain, and D. Rea for their helpful comments and critiques. We would like to acknowledge the Lamont-Doherty Geological Observatory and R. Larson for making available the LDGO magnetic data and W. Lynn for providing the Oregon State and University of Washington magnetic data. The help of S. Smith, U. Albright, V. Psarotulos, P. Forrestel, and J. Zwinakis is also gratefully appreciated. This work was supported by grants ONR-N-00014-80-C-0440 and NSF-OCE-80-18169 (for J. Mammerickx).

REFERENCES

Anderson, R. N., and E. E. Davis, A topographic interpretation of the Mathematician Ridge, Clipperton Ridge, East Pacific Rise system, *Nature, 241*, 191–193, 1973.

Anderson, R. N., and H. C. Noltimier, A model for the horst and graben structure of midocean ridge crests based upon spreading velocity and basalt delivery to the oceanic crust, *Geophys. J. R. Astron. Soc., 34*, 137–147, 1973.

Anderson, R. N., and J. G. Sclater, Topography and evolution of the East Pacific Rise between 5°S and 20°S, *Earth Planet. Sci. Lett., 14*, 433–441, 1972.

Anderson, R. N., G. F. Moore, F. S. Schilt, R. C. Cardwell, A. Trehu, and V. Vacquier, Heat flow near fossil ridge on the north flank of the Galapagos spreading center, *J. Geophys. Res., 81*, 1828–1838, 1976.

Anderson, R. N., M. A. Hobart, R. P. Von Herzen, and D. J. Fornari, Geophysical surveys on the East Pacific Rise–Galapagos Rise system, *Geophys. J. R. Astron. Soc., 54*, 141–166, 1978.

Atwater, T., Implications of plate tectonics for the Cenozoic tectonic evolution of western North America, *Geol. Soc. Am. Bull., 81*, 3513–3536, 1970.

Atwater, T., and H. W. Menard, Magnetic lineations in the northeast Pacific, *Earth Planet. Sci. Lett., 7*, 445–450, 1970.

Batiza, R., and C. G. Chase, Miocene spreading centre south of Isla Guadalupe, *Nature, 289*, 787–789, 1981.

Blakely, R. J., Geomagnetic reversals and crustal spreading rates during the Miocene, *J. Geophys. Res., 79*, 2979–2985, 1974.

Chase, C. G., The N plate problem of plate tectonics, *Geophys. J. R. Astron. Soc., 29*, 117–122, 1972.

Chase, C. G., H. W. Menard, R. L. Larson, G. F. Sharman III, and S. M. Smith, History of sea floor spreading west of Baja California, *Geol. Soc. Am. Bull., 81*, 491–498, 1970*a*.

Chase, T. E., H. W. Menard, and J. Mammerickx, Bathymetry of the North Pacific, Mercator projector, *Tech. Rep. Ser. TR-1–TR-15*, Scripps Inst. of Oceanog. Inst. of Mar. Resour., La Jolla, Calif., 1970*b*.

Chase, T. E., S. M. Smith, D. A. Newhouse, W. L. Crocker, M. Schoenbechler, L. Hydock, and U. Ritter, Track charts of SIO bathymetric data and track charts of SIO magnetic data in the Pacific Ocean, *Tech. Rep. Ser. TR-25*, Scripps Inst. of Oceanog. Inst. of Mar. Resour., La Jolla, Calif., 1972.

Couch, R., and S. Woodcock, Gravity and structure of the continental margins of southwestern Mexico and northwestern Guatemala, *J. Geophys. Res., 86*, 1829–1840, 1981.

Crane, K., The intersection of the Siqueiros transform fault and the East Pacific Rise, *Mar. Geol., 21*, 25–46, 1976.

Curray, J. R., et al., Leg 64 seeks evidence on development of basins, *Geotimes, 24*, 18–20, 1979.

Elvers, D., S. P. Srivastava, K. Potter, J. Morley, and D. Sdidel, Asymmetric spreading across the Juan de Fuca and Gorda rises as obtained from a detailed magnetic survey, *Earth Planet. Sci. Lett., 20*, 211–219, 1973.

Ewing, J. I., and R. P. Meyer, Rivera ocean seismic experiment (ROSE) overview, *J. Geophys. Res.*, in press, 1982.

Handschumacher, D. W., Post-Eocene plate tectonics of the eastern Pacific, in *The Geophysics of the Pacific Ocean Basin and Its Margin, Geophys. Monogr. Ser.*, vol. 19, edited by G. H. Sutton, pp. 177–202, AGU, Washington, D. C., 1976.

Haq, B., et al., Eastern Pacific Boundary currents, *Geotimes, 24*, 30–31, 1979.

Harrison, C. G. A., Poles of rotation, *Earth Planet. Sci. Lett., 14*, 31–38, 1972.

Hayes, D. E., and W. C. Pitman III, Magnetic lineations in the North Pacific, Geological Investigations of the North Pacific, edited by J. D. Hays, *Mem. Geol. Soc. Am., 126*, 291–314, 1970.

Heezen, B. C., The deep-sea floor, in *Continental Drift*, edited by S. K. Runcorn, pp. 235–288, Academic, New York, 1962.

Heirtzler, J. R., G. O. Dickson, E. M. Herron, W. C. Pitman III, and X. LePichon, Marine magnetic anomalies, geomagnetic field reversals, and motions of the ocean floor and continents, *J. Geophys. Res., 73*, 2119–2136, 1968.

Herron, E. M., Sea floor spreading and the Cenozoic history of the east-central Pacific, *Geol. Soc. Am. Bull., 83*, 1671–1691, 1972.

Isacks, B., J. Oliver, and L. R. Sykes, Seismology and the new global tectonics, *J. Geophys. Res., 73*, 5855–5899, 1968.

Karig, D. E., R. K. Cardwell, G. G. Moore, and D. G. Moore, Late

Cenozoic subduction and continental margin truncation along the northern Middle America trench, *Geol. Soc. Am. Bull., 89*, 265–276, 1978.

Kastens, K. A., K. C. Macdonald, K. Becker, and K. Crane, The Tamayo transform fault in the mouth of the Gulf of California, *Mar. Geophys. Res., 4*, 129–151, 1979.

Klitgord, K. D., J. D. Mudie, R. A. Larson, and J. A. Grow, Fast sea floor spreading on the Chile Ridge, *Earth Planet. Sci. Lett., 20*, 93–99, 1973.

Klitgord, K. D., S. P. Huestis, J. D. Mudie and R. L. Parker, An analysis of near-bottom magnetic anomalies: Sea floor spreading and the magnetized layer, *Geophys. J. R. Astron. Soc., 43*, 387–424, 1975

Larson, R. L., Bathymetry, magnetic anomalies, and plate tectonics history of the mouth of the Gulf of California, *Geol. Soc. Am. Bull., 83*, 3345–3360, 1972.

Larson, R. L., and C. G. Chase, Relative velocities of the Pacific, North America and Cocos plates in the Middle America region, *Earth Planet. Sci. Lett., 7*, 425–428, 1970.

Larson, R. L., H. W. Menard, and S. M. Smith, Gulf of California: A result of ocean floor spreading and transform faulting, *Science, 161*, 781–784, 1968.

Le Pichon, X., Sea floor spreading and continental drift, *J. Geophys. Res., 73*, 3661–3697, 1968.

Lonsdale, P., Regional shape and tectonics of the equatorial East Pacific Rise, *Mar. Geophys. Res., 3*, 295–325, 1977.

Lonsdale, P., and K. D. Klitgord, Structure and tectonic history of the eastern Panama Basin, *Geol. Soc. Am. Bull., 89*, 981–999, 1978.

Lonsdale, P.; and F. N. Spiess, Deep-tow observations at the East Pacific Rise, 8°45'N, and some interpretations, *Initial Rep. Deep Sea Drill. Proj., 54*, 43–62, 1980.

Ludwig, W. J., and P. D. Rabinowitz, Geophysical measurements across the East Pacific Rise in the vicinity of the Siqueiros fracture zone (survey area PT-4), *Initial Rep. Deep Sea Drill. Proj., 54*, 37–42, 1980.

Lynn, W. S., and Lewis, B. T. R., Tectonic evolution of the northern Cocos plate, *Geology, 4*, 718–722, 1976.

Mammerickx, J., Neogene reorganization of spreading between the Tamayo and the Rivera fracture zone, *Mar. Geophys. Res., 4*, 305–318, 1980.

Mammerickx, J., and K. D. Klitgord, Northern East Pacific Rise: Evolution from 25 m.y. B.P. to the Present, *J. Geophys. Res.*, this issue.

Mammerickx, J., and S. M. Smith, Bathymetry of the Northeast Pacific, *Maps Charts Ser. MC 43*, Geol. Soc. of Am., Boulder, Colo., 1981.

Mammerickx, J., R. N. Anderson, H. W. Menard, and S. M. Smith, Morphology and tectonic evolution of the east-central Pacific, *Geol. Soc. Am. Bull., 86*, 111–118, 1975.

Mammerickx, J., M. S. Reichle, and I. D. Reid, Bathymetry of the Rivera fracture zone, *Tech. Rep. Ser. TR-62*, Scripps Inst. of Oceanog. Inst. of Mar. Resour., La Jolla, Calif., 1978.

Mammerickx, J., E. Herron, and L. Dorman, Evidence for two fossil spreading ridges in the southeast Pacific, *Geol. Soc. Am. Bull., 91*, 263–271, 1980.

Mason, R. G., and A. D. Raff, A magnetic survey off the west coast of North America 32°N to 42°N, *Geol. Soc. Am. Bull., 72*, 1259–1265, 1961.

Menard, H. W., The East Pacific Rise, *Science, 132*, 1737–1746, 1960.

Menard, H. W., *Marine Geology of the Pacific*, 271 pp., McGraw-Hill, New York, 1964.

Menard, H. W., Fracture zones and offsets of the East Pacific Rise, *J. Geophys. Res., 71*, 682–685, 1966.

Menard, H. W., Elevation and subsidence of oceanic crust, *Earth Planet. Sci. Lett., 6*, 275–284, 1969.

Menard, H. W., Fragmentation of the Farallon plate by pivoting subduction, *J. Geol., 86*, 99–110, 1978.

Menard, H. W., and T. E. Chase, Fracture zones, in *The Sea*, vol. 4, edited by A. E. Maxwell, pp. 421–444, Interscience, New York, 1970.

Menard, H. W., and R. L. Fisher, Clipperton fracture zone in the northeastern equatorial pacific, *J. Geol., 66*, 239–253, 1958.

Menard, H. W., and J. Mammerickx, Abyssal hills, magnetic anomalies and the East Pacific Rise, *Earth Planet Sci. Lett., 2*, 465–472, 1967.

Minster, J. B., T. H. Jordon, P. Molnar, and E. Haines, Numerical modelling of instantaneous plate tectonics, *Geophys. J. R. Astron. Soc., 36*, 541–576, 1974.

Molnar, P., T. Atwater, J. Mammerickx, and S. M. Smith, Magnetic anomalies, bathymetry and the tectonic evolution of the South Pacific since the Late Cretaceous, *Geophys. J. R. Astron. Soc., 40*, 383–420, 1975.

Morgan, W. J., Rises, trenches, great faults, and crustal blocks, *J. Geophys. Res., 73*, 1959–1982, 1968.

Morton, W. T., and A. Lowrie, Regional geological maps of the northeast Pacific, Area NP-9, *Rep. RP-16*, U.S. Nav. Oceanog. Off., NSTL Station, Miss., 1978.

Mudie, J. D., J. Grow, K. Klitgord, and P. Larson, Shipboard cruise report on leg 2 of expedition SOUTH TOW in the southeast Pacific, *Ref. 72-66*, 40 pp., Scripps Inst. of Oceanog., La Jolla, Calif., 1972.

Ness, G., S. Levi, and R. Couch, Marine magnetic anomaly time scales for the Cenozoic and Late Cretaceous: A precis, critique and synthesis, *Rev. Geophys. Space Phys., 18*, 753–770, 1980.

Ness, G. E., O. Sanchez Z., R. W. Couch and R. S. Yeats, Bathymetry and oceanic crustal ages in the vicinity of the mouth of the Gulf of California illustrated using Deep Sea Drilling Project leg 63 underway geophysical profiles, *Initial Rep. Deep Sea Drill. Proj., 63*, 919–923, 1981.

Normark, W. R., Definition of the plate boundary along the East Pacific Rise off Mexico, *Mar. Geod., 4*, 29–43, 1980.

Pitman, W. C., III, E. M. Herron, and J. R. Heirtzler, Magnetic anomalies in the Pacific and seafloor spreading, *J. Geophys. Res., 73*, 2069–2085, 1968.

Project ROSE Scientists, Microearthquake activity on the Orozco fracture zone: Preliminary results from Project ROSE, *J. Geophys. Res., 86*, 3783–3790, 1981.

Prothero, W. A., I. Reid, M. S. Reichle, and J. N. Brune, Ocean bottom seismic measurements on the East Pacific Rise and Rivera fracture zone, *Nature, 262*, 121–124, 1976.

Raff, A. D., Seafloor spreading—Another rift, *J. Geophys. Res., 73*, 3699–3705, 1968.

Raff, A. D., and R. G. Mason, Magnetic survey off the west coast of North America, 40°N latitude to 50°N latitude, *Geol. Soc. Am. Bull., 72*, 1267–1270, 1961.

Rea, D. K., Evolution of the East Pacific Rise between 3°S and 13°S since the middle Miocene, *Geophys. Res. Lett., 5*, 561–564, 1978.

Rea, D. K., Tectonics of the Nazca-Pacific divergent plate boundary, Nazca Plate: Crustal Formation and Andean Convergence, edited by L. D. Kulm et al., *Mem. Geol. Soc. Am., 154*, 27–62, 1981.

Reichle, M. S., G. S. Sharman, and J. N. Brune, Sonobuoy and teleseismic study of Gulf of California transform fault earthquake sequences, *Bull. Seismol. Soc. Am., 66*, 1623–1641, 1976.

Rosendahl, B. R., and L. M. Dorman, Summary of the geology and geophysics of the East Pacific Rise in the vicinity of the Siqueiros fracture zone, *Initial Rep. Deep Sea Drill. Proj., 54*, 23–36, 1980.

Schilt, F. S., D. E. Karig, and M. Truchan, Kinematic evolution of the northern Cocos plate, *J. Geophys. Res., 87*, 2958–2968, 1982.

Schouten, J. A., A fundamental analysis of magnetic anomalies over oceanic ridges, *Mar. Geophys. Res., 1*, 111–144, 1971.

Schouten, H., and K. D. Klitgord, The memory of the accreting plate boundary and the continuity of fracture zones, *Earth Planet. Sci. Lett.*, in press, 1982.

Schouten, H., and K. McCamy, Filtering marine magnetic anomalies, *J. Geophys. Res., 77*, 7089–7099, 1972.

Schouten, H., and R. S. White, Zero offset fracture zones, *Geology, 8*, 175–179, 1980.

Sclater, J. G., R. N. Anderson, and M. L. Bell, Elevation of ridges and evolution of the central eastern Pacific, *J. Geophys. Res., 76*, 7888–7915, 1971.

Spencer, J. E., and W. R. Normark, Tosco-Abreojos fault zone: A Neogene transform plate boundary within the Pacific margin of southern Baja California, Mexico, *Geology, 7*, 554–557, 1979.

Sykes, L. R., Mechanism of earthquakes and nature of faulting on the mid-oceanic ridges, *J. Geophys. Res., 72*, 2131–2153, 1967.

Tamaki, K., M. Joshima, and R. L. Larson, Remanent Early Cretaceous spreading center in the Central Pacific Basin, *J. Geophys. Res., 84*, 4501–4510, 1979.

Taylor, P. T., J. A. Brennan, and N. J. O'Neill, Variable sea floor spreading off Baja California, *Nature, 229*, 396–399, 1971.

Theberge, A. E.; East Pacific anomaly map, 29°N to 40°N, 115°W to 127°W, Nat. Ocean Surv., Seattle, Washington, 1971.
Truchan, M., and R. L. Larson, Tectonic lineamonts on the Cocos plate, *Earth Planet. Sci. Lett., 17,* 426–432, 1973.
van Andel, T. H., G. R. Heath, and T. C. Moore; Cenozoic history and paleoceanography of the central equatorial Pacific Ocean, *Mem. Geol. Soc. Am., 143,* 134 pp., 1975.
von Huene, R., et al., Leg 67: The Deep Sea Drilling Project Mid-America trench transect off Guatemala, *Geol. Soc. Am. Bull., 91,* 421–432, 1980.
Weissel, J. K., and A. B. Watts, Tectonic evolution of the Coral Sea Basin, *J. Geophys. Res., 84,* 4572–4582, 1979.

(Received August 10, 1981;
revised January 26, 1982;
accepted February 19, 1982.)

Tectonophysics, 55 (1979) 107—126

THE RELATIONSHIP OF SOURCE PARAMETERS OF RIDGE-CREST AND TRANSFORM EARTHQUAKES TO THE THERMAL STRUCTURE OF OCEANIC LITHOSPHERE

SEAN C. SOLOMON and NORMAN C. BURR *

Department of Earth and Planetary Sciences, Massachusetts Institute of Technology, Cambridge, Mass. 02139 (U.S.A.)

(Submitted November 20, 1977; accepted for publication April 24, 1978)

ABSTRACT

Solomon, S.C. and Burr, N.C., 1979. The relationship of source parameters of ridge-crest and transform earthquakes to the thermal structure of oceanic lithosphere. In: J. Francheteau (Editor), Processes at Mid-Ocean Ridges. Tectonophysics, 55: 107—126.

The source parameters of large earthquakes on ridge crests and transform faults are closely related to the thermal and mechanical properties of oceanic lithosphere. Several characteristics of these earthquakes (including magnitude, seismic moment M_0, apparent stress $\eta\bar{\sigma}$ and stress drop $\Delta\sigma$) are synthesized according to local plate velocity v and, for transforms, to ridge—ridge offset L and average fault width W estimated by Brune's method. For ridge-crest (normal faulting) events: (1) the maximum M_0 decreases with v; (2) this decrease may be attributed to a particular isotherm limiting the depth of seismic failure if the largest crestal earthquakes are located 10—20 km off-axis; a constancy of the product of $\Delta\sigma$ and fault length for these events is implied; (3) $\eta\bar{\sigma}$ shows no systematic variation with v. For *transform* events: (1) the maximum M_0 decreases with v; (2) the maximum M_0 appears to increase with the maximum age contrast across the transform; (3) $\eta\bar{\sigma}$ does not clearly depend on either v or L; (4) the maximum estimated $W(v)$ decreases with v; (5) for fixed v, $W(L)$ increases with L; (6) the largest earthquakes on long transforms occur near the transform center; (7) an inversion of slip rate and magnitude data for 60 transforms supports the hypothesis that seismic failure occurs only at temperatures below a fixed value, and gives a nominal value of 100°—150°C to this limiting isotherm. Neither stress drops nor apparent stresses are resolvably different for ridge crest and transform fault earthquakes.

INTRODUCTION

Some general properties of mid-ocean ridge earthquakes are well known. It is known that earthquakes on transforms can be larger than those along ridge crests and that slow spreading ridges tend to be characterized by larger

* Present address: Lawrence Livermore Laboratory, University of California, Livermore, California 94550 (U.S.A.)

earthquakes and/or higher seismicity rates than faster spreading ridges (Isacks et al., 1968). But what are the key parameters governing the sizes of oceanic earthquakes? In particular, what controls the maximum size, or maximum seismic moment, of an earthquake on any particular ridge crest or transform?

In this paper we present a synthesis of earthquake source parameter data for ridge crest and oceanic transform earthquakes to support the hypothesis that earthquake size is controlled by thermal structure. More specifically, the seismic moment of an earthquake in a spreading center region appears to be limited by the depth to some fixed isotherm. Thus for ridge crests, the moment for normal faulting events is limited by the local spreading rate. For transform events the moment is limited by a combination of both spreading rate and ridge—ridge offset.

We also explore relations between the level of stress, as revealed by measurements of apparent stress and stress drop, and either plate boundary type or spreading rate. Data from earthquakes ranging in size from the largest observed to the smallest yet recorded with ocean-bottom seismometers are included. No difference in stress level is discernible between ridge crests and transforms, between fast and slow spreading systems, or between spreading centers and other seismic environments.

RIDGE-CREST EARTHQUAKES

Large earthquakes along the axes of mid-ocean ridge crests are characterized by a predominance of normal faulting (Sykes, 1967). For thirty earthquakes on or near ridge crests, published fault-plane solutions demonstrate that these events are of the normal-faulting class. Of these thirty, half (fifteen) appear to lie essentially along a ridge axis and half are demonstrably (≥ 50 km) off-axis or intraplate. A summary of the locations and pertinent source parameters for these earthquakes is given in Solomon (1978).

A common measure of earthquake size is magnitude. The body-wave magnitudes m_b of all ridge-crest earthquakes, both axial and off-axis, are plotted in Fig. 1 versus local spreading half-rate. Two conclusions are evident. First, at any given spreading rate the largest off-axis earthquakes are generally of greater magnitude than the axial events. Second, the largest magnitude of ridge-axis earthquakes appears to decrease with increasing spreading rate.

A measure of earthquake size more readily relatable to the fault dimensions and offset is the seismic moment (Aki, 1966). The known seismic moments of ridge-axis earthquakes are plotted versus local spreading half-rate in Fig. 2. The important characteristic of this figure is the envelope that bounds the data points from above. The maximum seismic moment appears to decrease by over an order of magnitude as spreading half-rate increases from 0.2 to 3 cm/yr.

Let us assert the premise that the envelope shown represents the true maximum moment at each spreading velocity. We admit there may be a problem

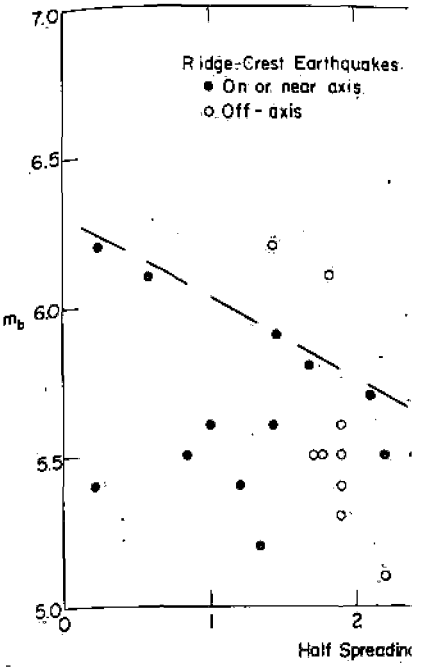

Fig. 1. Body-wave magnitude of ridg
Only earthquakes known to be norm
Solomon (1978). The dashed line g
rate for ridge-axis earthquakes.

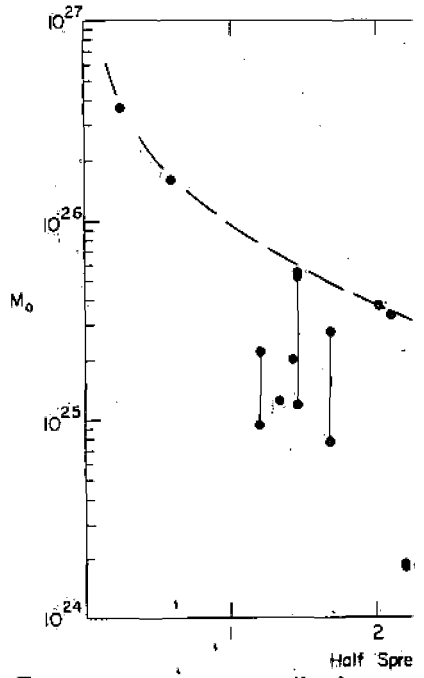

Fig. 2. Seismic moment (in dyne c
half-rate. Only earthquakes known
near or along a ridge axis are includ
dent measurements for the same e
Menahem and Aboodi (1971), Thatc
and Solomon (1978). The dashed c
spreading rate.

han faster spreading ridges
meters governing the sizes of
s the maximum size, or max-
iny particular ridge crest or

quake source parameter data
es to support the hypothesis
ucture. More specifically, the
g center region appears to be
i. Thus for ridge crests, the
the local spreading rate. For
mbination of both spreading

f stress, as revealed by mea-
d either plate boundary type
ig in size from the largest ob-
an-bottom seismometers are
ible between ridge crests and
stems, or between spreading

an ridge crests are character-
kes, 1967). For thirty earth-
-plane solutions demonstrate
ss. Of these thirty, half (fif-
is and half are demonstrably
f the locations and pertinent
in Solomon (1978).
gnitude. The body-wave mag-
axial and off-axis, are plotted
onclusions are evident. First,
earthquakes are generally of
nd, the largest magnitude of
increasing spreading rate.
relatable to the fault dimen-
i, 1966). The known seismic
l versus local spreading half-
his figure is the envelope that
num seismic moment appears
spreading half-rate increases

own represents the true max-
dmit there may be a problem

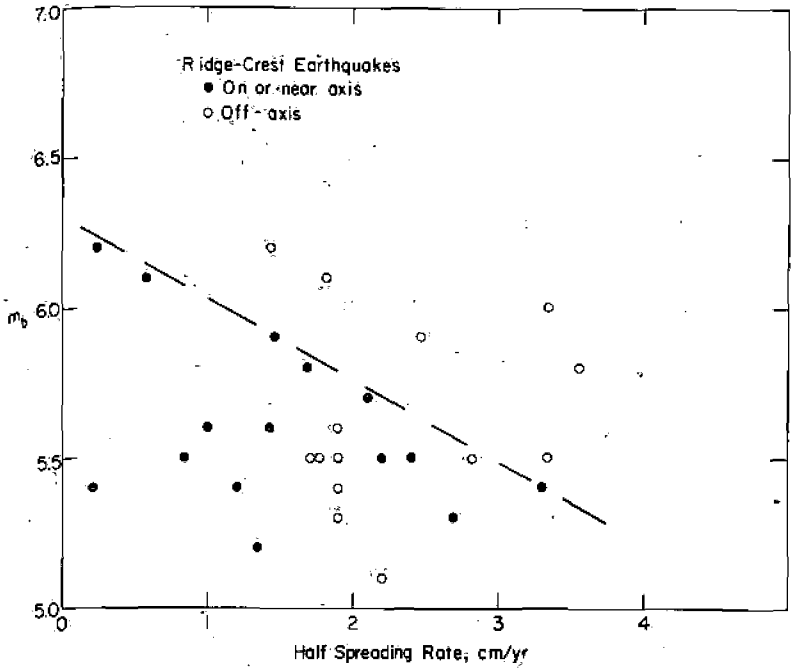

Fig. 1. Body-wave magnitude of ridge crest earthquakes versus local spreading half-rate. Only earthquakes known to be normal faulting events are included. Data are taken from Solomon (1978). The dashed line gives a nominal upper bound to m_b versus spreading rate for ridge-axis earthquakes.

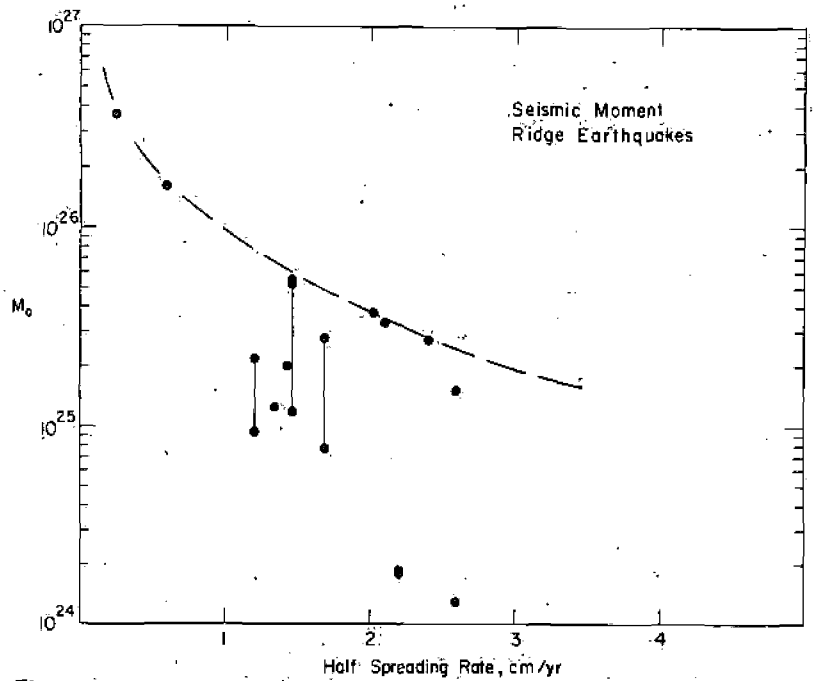

Fig. 2. Seismic moment (in dyne cm) of ridge-crest earthquakes versus local spreading half-rate. Only earthquakes known to be normal faulting events and known to be very near or along a ridge axis are included. Points connected by tie lines represent independent measurements for the same event. Data are from Tsai (1969), Wyss (1970), Ben-Menahem and Aboodi (1971), Thatcher (1972), Weidner and Aki (1973), Forsyth (1973), and Solomon (1978). The dashed curve is the postulated maximum M_0 as a function of spreading rate.

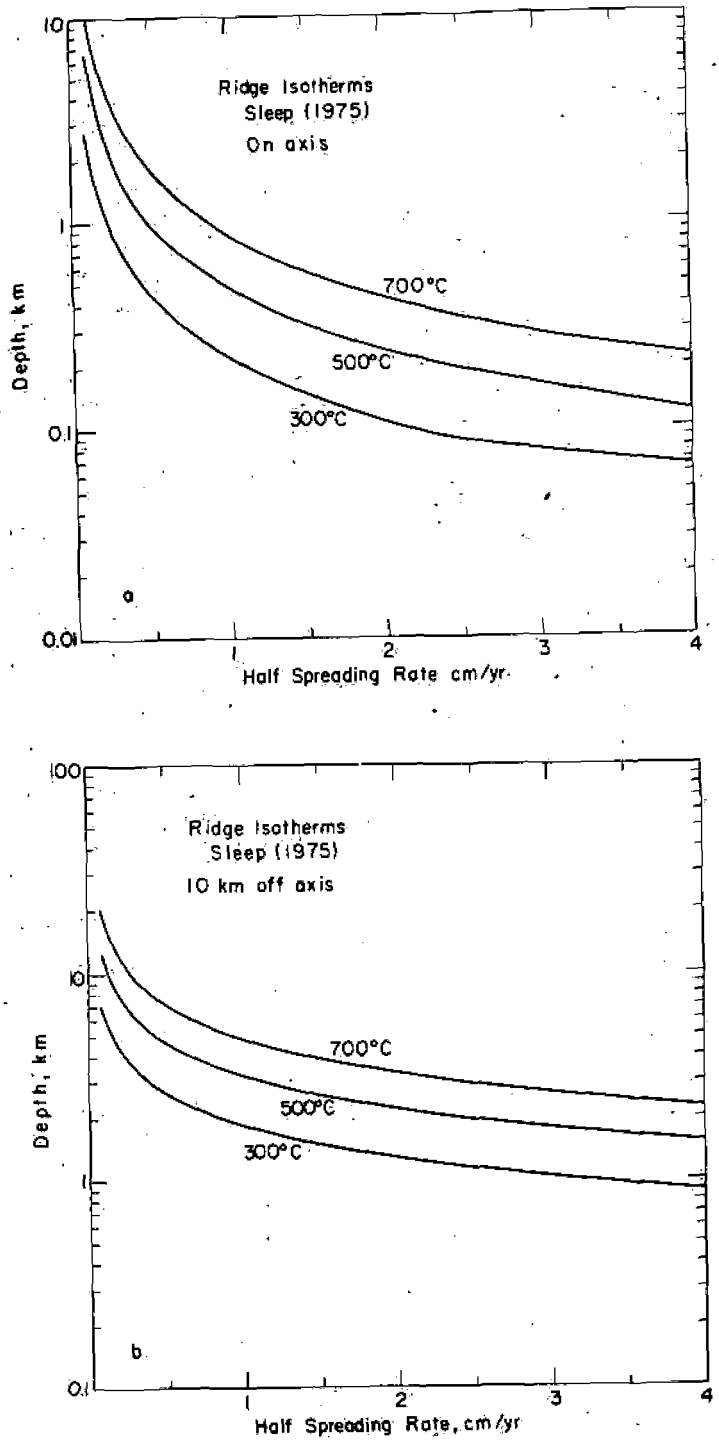

Fig. 3. a. Depth to various isotherms versus spreading rate along the ridge axis for the thermal model of Sleep (1975). b. Depth to various isotherms 10 km off-axis for the same model.

of limited sampling; one large ev show the premise to be untrue data.

With this premise we may test mum moment is controlled by th temperatures above this limiting rather than seismic. In other wo these largest ridge crest earthqu spreading rate varies.

How does an isotherm depth in Fig. 3a are isotherm depths at according to the most detailed Note the very rapid variation of Fig. 3b are isotherm depths vers axis. The variation is much mo greater distances off-axis, the i scale very much as those shown i ing rate is of course increased as t

To relate moment M_0 and isoth of length l and width w:

$$M_0 = clw^2\Delta\sigma$$

where $\Delta\sigma$ is the stress drop (equ final shear stress on the fault) an metry (Knopoff, 1958; Aki, 196 width w scales as isotherm depth sider three simple scaling laws for

$$M_0 \sim w$$

$$M_0 \sim w^2$$

$$M_0 \sim w^3$$

That is, M_0 may vary as the first hypothetical limiting isotherm fo 2a corresponds to $lw\Delta\sigma \sim$ consta stant, and relation 2c is equivalent

The observed curve of maxim may be tested against the relatio Fig. 3. Such a test is shown in Fi precisely along the ridge axis, th possibility is unlikely, because it v and fault area remains constant varies by more than a factor of 10

of limited sampling; one large event at a relatively rapidly spreading ridge can show the premise to be untrue. At least the premise is testable by future data.

With this premise we may test quantitatively the hypothesis that the maximum moment is controlled by the depth of a particular isotherm, i.e., that at temperatures above this limiting value the mode of stress release is aseismic rather than seismic. In other words, we suppose that the fault width w for these largest ridge crest earthquakes scales as the depth to an isotherm as spreading rate varies.

How does an isotherm depth at the ridge vary with spreading rate? Shown in Fig. 3a are isotherm depths at the ridge-axis as functions of spreading rate, according to the most detailed ridge-crest thermal models of Sleep (1975). Note the very rapid variation of isotherm depth with spreading velocity. In Fig. 3b are isotherm depths versus spreading rate for a distance 10 km off-axis. The variation is much more modest than along the axis proper. For greater distances off-axis, the isotherm depth-versus-spreading rate curves scale very much as those shown in Fig. 3b, but the depth at any given spreading rate is of course increased as the distance from the axis increases.

To relate moment M_0 and isotherm depth, note that for a rectangular fault of length l and width w:

$$M_0 = clw^2\Delta\sigma \tag{1}$$

where $\Delta\sigma$ is the stress drop (equal to the difference between the initial and final shear stress on the fault) and c is a constant that depends on fault geometry (Knopoff, 1958; Aki, 1966). Our working hypothesis is that the fault width w scales as isotherm depth. As the spreading rate varies, we might consider three simple scaling laws for seismic moment:

$$M_0 \sim w \tag{2a}$$

$$M_0 \sim w^2 \tag{2b}$$

$$M_0 \sim w^3 \tag{2c}$$

That is, M_0 may vary as the first, second or third power of the depth to the hypothetical limiting isotherm for seismic failure. From equation 1, relation 2a corresponds to $lw\Delta\sigma \sim$ constant, relation 2b corresponds to $l\Delta\sigma \sim$ constant, and relation 2c is equivalent to $\Delta\sigma \sim$ constant and $l/w \sim$ constant.

The observed curve of maximum moment versus spreading rate (Fig. 2) may be tested against the relations of equation 2 and the isotherm depths of Fig. 3. Such a test is shown in Fig. 4. If the largest ridge crest events occur precisely along the ridge axis, then maximum M_0 scales as w (Fig. 4). This possibility is unlikely, because it would imply that the product of stress drop and fault area remains constant for earthquakes for which the fault width varies by more than a factor of 10.

4

4

ıg; rate along the ridge axis for the
otherms 10 km off-axis for the same

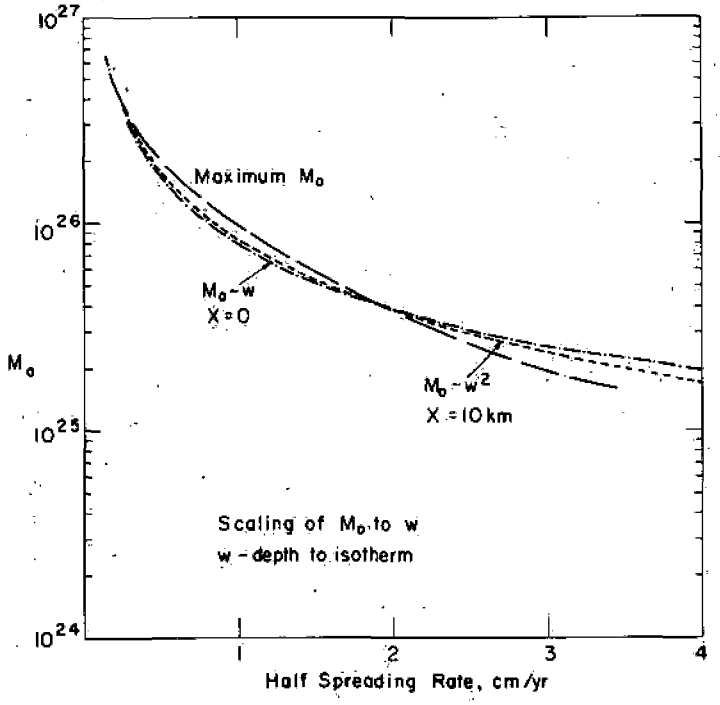

Fig. 4. Comparison of maximum M_0 versus spreading rate (from Fig. 2) with the 700°C isotherm depth w from Fig. 3a (different vertical scale) and with the squared depth to the 700°C isotherm from Fig. 3b (different vertical scale). The use of the 300°C or 500°C isotherms in Fig. 3 would give results indistinguishable from those shown.

If the largest ridge events occur 10 km or more off-axis, then maximum M_0 scales as w^2 (Fig. 4). This possibility leads to the more plausible implication that the product of stress drop and fault length is roughly constant for these largest ridge-axis earthquakes.

A predicted scaling of maximum M_0 to w^3 leads to too rapid a variation of maximum M_0 with spreading rate, even for ridge-axis offsets of several tens of kilometers. Thus unless new data on heretofore unobserved very large earthquakes on slow spreading centers are added at a future date, scaling relation 2c is not favored by the observed M_0 data (Fig. 2).

The hypothesis that the depth to an isotherm is the primary factor limiting earthquake size on mid-ocean ridge axes is therefore supported as long as the largest ridge-crest events occur slightly off center, probably beneath the rift valley walls or the edge of the rift mountains rather than directly beneath the central rift valley for slow spreading ridges. Further evidence for an off-center locus of seismic activity comes from the observation that micro-earthquakes along slowly-spreading ridges also tend to occur at the edge of the median rift valley rather than along the youngest central volcanic zone (Spindel et al., 1974; Francis et al., 1977).

If scaling relation 2b is val
ridge crests, then the produ
stant for these events. We sp
roughly constant for these
data, summarized in Solom
drop of 10—20 bars for such

Additional support for th
a strong function of spreadi
tity apparent stress (Aki, 19

$$\eta\bar{\sigma} = \mu E_s / M_0$$

where the apparent stress is
fault before and after faultii
is the shear modulus (taken
seismic energy. Determinat
energy—magnitude relation

$$\log_{10} E_s = 5.8 + 2.4 m_b$$

which is of doubtful applica

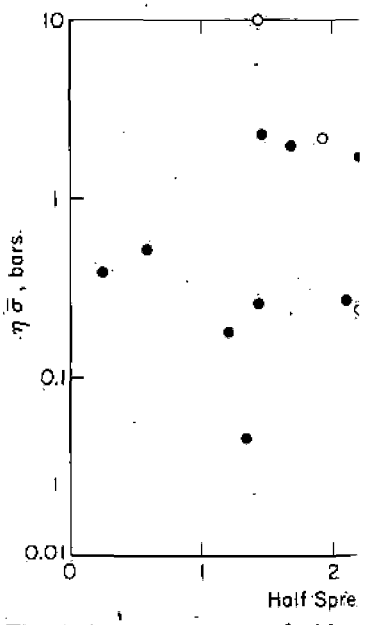

Fig. 5. Apparent stress of ridge
from Solomon (1978). The verti
March 1969 Gulf of California e
1972), at least one of which sh
and Brune, 1971).

If scaling relation 2b is valid for the largest normal-faulting earthquakes on ridge crests, then the product of stress drop and fault length is roughly constant for these events. We speculate that stress drop and fault length are each roughly constant for these largest crestal earthquakes. Limited stress drop data, summarized in Solomon (1978), support this notion and give a stress drop of 10—20 bars for such events.

Additional support for the idea that the state of stress at ridge crests is not a strong function of spreading rate comes from a consideration of the quantity apparent stress (Aki, 1966):

$$\eta\bar{\sigma} = \mu E_s / M_0 \tag{3}$$

where the apparent stress is the product of the average shear stress $\bar{\sigma}$ on the fault before and after faulting and an unknown seismic efficiency factor η, μ is the shear modulus (taken to be $3 \cdot 10^{11}$ dyne/cm^2), and E_s is the radiated seismic energy. Determination of E_s is not straightforward. We use the energy—magnitude relation of Gutenberg and Richter (1956):

$$\log_{10} E_s = 5.8 + 2.4 m_b \tag{4}$$

which is of doubtful applicability for modern determinations of m_b but does

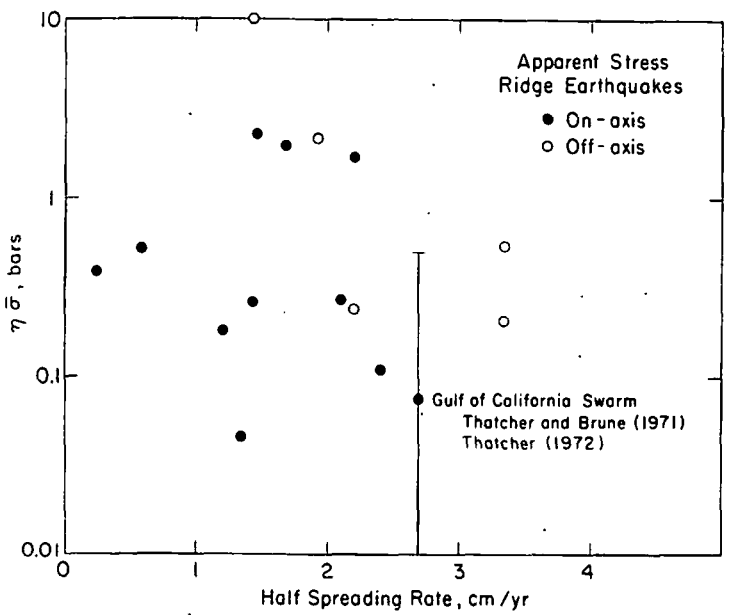

Fig. 5. Apparent stress of ridge-crest earthquakes versus local spreading rate. Data are from Solomon (1978). The vertical bar denotes the range in apparent stress found for a March 1969 Gulf of California earthquake swarm (Thatcher and Brune, 1971; Thatcher, 1972), at least one of which shows a normal-faulting earthquake mechanism (Thatcher and Brune, 1971).

provide an internally consistent means for estimating E_s when only relative variations in $\eta\bar{\sigma}$ among a population of events are desired, rather than rigorous measurements of absolute apparent stress levels. Apparent stress values so estimated, using m_b values reported by the International Seismological Centre, are shown in Fig. 5 versus the local spreading half-rate. No clear dependence on spreading rate is evident. There may be a tendency for off-axis earthquakes to show somewhat higher apparent stresses than axial events, though this may also be an artifact of an axial low-Q zone (Solomon, 1973) attenuating the amplitudes of body waves from the events nearest the median valley.

If the stress drop is constant for the events defining the bounding envelope in Fig. 2, then scaling relation 2b implies an approximate constancy of fault length l for the largest ridge crest earthquakes. The fault length corresponding to a 10—20 bar stress drop is 20—30 km, a figure in line with limited data from aftershock distributions (Ben-Menahem and Aboodi, 1971; Solomon, 1978). A characteristic bounding length to normal faults at mid-ocean ridge crests may represent the typical distance along a rift valley between major offsetting transforms.

TRANSFORM EARTHQUAKES

Along transform faults, temperatures should generally be less at any given depth than in the immediate vicinity of ridge crests. This provides simple qualitative grounds for the observation that earthquakes on oceanic transforms can be larger than those near ridge axes (Isacks et al., 1968). The thermal structure of a transform depends not only on the spreading rate but also on the transform offset L. Shown schematically in Fig. 6 is the area along a transform fault that is less than some temperature T_0 on *both* sides of the fault. If T_0 is the isotherm limiting seismic failure, then this shaded region represents the maximum fault area for an earthquake on this transform.

Source parameter data for 36 transform earthquakes and seismicity data for 60 transforms have been compiled by Burr and Solomon (1978). We use

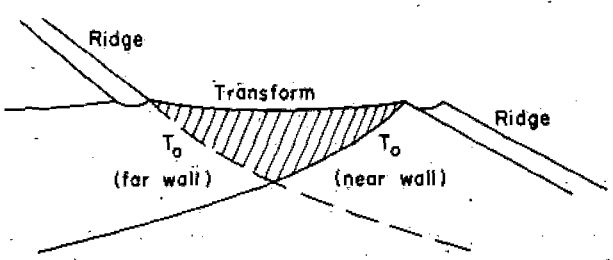

Fig. 6. Schematic view of how an isotherm may limit the area of a transform susceptible to seismic failure. The shaded region represents that portion of the transform on which temperature is less than a putative limiting value T_0 on both sides of the fault.

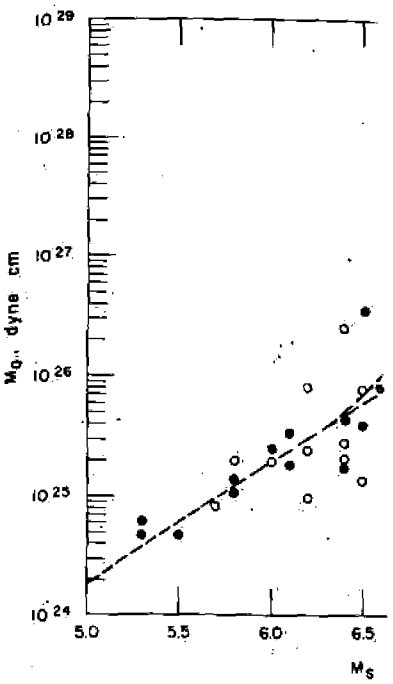

Fig. 7. Moment M_0 versus surface-v
Burr and Solomon (1978). Solid s
(1971) and an $M = 7.9$ event (Gut
ridge. Open symbols are those with
the ω^2 and ω^3 model of Aki (1967)

that data set below, with the
quakes: the three events of 14
4.2, $M_S = 4.3$, $M_0 = 1.3 \cdot 10^{23}$
and $m_b = 4.7$, $M_0 = 2.8 \cdot 10^{23}$
and the 25 March 1973 event i
$M_0 = 4.6 \cdot 10^{24}$ dyne cm, $l = 10$

Let us now examine several
meters of transform earthquak
set that support the notion th
undergoing seismic failure duri
considered two sets of earthqu
for transform faulting: the firs
with known seismic moment; th
quakes with known surface-v
moment and surface-wave mag
with known moment, and the p
Aki (1967). We have used the ω
the second earthquake data set
second set in the discussion belo

timating E_s when only relative
s are desired, rather than rigor-
s levels. Apparent stress values
he International Seismological
l spreading half-rate. No clear
re may be a tendency for off-
r apparent stresses than axial
an axial low-Q zone (Solomon,
ves from the events nearest the

events defining the bounding
olies an approximate constancy
earthquakes. The fault length
20—30 km, a figure in line with
n-Menahem and Aboodi, 1971;
ength to normal faults at mid-
al distance along a rift valley

d generally be less at any given
ge crests. This provides simple
earthquakes on oceanic trans-
(Isacks et al., 1968). The ther-
on the spreading rate but also
lly in Fig. 6 is the area along a
rature T_0 on *both* sides of the
ailure, then this shaded region
quake on this transform.
rthquakes and seismicity data
r and Solomon (1978). We use

the area of a transform susceptible
portion of the transform on which
both sides of the fault.

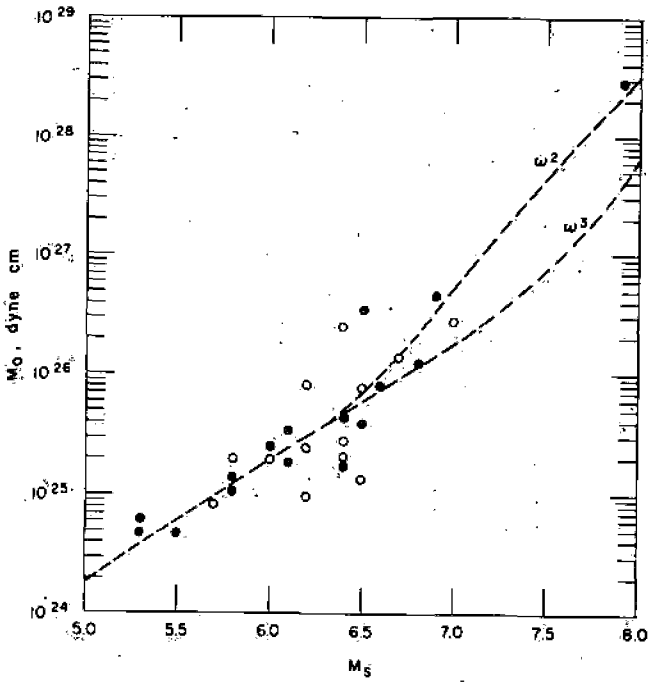

Fig. 7. Moment M_0 versus surface-wave magnitude M_S for transform earthquakes, from Burr and Solomon (1978). Solid symbols are those with M_S from the USGS or Udias (1971) and an $M = 7.9$ event (Gutenberg and Richter, 1954) on the southwest Indian ridge. Open symbols are those with magnitudes from Rothé (1969). Dashed lines are from the ω^2 and ω^3 model of Aki (1967).

that data set below, with the addition of the following transform earthquakes: the three events of 14/15 April 1974 on the Rivera transform (m_b = 4.2, M_S = 4.3, $M_0 = 1.3 \cdot 10^{23}$ dyne cm; m_b = 4.4, $M_0 = 2.1 \cdot 10^{23}$ dyne cm; and m_b = 4.7, $M_0 = 2.8 \cdot 10^{23}$ dyne cm, l = 4 km) studied by Reid (1976); and the 25 March 1973 event in the Gulf of California (m_b = 5.4, M_S = 5.5, $M_0 = 4.6 \cdot 10^{24}$ dyne cm, l = 10 km) studied by Reichle et al. (1976).

Let us now examine several empirical relations between the source parameters of transform earthquakes and either spreading rate or transform offset that support the notion that thermal structure is controlling the area undergoing seismic failure during an earthquake. Burr and Solomon (1978) considered two sets of earthquake data to explore these empirical relations for transform faulting: the first set consisted of all transform earthquakes with known seismic moment; the second set consisted of all transform earthquakes with known surface-wave magnitude. In Fig. 7 are shown the moment and surface-wave magnitude data for the transform earthquakes with known moment, and the predicted curves for the ω^2 and ω^3 models of Aki (1967). We have used the ω^2 curve to convert magnitude to moment for the second earthquake data set, and we consider only this more complete second set in the discussion below.

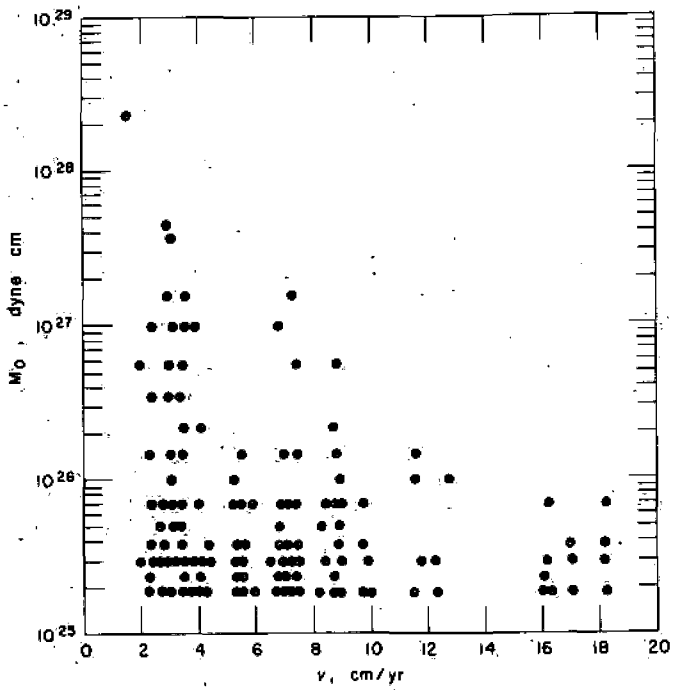

Fig. 8. Moment M_0 versus full spreading rate v for transform earthquakes using events with known magnitudes and the moment—magnitude relation given by the ω^2 model in Fig. 7.

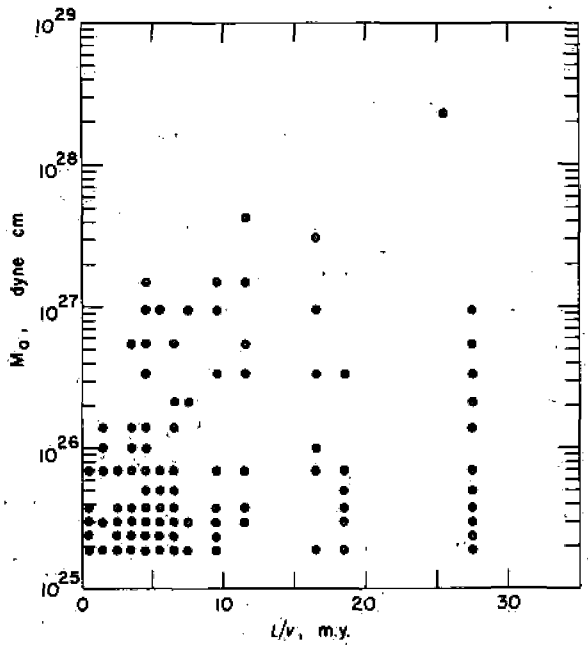

Fig. 9. Moment M_0 versus approximate transform age offset L/v using earthquakes with known magnitudes and the moment—magnitude relation given by the ω^2 model in Fig. 7. The values of L/v have been lumped in 1 m.y. wide bins; many of the symbols represent several events.

In Fig. 8 is shown the seis
events, using the data set
moment—magnitude relatior
maximum size of a transforn
Since higher spreading rate ir
sistent with temperature exer

In Fig. 9 is shown the seisr
approximate but simple me:
transform. The maximum n
maximum age contrast, thou
are too few to establish this
contrast implies deeper isoth
ing rate, the importance of
underscored.

As shown by Brune (1968
age depth interval of seismic
and the sum of the seismic n
a suitably long length of time

$$W = \Sigma M_0/\mu L v \tau$$

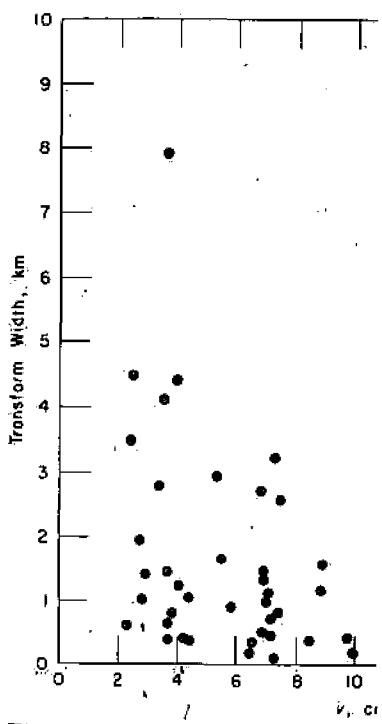

Fig. 10. Effective transform width
oceanic transforms. Data from Bur

In Fig. 8 is shown the seismic moment versus spreading rate for transform events, using the data set with known magnitudes and the assumed moment—magnitude relation. There appears to be a clear decrease in the maximum size of a transform earthquake as a function of spreading velocity. Since higher spreading rate implies shallower isotherms, these graphs are consistent with temperature exerting a strong control on fault area.

In Fig. 9 is shown the seismic moment plotted against the quantity L/v, an approximate but simple measure of the maximum age contrast across the transform. The maximum moment appears to increase with an increase in maximum age contrast, though the events with M_0 in excess of 10^{27} dyne cm are too few to establish this result with certainty. Again, since a greater age contrast implies deeper isotherms for either a given offset or a given spreading rate, the importance of temperature as a limit on earthquake size is underscored.

As shown by Brune (1968), the effective transform width W, or the average depth interval of seismic slip, can be estimated from the spreading rate v and the sum of the seismic moments for earthquakes on that transform over a suitably long length of time τ:

$$W = \Sigma M_0/\mu L v \tau \qquad (5)$$

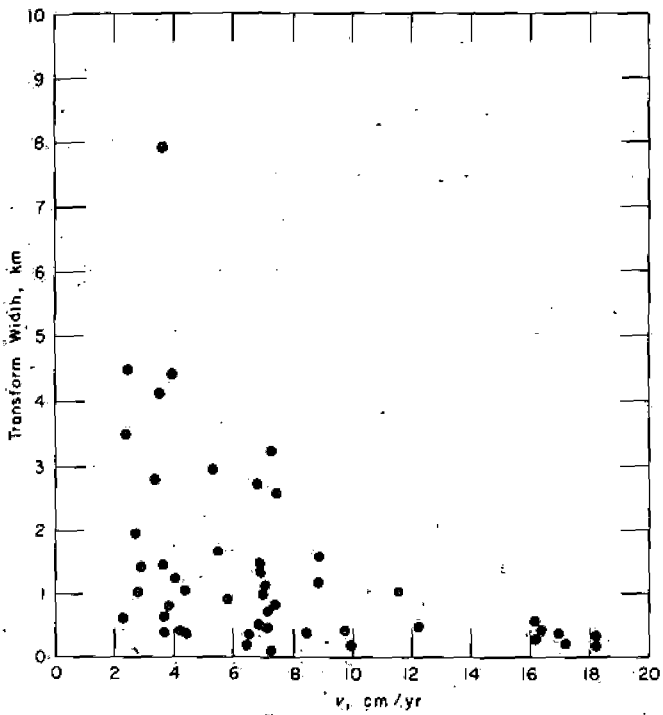

Fig. 10. Effective transform width W, from equation 5, versus full spreading rate for 60, oceanic transforms. Data from Burr and Solomon (1978).

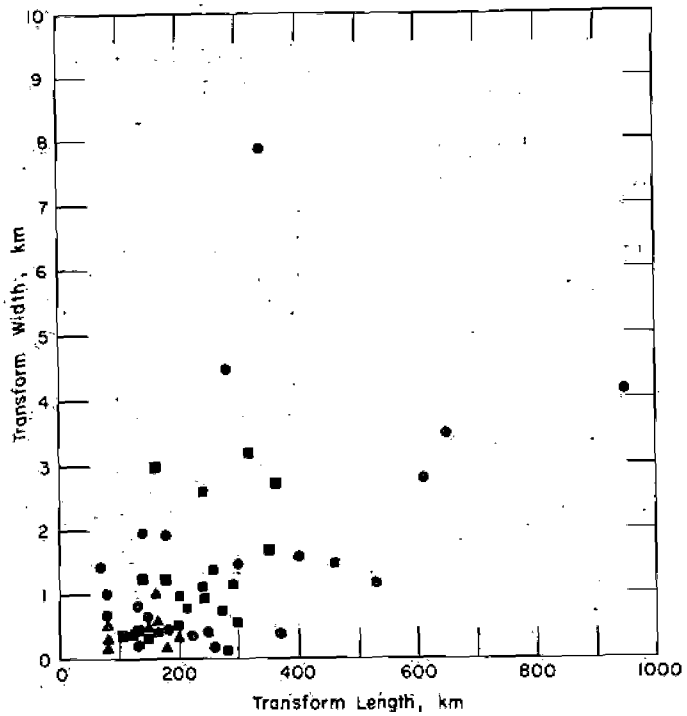

Fig. 11. Effective transform width W, from equation 5, versus transform length L. Symbols show trends of transforms with similar spreading rates: circles, v = 0—4 cm/yr; squares, v = 4—7.5 cm/yr; hexagons, v = 7.5—11 cm/yr; triangles, v = 11—18 cm/yr.

where L is the total transform length.

In Figs. 10 and 11 the transform width computed in this fashion is compared with the spreading rate and the transform length for 60 ridge—ridge transforms (Burr and Solomon, 1978), using approximately 50 years of magnitude data and the assumed moment—magnitude relation to determine the moment sums. In Fig. 10, the maximum effective transform widths may be

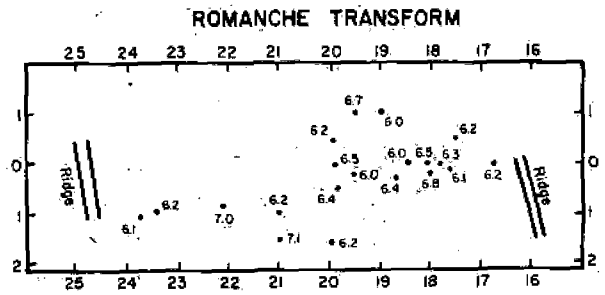

Fig. 12. Epicenters of earthquakes of magnitude 6.0 or greater on the Romanche transform, 1920—1975. Data from Gutenberg and Richter (1954) and USGS catalogs.

seen to decrease with spre
In Fig. 11, note that simila
a given spreading rate, the e
length.

The latter relation is als
quakes on the Romanche
events ($M \sim 7$) are confine
sumably because the fault
the transform ends.

The relation between t
earthquakes may be furthe
earthquakes on a particular
as the product of rigidity, fa

$$(\sum M_0)_i = \mu L_i W_i v_i \tau_i$$

Alternatively the moment s
tudes of the same earthquak

$$(\sum M_0)_i = \sum_j a_{ij} f_j(M_j)$$

where a_{ij} is the number of e
form, and f_j is the moment
a moment—magnitude relati
ture-limiting seismic failure,
transform from the spreadi
two pairs of equations may
The coefficients a_{ij} and the
for each transform but are l
the same for all transform
invert the system of equatio
ous assumed limiting temper

The results of one such set
are the moment—magnitude
therms shown after a least-s
magnitude relation resulting
inversion solutions and actu
temperature of about 150°
using somewhat different ass
Solomon (1978).

There are many reasons w
Our thermal model of the tra
tion across the transform, t
physical or chemical alteratic
culation, shear heating, and t
be leaky. Nonetheless, a lim

seen to decrease with spreading velocity, consistent with a thermal control. In Fig. 11, note that similar symbols denote comparable spreading rates. For a given spreading rate, the effective transform width increases with transform length.

The latter relation is also illustrated by looking at a plot of large earthquakes on the Romanche transform, as shown in Fig. 12. The very largest events ($M \sim 7$) are confined to the central portions of the transform, presumably because the fault width is greater in the cooler center than toward the transform ends.

The relation between temperature and seismic moments of transform earthquakes may be further quantified. The sum of the seismic moments for earthquakes on a particular transform i can be expressed, after Brune (1968), as the product of rigidity, fault area, spreading rate, and sampling time:

$$(\sum M_0)_i = \mu L_i W_i v_i \tau_i \tag{6}$$

Alternatively the moment sum can be expressed as a function of the magnitudes of the same earthquake set:

$$(\sum M_0)_i = \sum_j a_{ij} f_j(M_j) \tag{7}$$

where a_{ij} is the number of earthquakes of the magnitude M_j on the i^{th} transform, and f_j is the moment corresponding to the j^{th} magnitude, according to a moment—magnitude relation $f(M)$. For an assumed value for the temperature-limiting seismic failure, W_i in equation 6 may be determined for each transform from the spreading plate thermal models of Sleep (1975). These two pairs of equations may be written for each of 60 oceanic transforms. The coefficients a_{ij} and the spreading rate and transform area are different for each transform but are known. The magnitude-moment functions f_j are the same for all transforms, and are treated as unknowns. We may then invert the system of equations to find f_j and compare the solutions for various assumed limiting temperatures to the actual moment—magnitude data.

The results of one such set of inversions are shown in Fig. 13. In the figure are the moment—magnitude solutions for the various assumed limiting isotherms shown after a least-squares line has been fitted to the log moment—magnitude relation resulting from each inversion. From the comparison of inversion solutions and actual moment—magnitude data, a nominal limiting temperature of about 150°C is obtained. The results of other inversions using somewhat different assumptions are described more fully in Burr and Solomon (1978).

There are many reasons why this figure of 150°C is only a nominal value. Our thermal model of the transform is overly simple, ignoring lateral conduction across the transform, the sea floor topography of transforms, possible physical or chemical alteration of rocks in the fault zone, hydrothermal circulation, shear heating, and the possibility that some of the transforms may be leaky. Nonetheless, a limiting temperature of, at most, a few hundred

1000

versus transform length L. Symg rates: circles, v = 0—4 cm/yr; riangles, v = 11—18 cm/yr.

outed in this fashion is com-
m length for 60 ridge—ridge
roximately 50 years of mag-
de relation to determine the
ve transform widths may be

greater on the Romanche trans-
954) and USGS catalogs.

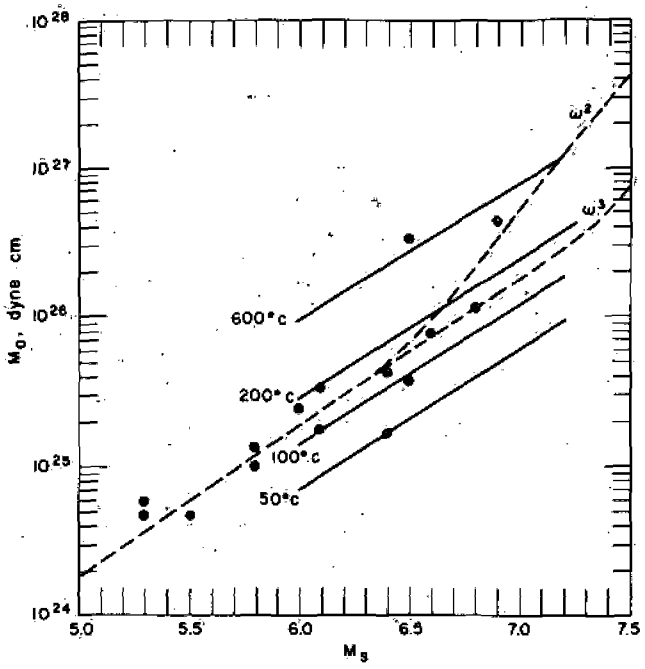

Fig. 13. Predicted log moment versus magnitude relations based on a least-squares linear representation of the results of inversion of slip rate and magnitude data from about 60 oceanic transforms. Each line represents the result of a different isotherm used to determine transform area as in Fig. 6. Data are the solid symbols in Fig. 7.

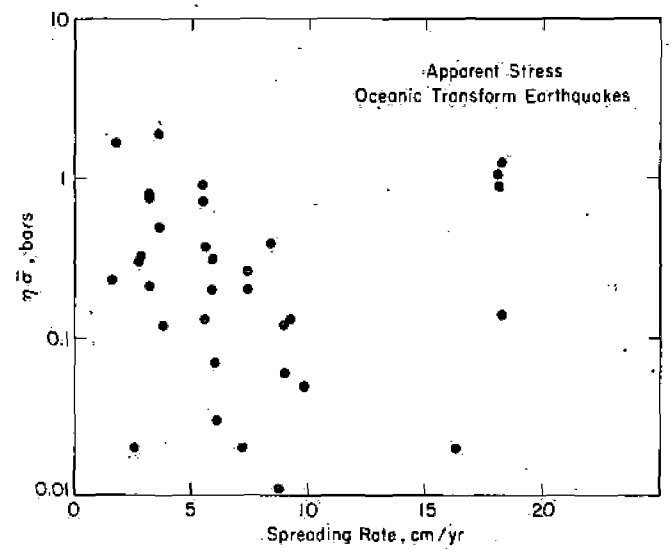

Fig. 14. Apparent stress of oceanic transform earthquakes versus local spreading rate. Data are from Burr and Solomon (1978), Reid (1976) and Reichle et al. (1976).

degrees Centrigrade is con
boundary between stick-slip
pressures appropriate to the
Byerlee, 1970; Stesky et al.
about a kilometer for the s
transforms are broadly consi
transform earthquakes (Tsai
1976; Prothero et al., 1976).

Apparent stresses for trans
4 and the I.S.C. as the source
14. As for ridge crest events,

FURTHER COMPARISONS OF S

It is of interest whether t
give any evidence for differe

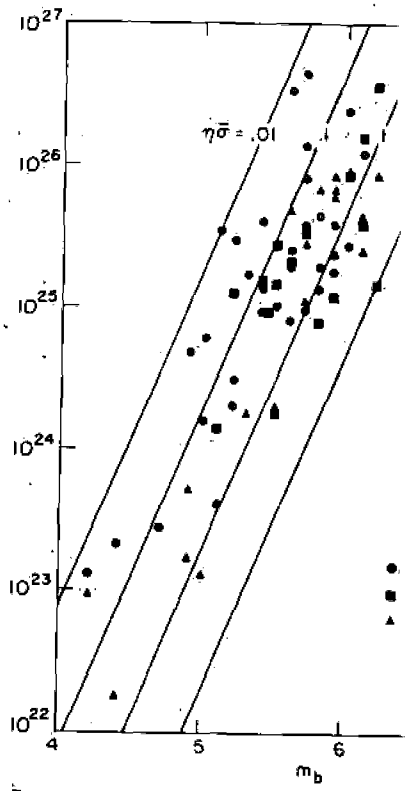

Fig. 15. Relationship between mo
transform, ridge crest and intraplate
and Solomon (1978), Reid (1976),
are from Solomon (1978). Data for
(1977) and from two earthquakes
Moments (vertical scale) are in dyne

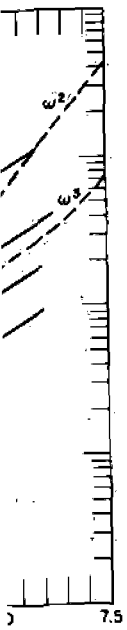

e relations based on a least-squares linear
p rate and magnitude data from about 60
sult of a different isotherm used to deter-
lid symbols in Fig. 7.

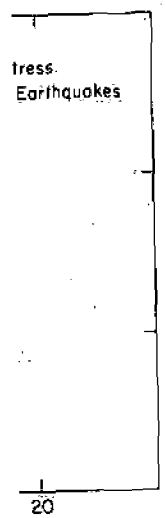

earthquakes versus local spreading rate.
1976) and Reichle et al. (1976).

degrees Centrigrade is consistent with laboratory measurements of the boundary between stick-slip and stable sliding in gabbros and peridotites at pressures appropriate to the oceanic crust and uppermost mantle (Brace and Byerlee, 1970; Stesky et al., 1974). Further, the predicted fault widths of about a kilometer for the shorter transforms and a few km for the longer transforms are broadly consistent with available data on the focal depths of transform earthquakes (Tsai, 1969; Weidner and Aki, 1973; Reichle et al., 1976; Prothero et al., 1976).

Apparent stresses for transform earthquakes, estimated using equations 3 4 and the I.S.C. as the source for m_b, are plotted versus spreading rate in Fig. 14. As for ridge crest events, no clear dependence of $\eta\bar{\sigma}$ on v is apparent.

FURTHER COMPARISONS OF STRESS STATES

It is of interest whether the available earthquake source parameter data give any evidence for differences in the state of stress between ridge axes

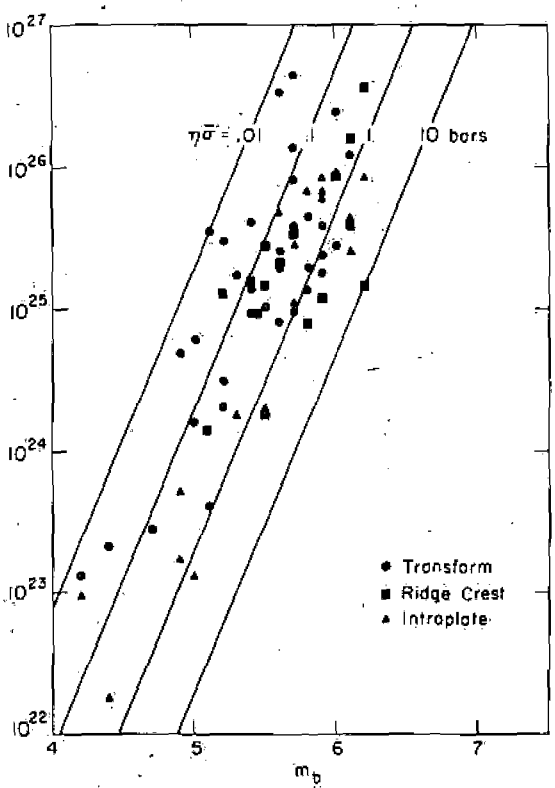

Fig. 15. Relationship between moment M_0 and body-wave magnitude m_b (I.S.C.) for transform, ridge crest and intraplate earthquakes. Data for transform events are from Burr and Solomon (1978), Reid (1976), and Reichle et al. (1976). Data for ridge crest events are from Solomon (1978). Data for intraplate events are from Richardson and Solomon (1977) and from two earthquakes on the Ninetyeast ridge by Stein and Okal (1978). Moments (vertical scale) are in dyne cm.

(rift valley normal faulting) and transforms (strike-slip faulting). We may consider either the apparent stress or the stress drop as a basis for such a comparison.

In Fig. 15 is shown a plot of M_0 versus m_b for ridge crest (including off-axis) and transform earthquakes; lines of constant $\eta\bar{\sigma}$ are indicated. Data for intraplate earthquakes (Richardson and Solomon, 1977; Stein and Okal, 1978) are also included. No pronounced difference in the distribution of apparent stresses among any of the three earthquake types is apparent. In particular, Fig. 15 strengthens the conclusion of Richardson and Solomon (1977) that intraplate earthquakes do not show systematically higher apparent stresses than plate boundary events.

A plot of seismic moment versus inferred fault length for ridge-crest and

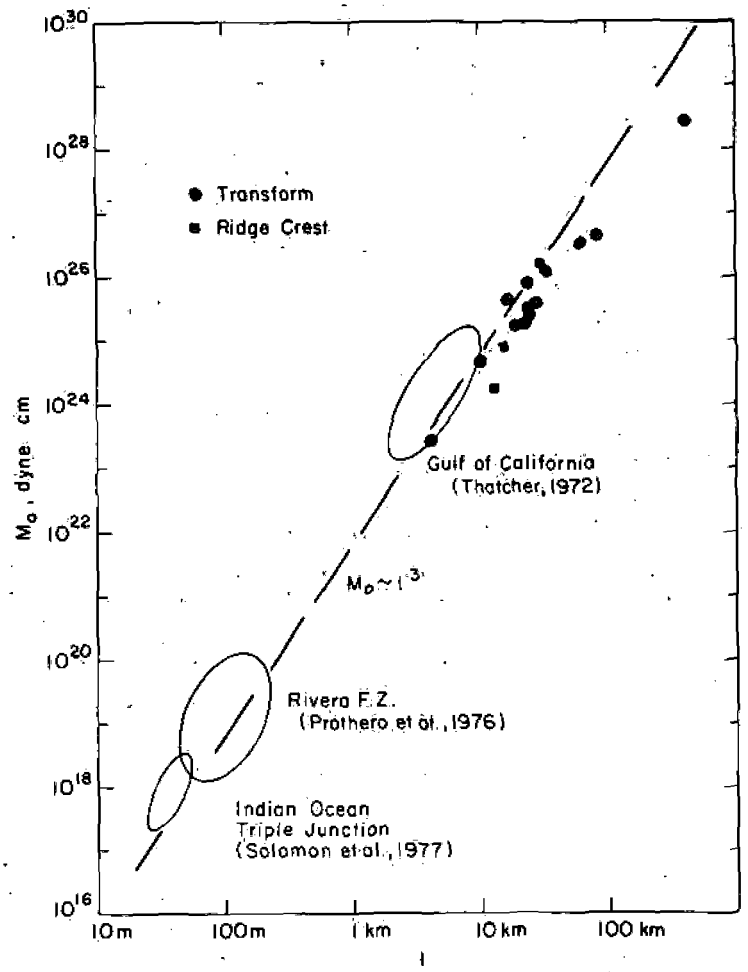

Fig. 16. Seismic moments M_0 and estimated fault lengths l for earthquakes on ridge crests and oceanic transform faults. Sources of data given in the text.

oceanic transform earthqual
ridge crest events are from Sc
aftershock distributions. Dat
from Burr and Solomon (19
Stewart (1976) for two event
frequencies for the remainde
shown, an $M = 7.9$ earthquak
Richter, 1954), for which th
length (Norton, 1976). Two
Reichle et al. (1976) and Rei
from the dimensions of the a
range of moments and fault
S wave spectra from the Marc
the Gulf of California (Thatch
microseismicity surveys durin
(Prothero et al., 1976) and c
triple junction in the centra
source theory of Madariaga (1
all corner frequencies to fault

The data in Fig. 16 are not
some of the mild departures
lar, the full suite of data is
that $M_0 \sim l^3$, or equivalently
geometrical similarity. The lir
for $l/w = 3$. (Note that dip sli
tor of ~3/4 for the same fa
events in Fig. 16 depart from
because of a lower stress drop

The main conclusion to b
ridge crest earthquakes are not
fault dimension relations or c
drops associated with divergen
quake size.

CONCLUSIONS

For both rift valleys and tr
large earthquakes support the
ronment is limited by the dep
seismic to aseismic slip.

For ridge-crest earthquakes,
mum observed moment is qua
perature limiting fault width
events are located 10–20 km
stress drops are approximately

oceanic transform earthquakes is shown in Fig. 16. Data points for large ridge crest events are from Solomon (1978); fault lengths are estimated from aftershock distributions. Data points for large transform events are mostly from Burr and Solomon (1978); fault lengths are taken from Kanamori and Stewart (1976) for two events, Udias (1971) for two events, and from corner frequencies for the remainder. One exception is the largest transform event shown, an $M = 7.9$ earthquake on the southwest Indian ridge (Gutenberg and Richter, 1954), for which the fault length was taken equal to the transform length (Norton, 1976). Two additional transform events shown are from Reichle et al. (1976) and Reid (1976); reported fault lengths were estimated from the dimensions of the aftershock zones. Shown also in Fig. 16 are the range of moments and fault lengths inferred from corner frequencies of S wave spectra from the March 1969 earthquake swarm (normal faulting) in the Gulf of California (Thatcher, 1972) and from ocean-bottom seismometer microseismicity surveys during March/April 1974 on the Rivera fracture zone (Prothero et al., 1976) and during March 1976 near the ridge—ridge—ridge triple junction in the central Indian Ocean (Solomon et al., 1977). The source theory of Madariaga (1977) for rectangular faults was used to convert all corner frequencies to fault lengths.

The data in Fig. 16 are not poorly approximated by a straight line, though some of the mild departures from a straight line fit may be real. In particular, the full suite of data is approximately consistent with the hypothesis that $M_0 \sim l^3$, or equivalently the hypothesis of constant stress drop and of geometrical similarity. The line shown in Fig. 16 amounts to $\Delta\sigma \sim 10$ bars for $l/w = 3$. (Note that dip slip events should have moments lower by a factor of $\sim 3/4$ for the same fault dimensions and stress drop.) The largest events in Fig. 16 depart from the line $M_0 \sim l^3$ by the greatest amount, either because of a lower stress drop or, more likely, a higher l/w ratio.

The main conclusion to be derived from Fig. 16 is that transform and ridge crest earthquakes are not distinguishable on the basis of moment versus fault dimension relations or on the basis of stress drop. Nor are the stress drops associated with divergent plate boundaries a strong function of earthquake size.

CONCLUSIONS

For both rift valleys and transform faults, the source parameter data for large earthquakes support the hypothesis that earthquake size in each environment is limited by the depth to an isotherm marking the transition from seismic to aseismic slip.

For ridge-crest earthquakes, the decrease with spreading rate in the maximum observed moment is quantitatively consistent with the notion of temperature limiting fault width as long as the epicenters of the largest ridge events are located 10—20 km from the rift center. Limited data suggest that stress drops are approximately constant for ridge axis events (10—20 bars) as

:orms (strike-slip faulting). We may
:he stress drop as a basis for such a

us m_b for ridge crest (including off-
f constant $\eta\bar{\sigma}$ are indicated. Data for
l Solomon, 1977; Stein and Okal,
ed difference in the distribution of
ree earthquake types is apparent. In
:lusion of Richardson and Solomon
o not show systematically higher
ents.
:rred fault length for ridge-crest and

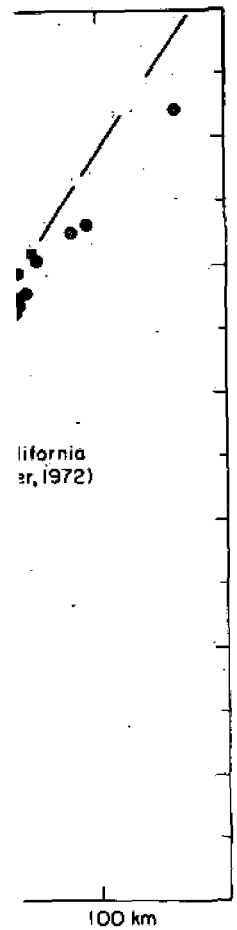

ılt lengths l for earthquakes on ridge crests
ven in the text.

a function of spreading rate. There may be a bound on fault length (20—30 km) for such earthquakes, independent of spreading rate, perhaps due to a characteristic spacing between transform faults.

For transform earthquakes, a number of empirical relations among maximum seismic moment, spreading rate, transform length, and average transform width all support the idea that temperature limits the depth of seismic failure in transform faults as well. An inversion of slip rate and magnitude data for 60 oceanic transforms provides an additional positive test of the hypothesis and gives an estimate for the nominal limiting temperature of 100°—150°C. There are many reasons why this nominal temperature must be assigned a large uncertainty, but the estimate is at least consistent with the shallow focal depths of transform earthquakes and with laboratory measurements of fault slip in rocks of compositions that may be representative of the oceanic crust and upper mantle.

Apparent stresses of transform and ridge-crest events show no obvious dependence on spreading rate and are not systematically different from each other or from apparent stresses of intraplate earthquakes. Moment versus fault length relations for transform and ridge-crest earthquakes are indistinguishable over eleven decades in moment and four decades in fault length. Thus there is no evidence that the general state of stress near spreading center boundaries varies from rift valley to transform or as a function of slip rate.

ACKNOWLEDGEMENTS

This research was supported by the Division of Earth Sciences, National Science Foundation, under NSF Grants EAR75-14812 and EAR77-69965. One of us (S.C.S.) also acknowledges the support of an Alfred P. Sloan Research Fellowship.

This paper was delivered to IASPEI/IAVCEI Symposium J3, Processes at Mid-Ocean Ridges, Durham/Great Britain in August 1977.

REFERENCES

Aki, K., 1966. Generation and propagation of G waves from the Niigata earthquake of June 16, 1964. Part 2. Estimation of earthquake moment, released energy, and stress-strain drop from the G wave spectrum. Bull. Earthquake Res. Inst., Tokyo Univ., 44: 73—88.

Aki, K., 1967. Scaling law of seismic spectrum. J. Geophys. Res., 72: 1217—1231.

Ben-Menahem, A. and Aboodi, A., 1971. Tectonic patterns in the northern Red Sea region. J. Geophys. Res., 76: 2674—2689.

Brace, W.F. and Byerlee, J.D., 1970. California earthquakes: why only shallow focus? Science, 168: 1573—1575.

Brune, J.N., 1968. Seismic moment, seismicity and rate of slip along major fault zones. J. Geophys. Res., 73: 777—784.

Burr, N.C. and Solomon, S.C., 1978. The relationship of source parameters of oceanic transform earthquakes to plate velocity and transform length. J. Geophys. Res., 83: 1193—1205.

Forsyth, D.W., 1973. Anisotropy
Mantle. Thesis, Mass. Inst. Techn
Francis, T.J.G., Porter, I.T. and Mc
tions on the Mid-Atlantic Ridge
Gutenberg, B. and Richter, C.F., 1
ena. Princeton Univ. Press, Princ
Gutenberg, B. and Richter, C.F.,
acceleration. Bull. Seismol. Soc.
Isacks, B., Oliver, J. and Sykes, L.
Geophys. Res., 73: 5855—5899.
Kanamori, H. and Stewart, G.S., 19
zone, Mid-Atlantic Ridge. Phys.
Knopoff, L., 1958. Energy release i
Madariaga, R., 1977. Implications
of stress drop from seismic obser
Norton, I.O., 1976. The present r
Planet. Sci. Lett., 33: 219—230.
Prothero, W.A., Reid, I., Reichle,
measurements on the East Pacif
214.
Reichle, M.S., Sharman, G.F. and I
Gulf of California transform fau
1623—1641.
Reid, I.D., 1976. The Rivera plate
University of California, San Die
Richardson, R.M. and Solomon, S.
earthquakes and the magnitude
115: 317—331.
Rothé, J.P., 1969. The Seismicity o
Sleep, N.H., 1975. Formation of
Res., 80: 4037—4042.
Spindel, R.C., Davis, S.B., Macdon
earthquake survey of median v
248: 577—579.
Solomon, S.C., 1973. Shear-wave
Ridge. J. Geophys. Res., 78: 604
Solomon, S.C., 1978. Sizes of ri
spreading centers. J. Geophys. R
Solomon, S.C., Mattaboni, P.J. and
Ocean triple junction. Geophys.
Stein, S. and Okal, E.A., 1978. Sei
dence for internal deformation o
Stesky, R.M., Brace, W.F., Riley, D
at high temperature and pressure
Sykes, L.R., 1967. Mechanism of e
ridges. J. Geophys. Res., 72: 213
Thatcher, W., 1972. Regional variat
California area. J. Geophys. Res.
Thatcher, W. and Brune, J.N., 197
in the Gulf of California. Geophy
Tsai, Y.B., 1969. Determination of
from Amplitude Spectra of Sur
144 pp.

Forsyth, D.W., 1973. Anisotropy and the Structural Evolution of the Oceanic Upper Mantle. Thesis, Mass. Inst. Technol., Cambridge, Mass., 254 pp.

Francis, T.J.G., Porter, I.T. and McGrath, J.R., 1977. Ocean-bottom seismograph observations on the Mid-Atlantic Ridge near lat 37°N. Geol. Soc. Am. Bull., 88: 664—677.

Gutenberg, B. and Richter, C.F., 1954. Seismicity of the Earth and Associated Phenomena. Princeton Univ. Press, Princeton, N.J., 310 pp. (2nd edition).

Gutenberg, B. and Richter, C.F., 1956. Earthquake magnitude, intensity, energy and acceleration. Bull. Seismol. Soc. Am. 46: 105—145.

Isacks, B., Oliver, J. and Sykes, L.R., 1968. Seismology and the new global tectonics. J. Geophys. Res., 73: 5855—5899.

Kanamori, H. and Stewart, G.S., 1976. Mode of the strain release along the Gibbs fracture zone, Mid-Atlantic Ridge. Phys. Earth Planet. Inter., 11: 312—332.

Knopoff, L., 1958. Energy release in earthquakes. Geophys. J. R. Astron. Soc., 1: 44—52.

Madariaga, R., 1977. Implications of stress-drop models of earthquakes for the inversion of stress drop from seismic observations. Pure Appl. Geophys., 115: 301—316.

Norton, I.O., 1976. The present relative motion between Africa and Antarctica. Earth Planet. Sci. Lett., 33: 219—230.

Prothero, W.A., Reid, I., Reichle, M.S. and Brune, J.N., 1976. Ocean bottom seismic measurements on the East Pacific Rise and Rivera fracture zone. Nature, 262: 121—214.

Reichle, M.S., Sharman, G.F. and Brune, J.N., 1976. Sonobuoy and teleseismic study of Gulf of California transform fault earthquake sequences. Bull. Seismol. Soc. Am., 66: 1623—1641.

Reid, I.D., 1976. The Rivera plate: a Study in Seismology and Plate Tectonics. Thesis, University of California, San Diego, Calif., 288 pp.

Richardson, R.M. and Solomon, S.C., 1977. Apparent stress and stress drop for intraplate earthquakes and the magnitude of tectonic stress in the plates. Pure Appl. Geophys., 115: 317—331.

Rothé, J.P., 1969. The Seismicity of the Earth. UNESCO, 336 pp.

Sleep, N.H., 1975. Formation of oceanic crust: some thermal constraints. J. Geophys. Res., 80: 4037—4042.

Spindel, R.C., Davis, S.B., Macdonald, K.C., Porter, R.P. and Phillips, J.D., 1974. Microearthquake survey of median valley of the Mid-Atlantic Ridge at 36°30'N. Nature, 248: 577—579.

Solomon, S.C., 1973. Shear-wave attenuation and melting beneath the Mid-Atlantic Ridge. J. Geophys. Res., 78: 6044—6059.

Solomon, S.C., 1978. Sizes of ridge crest earthquakes and lithospheric thickness at spreading centers. J. Geophys. Res., submitted.

Solomon, S.C., Mattaboni, P.J. and Hester, R.L., 1977. Microseismicity near the Indian Ocean triple junction. Geophys. Res. Lett., 4: 597—600.

Stein, S. and Okal, E.A., 1978. Seismicity and tectonics of the Ninetyeast ridge area: evidence for internal deformation of the Indian plate. J. Geophys. Res., 83: 2233—2245.

Stesky, R.M., Brace, W.F., Riley, D.K. and Robin, P.-Y.F., 1974. Friction in faulted rock at high temperature and pressure. Tectonophysics, 23: 177—203.

Sykes, L.R., 1967. Mechanism of earthquakes and nature of faulting on the mid-oceanic ridges. J. Geophys. Res., 72: 2131—2153.

Thatcher, W., 1972. Regional variations of seismic source parameters in the northern Baja California area. J. Geophys. Res., 77: 1549—1565.

Thatcher, W. and Brune, J.N., 1971. Seismic study of an oceanic ridge earthquake swarm in the Gulf of California. Geophys. J. R. Astron. Soc., 22: 473—489.

Tsai, Y.B., 1969. Determination of Focal Depths of Earthquakes in Mid-oceanic Ridges from Amplitude Spectra of Surface Waves. Thesis, Mass. Inst. Technol., Cambridge, 144 pp.

Udias, A., 1971. Source parameters of earthquakes from spectra of Rayleigh waves. Geophys. J. R. Astron. Soc., 22: 353–376.
Weidner, D.J. and Aki, K., 1973. Focal depth and mechanism of mid-ocean ridge earthquakes. J. Geophys. Res., 78: 1818–1831.
Wyss, M., 1970. Apparent stresses of earthquakes on ridges compared to apparent stresses of earthquakes in trenches. Geophys. J. R. Astron. Soc., 19: 479–484.

Tectonophysics, 55 (1979) 12

SEISMICITY AND EART MID-ATLANTIC PLATE AZORES

PÁLL EINARSSON

Science Institute, University o,

(Submitted December 19, 197

ABSTRACT

Einarsson, P., 1979. Seismicity plate boundary between Ice at Mid-Ocean Ridges. Tecto

The seismicity along the mi eral way consistent with the c seismicity of Iceland show, ho spreading ridges and transforn sula, for example, the plate bc acteristics. The Tjörnes fractur at least two parallel strike-slip quakes within the volcanic rift canoes and are not directly rel and the southern part of the F and of a spreading ridge, respe other hand, appears to be spre focal mechanism solutions of t stantial component of thrust f mantle plume activity under Ice

INTRODUCTION

Earthquake focal mech an important role in the c plate boundaries and fro infer the relative plate mo of view, it is unfortunate hidden under the ocean an

In the study of the seis usually limited by the larg quakes and the nearest se

Research for a Geothermal Field in a Zone of Oceanic Spreading: Example of the Asal Rift (French territory of the Afars and the Issas, Afar depression, East Africa)

LAURENT STIELTJES

Bureau de Recherches Géologiques et Minières, Service Géologique National, Département Géothermie, B. P. 6009, 45018, Orléans Cedex, France

ABSTRACT

Following a Bureau de Recherches Géologiques et Minières (BRGM) geothermal exploration in the Asal rift between 1970 and 1973, some borehole sites for steam research were planned on the southern margin of the rift. Attention was drawn to this zone by the presence of hot springs on the borders of the graben as well as by the rift structure itself.

A detailed petrological analysis of the rift lavas revealed a transitional volcanism which very closely resembled that which is found on oceanic ridges. The axial valley is affected by numerous open fissures, some of which are magma-productive. Its morphology and size are quite comparable to those of the mid-oceanic ridges. The present tectonic extension of the rift has been estimated at between 2 and 4 cm/year. Seismic activity is marked.

The average flux on the ridges is about three times higher than the flux in the oceanic basins. The gradient measured at Asal reaches 45°/100 m on the flanks of the tectonic swelling, whose diameter is about 10 km. This swelling is due to a magmatic intumescence probably connected with the upper mantle. The intumescence is the site of a differentiation phenomenon, strictly controlled by a fractioned crystallization process. This swelling affects all the central part of the rift.

The accretion band, which is 4 to 5 km wide, is hardly likely to favor the trapping of a geothermal field (marked dyke injection, fissuration, scarcity of thermal indications). The boreholes were therefore situated on the borders of this band where, in contrast, the stratigraphic series is normal, the tectonization is still intense, and superficial impermeability and hydrothermal indications exist along faults.

INTRODUCTION

Since 1970, the BRGM has undertaken geothermal prospecting of the French territory of Afars and Issas (TFAI), a small territory of 23 000 km^2 situated in the Afar depression (East Africa). The capital, Djibouti (80 000 inhabitants), is a port situated at the outlet of the Red Sea into the Gulf of Aden (Fig. 1). The other population centers are villages scattered in the bush, the largest of which are Dikhil and Ali Sabieh in the south and Tadjoura and Obock in the north.

The aim of this geothermic prospecting was initially to provide for an electrical power plant of 4 MW supplying the town of Djibouti. The TFAI is divided by the Gulf of Tadjoura and its western extension, the Ghoubbat al Kharab, which penetrate like a wedge into the TFAI, cutting into its center and thus determining a northern region and a southern region. The morphology of the TFAI is very irregular, and this marine indentation constitutes an important axis penetrating the heart of the territory.

In the first instance the prospecting concerned three rift areas in the south of the TFAI: the rifts of Gobaad, Hanleh, and Asal are recent subsidence structures which are seismically active and marked by numerous present-day and extinct hydrothermal occurrences and on faults and generally by volcanic activity of varying importance. Data on the geology, the geochemistry of the waters, gradient measurements, and geophysical soundings led us to concentrate our efforts on the Asal region, which has the most marked tectano-volcanic activity and where the geochemical indications concerning the springs were the most promising. Moreover, the fact that it is nearer to Djibouti than the other rifts would permit the construction of an electric power line over a shorter distance. It is easily accessible from the sea. The proximity of a brine deposit at Lake Asal (unexploited) might allow further development at a later date. Finally its central geographical position and its distance from the political frontiers confirm the interest of this region.

The prospecting work has been intensified over the past three years in the Asal zone, first at the instance of the BRGM and then with the impetus of the Ministry of Overseas Departments-Overseas Territories and the Ministry of Industry, in relation with the territorial authorities and the Electricité de Djibouti (EDD). The reconnaissance boreholes were drilled in spring 1975.

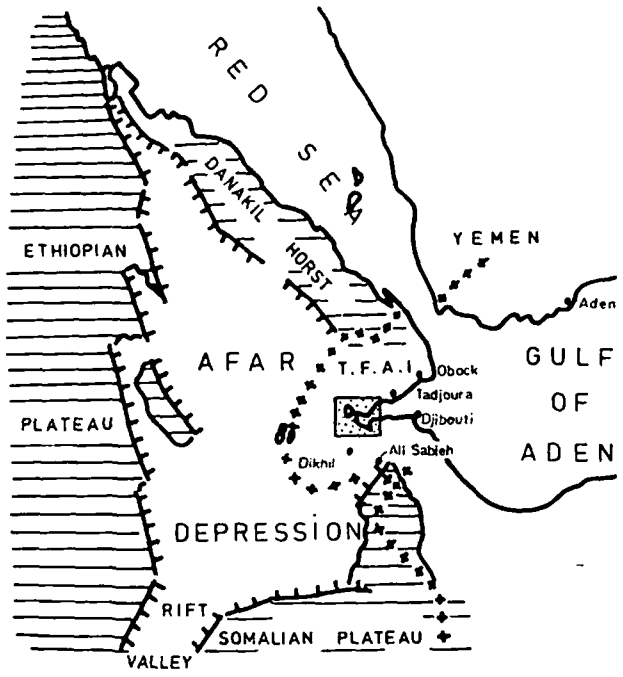

Figure 1. Location of TFAI and Asal rift in the Afar depression (Asal rift inserted).

In this report we set out the principal arguments which led to the establishment of the conditions of a geothermal field in this region and to the choice of the zone for the siting of the reconnaissance boreholes.

GEOLOGICAL AND GEOGRAPHICAL SETTING

The Afar depression, which is also called the Danakil depression, is triangular in form and extended over nearly 100 000 km² between the 10 and 15°N. parallels. It covers part of Ethiopia, the TFAI, and part of the Somalian republic. Its boundaries are constituted, to the east, by the Danakil horst and the coasts of the Red Sea and the Gulf of Adan; to the west, by the escarpment of the Ethiopian plateau, and to the south, by the border of the Somalian plateau, before opening into the great African rift valley (Fig. 1).

It is a low region whose average altitude is hardly more than a few hundred metres while the altitude of the neighboring Ethiopian and Somalian plateaus ranges from 2000 to 3000 m. Within the depression, several zones are situated below sea level, for instance, Asal (−155 m) and Dallol (−120 m).

The Afar depression is situated at the junction of three major tectonic structures of East Africa: the Red Sea, the Gulf of Aden, and the great African rift system. For a long time it was considered to be the transition zone between the African rift and the Red Sea Trough (Gregory, 1921; Mohr, 1967). However, it is now generally interpreted as part of the Red Sea-Gulf of Aden ridge (Barberi, et al., 1972). The transition between the Red Sea ridge and that of the Gulf of Aden is made across Afar by a series of active "rifts-in-rift" arranged in an *en echelon* structure.

The floor of the Afar region is largely covered with piles of Pliocene fissured basaltic lavas, while on its borders are found earlier basaltic or rhyolitic formations (Mio-Pliocene), (Varet, 1973). Afar is characterized by active distension tectonics emphasized by numerous fault escarpments, open fissures, and marked seismicity, as well as by a succession of recent volcanic chains oriented north-northwest to northwest (Barberi, et al., 1972). The Asal rift is the last of these chains.

GEOLOGICAL SETTING OF THE ASAL RIFT

The Asal rift opened during the Pleistocene within a stratified basaltic series with Mio-Pliocene rhyolitic intercalations characterizing the borders of the Afar depression (Stieltjes, 1973a). This ancient series is divided into a succession of monoclinal tectonic panels which are often strongly tilted (up to 30 degrees) towards the southwest (Fig. 2).

Tectonics

This typically dissymmetric fault trough is aligned northwest-southeast and is formed of successive steps descending gradually by normal faults (Stieltjes, 1973a). The rift is characterized by active distension tectonics—normal faults on the borders of the rift whose offset varies from several metres to several hundred metres; and open fissures in the axial band 3 to 8 km wide (Fig. 3). Some of these fissures are magma-producing. Important seismicity and active volcanism are associated with these tectonics. There are many indications of thermalism (fumaroles, hot springs, spring concretions; Stieltjes, 1973a).

The speed at which the two sides of the rift are separating has been estimated at 1.5 to 2 cm/year (Delibrias, Marinelli, and Stieltjes, 1974), while the amplitude of the vertical movements of the faults (normal within the axial valley and inverse on the borders) has been estimated at 1 to 2 mm/year (Harrison, Bonatti, and Stieltjes, 1974).

The piles of recent basalts in the central part of the rift are convex, forming a dome with a diameter of approximately

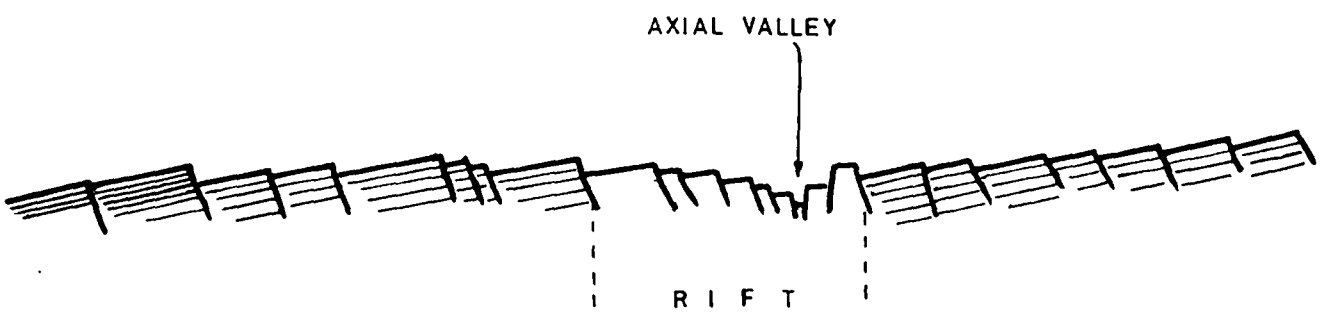

Figure 2. Recent opening of the Asal rift in monoclinal trap series.

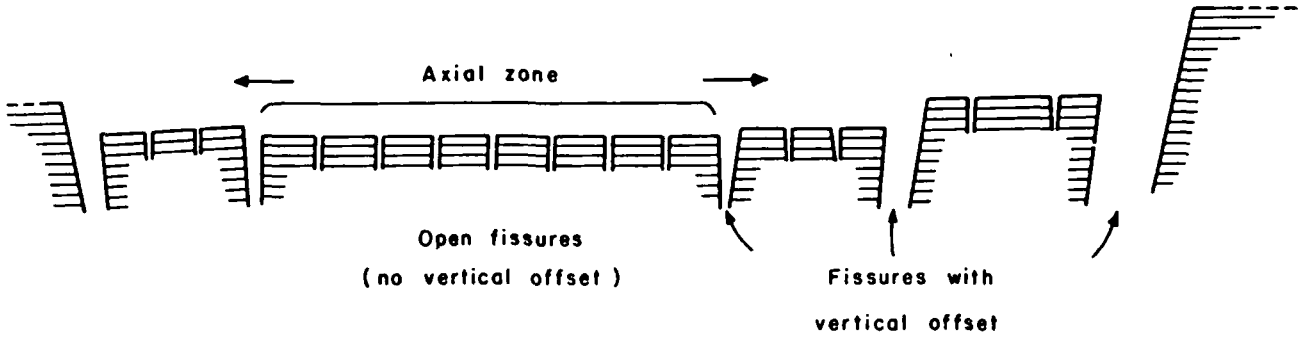

Figure 3. Open fissures and normal faults in the axial valley.

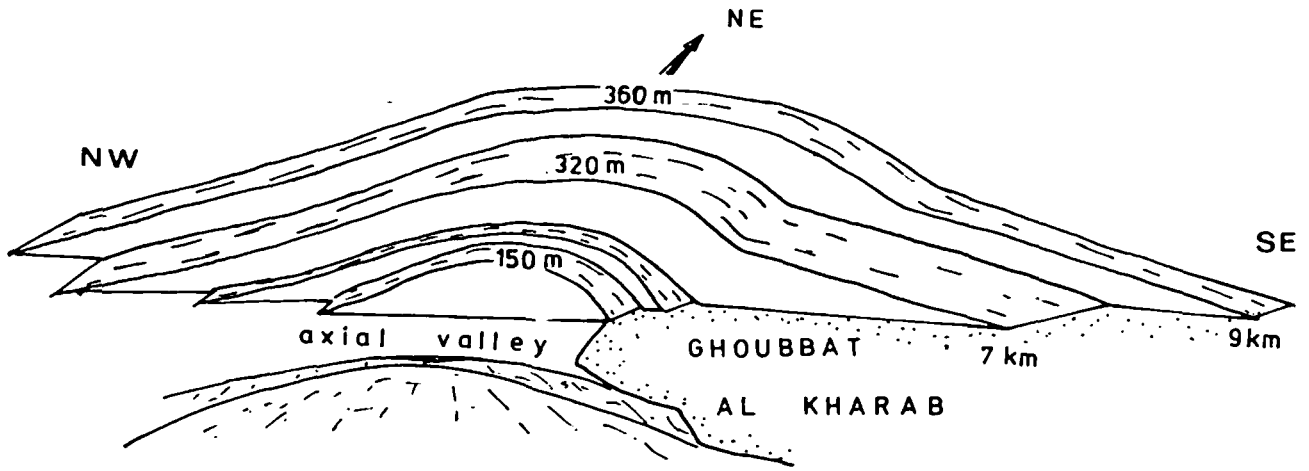

Figure 4. Scheme of the swelling in the axial part of the rift.

20 km, swelling the whole of the axial zone by at least 300 m (Fig. 4). The origin of this swelling could be linked with a magmatic intrusion of the diapiric type, determining an important thermic anomaly centered around the axis of the rift (Stieltjes, 1970, 1973a).

Gradient measurements made in this region have given values up to 45°C/100 m (Dague, et al., 1973).

Volcanology

The products of the volcanic activity associated with the rift, mainly basaltic, are spread out between the Gulf of Ghoubbat-al-Kharab (southeast) and Lake Asal (northwest) over an area 14 km long and about 10 km wide. The visible covered surface is approximately 110 km^2. The volume of these basaltic lavas has been estimated at 13.8 km^3 (Stieltjes, 1973b).

Two types of products from basaltic formations are associated with respective parts of the rift (Fig. 5):

1. On the tectonic compartments of the border and the floor of the rift, basaltic products of subaquatic origin crop out: hyaloclastic massifs at the bottom (palagonite tuffs), which can be spread over a radius of about 10 km around the massif, overlain by big piles of fissural subaqueous basaltic lavas characterized by their "pavement" structure (Tazieff, 1969), the absence of scoria, and their frequently mammillated surface.
2. In the axial valley, the subaqueous products are overlain by present-day subaerial basalts, fissural flows, eruptive bodies or scoria cones situated along open fissures or faults, and lava lakes (Stieltjes, 1973b). Some of these flows have already been cut by fissures (gja) which are open over lengths of several hundred metres or kilometres under the effects of the distension tectonics (Fig. 5).

Thus, a progressive emersion of the rift can be noted under the combined effects of the general upheaval of Afar over the last 200 000 years (Faure, Hoang, and Lalou, 1973; CNRS Afar team, 1973) and the rapid local up-arcing (about 1.5 cm/year) over the last 30 000 years (Stieltjes, 1973a).

Petrology

The stratified basaltic series earlier than the rift are alkaline in nature.

Definition and nature of the volcanism. The volcanic rocks belonging to the Asal rift are distinguished from the earlier stratified series by their nature and their chemical and mineralogical evolution. They constitute an incomplete differentiation series, going from olivine-rich to ferro-basaltic. All the intermediary compositions between these two extremes exist, and a remarkably regular decrease of the percentage volume of the different constituents during the differentiation may be noted (Fig. 6).

This differentiation from an initial liquid basalt is controlled by a fractioned crystallization process (Stieltjes,

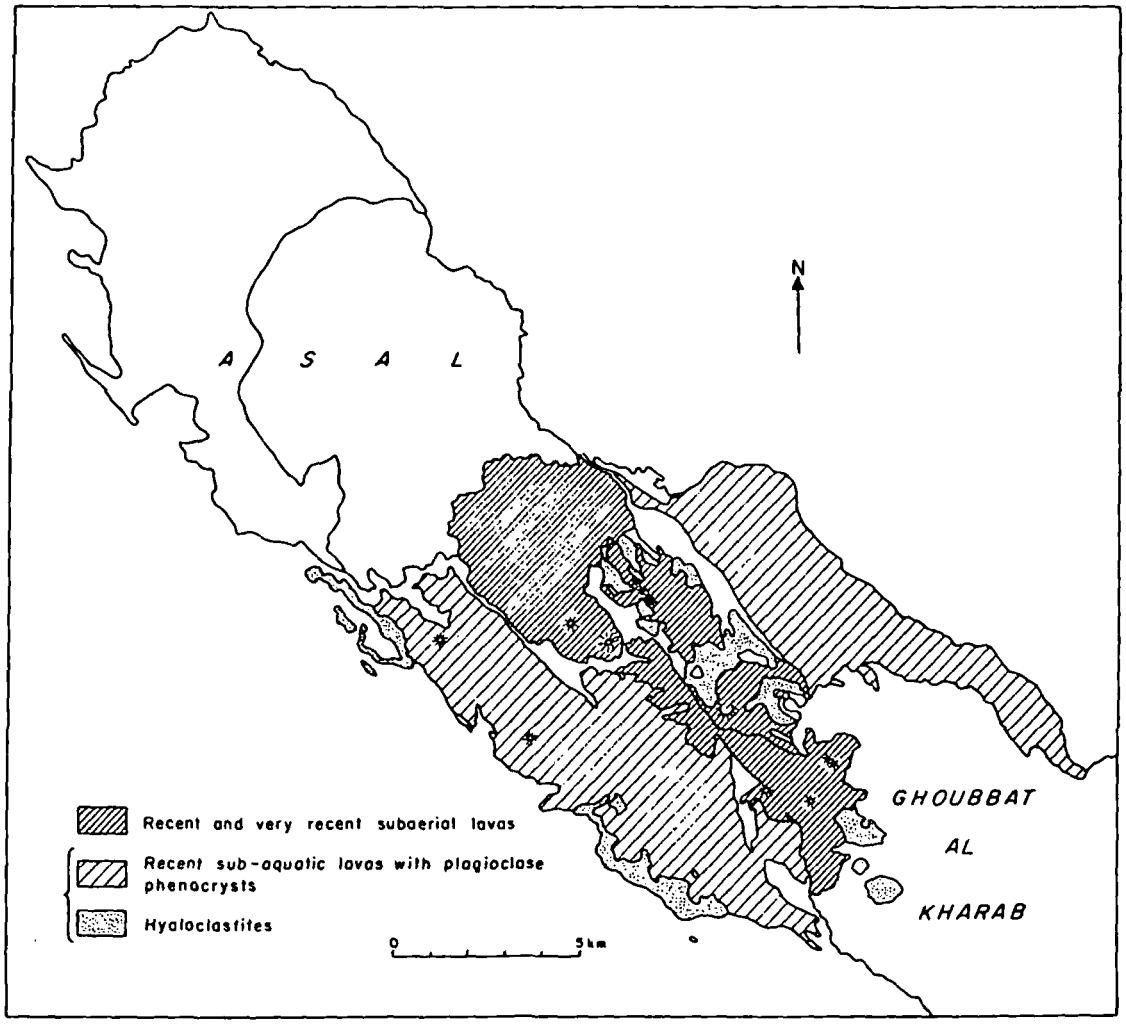

Figure 5. Repartition of subaqueous and subaerial volcanism in the Asal rift.

1973b): from the first stages of crystallization the separation of the olivines and the calcic plagioclases from the magmatic liquid causes the liquid to become poorer in Ca and Mg while it becomes richer in Fe. The enrichment in Fe of the liquid is greatly superior to that of the alkaline series and a little less than that of the tholeiitic series (Figs. 6 and 7).

The preparation of alkalines is low ($2\% < Na_2O < 5\%$ and $K_2O \leq 1\%$) and the relation $K:K + Na < 0.2$ is very low.

The mineralogical and petrochemical characteristics of this series reveal its intermediary nature between the alkaline and the tholeiitic series. The mineralogy is that of a typical alkaline series, while the normative composition is similar to that of olivine-tholeiites and even of tholeiites (Stieltjes, 1973b). This series can be considered as transitional between the alkaline series and the tholeiitic series (Fig. 7) comparable to that defined in the volcanic chains of northern Afar (Barberi and Varet, 1970).

Plagioclase "foam". Both the subaquatic (hyaloclastites, pavement lavas and the subaerial (fissural flows, scoria cones) basaltic lavas of the rift are characterized by their extremely abundant phenocrystals of calcic plagioclases ($^{An}60$ to $^{An}95$) together with the rarer olivines and pyroxenes of varying sizes from a few millimetres to several centimetres. These crystals are generally associated with numerous gas bubbles. Only a few of the subaerial flows (the most recent ones of the axial valley) are aphyric (no phenocrysts). It would seem as if all the mineral phases (olivine, plagioclase, pyroxene) separated from the initial magmatic liquid by fractioned crystallization, and were accumulated by flotation at the top of the magmatic reservoir, with gas bubbles, forming a "crystal foam." As the lava rises in the fissures, it carries with it a varying proportion of the plagioclases ($d = 2.73$) which, being lighter than the olivines and pyroxenes ($d = 3.33$), accumulate at the top of the pocket. The olivines and pyroxenes are only found in the last porphyritic flows just before the shrinking of the "foam" reservoir and the passage of an aphyric magma.

This "plagioclase foam" facies is very important for the qualitative evaluation of the local heat supply under the rift. This facies is discussed in greater detail later in this report in the paragraph dealing with the origin of the convexity of the rift and the conditions in which a local thermic flux was established.

Tectono-Volcanic Evolution

The tectonic and volcanic structures of the rift are progressively more recent from the margins towards the axial valley. The volcanic and petrological evolutions are closely

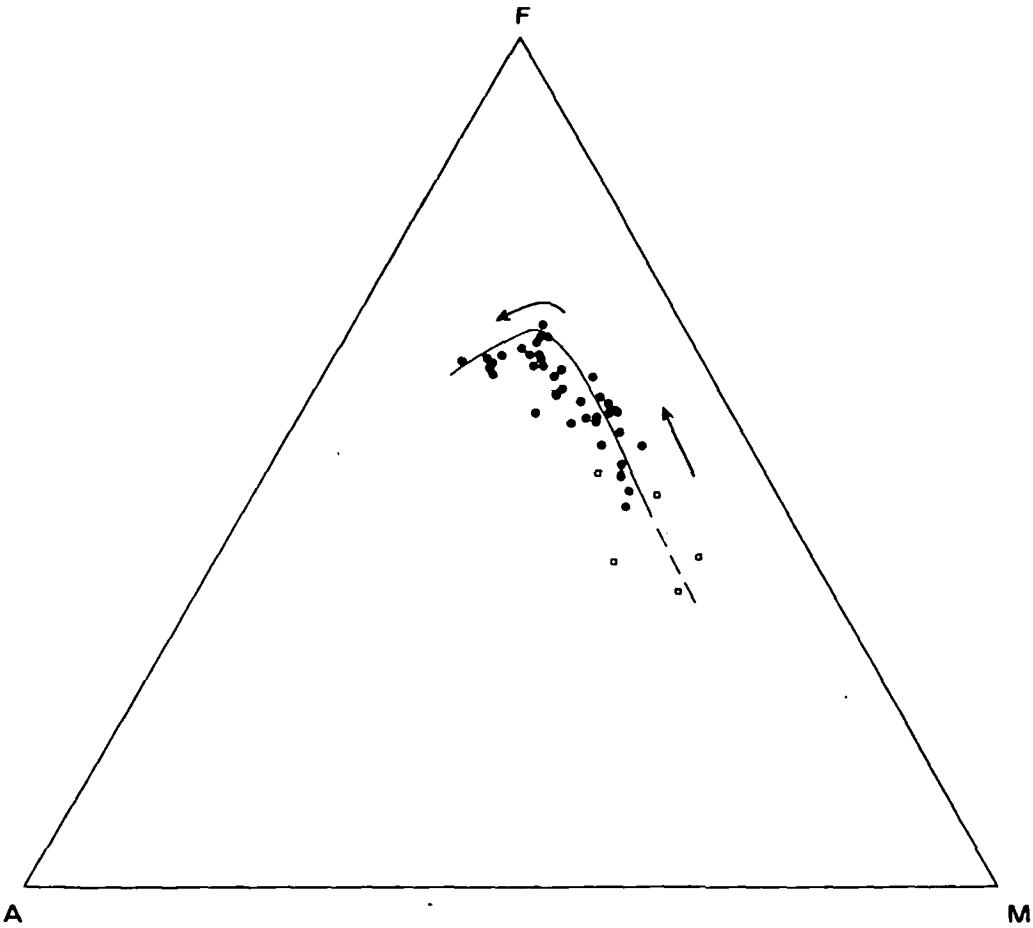

Figure 6. AFM diagram for volcanic rocks from the rift. Open squares represent total rock with plagioclase megacrysts. Filled circles represent magmatic liquids. Alkaline and magnesium components gradually decrease up to the ferro-basaltic stage. The differentiation process is controlled by crystal fractionation.

connected with the tectonic fracturation, which began as a continental rift with normal faults and a slight separation owing to the limited stretching, but which is now developing under the influence of the increasing injection of dykes in the axial zone as the system evolves (Stieltjes, 1974).

Thus, from the tectonic point of view, the normal faults of the rift borders have large scree slopes and consolidated smooth fault planes, while the faults of the axial valley have fresh, irregular, and unstable surfaces and limited scree slopes. The open fissures are situated in the axial valley which represents the most active zone at present.

From the volcanological point of view, the morphology of the flows and the eruptive bodies is increasingly well preserved towards the center of the rift. The volcanic products of the margins are typically subaquatic (hyaloclastites, pavement lavas) and affected by the normal tectonics of the rift. The volcanic products of the axial zone are subaerial, more recent, and only slightly affected by fracturation by normal faults. They are, however, often emitted and recut by open fissures.

From the petrological point of view, the basaltic series earlier than the rift are of an alkaline nature while the volcanism of the rift is of transitional nature. The most evolved differentiation products (ferro-basalts) are situated uniquely in the axial valley (aerial flows). They are sometimes very poor or lacking in phenocrysts of the plagioclases.

It would seem then that the tectonic evolution determines the volcanic and petrological activity, which evolves from the borders of the rift towards the axial valley where the present tectono-volcanic activity is essentially concentrated. This is evidenced by open fissures which may or may not generate magma, and the raising of a dome in the central zone of the rift.

Using these first data as a base we may consider and discuss the possibilities of the existence of exploitable geothermal fields.

Assessment

The size of the axial valley of the Asal rift is quite comparable to that of other known mid-oceanic ridges, such as the Gorda Ridge or the Mid-Atlantic Ridge (Fig. 8). Moreover, this rift is characterized by active distension tectonics, important apparent seismicity, active volcanism whose tholeiitic character is already marked, an important heat flow, and a thinning down of the continental crust together with the presence of an abnormal mantle (Lepine, Rwegg, and Steinmetz, 1972).

The Asal rift is situated in the western extension of the ridge of the Gulf of Tadjourah (which represents the western end of the Carlsberg Ridge). It presents a great number of analogies with the accretion zones of the mid-oceanic ridges and can actually be considered as the first emerged element of the "rifts-in-rift" formation of the Afar depres-

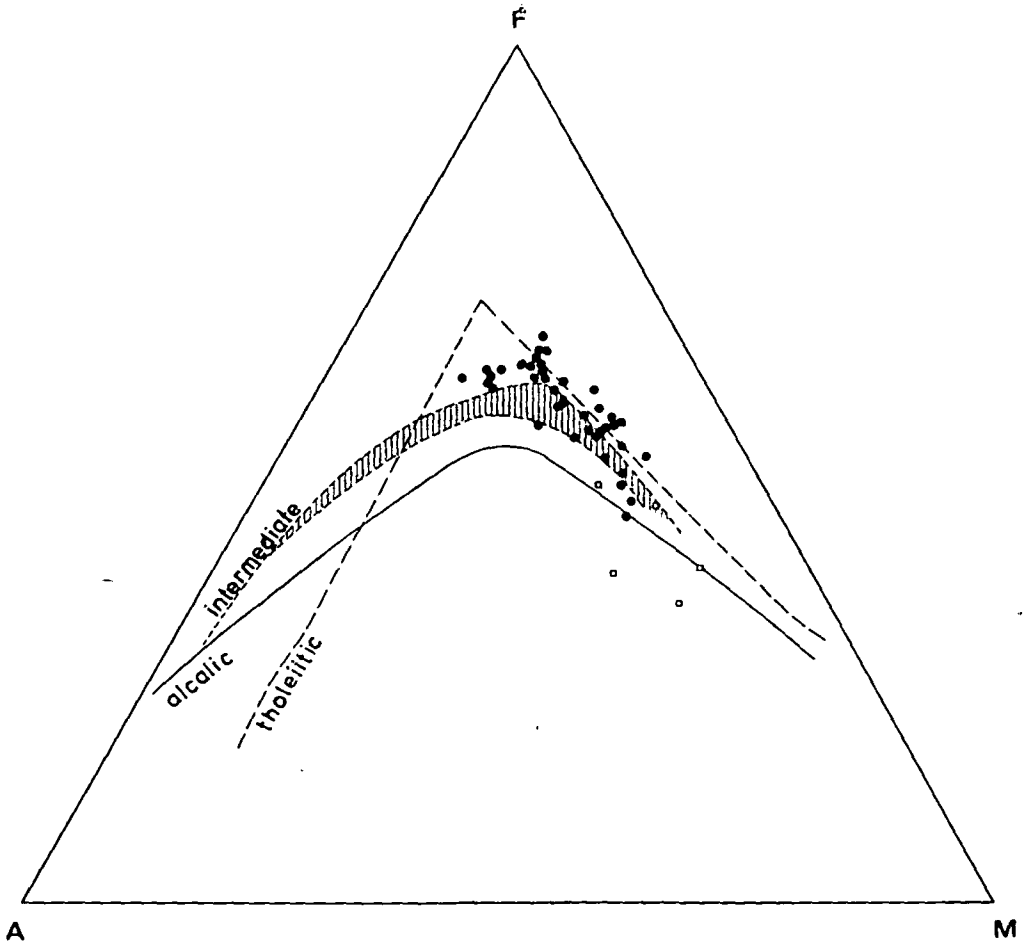

Figure 7. Comparison of Asal magmatic intermediate series with alkalic and tholeiitic series.

sion constituting the transition between the Carlsberg Ridge and that of the Red Sea (Barberi et al., 1972).

REGIONAL HEAT FLUX

Theoretical Considerations

The measurements of thermal flux taken since 1952 in the oceanic regions have shown that the mean flux on the ridges is high. The values obtained in the Gulf of Aden (3.9 Mcal/cm^2/sec) and in the Red Sea (3.4 Mcal/cm^2/sec) correspond to a very high flux compared with the mean values for the oceanic basins (1.28 Mcal/cm^2/sec).

The now-classic diagram of the distribution of flux values on a ridge compared with the structure of the crust (made by Menard in 1960), shows a correspondence between the crest of the ridge, the presence of an abnormal mantle, and exceptionally high heat flow values (Fig. 9).

MacKenzie in 1967 correlated these heat flow data with gravity data, and attributed this high heat flow to hot basic masses ascending from the upper mantle and cooling with time. As the two plates continue to move away, the parts distant from the ridge will progressively attain a normal heat flow value; then the axial part will always be hot because of the permanent basic magma supply. These accepted conclusions have been proposed for the Red Sea by Girdler in 1970, who nevertheless mentions the existence of remarkable anomalies at a certain distance from the axis of the ridge.

In fact the reality seems to be much more complex. The distribution of thermal flux values on a ridge according to the distance to its crest shows the presence of high and low values side by side. The highest values tend to be grouped over 150 km on each side of the crest (Fig. 10). It would seem that the high flux values correspond to the crest, while the low values correspond to transform faults. We may also note that the variation in the crust thickness induces different flux values on either side of the ridge.

Generally speaking, the Asal rift, which can be considered as an accretion zone evolving toward the ridge stage (Stieltjes, 1973b), should be the site of high thermal flux. A more accurate positioning was attempted during the geothermal prospection of this region.

The excess of heat in the axial regions of ridges causes a thermal dilation which could be responsible for the upheaval of these ridges and for the presence of light compensating masses beneath the crest (revealed by measurements of gravity). In fact, this thermal dilation seems to be insufficient to justify on its own the upheaval of the ridges. Phase changes could intervene in the axial zone; the most probable of these would be that of the partial fusion of materials.

In the Asal rift, the swelling of the central zone is the outstanding fact of this type of movement. The discussion

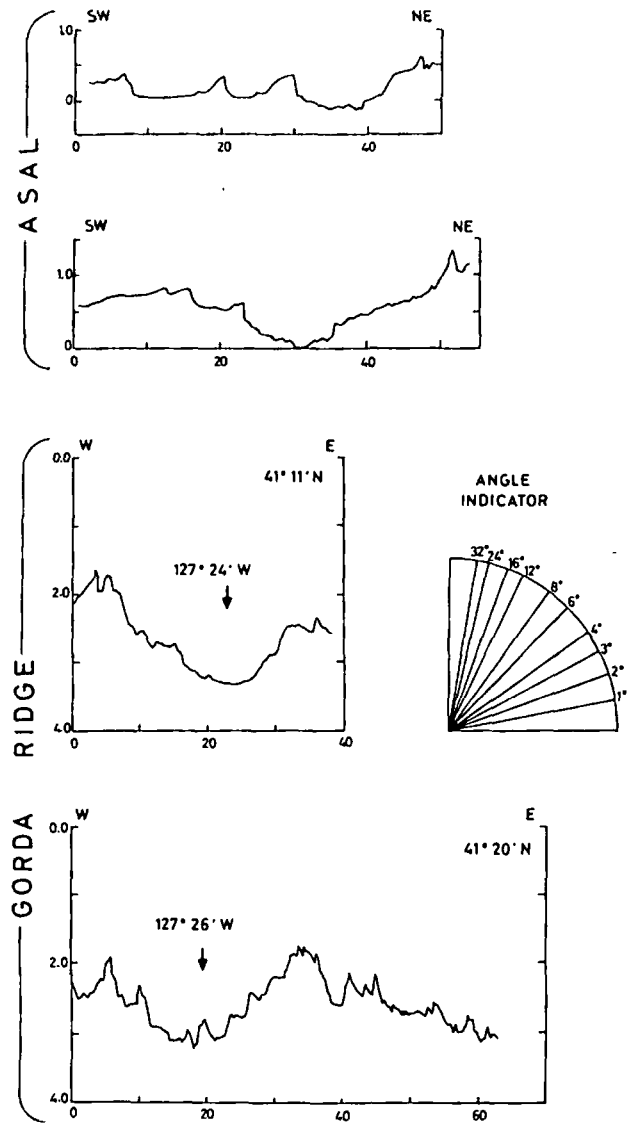

Figure 8. Topographic comparison between Gorda Ridge and Asal rift (after Harrison, Bonatti and Stieltjes, 1974). The extensions and the shapes of the axial valleys are similar between these two rifts. Asal may be assimilated to a mid-oceanic ridge.

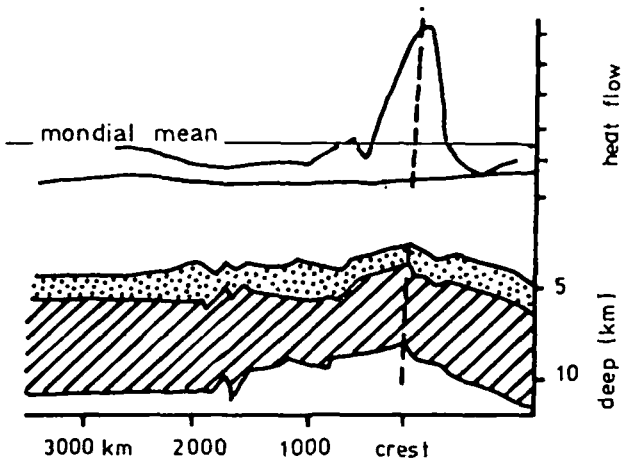

Figure 9. Comparison of the crust structure (low) and heat flow profile (high) in the East Pacific rise (after Menard in 1960).

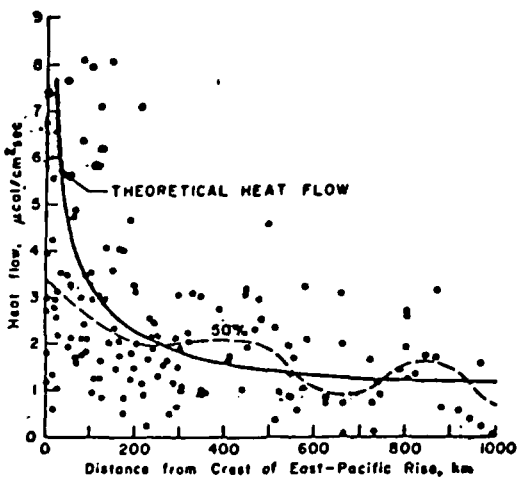

Figure 10. Heat flow as a function of distance from the East Pacific Ridge crest (after Lee and Uyeda, 1965).

below brings out the thermal implications of this local upheaval.

The Upheaval of the Central Zone

In the geological description of Asal, we have seen that the rift structure was affected by a doming of more than 300 m in height over a radius of about 10 km. We have also seen that the associated volcanism (13 km^3) was characterized by the presence of a remarkable quantity of large phenocrysts of plagioclase. In our opinion, these two phenomena are genetically linked and indicate a localized thermal anomaly.

1. The automorphic crystals of the calcic plagioclases (labradorite and bytownite) can attain dimensions of 4 to 5 cm. They are slightly or not at all zoned. Where the zoning exists, it only affects a thin rim on the border of the mineral. The crystallization must therefore have taken place in chemical balance with a magmatic liquid having a stable composition. Besides this, the quantity of plagioclase crystals should be negligible compared to the mass of magmatic liquid from which they split off. Finally, the massive crystallization of the plagioclases supposes their separation in the liquid before the pyroxenes; the magma must therefore be poor in water.

The model of the plagioclase crystallization is not the usual type. The rise of very fluid magmas (basalts) takes place along a system of very narrow fissures, that is, in a system causing very rapid heat loss, if only because of the small volumes of matter rising. We must therefore envisage the rise of an enormous quantity of magma whose high heat flow values can compensate almost entirely for the thermal dispersion of the magma during the crystallization.

The swelling of the central part of the rift cannot be due to an intrusion of the laccolith type in this case, since the rate of thermal dispersion is too high in such intrusions. We must envisage an intrusion of the diapiric type which

provides an abnormal heat supply to compensate for the normal thermal dispersion of the magma during its crystallization.

2. The transitional type of volcanism has a marked tholeiitic character. The fusion rate in the upper mantle which produced this magma must be slightly less than that which produced the tholeiites (30% approximately), but far above that which produced the alkaline basalts (5% approximately). The expansion rate of the rift (1.5 to 2 cm/year), which is comparable to that of the Mid-Atlantic Ridge, also supports this idea of a regional heat anomaly.

3. The differentiation phenomenon observed for the lavas of the rift in connection with the evolution of the structure of the rift presupposes a fractional crystallization in a shallow magmatic chamber. The rapid emission of a large quantity of magma must have emptied part of the chamber and created a certain settling or even subsidence structures. The absence of faults of this type in the raised zone indicates that this diapiric pocket is directly resupplied (by the upper mantle?), which would ensure an important and continuous heat supply.

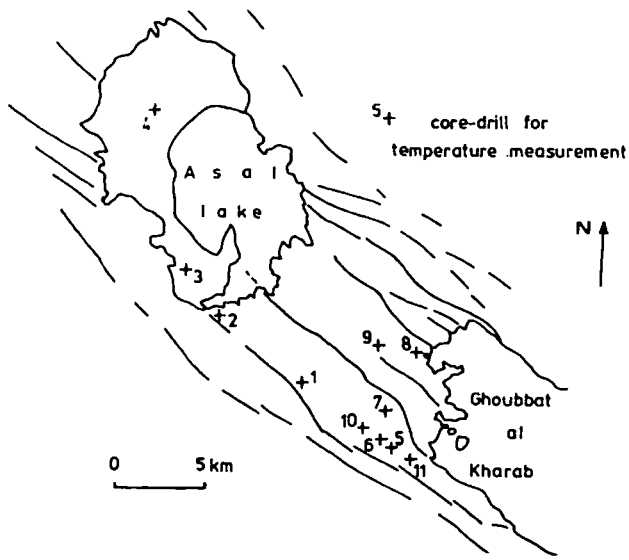

Figure 11. Positions of the heat flow measurement core drills during the BRGM prospecting effort.

Table 1. Temperature and temperature-gradient profile.

Borehole	Depth (m)	Maximum temperature (°C)	Mean gradient (°C/10 m)
1	49	64.8	+5.9
2	80	48.0	+0.2
3	78	34.6	+0.1
4	76	32.8	—
5	63	63.0	+3.1
6	90	75.0	+4.5
7	44	33.5	+1.8
8	50	29.1	−0.8
9	79	34.6	+0.15
10	177	100.5	+2.9
11	50	40.5	+0.75

Flux Measurements in the Rift

The BRGM team has taken flux measurements transversely to the axis of a rift during their 1972–73 operations. Altogether 862 m were drilled, divided between 17 boreholes with depths varying from 50 to 180 m. For reasons of accessibility and because of dissymmetric structure, only the tectonic compartments from the southern border up to the axial valley of the rift were prospected (Fig. 11).

A profile across the salt plain was attempted. Because the salt was not massive but subjected to horizontal brine circulations, the measuring conditions were not valid. The profile was eventually taken on the dome separating Lake Asal from Ghoubbat-al-Kharab (boreholes 5, 6, 7, 8, 9). It was completed by a longitudinal northwest-southeast profile on the southern panel of the rift (1, 10, 5, 6). The results obtained are given in Table 1 (from Dague et al., 1973).

In the axial zone of the rift, major sea water circulations along the faulted and fissured zones disturb the superficial thermic regime. Outside this axial zone, however, and in particular in the southern tectonic compartment, the measurement conditions were favorable and very high gradient values were obtained (2.9 to 5.9°C/10 m). In this southern region, the gradient values seem to increase from the southeast toward the northwest. However, the calculated correction of the influence of the topography shows that the isotherms deepen progressively toward the northwest (Fig. 12).

Depth measurements were taken, in particular on the

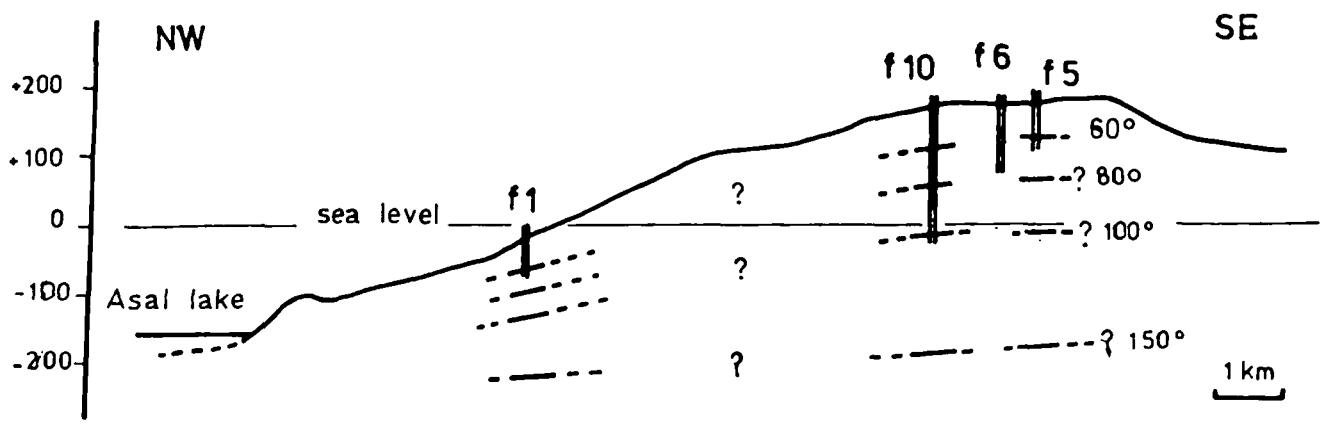

Figure 12. Measured and extrapolated temperatures in the core drills Nos. 1, 10, 6, 5 (after Dague et al., 1973).

150°C isotherm (as this corresponds to the minimum temperature for the circulation of hot waters at depth), according to the estimates of the geochemical studies conducted on the hot springs of the region.

LOCAL GEOTHERMAL CONDITIONS

Indications

The purely geological indications have been set out in detail above: active rift structure, upthrust of the central part, and active volcanism with a marked tholeiitic character.

The hydrothermal and fumarolic activity is developed throughout the rift; it is connected with the tectonic fracturation. Hot and salt springs emerge on the periphery and beneath Lake Asal and its salt plain. Submarine springs have also been detected in the Ghoubbat-al-Kharab (Fig. 13). Their temperature varies from 36 to 83°C. The generally low discharge (a few liters per second) sometimes reaches 100 l/sec for one of them.

At the level of the axial valley of the rift, the superficial sea water circulations towards the lake at −155 m—confirmed by geophysical methods—are found in the springs in the southeast bank of the lake. The springs' discharge is high, their temperature low (35 to 41°C), and their composition is very similar to sea water (Dague et al., 1973). On the northeast and southwest banks the situation is different: on the northeast bank, about 15 springs with temperatures varying between 37 and 83°C have been inventoried, while on the southwest bank there are only 3 visible springs, although these are on average hotter (59 to 80°C). The waters are generally more saline than sea water but have a different constitution. A relative enrichment in Ca^{++} and a relative reduction in Na^{+}, K^{+} and Mg^{++} as compared with sea water may be noted.

These waters are of dual origin: meteoric and marine waters, enriched in salts (50 to 70 g/l) by a deep washing of the high-temperature (>150°C) lavas (Bosch et al., 1974), after albitization and propylitization reactions of the basalts (Lopoukhine, 1973). These waters sometimes undergo slight mixing with the brine of the lake (Dague, et al., 1973).

The fumarolic activity is seen essentially in a few large fumarole areas connected with the tectonics, one in the axial valley and the others on the northern border of the rift. Small isolated fumaroles have been noted throughout the rift. Their temperature varies from 98 to 102°C, but the nature of the gases of these fumaroles reveals a very marked atmospheric contamination, which is normal in such a fractured zone. No grounds exist for establishing a relationship between this fumarolic activity and a possible geothermal field (Dague et al., 1973). We may note the absence of a fumarolic area on the southern border of the rift, which might indicate an efficient sealing.

Important concretions of travertine-forming peaks or crests, which may sometimes attain heights of several tens of meters, are situated around Lake Asal. Connected with older formations and tectonics, these indications of an earlier thermalism seem to correspond to different conditions from the present situation (Dague et al., 1973).

Discussion of Local Conditions of the Field

The axial valley of the rift, 4 to 5 km wide, would seem on *a priori* grounds to be the most favorable to the presence of a geothermal field because of its particular structure,

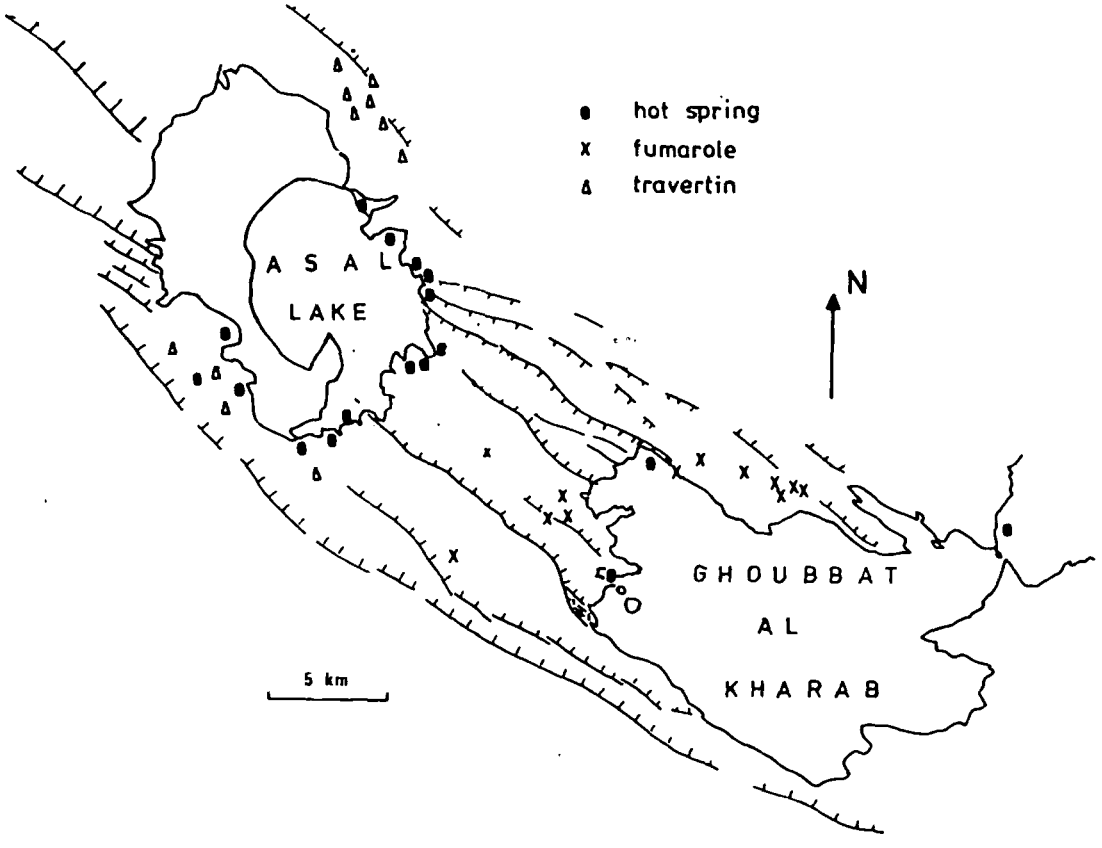

Figure 13. Hot springs, fumaroles and travertines in the Asal rift.

its accretion-zone character (where present volcanic and tectonic activity is concentrated), and the presence of fumarolic areas. However, this zone was rejected in the choice of prospecting zones in favor of the borders of the rift for reasons we set out below.

The axial valley corresponds roughly to the accretion band, a zone injected by dykes in a close network. The rock inclusions in the hyaloclastite massifs of the rift axis are constituted uniquely of lavas with "crystal foam." No rock inclusion from the border series has been found. This intense oceanization connected with the long distensive fissuration suggests an *open system:* absence of the normal geological series, of favorable trapping conditions, of satisfactory sealing and of the presence of fumarolic zones on active faults. The major superficial circulation of sea water masks the thermal flux values: although it was expected that this zone would be the hottest, the gradient measured was negative. The industrial problems which might arise for a power station located in the axial valley also should not be neglected: corrosion by volcanic gases, important seismicity, and risks of canalization ruptures and volcanic eruption.

In siting the prospecting drill holes, we aimed to avoid the accretion zone and find a more stable zone presenting a normal stratigraphic series, still subject to an important thermal flux. The problem therefore came down to estimating the extent of the band of intense oceanization and finding a better-sealed system (Fig. 14).

The southern and northern borders of the rift seem to fulfill these requirements. The southern border was chosen for the first drill campaign for two main reasons: (1) because of the dissymmetry of the rift, the whole of the southern side presents a wider area and a more obvious structure; and (2) it is more accessible by land and sea.

On the southern border of the rift, rock inclusions from older underlying series are found in the hyaloclastite massifs. The absence of any important hydrothermal indications on these panels should be a sign of good surface sealing (by the hyaloclastites and the detrital series of at least Pleistocene age) in such a tectonized region. The flux measured is still very high 45 to 59°C/100 m in surface) and the calculated tectonic and apparent seismic activity is sufficient to ensure the permanence of the fissuration or even a fracturation reservoir. The hot springs of this border indicate a deep circulation in the old lavas at temperatures of at least 170°C.

It was therefore on this southern border that the first reconnaissance boreholes were sited. The first of them is being drilled at present (Fig. 14).

CONCLUSIONS

The outstanding results of the prospecting have been set out above. They led us to a progressive adaptation of the ideas and research phases to the particular conditions of the region, including the unusual step in geothermal prospection of avoiding the outwardly most favorable zones. The borehole campaign is now in progress, but it is too early to draw any conclusions. It seemed worthwhile to set out the problems tackled *a priori* in the framework of a development policy for new and energetic research in the French overseas territories in a region which, geologically speaking, is practically unknown.

The hydrothermal indications suggest a deep circulation of waters of marine and meteoric origin, at temperatures exceeding 170°C. The geological study has revealed that the Asal rift presents characteristics of an active center of expansion connected with the Red Sea-Gulf of Aden ridge. The magmatic intumescence which affects the central zone of the rift over a diameter of about 10 km is attributed to a magmatic rise of the abnormal mantle. Throughout the rift, the thermal flux should therefore be very high. The measurements taken under valid conditions express gradients reaching 59°C/100 m in surface.

The accretion band, 4 to 5 km wide, which corresponds more or less to the axial valley of the rift, seems to be a system which is too open to trap a geothermal aquifer. We have tried to avoid it while still remaining in the recent part of the rift which is tectonically active. The southern margin, which is particularly wide due to the dissymmetry of the rift, seems to be an interesting geological and thermal structure although hydrothermal indications are practically nonexistent. We pose the hypothesis that this very absence of hot springs and fumaroles is in itself a very important indication. It should mean a good surface sealing by the hyaloclastites and Pliocene sediments, while the deep marine circulations in a hyperthermal cycle should be very important. The first borehole results confirm this.

The particular structure of an oceanic rift in progress of expansion, suggesting a considerable thermal flux particularly in the axial valley where the indications are the most developed (volcanism, hydrothermalism), led us to leave aside the hottest zones, because they have open and dispersive systems, in favor of research for thermal structures which, although less evident, should be geologically more reliable for purposes of trapping and sealing off a possible geothermal field.

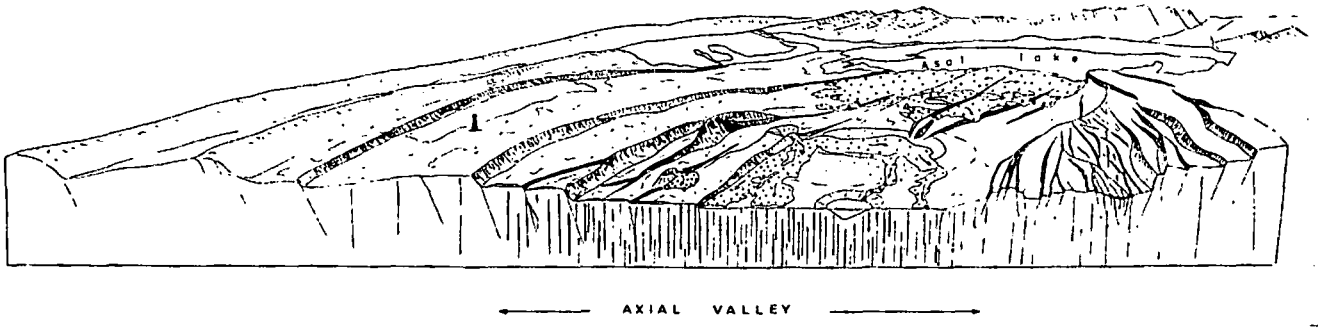

Figure 14. Block diagram of the Asal rift, showing the position of the exploration drill holes with respect to the accretion zone. The accretion zone consists of an open system, not very propitious for a geothermal trap.

ACKNOWLEDGMENT

I should like to thank Professor G. Marinelli (Pisa, Italy) for the many exchanges and discussions we have had in the field and in the laboratory on questions of volcanism and geothermy, and J. Goguel (BRGM) for his critical perspective during the prospecting phase.

REFERENCES CITED

Barberi, F., and Varet, J., 1970, The Erta'ale volcanic range (Danakil depression, northern Afar, Ethiopia): Bull. Volcanol., T, v. XXXIV, no. 4, p. 848-917.

Barberi, F., Giglia, G., Tazieff, H., and Varet, J., 1972, Tectonic significance of the Afar (or Danakil) depression: Nature, v. 235, no. 5334, p. 144-147.

Bosch, B., Deschamps, J., Leleu, M., Lopoukhine, M., Marce, A., and Vilbert, C., 1974, La zone géothermique du Lac ASAL (T.F.A.I.): Résultats de terrain et études géochimiques expérimentales: Bulletin du BRGM, section II, no. 4.

CNRS Afar Team, 1973, Geology of northern Afar depression (Ethiopia): Rev. Géographie Phys. et Géologie Dynam. (2), v. XV, fasc. 4.

Dague, Ph., Duroux, J., Lavigne, J., Lopoukhine, M., and Stieltjes, L., 1973, Prospection géothermique de la région d'ASAL—Rapport de syntèse: Rapport BRGM 73 SGN 144 GTH.

Delibrias, G., Marinelli, G., and Stieltjes, L., 1974, Spreading rate of the Asal rift: A geological approach: Afar Symposium, Bad Bergraben, Monograph.

Faure, H., Hoang, C., and Lalou, C., 1973, Structure et géochronologie (230 Th-234 U) des récifs coraliens soulevés à l'ouest du Golfe d'Aden (TFAI): Rev. Géographie Phys. et Géologie Dynam. (2), v. XV, fasc. 4, p. 393-404.

Gregory, J. W., 1921, The Rift Valleys and geology of East Africa: London, Seeley, 479 p.

Harrison, C. G. A., Bonatti, E., and Stieltjes, L., 1974, Tectonism of axial valleys in spreading centers: Data from the Afar rift: Afar Symposium, Bad Bergraben, Monograph.

Lee, W. H. K., and Uyeda, S., 1965, Review of heat flow data, *in* Terrestrial heat: Am. Geophys. Union Geophys. Mon. 8, p. 87-190.

Lepine, J. C., Rwegg, J. C., and Steinmetz, L., 1972, Seismic profiles in the Djibouti area: Tectonophysics, v. 15 (1/2), p. 59-64.

Lopoukhine, M., 1973, Rôle de la géochimie dans la recherche géothermique—Application au Territoire Français des Afars et des Issas [Thèse III° cycle]: Université de Paris VI.

Mohr, P. A., 1967, Major volcano-tectonic lineaments in the Ethiopian rift system: Nature, v. 21, p. 664-665.

Marinelli, G., 1971, La province géothermique de la dépression Dankali: Annales Mines (mai).

Stieltjes, L., 1970, Etude volcanologique et géothermique de la région Ghoubbat al Kharab—Lac Asal (Territoire Français des Afars et des Issas): Rapport BRGM 70 SGN 213 GTH.

——, 1973a, Evolution tectonique récente du rift d'Asal, TFAI: Rev. Géographie Phys. et Géologie Dynam. (2), v. XV, fasc. 4, p. 425-436.

——, 1973b, L'axe tectono-volcanique d'Asal (Afar Central-Territoire Français des Afars et des Issas) [Thèse III° cycle]: Université de Paris-Sud, centre d'Orsay, 7 nov. 1973.

——, 1974, Evolution volcano tectonique récente d'un rift: ex. d'Asal (TFAI-Depression Afar): 2° réunion annuelle des Sciences de la Terre, Pont à Mousson.

Tazieff, H., 1969, Volcanisme sous-marin de l'Afar: Acad. Sci. Comptes Rendus, t. 268, p. 2657-2660.

Varet, J., 1973, Critères pétrologiques, géochimiques et structural de la genèse et de la différenciation des magmas basaltiques: Exemple de l'Afar [Thèse de Doctorat]: Université de Paris-Sud, centre d'Orsay, 9 nov. 1973.

JOURNAL OF GEOPHYSICAL RESEARCH, VOL. 87, NO. B10, PAGES 8345–8357, OCTOBER 10, 1982

Summary of ROSE results

Rivera Ocean Seismic Experiment (ROSE) Overview

J. I. EWING

Department of Geology and Geophysics, Woods Hole Oceanographic Institution, Woods Hole, Massachusetts 02543

ROBERT P. MEYER

Geophysical and Polar Research Center, Department of Geology and Geophysics, University of Wisconsin—Madison, Madison, Wisconsin 53706

The Rivera Ocean Seismic Experiment (ROSE) was designed as a combined sea and land seismic program to utilize both explosive sources and earthquakes to study a number of features of the structure and evolution of a mid-ocean ridge, a major oceanic fracture zone, and the transition region between ocean and continent. The primary region selected for the experiment included the Rivera Fracture Zone, the crest and eastern flank of the East Pacific Rise north of the Rivera, and adjacent areas of Baja California and mainland Mexico. These areas were to be instrumented with land and ocean bottom seismographs in order to determine good source parameter and location data for natural events and to record these events along a large number of paths crossing various parts of the region. Explosive charges were to be detonated at sea to supplement the natural events. However, the necessary permission to conduct the experiment was not received from Mexican authorities; therefore an alternate plan was implemented whereby the marine program had to be moved southward outside of territorial waters. This had the effect of transforming this experiment into three almost independent components: (1) an experiment to study the East Pacific Rise south of the Orozco Fracture Zone primarily using ocean bottom recording and explosive sources, (2) a seismicity program at the Orozco, and (3) a land-based program of recording natural events along the coastal region of Mexico. A considerable amount of useful data was obtained in each of the three subprograms. In the marine parts of the experiment we were able to address a variety of problems including structure and evolution of young oceanic crust and mantle, structure and dynamics of the East Pacific Rise, seismicity of the Orozco Fracture Zone, and partitioning of energy transmission between the ocean volume and the crust/lithosphere. On land, the fortuitous occurrence of the Petatlan M7.6 earthquake of March 14, 1979, permitted the acquisition of an excellent data set of foreshocks and aftershocks of this large event, which provide new insight into the filling of a major seismic gap in the region. This overview describes the scientific rationale and the design of the experiments, along with some general results. Other articles in this volume give preliminary scientific results from certain components of the overall experiment or, in some cases, report on other data pertinent to the scientific goals of ROSE.

INTRODUCTION

Scientific and technological developments during the past several years have given seismologists encouragement to increase effort toward solving one of the salient problems posed by seafloor spreading and plate tectonics. The essence of the problem is to understand how new material emplaced at an accreting plate boundary becomes arranged into the 'typical' structure postulated for the outer 100 km of the earth's surface. A variety of observations indicates that at almost all depths in the crust and upper mantle there are detectable changes that relate to age. We felt that a large step could be made toward understanding the evolution of the lithosphere and the driving mechanism of plate tectonics if a sufficient set of quantitative, high-resolution seismological data on and near a substantial segment of a spreading ridge axis were acquired. Toward this end, we deployed ocean bottom seismographs (OBS), ocean bottom hydrophones (OBH), and other instrumentation for a 2-month period (January–March 1979) to record both earthquake and explosive events on the East Pacific Rise between the Clipperton and Orozco Fracture Zones (Figure 1) and on the adjacent coastal region of mainland Mexico. The combined suite of investigations is called the Rivera Ocean Seismic Experiment (ROSE).

Paper number 1B1833.
0148-0227/82/001B-1833$05.00

The rationale for a seismological experiment utilizing both earthquake and explosive sources is based on several considerations. Earthquakes generate more shear, as well as surface wave energy, than do explosions and thus provide a significantly more diagnostic data set for determining many of the physical properties of the propagating medium. However, much of what is known about the structure of the oceanic crust and upper mantle has been derived from the study of compressional waves generated by explosives. Therefore we wanted to carry out an experiment which permits the direct comparison of broadband, multiphase data from earthquakes with the more commonly used data from explosion seismology. Not only would we have a complete study of a section of the East Pacific Rise (EPR) system, including one of its fracture zones, but we would also have data that may be directly compared with the substantial quantity of data acquired by explosion seismologists from many regions of the world oceans. For example, the rise crest and eastern flank of the EPR between the two ROSE deployment areas (Figure 1) had already been studied intensively in an OBS experiment conducted by University of Washington [*Lewis and Snydsman*, 1977], so these two experiments together provide an enormous amount of data in the region from the Orozco Fracture Zone southward almost to the Clipperton.

The timing of the experiment seemed appropriate for the following reasons: Data already acquired had given significant insights into some aspects of the problems and offered

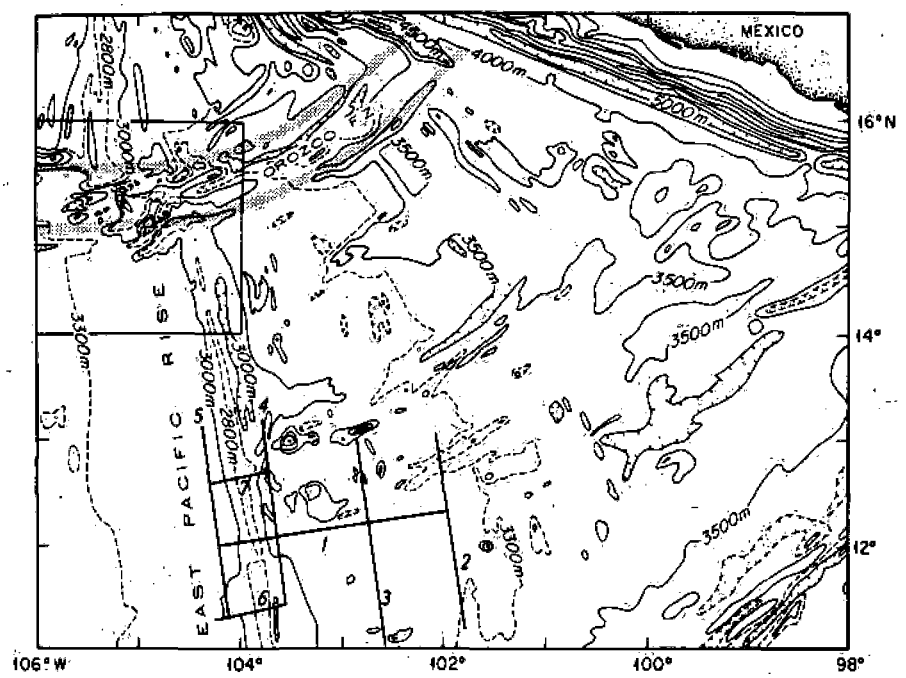

Fig. 1. Map showing the ROSE deployment areas for phase 1 (explosive) centered on 12°N, 103°W and phase 2 (earthquake) centered on the Orozco Fracture Zone at 15°N, 105°W. The major line numbers (1–7) and subarrays (A and B) are designated for the phase 1 deployment. Bathymetry after *Mammerickx and Klitgord* [1982]. Deployment details are shown in Figures 2, 3, and 4. The stippled lines indicate fracture zone trends.

effective guidance in designing additional tests. Instrument development had progressed to the point that substantial numbers of OBS, OBH, and portable land seismograph units existed, and a considerable amount of experience in their use had been accumulated. The development of new analytical procedures (e.g., inversion techniques and synthetic seismogram modeling) had made it possible to derive an increasing amount of geologic information from the recorded data. Further, a large proportion of the seismological community were convinced that a pooling of personal and instrumental resources into the project would likely produce results whose significance would far exceed those obtainable from a number of smaller experiments carried out separately by individual groups.

Our intent originally was to conduct the experiment on the Rivera Fracture Zone and on the rise crest to the north. However, diplomatic clearance was not received to work in the area, which is within Mexico's 200-mile limit, and the experiment was relocated but not renamed. The necessity of having to move the experiment from the Rivera Fracture Zone, which generates a substantial number of teleseismic earthquakes, eliminated much of the purpose of a combined land and sea operation. The hope of recording good source parameter and location data for the fracture zone shocks by local instrument arrays and of recording the same events at more distant marine and land stations was not realized. The only events recognized to date that were recorded by both land and marine instruments were the magnitude 7.6 Petatlan earthquake of March 14, 1979, at 17.5°N, 101.5°W and some of its foreshocks and aftershocks.

Because of the events that caused the original experiment to be fragmented, we present the scientific rationale and experiment design in two parts: part 1, the marine component, and part 2, the land component.

Scientific laboratories that took part in ROSE (Sea) were: Hawaii Institute of Geophysics; Lamont-Doherty Geological Observatory; Massachusetts Institute of Technology; U.S. Naval Ocean Research and Development Activity; U.S. Naval Research Laboratory; U.S. Naval Undersea Systems Center; Oregon State University; Scripps Institution of Oceanography; University of California, Santa Barbara; University of Texas at Galveston; University of Washington; Woods Hole Oceanographic Institution; and Instituto Oceanografico at Manzanillo.

Scientific laboratories that took part in ROSE (Land) were: Hawaii Institute of Geophysics; University of Wisconsin at Madison and Oshkosh; University of Mexico, Instituto de Geofisica and Instituto de Ingenieria; and Centro de Investigaciones Cientifica y Education Superior de Ensenada.

Research ships used during the experiment were: R/V *Robert D. Conrad*, Lamont-Doherty Geological Observatory; USNS *DeSteigeur*, NORDA/NAVOCEANO; USNS *Hayes*, Office of Naval Research/Naval Research Laboratories; R/V *Kana Keoki*, Hawaii Institute of Geophysics; and R/V *Thomas G. Thompson*, University of Washington.

PART 1: SCIENTIFIC RATIONALE AND OBJECTIVES (MARINE)

Explosion Seismology

Experimental and analytical techniques in marine seismology have evolved rapidly in recent years due both to the employment of ocean bottom seismographs and to the development of methods of analysis which permit a more flexible view of the variation of velocity with depth [*Helmberger*, 1968; *Fuchs and Müller*, 1971; *Bessonova et al.*, 1974; *Kennett*, 1977]. This has, in turn, greatly altered our conception of the structure of the oceanic crust and upper mantle and has emphasized the need for detailed studies of specific areas and problems rather than less well directed

surveillance expeditions. Several important hypotheses can now be tested or refined by a detailed field experiment using the currently available OBS systems. Among these hypotheses are:

1. The low-velocity zone (LVZ), observed in several places along the East Pacific Rise, is a magma chamber or, at least, is a zone of partial melt.
2. The low-velocity zone (magma chamber?) underlying the rise crest is geographically discontinuous.
3. A low-velocity zone, perhaps a region of serpentinized mafic rocks, lies at the base of the oceanic crust.

LVZ's have been found by *Orcutt et al.* [1976] north of the Sequieros Fracture Zone and by *Reid et al.* [1977] at 21°N using single ended OBS refraction profiles interpreted in terms of flat-lying homogeneous layers. *McClain and Lewis* [1980] used refracted arrivals across the rise axis to find evidence for a narrow LVZ at 22.5°N, south of the Tamayo Fracture Zone. However, crustal LVZ's have also been found well away from the rise [*Lewis and Snydsman*, 1977] leaving some question as to the cause of the low velocity.

4. The velocity structure of the oceanic crust changes smoothly with increasing depth rather than discontinuously.

Most of the refraction measurements of recent years, in which amplitude information has been utilized in the analysis, have been interpreted as supportive of this hypothesis [cf. *Orcutt et al.*, 1976; *Lewis*, 1978; *Whitmarsh*, 1978; *Stephen et al.*, 1979; *Detrick and Purdy*, 1980]. Most results from reflection seismology give further support, in that intercrustal reflections are seldom observed, while reflections from the crust-mantle transition are relatively common in variable angle reflection profiles [*Ewing and Houtz*, 1969; *Houtz*, 1977] and in near-normal incidence multichannel profiles [*Grow and Markl*, 1977; *Buhl et al.*, 1978; *Stoffa and Buhl*, 1979].

5. Crustal and upper mantle structure and seismic velocities vary with increasing age.

From other experiments on and near the East Pacific Rise [e.g., *Phillips*, 1964; *Lewis and Snydsman*, 1977; *Bibee and Shor*, 1976; *McClain and Lewis*, 1980; *Clowes and Malecek*, 1976; *Houtz and Ewing*, 1976] it has been found that at least three important changes occur in the crust and upper mantle with age: (1) the upper crustal velocities increase with age, (2) the crust thickens with age in some areas, and (3) the upper mantle velocities increase with age.

To explain these effects, it has been suggested that cracks, voids, and rubble zones associated with newly formed crust are filled and cemented by mineralization as the crust ages, resulting in a gradual increase in upper crustal velocities; that convective circulation of water in the crust penetrates to depths of about 8 km causing varying degrees of serpentinization of the ultramafics in the lower crust; and that cooling of the upper mantle causes the increase in upper mantle velocity with age. From an experiment on the Cocos Plate, *Lewis* [1978] also found that the degree of upper mantle anisotropy changes with age, being higher near the rise axis than in older parts of the Pacific [*Raitt et al.*, 1971].

6. Major features of the oceanic crust, such as the sharpness of the transition from crust to mantle, vary significantly over geographic wavelengths of as little as 10 km [*Grow and Markl*, 1977]. Evidence of variations in the crust-mantle transition is apparent in both refraction and reflection profiles. In some areas, reflection data at normal incidence indicate that the moho is essentially a first-order discontinuity for wavelengths as short as 600–800 m. In other places the transition appears to be more gradual, producing only refracted arrivals. An objective of the ROSE experiment was to acquire a sufficient body of data to permit a better realization and understanding of the variability in the transition in the hope of gaining further insight into accretion and aging processes.

7. The shear velocity structure of the oceanic crust excludes the likelihood of a high degree of serpentinization at any depth within the crust [*Christensen and Salisbury*, 1975].

Some of these hypotheses, such as 3 and 7, are, at first glance, mutually exclusive. Unfortunately, many of the conclusions about the nature of the oceanic crust have been developed by statistical analyses of survey data from many different geographic areas. This statistical treatment of data is of questionable validity because of evidence for significant heterogeneity in the crust and upper mantle and because of the realization that each of the listed hypotheses has observational examples and counter examples. ROSE was conceived to concentrate enormous attention on the details of the seismic structure of a specific area, to link the fine scale structures observed in submersible and deep tow operations to the grosser scales addressed by more traditional seismic techniques, and to employ new seismic methods in learning about the details of the velocity structure.

An overall goal of ROSE, which embodies most of the topics in the preceding discussion, was to gain insight into the nature and geometry of a young lithosphere/asthenosphere boundary through the study of seismic velocity structure and energy partitioning along paths at various distances from the accretion axis, as well as along paths through different levels of the accretion zone. Some specific questions to be addressed were:

1. Does the boundary dip as steeply away from an accretion axis as is suggested by thermal models, for example, *Parker and Oldenburg* [1973]?
2. Is there a high-velocity lid at the base of young lithosphere?
3. What is the effect of aging on seismic attenuation in the lithosphere?
4. Does the moho exist under the ridge axis? If not, at what lithospheric age is it identifiable?

Orozco Seismicity

The three principal scientific objectives of the seismicity phase of the ROSE studies were (1) locations of earthquakes, including depth, (2) focal mechanism studies, and (3) structural evolution of the plate with age using body waves, especially shear.

A few OBS microearthquake surveys in the Rivera region have previously been conducted, and several large earthquakes have been studied with teleseismic techniques, though none of these investigations extended to the region included in Figure 1. *Prothero et al.* [1976] reported microearthquake seismicity rates, moments, and rough source depths and dimensions for events recorded at two sites on the Rivera Fracture Zone using tripartite OBS arrays. A third site on the rise crest was quiet for an 8-day deployment. Combined analysis of OBS and teleseismic records from three of the largest shocks has yielded more precise estimates of focal depth (<5 km) and stress drop (~10 bars) and a measure of teleseismic *P* delay [*Reid and Prothero*, 1981].

Fault plane solutions for large earthquakes in the Rivera area have been published by *Sykes* [1967, 1970] and *Molnar* [1973], and moments for three events are given by *Tsai* [1969]. These results will provide a useful basis for comparison with ROSE data on the Orozco.

1. The spatial and temporal patterns of seismicity on the Orozco transform fault and the adjacent segments of the East Pacific Rise are of fundamental interest for studying the details of crustal spreading and transform faulting. Precise locations and source excitations are also prerequisites for the propagation experiments using earthquake-generated phases as described below.

Additional source characterization of the oceanic earthquakes of this study is possible to a unique degree because of the large number and variety of near-source sensors simultaneously in operation. Focal mechanisms of the larger events will be possible from P and S wave motions. The seismic moment, magnitude, source dimension, apparent stress, and stress drop will be derivable from spectral analysis for some earthquakes. For a few well-recorded events, such additional source parameters as rupture velocity and rise time may also be estimable. Determination of the detailed pattern of seismicity during ROSE allows the definition of the active portions of the plate boundary and constrains the nature of the faulting processes on a scale and with a spatial resolution not heretofore possible in marine experiments. Of particular interest is the potential variation of earthquake focal depths along the transition from the rise crest to the transform fault and with decreasing age contrast across the transform fault. Since the distribution of earthquake foci is related to the regime of brittle fracture in the earth, this experiment may provide a quantitative measure of the change in the depth to a brittle-ductile transition in the crust or mantle as a function of plate aging.

2. Focal mechanisms for the larger earthquakes can be reasonably well constrained by body wave first motion. The concentration of receivers provides the essential azimuthal control for a more complete description of the focal mechanisms than has been possible with other oceanic microearthquake seismicity studies to date.

3. Several seismological studies, as noted above, have provided convincing evidence that seismic wave velocities in the oceanic mantle and perhaps in the crust increase with lithosphere age. These velocity increases may be associated with the decrease in temperature and the motion of temperature-controlled phase boundaries in the cooling oceanic plate as it moves away from a spreading center. Thus an accurate determination of the variation of velocity with depth and with age in oceanic lithosphere can help constrain both the thermal structure and the mineralogy and petrology of the crust and mantle.

Shear wave velocity structure is particularly sensitive to seafloor age, and the seismological evolution of the lithosphere has been best demonstrated from measurements of S_n [*Hart and Press*, 1973] velocity and of the phase and group velocities of Love and Rayleigh waves [e.g., *Leeds et al.*, 1974; *Yoshii*, 1975; *Forsyth*, 1975]. The high-frequency S_n phases yield information on the lithospheric mantle, possibly of high-velocity waveguides, and the longer-period surface waves provide abundant information on the shear velocity and density structure of crustal layers and of the lithospheric and asthenospheric mantle, including the important question of anisotropy. Unfortunately, all such studies to date have been confined of necessity to long and heterogeneous paths from oceanic sources to seismic stations on land, usually on continents. So-called 'pure path' measurements have been extracted from large sets of mixed-path data by a combination of simplifying assumptions and statistical analysis, but the way 'pure path' data so derived average actual structure is not at all clear. Further, these teleseismic studies have used surface wave data primarily of periods longer than 15 s. Shorter-period (1–15 s) fundamental and higher-mode surface waves, and their valuable constraints on shallow crustal properties, have rarely been used to study oceanic structure. Unambiguous determination of path characteristics for body and surface waves requires oceanic sources and ocean bottom sensors aligned along profiles of constant lithosphere age. Efficient generation of diagnostic S_n and surface waves requires that the sources be earthquakes.

The Orozco experiment provided an excellent opportunity to characterize S_n propagation along truly pure oceanic paths of nearly constant age. The strike-slip earthquakes on East Pacific Rise transforms generate SH waves that have maximum amplitudes along north-south isochron paths. From the Orozco data set, the shear wave structure for young lithosphere (2 m.y.) may be derived, with the distinct advantage that the variation in structure with age derived from this experiment will be tightly controlled by the pure path data.

Experiment Design (Marine)

Explosion Seismology

The scientific rationale discussed above led us to an experiment design based on the deployment of 60 to 80 OBS and OBH units in the patterns shown in Figures 2, 3, and 4. (See Table 1 for instrument designations used in Figures 2–4.) The first deployment was designed primarily for explosion seismology but clearly could also provide earthquake-generated data to supplement that recorded during the second deployment. The ability to locate explosive sources at will obviously permits more flexibility in experiment design than is possible when natural events are depended upon. Therefore a considerable part of the explosive phase of the experiment was devoted to studying specific structural problems, such as the extent and distribution of magma chambers, and to investigating the details of velocity structure and propagation parameters from the ridge crest (0 age) out to a crustal age of about 4 m.y.

The shot and detector patterns outlined in Figures 2 and 3 permit comparisons of travel times, arrival structure, and energy levels for various propagation paths over a wide

TABLE 1. Instrument Designations Used in Figures 2, 3, and 4

Organization	Numbering
Woods Hole Oceanographic Institution	1–8
Lamont-Doherty Geological Observatory	101–107
University of Texas Marine Sciences Institute	201–212
Scripps Institution of Oceanography	301–305
University of Washington	401–408
Hawaii Institute of Geophysics	501–527
Oregon State University	601–612
Massachusetts Institute of Technology	1001–1003
University of California, Santa Barbara	801–802

In both phase 1 and phase 2, Woods Hole Oceanographic Institution instruments were deployed twice. The second deployments are designated by primed numbers in Figures 2, 3, and 4.

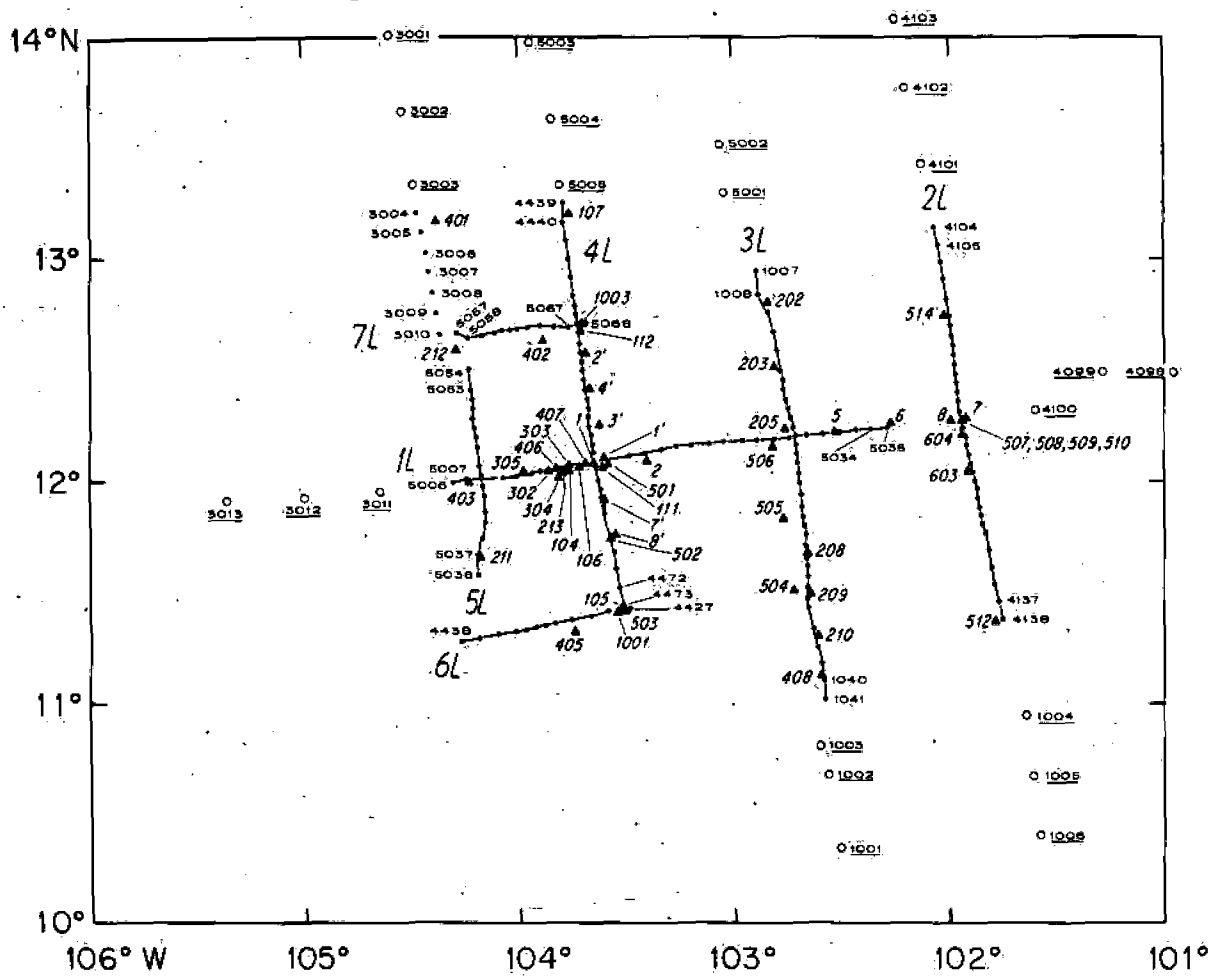

Fig. 2. Details of instrument deployment and locations of large shots in phase 1. Instrument designations are given in Table 1. Open circles denote 800-kg shots. Solid circles are 200-kg or 80-kg charges with the larger size generally spaced farther apart and located near the ends of the shot lines.

range of distances and azimuths and through a variety of crustal and upper mantle structural configurations. A large number of shots of several sizes and spectra are distributed in the study area, providing a unique opportunity to study propagation quantitatively over a substantial range of frequencies and medium parameters. The following comments are pertinent to the deployment and shooting rationale.

1. Shot lines fired between array elements as indicated in Figures 2 and 3 produced excellent refraction control at each position for determination of both shallow and deep structures. The distribution of large shots (200–800 kg) within and outside of the array provided a large number of shots with potential to be recorded by most elements of the array, covering a broad range of distances, azimuths, and ages. With control on the upper structure provided by the smaller shots, the variations in seismic parameters of the entire area should be extremely well determined.

2. Array A was planned as a vertical array of hydrophones and an L-shaped array of OBS's distributed in a log periodic fashion. The maximum length of each leg was to be about 5–8 km with the minimum spacing being about 100 m. As well as being used for structure determination, this array was to be used for measurements of wavefront distortion due to inhomogeneities, signal and noise coherency, energy partitioning, attenuation, and impedance. Because of some OBS failures and deployment problems the desired array configuration was not achieved exactly. Nevertheless, the data set recorded by the array is unique and potentially of considerable value to the whole experiment.

3. The main objective of the deployment of array B was to utilize propagation paths from shots, particularly along line 1, which pass through the rise crest and its flanks at many different depths, permitting a detailed study of the rise structure. The shots along lines 4 and 5 also provide some insight into structural variation in the dimension parallel to the rise.

4. The studies with the main OBS array, as well as those connected with the tight arrays at points A and B, were supplemented by receiving many of the lines of explosive shots with a towed multichannel seismic array in 'expanding spread' mode. Not only does this method provide seismic and acoustic data of exceptionally high resolving power, but also we considered it important to be able to compare results obtained with fixed bottom receivers with those obtained with a mobile line array. Details of the expanding spread method are given by *Stoffa and Buhl* [1979].

5. To achieve a denser population of detectors on lines 1 and 4, the Woods Hole Oceanographic Institution OBH's were deployed on line 1 while it was being shot and redeployed on line 4 for the shooting there.

6. In addition to the work along the main lines of the instrument grid, some periods of time during the experiment

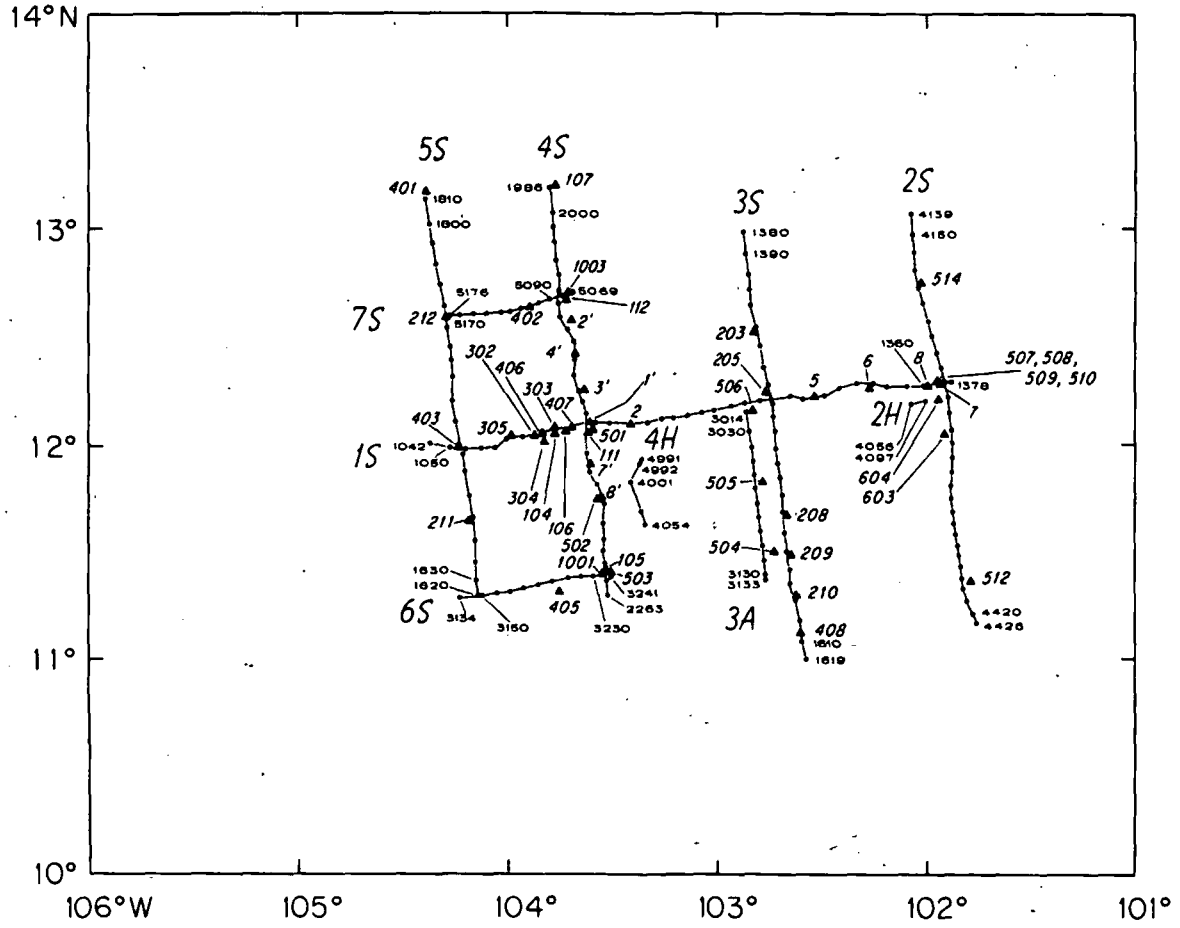

Fig. 3. Instrument deployments and locations of small shots in phase 1. Instrument designations are given in Table 1. Small shots alternating 2-kg and 10-kg charge fired approximately every kilometer. Figure shows location of every tenth shot.

were devoted to firing detailed shot patterns around individual instruments using deep explosives, airguns, and maxipulse as sources. Some of the exercises of this type were based on vertical array recording to measure arrival structure, coherence, reflection coefficients, and bottom impedance, while others were designed for high-resolution measurements of crustal structure at various OBS locations.

7. Following the main ROSE field program, R/V *Conrad* conducted a 24-channel CDP reflection survey along the major lines of the phase 1 grid. This survey was expected to provide important data on the geometry and reflectivity of the crust-mantle transition and on possible intracrustal discontinuities [*Buhl et al.*, 1978; *Herron et al.*, 1978].

8. Other separate, but related, experiments conducted during or after ROSE included further tests with the University of Washington deep-towed seismic array, a deployment by R/V *Kana Keoki* of Oregon State University OBS's in the Petatlan aftershock region, and deployment by R/V *Thompson* of electromagnetic recording instruments operated by J. Filloux of Scripps Institution of Oceanography.

Orozco Seismicity

The second deployment of the instruments (Figure 4) was primarily for earthquake recording at the Orozco Fracture Zone. The receiving array was designed with two primary objectives in mind: (1) to instrument portions of the fracture zone to accurately locate earthquakes occurring along it and to measure the source parameters as a function of position along the transform, and (2) to instrument the neighboring regions of the rise crest and flank to record body and surface waves from the fracture zone shocks.

In short, the second deployment was planned to use natural seismic events to investigate the tectonic behavior of a fracture zone, to interpret the behavior in terms of crustal and lithospheric properties, and to use the earthquake sources for studying the variation of crustal and lithospheric structures as a function of age. Additional source-receiver propagation paths might be expected from local ridge crest and from teleseismic events. In this instrument deployment, most of the units were expected to be recording for a period of 2–3 weeks with a high probability that a few earthquakes would be recorded by all instruments. Not only was this expectation realized, but also a large number of smaller shocks from the fracture zone were detected by the closer units. Several 200 kg and 800 kg shots were fired within and outside the Orozco array to provide a direct comparison of earthquake and explosive sources. In addition, four lines of smaller explosive charges were fired to provide crustal velocity information for aid in location of the seismic events. The locations of the explosive charges are shown in Figure 4. Most of these objectives, as well as several others, were more realizable at a large fracture zone like the Rivera. Nevertheless, the Orozco data base is substantial and is expected to add significantly to our understanding of accreting plate boundaries and oceanic transform faults.

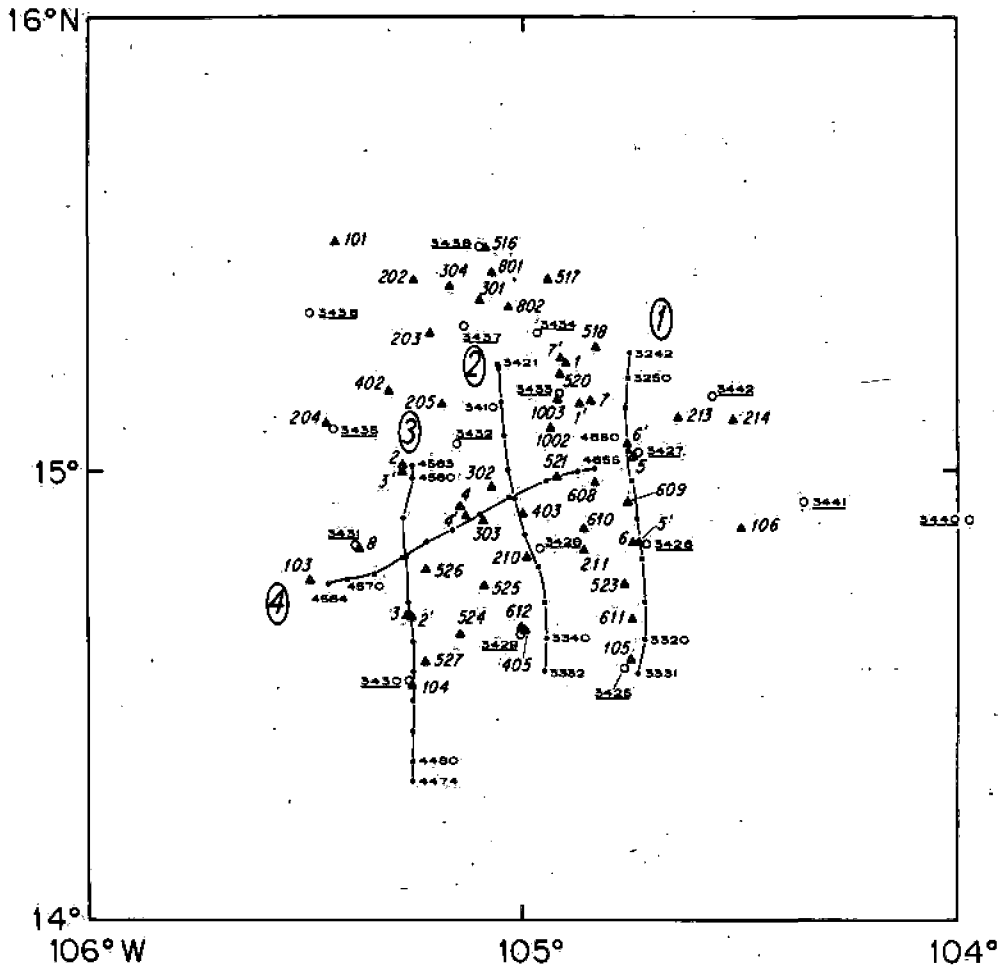

Fig. 4. Instrument deployments and shot positions for phase 2. Instrument designations are given in Table 1. Open circles are 200-kg charges, except 3440 and 3441, which are 800 kg. There was no shot 3439. Charges of 2 kg each were fired along lines 1–4 approximately every kilometer.

PART 2: SCIENTIFIC RATIONALE AND OBJECTIVES (LAND)

The land portion of the Rivera Ocean Seismic Experiment (ROSE) began with the same question as the parent marine program: to understand how new material emplaced at an accreting plate boundary becomes arranged into the 'typical' structure postulated for the outer 100 km of the earth's surface. During the decade preceding ROSE, both active and passive margins had been examined by combined oceanographic and land seismic experiments, with uniformly favorable experience observing sea shots at land seismographs to ranges as great as 1500 km. These experiments had resulted in estimates of the depth of the lithosphere-asthenosphere boundary under the Gulf of Mexico [*Hales et al.*, 1970] and in considerable insight concerning the region where subduction begins off Mexico [*Helsley et al.*, 1975; *Mooney et al.*, 1975], Peru [*Geitrust et al.*, 1973; *Luetgert and Meyer*, 1978], and Colombia [*Meissner et al.*, 1976; *Meyer et al.*, 1976; *Ocola et al.*, 1975]. The ROSE experiment provided the first opportunity to examine a spreading center in a similar way.

The advantages of adding observations on land during both the explosion and the earthquake-recording phases of the ROSE oceanographic program were several. With sea shots as sources, we expected observations at quiet land sites along parallel several-hundred-kilometer lines in Baja California and southeast along the Mexican coast (Figure 5), thereby extending the lines of measurements to greater range than available to the marine program. Because of this extended range, it was likely that the land seismographs could sample deeper regions beneath the East Pacific Rise, for regardless of marine experience showing little or no energy transmission across a spreading center at shorter ranges, our expectation here was that, as the range increased, energy via Fermat paths crossing the divergent margin would be seen (a common observation, as teleseismic arrivals attest) and the depth of penetration beneath the spreading center would increase continuously or discontinuously with increasing range. We also expected to obtain data to compare the velocity-depth structure of the coastal mainland Mexico with that of formerly adjacent Baja California, addressing, among other things, the question of the effect of the rafting of Baja on its underpinnings. Further, from lines of shots northeast, at right angles to those above, we would examine the deep structure along seafloor isochrons. Based on the results of shooting across the Gulf of Mexico [*Hales et al.*, 1970], we expected high P wave velocities at approximately 60-km depth even under the very young ocean floor here, and the greater ranges afforded by the land seismographs improved the chance of observing them.

A land extension of the second, earthquake recording,

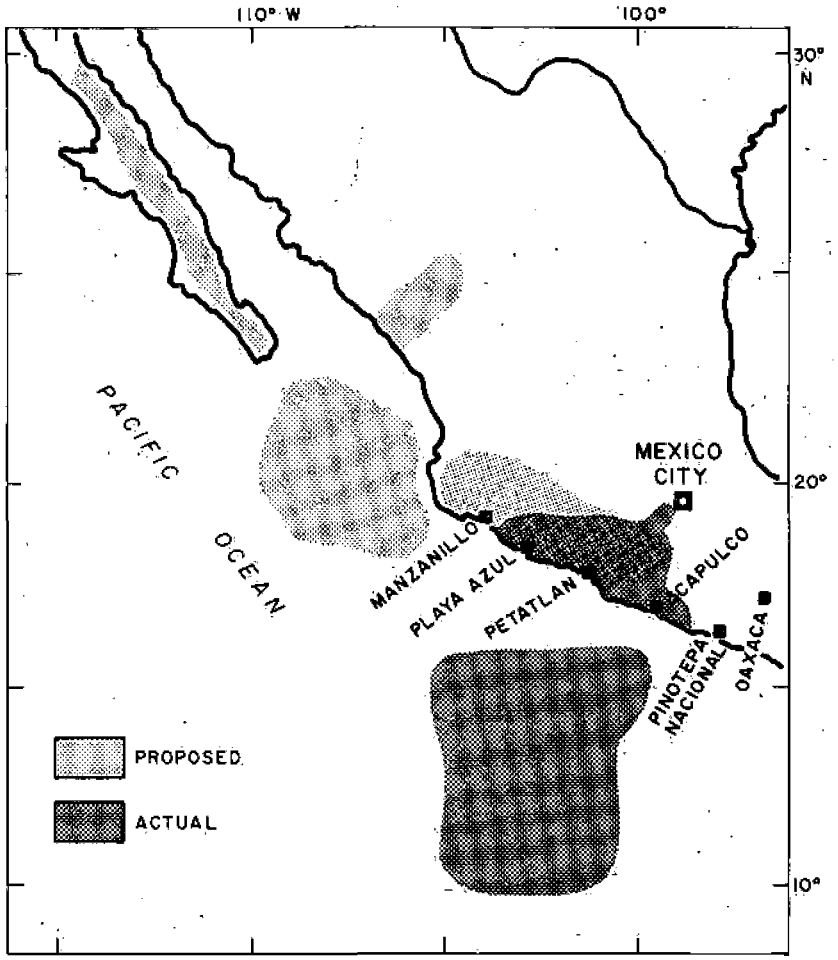

Fig. 5. Proposed and actual locations of seismic observations. Not shown is the region off Petatlan occupied by OBS's for aftershock studies.

phase of the ROSE program was planned because of the high seismicity, not only of the East Pacific Rise, Rivera Fracture Zone, and Tamayo fracture Zone, but also of the mainland adjacent to these areas. Because of the proximity of the sources, we expected that well-located earthquakes on land or sea could be seen by counterpart arrays at sea or on land (Figure 6), providing a prime opportunity to study S wave parameters, which are essentially unavailable from explosion data.

Land Program Modified

The land field parties assembled in Mexico in January were left with greatly diminished opportunities when diplomatic clearance was not received for the ships of the ROSE consortia to work within Mexico's 200-mile territorial limit. The explosive phase of the experiment was relocated some 400–500 km farther out to sea and to the south, over the East Pacific Rise south of the Orozco Fracture Zone, interposing a minimum of over 400 km and a subduction zone between the land and marine programs.

The gap between land and marine programs was not thought insurmountable for recording either sea shots or well-located land or sea earthquakes at counterpart arrays, and we thought some connection, although not a continuous profile, could be expected between the programs. In 1974, Universidad Nacional Autónoma de México, University of Wisconsin—Madison, Hawaii Institute of Geophysics, and University of Washington had recorded an onshore-offshore profile perpendicular to the subduction zone, passing close to the city of Pinotepa Nacional (Figure 5) midway between Oaxaca and the newly chosen region for the ROSE land observations. In that earlier profile we had easily recorded shots seaward of the trench at land seismographs [*Mooney et al.*, 1975; *Helsley et al.*, 1975]. Therefore we were surprised when energy from ROSE shots, some of which were larger than those used in 1974, was not seen at the land array at similar ranges; although some large earthquakes located on land were received at the sea array, shots of 1 to 5 tons exploded on four occasions just outside the 200-mile limit were not seen on land, with the exception, perhaps, of T phases. Since ROSE we have found that other investigators have had similar, anomalous, results recording in areas of subduction, for example, in the Aleutian subduction region, where earthquakes located seaward of the trench by OBS's were not seen by a land array [*Frohlich et al.*, 1981].

Since a continuous onshore-offshore profile was not possible in any case, revised goals were needed for the land program unless it was to be abandoned, and an additional objective was adopted: delineation of the P and S wave velocity-depth structure of the edge of the continent in order to refine the velocity-depth model for the aftershock area of a major earthquake near Puerto Escondido, Oaxaca, on November 29, 1978, and because we were seeking an improved interpretation of the 1974 onshore-offshore profile. We planned to use well-located aftershocks as sources for profiling between two recent earthquakes, the Oaxaco earth-

quake (M = 7.8), and the Tecpan, Guerrero, earthquake of January 26, 1979 (M_s = 6.5). Further, seismic gaps had previously been recognized in this area [*Kelleher et al.*, 1973; *McCann et al.*, 1978], with major earthquakes and their foreshocks and aftershocks recurring in fairly discrete zones at fairly regular intervals. We were interested in studying the variations in parameters along the profile, including structure that might correlate with gap boundaries, such as zones of low rigidity and low Q at the edges of the gaps. If they existed, could they be the controls on the largest-size rupture possible in a given area?

The immediate goals, then, were twofold: (1) to set up lines of receivers at azimuths appropriate for the shots being fired at sea in hopes of fulfilling some of the original objectives and (2) to profile along the coast. For the first five 1-ton shots, 100- to 150-km profile lines were established perpendicular to the coast inland from Acapulco, principally using long-term AM-recording seismographs (Hawaii Institute of Geophysics), and inland from Playa Azul 300 km to the northwest with FM-recording seismographs requiring daily service (University of Wisconsin—Madison). The Playa Azul line was later partially instrumented by the Hawaii Institute of Geophysics AM-recording seismographs to lessen the logistic load of daily service, and a regional array including profile lines of recorders to locate earthquakes and to receive shots was formed, covering a 100- by 300-km block [*Getirust et al.*, 1981]. To profile along the coast, the University of Wisconsin—Madison planned to locate regions of current high seismicity and then, with Universidad Nacional Autónoma de México install a tight array over the zones of highest seismicity to provide precise locations of earthquakes used as profile sources. It was also expected that some of the best located earthquakes could be seen by the ocean arrays.

With the March 14, 1979, M_s = 7.6 earthquake near Petatlan, Guerrero, the most important objective on land became recording the aftershock sequence. On March 12, two smoked-paper recorders had been installed near Petatlan based on our recalculation of the aftershock area of the Tecpan, Guerrero, earthquake. Near the end of February, 15 newly completed three-component digital seismographs (University of Wisconsin—Madison) arrived in Mexico; these seismographs, after checkout, had been moved to the vicinity of Petatlan on March 13. The University of Wisconsin—Madison and the Universidad Nacional Autónoma de México quickly installed a dense local network including the digital seismographs in the epicentral area, and the Hawaii Institute of Geophysics maintained the seismograph positions that they had instrumented a month or more before the earthquake. Subsequently, the University of Wisconsin—Madison and Universidad Nacional Autónoma de México made overlapping, interleaved measurements on profiles away from the aftershock region both parallel to the coast and perpendicular to it toward Mexico City, where there had been considerable earthquake damage [*Meli*, 1979]. In addition, three of Oregon State University's OBS's were moved to the epicentral area by the R/V *Kana Keoki* (Hawaii Institute of Geophysics) for two weeks recording starting March 25; they were picked up later by the Instituto Oceanografico (Manzanillo), using a Mexican Navy vessel. The land recording program was extended through mid-April, beyond the end of the oceanographic program.

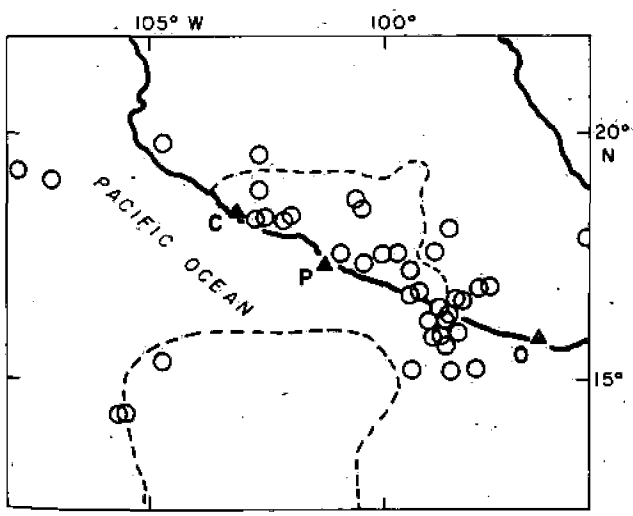

Fig. 6. Teleseismically recorded earthquake epicenters during 1975 (source: National Geophysical and Solar-Terrestrial Data Center, Boulder, Colorado). Dashed lines outline the regions occupied by land and sea arrays during Project ROSE. C denotes the Colima earthquake (1973, M = 7.5); P is Petatlan (1979, M = 7.6); O is Oaxaca (1978, M = 7.8).

In the final analysis, the opportunities afforded because of the ROSE land program were unpredicted and exceptional, leading to an excellent data set of approximately 10,000 events and 100–200,000 seismograms before and after a major earthquake associated with a subduction zone and in a region previously recognized as a seismic gap. An efficient means of assembling and analyzing this large natural events data set is the current thrust of efforts at the Hawaii Institute of Geophysics and the University of Wisconsin—Madison.

Questions That Can Be Addressed Using the ROSE Land Program Data

The major questions we can address are associated with source properties (e.g., location, stress drop) and their variation with time and space as possible predictive tools, the structure of the subduction zone and volumes adjacent to it, and the use of land, OBS, and combined arrays. The following are some of the questions now under discussion:

1. Is there predictive value in the space-time hypocenter history of the seismic events as observed by a regional network starting a few months before an earthquake associated with a subduction zone and a seismic gap [*Hsu et al.*, this issue; *Granet and Trong*, 1980].

2. Are the foreshocks and aftershocks in the same or in different plates? (Results to date suggest that the foreshocks seem most likely to be in the continental plate and the aftershocks more closely associated with the deeper Benioff zone between the continental and oceanic lithospheres [*Getirust et al.*, 1981].) Does this imply a fundamental means for differentiating foreshocks and aftershocks in subduction zones? If foreshocks lie in a different volume than aftershocks, how is quiescence of foreshock activity, which may outline the zone of the mainshock, related to it and to the aftershocks?

3. How do the source parameters of the foreshock series compare with those of the aftershock series? *Valdes et al.* [this issue] suggest that the b value changes sharply between the foreshock and aftershock sequences. On average, does the direction of faulting, or of compressional or tensional axis, shift between foreshocks and aftershocks? If so, what might this imply about gradual shifts in the future? Can shifts

of any of these parameters be detected between 1941, when the previous major shock near Petatlan occurred, and 1979, up to the recent Petatlan event? Do apparent stress, stress drop, source dimensions, magnitude, or moment show systematic areas or temporal change before and after the major shock? Are there changes in the path parameters with time before or after the main event; for example, does apparent V_P/V_S ratio or Q change with time following a major event [*Shibuya*, 1979]?

4. Are there changes in source and path parameters starting a few months before a major event? If so, what is their predictive value? Analog instruments were used for the regional network that covered the likely foreshock area, and some questions that can be addressed because of these data are: Does Poisson's ratio here change areally or with time [*Fitch and Rynn*, 1976; *Wadati*, 1931]? Can the relative stress drop for various parts of the area be estimated—for example, by observing the areal distribution of the moment of earthquakes with identical corner frequencies [*Takemura et al.*, 1980]? Is it possible that the b value, including changes with time and with area, could also be predictive? (Initial estimates of b value in the region of the Petatlan event before the earthquake show it to be the lowest of those in several active volumes covered by the regional array [*Hsu et al.*, this issue, personal communication, 1981].)

5. What part of the convergence as estimated from the convergence rate and major earthquake recurrence time is relieved by major shocks? (Initial estimates are that approximately 51% of the slip estimated for the 36-year period since the 1941 major event in the Petatlan region was accounted for by the 1979 earthquake [*Valdes et al.*, this issue].) How much of the convergence can be accounted for by deformation of the continental block as manifest by the continuing activity in the continental block between the times of major subduction events, and how much can be assigned to aseismic deformation?

6. Can the regions of transition between brittle failure and ductile failure be discovered by the study of stopping phases and their variations with depth [*House and Boatwright*, 1980; *Boatwright*, 1980]? Is the stress drop of major earthquakes controlled by basal shear stress? How is stress drop related to magnitude? (There is already clear evidence that for the aftershocks there is a tendency for larger events to have higher stress drops [*Valdes et al.*, this issue]. Correlation with earthquake location in relation to structure, for example, is latent in the data.)

7. What was the cause of the very high apparent attenuation of the sea shots along paths to land receivers? How much can be related to the Orozco Fracture Zone, which is incident on the coast at Petatlan? The earthquake energy that traversed similar paths to those expected for the shots may provide a measure of the attenuation and possibly an explanation. (It is also to be noted that large sea shots were not seen at great distances at sea.)

8. Can local P and S velocity-depth structure models within the aftershock volume be improved by using earthquakes as controlled sources for refraction and wide-angle reflection profiling measurements, or through the minimum apparent velocity method [*Matumoto et al.*, 1977], or other methods of inverting earthquake data for velocity and depth [e.g., *Crosson*, 1976; *Aki and Lee*, 1976]?

9. To what extent can the error resulting from teleseismic hypocentral locations for subduction-related events be removed by a regional land array, by a more local epicentral array, by regional and local land arrays augmented by OBS's in the epicentral region? (We find that the epicentral location for the main shock constrained either by an array near Mexico City and two local stations [*Meyer et al.*, 1980] or by the regional array of the Hawaii Institute of Geophysics agree within 10 km for the main shock, and both are in disagreement with the PDE location, which is about 50 km farther inland [*Hsu et al.*, this issue; *Valdes et al.*, this issue].) Further, for the few aftershocks tested so far, the locations of these with or without the addition of OBS arrival time data are very little different from those determined solely from local land arrays, even though the events lie seaward of the land array [*Valdes et al.*, this issue].

An auxilliary question relates to the large number of earthquakes that are routinely not satisfactorily located (as judged, for example, by high origin time residuals) and thereby eliminated from consideration. Is this an acceptable procedure, or are these earthquakes of critical importance? Will their numbers decrease if OBS data are available in the epicentral region, or do these unsatisfactory locations result largely from instrument or reading error? Or, alternately, are their associated error estimates high because the flat-layered model so far assumed is too simple for their unusual locations, allowing 'satisfactory' location (e.g., ±0.23-s average origin time residuals for less than 65% of the aftershocks analyzed so far [*Valdes et al.*, this issue]) only for earthquakes whose locations fit the model?

Results of the Experiment

Scientific Results

Most of the papers in this volume related to the marine part of ROSE focus on problems that have solutions attainable with data from a limited number of instruments, primarily those operated by the authors' institution. They constitute partial answers to some of the questions posed earlier in this text and, as usual, raise some new questions. There is good reason to expect much more from the entire ROSE data set as larger subsets are utilized, the purpose for which the ROSE data archive was established [*LaTraille et al.*, this issue]. The scientific results of the ROSE land program reported in this issue are essentially independent of those of the ROSE marine program, fulfilling different objectives than could have been envisaged beforehand. The feature that can be studied most completely is a subduction zone before, during, and after a major earthquake.

Preliminary results can be grouped into a few general topics and provide a considerable amount of new insight into some of the fundamental questions we sought to answer.

1. Seismic structure and aging of the crust (see papers in this issue by Ewing and Purdy, Furukaya et al., Garmany, Kempner and Gettrust, Purdy).

Several papers have addressed this question in one way or another, although the rather narrow range of crustal age (0–4 m.y.) in the ROSE area permits a study of only the effects associated with the early stages of aging. The preliminary results indicate that the uppermost crust has a very low p velocity (2.5–3 km/s), which increases with depth at a high rate (3–4 s^{-1}) in the upper 500–800 m. The early effects of aging on crustal velocity structure are subtle, apparently because the influences of fracture zones, local topography, etc., are more pronounced than weathering or sealing of cracks and voids for at least the first few million years. A relatively rapid change in layer 3 is postulated in the close

vicinity of the spreading axis, and evidence is presented for *p* wave velocity anisotropy in layer 3, with high velocity in the spreading direction. Synthetic seismogram modeling results are presented to support similarity of young oceanic crust to the Samail ophiolites and of mature oceanic crust to the Bay of Islands ophiolites.

2. Rise axis structure and processes (see papers in this issue by Filloux, Lewis, Lewis and Garmany, McClain and Lewis).

Electromagnetic observations north of the Rivera fracture zone and south of the Orozco indicate a signifiant shoaling of high conductivity under the rise axis, as compared with the off-axis measurements, suggestive of relatively shallow (a few kilometers) magmatic activity. Seismic data from profiles across the rise axis at 12°N latitude indicate a low-velocity zone, presumably magma or partial melt, within the crust. The LVZ appears to be only a few kilometers wide but has appreciable along-axis extent, as deduced from results of fan profiles. In contrast with these results from the ROSE area, McClain and Lewis report having found no indication of a crustal magma chamber under the Juan de Fuca ridge. Combined gravity and topography inversion reveals the presence of a relatively narrow body of excess mass under the rise axis that is postulated to be peridotitic mantle material supported dynamically above isostatic equilibrium by plate driving forces.

3. Crust-mantle transition (see paper in this issue by Garmany).

Comparison of refraction profiles parallel and perpendicular to the rise axis permits a characterization of the crust-mantle transition in terms of the rate at which the high-velocity gradient in the moho changes to the lower gradient in the mantle. The rate of change of gradient is found to be more gradual in perpendicular (fast) direction than in the parallel (slow) direction. These results have been interpreted by *Garmany* [1981] as indicating anisotropy gradients in the moho transition region.

4. Microseismicity of fracture zones (see papers in this issue by Ouchi et al., Prothero and Reid).

Two papers in this volume report on observations of fracture zone seismicity. An earlier report on the Orozco has been published [*Project ROSE Scientists*, 1981]. Data from the rise axis near the Rivera and the Orozco show a tendency for microearthquake activity to be swarmlike and possibly associated mainly with magmatic or hydrothermal processes. Events occurring in clearly defined transform regions of the fracture zones give strike-slip focal mechanism solutions, as expected, but one region of high activity in the Orozco is complex, both morphologically and seismically, and may correspond to stress release associated with recent changes in plate motion [*Klitgord and Mammerickx*, 1982].

5. Regional tectonics [see *Klitgord and Mammerickx*, 1982; *Mammerickx and Klitgord*, 1982].

Magnetic and bathymetric data on the East Pacific Rise north of the equator have been summarized by *Klitgord and Mammerickx* [1982] and a detailed picture of the history of seafloor spreading during the past 25 m.y. has been produced. Four periods of reorganization of plate motions have been recognized during this time period. The information provided by this study on crustal age patterns, fracture zone locations, and extinct spreading axes is crucial to interpreting the ROSE and other data sets in the context of plate structure and evolution.

6. Experimental techniques (see the paper in this issue by Creager and Dorman).

Several of the papers already mentioned include some new ideas on methods. The paper by Creager and Dorman addresses the problem of locating ships (and explosive charges deployed by ships) and ocean bottom recording units in a relative and an absolute sense. The locations of sources and receivers are obviously very important parameters in the seismic data analysis. The importance of the positioning information increases as larger and larger subsets of the total data base are employed in particular studies, so this paper is timely.

7. Petatlan earthquake (see papers in this issue by Hsu et al., Valdes et al.).

Two papers describe results of land-based seismicity studies related to the Petatlan earthquake. Hsu et al. concentrate mainly on foreshock activity and the filling of a major seismic gap by three earthquakes—Acapulco, December 12, 1978; Tecpan, January 26, 1979; and Petatlan, March 14, 1979. Their results suggest that the seismicity pattern preceding the Petatlan event might have permitted a forecasting of the earthquake. Valdes and others report on the Petatlan aftershock activity, presenting results on the rupture area and geometry, seismic moment, slip, and stress drop, for the main event and for a number of aftershocks, along with a variety of other parameters of the aftershocks.

Operations and Instrument Performance

The ROSE marine program was a complex experiment operationally, requiring the coordinated efforts of 12 research groups working with five ships deploying a large number of instruments and firing about 1600 explosive shots on a rigid schedule. These operations proceeded very smoothly with very little deviation from the original plan. Instrument performance left something to be desired, with 11 lost in 153 total deployments and an information recovery percentage only slightly above 50%. In postmortem discussions we tend to put primary blame for losses on the ballast releases, both acoustic and timed. The primary cause of failure to acquire data from some of the recovered instruments was malfunctioning of tape recorders.

The ROSE data set is expected to contribute toward determining those OBS design parameters most important to data quality, in view of the considerable variation in style of instruments used in the experiment. In this respect, attention is called to *Sutton et al.* [1980] for a report on an OBS intercomparison study made prior to ROSE in a shallow water environment at Lopez Island in Puget Sound. The basic designs and response characteristics of most of the instruments used in ROSE are shown in that report. The ROSE data will provide some further intercomparison results for the deep-sea environment.

The ROSE land program investigators were placed in a most fluid situation by the move of the marine program. Logistically the land program was difficult, in that about six to eight small parties, each made up of Mexican and U.S. investigators, needed coordination with each other, and with the parties at sea, to meet both scientific and diplomatic objectives. There were, as expected, access problems on land, especially related to the coastal Sierra Madre range, which is sparsely served by roads; these were lessened by use of the Aerocommander 500B aircraft of the University of Wisconsin—Oshkosh, which reduced the time for seismo-

graph deployment and servicing from days of truck travel to less than an hour of air travel.

The older (analog) equipment performed well; malfunctions were, as with most of the equipment, often related to tape recorder failures. Of two sets of new digital equipment, one set proved fully as fieldworthy as analog equipment. One digital seismograph survived being removed from its site and subsequently recovered, after having its parts distributed more or less evenly around a village; another fell out of a truck on a rough road; in each case, the abused seismograph was fully operational shortly after recovery, leading us to the conclusion that fieldworthy digital seismographs are an achievable goal.

Acknowledgments. The authors and the other ROSE scientists gratefully acknowledge funding support from the Office of Naval Research, the National Science Foundation, the Naval Ocean Research and Development Activity, the Instituto de Ingeneria and the Instituto de Geofisica (University of Mexico), and the Instituto Oceanografico (Manzanillo). This operationally complex experiment could not have been successful without the exemplary spirit of cooperation displayed by all of the scientific and technical participants, as well as by the officers and crews of *Conrad, Desteiguer, Hayes, Kana Keoki,* and *Thompson.* It is also a pleasure to acknowledge the considerable assistance of the Mexican Navy. Through the good offices of Admiral Piana Lara and of the Naval Authorities in Manzanillo, we were given all possible support. We are particularly indebted to Gustavo Calderon Riveroll, Director of the Instituto Oceanografico in Manzanillo. Not only did he provide great assistance with logistics, communication, and clearances, but also he rendered a great service by securing the use of Mexican Naval vessels to rescue three OBS's prematurely deployed in the Rivera area and three units later deployed in the Petatlan region. Many other individuals in Mexico made efforts on behalf of the ROSE program that typify unselfish cooperation in science. In chronological order we thank L. Ponce and A. Reyes for support of the original concept. For assistance in restructuring the land program, general counsel, and/or immediate response after the Petatlan earthquake, we thank L. Ponce, K. Singh, I. Galindo, D. Resendiz, J. Havskov, and J. Yamamoto. Universidad Nacional Autónoma de México students who assisted in the field included C. Valdes, R. Zuniga, M. Guzman Speziale, R. Ruiz Kitchnmer, F. Gomez C., and J. Hirata Merre. Participants on the ships were M. Muguerza Pacho, C. Mortera Gutierrez, and S. Lopez Sandoval. Most of the participants in ROSE contributed to the conception and planning of the experiment, and hence to the text of this paper. Special thanks are due Michael Purdy, Sean Solomon, and Anne Trehu for their constructive reviews of the manuscript.

REFERENCES

Aki, K., and W. H. K. Lee, Determination of three-dimensional velocity anomalies under a seismic array using first *P* arrival times from local earthquakes, 1, A homogeneous initial model, *J. Geophys. Res.*, *81*(23), 4381–4399, 1976.

Bessonova, E. N., V. M. Fishman, V. Z. Ryaboyi, and G. A. Sitnikova, The Tau method for the inversion of travel times, I, Deep seismic soundings data, *Geophys. J. R. Astron. Soc.*, *36*, 377–398, 1974.

Bibee, L. D., and G. G. Shor, Jr., Compressional wave anisotropy in the crust and upper mantle of the Pacific (abstract), *Eos Trans. AGU*, *57*, 333, 1976.

Boatwright, J., A spectral theory for circular seismic sources: Simple estimates of source dimension, dynamic stress drop, and radiated seismic energy, *Bull. Seismol. Soc. Am.*, *70*(1), 1–26, 1980.

Buhl, P., P. L. Stoffa, T. K. Kan, M. Talwani, and J. Ewing, Observations of reflections from the *M*-discontinuity in the western Pacific by near vertical incidence multi-channel profiling (abstract), *Eos Trans. AGU*, *59*, 321, 1978.

Christensen, N. I., and M. H. Salisbury, Structure and constitution of the lower oceanic crust, *Rev. Geophys. Space Phys.*, *13*, 57–86, 1975.

Clowes, R. M., and S. J. Malecek, Preliminary interpretation of a marine deep seismic sounding survey in the region of Explorer Ridge, *Can. J. Earth Sci.*, *13*, 1545–1555, 1976.

Creager, K. C., and L. M. Dorman, Location of instruments on the seafloor by joint adjustment of instrument and ship positions, *J. Geophys. Res.*, this issue.

Crosson, R. S., Crustal structure modeling of earthquake data, 1, Simultaneous least squares estimation of hypocenter and velocity parameters, *J. Geophys. Res.*, *81*, 3036–3046, 1976.

Detrick, R. S., Jr., and G. M. Purdy, The crustal structure of the Kane Fracture Zone from seismic refraction studies, *J. Geophys. Res.*, *85*, 3759–3777, 1980.

Ewing, J., and R. Houtz, Mantle reflections in airgun-sonobuoy profiles, *J. Geophys. Res.*, *74*, 6706–6709, 1969.

Ewing, J. I., and G. M. Purdy, Upper crustal velocity structure in the ROSE area of the East Pacific Rise, *J. Geophys. Res.*, this issue.

Filloux, J. H., Magnetotelluric experiment over the ROSE area, *J. Geophys. Res.*, this issue.

Fitch, T. J., and J. M. W. Rynn, Inversion for V_P/V_S in shallow source regions, *Geophys. J. R. Astron. Soc.*, *44*, 253–267, 1976.

Forsyth, D. W., The earth structural evolution and anisotropy of the oceanic upper mantle, *Geophys. J. R. Astron. Soc.*, *43*, 103–162, 1975.

Frohlich, C., S. Billington, and E. R. Engdahl, Final results from the OBS experiments in the central Aleutians in 1978 (abstract), *Eos Trans. AGU*, *62*(17), 335, 1981.

Fuchs, K., and G. Muller, Computation of synthetic seismograms with the reflectivity method and comparison with observations, *Geophys. J. R. Astron. Soc.*, *23*, 417–433, 1971.

Furukawa, K., J. F. Gettrust, and W. C. Kempner, Variation in young oceanic crustal structure with age: Preliminary report on the ROSE seismic refraction data, *J. Geophys. Res.*, this issue.

Garmany, J. D., Anisotropic gradients in the upper mantle, *Geophys. Res. Lett.*, in press, 1981.

Garmany, J., Amplitude constraints in linear inversions of seismic data, *J. Geophys. Res.*, this issue.

Gettrust, J. F., R. P. Meyer, and L. C. Ocola, Crustal structure in the western-central cordillera region of southern Colombia, paper presented at the meeting of the Int. Assoc. of Seismol. and Phys. of the Earth Interior, Lima, Peru, Aug. 20–31, 1973.

Gettrust, J. F., V. Hsu, C. E. Helsley, E. Herrero, and T. Jordan, Patterns of local seismicity preceding the Petatlan earthquake of 14 March 1979, *Bull. Seismol. Soc. Am.*, *71*(3), 761–770, 1981.

Granet, M., and P. H. Trong, Some medium properties at Friuli (Italy) from amplitude spectrum analysis: A possible change in time or in space, *Tectonophysics*, *68*, 167–182, 1980.

Grow, J. A., and R. G. Markl, IPOD-USGS multichannel seismic reflection profile from Cape Hatteras to the Mid-Atlantic Ridge, *Geology*, *5*, 625–630, 1977.

Hales, A., C. E. Helsley, and J. Nation, *P* travel times for an oceanic path, *J. Geophys. Res.*, *75*(35), 7362–7381, 1970.

Hart, R. S., and F. Press, S_n velocities and the composition of the lithosphere in the regionalized Atlantic, *J. Geophys. Res.*, *78*, 407–411, 1973.

Hedgal, J. S., and J. D. Garmany, Observations of the fine structure of caustics, *J. Geophys. Res.*, this issue.

Helmberger, D. V., The crust-mantle transition in the Bering Sea, *Bull. Seismol. Soc. Am.*, *58*, 179–214, 1968.

Helsley, C. E., J. B. Nation, and R. P. Meyer, Seismic refraction observations in southern Mexico (abstract), *Eos Trans. AGU*, *56*, 452, 1975.

Herron, T. J., W. J. Ludwig, P. L. Stoffa, T. K. Kan, and P. Buhl, Structure of the East Pacific Rise crest from multichannel seismic reflection data, *J. Geophys. Res.*, *83*, 798–804, 1978.

House, L., and J. Boatwright, Investigation of two high-stress-drop earthquakes in the Shumagin seismic gap, Alaska, *J. Geophys. Res.*, *85*(B12), 7151–7165, 1980.

Houtz, R., Interval velocities in crustal layers from sonobuoy records of mantle reflections, *J. Geophys. Res.*, *82*, 5385–5400, 1977.

Houtz, R., and J. Ewing, Upper crustal structure as a function of plate age, *J. Geophys. Res.*, *81*, 2490–2498, 1976.

Hsu, V., J. F. Gettrust, and C. E. Helsley, Filling of a seismic gap: Local seismicity preceding the March 14, 1979, Petatlan earthquake, *J. Geophys. Res.*, this issue.

Karl, J. H., and D. G. Kilday, Continental shelf magnetic linea-

ments of Magdalena Bay, Baja California, *J. Geophys. Res.*, this issue.
Kelleher, J., L. Sykes, and J. Oliver, Possible criteria for predicting earthquake locations and their application to major plate boundaries of the Pacific and Caribbean, *J. Geophys. Res.*, *78*, 2548–2585, 1973.
Kempner, W. C., and J. F. Gettrust, Ophiolites, synthetic seismograms, and ocean crustal structure, 1, Comparison of OBS data and synthetic seismograms for the Bay of Islands ophiolite, *J. Geophys. Res.*, this issue, *a*.
Kempner, W. C., and J. F. Gettrust, Ophiolites, synthetic seismograms, and ocean crustal structure, 2, A comparison of synthetic seismograms of the Samail ophiolite, Oman, and the ROSE refraction data from the East Pacific Rise, *J. Geophys. Res.*, this issue, *b*.
Kennett, B. L. N., Towards a more detailed seismic picture of the oceanic crust and mantle, *Mar. Geophys. Res.*, *3*, 7–42, 1977.
Klitgord, K. D., and J. Mammerickx, Northern East Pacific Rise: Magnetic anomaly and bathymetric framework, *J. Geophys. Res.*, *87*, 6725–6750, 1982.
LaTraille, S. L., J. F. Gettrust, and C. E. Helsley, The ROSE seismic data archive system, *J. Geophys. Res.*, this issue.
Leeds, A. R., L. Knopoff, and E. G. Kausel, Variation of upper mantle structure under the Pacific Ocean, *Science*, *186*, 141–143, 1974.
Lewis, B. T. R., Evolution of ocean crust seismic velocities, *Annu. Rev. Earth Planet. Sci.*, *6*, 377–404, 1978.
Lewis, B. T. R., Constraints on the structure of the East Pacific Rise from gravity, *J. Geophys. Res.*, this issue.
Lewis, B. T. R., and J. D. Garmany, Constraints on the structure of the East Pacific Rise from seismic refraction data, *J. Geophys. Res.*, this issue.
Lewis, B. T. R., and W. E. Snydsman, Evidence for a low velocity layer at the base of the oceanic crust, *Nature*, *266*, 340–344, 1977.
Luetgert, J. H., and R. P. Meyer, Seismic refraction observations across the continental leading edge in southern Peru (abstract), *Eos Trans. AGU*, *59*(4), 332, 1978.
Mammerickx, J., and K. D. Klitgord, East Pacific Rise: Evolution from 25 m.y. B.P. to the present, *J. Geophys. Res.*, *87*, 6751–6759, 1982.
Matumoto, T., M. Ohtake, G. Latham, and J. Umana, Crustal structure in southern Central America, *Bull. Seismol. Soc. Am.*, *67*(1), 121–134, 1977.
McCann, W., S. P. Nishenko, L. R. Sykes, and J. Krause, Seismic gaps and plate tectonics: Seismic potential for major boundaries, *U.S. Geol. Surv. Open File Rep.*, *78-943*, 1978.
McClain, J. S., and B. T. R. Lewis, A seismic experiment at the axis of the East Pacific Rise, *Mar. Geol.*, *35*, 147–169, 1980.
McClain, K. J., and B. T. R. Lewis, Geophysical evidence for the absence of a crustal magma chamber under the northern Juan de Fuca Ridge, a contrast with ROSE results, *J. Geophys. Res.*, this issue.
Meissner, R. O., E. R. Flüeh, F. Stibane, and E. Berg, Dynamics of the active plate boundary in south west Colombia according to recent geophysical measurements, *Tectonophysics*, *35*, 115–136, 1976.
Meli, R., Evaluacion de los efectos del sismo del 14 de Marzo 1979 en las edificaciones del Distrito Federal, Prelim. Rep., Inst. de Ingenieria, Univ. Nac. Autónoma de México, May 7, 1979.
Meyer, R. P., W. D. Mooney, A. L. Hales, C. E. Helsley, G. P. Woollard, C. M. Hussong, L. M. Kroenke, and J. E. Ramirez, Project Narino III: Refraction observations across a leading edge, Malpelo Island to the Colombian Cordillera Occidental, in *Geophysics of the Pacific Ocean Basin and Its Margin*, *Geophys. Monogr. Ser.*, vol. 19, edited by G. H. Sutton, M. H. Manghnani, and R. Moberly, pp. 105–132, AGU, Washington, D. C., 1976.
Meyer, R. P., W. D. Pennington, L. A. Powell, W. L. Unger, M. Guzman, J. Havskov, S. K. Singh, C. Valdes, and J. Yamamoto, A first report on the Petatlan, Guerrero, Mexico, earthquake of 14 March 1979, *Geophys. Res. Lett.*, *7*(1) 97–100, 1980.
Molnar, P., Fault plane solutions of earthquakes and direction of motion in the Gulf of California and on the Rivera Fracture Zone, *Geol. Soc. Am. Bull.*, *84*, 1651–1658, 1973.
Mooney, W. D., R. P. Meyer, C. E. Helsley, C. Lomnitz, and B. T. R. Lewis, Refracted waves across a leading edge: Observations of Pacific shots in southern Mexico (abstract), *Eos Trans. AGU*, *56*, 452, 1975.
Ocola, L. C., J. F. Gettrust, R. P. Meyer, and G. P. Woolard, Seismic energy transmission from ocean to continent in western South America, *Geophys. Res. Lett.*, *2*(6), 361–364, 1975.
Orcutt, J. A., B. L. N. Kennett, and L. M. Dorman, Structure of the East Pacific Rise from an ocean bottom seismometer survey, *Geophys. J. R. Astron. Soc.*, *45*, 305–320, 1976.
Ouchi, T., A.-B. K. Ibrahim, and G. V. Latham, Seismicity and crustal structure in the Orozco Fracture Zone: Project ROSE phase 2, *J. Geophys. Res.*, this issue.
Parker, R. L., and D. W. Oldenburg, Thermal model of ocean ridges, *Nature*, *242*, 137–139, 1973.
Phillips, R. P., Seismic refraction studies in Gulf of California, in *Marine Geology of the Gulf of California*, edited by T. H. van Andel and G. G. Shor, pp. 90–121, American Association of Petroleum Geologists, Tulsa, Okla., 1964.
Project ROSE scientists, Microearthquake activity on the Orozco Fracture Zone: Preliminary results from Project ROSE, *J. Geophys. Res.*, *86*, 3783–3790, 1981.
Prothero, W. A., Jr., and I. D. Reid, Some microearthquake results from the East Pacific Rise at 21°N and the Rivera Fracture Zone, *J. Geophys. Res.*, this issue.
Prothero, W. A., I. Reid, M. S. Reichle, and J. N. Brune, Ocean bottom seismic measurements on the East Pacific Rise and Rivera Fracture Zone, *Nature*, *262*, 121–124, 1976.
Purdy, G. M., The correction for the travel time effects of seafloor topography in the interpretation of marine seismic data, *J. Geophys. Res.*, this issue, *a*.
Purdy, G. M., The variability in seismic structure of layer 2 near the East Pacific Rise at 12°N, *J. Geophys. Res.*, this issue, *b*.
Raitt, R. W., G. G. Shor, G. M. Morris, and H. K. Kirk, Mantle anisotropy in the Pacific Ocean, *Tectonophysics*, *12*, 173–186, 1971.
Reid, I., and W. A. Prothero, An earthquake sequence studied with ocean bottom seismographs, *Geophys. J. R. Astron. Soc.*, *64*, 381–391, 1981.
Reid, I., J. A. Orcutt, and W. A. Prothero, Seismic evidence for a narrow zone of partial melting underlying the East Pacific Rise at 21°N, *Geol. Soc. Am. Bull.*, *88*, 678–682, 1977.
Shibuya, K., Attenuation of seismic waves in the aftershock region—A case of the Off-Izu Peninsula earthquake of 1974, *J. Phys. Earth*, *27*, 141–170, 1979.
Stephen, R. A., K. E. Louden, and D. H. Matthews, The oblique seismic experiment on DSDP leg 52, in *Initial Reports of the Deep Sea Drilling Project*, Legs 51, 52, and 53, Part 1, edited by T. Donnelly et al., pp. 675–704, U.S. Government Printing Office, Washington, D. C., 1979.
Stoffa, P. L., and P. Buhl, Two-ship multichannel seismic experiments for deep crustal studies: Expanded spread and constant offset profiles, *J. Geophys. Res.*, *84*, 7645–7660, 1979.
Sutton, G. H., B. T. R. Lewis, J. Ewing, F. K. Duennebier, B. Iwatake, J. D. Tuthill, et al., Lopez Island ocean bottom seismometer intercomparison experiment, *Tech. Rep. HIG-80-4*, Ha. Inst. of Geophys., Honolulu, 1980.
Sykes, L. R., Mechanism of earthquakes and nature of faulting on the mid-oceanic ridges, *J. Geophys. Res.*, *72*, 2131–2153, 1967.
Sykes, L. R., Focal mechanism solutions for earthquakes along the world rift system, *Bull. Seismol. Soc. Am.*, *60*, 1749–1752, 1970.
Takemura, M., T. Masuda, K. Goto, A. Ito, and H. Hamaguchi, Spectral analysis of aftershocks of the 1978 Miyagiken-oki earthquake, *Sci. Rep. Tohoku Univ. Ser. 5*, *26*(3–5), 101–110, 1980.
Tsai, Y. B., Determination of focal depths of earthquakes in mid-oceanic ridges from amplitude spectra of surface waves, Ph.D. thesis, 144 pp., Mass. Inst. of Technol., Cambridge, 1969.
Valdes, C., R. Meyer, R. Zuniga, J. Havskov, and K. Singh, Analysis of Petatlan aftershock having coda lengths greater than 60 seconds, *J. Geophys. Res.*, this issue.
Wadati, K., Shallow and deep earthquakes, *Geophys. Mag.*, *5*, 231–283, 1931.
Whitmarsh, R. B., Seismic refraction studies of the upper igneous crust in the North Atlantic and porosity estimates for layer 2, *Earth Planet. Sci. Lett.*, *37*, 451–464, 1978.
Yoshii, T., Regionality of group velocities of Rayleigh waves in the Pacific and the thickening of the plate, *Earth Planet. Sci. Lett.*, *25*, 305–312, 1975.

(Received May 11, 1981;
revised November 6, 1981;
accepted December 4, 1981.)

Geophys. J. R. astr. Soc. (1976) **45**, 305–320.

Structure of the East Pacific Rise from an Ocean Bottom Seismometer Survey

John A. Orcutt and Brian L. N. Kennett*

Institute of Geophysics and Planetary Physics, Scripps Institution of Oceanography, La Jolla, California 92093, USA

LeRoy M. Dorman

Geological Research Division, Scripps Institution of Oceanography, La Jolla, California 92093, USA

(Received 1975 December 2; in original form 1975 September 2)

Summary

Three seismic refraction profiles have been recorded on the East Pacific Rise near the Siqueiros fracture zone. These profiles have been interpreted using both travel-time analysis and waveform and amplitude studies with the aid of synthetic seismograms.

For the profile at the Rise Crest a pronounced low velocity zone has been found at about 2 km below the seabed. The *P*-wave velocities increase quite rapidly from about 5 km s^{-1} at the sea floor to 6·7 km s^{-1} at the lid of the low velocity zone. Mantle arrivals from below this zone indicate a low *P*-wave velocity of 7·7 km s^{-1}. A second profile, on 2·9 My old crust shows a shallow region of strong velocity gradients which grades into velocities typical of the 'oceanic' layer without any clear stratification. The mantle velocity is again low at 7·6 km s^{-1}. The third profile situated on 5 My old crust, shows more distinct layering but velocity gradients exist within the stratification. The velocities here are more typical for Pacific refraction profiles and we have a mantle velocity of 8 km s^{-1}.

The results show that radical changes occur in the structure of the oceanic crust within a few million years in this region and that stratification becomes more pronounced with age.

The most rapid change in seismic velocity with age appears to occur in the top 2 km of the structure and the low velocity zone is certainly absent for crustal ages greater than 1·5 My.

1. Introduction

During the past decade a considerable number of refraction surveys have been conducted at, or near, the crest of the Mid-Atlantic Ridge (Talwani, Windisch & Langseth 1971; Keen & Tramontini 1970; Whitmarsh 1973; Fowler & Matthews 1974; Poehls 1974). This slow-spreading ridge has extremely rough topography with a well-developed axial trough. The ambiguity of the position of the receiver when using

* Present address: Department of Geodesy and Geophysics, Cambridge University, Cambridge CB3 0EZ.

drifting surface sensors, and the presence of the median valley walls when conducting an axial survey present significant problems in interpretation.

Comparatively few profiles have been carried out on the crest of the East Pacific Rise (Shor, Menard & Raitt 1970; Snydsman, McClain & Lewis 1974). Here the spreading rate is much faster, there is no axial trough and the topography is attenuated, which hopefully implies that the subsurface structure is more amenable to interpretation in terms of a laterally homogeneous model.

Le Pichon, Francheteau & Bonnin (1973) have summarized the seismic evidence on the development of the oceanic crust. They conclude that the thickness of layer 2 varies between 1 and 2 km and its seismic *P*-wave velocity is highly variable between 4 and 6 km s^{-1}. No systematic changes in thickness or velocity were found to be related to the spreading rate. The thickness of the oceanic layer appears to increase with age from about 3 to 5 km or more, and the *P*-wave velocity in this layer at a slow-spreading ridge crest is probably low. The *P*-velocity in the mantle near the rise crest for fast and slow rates of spreading appears to be universally low, 7·6 km s^{-1} rather than the 'normal' 8·1 km s^{-1} observed in the ocean basins.

Seismic work conducted since Le Pichon *et al.*'s summary has generally tended to substantiate their outline. In one case (Whitmarsh 1973) a profile in the median valley of the Mid-Atlantic Ridge yielded a mantle *P*-wave velocity of 8·16 km s^{-1}. This

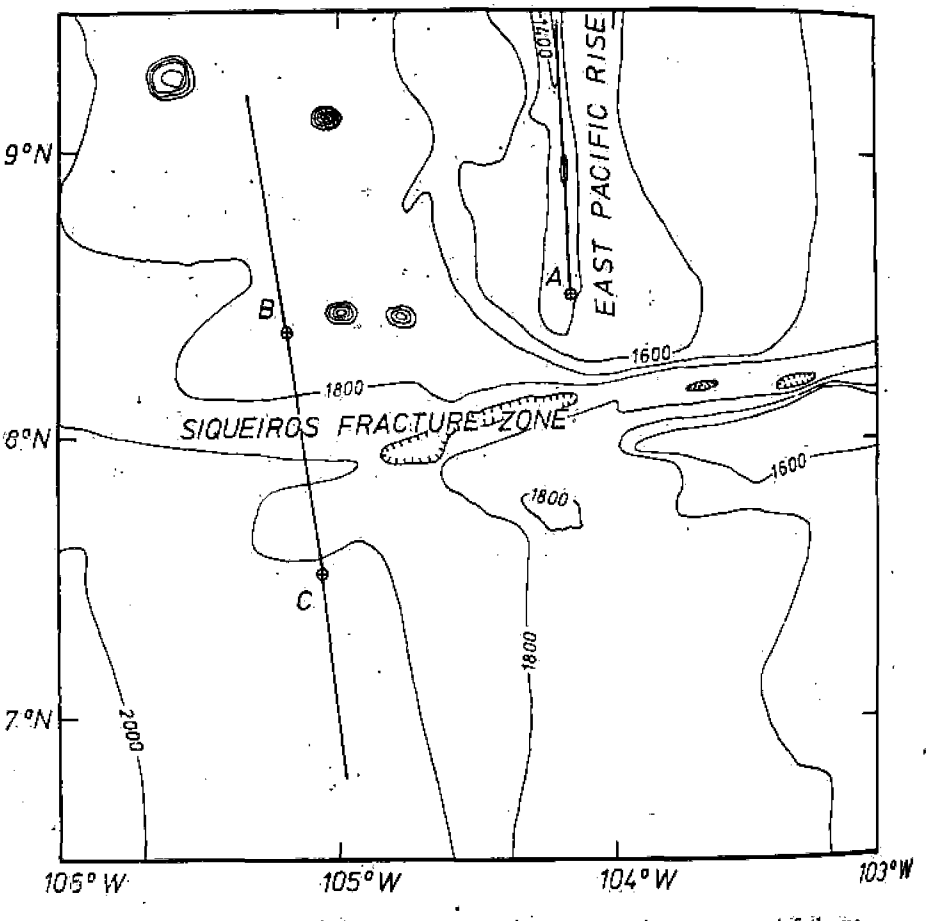

FIG. 1. Bathymetry of the survey area with contours in uncorrected fathoms. The crosses indicate the location of the OBS and the solid lines the seismic refraction profiles.

profile, however, crossed a fracture zone thus creating the possibility that the observed phase velocity is contaminated by the presence of the fracture zone. Poehls (1974), using surface sonobuoys, found a mantle velocity in excess of 8 km s^{-1} but acknowledged that the solution might be suspect because of the poor quality of mantle arrivals.

Since previous refraction results have shown considerable variability we designed our field experiments to attempt to maximize the systematic effects of ageing whilst minimizing the effects of other variables such as spreading rate, azimuth and position along the spreading centre. We have, therefore, chosen to concentrate our attention on the vicinity of the spreading centre in the hope that the effects of ageing which change as $t^{\frac{1}{2}}$ (Parker & Oldenburg 1974) will dominate those processes in which we have less interest. By shooting our profiles, parallel to the isochrons we reduce the effects of anisotropy (Raitt *et al.* 1971) and aim to minimize the lateral variation along the profiles.

During June and July 1974, a seismic refraction and gravity survey of the East Pacific Rise near the Siqueiros Fracture Zone was carried out by Scripps Institution of Oceanography in association with the Hawaii Institute of Geophysics. We discuss here the data taken on three long refraction profiles recorded on digital ocean bottom seismometers. (OBS). The location of these profiles is shown on Fig. 1. In addition to obtaining refraction profiles at several ages we wished to record long gravity profiles across a fracture zone for use in the analysis of the gravity edge effect (Dorman 1975), which should indicate the evolution of the density structure of the lithosphere. The experiment was centred about the two long lines shown in Fig. 1. The eastern line (A) is aligned with the rise crest and thus crosses the Siqueiros fracture zone at the point of maximum topographic relief giving the maximal, though not necessarily the most interpretable, edge effect. The western long line, comprising profiles B and C, crosses the fracture zone at the 2·9–5 My boundary. Our refraction results from this line indicate that the fracture zone can be quite well modelled as a sharp discontinuity.

For each of the three refraction profiles A, B and C we have used both travel-time analysis and matching of amplitudes and waveforms using synthetic seismogram calculations to deduce velocity models compatible with the observations.

2. Conduct of the experiment

The OBS which we used in this study contained a vertical, 1-s natural period Ranger seismometer (Prothero 1974), the output of which was digitized at 128 samples s^{-1} after passing through an aliasing filter. The OBS recording system was turned on at preprogrammed intervals to record ground and water-borne waves from an explosive charge set by the shooting ship, R/V *Thomas Washington*.

The charge sizes used varied from 0·45 to 436 kg of TOVEX explosive. The charges were fired by slow-burning fuse timed to explode the shot at optimum depth to obtain constructive interference between the first bubble pulse and the surface reflected initial pulse. The shot time was recorded on the ship using a towed hydrophone streamer and the time was subsequently corrected for the shot-to-ship travel time.

The shot range was determined by the time interval between shot time and the water-borne wave arrival times. Generally, the arrival of the direct water-borne wave and two waves multiply reflected from the bottom and surface prior to reaching the OBS could be seen on the records. These times were converted to horizontal distance by tracing acoustic rays through a vertically inhomogeneous ocean. The velocity structure of the upper 450 m of water was determined from bathythermograph deployments every 6 hr. This velocity structure was coupled to a deeper, more stable, velocity profile obtained by a hydrocast obtained on the August 1952 Scripps Shellback Expedition. The acoustic velocity at the ocean bottom in the relatively shallow water atop the East Pacific Rise was lower than the surface velocity so that the direct water

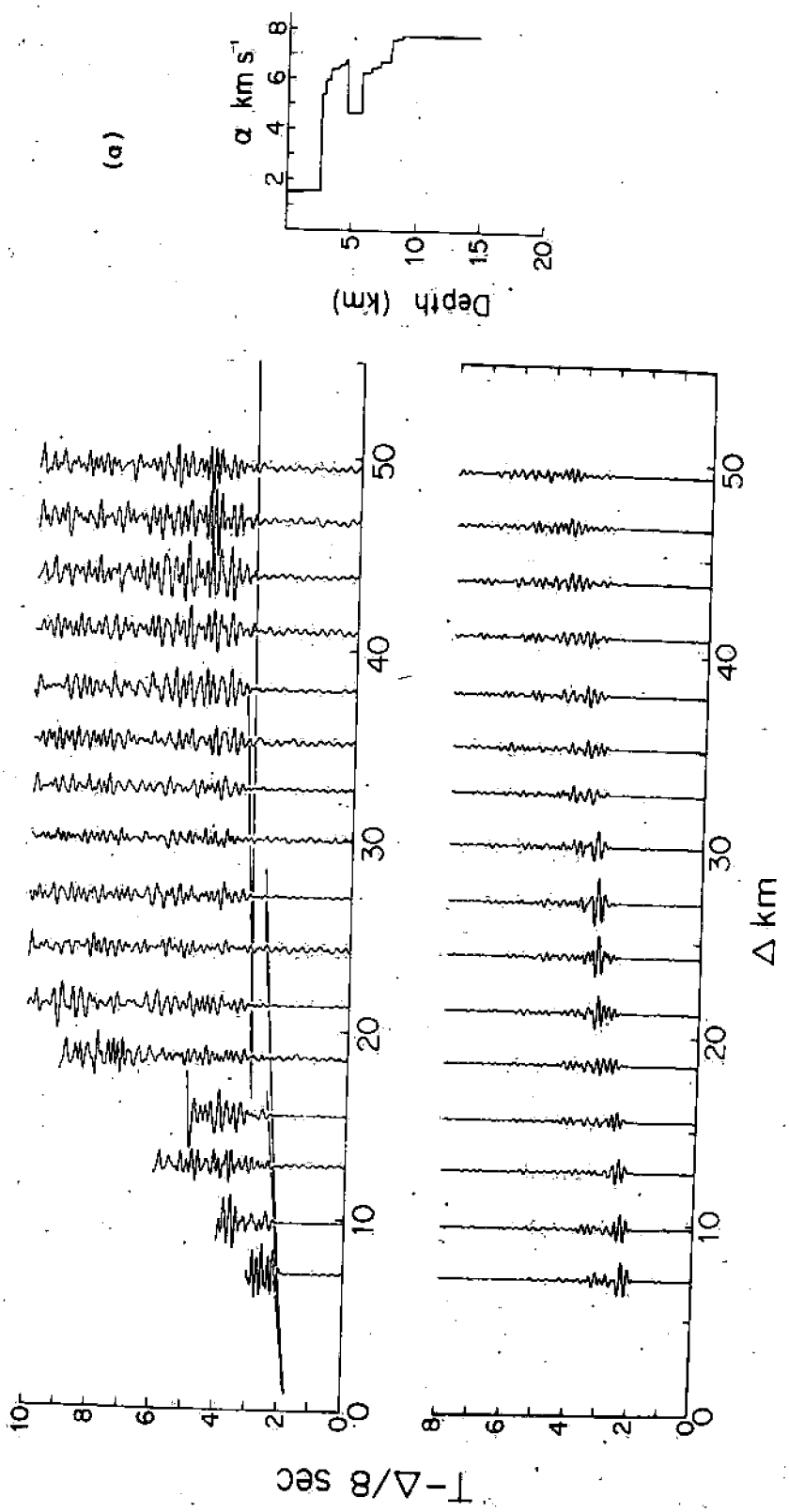

Fig. 2(a)

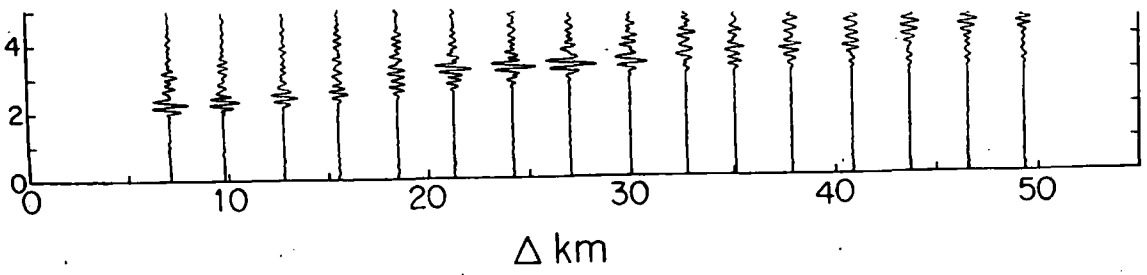

FIG. 2(a)

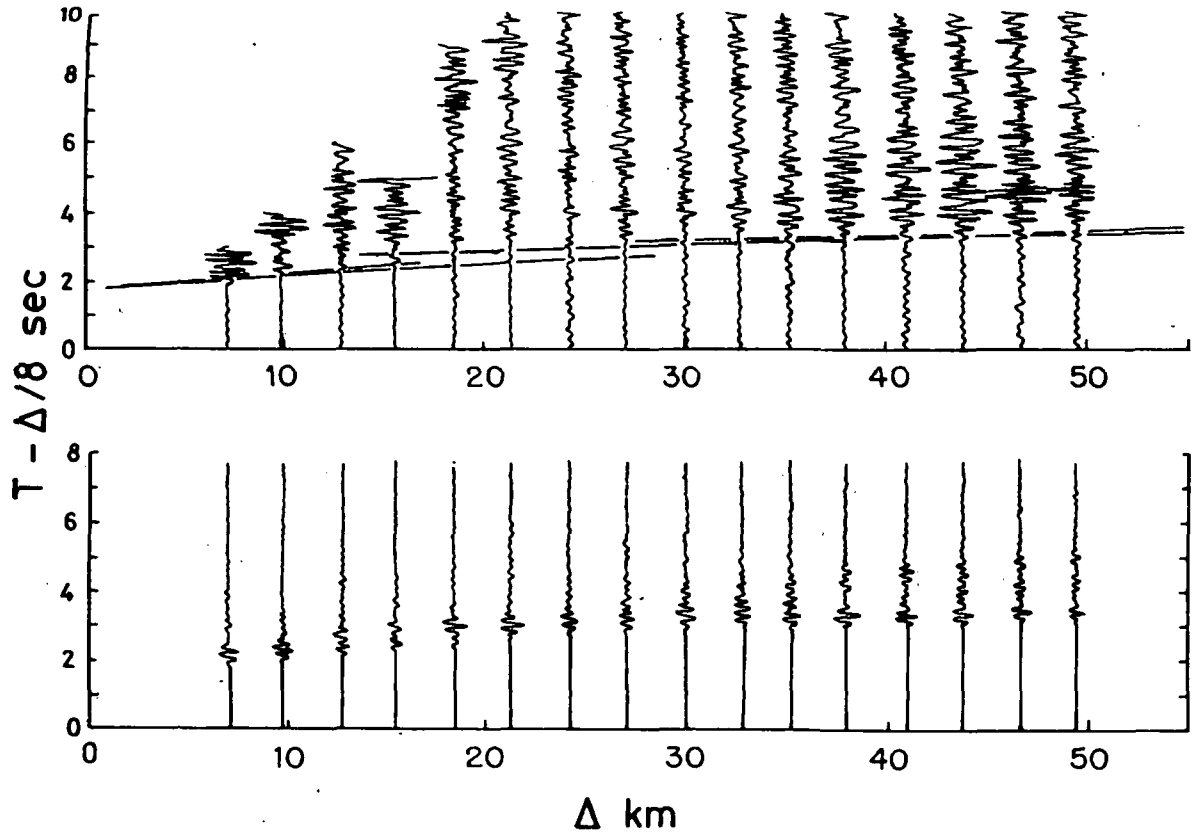

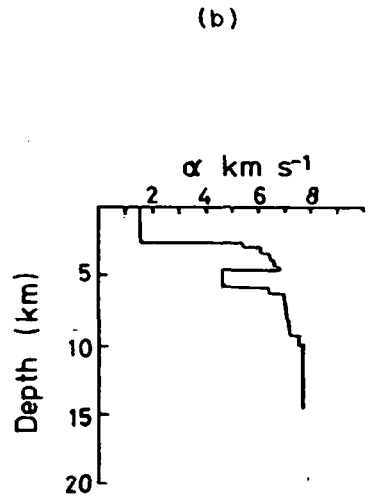

FIG. 2 (a) and (b). The ridge crest profile composite record sections. In (a) and (b), the upper section shows the filtered observed records (1–9 Hz) with the travel-time curve for the model superimposed. The lower section shows the synthetic seismograms for the *P* wave velocity model shown at the right-hand side.

wave reached the OBS in all cases. However, the component of longitudinal acoustic wave motion in the direction of the OBS vertical seismometer decreases with distance causing a diminution of the direct wave amplitude. At large ranges it was necessary to use the travel times for the two observed bounce modes. The distances calculated by ray tracing were checked for consistency against the ranges obtained from the navigation positions calculated by a computer controlled satellite navigation system. The OBS locations were determined by echo ranging to acoustic transponders on each OBS. The maximum difference between the two sets of calculated ranges was less than 450 m.

The observed record sections for the three profiles are shown in Figs 2, 3 and 4. The observed amplitudes on all the profiles have been corrected to a single shot size by applying an empirical scaling factor to each record. We have scaled the amplitude by $(W_0/W)^{0.65}$, where W is the shot weight and W_0 is the reference weight (O'Brien 1967). Arrival times have been corrected to the OBS depth assuming that the rock layering follows the seabed. Since all shots on the same profile were recorded with the same instrument there is no problem with variability of instrument response.

All the observed seismograms have been passed through a zero phase shift 1–9 Hz digital bandpass filter and all the synthetic seismograms we have calculated in the course of the interpretation have had the same frequency pass band. By looking at only relatively low frequencies we gain significant advantages when we wish to use amplitude and waveform data. We dramatically reduce the effect of small scale inhomogeneities along the profile and are able to improve the correlation between successive records. We do reduce our ability to resolve fine detail, but gain a broad picture of the structure.

The three refraction profiles conducted on oceanic crust of different ages show remarkable diversity in the observed seismograms. Profile A (Fig. 2) conducted at the rise crest along a horsted block about 10 km wide, has fairly complex seisograms with significant late energy. At short ranges we see first arrivals with a velocity around 6 km s^{-1} which may be traced out to nearly 30 km. Beyond this range a first arrival appears with a velocity of about 7·5 km s^{-1}, but with a definite offset in intercept time.

The northern profile B (Fig. 3), situated on 2·9 My old crust, presents very simple seismograms with the main energy concentrated into about 1 s after the first arrival. The records on this profile show a particularly clear reflection from the sea surface at about 8 s reduced time.

The southern profile C (Fig. 4), separated from B by the Siqueiros fracture zone is on somewhat older (5 My) crust. The records on this profile show considerable persistence of energy and there is no longer a clear sea surface reflection. On this profile we see, for the first time, the appearance of an arrival with a velocity in excess of 8 km s^{-1} at ranges from 40 to 85 km with a strong second arrival over the same interval. Examination of 3·5-kHz profiler records shows that the OBS for profile C was sited in a sediment pond, which would lead to enhanced reverberation in the seismograms, while the OBS for profile B was sited on rock.

3. Interpretation techniques

For each of the profiles we have measured travel times of first arrivals and prominent second arrivals from unfiltered records and used this data to construct preliminary laterally homogeneous models satisfying the arrival times.

For profile A the jump in intercept time suggests the presence of a low velocity zone and the relatively dense system of observations allows a detailed travel-time inversion. From the travel-time (t, x) data we construct estimates of the relation between the delay time $\tau(p)$ and the ray parameter p (Kennett 1976), using both the graphical

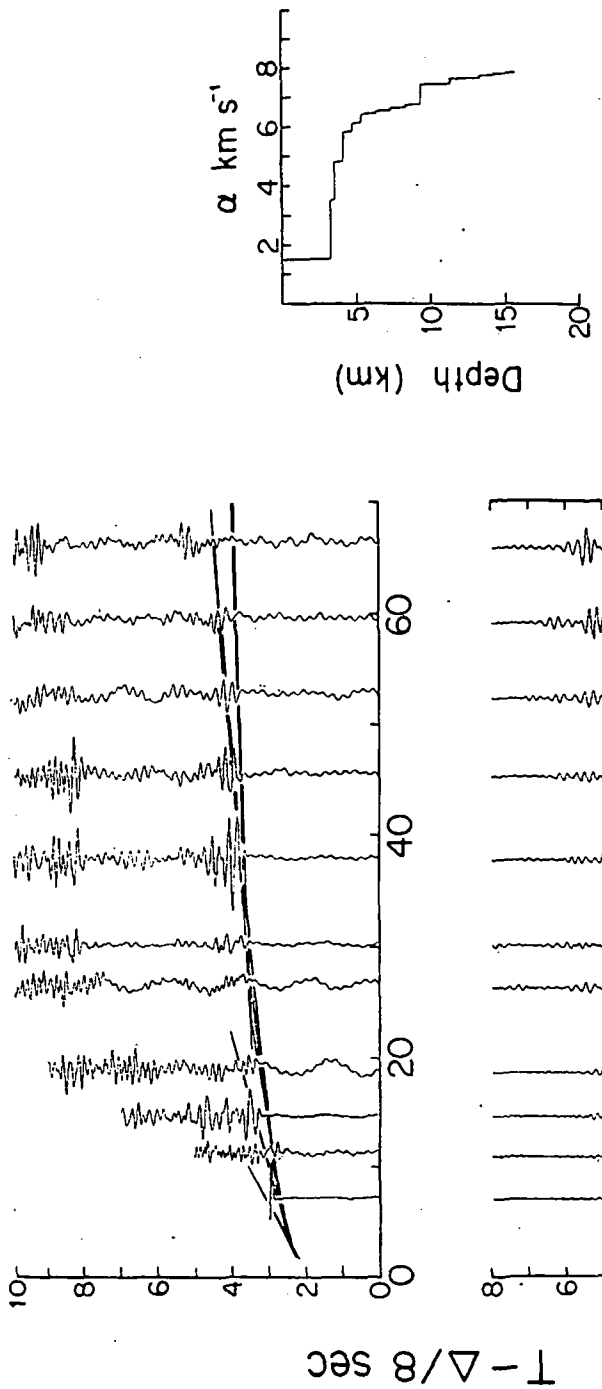

FIG. 3. Composite record section for profile B (2·9 My), the configuration follows Fig. 2.

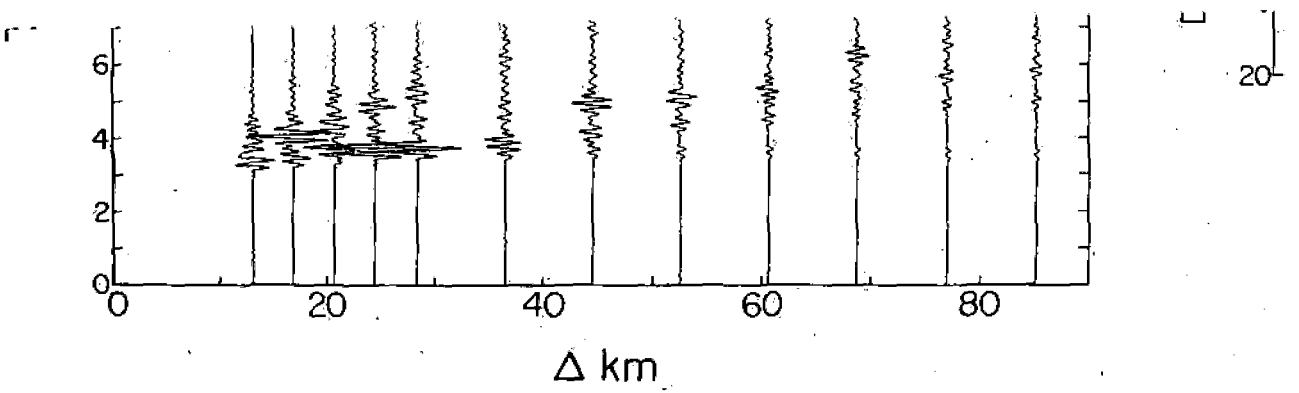

FIG. 4(a). Detailed sections with velocity model.

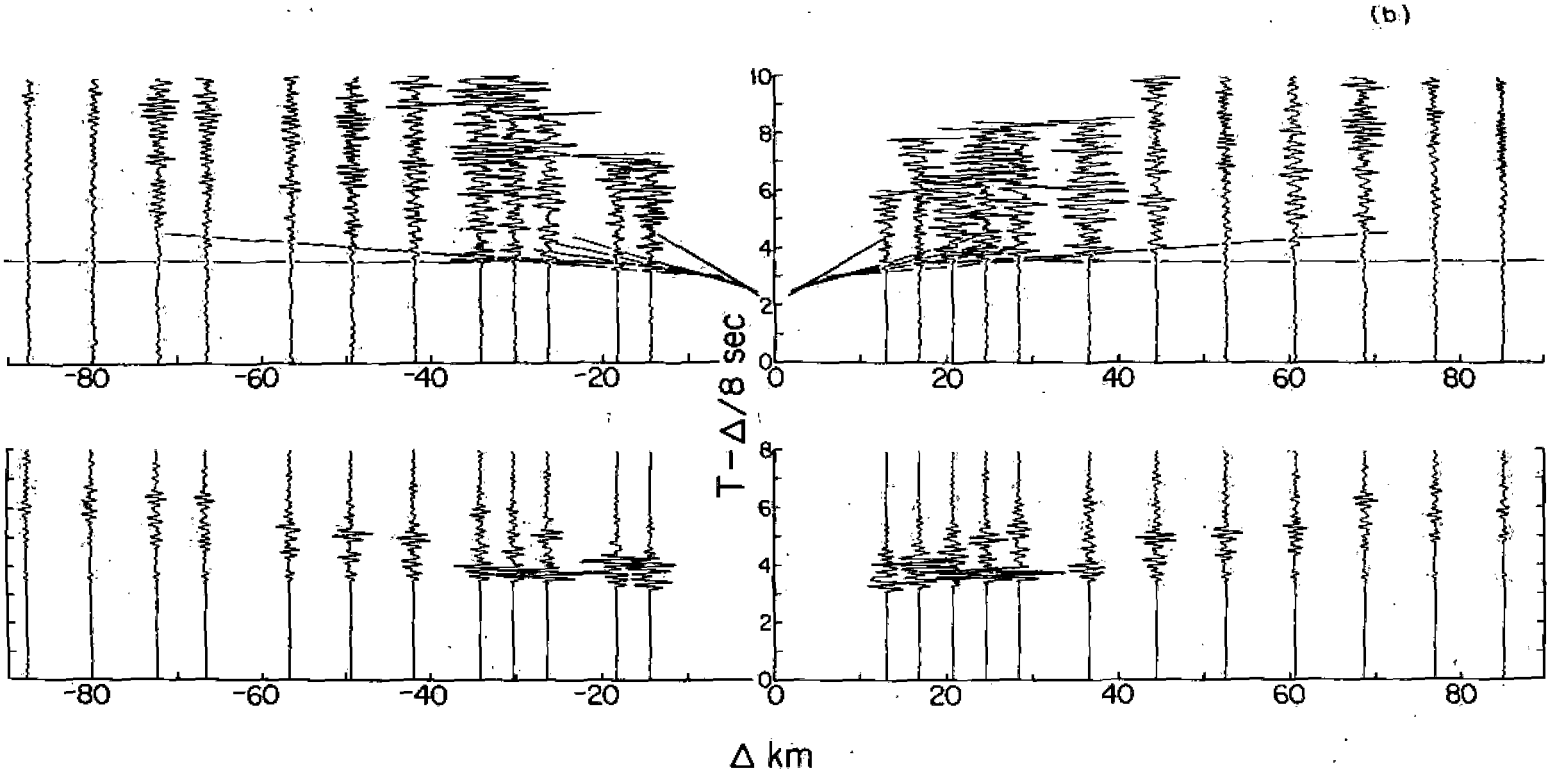

FIG. 4(a) and (b). Composite record section for profile C (5·0 My). (b) Section for the full split profile C illustrating the lateral homogeneity along the profile. The upper section is the filtered observed records and the lower the synthetic seismograms.

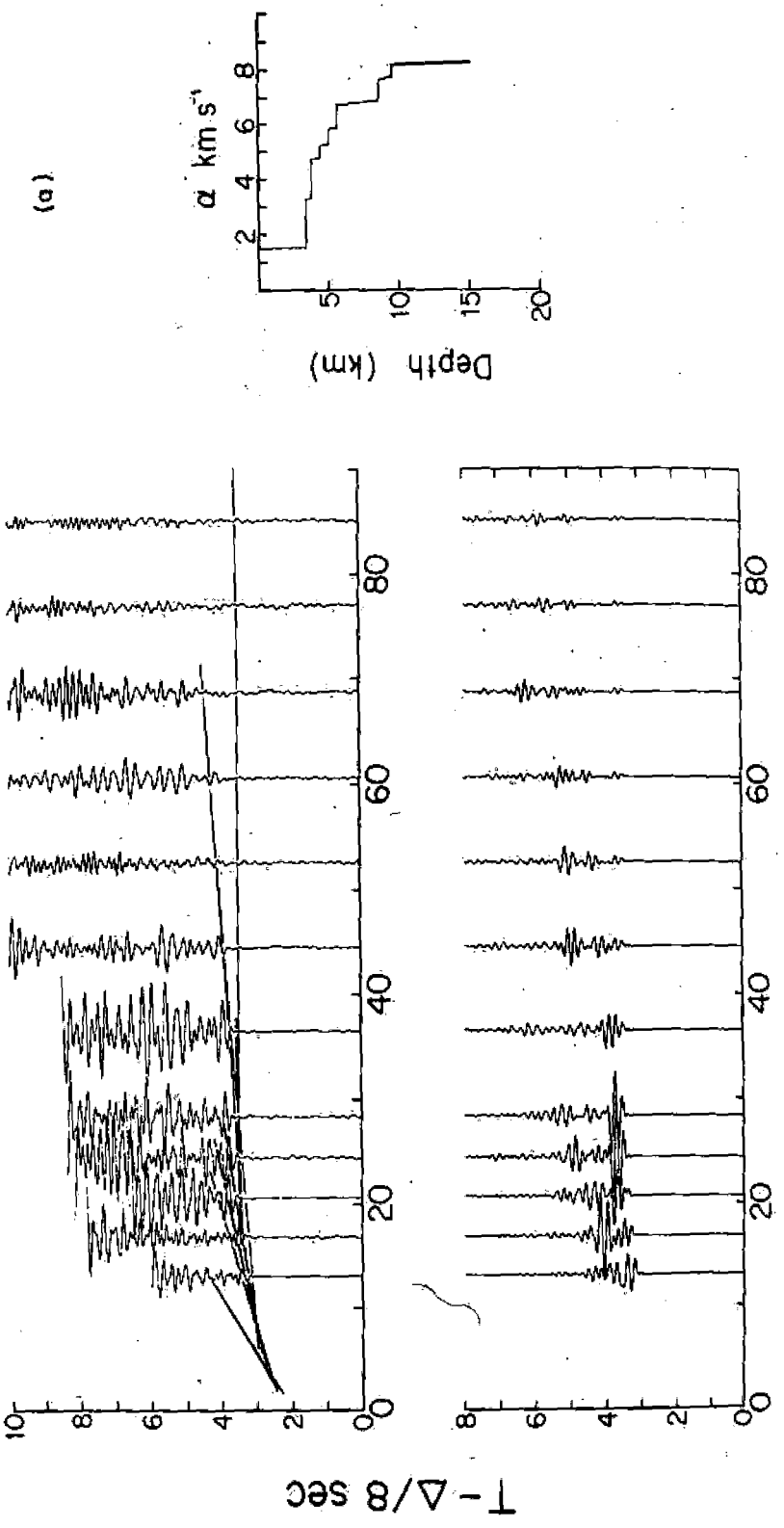

Fig. 4(a). Detailed seismograms with velocity model.

construction technique of Bessonova *et al.* (1974) and by fitting a smoothed spline interpolate (Reinsch 1967).

The ray parameter, p, corresponds to the local slope of the travel-time curve and $\tau(p)$ to the time intercept at zero distance made by a tangent to the travel time with this slope. The advantages of working with the delay time $\tau(p)$ are that it is a monotonically decreasing function of p and exhibits a discontinuity for p equal to the reciprocal of the velocity at the lid of any low velocity zone. As we have previously noted (Orcutt *et al.* 1975), for profile A the τ *vs* p curve has two distinct branches separated by a jump of 0·4 s between the values for phase velocities of 6·70 km s^{-1} and 7·00 km s^{-1} which suggest the probable existence of a low velocity zone with a lid of 6·70 km s^{-1}. Analysis of the sonobuoy records for the same profile gives independent evidence for velocities around 6·7 km s^{-1}.

Bounds on the $\tau(p)$ relation were inverted by the method of Bessonova *et al.* (1974) to yield upper and lower bounds on the depths at which particular velocities could occur outside the low velocity zone. These bounds were used as constraints on the models considered for profile A. In addition we performed a linearized inversion on the $\tau(p)$ data (Kennett 1976). Comparison of velocity structures obtained from different initial models showed that the shallow structure down to 2 km below the seabed was well resolved, and this was incorporated into our preliminary model for this profile.

Once we have found a model which provides a satisfactory fit to the travel times we have calculated synthetic seismograms by the reflectivity method (Fuchs & Müller 1971; Kennett 1975a, b—see also the Appendix) and compared these to the filtered observed records. A successful model should ideally not only match the relative amplitudes of arrivals on the same record but also the pattern of energy distribution with distance. In practice the problems of an inadequate allowance for shot amplitude normalization and particularly the existence of lateral heterogeneities makes detailed matching rather difficult. In all our calculations of synthetic seismograms we have used a simple analytical source function of the type described by Fuchs & Müller (1971).

The amplitudes in the synthetic calculations are most sensitive to the velocity gradients within the model so that the constraints on gradients are better than those on absolute velocity values. As yet no formal inversion scheme for velocity structure has been devised which uses the whole waveform so that we are unable to place confidence limits on our models. However, the comparison of observed and synthetic seismograms does provide an effective discriminant between models and allows an iterative (and hopefully convergent!) procedure for generating a velocity structure for which the synthetic waveforms and travel times are in good agreement with observations.

We have normally based our modelling on determining the P wave velocity distribution (α), have taken the S wave velocity (β), to be given by $\alpha/\beta = 1{\cdot}75$ and determined the density from the Nafe–Drake relation. We have also the possibility of varying the attenuation within the model. We have usually assumed all attenuation arises in shear and used $Q_\alpha = 575$, $Q_\beta = 250$, but have introduced increased attenuation for sediments.

4. Interpretation of the profiles

Composite record sections for the three profiles are shown in Figs 2, 3 and 4 at a reduction velocity of 8 km s^{-1}. For each profile we show the filtered observed records with shot weight normalization and the synthetic seismograms calculated for the model proposed for the profile. For ease of comparison the synthetics are calculated at the same ranges as the observed records and for display purposes an amplitude scaling factor of (Δ/10), where Δ is the range in kilometres, is applied to both observed and synthetic records. On each of the observed profiles we have superimposed the travel-time curves appropriate to our proposed P-wave velocity model which is shown at the side

For profile A, on the ridge crest (Fig. 2(a)), it has proved very difficult to fit both the relatively small amplitudes between 20 and 30 km and the large later arrivals between 40 and 50 km. The model shown in Fig. 2(a) represents the best compromise we have been able to achieve (Orcutt *et al.* 1975). The shallow structure is quite close to that obtained from the linearized travel-time inversions and shows a strong velocity gradient weakening with depth and reaching a velocity of 6·7 km s^{-1} at 2 km below the sea floor. This is underlain by a low velocity channel some 1·4 km thick in which the velocity decreases to around 4·8 km s^{-1}. Below this there is a velocity gradient from 6·2 to 6·8 km s^{-1} and mantle velocities of 7·7 km s^{-1} are reached 6 km below the sea floor. The amplitude of the first arrival from 30 to 50 km decreases too slowly for the transition to the highest velocity to be a discontinuity in velocity but the behaviour can be modelled well with a gradient zone. An improved fit to the observations is achieved by reducing the ratio of S to P wave velocities in the channel and increasing the attenuation to $Q_\beta = 100$.

The fit to the observed seismograms is quite good to 20 km range but the synthetic amplitudes are too large between 20 and 30 km. These amplitudes may be reduced by raising the velocity below the channel to about 7 km s^{-1}, as in Fig. 2(b). This has the effect of reducing velocity contrast at the Moho and thus the amplitude of the Moho reflection. This does, however, strongly reduce the later energy between 40 and 50 km. Increased energy in this latter region can be achieved by introducing a more strongly developed low velocity zone with lower velocities extending to the mantle, but this generates very considerable amplitudes between 20 and 30 km. A comparison of the synthetic seismograms for models in Fig 2(a) and 2(b) indicates the sensitivity of the waveforms to the detailed velocity gradient, particularly within such reverberative structures as low velocity zones.

These results, of course, apply to laterally homogeneous models but they suggest that there is a progression in the structure of the low velocity zone as one moves away from the fracture zone. At relatively short distances there would only be a thin, low velocity channel but as the distance from the OBS, and thus the fracture zone, increases the low velocity zone would become thicker leading to the large, late amplitude. We are unable to check this hypothesis by direct calibration of synthetic seismograms for a laterally heterogeneous model. However, if the shallow crustal structure has a nearly constant delay time we would expect that the sonobuoy results, where multiple coverage gives good lateral control, would show an increase in the delay time to mantle moving away from the fracture zone. This effect is indeed seen (Rosendahl *et al.* 1976) and is too large to be accounted for by crustal thickening. There may thus be slight dip along the profile at the bottom of the low velocity zone with the result that our mantle velocity is probably an underestimate.

As we have already noted, the northern profile B situated on 2·9 My crust, shows a very clear arrival of about 1-s duration on most records (Fig. 3). In order to model these pulses we need to introduce a velocity model for which there are tightly overlapping travel-time branches. This implies the velocity model should have convex upward curvature in the upper layering. The structure which we propose has somewhat similar shallow structure to that seen on profile A. An initially steep velocity gradient weakens with depth until a velocity of 6·5 km s^{-1} is reached at a depth of 2 km below the sea floor. Below this we have a relatively homogeneous region with only a slight velocity increase with depth until the mantle is reached. There is not a very strong Moho reflection which suggests that the contrast at the Moho is not too large. The apparent mantle velocity is here 7·6 km s^{-1} and a slight gradient below the Moho is needed to support the amplitude of the first arrivals. Sonobuoy studies in this region give mantle velocities of 7·7 km s^{-1}.

The agreement between observed and synthetic sections for this profile is good. We have been able to model the change in the character of the records out to 20 km and

particularly the large arrival at 35 km. We have also been reasonably successful in modelling the late energy near 70 km.

The profile C, situated on 5 My old crust, has a very different appearance from the other profiles (Fig. 4(a)). On this section we see for the first time evidence of distinct layering in the structure. We have included a sediment layer which contributes to reverberations in the synthetic records. Our proposed model shows a relatively distinct 'layer 2' but we were unable to characterize this by a single velocity and needed to introduce a gradient to bring the amplitudes into agreement with the observations. Below this we have a weak gradient with a lid velocity of 6·7 km s^{-1}. In order to model the nature of the mantle arrival and the late second arrival beyond 40 km, we need to introduce an intermediate step, before reaching mantle velocities of 8·1 km s^{-1}. This would seem to correspond to the higher velocity layer 3B found in recent sonobuoy studies. This profile is in fact only one side of a split profile and the full section with the superimposed travel-time curves of our model is shown in Fig. 4(b). We see that the record character to the North, closer to the fracture zone is very similar to that for the southern side of the OBS, and that there is no indication of appreciable dips. The synthetic records shown in Fig. (4b) agree very well over the whole profile.

Profiles B and C were separated by the Siqueiros fracture zone, and have quite different crustal ages and also show distinctly different crustal structures. For shots between the two OBSs we find that the character of the seismograms recorded at each OBS is maintained provided the bottoming point of the mantle arrivals is on the same side of the fracture zone as the OBS. Once this point crosses the fracture zone there is a distinct change of character. This suggests that the approximation of considering two laterally homogeneous structures on the two sides of the fracture zone should be quite good.

5. Discussion

In the three profiles we have examined we see a significant change in the structure with age. For both the younger profiles A and B we have no indication of distinct layering—there is a significant non-uniform velocity gradient which is interrupted by a low velocity zone at the ridge crest and which grades into velocities more typical of the 'Oceanic' layer in the 2·9 My profile. Even on profile C at 5 My we have velocity gradients existing within a more distinct stratification. The structure we have proposed for profile C is in quite good agreement with the model suggested by Le Pichon, Francheteau & Bonnin (1973) for crust of that age. The velocity structures for the three profiles we have considered are compared in Fig. 5, where the depth origin has been taken to be the sea floor. It is difficult to estimate confidence limits for these models but except for the details of the velocity distribution within the low velocity zone the tolerance would be about $\pm 0{\cdot}1$ km s^{-1}.

The most rapid changes in velocity structure between the three profiles occur within 2 km below the seabed in the 'volcanic' layer. This region seems to be evolving with age and to be developing a sharper lower boundary. The transition between the crust and mantle, however, is becoming more complex over this age range.

The velocity gradients we have found in the 'volcanic' layer are possibly related to compositional gradients within this region. Deep Sea Drilling Project—Leg XXXVII, conducted at crustal ages ranging from 3·5 to 16·5 My, demonstrated that the volcanic layer is probably composed of basalt flows interlayed with deep sea sediments (Aumento 1975). The relative abundance of inferred sediment contained in the basalt flows decreases with depth until only volcanic rocks are encountered. The formation of the volcanic layer apparently occurs at a cyclic eruption of basalt flows over accumulated sediments. The frequency of the eruptions decreases as the age and hence distance from the axial trough increases. Such behaviour in the genesis

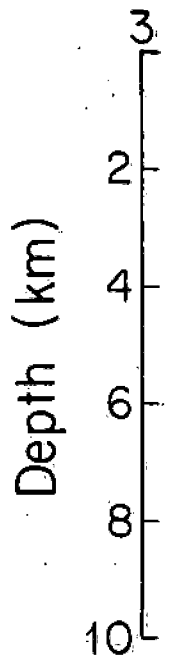

FIG. 5. Comparis

of the volcanic layer w
the structure rather tha
The low velocity z
hypothesized to be a zc
(1973) predicted from
spreading half-rate anc
so $l = 0{\cdot}72$ km. If we
the low velocity zone i
motion, then the lithos
approximately 2 km.
$9{\cdot}4\,t^{\frac{1}{2}} = 16$ km (Parke
represents the structur
5 My the lithosphere w
crust has become a sep
exceeded 8 km s^{-1}.
The presence of a l
studies at a rise crest, i
teleseismic data from t
low Q at the crest acro
1969; Solomon 1973).
lateral velocity gradien
the unusual fault plane
crest. Francis & Porte
depth of about 2·5 km
of observation for micr

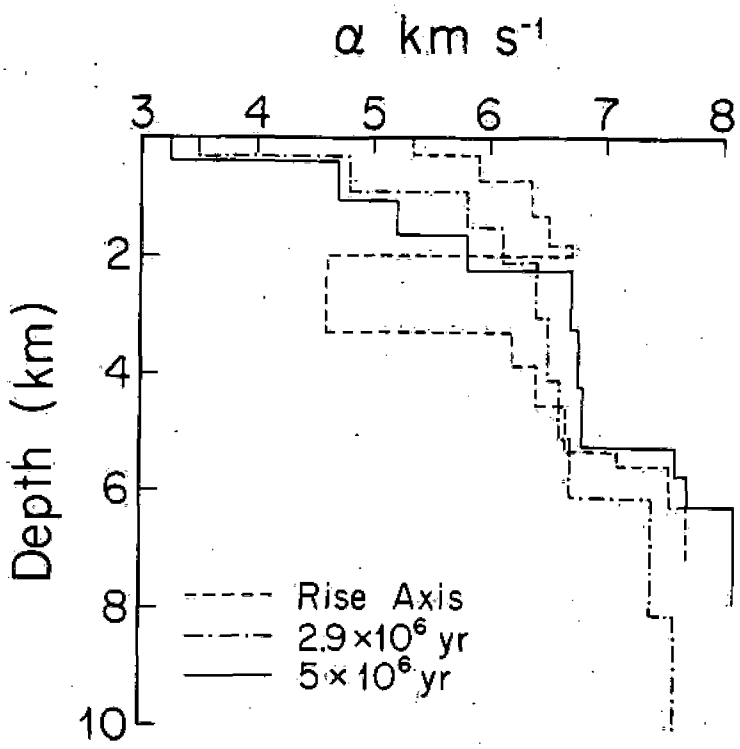

FIG. 5. Comparison of velocity models for the three profiles, the depth origin is taken at the sea floor.

of the volcanic layer would lead to the sort of velocity gradients we have derived for the structure rather than the series of homogeneous layers generally hypothesized.

The low velocity zone underlying the high velocity crust at the rise crest is hypothesized to be a zone of partial melt or a magma chamber. Parker & Oldenburg (1973) predicted from their thermal model that $vl = 43\ m^2\ yr^{-1}$ where v is the spreading half-rate and l the intrusive zone depth. In this case $v = 6 \times 10^{-2}\ m\ yr^{-1}$ so $l = 0{\cdot}72$ km. If we regard this thickness as an order of magnitude estimate and the low velocity zone is regarded as a layer with no enduring resistance to shearing motion, then the lithosphere–asthenosphere boundary occurs at a crustal thickness of approximately 2 km. At an age of 2·9 My the lithosphere would have thickened to $9{\cdot}4t^{\frac{1}{2}} = 16$ km (Parker & Oldenburg 1973). Our model for the intermediate age crust represents the structure of virtually the entire lithosphere at that age. At an age of 5 My the lithosphere would be 21 km thick. The data indicate, at that age, that the crust has become a separate entity within the lithosphere and the mantle velocity has exceeded 8 km s^{-1}.

The presence of a low velocity zone, though not reported in previous refraction studies at a rise crest, is not an unusual or unaccountable result. Seismologists using teleseismic data from the Mid-Atlantic Ridge have hypothesized a localized region of low Q at the crest across which S_n will not propagate (Molnar & Oliver 1969; Francis 1969; Solomon 1973). Solomon & Julian (1974) require a velocity model with high lateral velocity gradients and a degree of partial melting at shallow depths to explain the unusual fault plane solution patterns for normal faulting earthquakes on the rise crest. Francis & Porter (1973) hypothesized the presence of a low velocity zone at a depth of about 2·5 km beneath the crustal surface in order to explain the limited range of observation for microearthquakes with OBSs. Cann (1974) has required the presence

Table 1

Summary of seismic refraction profiles conducted on the Mid-Atlantic Ridge. References are Talwani: (Talwani et al. 1971); Poehls (Poehls 1974); Whitmarsh (Whitmarsh 1974) and Keen/Tramontini (Keen & Tramontini 1970).

Author	Profile	Sediment velocity / thickness	Basement velocity thickness	Oceanic layer / velocity thickness	Mantle velocity	Delay time	Age
Talwani	35		2·33/0·96	4·63/2·31	7·59	1·57	0
Talwani	36		2·79/0·81	4·77/0·81	7·79	1·43	0
Talwani	33	1·52/0·038	3·84/1·81	5·92/2·57	7·40	1·50	1·5 My
Talwani	34		3·57/1·05	4·85/2·20	7·40	1·49	1·5 My
Talwani	26	1·60/0·176	4·05/2·11		7·40	1·09	10 My
Poehls	1a		3·11/1·41	6·34/2·93	8·34	1·44	0
Poehls	2b	1·8/0·24	3·77/0·52	5·66/2·4	7·21	1·02	2·0 My
Whitmarsh mean			2·8/1·00	6·37/4·78	8·16	1·61	0
Keen–Tramontini mean			4·58/1·64	6·62/3·38	8·11	1·18	1·18 1·5–6·5 My

of a shallow magma chamber in developing a petrological model for crustal synthesis.

Table 1 summarizes some of the refraction work conducted on the Mid-Atlantic Ridge and its immediate flanks. Approximate ages of the profiles are listed along with the crustal delay time to mantle. Delay time was computed by integrating the vertical slowness, $\eta = (\alpha(z)^{-2} - \alpha_m^{-2})^{\frac{1}{2}}$ over the crustal depth, equating α_m to the individual investigator's determination of mantle velocity.

The delay time to mantle is the most stable datum resulting from the conduct of a seismic refraction experiment. Generally mantle arrivals occur over large portions of the refraction profile from near 35 km to as far as 120 km and the delay time to mantle calculated by extending a line drawn through the mantle arrivals back to the time axis is an accurate determination. Furthermore, if the Moho is treated as an interface between two homogeneous media, in the conventional manner of data reduction, the delay time to mantle is independent of dip even though the mantle velocity is heavily dependent on dip. Note that throughout Table 1 there is a sudden 0·5 s drop in delay time to the mantle at a crustal age of approximately 1·5 My. Because the delay times possess errors generally no larger than ±0·1 s the 0·5 s drop is highly significant.

Both the results presented here and the previous work conducted on the Mid-Atlantic Ridge confirm that radical change in the nature of the crust occurs in the age range 0–5 My. The increased delay time to the mantle at the rise crest can be obtained in two ways: (1) Increased crustal thickness (3 km of 6·7 km s^{-1} material has a delay of about 0·5 s), or (2) Lower mean crustal velocity. Generally all work conducted has employed the second solution. Other authors have accepted a crust whose velocity is uniformly low but we have introduced a low velocity zone with normal crustal velocities outside the zone. The similarity of the 0·4 s jump in delay time at a velocity of nearly 6·7 km s^{-1} observed in our data to the 0·5 s jump shown in Table 1 suggests that a low velocity zone may have been present in some or all of the Atlantic profiles. Our sonobuoy work on the East Pacific Rise (Rosendahl *et al.* 1976) indicate that here the low velocity zone is probably confined to the region immediately beneath the 10 km or so wide central block.

Acknowledgments

We thank Drs K. Fuchs and G. Müller for furnishing their reflectivity program on which the program used in this paper was based. This work was funded mainly by NSF grant DES 74-11909. Brian Kennett thanks the Lindemann Trust for a fellowship.

References

Aumento, F., 1975. Deep drilling reveals the complexities of oceanic layer 2, *E.O.S.*, **56**, 467.

Bessonova, E. N., Fishman, V. M., Ryaboyi, V. Z. & Sitnikova, G. A., 1974. The tau method for the inversion of travel times—I Deep seismic sounding data, *Geophys. J. R. astr. Soc.*, **36**, 377–398.

Cann, J. R., 1974. A model for oceanic crustal structure developed, *Geophys. J. R. astr. Soc.*, **39**, 169–187.

Dorman, LeRoy M., 1975. The gravitational edge effect, *J. geophys. Res.*, **80**, 2949–2950.

Fowler, C. M. R. & Matthews, D. H., 1974. Seismic refraction experiment on the Mid-Atlantic Ridge in the FAMOUS area, *Nature*, **249**, 752–754.

Francis, T. J. G., 1969. Upper mantle structure along the axis of the Mid-Atlantic Ridge near Iceland, *Geophys. J. R. astr. Soc.*, **17**, 507–520.

Francis, T. J. G. & Porter, I. T., 1973. Median valley seismology: The Mid-Atlantic Ridge near 45° N, *Geophys. J. R. astr. Soc.*, **34**, 279–311.

Fuchs, K. & Müller, G., 1971. Computation of synthetic seismograms with the reflectivity method and comparison with observations, *Geophys. J. R. astr. Soc.*, **23**, 417–433.

Keen, C. & Tramontini, C., 1970. A seismic refraction survey on the Mid-Atlantic Ridge, *Geophys. J. R. astr. Soc.*, **20**, 473–491.

Kennett, B. L. N., 1975a. Theoretical seismogram calculation for laterally varying crustal structures, *Geophys. J. R. astr. Soc.*, **42**, 579–589.

Kennett, B. L. N., 1975b. The effects of attenuation on seismograms, *Bull. seism. Soc. Am.*, **65**, 1600.

Kennett, B. L. N., 1976. A comparison of travel time inversions, *Geophys. J. R. astr Soc.*, **44**, 517–536.

LePichon, X., Francheteau, J. & Bonnin, J., 1973. *Plate tectonics*, Elsevier Scientific Publishing Co., Amsterdam.

Molnar, P. & Oliver, J., 1969. Lateral variations of attenuation in the upper mantle and discontinuities in the lithosphere, *J. geophys. Res.*, **74**, 2648–2682.

O'Brien, P. N. S., 1967. The use of amplitudes in seismic refraction survey, *Seismic refraction prospecting*, 85–118, ed. A. W. Musgrave, Soc. of Exploration Geophysicists, Tulsa, Oklahoma.

Orcutt, J.. Kennett, B., Dorman, L. & Prothero, W., 1975. A low velocity zone underlying a fast-spreading rise crest, *Nature*, **256**, 475–476.

Parker, R. L. & Oldenburg, D. W., 1973. Thermal model of ocean ridges, *Nature*, **242**, 137–139.

Poehls, K. A., 1974. Seismic refraction on the Mid-Atlantic Ridge at 37° N, *J. geophys. Res.*, **79**, 3370–3373.

Prothero, W. A., 1974. A short period ocean bottom seismograph, *Bull. seism. Soc. Am.*, **64**, 1251–1262.

Raitt, R. W., Shor, G. G., Morris, G. B. & Kirk, H. K., 1971. Mantle anisotropy in the Pacific Ocean, *Tectonophysics*, **12**, 173–186.

Reinsch, C. H., 1967. Smoothing by spline functions, *Num. Math.*, **10**, 177–183.

Rosendahl, B., Raitt, R. W., Dorman, L. M. & Bibee, L. D., 1976. Evolution of ocean crust, Part I: A geophysical model of the East Pacific Rise Crest derived from seismic refraction data, *J. geophys Res.* in press.

Shor, Jr., G. G., Menard, H. W. & Raitt, R. W., 1970. Structure of the Pacific basin *The Sea*, Vol. 4, Part II, 3–27, ed. A. E. Maxwell, John Wiley and Sons, New York.

Solomon, S. C., 1973. Shear wave attenuation and melting beneath the Mid-Atlantic Ridge, *J. geophys. Res.*, **78**, 6044–6059.

Solomon, S. C. & Julian, B. R., 1974. Seismic constraints on ocean ridge mantle structure: anomalous fault-plane solutions from first motions, *Geophys. J. R. astr. Soc.*, **38**, 265–285.

Snydsman, W., McClain, J. & Lewis, B., 1974. Seismic refraction results from the Northern Cocos Plate, *E.O.S.*, **56**, 1147.

Talwani, M., Windisch, C. C. & Langseth, M. G., 1971. Reykjanes Ridge Crest: A detailed geophysical study, *J. geophys. Res.*, **76**, 473–517.

Whitmarsh, R. B., 1973. Median valley refraction line, Mid-Atlantic Ridge at 37° N, *Nature*, **246**, 297–298.

Appendix

The Reflectivity Method

We have adapted the reflectivity method (Fuchs & Müller 1971) to calculate synthetic seismograms for vertical component ocean bottom seismometers. The modifications which need to be made parallel those discussed by Kennett (1975a, b).

The essence of the reflectivity technique is to divide a velocity structure into two parts, in the lower part all multiples and interconversions are included whereas ray-tracing is employed in the upper part of the section. For marine crustal profiles it is very convenient to break the layering at the sea floor and to consider the reflection response from the sub-bottom structure.

The synthetic seismograms are computed by Fourier synthesis of a plane wave representation. For a horizontal range between source and receiver r the vertical displacement at an OBS from an explosion in the sea will be given by (*cf.* Fuchs & Müller 1971; Kennett 1975a)

$$W(r, 0, t) = \int_{-\infty}^{\infty} d\omega\, \bar{S}(\omega)\, e^{i\omega t}(\omega^2/\alpha_m^2) \int_{\gamma_1}^{\gamma_2} d\gamma \sin\gamma \cos\gamma\, J_0(\omega r \sin\gamma/\alpha_m) \times R_{pp}(\omega, \gamma)\, T_0(\omega, \gamma)$$

where

α_m = P wave velocity at the sea bed,

$\bar{S}(\omega)$ = source spectrum (including recording effects),

$R_{pp}(\omega, \gamma)$ = reflection coefficient from the sub-bottom structure,

$T_0(\omega, \gamma)$ = overall transmission coefficient to the sea bed from the explosion.

The integration variable is the angle of incidence at the sea bed and the limits are specified by

$$\gamma_{1,2} = \cos^{-1}(\alpha_m/c_{1,2})$$

where c_1 is the largest and c_2 the smallest phase velocity considered.

In the calculations in this paper we have used phase velocity limits of 60·0 km s^{-1} and 4·0 km s^{-1} which corresponds to a relatively narrow cone of rays (<25° from the vertical) propagating downward through the ocean. The sub-bottom velocity structure is represented by a stack of thin layers with uniform properties and its reflection response is calculated by efficient matrix methods so that all multiple reflections within the layers and interconversions of wave type between P and S waves are included. For each layer the P and S wave velocities and density need to be specified and allowance may be made for attenuation in the layering (Kennett 1975b). As noted above we have normally taken the ratio of P to S wave velocities to be 1·75 and determined the density from the Nafe–Drake relations. Our primary input parameters are thus the P wave velocities in each of the layers and their respective thicknesses.